Oxygen in the Universe

G. Stasińska,

N. Prantzos, G. Meynet, S. Simón-Díaz,

C. Chiappini, M. Dessauges-Zavadsky, C. Charbonnel,

H.-G. Ludwig, C. Mendoza, N. Grevesse, M. Arnould,

B. Barbuy, Y. Lebreton, A. Decourchelle, V. Hill, P. Ferrando,

G. Hébrard, F. Durret, M. Katsuma and C.J. Zeippen

November 2011

EDP SCIENCES

Cover Figure

Planetary nebula Abell 39
http://www.noao.edu/image_gallery/html/im0636.html
Credit WIYN/NOAO/NSF
The spiral galaxy UGC 12158
Credit ESA/Hubble & NASA
http://www.spacetelescope.org/images/potw1035a/
Sun
http://sdo.gsfc.nasa.gov/data/rules.php
Courtesy of NASA/SDO and the AIA, EVE, and HMI science teams.

Authors Affiliations

M. Arnould, Institut d'Astronomie et d'Astrophysique, Université Libre de Bruxelles, CP. 226, Campus Plaine, Boulevard du Triomphe, 1050 Brussels, Belgium

B. Barbuy, Universidade de São Paulo - IAG, Rua do Matão 1226, 05508-900 São Paulo, Brazil

C. Charbonnel, Geneva Observatory, University of Geneva, Chemin des Maillettes 51, 1290 Versoix, Switzerland & IRAP, UMR 5572 CNRS, and Université de Toulouse, 14 Av. E. Belin, 31400 Toulouse, France

C. Chiappini, Leibniz-Institut für Astrophysik Potsdam (AIP), An der Sternwarte 16, 14482 Potsdam, Germany

A. Decourchelle, Service d'Astrophysique SAp/IRFU/DSM and Laboratoire AIM, CEA-IRFU/CNRS/Université Paris Diderot, CEA Saclay, L'Orme des Merisiers, Bât. 709, 91191 Gif-sur-Yvette Cedex, France

M. Dessauges-Zavadsky, Geneva Observatory, University of Geneva, Chemin des Maillettes 51, 1290 Versoix, Switzerland

F. Durret, UPMC-CNRS, UMR 7095, Institut d'Astrophysique de Paris, 75014 Paris, France

P. Ferrando, CEA/DSM/IRFU/ Service d'Astrophysique & UMR APC, CEA Saclay, 91191 Gif-sur-Yvette, France

N. Grevesse, Centre Spatial de Liège, Université de Liège, Avenue du Pré Aily, 4031 Angleur-Liège, Belgium and Institut d'Astrophysique et de Géophysique, Université de Liège, Allée du 6 Août, 17, B5C, 4000 Liège, Belgium

G. Hébrard, UPMC-CNRS, UMR 7095, Institut d'Astrophysique de Paris, 75014 Paris, France

V. Hill, Université de Nice Sophia Antipolis, CNRS, Observatoire de la Côte d'Azur, Bd. de l'Observatoire, BP. 4229, 06304 Nice Cedex 4, France

M. Katsuma, Institut d'Astronomie et d'Astrophysique, Université Libre de Bruxelles, CP. 226, Campus Plaine, Boulevard du Triomphe, 1050 Brussels, Belgium

Y. Lebreton, GEPI & UMR CNRS 8111, Observatoire de Paris, 92195 Meudon Cedex, France and Université de Rennes 1, IPR, Bât. 11B, Case 1107, Campus de Beaulieu, 35042 Rennes Cedex, France

H.-G. Ludwig, ZAH, Landessternwarte, Königstuhl 12, 69117 Heidelberg, Germany

C. Mendoza, Centro de Física, Instituto Venezolano de Investigaciones Científicas (IVIC), Apdo. Postal 20632, Caracas 1020A, Venezuela, and Centro Nacional de

Cálculo Científico Universidad de Los Andes (CeCalCULA), Corporación Parque Tecnológico de Mérida, Mérida 5101, Venezuela

G. Meynet, Geneva Observatory, University of Geneva, Chemin des Maillettes 51, 1290 Versoix, Switzerland

N. Prantzos, UPMC-CNRS, UMR 7095, Institut d'Astrophysique de Paris, 75014 Paris, France

S. Simón-Díaz, Instituto de Astrofísica de Canarias, 38200 La Laguna, Tenerife, Spain and Departamento de Astrofísica, Universidad de La Laguna, 38205 La Laguna, Tenerife, Spain

G. Stasińska, LUTH, Observatoire de Paris, CNRS, Université Paris Diderot, 5, Place Jules Janssen, 92190 Meudon, France

C.J. Zeippen, LERMA, Observatoire de Paris, ENS, UPMC, UCP, CNRS, 5, place Jules Janssen, 92190 Meudon, France

List of abbreviations

AGB	asymptotic giant branch
CEL	collisional emission line
DLA	damped lyman alpha system
GRB	gamma-ray burst
IGM	intergalactic medium
IMF	initial mass function
ISM	interstellar medium
LMC	Large Magellanic Cloud
LTE	local thermodynamic equilibrium
MS	main sequence
MW	Milky Way
NLTE	out of local thermodynamic equilibrium
ORL	optical recombination line
QSO	quasar
RGB	red giant branch
SFH	star formation history
SFR	star formation rate
SMC	Small Magellanic Cloud
SN	supernova
SNIa	Type Ia supernova
SNII	Type II supernova
SNR	supernova remnant
SoS	solar system
WR	Wolf-Rayet
ZAMS	zero-age main sequence

NOTATIONS

All the wavelenghts are in Angstroms, unless specified otherwise

Contents

Foreword

This book is the result of a collaboration between specialists of various areas of astronomy to summarise what we understand of the production and distribution of oxygen in the Universe. A large part is devoted to the methods of oxygen abundance determination in various media, as those are the fundaments on which our knowledge is built.

Why concentrate on oxygen? Oxygen is the most abundant of the metals, its abundance can be measured in many sites and with a variety of techniques, its formation process is now rather well understood: yet there are many unsolved questions. We believe that it is by showing the problems and facing them that progress is better made.

Following the thread of oxygen, the reader can gain a view of the Universe which is quite different from the perspective usually adopted in manuals, and therefore hopefully rewarding. We believe that this book is suitable for students, provided that they have sufficient background knowledge in astrophysics.

This volume contains a lot of original material in the form of figures and tables as well as an extensive list of references. However, since this book took about 4 years to get assembled, and its parts were written at different epochs, not all the references have been updated. The field is progressing so fast that any update would have quickly become obsolete anyway. As a matter of fact, the major aim of this book is not to describe the latest results, but rather to provide the reader with tools for a deeper understanding of how these results are obtained. This is why this book not only provides a careful mapping of oxygen in the Universe but also introduces some fundamental astronomical concepts (*e.g.* theory of line formation, stellar evolution principles, basic equations for chemical evolution of galaxies), and discusses the methods to derive the chemical composition of astronomical bodies (stars, nebulae, cosmic rays, meteorites, etc.) and their uncertainties. The reliability of the atomic and nuclear data is also addressed.

We undertook this collective endeavour so that the reader could benefit from the best of our experience in our respective fields, perhaps at the expense of homogeneity in style or notation. We hope that the usefulness of this book will overcome its imperfections.

The authors

Chapter 1

HOW TO DERIVE OXYGEN ABUNDANCES

1.1 Oxygen abundance scales and notations

Before describing the many ways to determine the abundance of oxygen in various regions of the Universe, let us first present the different scales and notations that are used for this purpose. For historical reasons, each field of astronomy has developed its own metrics.

In astronomy, the word *abundance* applied to an element, for example oxygen, usually refers to the ratio of its number density, $n(\mathrm{O})$, to that of hydrogen, $n(\mathrm{H})$. It is usually simply written O/H. The abundance of the element is often given on a logarithmic scale in which the value for hydrogen is 12:

$$A(\mathrm{O}) = \log \epsilon(\mathrm{O}) = \log n(\mathrm{O})/n(\mathrm{H}) + 12. \tag{1.1}$$

This is the so-called *astronomical scale*.

Another important quantity is the *mass fraction* of an element. For oxygen, it is written $X(\mathrm{O})$ and given by

$$X(\mathrm{O}) = \frac{\mu_{\mathrm{O}} n(\mathrm{O})/n(\mathrm{H})}{\sum \mu_{\mathrm{E}} n(\mathrm{E})/n(\mathrm{H})}, \tag{1.2}$$

where μ_{E} is the atomic weight of element E and the summation in the denominator includes all the elements. The value of the denominator is the same in all the parts of the Universe and does not change with time.

The metallicity, Z, is the sum of the mass fractions of all the elements heavier than helium[1]. Due to its high cosmic abundance, oxygen accounts for almost half of the total mass fraction of metals in the Sun.

In studies dealing with atmospheres of cool stars, the abundances of the elements are traditionally expressed in *logarithm with respect to the solar value* and use a notation with brackets. For oxygen it may be expressed

$$[\mathrm{O/H}] = \log(\mathrm{O/H}) - \log(\mathrm{O/H})_{\odot}. \tag{1.3}$$

---

[1]In astronomy, all the elements except H and He are called *heavy elements* or *metals*, although not all of them are heavy elements or metals in the chemical sense.

This has the advantage of an easy visualisation of how much the chemical composition of a given region differs from that in the Sun. The drawback is that whenever the solar chemical composition is revised – and this happened several times recently – a simultaneous revision of all the previously published abundances is required as well, if those are to be compared with the abundances in other celestial bodies. For this reason, it would seem much more logical to express abundances with respect to hydrogen. However, the reason for using such a scale in cool star atmospheres is that abundances are determined with respect to a reference value – usually the solar one – and not in absolute value.

For objects in which hydrogen is only a trace element, like in the atmospheres of some evolved stars, a scale based on hydrogen would not be appropriate and one rather uses mass fractions.

The *meteoritic scale* (also called *cosmochemical scale*) uses numbers of atoms relative to 10^6 atoms of Si.

In ionised nebulae, the metallicity is generally expressed in units of solar metallicity denoted by $Z_\odot$. Thus, a nebula with twice the solar metallicity would have $Z = 2\,Z_\odot$. Since oxygen represents a large fraction of the total mass of the metals, and since the abundances of most elements contributing significantly to the metallicity generally vary in lockstep in the Universe, the oxygen abundance in such a nebula would be almost equal to twice the solar value – except if the nebula is close to a region of production of oxygen or of other elements contributing significantly to the metallicity.

Therefore, in practice, the metallicity Z has a slightly different meaning for the stellar and the nebular astrophysicists. In both cases, oxygen plays a dominant role in the definition. In nebular astronomy, as just mentioned, the metallicity is synonym of the oxygen abundance. This is justified by the fact that oxygen generally plays a dominant role in the cooling. In stellar astronomy, it is strongly related to the oxygen abundance, since oxygen is the element that contributes most to the total mass of elements heavier than metals. However, the dominant sources of opacity that control the stellar internal structure as well as stellar evolution are iron and other heavy elements. In first approximation, the oxygen and iron contents in astronomical objects vary in lockstep, so the distinction between the two definitions does not lead to major problems. However, it is now known that the O/Fe ratio is not exactly constant in the Universe, but is a function of the history of star formation (see Chapter 4). Besides, the abundance of oxygen (and metals) that is considered as the solar value has changed several times (see Chapter 2). Therefore, the word *metallicity* must be correctly deciphered in every paper.

Absorption line studies often give the chemical composition in number of atoms per 10^6 H atoms (the unit is abbreviated as ppm, for *part per million*).

One thus has to adapt to different scales and units according to the objects under consideration, and be able to easily transform one into another when changing the area of interest.

As an illustration, we give in the table below the value of the solar oxygen abundance in different scales for two different estimates that have been widely

Table 1.1. The solar oxygen abundance in various scales.

Reference	O/H	$A(O)$	$Z(O)$	$[O/H]^a_{AG89}$	$[O/H]^b_{Aspl09}$
AG89[a]	8.51×10^{-4}	8.93	9.60×10^{-3}	0	0.24
Aspl09[b]	4.90×10^{-4}	8.69	5.77×10^{-3}	-0.24	0

[a] Anders & Grevesse (1989)
[b] Asplund *et al.* (2009)

quoted in the literature as a reference: Anders & Grevesse (1989) and Asplund *et al.* (2009).

1.2 Spectroscopic methods

1.2.1 Basics of line formation

The emission of light by an astronomical object is the result of interactions between its constituting matter and the ambient electromagnetic field. The discrete character of possible internal energy states of the involved matter particles (here atoms or molecules) often gives such interactions the character of resonances taking place at specific (temporal) frequencies. The frequency spectrum exhibits localised intensity features – *spectral lines*. If the intensity in a spectral line is larger than in its immediate spectral vicinity one speaks of an *emission line*, in the case of a reduced intensity, of an *absorption line*. The lines are often superimposed on a slowly changing background – the *spectral continuum*. A spectral line encodes properties of the particles responsible for its formation and the environment in which the formation took place. In particular, spectral lines allow the derivation of the *abundance* of the interacting particles and thus the study of the chemical composition of astronomical objects by remote sensing – in astronomy obviously a very valuable capability. Depending on environment the abundance of oxygen is derived from emission or absorption lines whose specific aspects and intricacies of formation are discussed in the corresponding sections below. For now, we leave out the complexities of the microscopic processes governing the emission and absorption of light and give an elementary, phenomenological account of the formation of spectral lines to provide the reader with an intuitive picture[2].

A beam of light travelling through a medium in the positive direction s experiences a change of intensity according to

$$\frac{dI_\nu}{ds} = -\rho \chi_\nu \left(I_\nu - S_\nu \right), \tag{1.4}$$

---

[2]We would like to acknowledge inspiration for the following considerations obtained from R.J. Rutten's lecture notes on "Radiative Transfer in Stellar Atmospheres". We further assume that the reader is familiar with the basic definition and meaning of intensity, source function and absorption coefficient.

where I_ν is the specific intensity per frequency interval, χ_ν the frequency-dependent mass absorption coefficient, S_ν the source function per frequency interval and ρ the mass density. Introducing the optical depth

$$\tau_\nu(s) \equiv \int_0^s \rho\chi_\nu ds' \tag{1.5}$$

measured from the origin to coordinate s in the direction of beam propagation we can write Equation (1.4) as

$$\frac{dI_\nu}{d\tau_\nu} = -I_\nu + S_\nu. \tag{1.6}$$

The general solution of the differential Equation (1.6) in the interval $[0, \tau_\nu]$ can be written as

$$I_\nu(\tau_\nu) = I_\nu(0)e^{-\tau_\nu} + \int_0^{\tau_\nu} S_\nu(t_\nu)e^{-(\tau_\nu - t_\nu)}dt_\nu \tag{1.7}$$

with $I_\nu(0) \equiv I_\nu(\tau_\nu = 0)$. This is an example of the so-called *formal solution* of a given radiative transfer problem, *i.e.* the solution of the radiative transfer equation for a given source function as function of optical depth.

While generally the mass density and the absorption coefficient are complex functions of location s we now consider a very simple model: a homogeneous medium of finite geometrical thickness – say, a gas cloud – stretching from $s = 0$ to $s = d$ in which source function, mass density and absorption coefficient are constant. Moreover, we assume it is illuminated at $s = 0$ with radiation of intensity $I_\nu(0)$, and an observer records the emitted intensity at $s = d$. We note in passing that if the observer were located at $s > d$ and no matter were present in-between $s = d$ and the observer, the recorded intensity would remain the same: the specific intensity is a distance-independent quantity. For a homogeneous medium the integral in Equation (1.7) can be easily solved analytically, and one obtains

$$I_\nu(d) = S_\nu + (I_\nu(0) - S_\nu)\, e^{-\tau_\nu(d)}. \tag{1.8}$$

We now evaluate Equation (1.8) at frequencies within and outside of a line. The presence of a line adds some extra absorption and increases the optical depth at $s = d$ from the continuum optical depth τ_c to $\tau_{l+c} = \tau_l + \tau_c$. For the difference of the intensity in the line including the contributions from the continuum I_ν^{l+c} and the neighbouring continuum I_ν^c we obtain from Equation (1.8)

$$I_\nu^{l+c} - I_\nu^c = [S_\nu - I_\nu(0)]\, e^{-\tau_c}\left(1 - e^{-\tau_l}\right). \tag{1.9}$$

From Equation (1.8) a first conclusion can be drawn for our simple model. In case of a very large optical thickness in the continuum $\tau_c(d) \gg 1$ and consequently even more so in the line, the observed intensity corresponds to the source function in the cloud S_ν. In the case of local thermodynamic equilibrium (LTE) the source function within a spectral line and the continuum are identical and equal to the

black body radiation function[3] B_ν. In other words, an isothermal, optically thick medium in LTE emits a line-free continuum given by the black body radiation function of the given temperature. For the formation of a spectral line at least one of the conditions of thermal homogeneity, large optical thickness or LTE has to be violated. However, in astronomical objects all three conditions are hardly ever met simultaneously so that the formation of spectral lines is a ubiquitous phenomenon.

From Equation (1.9) we see that depending on the optical thickness in the continuum and the intensity of the illuminating radiation $I_\nu(0)$ the "modulation" of the optical depth scale by the presence of the line is responsible for the formation of a spectral line. In case that the background illumination is weak $I_\nu(0) < S_\nu$ the line appears in emission. If the background illumination is increased $I_\nu(0) > S_\nu$ the line appears in absorption. At first sight it may appear counter-intuitive that by adding intensity a previously brighter spectral feature becomes dark. The reason is that the added background intensity is more strongly blocked in the line than in the continuum and cannot contribute anymore to the observed line intensity. One might take this situation as a crude model of a stellar atmosphere while the lack of background illumination is a typical situation in nebulae. From the discussion it is clear that emission and absorption lines are of the same nature, and that broadening mechanisms operate in the same way. Their distinction in the following sections is motivated by differences in their practical analysis in the various astronomical environments.

1.2.1.1 LTE and NLTE

For calculating the detailed interaction between matter and radiation one needs to know the population numbers of the involved quantum states – of the radiating atoms or molecules as well as of the radiation field itself. For rendering this complex problem tractable the approximation of Local Thermodynamic Equilibrium (LTE) was introduced. Depending on the physical system the LTE approximation can be refined by explicitly considering non-equilibrium processes which is referred to as the treatment of the problem in Non Local Thermodynamic Equilibrium (NLTE, or non-LTE). In the following we give a brief discussion of the concepts in connection to the formation of spectral lines.

The second law of thermodynamics states that a closed thermodynamic system (a system with a large number of internal degrees of freedom) always evolves towards a state of larger disorder – into thermodynamic equilibrium. Under such circumstances the system can be characterised by a single temperature, and the populations of the various quantum states – in NLTE parlance usually referred to as *level populations* – can be calculated without explicit knowledge of the microscopic processes populating and de-populating a particular state. Obviously, this

---

[3]Often also called the Kirchhoff-Planck function.

is a tremendous simplification of the situation since the level populations can be calculated from statistics known from equilibrium thermodynamics:

- the levels within an atom or molecule are populated according to Boltzmann statistics

- the ionisation of atoms is following Saha-Boltzmann statistics

- analogous to ionisation processes the association and dissociation of molecules follows the mass action (or Guldberg-Waage) law

- the thermal motion of the matter particles follows Maxwell statistics

- the source function is given by the black body function.

While indeed the above conditions alleviate the solution of the overall problem tremendously, one has to keep in mind that depending on the number of involved plasma constituents theoretical calculations can still be rather cumbersome even when assuming strict LTE. They can involve the solution of large systems of equations. Moreover, the partition functions of all involved species need to be known, hence demanding detailed knowledge of all relevant energy levels of the constituents − information which is not always available.

Stellar atmospheres as well as interstellar gas clouds (astrophysical systems which will be of particular interest in later sections) are open systems since, *e.g.* energy is flowing through them driven by temperature gradients. Hence, the conditions of thermodynamic equilibrium cannot be met globally. However, equilibria may in fact be established locally (motivating the term *local* thermodynamic equilibrium) in regions over which the physical conditions vary little. Since such local sub-systems interact with their environment two conditions need to be fulfilled such that local thermodynamic equilibrium can indeed be reached: (i) there is sufficient time that microscopic randomising processes can take effect to establish equilibrium and (ii) there is no external forcing inhibiting processes necessary for establishing equilibrium.

In astrophysical plasmas collisions among the particles due to their thermal motion are often the main driving agent towards thermodynamic equilibrium. Electrons are particularly effective since they have a large interaction cross section (due to their charge) and high thermal velocity (due to their small mass). Thermodynamic equilibrium conditions are thus usually established on a time scale controlled by the time interval between particle collisions. In the optically thin case the radiation field has a non-local character, inter-connecting regions where different physical conditions – particularly temperatures – prevail. This tends to drive the coupled systems out of LTE. A typical situation is encountered in stellar atmospheres where the hot radiation field emerging at deeper layers is impinging on higher atmospheric layers of lower temperature. While collisions try to establish level populations corresponding to the local kinetic temperature of the gas the radiation field introduces changes of the level populations corresponding to a higher temperature. The competition between the various processes determines

how close LTE conditions are actually met. This is the classic problem of NLTE in predicting level populations and, ultimately, the detailed strengths and shapes of spectral lines. This is of particular importance in hot stars. In this kind of NLTE problem one seeks a stationary solution of the kinetic equations describing the microscopic processes governing the level populations coupled to the equation of radiative transfer. In this approach one usually assumes the existence of partial equilibria, in particular a well-defined kinetic temperature of the electron gas, *i.e.* that the velocity distribution of the electrons follows Maxwellian statistics. Since collisions are important for establishing LTE it is to be expected that at low mass densities it is less and less likely that LTE conditions will be met. Indeed, stellar chromospheres and coronae as well as interstellar clouds commonly exhibit conditions far away from LTE. In nebulae the idealised concept of LTE has often little bearing on the actual situation.

The classic NLTE problem assumes stationarity, and deals with the non-local forcing of the radiation field driving level populations out of LTE. As stated before, also the time dependence of physical conditions can lead to a situation that prevents the establishment of LTE. In recent years this possibility acquired particular attention in the context of time-dependent hydrodynamical model atmospheres (see Sect. 1.2.2.1). Typically, passing shock fronts lead to strongly time-variable thermodynamic conditions in the atmospheres of cool stars. In the upper photospheres and above collisions are not sufficiently frequent to maintain LTE. Examples of prominent consequences are deviations in the ionisation balance of hydrogen (Carlsson & Stein 2002; Leenaarts & Wedemeyer-Böhm 2006) and the formation of carbon-monoxide molecules (Asensio Ramos *et al.* 2003; Wedemeyer-Böhm *et al.* 2005) in the solar atmosphere. Another environment where departures from LTE are caused by the time dependence of the thermodynamic conditions is expanding supernova atmospheres (De *et al.* 2010).

In the present section we have discussed the very basics concerning the formation of spectral lines with emphasis on nebulae and stellar atmospheres. In the following we provide more details about the mechanisms responsible for the broadening of lines.

1.2.1.2   Broadening of spectral lines in gaseous media

Gaseous oxygen can be observed and measured in absorption, in the interstellar medium on the sight lines of stars or in the intergalactic medium on the sight lines of quasars. The method is similar for interstellar and intergalactic diffuse clouds as described below.

For a given transition of a given element (here oxygen) in a given ionisation state, each absorbing cloud along a sight line produces an absorption line that can be modelled with a Voigt profile. A Voigt profile is the convolution of Lorentzian and Gaussian profiles (see below); it is defined by three atomic parameters and four parameters of the cloud. The atomic parameters are the wavelength, the oscillator strength and the natural broadening of the transition. The parameters of the cloud are the radial velocity V_{r} of the cloud (in $\mathrm{km\,s^{-1}}$), the column density

N of the element (in cm^{-2}), the temperature T of the gas (in K) and its turbulent velocity ξ (in km s^{-1}). If there are several components on the sight line, each cloud produces an absorbing line with its proper four parameters.

We describe here how to measure the parameters of the clouds and especially the column density of oxygen from the study of the absorption lines.

Absorption from an interstellar or intergalactic cloud.   The specific intensity $I(\lambda)$ (in W m^{-2} s^{-1} Hz^{-1}) of a cloud observed in absorption on the sight line of a target (a star or a quasar) is, assuming this cloud is homogeneous and purely absorbing,

$$I(\lambda) = I_\star(\lambda)\, e^{-\tau_\lambda}$$

where $I_\star$ is the specific intensity of the target, *i.e.* its continuum, and τ_λ is the optical depth at wavelength λ. The wavelength dependency of τ_λ makes the spectrum; if it varies strongly in a short wavelength range, there is a spectral line.

A spectral line is not a Dirac delta function at the frequency ν_0 of the transition but is always broadened and thus presents a profile. This profile is given by the function $\Phi(\nu)$, where $\Phi(\nu)\, d\nu$ is the probability (normalised to unity) to have an absorption at the frequency ν near ν_0.

Line broadening.   Two processes can broaden absorbing lines in diffuse clouds[4].

- *Natural broadening*

  The lifetime of an electronic level is the inverse of its damping constant γ_n, which is the sum of Einstein's probabilities (only the induced absorption is taken into account here; induced and spontaneous emissions are negligible in diffuse media). These probabilities are typically $\sim 10^8$ s^{-1} for allowed lines and $\sim 10^{-15}$ s^{-1} for forbidden lines. The Heisenberg uncertainty relation between energy and lifetime for a level n thus implies a natural broadening, *i.e.* damping broadening. The natural profile of a line is a Lorentzian:

  $$\Phi(\nu) = \frac{1}{\pi}\, \frac{\delta_n}{\delta_n{}^2 + (\nu - \nu_0)^2}$$

  where $\delta_n = \gamma_n/4\pi$. The total width of this natural broadening is typically $2\delta_n$.

- *Doppler thermic broadening*

  The velocity dispersion of absorbing particles implies a broadening of the lines due to the Doppler effect. In a gaseous cloud in thermal equilibrium with a temperature T, this dispersion is described by Maxwell distribution law, and the thermal profile is a Gaussian given by

  $$\Phi(\nu) = \frac{1}{\sqrt{\pi}\, \Delta\nu_D}\, e^{-\left(\frac{\nu - \nu_0}{\Delta\nu_D}\right)^2}$$

---

[4]The low density of diffuse media allows collisional broadening to be neglected.

where $\Delta\nu_D = \frac{\nu_0}{c}\, b$ is the Doppler width. The b-value is the characteristic velocity of the broadening. In addition to the purely thermic part, it can include a non-thermic part ξ due to the turbulence in the cloud. It is given by $b^2 = \frac{2kT}{M} + \xi^2$, where k is the Boltzmann constant and M the mass of the particles.

Voigt profile.   The profile of an absorbing interstellar or intergalactic line is thus the convolution of a Lorentzian and a Gaussian. It is given by the Harris function H. We thus have $\tau_\lambda = H\,\tau_{\lambda_0}$ where τ_{λ_0} is the optical depth at the centre of the line without damping. The H function, also referred to as the *Voigt profile*, is

$$H(a, u) = \frac{a}{\pi} \int_{-\infty}^{+\infty} \frac{e^{-y^2}}{a^2 + (u - y)^2}\, dy$$

where:

- $a = \frac{\delta}{\Delta\nu_D}$ is the ratio between the two widths (usually small);

- $u = \frac{\nu - \nu_0}{\Delta\nu_D}$ is the shift to ν_0 in units of Doppler width $\Delta\nu_D$;

- $y = \frac{V_r}{c}\frac{\nu_0}{\Delta\nu_D}$ is the Doppler shift. This shift scans all possible values in the convolution integral (V_r being the radial velocity along the sight line).

The Harris function can be developed as a function of a. One can use for example the empirical analytical approximation from Hui *et al.* (1978).

Curves of growth.   The equivalent width W is defined as

$$W = \int_{-\infty}^{+\infty} \frac{I_\star - I}{I_\star}\, d\lambda = \int_{-\infty}^{+\infty} (1 - e^{-\tau_\lambda})\, d\lambda.$$

W is the line surface as compared to the continuum, *i.e.* the width of a normalised rectangular absorption line with the same surface; thus, W is in units of wavelength, and theoretically does not depend on spectral resolution.

From the Harris function, three distinct domains appear. They can be used to describe the curve of growth, *i.e.* the variation of W as a function of the column density N.

- *Unsaturated mode (optically thin, linear case)*

  This is the domain of low values for N, thus low values for τ_0. The damping wings are negligible and the profile is mainly Gaussian. N is insensitive to the Doppler width $\Delta\nu_D$ and proportional to W:

  $$N(\mathrm{cm}^{-2}) = 1.13 \times 10^{20}\, \frac{W(\text{Å})}{\lambda(\text{Å})^2\, f}$$

  where f is the oscillator strength of the transition. This unsaturated case is thus particularly favourable for column density measurements of numerous species, including oxygen.

- *Intermediate mode (flat part of the curve of growth)*

  For larger W values, W is weakly sensitive to N but strongly depends on $\Delta\nu_D$. We have here

  $$\frac{W}{\Delta\nu_D} \simeq \text{constant}.$$

  This case is favourable for the measurement of b but not of the column density.

- *Saturated mode (optically thick, square-root case)*

  This is the mode of large values of N ($\tau_0 >> 1/a$). The damping wings become visible, so there is a strong dependence on δ. Here we have

  $$\frac{W}{\lambda} = 2\pi^{1/4}\,\frac{\pi e^2}{m_e c^2}\,\sqrt{\delta N f \lambda}$$

  and W varies as $\sqrt{N}$. Few species reach this mode in interstellar and intergalactic media. They include neutral hydrogen at Ly-α or in the first lines of the Lyman series, or molecular hydrogen for dense sight lines. As abundances are usually relative to hydrogen, oxygen abundance measurements require hydrogen column density measurements that are usually in the damped regime.

1.2.1.3   Emission lines

Emission lines are produced whenever an excited atom (or ion) returns to lower-lying levels by emitting discrete photons. Emission lines can be produced both in neutral and ionised gas. However only those arising in ionised (or partially ionised) gas are used for abundance determinations. The good thing about emission lines used for abundance determinations in nebulae is that, once a photon is emitted, it is generally not reabsorbed in the nebula, so one does not have to care about complicated transfer problems[5].

There are several mechanisms which can produce atoms (ions) in excited levels. Lines used for abundance determinations are produced by recombination or by collisional excitation.

Recombination lines.   The recombination of an ion can occur either directly to the ground state or to excited states from which de-excitation proceeds by cascades down to the ground state. The resulting emission lines are called recombination lines. They are labelled with the name of the *recombined* ion, but their intensities are proportional to the abundance of the *recombining* species.

The energy ϵ_{ijl} emitted per unit time in a line l due the recombination of the ion j of an element X^i can be written as

$$\epsilon_{ijl} = n_e n(X_i^j)\alpha_{ijl}, \tag{1.10}$$

---

[5]If the ionised part of the nebula contains dust grains, absorption by internal dust grains may be a concern. Absorption by foreground grains can be dealt with as explained in Section 1.2.3.1.

where α_{ijl} is the effective recombination coefficient of the line which is roughly inversely proportional to the electron temperature.

The strongest recombination lines are those of H I since hydrogen is by far the most abundant element. Usually, it is the Hβ line which is taken as a reference in abundance determinations based on optical spectra. Concerning oxygen, recombination lines from various ions have been observed mostly in planetary nebulae (see *e.g.* Zhang *et al.* 2005). The most commonly observed is O II λ4651 produced by the recombination of O^{++}, and its intensity is typically about one thousandth of Hβ.

Collisionally excited lines. Another way to populate excited states is via collisions with thermal electrons. Obviously, levels corresponding to high excitation energies can be excited only if the thermal electrons are energetic enough, *i.e.* if the electron temperature is high enough.

In the simple two-level approximation, assuming that statistical equilibrium holds between the ground level, 1, and the excited level, 2, one may state that

$$n(X_i^j)n_e r_{12} = n(X_i^{j+1})(n_e r_{21} + A_{21}), \qquad (1.11)$$

where r_{12} is the collisional excitation rate, r_{21} is the collisional de-excitation rate and A_{21} is the radiative de-excitation rate or transition probability. In the limit where $n_e r_{21} << A_{21}$, *i.e.* at low densities and/or large transition probabilities, each excitation is followed by a radiative de-excitation, and the energy ϵ_{ijl} emitted per unit time in a line l due to collisional excitation of an ion j of an element X^i can be written as

$$\epsilon_{ijl} = n_e n(X_i^j)q_{ijl}h\nu_l = 8.63\,10^{-6}n_e n(X_i^j)\Omega_{ijl}/\omega_{ijl}T_e^{-0.5}\mathrm{e}^{(\chi_{ijl}/kT_e)}h\nu_l, \quad (1.12)$$

where Ω_{ijl} is the collision strength, ω_{ijl} is the statistical weight of the upper level and χ_{ijl} is the excitation energy.

Collisionally excited lines (CELs) can be divided into forbidden[6], semi-forbidden and permitted [7] according to the type of electronic transition involved. Forbidden lines have transition probabilities of the order of 10^{-2} s^{-1} (or less for infrared lines), semi-forbidden (or inter-combination) lines of the order of 10^2 s^{-1}, and permitted lines of the order of 10^8 s^{-1}. This means that, for forbidden lines, the critical density (*i.e.* the density at which the collisional and radiative de-excitation rates are equal) is much smaller than that for inter-combination lines or permitted lines.

Note that the levels emitting the collisionally excited lines can also be populated by recombination. In most cases, the contribution of recombination is

---

[6]The word *forbidden* means that the transition cannot occur by electric dipole radiation; but it can occur by magnetic dipole or electric quadrupole radiation.

[7]The square brackets enclosing the name of the emitting ion indicate a forbidden line, the square bracket to the right of it indicates a semi-forbidden line. Permitted lines have no special sign to identify them. Permitted lines that are collisionally excited are named with the ion being excited, while permitted lines that arise from recombination are named with the recombined ion.

negligible. However, at low temperatures (below, say, 5000 K), the contribution of recombination to the intensities of [N II] $\lambda5755$ and [O II] $\lambda\lambda7320, 7330$ must be considered (see Stasińska 2005).

1.2.2   Methods using absorption lines

1.2.2.1   Stellar atmospheres

The *stellar atmosphere* is defined as the light emitting surface layer of a star. It is thus the layer directly amenable to remote observations, and constitutes our most important source of information about the chemical composition of stars. Within a stellar atmosphere, one can often further distinguish between photosphere, chromosphere, corona and the wind according to the dominant physical processes in operation. We shall concentrate on stellar photospheres since the bulk of the radiative energy output of a star originates from its photosphere, and most spectral line diagnostics suitable for abundance measurements are emerging from these layers.

Physically, stellar atmospheres are characterised by the effective temperature, surface gravity, chemical composition and degree of sphericity. Due to our limited understanding of the atmospheric physics and modelling abilities, additional auxiliary parameters are usually introduced to describe the microturbulent velocity, level of turbulent pressure, efficiency of the convective energy transport and properties of a potentially present stellar wind. For extracting abundance information from observed stellar spectra it is necessary to have a suitable model at hand describing the physical structure of a stellar atmosphere. In the following we give an overview of the concepts entering the construction of such *stellar model atmospheres* and aspects related to the formation of spectral lines. Stellar model atmospheres and the analysis of stellar photospheres are broad subjects in their own right, and we refer the reader to the books of Mihalas (1978) and Gray (2005) as examples for in-depth reading.

The properties of stellar atmospheres and consequently the methodology of their analysis vary significantly across the Hertzsprung-Russell diagram. We split the ensuing discussion between cool and hot stars taking spectral type A ($T_{\text{eff}} \approx 10\,000$ K) as the demarcation line. Stars cooler than spectral type A usually have very rich line spectra of atomic or molecular species. They also exhibit convective outer envelopes which drive hydrodynamical flows in their photospheres, which in turn lead to the development of a class of model atmospheres capable of representing such flows. Stars hotter than spectral type A exhibit line spectra for which the inclusion of departures from local thermodynamic equilibrium (NLTE) is important for their interpretation. Moreover, their stronger radiation fields might lead to the presence of stellar winds.

Basics of model atmosphere construction.   In this section we discuss the basic physics of stellar atmospheres and the related construction of models. Strictly speaking, a model atmosphere requires the solution of the full magneto-hydrodynamical problem describing the dynamical and thermal evolution of a

gravitating plasma flow coupled to radiative transport in the surface layers of a star, where all relevant spatial and temporal scales have to be taken into consideration. Stars often exhibit coherent structures on scales of the star as a whole, *e.g.* a global magnetic field or pulsational motions. Realistic analytical solutions of such a problem are out of reach, due to the non-linear character of the equations as well as the complex functional dependence of material properties described by an equation-of-state and opacities on the thermodynamic properties of the plasma. One has to resort to numerical solutions and to reducing the complexity of the problem to a manageable level. For the sake of simplicity, current standard model atmospheres usually rely on the following.

- One-dimensional geometry (1D) assuming either plane-parallel or spherical symmetry. The stellar atmosphere is described by a stacking of layers in the radial direction. The plane-parallel symmetry is obviously only meaningful if the extent of the atmosphere is small in comparison to the stellar radius. However, this assumption is well met in stellar photospheres of dwarf and not too extreme giant stars.

- Time independence. For the kinematics one either assumes static conditions or constant flow speeds (potentially still variable in space). This assumption reduces the momentum equation to the equation of hydrostatic balance with an inertial term if macroscopic flows are present. For the energy equation it implies a balance of all heating and cooling processes at a particular location. If radiative transfer is the only energy transport *radiative equilibrium* is held.

- Chemical homogeneity. One assumes that the relative mixture of chemical elements is everywhere the same. Ionisation and molecular formation processes might alter the actual composition, however, leaving the number fractions of involved atomic nuclei unaltered.

- Absence of magnetic fields.

The above list of assumptions constitutes perhaps the most stringent set of simplifications, and depending on model application, considerable effort has been invested to overcome some of them. For instance, in the field of chemically peculiar stars chemical homogeneity was replaced by a layering of the chemical species according to the competing effects of gravitational sedimentation and radiative levitation (*e.g.* Alecian & Stift 2007; Leblanc *et al.* 2009). For late-type stars in which convective flows produce pronounced atmospheric inhomogeneities model atmospheres were constructed which overcome the assumptions of one-dimensional geometry and time independence (see next paragraph).

In standard 1D models the largest emphasis is put on the energetics which controls the temperature structure of a stellar atmosphere, and eventually has the largest influence on the formation of spectral lines. In hot stars the energy balance is essentially controlled by radiation while in cool stars convection can contribute substantially to the energy transport, and has to be taken into account in order to obtain reliable temperatures. The convective energy transport is commonly

treated within the framework of the so-called mixing-length theory. Originally formulated in the contexts of meteorology (Taylor 1915) and aerodynamics (Prandt 1926), it was introduced into astrophysics by Biermann (1932) and Vitense (1953).

Besides the transport of energy, convectively driven flows also influence the momentum balance of an atmosphere, and the influence of *turbulent pressure* can become substantial, particularly in late-type giants. Modelling the influence of turbulent pressure on the hydrostatics within mixing-length theory has its limitations since formally the turbulent pressure gradient becomes infinite at the stability boundary of a convective region. Physically, convectively driven flows are not strictly confined to convectively unstable regions, and *overshooting* motions occur. These are absent in the standard (and most widely applied) formulation of mixing-length theory, leading to the unphysical behaviour of the theory in the vicinity of convective boundaries. In the following section we introduce hydrodynamical model atmospheres as a remedy to these shortcomings. For 1D standard models, one has to keep in mind that the rather *ad-hoc* modelling of hydrodynamical effects leads to limits in their predictive capabilities.

For cool stars essentially two techniques were established to deal with the tremendous complexity of the wavelength dependence of the radiative transfer due to the presence of a large number of spectral lines (line blanketing): opacity distribution functions (Labs 1951; Strom & Kurucz 1966) and opacity sampling (Peytremann 1974; Sneden *et al.* 1976). Both techniques are of statistical nature taking advantage of the fact that the distribution of the line absorption of the many involved elements at various ionisation stages is rather irregular and unsystematic, and thus amenable to a statistical treatment. Standard models based on opacity sampling typically use 10^5 wavelength points in opacity distribution functions with typically 10^4 equivalent wavelengths. Model atmospheres based on opacity distribution functions are thus computationally less demanding although less flexible since the opacity distribution functions are pre-tabulated for thermodynamic conditions of interest from extensive line lists. This makes it difficult to include effects such as stemming from chemical inhomogeneities in the radiative transfer. Moreover, the opacity distribution function approach does not easily allow the inclusion of NLTE effects in the calculation of a model atmosphere. They can be included in an iterative manner (Haberreiter *et al.* 2008) demanding a re-calculation of the opacity distribution functions in each iteration step.

For hot stars line blanketing is treated somewhat directly by including the relevant lines explicitly, *i.e.* the wavelength grid of the numerical model resolves the individual line profiles. This approach is natural since NLTE effects in the lines have to be dealt with anyway. However, this strict treatment is only possible for light elements without overly complex term systems. In particular, for the treatment of the important line blanketing of the iron group elements one has to resort to approximations. One reduces the number of involved energy levels to be explicitly treated in NLTE by grouping levels sharing similar properties into so-called "superlevels" (Anderson 1985, 1989) of levels sharing similar properties. The relative population numbers within each superlevel are assumed to be in LTE. For treating the numerous transitions between the levels within the superlevels one

Table 1.2. Overview of 1D model atmosphere codes. For each code the name is listed specifying whether it employs plane-parallel (P) or spherical (S) geometry (geo.), whether line blanketing (blank.) is treated in LTE or NLTE (with approximations "$\approx$"), whether a wind is included and the main application domains. The application domains are denoted by the stellar spectral type or particular classes of objects such as brown dwarfs (BD), planets (Pl), novae (N), supernovae (SN), Wolf-Rayet (WR) stars or central stars of planetary nebulae (CSPN).

Name	geo.	blank.	wind	main application
ATLAS[1]	P	LTE	no	AFGKM
MARCS[2]	P	LTE	no	AFGKM
MAFAGS-OS[3]	P	LTE	no	AFGKM
TLUSTY[4]	P	NLTE	no	OBAFGKM, BD, Pl
PHOENIX[5]	P,S	NLTE	yes	AFGKM, N, SN, BD, Pl
Detail/Surface[6]	P	–	no	BA
TMAP[7]	P,S	NLTE	no	hot compact stars
PoWR[8]	S	NLTE	yes	WR
CMFGEN[9]	S	NLTE	yes	OBA, WR, SN, CSNP
WM-*basic*[10]	S	NLTE	yes	OB with winds, SN, CSPN
FASTWIND[11,12]	S	$\approx$NLTE	yes	OBA

References : (1) Kurucz (1979, 2005a, b, c, d, e) - (2) Bell *et al.* (1976); Gustafsson *et al.* (1975, 2008); Plez (2008) - (3) Grupp *et al.* (2009) - (4) Hubeny (1998) - (5) Hauschildt (1992); Hauschildt & Baron (1999) - (6) Butler & Gidding (1985); Giddings (1981) - (7) Rauch & Deetjen (2003); Werner *et al.* (2003) - (8) Gräfener *et al.* (2002) - (9) Hillier & Miller (1998) - (10) Pauldrach *et al.* (2001) - (11) Puls *et al.* (2005) - (12) Santolaya-Rey *et al.* (1997).

again resorts to a statistical treatment by applying the same ideas of opacity distribution functions or opacity sampling as used in cool stellar atmosphere models (see Puls 2009, and references therein).

Stellar model atmosphere codes.   In this section we provide a brief overview of 1D model atmosphere codes which are commonly applied in the analysis of stellar spectra. Our list (see Table 1.2) is not complete, but nevertheless covers the majority of codes currently in routine operation. We tried to provide the main application domains of the listed codes. A particular code might be technically capable of calculating model atmospheres in a wider range than given. However, certain approximation might become physically questionable, or users simply did not apply the code outside the range given. ATLAS – one of the "workhorses" among the stellar atmosphere codes – is an example. Technically, it can also be applied to O-type stars; however, line blanketing treated in LTE results in inaccurate models.

Table 1.3. Behaviour with respect to spectral type of the diagnostic lines commonly used to derive oxygen abundances in stars.

Line	spectral domain	Spec. type range
OH	IR	G – M
OH	UV	F – M
[O I]	Op	G – K
O I	Op & NIR	Mid B – late F
O II	Op	Late O – B3

To some extent there is a distinction between codes primarily used for cool and codes primarily used for hot stellar atmospheres. The strong radiation fields in hot stars require the treatment of line blanketing in NLTE. Moreover, winds are commonly driven by the radiation fields of hot stars so that the codes for hot stars often include a consistent treatment of stellar winds.

The listing of a code in Table 1.2 does not imply that it is publicly available. The distribution policies of the codes vary. The ATLAS code is an example of a freely available code. Such liberal policy has certainly contributed to its wide-spread use, and also spawned efforts to port the code to various computer architectures (*e.g.* Sbordone 2004). From the user perspective it is often sufficient to have the final products of atmosphere codes such as atmospheric structures, spectra and colours. Again, the situation is heterogeneous, and we only point to the work of Castelli *et al.* (2003) and the MARCS model atmosphere site (see `http://marcs.astro.uu.se`) as examples where larger model atmosphere grids are made available.

Oxygen abundance indicators for different stellar types. Different oxygen abundance indicators are available depending on the effective temperature of the star under study. These are summarised in Table 1.3. In the case of cool stars (*i.e.* with spectral types later than F), four types of indicators are accessible more or less simultaneously. These refer to the OH lines present in the UV and IR, the forbidden [O I] $\lambda6300$, $\lambda6363$ lines and the three permitted O I triplets found in the $6150-9270$ Å range. Only the O I lines remain present in the spectra of A-type stars, becoming very faint in late B-type stars and finally disappearing in earlier spectral types. Although no clear oxygen features appear in the spectrum of stars in the spectral type range between $\sim$B9 and B3 (making it quite difficult to measure oxygen abundances in these objects), a large number of O II lines begin to populate the stellar optical spectrum ($3800-7000$ Å) in early B-type stars. The forest of O II lines disappear again for spectral types earlier than $\sim$O9 (the maximum strength of these lines is found for $\sim$B1). Finally, for the mid and early O-type stars, oxygen abundance determinations rely on a few strong O III-V lines.

In the next sections we describe in detail the methods and abundance indicators used to derive oxygen abundances in stars. Although the basics of the methodology

is similar, we differentiate between cool (A-type and later) and hot star (OB-type) strategies mainly according to the diagnostic lines and techniques used in the stellar parameter determination and the abundance analysis.

Cool stars.

Hydrodynamical model atmospheres of cool stars.   In the late 1970s computing power had evolved to a level which allowed the removal of the simplifying assumptions of stationarity and 1D geometry made in standard model atmospheres of cool stars. The presence of granulation – directly observable on the Sun – is the tantalising sign that the surfaces of cool stars are not homogeneous as assumed in the 1D models. This motivated the development of a class of models capable of representing convective flows which are the driving ingredient behind the surface inhomogeneities. While 1D standard models were (and are) fairly successful when used in the interpretation of observed spectra, the standing question is whether major revisions of measured atmospheric quantities – particularly abundances – might emerge when the inhomogeneous nature of the atmosphere is accounted for. Nordlund & Dravins (1990) give a brief historic overview (see their Sect. 7.3) about the early hydrodynamical model atmospheres (hereafter "3D models" for short). Here, it suffices to mention the milestone paper of Nordlund (1982) who most consequently pushed 3D models towards their application in solar and stellar spectroscopy during the initial development phases.

Today, a number of different codes exist for the calculation of hydrodynamical models of stellar surface flows and the atmospheric structure. Due to the fact that computing power is still a limiting factor for the realism that can be achieved, the codes are usually optimised for specific purposes. Roughly speaking, they can be divided into codes developed for the study of dynamical phenomena such as magnetic fields and their evolution, and 3D stellar model atmospheres that intend to represent as accurately as possible the properties of the stellar atmosphere which are relevant for spectroscopy. The energy budget governed by radiative transport and the controlling of temperatures is carefully accounted for, together with the kinematics of the flow field important for line broadening. For abundance work essentially two different codes have been up-to-now applied extensively: the convection code originally developed by Nordlund & Stein (Stein & Nordlund 1998) and refined by Asplund and collaborators (Asplund *et al.* 2000), and CO^5BOLD[8] developed by Freytag & Steffen (Freytag *et al.* 2002; Wedemeyer *et al.* 2004) with contributions by several collaborators (Leenaarts & Wedemeyer-Böhm 2005; Ludwig *et al.* 2009; Schaffenberger *et al.* 2005; Wedemeyer-Böhm *et al.* 2005).

Hydrodynamical model atmospheres intend to overcome the simplified treatment of the gas-dynamical processes in standard 1D models based on mixing-length theory or similar concepts. The large spatial scales in combination with the small molecular viscosity of the stellar plasma render the gas-dynamical problem at very

---

[8]COnservative COde for the COmputation of COmpressible COnvection in a BOx of L Dimensions with L = 2,3.

high Reynolds number, with resulting flows which are often turbulent and intermittent, as well as having the tendency to form shocks. The dominant mode of energy exchange among gas elements is radiative transfer, and an accurate description is mandatory in order to obtain a realistic description of the stellar atmosphere. All this is coupled to material quantities (given by an equation-of-state and opacities) which have complex functional dependencies. The combination of both problems makes the construction of hydrodynamical model atmospheres demanding, and judicious approximations have to be introduced. These approximations are sources of potential errors, and we will discuss them in the following. The recent review of Carlsson (2009) provides a summary of the present state-of-the-art with emphasis on further development steps.

The non-linear hydrodynamical equations in combination with the non-linear material functions make the analytic treatment of the problem largely intractable so that one has to resort to numerical solutions. The almost inviscid conditions in stellar atmospheres make the Euler equations an appropriate model for the gas dynamics. The Euler equations are augmented by force terms due to gravity and by a model for viscous effects, either by introducing explicit viscosity terms (artificial viscosity, often in the form of a so-called hyperviscosity) or implicit to the numerical scheme (numerical viscosity) applied in the solution of the hydrodynamical equations, or a combination of both. At present all codes for modelling the dynamics of stellar atmospheres are grid-based (as opposed to grid-less smooth particle hydrodynamics), and use discrete representations of the governing equations. Turbulence and shocks tend to create structures on spatial scales governed by the molecular viscosity which are commonly far smaller than the resolution of the numerical grid. The viscosity in the numerical schemes plays a two-fold role in this context: on the one hand it is used for stabilising the scheme, on the other hand it is intended to model the dissipative effects on unresolved spatial scales. The most important design goal of the numerical schemes in hydrodynamics is perhaps to restrict the influence of the sub-grid scales on the resolved scales as little as possible – of course, without rendering the overall numerical scheme unstable and hence useless. Since the introduction of artificial viscosity in numerical hydrodynamics by Von Neumann & Richtmyer (1950) a great number of numerical schemes were devised, and the literature is extensive. We recommend the collection of papers edited by Steiner & Gautschy (1998) as a starting point for further reading.

The radiative exchange of heat is the dominant non-adiabatic process in the atmospheric flows and governs their thermal structure and evolution. Like in 1D standard models great care has to be taken to represent this process sufficiently accurately. In 3D, the radiation intensity becomes a six-dimension field (three spatial, two directional and one wavelength coordinates) whose evolution has to be followed in time. Even at modest resolution in space, solid angle and wavelength the computational demand becomes high, and, indeed, in hydrodynamical model atmospheres most of the computer time is spent on the calculation of the radiation field. As a consequence, resolution is limited to the affordable minimum. In particular, the wavelength resolution is limited, and the wavelength

dependence of the radiative transfer is commonly treated using the concept of "opacity binning" (Nordlund 1982) which is a multi-group method related to opacity distribution functions. The basic idea is to classify wavelength points, and sort them into groups representing the continuum and spectral lines of increasing strength. Within each group the source function is integrated, and the variable opacity approximated by a suitable average value. As a result the radiative transfer needs to be solved only once per group, instead of many times for each individual wavelength point falling into the group. However, while in 1D typically 10^4 to 10^5 wavelength points can be afforded, this number is reduced to four to twelve opacity groups in present 3D models. Since the grouping treats the wavelength dependence only approximately, the rather coarse resolution is obviously a point of concern. As a consequence, in present developments the ever increasing computing power is directed to improve this aspect. Looking at the overall situation, present developments go almost parallel to the developments of 1D models some 40 years ago, and again opacity distribution functions or opacity sampling are competing concepts for the future treatment of the radiative energy exchange in 3D models. Ultimately, opacity sampling is the method of choice since it allows one to naturally include refinements like Doppler shifts when treating the absorption in spectral lines. At the moment, however, it is unclear whether the modest number of affordable wavelength points (or groups) is not more effectively invested in an approach using opacity distribution functions or a refined opacity binning.

Today, hydrodynamical model atmospheres employ at best a few hundred grid points per spatial dimension, which renders the effective Reynolds number of the simulated flows by many orders of magnitude smaller than present in reality. The wavelength dependence of the radiative energy exchange is treated at very modest wavelength resolution. These two approximations have understandably spawned some criticism. However, using the Sun as the obvious testbed, 3D models exhibited excellent performance concerning the kinematics and thermodynamics of the flow as measured by line properties (Asplund *et al.* 2000), granulation contrast (Wedemeyer-Böhm & Rouppe van der Voort 2009), and centre-to-limb variation of the radiation field (Asplund *et al.* 2009; Ludwig *et al.* 2010). Hence, 3D models capture the essential physics, and in this way eliminate the need of free parameters in 1D models such as the mixing-length, as well as micro- and macro-turbulent velocities. The correspondence between observation and theory is not yet perfect (see, *e.g.* Steffen *et al.* 2009), but improving resolution is a clear pathway towards even higher degrees of realism.

When a 3D model run is completed, detailed spectral information is calculated in a subsequent step from its thermal and kinematic properties. This is illustrated in Figure 1.1. First of all, the model represents a small volume at the stellar surface embedding the energetically dominant flow feature – the granulation. The representation is statistical in nature since the convective flow is deterministically chaotic – similar to the weather on Earth. The 3D model has to be considered as a Monte-Carlo experiment representing a possible realisation of the atmospheric flows, and sufficient spatial and temporal statistics has to be gathered for an
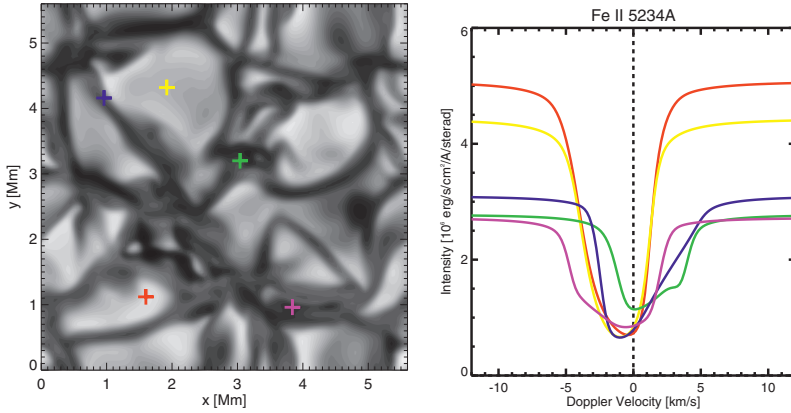
Fig. 1.1. *Left panel:* snapshot of the emergent intensity obtained from a hydrodynamical model atmosphere of the Sun. Lighter shades correspond to greater brightness. *Right panel:* synthetic Fe II line calculated at the positions marked by the crosses of the same colour in the intensity pattern. The line profiles show a strong variation dependent on the selected line of sight.

accurate prediction of the flow properties. The left panel of Figure 1.1 shows the emergent intensity pattern obtained from a solar 3D model atmosphere at a particular instant in time during its temporal evolution. The right panel of the figure shows synthetic line profiles calculated for various locations in the 3D model volume. The line of sight, along which the radiative transfer equation is solved, traverses the model perpendicular to the depicted surface. For the interpretation of observed spectral lines these spatially resolved line profiles have to be suitably averaged also taking into account their centre-to-limb variation. Finally, the spectral synthesis calculations have to be performed for several instances in time and averaged temporally. Since usually a large number of convective cells are present on the surface of a late-type star, statistical fluctuations are minor, and then the modelled synthetic line profiles can be directly confronted with observations.

Derivation of stellar parameters in cool stars. The derivation of elemental abundances in cool stars requires the basic stellar parameters to be known, namely effective temperature $T_{\rm eff}$, gravity $\log g$, metallicity [Fe/H] and microturbulence velocity $v_{\rm t}$. The detailed abundance analysis of cool stars consists in using a set of Fe I and Fe II lines to derive the four basic parameters. The reason to use Fe I and Fe II lines is that there are hundreds of lines of these species in the spectra of cool stars, from the UV to the infrared. Therefore given their large numbers, it is possible to combine lines of different excitation potentials and different strengths, and test their behaviour as a function of the stellar parameters.

The formation of absorption lines by means of sophisticated model atmospheres consists in the radiative transfer from deeper to shallower layers (optical depths $2 \gtrsim \log \tau \gtrsim -5$), more often considering conditions of LTE and building up the line along the layers. Since the effects of the four stellar parameters are interdependent,

the analysis has to consider simultaneously excitation equilibrium, ionisation equilibrium, and a best v_t value that satisfies a range of equivalent widths. Once the stellar parameters are settled, the abundances of different elements are derived line-by-line, either using their equivalent widths or by fitting line profiles.

Effective Temperature. In the optical the effective temperature is preferentially derived from the excitation equilibrium of Fe I and Fe II lines of different excitation potentials. A change of 100 K in $T_{\rm eff}$ causes a recognisable trend in the plane Fe I abundance *versus* excitation potentials, such that this can be considered as a reasonable uncertainty value.

In the near-infrared (H, K) band regions, the Fe I lines have high excitation potentials around 5.5–6.5 eV; therefore the line strengths are not sensitive to errors in temperature. Consequently, in studies using H and K bands, temperatures rely preferentially on photometric colours. In using colours there is however a dependence on interstellar extinction, which is considerably lower in the infrared than in the optical but still has to be considered. A check with the Fe I lines is useful.

Gravity. The surface gravities $\log g$ are in general derived using the effective temperature and, when available, also the parallax as input (in which case the bolometric magnitude is derived using a parallax value), and adopting the Sun as the reference star with the classic relation

$$\log \frac{g_*}{g_\odot} = 4\,log\,\frac{T_*}{T_\odot} + 0.4\,(\mathcal{M}_{\rm bol}^* - \mathcal{M}_{\rm bol}^\odot) + log\,\frac{M_*}{M_\odot}.$$

Spectroscopic gravities $\log g$ can be derived from the ionisation equilibrium of Fe I and Fe II lines. In general the photometric gravity is adopted as the initial value which is further improved through the ionisation equilibrium. Gravity values show typical uncertainties of ± 0.30 dex.

Microturbulence. The microturbulent velocities v_t are usually determined using Fe I lines. Line growth proceeds in three phases, For weak lines the depth of the line as well as its equivalent width grow proportionally with the abundance. The second growth phase occurs when the line depth reaches its maximum and the line saturates; the equivalent width grows asymptotically to a constant value. The third growth phase starts with the development of the wings, and therefore dependent on the damping constant γ. If γ were constant, then the equivalent width would grow roughly as the square root of the abundance. The saturated part of the curve of growth is sensitive to the microturbulence velocity, and is used to establish the optical value of v_t. More details on the curve of growth are given in Section 1.2.2.

The uncertainty derived from the Fe I abundance *versus* W_λ is in general around 0.2 km s^{-1}.

Oxygen abundance indicators in cool stars. There is agreement in the literature concerning an overabundance of oxygen relative to iron in metal-poor stars. This result was first established by Conti *et al.* (1967) and Sneden *et al.* (1979). However there is no agreement on the overabundance value itself. These

discrepancies have triggered discussions in the literature about the oxygen abundance indicators. The reasons for the discrepancies come from the fact that four sets of lines can be used to derive oxygen abundances in metal-poor stars: (i) the forbidden [O I] $\lambda6300$, $\lambda6363$ lines measurable in giants of [Fe/H] > -3.0; (ii) the permitted O I $\lambda7771$, $\lambda7774$ and $\lambda7775$ lines measurable in dwarfs and subgiants or the weaker triplet at O I $\lambda6156$, $\lambda6157$ and $\lambda6158$ in supergiants; (iii) the ultraviolet (UV) OH lines ($A^2\Sigma - X^2\Pi$ electronic transition) and (iv) the infrared (IR) OH lines ($X^2\Pi$ vibration-rotation transition).

Therefore there are only a few lines available, and in most cases the different lines are not present in the same stars.

(i) The forbidden doublet [O I] $\lambda6300$ and $\lambda6363$ lines are reliable oxygen abundance indicators in cool giant stars, given that the lower level is the ground state and the upper level is controlled by collisions (Kiselman 2001); therefore it is not affected by NLTE effects. Hydrodynamical 3D model atmospheres show that this line is affected by granulation, as discussed by Nissen *et al.* (2002).

(ii) The permitted lines appear strong in dwarf stars hotter than $\gtrsim 5500$ K. In general, O I permitted lines give systematically higher values than the [O I] forbidden lines. Kiselman & Nordlund (1995) computed equivalent widths of the O I $\lambda7770$ triplet for solar type stars, showing that they are subject to NLTE effects and also probably to granulation effects, concluding that the O I $\lambda7770$ nm triplet is not understood even in the Sun. Therefore, they do not recommend to use it for abundance determinations in stars. Asplund *et al.* (2004) reanalysed [O I], O I and OH lines with a more complete oxygen atom taking into account NLTE calculations within 3D, time-dependent, hydrodynamical models, and found agreement between the different oxygen abundance indicators in the Sun.

The O I $\lambda6158$ triplet, weaker than the O I $\lambda7770$ triplet, is a better option in cases where the latter is too strong, and has been shown to be suitable in supergiants (Barbuy *et al.* 1994) and in hot turn-off dwarfs (Clegg *et al.* 1981). The O I $\lambda8446$, $\lambda8447$ and $\lambda9266$ triplet lines are rarely used in the literature of cool stars, because of severe blends with telluric lines.

(iii) UV OH lines are strongly affected by granulation in metal-poor stars. The derivation of oxygen abundances from these lines would be however very important in the most metal-poor stars, given that they are the only oxygen lines strong enough to be measured in these stars. UV OH lines show NLTE effects (Hinkle & Lambert 1975). Asplund & García Pérez (2001) and González Hernández *et al.* (2008) carried out calculations of UV OH lines with 3D model atmospheres, showing that such effects can be large, affecting mostly metal-poor stars.

(iv) The infrared (IR) $X^2\Pi$ vibration-rotation transitions of OH lines in the H band have measurable intensities down to metallicities [Fe/H] ~ -3.0 for giants with effective temperatures $T_{\text{eff}} \sim 4300$ K. For dwarfs the lines are stronger, and for $T_{\text{eff}} \sim 4500$ K, these lines can be measured down to metallicities [Fe/H] ~ -3.5. These lines were first used in halo stars by Balachandran & Carney (1996) for the dwarf HD 103095 characterised by [Fe/H] $= -1.22$ and [O/Fe] $= 0.29$. Balachandran *et al.* (2001), Balachandran *et al.* (2002), Meléndez *et al.* (2001) and Meléndez & Barbuy (2002) presented further oxygen abundance determinations
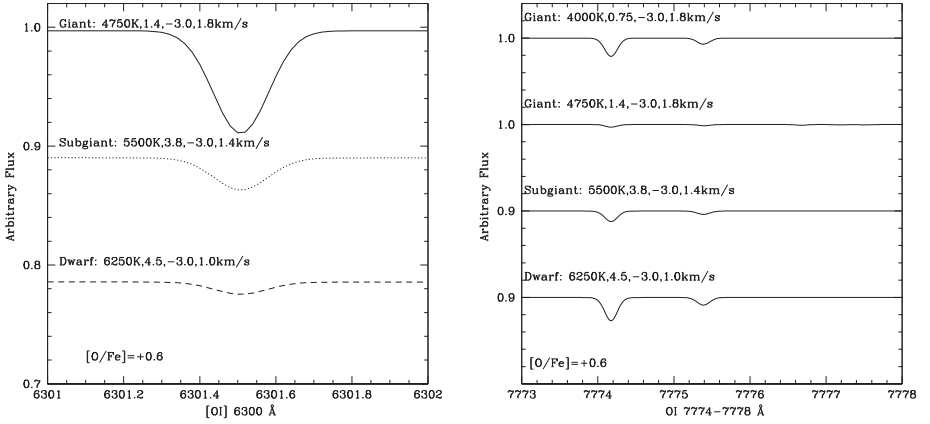
Fig. 1.2. (Left) the [O I] $\lambda 6300$ forbidden line, computed for a cool giant, a typical red giant, a subdwarf and a turn-off dwarf, with parameters: (T_{eff}, log g, [Fe/H], v_t) = (4000, 0.8, -3.0, 1.8), (4750, 1.4, -3.0, 1.8), (5500, 3.8, -3.0, 1.4) and (6250, 4.5, -3.0, 1.0) respectively; (right) O I $\lambda 7770$ permitted triplet lines, for a typical metal-poor giant, a subgiant and a dwarf, with parameters (T_{eff}, log g, [Fe/H], v_t) = (4750, 1.4, -3.0, 1.8), (5500, 3.8, -3.0, 1.4) and (6250, 4.5, -3.0, 1.0) respectively.

in metal-poor stars from OH lines in the H band. Their [O/Fe] values tend to show agreement with those derived from [O I] lines in the metallicity range $-2.5 \lesssim$ [Fe/H] $\lesssim -1.0$. Most analysed stars of lower metallicities than [Fe/H] < -2.5 give oxygen abundances higher than permitted line values, probably due to non-LTE effects in the formation of the IR vibration-rotation OH lines (Asplund & García Pérez 2001; Hinkle & Lambert 1975). This line is present in both dwarf and giant stars.

Besides the OH lines in the H band, only the fundamental transition lines at 3.5 μm in the L band are measurable (the difficulty with the latter lines comes however from the thermal background and lower sensitivity of the instruments). The relative intensities of the OH lines can be found in Hinkle *et al.* (1995) for Arcturus (L and H bands) and in Livingston & Wallace (1991) for the Sun (L band only).

In Figures 1.2a,b we show the forbidden [O I] $\lambda 6300$ and the O I $\lambda 7770$ triplet lines computed for a cool giant of parameters (T_{eff}, log g, [Fe/H], v_t) = (4000 K, 0.8, -3.0, 1.8 km s^{-1}), a typical metal-poor red giant BD-18°5550 with parameters = (4750 K, 1.4, -3.0, 1.8 km s^{-1}) (Cayrel *et al.* 2004); a subgiant where both the forbidden and the permitted lines are detected, taken from the study of Spite & Spite (1991); HD 132475 of parameters (5500 K, 3.8, -1.60, 1.2 km s^{-1}), but lowering the metallicity to [Fe/H] $= -3.0$ for comparison purposes; and a metal-poor turn-off dwarf CS 22177-009 of parameters (6257 K, 4.5, -3.1, 1.2 km s^{-1}) adopted from Bonifacio *et al.* (2007).

Abundance uncertainties in cool stars.   Abundance ratios such as [O/Fe] are more accurate than abundances relative to hydrogen such as [O/H], because possible uncertainties in model atmospheres cancel out when the abundance ratios are considered. In general, ionised lines are combined to Fe II and neutral species to Fe I. Some ratios are more reliable when compared with Fe II, such as oxygen derived from [O I] $\lambda6300$, since these lines form in similar layers. The use of Fe II is more reliable also regarding concerns of non-LTE, since Fe II lines are far less susceptible to NLTE than Fe I lines (Thévenin & Idiart 1999).

Another source of errors is the use of 1D model atmospheres, since the strengths of lines depend on the detailed structure of the atmospheres. Stellar granulation, including effects of temperature gradients, atmospheric inhomogeneities and velocity fields caused by convection, affect the ratio of line to continuous absorption (Asplund 2005). These effects are taken into account in 3D (time-dependent) hydrodynamical model atmospheres. Such calculations applied to [O I]$\lambda6300$ and Fe II lines by Nissen *et al.* (2002) showed that for metal-poor stars the derived oxygen abundances using 1D model atmospheres have to be corrected downwards by an amount of 0.2 dex. On the other hand, essentially no difference is found for metal-rich stars. Another point is that 3D effects compensate for NLTE effects, so that both improvements have to be considered at the same time. In the case of [O I]$\lambda6300$ the NLTE effects are negligible, so that the predictions by Nissen *et al.* (2002) should apply, and they do not change the results for metal-rich stars. For infrared OH lines, corrections could have some effect, and stronger corrections apply to UV OH lines (Asplund & García Pérez 2001).

It should be noted that abundances in cool stars are often presented with respect to the solar values. This stems from the fact that the line oscillator strengths needed to derive the abundances are not known with good accuracy from atomic physics computations, and are often calibrated so as to reproduce the "standard" value of the abundances for the Sun, using the same methodology (atmosphere model, code, etc.)

Hot stars.   This section is mainly devoted to the methods applied to derive oxygen abundances in the so-called OB-type stars – a spectral subgroup comprising late O- and early B-type stars (Jaschek & Jaschek 1995), in which both dwarfs and supergiants are included. As commented above the optical spectrum of these stars is characterised by the presence of a large number of O II lines, along with other H I, He I-II and Si II-IV lines which can be used to establish the stellar parameters (see Fig. 1.3). These methods are based on the spectroscopic analysis of the optical spectrum of the stars by means of stellar atmosphere codes. Although the basic ideas behind this method are similar to those presented in the previous section one should note that:

1. The physical conditions characterising the atmospheres of OB-type stars are quite different from those present in cooler stars, and hence different assumptions have to be considered for the stellar atmosphere model calculations.

2. The spectral features used to establish the stellar parameters are different.
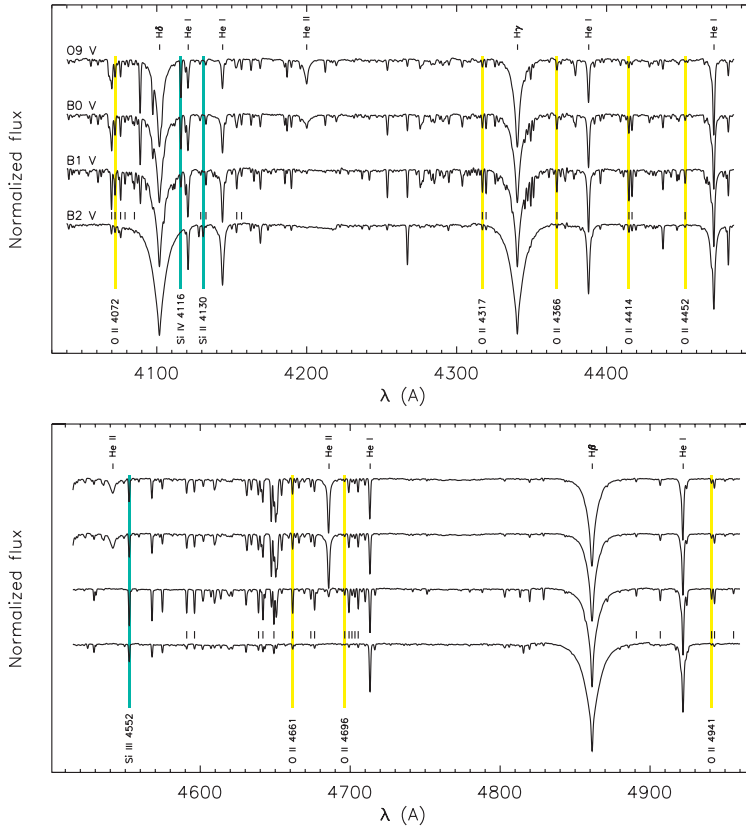
Fig. 1.3. Representative spectra of four OB-type dwarfs with low $v \sin i$ (from the IACOB spectroscopic database, Simón-Díaz *et al.* 2011). The optical range between 4000 and 5000 Å contains several H Balmer lines along with various Si II-IV and/or He I-II lines (depending on the effective temperature of the star) which make it possible to derive the stellar parameters ($T_{\rm eff}$ and $\log g$). These lines are indicated in the upper part of the figure. In addition, more than 25 O II lines (in the best cases) are available for the determination of the oxygen abundance. These are indicated just above the spectrum of the B2 V star. Marked in blue and yellow we identify some representative Si II-IV and O II lines, respectively, to bring forth their behaviour with spectral type (*i.e.* effective temperature).

3. The atomic models required for the oxygen abundance determination are different. Specifically, a detailed O II model atom is needed for the study of OB-type stars.

4. In the best cases, more than 25 O II lines covering a large range in equivalent widths are present in the optical spectrum of OB-type stars. If the projected rotational velocity of the star is low enough (say below $\sim$60 km s^{-1}), these

lines are well separated from other absorption line features also appearing in the spectrum (H I and He I-II lines, as well as lines from other light elements: C, N, Si, Mg, etc.). The availability of a large sample of O II lines makes it possible to account for the effect of microturbulence on the oxygen abundance determination consistently (*i.e.* microturbulence can be constrained using the O II lines themselves).

In this section we treat all these points in detail, and show how the most commonly used method to derive oxygen abundances in OB-type stars (the *curve of growth method*) can also be used to establish the error associated with the various sources of uncertainty affecting the final value, as well as to identify problematic lines. The *curve of growth* method is not applicable in some cases, such as the study of fast rotators (when line blending is severe due to the high $v \sin i$ of the star) or when the spectral resolution is not good enough for resolving individual lines (for example, in extragalactic studies beyond the Local Group). In those cases, the abundance analysis is performed by the so-called *synthesis method*. We will also give some notes on this method.

Model atmospheres for hot stars. Similarly to the case of cool stars, stellar atmosphere models are needed to perform quantitative abundance analyses of OB-type stars. The basics of stellar atmospheres were described in Section 1.2.2.1. As already mentioned there, in the modelling of hot star atmospheres it is important to correctly account for NLTE and line blanketing effects. In addition, in the case of OB supergiants, one needs also to account for departures from plane parallel geometries and hydrostatic equilibrium. This is nowadays feasible using the modern generation of stellar atmosphere codes (FASTWIND and CMFGEN in a more general case, and TLUSTY when the plane-parallel assumption is valid); however, previous to the 90s this was not possible, and one had to relax some of the physical processes considered.

In order to understand the various approaches followed in the literature (corresponding to the studies presented in Chapter 2), it is important to remark that the abundance analysis is performed in two (traditionally separate) steps. In the first one the structure of the atmosphere is computed using a stellar atmosphere code. In this step one must decide the type of approximations to be considered (*i.e.* fully blanketed *vs.* HHe models, NLTE *vs.* LTE, plane-parallel *vs.* spherical geometries). In a second step, line formation calculations are performed on the resulting model atmosphere. The coupled radiative transfer and statistical equilibrium equations are solved, and spectrum synthesis with refined line-broadening theories is performed by means of a line formation code (either in LTE or NLTE). This way one can find studies in the literature which perform the full analysis in NLTE using a stellar atmosphere code including line blanketing and spherical geometry (*e.g.* Simón-Díaz 2010; Trundle *et al.* 2004; Urbaneja *et al.* 2005b) or a plane-parallel code (*e.g.* Hunter *et al.* 2007; Trundle *et al.* 2007) studies which couple a plane-parallel LTE blanketed atmosphere with NLTE line formation computation (*e.g.* Gummersbach *et al.* 1998; Kilian 1992; Przybilla *et al.* 2008), or those which

combine plane-parallel LTE blanketed atmospheres with LTE abundance determinations (*e.g.* Cunha & Lambert 1992; Rolleston *et al.* 2000; Trundle *et al.* 2002).

Model atoms are another crucial ingredient in the abundance analysis. It is important to remark that detailed non-LTE line formation calculations became possible only once elaborate model atoms using accurate data for energy levels, radiative and collisional transitions and line broadening data were constructed. For the case of oxygen, the extensive model atom presented by Becker & Butler (1988) has been mainly used. In view of progress in the relevant atomic data (see the Appendix), this model atom should perhaps be revised. Other model atoms which are also needed are those of H and He I-II, as well as Si II-IV. Lines of these elements are commonly used to establish the stellar parameters of a star, prior to the oxygen abundance determination.

Derivation of stellar parameters in hot stars. The first step in an abundance analysis is the selection of an appropriate model atmosphere from which to compute the theoretical equivalent widths for the lines of the element one would like to analyse. A stellar atmosphere model is characterised by a set of stellar parameters (T_{eff}, $\log g$, $A(\mathrm{He})$, Z, plus parameters characterising the wind in the case of spherically extended codes).

Nowadays, it has become clear that the most accurate and reliable way to obtain abundances in OB-type stars is to adopt a self-consistent *spectroscopic approach* (see *e.g.* Kilian 1992; Nieva & Simón-Díaz 2011; Przybilla *et al.* 2008; Simón-Díaz 2010). This method requires (i) the full analysis (stellar parameters + abundance determination) to be completed using the same stellar atmosphere model computations, and (ii) the stellar parameters to be determined using only spectroscopic indicators.

The most common diagnostics used for the stellar parameter determination in this approach are the H and He line profiles and/or the equivalent widths of Si lines from different ionisation stages. In this approach, the stellar parameters (T_{eff} and $\log g$) are discussed together with the He and/or Si abundance and the microturbulence, since the derivation of the four quantities is interdependent.

However, the application of this method was not always feasible in the past, and previous abundance determinations often used *photometric* indices to derive the stellar parameters. We can find examples of the use of photometric calibrations in Kane *et al.* (1980), Balona (1984), Brown *et al.* (1986b) and Gies & Lambert (1992). In brief, a grid of stellar atmosphere models is used to obtain theoretical colours (normally corresponding to ubvyβ photometry) by convolving the predicted emergent fluxes with the corresponding filter functions. A calibration of photometric indices *versus* T_{eff} and/or $\log g$ is created (note: although some authors used a photometric calibration for the determination of $\log g$, soon the use of theoretical Hβ line profiles to be fitted to the observed ones was preferred). Finally, stellar parameters are derived from observed photometry using a given calibration. Similarly to the *spectroscopic approach*, since the colour index used as T_{eff} indicator and the width of the Balmer lines are somewhat dependent on both

T_{eff} and $\log g$, an iterative scheme must be used to arrive at the final result (this scheme usually converges to a solution in less than four iterations).

Abundance analysis in hot stars.   There are two different approaches for the abundance analysis in stellar objects: the *curve of growth* method and the *spectral synthesis* method. The *curve of growth* method is based on the behaviour of the line strength with an increase in the chemical abundance of the absorber (see Sect. 1.2.1) and, as in the case of cool stars, incorporates the effect of microturbulence[9]. This method uses line equivalent widths, and hence does not require any knowledge of the exact rotational and macroturbulent broadening mechanisms affecting the line profile.

The applicability of the *curve of growth* method is limited to those cases when equivalent widths of individual lines can be measured. When the projected rotational velocity of the star is high (*i.e.* fast rotators), or when the spectral resolution is not good enough for resolving individual lines (*e.g.* in extragalactic studies beyond the Local Group), a different approach must be considered: the *spectral synthesis* method, one of the few techniques that can be applied when blending is severe. This method is based on the computation of a synthetic spectrum including all the observed lines, which is directly compared to the observed spectrum. In contrast to the *curve of growth* method, this method requires a correct broadening of the line profiles.

We describe below the basics of these methods, giving some notes on the effect of the various sources of uncertainty.

The curve of growth method.   Once the stellar parameters have been established, a grid of stellar atmosphere models whereby the abundance for the studied element and the microturbulence ξ_{t} are varied (the remaining parameters are kept fixed) is computed. In this way, the curves of growth for each line can be constructed by plotting the theoretical equivalent width for each value of ξ_{t} as a function of the abundance (see Fig. 1.4a). From the observed equivalent width and its error, an abundance (and its uncertainty) can be derived for each line and each value of ξ_{t}. The individual line abundances are dependent on the microturbulence, which affects more the strong lines than weak lines. Figure 1.4b shows the $A(\mathrm{O})$ – $\log EW$ diagrams for two different values of ξ_{t} in the case of HD 36591, a B1 V star in the Orion OB1 association (see Simón-Díaz 2010). The value of ξ_{t} that minimises the dependence of the line abundances on the line strength in the $A(\mathrm{O})$ – $\log EW$ diagrams (*i.e.* produces a zero slope) will be the adopted microturbulence[10]. Figures 1.4c.1 and 1.4c.2 show the dependence of the slope of the $A(\mathrm{O})$ *vs* $\log EW$ relation and of $A(\mathrm{O})$ on ξ_{t}, respectively. These figures

---

[9]Microturbulence (ξ_{t}) is a free parameter that was included in the stellar abundance analyses to solve the discrepancy found in the line abundances derived from weak and strong lines. Its physical meaning is supposed to be related to the small scale turbulent motions of the stellar plasma which would mainly affect the strong lines close to saturation.

[10]These diagrams can also be used as a diagnostic tool to check the reliability of the various lines available for the abundance determination.
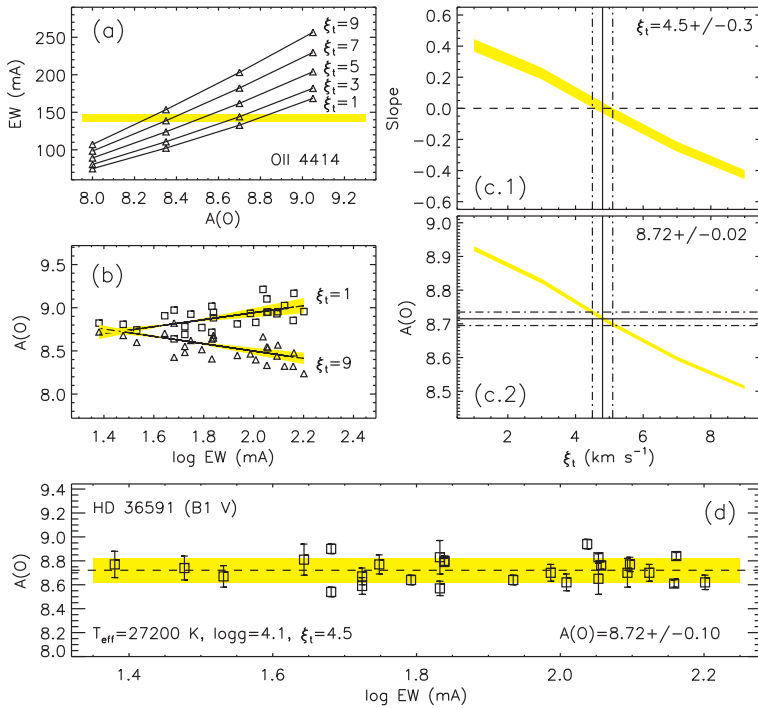
Fig. 1.4. Example of the steps followed in the oxygen abundance analysis of an early-B type star by means of the *curve of growth* method. See the text for explanations.

allow one to estimate the uncertainties in ξ_t by considering the errors derived for the slope (due to errors in the individual line abundances), and the contribution of this uncertainty to the total error associated with the final oxygen abundance value. This uncertainty depends mainly on the quality of the spectra via the errors associated with the *EW* measurement (in the example shown in Fig. 1.4 this is ~ 0.02 dex). In the last step, abundance values for each line as well as their uncertainties are calculated for the adopted microturbulence (Fig. 1.4d). The final abundance value is estimated through a weighted mean of the linear individual line abundance, and its uncertainty is associated with this mean. The final uncertainty in the total abundance takes into account three different sources of errors: those associated with the line-to-line abundance dispersion, those derived from the error in the determined microturbulence and finally those referred to the uncertainties in the stellar parameters (see comment below and Fig. 1.5). All these sources of error are added quadratically to estimate the final abundance uncertainty.

The spectral synthesis method. There are certain cases in which the measurement of equivalent widths of individual lines is not feasible because the diagnostic lines are blended with lines from other elements. It is then possible to select one or
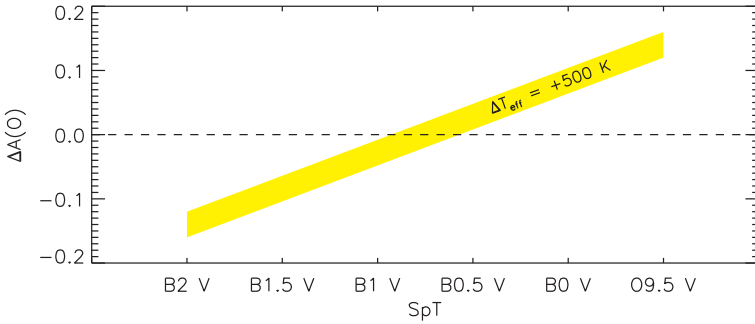
Fig. 1.5. Deviation from the actual oxygen abundance resulting from an overestimate of 500 K in early-B dwarfs. Maximum deviations of −0.15 and +0.15 dex can be found in B2 V and O9.5 V stars, respectively. Minimum deviations are obtained for spectral types B1 − B1.5, where the equivalent width of the O II lines is maximum and hence only slightly dependent on temperature.

several groups of blended lines and perform the abundance analysis by comparing a synthetic spectrum with the observed spectrum.

Similarly to the *curve of growth* method, the abundance analysis by means of the *spectral synthesis* method is performed on the basis of a previously defined stellar atmosphere model once the stellar parameters have been determined.

All the elements whose lines are present in the blending must be included in the line formation calculations. Also, the broadening of the lines must be correctly assumed when computing the final broadened synthetic spectrum to be compared with the observed one.

Abundance uncertainties in hot stars. Several sources of systematic uncertainties must be considered.

- *Equivalent width measurements.* The *curve of growth* method for abundance determination is based on the comparison of theoretical and observed equivalent widths. Therefore, a proper determination of line equivalent widths in the observed spectrum is crucial. There are several factors that may affect the accuracy and the reliability of these measurements: (i) the quality of the spectrum (spectral resolution and signal-to-noise ratio), (ii) the continuum placement, (iii) the integration limits, (iv) the scattered light, (v) the effect of binarity, (vi) the presence of blended lines and (vii) the use of a Gaussian fit or more elaborated methods (in supergiants, the use of a Gaussian fit may slightly underestimate the contribution of the extreme wings). Also, weak line measurements are limited by the signal-to-noise ratio, and are more difficult if $v \sin i$ is large.

- *Atomic data and line abundance dispersion.* The typical accuracy in the atomic data needed to calculate the oxygen abundance in hot stars is

$\simeq 10-15\%$ (see Appendix). Even though lines from the same multiplet should give similar abundances, large discrepancies are found in some cases. This may indicate an error in the equivalent width measurement, the presence of a blended line and/or an incorrect determination of the line $\log gf$ value. The resulting consequence is a dispersion in the individual line abundances which not only contributes to the final uncertainty of the derived abundance, but also to the microturbulence determination.

- *Microturbulence.* This is a key parameter in abundance analyses of OB-type stars. Even if microturbulence is considered a free parameter (we do not enter here in a discussion about its physical origin and interpretation in the case of hot stars), the choice of the microturbulent velocity in the abundance analysis is not always straightforward. As mentioned above, this quantity was included in the analyses to force weak and strong lines to yield the same abundance.

- *Stellar parameters.* This is probably the main source of systematic errors affecting the oxygen abundance determination in OB-type stars. The basic idea is that a bad determination of the stellar parameters implies incorrect abundances, with larger effects produced when the actual effective temperature of the star is far from the temperature regime where the equivalent width of the O II lines is maximum. This is illustrated in Figure 1.5 for the case of B dwarfs.

- *Metallicity.* The common assumption made in OB-type star studies is that the metallicity of the underlying atmosphere has no impact on line formation. However, as pointed out by Gummersbach *et al.* (1998), the metallicity of the underlying atmosphere has a non-negligible impact on the temperature structure and the subsequent line formation. For example, the effect of an increased metallicity on a subsolar-abundance atmosphere with a $T_{\rm eff} \geq 28000$ K is to raise the stellar parameters $T_{\rm eff}$ and microturbulence, to leave $\log g$ roughly unaffected and to lower the chemical abundances. The effect would be the contrary for stars with $T_{\rm eff} \leq 27000$ K. This may have important consequences in the study of oxygen abundance gradients in spiral galaxies.

The *curve of growth* method allows the identification of several of the sources of uncertainty (*e.g.* blended lines not initially identified, or cases in which the $\log gf$ values considered in the atomic models are not correct) and to study the effects that each of them has on the final abundance. With the *spectral synthesis* method, the various effects are not so easily identified and/or isolated. Therefore, the application of the *spectral synthesis* method should be ideally preceded by the *curve of growth* analysis of a star with similar parameters in order to gain some experience. Thus one can take decisions about, for example, the assumed microturbulence or the best diagnostic lines to use.

1.2.2.2   Interstellar medium

Neutral ISM.

Local ISM.   Gaseous oxygen can be observed and measured in absorption in the interstellar medium of our Galaxy on the sight lines of stars, or in the interstellar medium of high-redshift galaxies and the intergalactic medium on the sight lines of quasars. The method, which is the same in all those cases, is described as follows.

Column density measurements. The equivalent widths can be measured and directly translated into column densities for unsaturated absorption lines. If several transitions of a given element are available with different oscillator strengths, their equivalent widths can be measured and an empirical curve of growth can be drawn, allowing the ionic column density, N, and the Doppler broadening, b, to be measured, and the possible saturation to be evaluated.

The apparent optical depth method (AODM) allows similar studies by measuring the optical depth as a function of the wavelength (Savage & Sembach 1991). Indeed, the apparent column density of an ion in each velocity bin, $N_a(v)$ in units of atoms cm^{-2} (km s^{-1})$^{-1}$, is related to the apparent optical depth in that bin, $\tau_a(v)$, by the expression

$$N_a(v) = \frac{m_e c}{\pi e^2} \frac{\tau_a(v)}{f \lambda_{\mathrm{lab}}} = 3.768 \times 10^{14} \frac{\tau_a(v)}{f \lambda_{\mathrm{lab}}(\mathring{A})} \,, \qquad (1.13)$$

where f is the oscillator strength of the transition at the wavelength λ_{lab} in Å. The apparent optical depth is deduced directly from the observed intensity in the line at velocity v, $I_{\mathrm{obs}}(v)$, by

$$\tau_a(v) = -\ln \left[I_{\mathrm{obs}}(v)/I_c(v) \right], \qquad (1.14)$$

where I_c is the intensity in the continuum. The total column density of an ion X, $N_{\mathrm{aod}}(X)$, is obtained by summation of Equation (1.13) over the velocity interval where the line absorption takes place. This method is solely applicable when the profiles of the absorption lines are fully resolved. The apparent optical depth method provides, in addition, a stringent consistency check when several ISM lines arising from the same ground state of an ion, but with different values of the product $f\lambda_{\mathrm{lab}}$, are analysed. The run of $N_a(v)$ with v should be the same for all such lines. In general, this condition will not be satisfied if there are *saturated* components in the absorption lines: the deduced value of $N_a(v)$ will appear smaller for lines with higher values of $f\lambda_{\mathrm{lab}}$.

The Voigt profile fitting of absorption lines, via a χ^2 minimisation of the difference between the theoretical and observed profiles, also allows a measure of the ionic column density and the Doppler broadening (Fig. 1.6). Profile fitting is a particularly powerful tool, especially in the case of line blending and/or when several species of different elements but from the same cloud are detected.
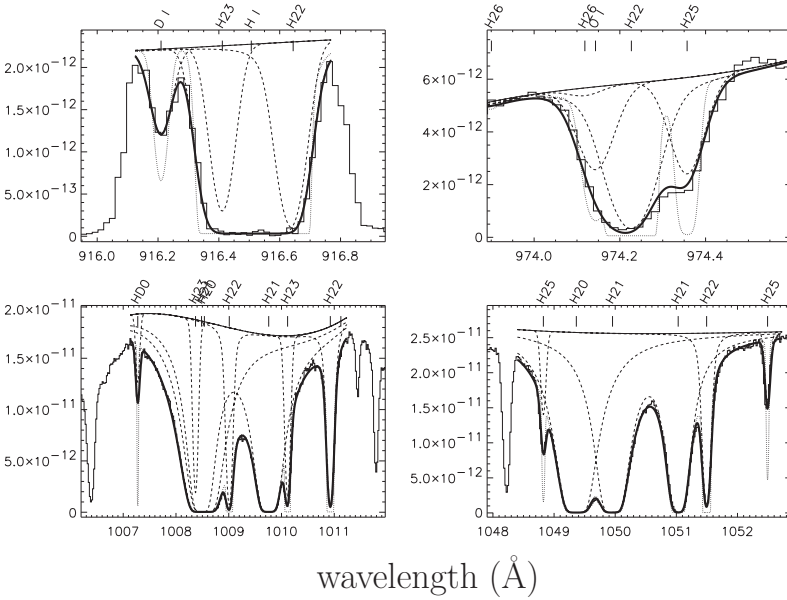
Fig. 1.6. Examples of absorption line profile fittings. The histogram lines are the data (FUSE observations of the distant star HD 90087), the solid lines are the fits (thick) and continua (thin). The dashed lines are the fits for each species. The dotted lines are the model profiles prior to convolution with the line spread function. The Y-axis is flux in erg/cm^2/s/Å. The species are identified at the top of the plots for each line. The H$_2$ lines of the levels $J = 0$ to $J = 6$ are labelled H20 to H26 and HD ($J = 0$) is labelled HD0. Figure reproduced from Hébrard *et al.* (2005).

The abundances relative to hydrogen are hence defined as

$$X/H = \log(N(X)/N(H)). \qquad (1.15)$$

Source of uncertainties in column density measurements. Statistical error bars on column density measurements can be evaluated from the error on the equivalent width measurements or from the χ^2 variations computed in the line profile fits. These errors are directly linked to the uncertainties in the flux and wavelength calibrations. Additional uncertainties linked to the method itself are also present. We try to list here these potential systematic uncertainties:

- *Atomic data.* Whereas the atomic data of the hydrogen atom are well known, this is not the case for species with more complex electronic structures, and especially oxygen. It is common to have $\sim$20% uncertainties in the oscillator strength values of oxygen transitions.

- *Line spread function shape.* An observed line is the actual line convolved by the line spread function of the spectrograph used, and this function is not

always perfectly known. This source of uncertainty is present in line profile fitting, but it can also be significant in equivalent width measurements if the line spread function presents wings that can be lost in the continuum.

- *Flux background.* Some spectrographs might have scattered light, especially the high resolution ones, which can make uncertain the zero flux level of the spectra, and thus the depth of the absorption lines.

- *Continua.* Each line detected is in absorption against the continuum of a star or a quasar. These continua can be simple but they can also be non-trivial, especially in crowded spectra with numerous absorption lines. They can be fitted by physical models or simple mathematical functions.

- *Velocity structure.* The number of clouds, and more generally the velocity structure along the sight line, can be uncertain, especially if the spectral resolution is low. Some components may be unresolved. The effect of the spectral resolution on the line profile is illustrated in Figure 1.7. The spectral resolution is, indeed, a key parameter in the measurement accuracy of column densities. The multi-ion, single-component curve of growth analysis technique systematically underestimates the column densities of metal-line profiles which comprise several clouds (see the discussion in Prochaska 2006).

Numerous potential systematic errors could be reduced by using unsaturated lines only, located on the linear part of the curve of growth. Column densities measured from such lines are less dependent on the line spread function and the velocity structure on the sight line. They are also weakly sensitive to the temperature or to the turbulence in the absorbing gas.

Available lines. Lines of ionised oxygen and of molecules including oxygen atoms are available, but most of the measurements of oxygen are performed on neutral oxygen (O I). The neutral oxygen resonance lines are located in the ultraviolet range, so space telescopes such as Copernicus, FUSE or the Hubble Space Telescope are essential to observe them in the interstellar medium. Toward quasars, some distant interstellar and intergalactic clouds are redshifted enough to allow O I observations from ground-based telescopes. Hydrogen lines, mandatory to perform O/H abundance measurements, are in a similar wavelength domain.

All the resonance lines of neutral oxygen are listed in Table 1.4, sorted by decreasing oscillator strength. The ones at the top of the list are useful for the lowest oxygen column densities, but they become saturated as the column density increases. The ones at the bottom of the list are those that can remain unsaturated for the highest column densities, but they are not detected if the column density is too low.

These oxygen abundance measurements, although being derived in the gas phase, are unaffected by dust depletion and ionisation effects. Indeed, oxygen is only very mildly refractory (Savage & Sembach 1996), and O I is thought to follow H I closely due to charge exchange reactions (Field & Steigman 1971), implying that the O I/H I ratio accurately determines O/H without having to apply ionisation corrections.
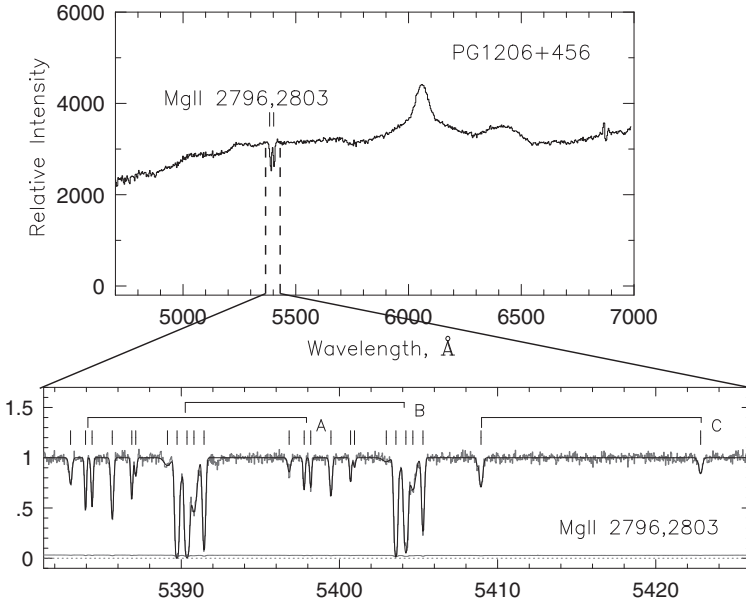
Fig. 1.7. This figure illustrates the dramatic effect of the spectral resolution on the Mg II doublet. *Upper panel:* spectrum at $R = 3000$ of PG 1206 + 459. The absorption lines that are apparent at an observed wavelength of ∼5400 Å are the Mg II $\lambda2796$, $\lambda2803$ lines from a system at $z_{abs} = 0.927$. *Lower panel:* the remarkable kinematic structure revealed at a resolution of $R = 45\,000$ for the same system. The system can be separated into two "clusters" of clouds, labelled A and B. Another weaker Mg II doublet is observed at 5409 and 5423 Å from a system at $z_{abs} = 0.934$, labelled C. The solid line is the result of multiple Voigt profile fitting with a cloud component centred on each of the vertical bars drawn above the spectrum. Figure reproduced from Charlton *et al.* (2000).

High redshift ISM.   The method to measure the oxygen abundance in high-redshift galaxies is closely related to their selection technique. Different techniques to detect high-redshift galaxies have indeed been elaborated in different wavelength ranges, depending on their star formation activity and their luminosity.

Prior to the advent of 8–10 m class telescopes which made it possible to identify and study high-redshift galaxies directly, our knowledge of the galaxy population at $z > 0.5$ relied almost exclusively on galaxies detected in absorption in the spectra of background quasars. Among the different classes of quasar absorbers, damped Lyα systems (DLAs) – with column densities of neutral hydrogen in excess of $N(\text{H I}) = 2 \times 10^{20}\,\text{cm}^{-2}$ – have received great attention. These absorbers account for most of the neutral gas seen in absorption along random sight lines to distant quasars, and dominate the neutral gas content of the Universe available for star formation. They are therefore believed to be the progenitors of present-day galaxies (see Wolfe *et al.* 2005, for a review).

Table 1.4. Neutral oxygen O I lines from Morton (1991) and Morton (2003).

Vacuum rest-frame wavelength (in Å)	Oscillator strength
988.7734	4.65×10^{-2}
1302.1685	4.80×10^{-2}
971.738†	1.38×10^{-2}
1039.2304	9.20×10^{-3}
988.6549	8.30×10^{-3}
948.6855	6.31×10^{-3}
936.6295	3.65×10^{-3}
976.4481	3.31×10^{-3}
929.5168	2.29×10^{-3}
950.8846	1.58×10^{-3}
924.9500	1.54×10^{-3}
921.8570†	1.19×10^{-3}
919.6580†	9.47×10^{-4}
918.0440	6.14×10^{-4}
988.5778	5.53×10^{-4}
930.2566	5.37×10^{-4}
916.8150†	4.74×10^{-4}
915.8660	3.74×10^{-4}
925.4460	3.50×10^{-4}
915.0960	2.98×10^{-4}
922.2000	2.45×10^{-4}
919.9170	1.78×10^{-4}
915.9880	7.86×10^{-5}
915.1990	6.25×10^{-5}
974.0700	1.56×10^{-5}
1355.5977	1.16×10^{-6}

† Triplet structure used.

As discussed above, resonance absorption lines in the rest-frame ultraviolet are the main available tools for determining the abundances in the cool interstellar gas. They have been widely used in the ISM of the Milky Way. The gas revealed in DLAs corresponds to the ISM of the associated galaxy. Therefore, similarly to the ISM studies in the Milky Way, the ultraviolet resonance absorption lines can be used to determine the abundances of the DLA galaxies, with the advantage that, thanks to their high redshifts, these lines are shifted to the optical domain and are hence accessible from ground-based facilities. This method is capable of achieving high precision. Indeed, the relatively strong brightness of a large number of background quasars – with magnitudes between 15 and 18.5 – allows one to obtain high resolution ($R \sim 40\,000$) and high signal-to-noise ratio spectra of DLAs at redshifts up to 5.5 on $8-10$ m class telescopes.

These high-quality spectra are usually rich in interstellar metal lines which accompany the strong Lyα line. They may lead to accurate abundance measurements

of up to 25 elements in DLAs (*e.g.* Dessauges-Zavadsky *et al.* 2004, 2006; Prochaska *et al.* 2003). Indeed, the Voigt profile fitting of the damped Lyα line and of the metal lines allows the determination of accurate column densities of H I, N(H I) and of metal ions, N(X), respectively. The abundances relative to hydrogen are obtained as X/H = log(N(X)/N(H)). This is, however, only valid provided:

  (i) one is in a regime where the metal absorption line optical depth is low, *i.e.* line saturation is not a concern;

 (ii) the line blending with other metal lines or with H I lines from the Lyα forest is excluded;

(iii) ionisation corrections are negligible; and

 (iv) dust depletion can be accounted for.

These are all tractable problems in DLAs, but some elements are more affected by them than others.

The abundance of oxygen is among the most difficult abundances to determine in DLAs. While both the dust depletion and ionisation are not big issues for this element as in the local ISM (see above), the atomic parameters of the O transitions (rest-wavelength positions and oscillator strengths) are. There are usually only two O I lines at $\lambda_{\rm rest} = 1302$ and $1355\,$Å available redwards of the Lyα forest and these lines are, respectively, either strongly saturated or extremely weak (never detected). They hence only lead to a lower and an upper limit, respectively, differing by over an order of magnitude. All the other O I transitions with a large range of oscillator strengths fall shortwards of the quasar's Lyα emission, *i.e.* in the Lyα forest. This severely limits the success of O abundance determination, because of possible line blends with H I lines, and restrains the access of these O I transitions to DLAs with redshifts higher than $z = 2.1$ – the minimum redshift at which these transitions are redshifted beyond the atmospheric cutoff.

With the discovery that long-duration ($t > 2\,$s) gamma-ray bursts (GRBs) are extragalactic events (Metzger *et al.* 1997), it was immediately realised that these phenomena offer a means of probing the gas in the early Universe similar and complementary to the quasar absorption lines. Identified exclusively with star-forming galaxies (Fruchter *et al.* 2006), GRB events are believed to result from the death of a massive star (Woosley & Bloom 2006). The majority emit a bright, power-law afterglow due to the deceleration of the relativistic jet in the surrounding interstellar or circumstellar medium. The extraordinary luminosity of these events allows their detection and analysis up to very high redshifts ($z > 10$), potentially enabling research on the epoch of reionisation when bright quasars were extremely rare (Lamb & Reichart 2000).

Like quasars, GRBs provide a bright – albeit transient – light beam. Many of the recent advances were enabled by the launch of the *Swift* satellite. Thanks to its rapid and precise localisation of GRBs and thanks to the target-of-opportunity programmes on 8–10 m class telescopes, high-quality and high-resolution spectroscopy has been achieved for a number of afterglows. In addition to studies of

the intergalactic medium, the GRB afterglow spectrum records data on the gas local to the event as well as the ISM of the GRB host galaxy surrounding the star-forming region. In turn, analysis yields constraints on the physical conditions within star-forming galaxies in the early Universe.

Most of the GRB host galaxies are characterised by a damped Lyα absorption with a very large H I column density – the median value being $N(\text{H I}) = 10^{21.7}\,\text{cm}^{-2}$ (Prochaska $et\ al.$ 2007). Accurate chemical abundances in high-redshift GRB host galaxies for which the Lyα line is accessible in optical spectra ($z > 1.5$) are thus derived in the same way as in the DLAs. We are hence confronted not only with the same technique, but also with the same uncertainties and difficulties as those encountered in DLAs. The O abundance determination in GRB hosts has an additional difficulty: the often insufficient signal-to-noise ratio in the blue spectral regions ($\lambda_{\text{rest}} < 4500\,\text{Å}$) because of the lack of long enough exposure times. These regions are nonetheless necessary for the recovery of most of the O I lines that have rest-frame wavelengths bluewards of the Lyα line.

Warm ISM.   The best ultraviolet lines available for studying the warm-hot interstellar plasma ($T > 10^5\,\text{K}$) are the O VI λ1031, λ1037 doublet. To create the O VI ions from the preceding oxygen ionisation stages requires 114 eV. In principle, these ionisation energies can be supplied either by electron collisions in hot plasma or by extreme UV photons.

O VI peaks in abundance at $T = 3 \times 10^5\,\text{K}$ under collisional ionisation equilibrium conditions (Gnat & Sternberg 2007; Sutherland & Dopita 1993). Surveys of O VI absorption have been used to establish the presence of warm-hot ionised medium in the Milky Way and its surrounding network of high-velocity clouds (Fox $et\ al.$ 2006; Savage $et\ al.$ 2003; Sembach $et\ al.$ 2003). Additionally, O VI formed by photoionisation has been reported for narrow O VI absorbers in the intergalactic medium at $z \gtrsim 2$ (Bergeron & Herbert-Fort 2005; Bergeron $et\ al.$ 2002; Carswell $et\ al.$ 2002; Levshakov $et\ al.$ 2003; Lopez $et\ al.$ 2007). On the other hand, very little is known so far about the presence or properties of a warm-hot ionised medium in the high-redshift galaxies associated with the damped Lyα absorbers (Fox $et\ al.$ 2007). Besides the neutral gas phase, spectroscopic observations of DLAs have revealed both cold molecular ($T \lesssim 300\,\text{K}$, Ledoux $et\ al.$ 2003; Petitjean $et\ al.$ 2000; Srianand $et\ al.$ 2005) and warm ionised ($T \sim 10^4\,\text{K}$, Ledoux $et\ al.$ 1998; Lu $et\ al.$ 1996; Wolfe & Prochaska 2000) components with a multiphase structure resembling that seen in the Galactic interstellar medium. Since, in addition, there is evidence for star formation in DLAs (see Wolfe et al. 2005), Type II supernovae should create observable regions of hot, shock-heated interstellar plasma. The separate processes of accretion and shock-heating of intergalactic gas may also lead to the production of a warm-hot ionised medium. Thus, a warm-hot ionised medium is expected to be present in DLAs.

O VI is only accessible from the ground at $z > 2$ where the transitions become redshifted enough to overcome the atmospheric cutoff near 3100 Å. Since they lie in the Lyα forest, there is a high level of confusion in separating O VI from

Table 1.5. X-ray oxygen absorption lines. The calculations are done for a hydrogen column density of 10^{24} m^{-2}. W_{max} corresponds to the peak of the equivalent width, reached at a temperature T_{max} (in K). They are obtained assuming a plasma in collisional ionisation equilibrium with proto-solar abundances (Lodders 2003) and only thermal broadening.

λ (Å)	W_{max} (mÅ)	log T_{max}	ion
16.006	2.6	6.37	O VIII
17.306	2.8	6.06	O VII
17.768	4.4	6.11	O VII
18.629	6.9	6.19	O VII
18.967	8.7	6.41	O VIII
18.973	6.5	6.39	O VIII
21.602	12.1	6.27	O VII

H I interlopers that becomes more difficult with increasing redshift. The expected doublet ratio $\tau(\mathrm{O\ VI}\ \lambda1031)/\tau(\mathrm{O\ VI}\ \lambda1037)$ is equal to 2 in all pixels through the line profile. It helps to highlight the presence of contaminations by H I interlopers.

We can calculate the total hydrogen column density in the warm-hot, O VI-bearing phase using the relation

$$N_{\mathrm{HII}}^{\mathrm{Hot}} = \frac{N_{\mathrm{Ovi}}}{f_{\mathrm{Ovi}}(\mathrm{O/H})_{\mathrm{Hot}}} = \frac{N_{\mathrm{Ovi}}}{f_{\mathrm{Ovi}}(\mathrm{O/H})_{\mathrm{Neut}}} \frac{(\mathrm{O/H})_{\mathrm{Neut}}}{(\mathrm{O/H})_{\mathrm{Hot}}} \qquad (1.16)$$

where $f_{\mathrm{O\ vi}} = N_{\mathrm{O\ vi}}/N_{\mathrm{O}}$ is the fraction of oxygen atoms in the five-times ionised state. Assuming solar relative abundance ratios in both the neutral and plasma phases, we have [O/H]$_{\mathrm{Hot}}$=[Z/H]$_{\mathrm{Neut}}$. By using Z$_{\mathrm{Hot}}$ and Z$_{\mathrm{Neut}}$ as shorthands for the absolute metallicities in the hot and neutral phases, we can write

$$N_{\mathrm{H\ II}}^{\mathrm{Hot}} = \frac{N_{\mathrm{O\ vi}}}{f_{\mathrm{O\ vi}}10^{[\mathrm{Z/H}]_{\mathrm{Neut}}}(\mathrm{O/H})_{\odot}} \frac{\mathrm{Z}_{\mathrm{Neut}}}{\mathrm{Z}_{\mathrm{Hot}}}. \qquad (1.17)$$

We cannot directly measure the metallicity of the plasma phases so we assume Z$_{\mathrm{Neut}}$/Z$_{\mathrm{Hot}}$ is equal to 1. The remaining unknown is $f_{\mathrm{O\ vi}}$ which will depend on the ionisation mechanism. The *maximum* value $f_{\mathrm{O\ vi}}$ reaches in a collisionally ionised plasma is 0.2 at $10^{5.45}$ K (Sutherland & Dopita 1993). We can therefore estimate *lower* limits to the warm-hot hydrogen column densities using the maximum values of $f_{\mathrm{O\ vi}}$.

Hot ISM. Oxygen lines are among the most important X-ray absorption lines. The best known oxygen X-ray absorption lines are the 1s-2p line of O VII at 21.60 Å and the O VIII Lyα doublet at 18.97 Å. The well known 2s-2p doublet of O VI is observed in the FUV at 1032 and 1038 Å (see Sect. 1.2.2.2). While the spectral line characteristics of only highly ionised oxygen ions are given in Table 1.5, note that spectral lines of all ionisation stages are present in the 17−24 Å band (see

Table 6 in Kaastra *et al.* 2008). Observations of absorption lines allow one to determine the *density and ionisation of the absorbing material*. Note that all the phases of the ISM (if present in the line of sight) can be seen in X-ray absorption towards bright X-ray sources, while only the hot phase is seen in X-ray emission. Regarding the photoelectric continuum absorption, it is at the lowest energies that X-rays are the most strongly absorbed. Oxygen contributes significantly to the interstellar absorption cross section above 0.5 keV while below the carbon edge, hydrogen and helium dominate. At the highest energy, above 7.1 keV, iron is the main opacity. The absorption edges shift to higher energies for higher ionisation.

1.2.3   Methods using emission lines

1.2.3.1   Photoionised nebulae

Photoionised nebulae in a nutshell.   The most common case is that of nebulae that are photoionised by a star, a group of stars or by radiation from an active galactic nucleus. However, ionisation can also be produced in shocks, where kinetic energy is transformed into thermal energy, and where the thermal electrons – if they are energetic enough – can ionise the gas. The cooling radiation from shocks also produces high energy photons that contribute to the ionisation. In the astronomical universe, shocks can be produced for example by the impact of supernovae or of jets on the interstellar medium, but also by stellar winds. Most of the nebulae that are studied for abundance determinations with emission lines are photoionised nebulae. In such nebulae, shocks may play a role in shaping the gas distribution, but their impact on the ionisation and overall temperature of the nebula are expected to be minor.

In most photoionised nebulae, the gas is in ionisation and thermal equilibrium, as the dynamical and stellar timescales are larger than the atomic time scales. This is fortunate because one need not care about the history of the nebulae to derive their chemical composition. At each point in the nebula, the relative populations of the different ions of an element are determined by the equilibrium between ionisation (essentially photoionisation) and recombination processes.

The ionisation structure results from the spatial variation of the ionising radiation field inside the nebula, which is modified by absorption and by dilution. The ionisation parameter is a very useful concept to characterise the general ionisation level of a nebula (under the assumption of constant density). It is usually defined by

$$U = Q(\mathrm{H}^0)/(4\pi R^2 n c), \tag{1.18}$$

where $Q(\mathrm{H}^0)$ is the number of ionising photons, R is either the Strömgren radius or a typical distance from the gas cloud to the ionising star and c is the speed of light. U is thus approximately the ratio of the ionising photon pressure to the gas pressure, and the nebular ionisation structure – for a given "hardness" of the ionising radiation field – depends essentially on U.

The temperature is the result of the balance between heating processes (essentially photoionisation of H and He which produces photoelectrons that share their energies with the thermal electrons) and cooling processes (free-free radiation, recombination and, most of all, collisional excitation of low-lying levels of metals − principally oxygen – followed by line emission). The electron temperature in a nebula is thus higher for hotter ionising sources and lower at higher metallicity. What is less intuitive is that, in general, the electron temperature does not vary much across the nebula, and does not necessarily decrease outside; indeed, it is not the total intensity of the ionising radiation field which determines the heating rate per unit volume, but only its spectral energy distribution above 13.6 eV. What counts is the amount of energy gained per ionisation, since the number of ionisations is exactly balanced by the number of recombinations.

Methods for oxygen abundance determinations. Methods to derive abundances in nebulae can be grouped into four classes: (i) the so-called direct method, which derives the abundance using information directly from the observed spectrum of a given nebula; (ii) statistical methods, which use relations obtained from families of objects; (iii) the third class has no particular denomination, it compares a given object with a grid of photoionisation models and (iv) tailored photoionisation modelling, in which the abundance is inferred from the model giving the best fit to the data. The latter method is often considered the best, but as we will see, this is not necessarily the case in practice.

Direct methods. Here, one uses the observed line ratio

$$\frac{I(O_l^j)}{I(H\beta)} = \frac{\int n(O^j) n_e \epsilon_{jl}(T_e, n_e) dV}{\int n(H^+) n_e \epsilon_{H\beta}(T_e, n_e) dV}, \tag{1.19}$$

where $I(O_l^j)$ is the intensity of a line l emitted by an oxygen ion O^j, $I(H\beta)$ is the intensity of the $H\beta$ line and the ϵ's are the line emissivities in erg cm^{-6} s^{-1}, directly to obtain the ionic abundance ratio:

$$\frac{\int n(O^j) n_e dV}{\int n(H^+) n_e dV} = \frac{I(O_l^j)/I(H\beta)}{\epsilon_{jl}(T_l, n_l)/\epsilon_{H\beta}(T_\beta, n_\beta)}, \tag{1.20}$$

where T_l and n_l are respectively the electron temperature and density representative of the emission of the line l, and T_β and n_β are the electron temperature and density representative of the emission of $H\beta$. The direct methods for abundance determinations are also called temperature-based methods, because they require the electron temperature to be measured directly from the spectrum.

Assuming that the chemical composition is uniform in the nebula, one then obtains the oxygen abundance

$$\frac{n(O)}{n(H)} = \frac{I(O_l^j)/I(H\beta)}{\epsilon_{jl}(T_l, n_l)/\epsilon_{H\beta}(T_\beta, n_\beta)} \; icf, \tag{1.21}$$

where icf is the ionisation correction factor, equal to

$$icf = \frac{\int n(O^j)/n(O)n_e dV}{\int n(H^+)/n(H)n_e dV}. \tag{1.22}$$

In the case where several ions of a same element are observed, which is generally the case for oxygen, one can use a "global" icf adapted to the ions that are observed (e.g. $icf(O^+ + O^{++})$ for planetary nebulae in which oxygen may be found in higher ionisation stages.

The oxygen ions that are commonly used for oxygen abundance determinations in ionised nebulae[11] are O^+ ([O II] $\lambda3726+29$) and O^{++} ([O III] $\lambda5007$[12]). O^{3+} has strong lines only in the UV ([O IV] $\lambda1661$) and in the IR ([O IV] $\lambda25.8$ μm) and O^{4+} and O^{5+} only in the UV ([O V] $\lambda1213$ and [O VI] $\lambda1031$).

In H II regions, one has $icf(O^+ + O^{++})=1$, making the direct abundance determination of the oxygen abundance very straightforward[13]. Oxygen is the only element for which the abundance can be derived in such a simple manner. This is very lucky, in view of the important role that oxygen plays in astronomy.

In planetary nebulae, whose exciting stars are evolved intermediate-mass stars, with temperatures often higher than those of massive stars, ionisation stages higher than O^{++} are present. To correct for those, one generally uses the ionisation correction factors proposed by Kingsburgh & Barlow (1994), which are based on photoionisation models for a dozen planetary nebulae.

The [O III] $\lambda4363/5007$ and [O II] $\lambda7320+30/3726+29$ line ratios are direct measures of the electron temperature in the O^{++} and O^+ zones, respectively, while the [O II] $\lambda3726/3729$ ratio measures the electron density in the O^+ zone. In practice, one rather uses the [N II] $\lambda5755/6584$ ratio to measure the electron temperature and the [S II] $\lambda6716/6730$ ratio to measure the electron density in the O^+ zone because these ratios are easier to measure. There is no practical way to measure the temperature of higher ionisation zones, which may occur in planetary nebulae excited by stars with temperatures above, say, 60 000 K. In practice, this is not a problem if only lines of O^+ and O^{++} ions are used.

An interesting revision of the classic direct method for abundance determination has been proposed by Milanova & Kholtygin (2009), which aims at accounting at the same time for temperature and density fluctuations, as well as errors in the line intensities. However, a thorough discussion of the limits of this method would be needed.

---

[11] Due to the fact that the ionic abundances are obtained with reference to H^+ and that O^0 and H^0 are strongly linked by charge exchange, one does not compute the abundance of neutral oxygen to obtain O/H.

[12] It sometimes happens that the [O III] $\lambda5007$ line, which can be very strong, is saturated. Then, the [O III] $\lambda4959/5007$ ratio strongly deviates from its theoretical value of 2.98. In that case, [O III] $\lambda4959$ is used instead of [O III] $\lambda5007$ for abundance determinations.

[13] The only case where this relation is not exactly verified is in objects which show some He II line emission (due to the presence of hot Wolf-Rayet stars or to some X-ray sources), but then the correction for unseen stages of oxygen is negligible with respect to other sources of errors.

Statistical methods. In many cases, the weak [O III] $\lambda4363$ or [N II] $\lambda5755$ lines are not available. This can happen for different reasons: the gas temperature is too low, the spectra are too noisy, or else the data consist of narrow band images only in the stronger lines. In such cases, it is still possible to estimate the oxygen abundance – or rather the metallicity – by using the so-called "strong line methods". Such methods are very different from the temperature-based methods in that they are statistical in nature: they allow one to derive the metallicity of an object only on the assumption that it shares the same properties as those of the objects used to calibrate the method. In practice, such methods work rather well for giant H II regions, since it appears that giant H II regions form a narrow sequence (see *e.g.* McCall *et al.* 1985), where the hardness of the ionising radiation field and the ionisation parameter are closely linked to the metallicity. Indeed, an increased metallicity enhances the metal line blocking of the emergent stellar flux in the extreme ultraviolet and softens the ionising spectrum. In addition, the pressure exerted on the nebular gas increases with the strength of the stellar winds, which are related to metallicity, and this in turn decreases the ionisation parameter (Dopita *et al.* 2006). On the other hand, for planetary nebulae, there is no such sequence, since the temperature of the ionising star depends above all on the evolutionary state of the nebula.

Unlike direct methods for abundance determinations, statistical methods have to be calibrated. The reliability of these methods depends not only on the choice of an adequate indicator, but also on the quality of the calibration. This calibration can be done using grids of *ab initio* photoionisation models (McGaugh 1991), or some tailored photoionisation models (Pagel *et al.* 1979), abundances derived from direct methods (Pilyugin & Thuan 2005), or objects other than H II regions thought to have the same chemical composition (Pilyugin 2003).

The oldest and still most popular statistical method is the one based on oxygen lines. Pagel *et al.* (1979) introduced the ([O II] $\lambda3727$ + [O III] $\lambda4959,5007$)/Hβ ratio (later referred to as R_{23} and then O_{23}) to estimate O/H. This method has been calibrated many times with results that may differ by about 0.5 dex. McGaugh (1991) and later Pilyugin (2000, 2001) refined the method to account for the ionisation parameter.

Many other metallicity indicators have been proposed: [O III] $\lambda5007$/[N II] $\lambda6584$ (O_3N_2) by Alloin *et al.* (1979); [N II] $\lambda6584$/Hβ (N_2), by Storchi-Bergmann *et al.* (1994); ([S III] $\lambda9069$+[S II] $\lambda6716,6731$)/Hα (S_{23}) by Vilchez & Esteban (1996); [N II] $\lambda6584$/[O II] $\lambda3727$ (N_2O_2) by Dopita *et al.* (2000); [Ar III] $\lambda7135$/[O III] $\lambda5007$ (Ar_3O_3) and [S III] $\lambda9069$/[O III] $\lambda3869$ (S_3O_3) by Stasińska (2006); [Ne III] $\lambda9069$/[O II] $\lambda3727$ (Ne_3O_2) by Nagao *et al.* (2006).

There are however some points to be aware of. Methods such as O_{23} or S_{23} are bound to be double-valued as illustrated *e.g.* by Figure 7 of Stasińska (2004). This is because, at low metallicities, such ratios increase with increasing metallicity but, at high metallicities, they decrease due to the increased cooling by infrared lines, which lowers the temperature below the excitation threshold of optical CELs. In such circumstances, external arguments must be found to determine whether the object under study is on the "high abundance" or "low abundance" branch. The

most common argument is based on the [N II] $\lambda6584$ line. The reason why this argument works is that, in giant H II regions, N/O tends to increase as O/H increases at least at high metallicities. In addition, high metallicity H II regions have lower ionisation parameters, favouring low-excitation lines such as [N II] $\lambda6584$. The biggest problem is when the O_{23} (or the S_{23}) ratio is close to its maximum value, which occurs around log O/H +12 = 8 for O_{23} and 8.6 for S_{23}. Then the metallicity is very ill-determined with an error bar of perhaps ±0.3 dex. By using both O_{23} and S_{23} indexes at the same time, it would perhaps be possible to reduce this uncertainty.

Methods that use the [N II] $\lambda6584$ lines have another potential difficulty. Chemical evolution of galaxies changes the N/O ratio in a complicated and non-universal way. Therefore, one must really ask whether the calibration used is relevant for the group of objects under study.

Perhaps the most satisfactory methods, on the theoretical side, are the ones using the Ar_3O_3 or S_3O_3 indicators, since these indicators are monotonic and work for well-understood reasons directly linked to metallicity.

On the contrary, the Ne_3O_2 index, which is seen to decrease as metallicity decreases, behaves in such a way *only* because more metal rich giant H II regions are excited by a softer radiation field and have a lower ionisation parameter. This is a very indirect metallicity indicator!

It is important to be aware that, in principle, strong line methods can be safely used only when applied to the same category of objects that were used for the calibration. The meaning of the results in the case of integrated spectra of galaxies, for example, is far from obvious. Such spectra contain the light from H II regions differing in chemical composition and extinction as well as the light from the diffuse ionised interstellar medium. In addition, inclination effects may be important. A few studies have addressed these issues from an observational point of view (Kobulnicky *et al.* 1999; Moustakas & Kennicutt 2006; Zaritsky *et al.* 1994), but clearly the subject is not closed.

A further step in strong line abundance determinations has been made by using ratios of line equivalent widths instead of intensities (Kobulnicky *et al.* 2003). The advantage of using equivalent widths is that they are almost insensitive to interstellar reddening, which allows one to apply the method even when reddening corrections are not available, especially at redshifts larger than 1.6. The reason why equivalent widths work well for integrated spectra of galaxies is that there is empirically a very close correlation between line intensities and equivalent widths, meaning that, statistically, stellar and nebular properties as well as reddening are closely interrelated.

As stated above, strong line methods have to be calibrated. Calibrations by different authors, based on different samples and using different methods, lead to substantial differences in oxygen abundances derived for the same object – up to 0.6 dex (see Kewley & Ellison 2008, who provide the most complete method compilation). Low abundances are generally less problematic than high abundances. Kewley & Ellison (2008) provide useful metallicity conversions between different strong-line calibrations.

Using grids of photoionisation models. It is relatively easy, with presently available photoionisation codes and with the speed and capacity of modern computers, to build extensive grids of photoionisation models[14], in which one varies the main input parameters (the effective temperature of the ionising radiation, the ionisation parameter and the chemical composition for a basic grid of models). Since one of the outputs of such models (which involve a self-consistent treatment of the transfer of ionising radiation and of the ionisation and thermal balance in each nebular zone) is to predict the intensities of emission lines, one can think of using such grids of models to infer the chemical composition of observed objects by comparing observed line ratios with those of model grids.

A nice example of such an approach is provided by the work of Charlot & Longhetti (2001) or of Brinchmann *et al.* (2004). However, this is not as simple as it appears. First, one must find a suitable interpolation technique for such a multi-parameter problem. Another approach is to use Bayesian methods. It must also be realised that such a method can give reliable results only if the model grid is appropriate, *i.e.* if it contains models that are sufficiently close to the studied objects in all relevant aspects. For example, Yin *et al.* (2007) noted that the abundances derived with Bayesian methods by Tremonti *et al.* (2004) for a sample of galaxies from the Sloan Digital Sky Survey (York *et al.* 2000) with measured [O III] $\lambda 4363$ were significantly larger than those derived with direct, temperature-based methods for the same objects. As suggested by Yin *et al.* (2007), the reason lies in the abundances chosen in the model grid. Since the procedure uses simultaneously all the strong lines to derive O/H, any offset between the real N/O and the N/O adopted in the model grid induces an offset in the derived O/H. Nevertheless, this technique to derive the chemical composition of nebulae is bound to have a bright future. Detailed studies of individual objects are however necessary to validate the methods, otherwise important biases may remain uncovered.

Tailored photoionisation modelling. We now turn to the most sophisticated way to determine the oxygen abundance in a photoionised nebula, which is to construct a detailed photoionisation model of the object under study. In a perfect world, this would be the most accurate way to derive the oxygen abundance. In practice, this is not always so, as will be made clear below.

The general procedure is as follows:

1. Assign values to the input parameters, which, in a sophisticated approach, are: (i) the characteristics of the ionising radiation field (luminosity, spectral energy distribution); (ii) the density distribution of the nebular gas; (iii) the chemical composition of the nebular gas; (iv) the dust content (composition, distribution in the nebula) and (v) the distance.

---

[14]A dozen of photoionisation codes have been benchmarked and described in Péquignot *et al.* (2001). A list of publicly available photoionisation codes is given in Stasińska (2009).

2. Use an appropriate photoionisation code and compute a model.

3. Compare outputs with observations.

4. Return to step 1 and iterate until the observations are satisfactorily reproduced. Here "satisfactorily" means that *all* the observational data are reproduced within acceptable limits, taking into account both the observational errors and the approximations of the model.

During the model-fitting process, one should:

1. Use as many observational constraints as possible (not only line intensity ratios): (i) the total observed Hα flux; (ii) the Hα surface brightness distribution and the angular size of Hα emitting zone; (iii) the line intensities and (iv) the infrared continuum produced by internal dust. All the observational data that can be affected by extinction due to intervening dust must be corrected for it in advance.

2. Keep in mind that the importance of the constraint has nothing to do with the strengths of the lines. For example He II $\lambda 4686$/Hβ, which is of the order of a few percent at most in H II regions, indicates the presence of photons above 54.4 eV, which are not expected in main sequence, massive stars (unless they are part of an X-ray binary system); [O III] $\lambda 4363$ and [N II] $\lambda 5755$ are weak lines, but they indicate whether the energy budget is well reproduced by the model. If these lines are not fitted, the abundance derived from the model is not reliable.

3. In the comparisons of models with observations, take into account the fact that the spectroscopic slit does not necessarily encompass the entire object.

4. Choose a proper estimator for the "goodness of fit", *e.g.* avoid using a χ^2 minimisation technique without being convinced that this is the most appropriate test in the case under study.

A priori, the most satisfactory situation is when *all* the observations are fitted within the error bars. Then, *if the number of constraints are sufficient to fully determine the problem*, the chemical composition of the object under study is given by the input of the successful model. There is no general and easy way to determine the error bars on the derived abundances. Note that the available observational constraints do not necessarily determine the problem. For example, if there is no line to constrain the electron temperature, two families of solutions can be found, one with high metallicity, one with low metallicity. This is related to the double-value problem mentioned in the section on statistical methods.

It is often the case, however, that some of the observations cannot be fitted. This means either that the observations are not as good as thought, or that some assumptions in the modelling are incorrect. For example: the nebula has a different geometry than assumed, or the stellar ionising radiation field is not well described, or an important heating mechanism is missing. In such a situation, one cannot be

sure of the chemical composition to the desired accuracy. This is for example the case of the extremely metal-poor galaxy, IZw 18, for which the oxygen abundance is $\log O/H + 12 \simeq 8.1$. For this object, Stasińska & Schaerer (1999) were not able to reproduce the observed temperature structure, and argued that this implied an uncertainty in O/H by about 30%. Péquignot (2008) disputed this result, and produced a model with a more complex density structure which was able to explain the observed [O III] $\lambda 4363/5007$ ratio in the central zone of the object (but not over the entire face of it, as observed . . .).

It should have thus become clear to the reader that tailored photoionisation modelling is a heavy procedure, that is not necessarily rewarding in terms of abundance determinations. If all the relevant observational information is available, and the model fits the data well, the abundance derived from a photoionisation model is generally very close to what would have been obtained using a direct empirical method (the only exceptions being the case of a very high excitation nebula for which the icf could be wrong). If the data are not well fitted, the abundance is uncertain. For this object, the abundance obtained by direct methods would also be uncertain. In that case, one can say that the advantage of photoionisation modelling is to demonstrate that the abundance is uncertain. Furthermore, if some important observational constraint is missing, photoionisation modelling may lead to a solution which would not be the correct one!

H II regions.[15] There are a few important aspects which have not been mentioned above, for the sake of a more linear presentation. Most of them have been extensively treated in Stasińska (2004), and will be mentioned here only briefly with some updates if necessary.

Atomic data. The atomic data involved in abundance determinations from optical lines are generally believed to be quite accurate (within $5-10\%$) (see Appendix). Atomic data accuracy is presently not the major issue for abundance determinations in planetary nebulae from optical data.

Correction for reddening and underlying stellar absorption. Before being analysed in terms of abundances, the intensities of observed lines must be corrected for various effects. The presence of dust between the zone of emission and the observer attenuates the collected radiation and modifies its colour.

The usual dereddening procedure is to derive the logarithmic extinction at Hβ, C, from the observed Hα/Hβ ratio, assuming that the intrinsic one has the value $(H\alpha/H\beta)_B$ predicted by case B recombination:

$$C = [\log(H\alpha/H\beta)_B - \log(H\alpha/H\beta)_{obs}]/(f_\alpha - f_\beta), \qquad (1.23)$$

---

[15]Most topics discussed in this paragraph are also relevant for planetary nebulae. Indeed H II regions and planetary nebulae share the same global physics, even if they have very different origins (and also timescales and masses).

where f_α and f_β represent the values of the "reddening law" at the wavelengths of the Hα and Hβ lines, respectively.

Then, for any observed line ratio $(F_{\lambda 1}/F_{\lambda 2})_{obs}$ one can obtain the reddening corrected value $(F_{\lambda 1}/F_{\lambda 2})_{corr}$ from

$$\log(F_{\lambda 1}/F_{\lambda 2})_{corr} = \log(F_{\lambda 1}/F_{\lambda 2})_{obs} + C(f_{\lambda 1} - f_{\lambda 2}). \qquad (1.24)$$

Ideally, one can iterate after having determined the electron temperature of the plasma so as to use a value of $(\mathrm{H}\alpha/\mathrm{H}\beta)_\mathrm{B}$ at the appropriate temperature.

Thus, the reddening correction in ionised nebulae is in principle straightforward. There are however a few points that deserve attention.

The "reddening law", once considered universal, is actually a one-parameter function characterised by the value of the total-to-selective extinction $R_V = A_V / E(B - V)$ (Fitzpatrick 1999, 2004). The canonical value of R_V, generally used for reddening corrections, is 3.1 or 3.2. However, the measurement of R_V using 258 Galactic O stars yields a distribution around this value with a dispersion of $\pm$ 0.5. Values of R_V as small as 1.6 or as large as 5 are found (Patriarchi et $al.$ 2003). In general, the value of R_V applying to a specific observation is not known. Therefore, there is an intrinsic uncertainty in the dereddening process that cannot be reduced. Fortunately, it translates into an uncertainty of typically less than 5% in O^+/H^+, and even smaller in O/H.

A further point is that, in emission line galaxies and in giant H II regions (as well as in unresolved planetary nebulae), the observed Balmer lines are affected by the underlying assumption from the stellar component. This absorption can be determined empirically together with the extinction by fitting several Balmer lines to the theoretical Balmer decrement (as in, for example, Izotov et $al.$ 1994). In the case of a planetary nebula, if a high resolution spectrum of the central star is available and can be modelled, one can take the modelled spectrum of the star as the continuum against which the nebular lines are seen. This procedure, feasible in practice at least for objects located at galactic distances, is almost never applied as it is rather heavy. In the case of emission line galaxies, the observed continuum can be modelled, using spectral synthesis techniques, to reproduce the stellar absorption features after clipping out the spectral zones where emission lines are found. Then, the emission lines are measured after subtracting the full continuum model from the observed spectrum (Cid Fernandes et $al.$ 2005). One can avoid such a lengthy procedure by using an empirical relation between the discontinuity at 4000 Å, $D_n(4000)$ (easy to measure in galaxies) and the stellar absorption equivalent widths in Hα and Hβ (see Stasińska et $al.$ 2007):

$$EW_{\mathrm{abs}}(\mathrm{H}\alpha) = 9 \exp(-1.2x) + 1.3 \qquad (1.25)$$

and

$$EW_{\mathrm{abs}}(\mathrm{H}\beta) = 400 \exp(-4.x + 0.5) + 2.5, \qquad (1.26)$$

where $x = D_n(4000)$.

It is always a good idea to check, after dereddening, whether Hγ /Hβ has the value predicted by recombination theory. If not, the [O III] λ4363/5007 ratio will
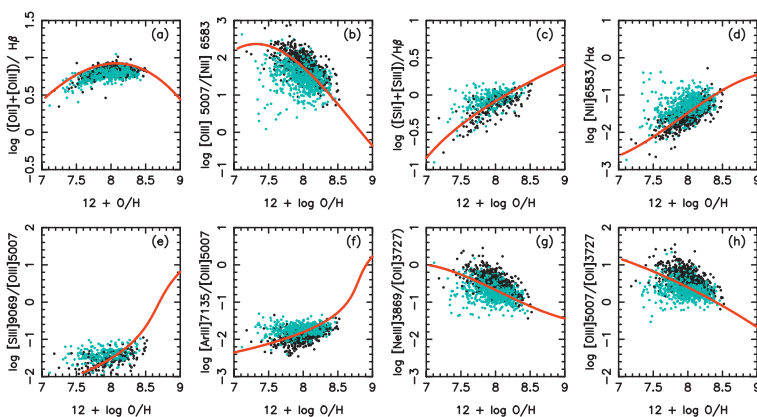
Fig. 1.8. Abundance-indicator strong-line ratios plotted as functions of the oxygen abundance. The curves represent various calibrations. The dots represent galaxies from the SDSS for which O/H was derived with a temperature-based method. Black dots represent galaxies with $W(\mathrm{H}\beta) \geq 100$ Å. Cyan dots represent galaxies with $W(\mathrm{H}\beta) < 100$ Å.

likely be in error by a similar amount, which may have an important effect on the derived oxygen abundance. Typically, a 20% error in [O III] $\lambda4363/5007$ for a nebula at a temperature of 10 000 K will induce a $20-30\%$ error on O/H in the opposite direction. To avoid this, it is better to "force" the entire Balmer decrement to the theoretical one, and then deredden the adjacent line intensities by interpolation.

Aperture effects. Another issue is when the objects under study are more extended than the observing beam. This fact must be taken into account in the analysis. For example, spectra obtained with several instruments must be carefully combined. This is especially important – and difficult – when merging ultraviolet or infrared data with optical data, since in that case flux calibration problems may arise. It is theoretically possible to combine all the data by comparing each observation to the results of a tailored photoionisation model seen through an appropriate aperture. Most of the time, however, aperture corrections are performed in an approximate way, neglecting the effect of the ionisation structure of the nebulae on the line fluxes recorded through small apertures.

Dangers of strong line methods. As shown by Stasińska (2010), abundances derived with strong line methods may be significantly biased, if the objects under study have different structural properties (hardness of the ionising radiation field, morphology of the nebulae) than those used to calibrate the methods (see Fig. 1.8).

Strong line methods to derive nebular abundances, while very easy to apply, are thus particularly prone to systematic errors. In principle, they should be used

only for objects whose H II regions have the same structural properties as those of the calibrating samples. This recommendation is not easy to follow, but at least one should be aware that using the same calibration for different samples may produce important biases.

In particular, claims on differences in oxygen abundance

- between samples of galaxies with different chemical evolution histories

- between samples of galaxies with different star formation histories

- between samples of galaxies at different redshifts (observational selection effects may play a role)

should be taken at least with a grain of salt.

A further problem, when dealing with spectra of entire galaxies, is the physical meaning of the derived abundance, especially in presence of abundance gradients. This issue, which is also relevant to the simple "strong line indicators" approach, has not yet been fully addressed.

The temperature structure.   In many cases, the electron temperature can be derived from only one line ratio (usually [O III] $\lambda4363/5007$ or [N II] $\lambda5755/6584$). It is often adopted that this is the temperature to use for all ions (actually, for oxygen, only O^+ and O^{++} in the vast majority of cases, the other ions not being observed). For H II, empirical relations have been proposed between $T(4363/5007)$ and $T(5755/6584)$ (*e.g.* Garnett 1992 or Izotov *et al.* 2006), based either on grids of photoionisation models or on fitting a formula to observed values. It must be noted, however, that observations show a very large dispersion about those relations. It is not clear whether this is due to underestimated observational error bars, or whether the dispersion is really so large. At high metallicities, the relevance of any empirical relation between the various T_l's is even more questionable, due to the existence of large temperature gradients in the nebulae, which are strongly dependent on the physical conditions (see below).

The special case of metal-rich giant H II regions.   Until recently, it was not possible to measure the electron temperature in metal-rich H II regions. The usual temperature diagnostics involve weak auroral lines which easily fall below the detection threshold at low temperatures. With very large telescopes such temperature-sensitive line ratios as [O III] $\lambda4363/5007$, [N II] $\lambda5755/6584$ and [S III] $\lambda6312/9532$ can now be measured even at high metallicities (*e.g.* Bresolin *et al.* 2005, 2007; Kennicutt *et al.* 2003). However, due to the large temperature gradients expected in high-metallicity nebulae, which are a consequence of the extremely efficient cooling in the O^{++} zone due to the infrared [O III] lines, [O III] $\lambda4363/5007$ does not represent the temperatures of the O^{++} zone. As a consequence, the abundances derived by empirical methods can be strongly biased, as shown by Stasińska (2005). The magnitude of the bias depends on the physical properties of the H II region and on the temperature indicators available. Therefore, any empirical determination of the oxygen abundance in zones suspected of

being oxygen-rich must be critically analysed and should be confirmed by detailed photoionisation modelling.

A further problem in the estimation of T_e at high metallicity is the contribution of recombination to the intensities of collisionally excited lines, which becomes important at low values of T_e. For example, the contribution of recombination from O^{++} to the intensity of [O II] $\lambda 7320+30$ can be very important. It can be corrected for using the formula given in Liu *et al.* (2000), provided that the temperature characteristic of the emission of the recombination line is known (which is not the case if the temperature is obtained from CEL ratios). Only photoionisation modelling − which takes this into account implicitly – can deal with this properly.

The importance of stellar energy distribution in photoionisation models. The outcome of photoionisation models depends critically on the spectral energy distribution of the ionising radiation, especially regarding the nebular ionisation structure.

The exciting stars of H II regions have generally extended atmospheres in which important deviations from LTE occur. Hundreds of thousands of metallic lines produce line blanketing and line blocking effects, and are at the origin of radiative driven winds. Modern stellar atmosphere codes are able to handle these aspects, although each one works with some degree of approximation in one aspect or another. As a result, the codes give different descriptions of the hydrogen Lyman continuum. A few studies have started using H II regions to probe the Lyman continuum radiation predicted by stellar atmosphere models (Morisset *et al.* 2004; Simón-Díaz & Stasińska 2008) but there is no clear answer yet.

In the case of giant H II regions, where the ionisation is produced by a group of stars, there are several additional issues. The usual way to deal with this is to take the spectrum predicted by spectral synthesis codes, such as Starburst 99 (Leitherer *et al.* 1999; Smith *et al.* 2002), which, of course, rely on model atmospheres for individual stars. Additional problems are the spatial distribution of the ionising stars (partly addressed by Ercolano *et al.* 2007) and the statistical sampling issues in the case when the total mass of the ionising cluster is below a certain value (typically $10^5 M_\odot$), so that the number of ionising stars is too small to be represented by the analytic formulation in synthesis codes (Cerviño & Luridiana 2004, see also Jamet *et al.* 2004). Although these are only second order problems for the determination of oxygen abundance in H II regions, it is good to keep them in mind.

Temperature fluctuations and the ORL/CEL discrepancy. If, for some reason, the electron temperature in the zone occupied by a given ion presents spatial fluctuations, abundances derived from collisional emission lines (CELs) by the temperature-based techniques described above will be too small. Indeed, the hottest zones will favour the lines of higher excitation potential. As a result, the temperature derived from line ratios ([O III] $\lambda 4363/5007$, for example) will overestimate the temperature of the O^{++} zone, and result in an underestimate of

the O^{++} abundance. Peimbert (1967) and Peimbert & Costero (1969) developed a mathematical formulation to correct for this bias. It is based on the Taylor expansion of the average temperature

$$T_o(X_i^j) = \frac{\int T_e n(X_i^j) n_e dV}{\int n(X_i^j) n_e dV} \tag{1.27}$$

defined for each ion X_i^j, using the *r.m.s.* temperature fluctuation

$$t^2(X_i^j) = \frac{\int (T_e - T_o(X_i^j))^2 n(X_i^j) n_e dV}{T_o(X_i^j)^2 \int n(X_i^j) n_e dV}. \tag{1.28}$$

From a comparison of temperatures measured by different methods (for example Balmer jump *versus* [O III] $\lambda 4363/5007$), it was concluded that temperature fluctuations are common in H II regions, with typical values of $t^2 = 0.03-0.05$ (see more recent references in Peimbert 1996; Esteban 2002), leading to an underestimate of the oxygen abundance from optical CELs by about $0.2-0.3$ dex if no correction for temperature fluctuation is applied. However, these conclusions were not commonly accepted and, forty years after the seminal paper by Peimbert (1967), specialists are still debating about

1. The existence of temperature fluctuations at a level that significantly biases the abundances from CELs;

2. The relevance of procedures to correct for this bias;

3. The possible causes of such temperature fluctuations (shocks? dust heating? etc.).

Some aspects of the discussion can be read in Stasińska (2004) and Stasińska *et al.* (2007) and references therein.

   An important argument is that a high spatial resolution map of the Orion nebula with the *Hubble Space Telescope* did reveal fine-scale fluctuations of the columnar temperature, implying a three dimensional $t^2 = 0.028 \pm 0.006$.

   A possibly related aspect is that of the famous ORL/CEL discrepancy, *i.e.* the fact that abundances derived from recombination lines are higher than abundances derived from collisionally excited lines, typically by a factor of 2 in H II regions (see García-Rojas & Esteban 2007). Oxygen is the element for which this discrepancy is best seen. Peimbert and coworkers assign it to the presence of temperature fluctuations. As a matter of fact, the value of t^2 derived from the comparison of Balmer jump and [O III] $\lambda 4363/5007$ temperatures is close to the one needed to reconcile the oxygen abundance derived from CELs and ORLs. Other authors (Tsamis & Péquignot 2005; Tsamis *et al.* 2003) ascribe it to abundance inhomogeneities (which, actually, is the easiest way to produce temperature fluctuations). The question to answer is then: what is the cause of such abundance inhomogeneities? Stasińska *et al.* (2007) examined quantitatively the scenario proposed

by Tenorio-Tagle (1996) of oxygen-rich "droplets" containing the supernova ejecta from previous stellar generations. From order-of-magnitude estimates of processes occurring at all scales (from the galactic scale to the atomic scale), they concluded that this scenario was a good candidate to explain the ORL/CEL problem in H II regions. They also warned that, in such a hypothesis, the recombination lines strongly overestimate the oxygen abundance of the fully mixed H II regions, and even collisionally excited lines lead to some bias (although much smaller). In absence of any recipe for correcting these biases, they recommend to discard H II regions with large ORL/CEL discrepancies when testing models of galactic chemical evolution. On the other hand, Peimbert & Peimbert (2006) argue that one should use only ORLs (insensitive to temperature fluctuations) to study abundance gradients in galaxies, and that one should calibrate strong-line methods with oxygen abundances derived from ORLs. Definitely, there is no consensus here!

Summary of oxygen abundance determinations in H II regions. The methods are generally straightforward in their principle. In the best cases (temperature-based method, high signal-to-noise observations, careful analysis of the data), one can hope for an accuracy of 0.1 dex in the oxygen abundance. In absence of any direct information on the electron temperature, however, the accuracy deteriorates significantly. When using a double-valued method, there is a whole range of abundances, typically between log O/H +12 = 8. and 8.6 which is totally undetermined. The absolute value of the derived oxygen abundances at the high metallicity end strongly depends on the calibration choice. While earlier calibrations (Dopita & Evans 1986; Edmunds & Pagel 1984) led to values of log O/H +12 as large as 9.4 in the central parts of some spiral galaxies, some recent calibrations (*e.g.* Pilyugin & Thuan 2005) give a value of log O/H +12 that never exceeds 8.9.

Shocks and related issues. Photoionisation is not the only process leading to the formation of emission lines. Cooling flows (Cox & Smith 1976; Fabian & Nulsen 1977) and interstellar shocks can also produce emission lines. Shocks are ubiquitous in galaxies, caused by jets (jets associated to brown dwarfs, protostars or massive black holes), winds (stellar winds, protostars, active galactic nuclei) or supersonic turbulence. Dopita & Sutherland (1995, 1996) and more recently Allen *et al.* (2008) have provided grids of models of line emission produced by pure shocks[16]. The efficiency of ionisation by stellar photons is so high that, whenever hot stars are present, they are likely to dominate the ionisation budget of the surrounding gas. The same can probably be said for radiation arising from accretion onto a massive black hole. However, in order to explain observed emission

---

[16]It is with similar grids of pure shock models that some authors (*e.g.* Dopita *et al.* 1984) have determined the chemical composition of supernova remnants. These techniques, however, seem to have been abandoned, probably because of their lack of robustness and of the necessity to rely on extensive grids.

line ratios, the possible contribution of shock heating to photoionisation must be examined.

The effects of shocks that leave a signature on emission line spectra in photoionised nebulae can be summarised as follows:

1. Shocks generate compression and thus high gas densities.

2. This compression locally reduces the ionisation parameter, and thus enhances the low ionisation emission lines such as [O II], [N II], [S II] and [O I].

3. Shock heating produces very high temperatures (of the order of million degrees), which lead to collisional ionisation and the production of ions such as O^{3+} or He^{++}.

4. This high temperature gas emits X-rays, which contribute to the ionisation in front of the shock and behind it.

5. In the region between the X-ray emitting zone and the low excitation zone, the temperature of the gas passes through intermediate temperatures of several tens of thousands of K, boosting the emission of ultraviolet CELs and of auroral lines. The [O III] $\lambda4363/5007$ ratio can be significantly enhanced.

However, it must be realised that effects 2, 3 and possibly 4 are spectroscopically indistinguishable from the effects of photoionisation by an external X-ray source. As for the enhancement of the low ionisation lines, it can simply be due to a small ionisation parameter without the necessity of invoking shock heating (see *e.g.* the explanation proposed by Stasińska & Izotov 2003 for the behaviour of the [O I] lines in H II galaxies).

Finally, dynamical heating and cooling as well as non-equilibrium photoionisation may be an issue in certain cases, when the dynamical times are shorter than the radiative time. Only a few works have started exploring these avenues, which require important computing power and therefore cannot use the same approach to real nebulae as the ones discussed in the present text. An enlightening introduction to the role of dynamics in photoionised nebulae is given by Henney (2007).

Planetary nebulae.   The problems in abundance determinations that one faces in H II regions are also encountered in planetary nebulae. However, there are a few additional problems in the latter which will be now discussed.

Densities.   While most of the H II regions that are studied for their abundances have rather low electron densities (<500 cm^{-3}), many planetary nebulae have measured electron densities of $10^3 - 10^4$ cm^{-3} or larger. An error of a factor of 3 at $n = 10^4$ cm^{-3} (which results from a 10% uncertainty in the [S II] $\lambda6731/6717$ ratio) induces an error of a factor of 2 on the O^+ abundance in the same direction when measured from the [O II] $\lambda3727$ line, and an error of 25% in the opposite direction when measured from [O II] $\lambda7320, 7330$.

Correction for unseen oxygen ions. Most planetary nebulae show the He II $\lambda4686$ line, meaning that their central stars emit photons with energies above 54.4 eV, which are able to ionise O^{++}. [Ne V] lines are common in planetary nebulae, implying that O^{3+} and O^{5+} are present in the nebula, and can easily represent half of the total oxygen. In the case where the oxygen abundance is obtained using the general formula for the *icf*, the correction can be wrong by as much as, say, 30% for the planetary nebulae with highest excitation. It is not granted that, observing O^{3+} in the ultraviolet or in the infrared will really improve the oxygen abundance, because of the uncertainties in the observed fluxes and of the difficulties in combining spectral information from different instruments and obtained through different apertures. The most reliable result, in such circumstances, is in principle obtained through a photoionisation model fitting of the observations – but this heavy procedure is not fully reliable either, because the spectral energy of the ionising radiation field is not well known, especially at the highest energies.

Large ORL/CEL discrepancies. As in the case of H II regions, the temperature derived from the Balmer jump is systematically lower than that derived from [O III] $\lambda4363/5007$, and the oxygen abundance derived from ORLs is larger than that derived from CELs. The problem is even more severe, since the abundance discrepancy factor (which has now been measured in nearly 100 planetary nebulae) is >5 for 20% of planetary nebulae and >10 for 10% of planetary nebulae (Liu 2002). All the oxygen abundances derived from ORLs are larger than solar. In one extreme planetary nebula, Hf $2-2$, the abundance discrepancy factor is 70, and the Balmer jump temperature is as low as 900 K for an [O III] $\lambda4363/5007$ temperature of 8800 K (Liu *et al.* 2006)! In contrast with what seems the rule in H II regions, the temperature fluctuation estimated from the comparison of the Balmer jump temperature and the [O III] $\lambda4363/5007$ temperature is not sufficient to explain the observed abundance discrepancy factor. In planetary nebulae, abundance discrepancy factors have also been measured for other elements (C, N and Ne). The dual abundance model, first suggested by Liu *et al.* (2000) for the planetary nebula NGC 6153, is presently the only way to explain the observed large abundance discrepancy factors. According to Liu (2006) a few Jupiter masses of hydrogen-poor material inside the nebula can account for the observed recombination lines of C, N, O and Ne. A detailed dual-abundance photoionisation model of NGC 6153 now exists (Yuan *et al.* 2011) which reproduces satisfactorily all the observed line ratios including the temperature diagnostics, adding physical consistency to this scenario. However, the origin of this hydrogen-poor material is not clear. It was first thought to be processed material from the central star. However, this explanation is difficult to reconcile with the fact that the C:N:O:Ne ratios in the hydrogen-poor component seem to be roughly solar, while it is expected that these ratios are modified by nucleosynthesis in the progenitor followed by dredge-up episodes. Another possibility suggested by Liu (2002) is that the hydrogen-poor material comes from photo-evaporation of planetesimals.

In view of this ORL/CEL discrepancy, what are the abundances that one can consider as representative of planetary nebulae? There seems to be agreement

that, except for the planetary nebulae with the largest abundance discrepancy factors, the oxygen abundance derived from CELs represents the average oxygen abundance in the nebula fairly well. But which value of it? The one computed assuming t^2=0? Or that computed using t^2 derived from the difference between the Balmer jump and [O III] $\lambda 4363/5007$ temperatures? Peimbert & Peimbert (2006) argue for the latter values.

High-redshift galaxies. Galaxies in different, well determined, redshift intervals are now readily identified by the application of appropriate broad-band photometric pre-selection criteria, of which the Lyman-break technique is the best known example. These high-redshift galaxy candidates are then observed with efficient multi-object spectrographs on 8–10 m class telescopes to confirm their redshifts. The original $U_n GR$-based colours of Steidel *et al.* (1995) have more recently been "tuned" to select star-forming galaxies at the mean redshifts of $\langle z \rangle = 3$ (Lyman break galaxies, LBGs), $\langle z \rangle = 2.2$ (BX galaxies) and $\langle z \rangle = 1.7$ (BM galaxies), in each case with a redshift dispersion of about 0.3 (Adelberger *et al.* 2004).

Nebular emission lines from H II regions are the main tools available for measuring the element abundances and their radial gradients in nearby galaxies. When it comes to applying at high redshifts the same abundance diagnostics, based on the ratios of the strongest nebular lines, we are faced with a number of problems. The obvious one is the reduction in the flux received, which may be in some objects compensated by a strong starburst, *i.e.* a high star formation rate. When the nebular emission lines are redshifted to near-infrared wavelengths, only a subset of the strong lines often become accessible, namely those which are free from water vapour absorption and OH emission from the sky.

The most commonly used strong-line abundance indicator is R_{23} (see above) method, which relates the oxygen abundance to the ratio of ([O II] + [O III])/Hβ (Pagel *et al.* 1979). The R_{23} method has been employed to determine the metallicities of individual H II regions in the local Universe and the average metallicities of entire star-forming galaxies in the distant Universe (Kobulnicky *et al.* 2003; Lilly *et al.* 2003). However, the double-valued nature of the R_{23} calibration limits its usability, unless an independent line ratio can be used to determine whether a galaxy is on the upper, metal-rich branch or the lower, metal-poor branch.

For this reason, and for the often limited access to several nebular lines in the same object at high redshift, the usability of the N_2 index has recently been revisited empirically by Pettini & Pagel (2004). Their new calibration yields: $12 + \log(\text{O/H}) = 8.90 + 0.57 \log N_2$. Unlike R_{23}, the [N II]/Hα ratio increases monotonically with increasing metallicity (at least up to solar metallicity). Another benefit of the [N II]/Hα ratio is the small difference in wavelength between the two features, which reduces the importance of accurate flux-calibration and dust extinction correction. Limitations of the N_2 method include the fact that N_2 is sensitive to the value of the ionisation parameter, as well as to metallicity. In addition, the N/O ratio is very dependent on the star formation history and age of galaxies, which makes its calibration non-trivial. Despite these limitations, the N_2 indicator offers rough estimates of the H II region abundances, under the

assumption that the observed emission lines originate in H II regions excited by the photoionising radiation from massive O and B stars. The contribution from diffuse ionised gas to the integrated emission-line spectra of local star-forming galaxies gas can enhance the [N II]/Hα ratio by different amounts ranging from less than 0.1 dex to as much as a factor of 2, relative to what is measured in individual H II regions (Lehnert & Heckman 1994). The diffuse ionised gas component could potentially bias the interpretation of [N II]/Hα ratios toward higher metallicities. Currently, there are no constraints on the contribution of diffuse ionised gas to the high-redshift galaxy spectra, which would require spatially resolved Hα narrowband imaging of the cosmologically distant galaxies.

The main uncertainty in the measure of metallicities in the high-redshift star-forming galaxies is precisely the use of several metallicity calibrators. Indeed, depending on the nebular emission lines detected, which will vary according to spectral coverage, redshift, galaxy properties, etc., a different metallicity calibrator is used (*e.g.*, Izotov *et al.* 2006; Kewley & Dopita 2002; Kewley & Ellison 2008; Pettini & Pagel 2004). Kennicutt *et al.* (2003), for instance, showed that the metallicity based on an electron-temperature sensitive method is on average a factor of 2.5 lower than that derived using the empirical method by Kewley & Dopita (2002). Therefore, when comparing the metallicities of the various surveys of galaxies at high redshift, we need to keep in mind that the intrinsic metallicities can vary by a factor of at least 2.

1.2.3.2   Collisionally ionised media

We have already mentioned in Section 1.2.3.1 the effect that shocks have on optical and ultraviolet emission lines. Here we concentrate on X-ray lines.

Thermal X-ray radiation provides an important diagnostic tool for studying the hot phase of various media, including the interstellar medium. They are characteristic of plasma at temperatures of the order of million degrees. In the following, we focus upon the properties of the oxygen lines in the X-ray spectrum of tenuous plasma, considered to be optically thin (mean free path of photons large compared to the plasma characteristic size).

Emission lines arise from the de-excitation of ions from a high energy state to the ground state or any other lower energy level. Oxygen being the most abundant metal, its X-ray lines, as well as those of iron, are among the strongest. Despite a much lower iron abundance (6% of the cosmic oxygen abundance), iron lines are often of similar strength than those of oxygen. The reason is that ion emissivity increases with a high power of the nuclear charge. The characteristics of oxygen emission lines are given in Table 1.6. They correspond to K-line excitation and arise from highly ionised ions (hydrogen- and helium-like ions) with only one or two electrons left in the electronic shells. With current charged coupled device detectors, as those used in the *XMM-Newton*, *Chandra* and *Suzaku* satellites, these spectral lines are roughly resolved. The observation and modelling of these spectral lines allow one to determine *the abundance of oxygen*, *its ionisation state* and *radial bulk velocities* through Doppler line shift measurements.

Table 1.6. X-ray oxygen emission lines. T_{max} is the temperature at which the emissivity peaks, $Q_{max} = P/(n_e n_H)$, with P the power per unit volume at T_{max}, and Q_{max} is in units of 10^{36} W m^3. T_{max} and Q_{max} are provided assuming collisional ionisation equilibrium conditions.

E (eV)	λ (Å)	-log Q_{max}	log T_{max}	ion	iso-el seq.	lower level	upper level
561.0	22.101	0.86	6.32	O VII	He	1s ^{1}S$_0$	2s ^{3}S$_1$(f)
568.5	21.807	1.45	6.32	O VII	He	1s ^{1}S$_0$	2p ^{3}P$_{2,1}$(l)
573.9	21.602	0.71	6.33	O VII	He	1s ^{1}S$_0$	2p ^{1}P$_1$(r)
653.5	18.973	1.05	6.49	O VIII	H	1s ^{2}S$_{1/2}$	2p ^{2}P$_{1/2}$(Lyα)
653.7	18.967	0.77	6.48	O VIII	H	1s ^{2}S$_{1/2}$	2p ^{2}P$_{3/2}$(Lyα)
665.6	18.627	1.58	6.34	O VII	He	1s ^{1}S$_0$	3p ^{1}P$_1$
774.6	16.006	1.55	6.50	O VIII	H	1s ^{2}S$_{1/2}$	3p ^{2}P$_{1/2,3/2}$(Lyβ)

1.3 *In situ* Methods

A large variety of extraterrestrial material is now available for investigation in the laboratory, and in particular for elemental or isotopic abundance determinations. This material includes meteorites (of asteroidal, lunar and martian, as well as possibly cometary origin), micrometeorites (of asteroidal or cometary origin) and samples from the Apollo and Luna missions. The solar wind, solar energetic particles and cosmic rays of Galactic or extra-galactic origins are also amenable to laboratory investigation, although perhaps only indirectly. In the following, we concentrate on meteorites and Galactic cosmic rays.

1.3.1 Meteorites

Meteorites are currently broadly classified into chondrites, primitive achondrites and achondrites, based largely on their mineralogical and petrographic characteristics, as well as on their whole-rock chemical and isotopic compositions. These broad classes are further divided into groups some of which contain different subgroups (see *e.g.* Weisberg *et al.* 2006). Note that some meteorites do not fit into the existing classification.

Almost all analytical methods known to scientists have been used to analyse meteorites, and it is impossible to review them all here in any detail. Texture and mineralogy is determined by conventional thin-section techniques, after which structure and major, minor, trace-element and isotopic chemistries are determined using a large variety of techniques.

These include (i) optical and electron microscopy, (ii) electron, proton and X-ray probes, (iii) stable and radioactive isotope and organic mass spectroscopy (using thermal, resonance, acceleration or plasma ionisation) and (iv) optical,

infrared, ultraviolet, Mössbauer, nuclear magnetic resonance and Raman spectroscopy. All the necessary instrumentation is becoming increasingly precise. It requires the use of ever smaller amounts of material, allowing subtle effects to be traced and very minor meteoritic components to be identified.

As a remarkable example of these achievements is the development of the secondary ion mass spectrometry (SIMS) technique that has made possible the full scientific exploitation of the stardust grains identified in some meteorites (see Sect. 2.1.3.4). In SIMS, a solid sample is bombarded by a finely focussed beam of about 20 keV ions. The sputtered ions from the sample are transported through a mass spectrometer that determines their masses using electric and magnetic fields. The high SIMS sensitivity allows isotopic measurements of many major and minor elements in individual tiny dust grains. Until recently, the critical grain size was of the order of one μm. A new generation of SIMS instruments, referred to as NanoSIMS, bring this critical limit down to about 0.1 μm with increased sensitivity. This novel technique has opened new routes to stardust analyses. The study of the mineralogical and structural characteristics of these grains has also largely progressed thanks to the scanning electron microscopy and transmission electron microscopy techniques. In particular, transmission electron microscopy is able to characterise crystal structures and defects on a nanometre scale and to search for subgrains embedded into individual stardust particles (see Clayton & Nittler 2004; Meyer & Zinner 2006 for more details and references).

1.3.2 Cosmic Rays
1.3.2.1 Cosmic-ray basics

The discovery of an extraterrestrial ionising radiation was made in 1912 by Victor Hess, while he was carrying electroscopes in high altitude balloons. He wanted to understand the origin of the radiation responsible for their spontaneous discharge, a true mystery at that time (Hess 1912). Since then, this radiation, named cosmic rays by Millikan in 1925, has been the object of extensive studies. The fact that cosmic rays are charged particles, essentially protons, was assessed in the late 1920s thanks to measurements of the latitude dependence of their flux by J. Clay, while the discovery of the presence of heavy ions in cosmic rays was achieved by Bradt & Peters (1948) through measurements of their tracks in nuclear emulsions.

The interest in studying cosmic rays came initially from particle physicists, who found in this radiation ways to study the nature of matter prior to the building of powerful accelerators. For example, it is in cosmic rays that C. Anderson discovered the positron (Anderson 1932), which granted him the Nobel Prize in 1936, shared with V. Hess for his discovery of cosmic rays. Even today, the energy carried in cosmic rays goes far beyond what can be achieved in man-made accelerators, with a current detection record of 3×10^{20} eV in one particle.

From the astrophysics point of view, cosmic rays are of fundamental interest for several reasons. First they are an important component of the equilibrium of our Galaxy, as their energy density (~ 1 eV/cm^3) is comparable to that of the magnetic field, the starlight or the kinetic energy of the interstellar gas (*e.g.*

Berezinsky *et al.* 1990). Second, their acceleration represents a challenge to particle acceleration theories. If it is widely believed that young supernova-remnant shocks are the accelerators up to the "knee" in the spectrum ($\sim 3-4 \times 10^{15}$ eV), there is no consensus regarding what process can accelerate cosmic rays up to the highest energies observed so far, and in which astrophysical context this happens.

The last, but not least, astrophysical interest is that they are, together with neutral atoms from the very local interstellar medium, the only sample of matter from outside the solar system that can be directly measured. Unfortunately, being charged particles, cosmic rays do not travel in straight lines from their source to our detectors, but have a diffusive walk in the disordered and fluctuating magnetic fields that they encounter both in the interstellar medium and in the solar wind. To learn about their source and history, one has to use their chemical and isotopic composition as tracers of the different processes they have suffered. A lot of efforts have therefore been devoted to measuring the heavy-ion composition of cosmic rays.

1.3.2.2   Measurement techniques

When entering the Earth atmosphere, cosmic-ray ions suffer inelastic nuclear collisions which strongly suppress their flux after the traversal of a few g/cm^2 of residual atmosphere. Experiments to measure the cosmic-ray composition must therefore be conducted either by instruments flown in high altitude balloons, above 40 km, or embarked on satellites. The instruments are all based on stacking several detectors which when crossed by a particle give simultaneous signals related to the particle charge, speed or total energy.

At the lowest energies, below a few hundreds MeV/nucleon (hereafter MeV/n), it is possible to stop the particles before they break up by nuclear interactions with the detector material. The detection principle used in low energy electronic instruments is then to combine two measurements: the ionisation energy loss dE/dx in the first detector encountered by the particle and the total energy, E, deposited in the second detector where the particle stops. In the non-relativistic limit, dE/dx is $\approx (Z/v)^2$ and $E = 1/2Mv^2$; taking advantage that Z^2M is unique for every nucleus, the combination of the two gives both the charge Z and mass M of the particle. The best detector flown today is the Cosmic Ray Isotope Spectrometer (CRIS, Stone *et al.* 1998) on the Advance Composition Explorer Mission which is orbiting the Earth. Figure 1.9 shows the very clear isotopic measurements, in particular for oxygen, which have been achieved by CRIS (Wiedenbeck 2007). It is worth noting that instruments of the same kind, although less sophisticated than CRIS, have been put on board the Ulysses and Voyager spacecrafts, obtaining chemical and isotopic measurements out of the ecliptic plane and far in the outer heliosphere (see *e.g.* Simpson & Connell 2001; Lukasiak *et al.* 1994).

At higher energies the above mentioned dE/dx *versus* total energy identification cannot be used anymore. Moreover, much larger collecting powers are needed as the cosmic-ray flux is strongly decreasing with energy. Instruments usually make use of Cherenkov detectors which give a signal proportional to $Z^2(1 - (P_0/P)^2)$,
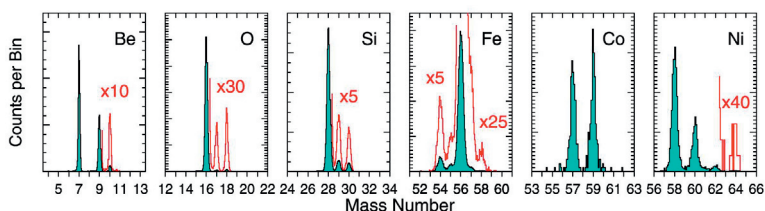
Fig. 1.9. Isotopic measurements at ∼200 MeV/n for elements between Be and Ni performed by the CRIS instrument onboard ACE. The three oxygen isotopes are fully separated. Figure reproduced from Wiedenbeck (2007).
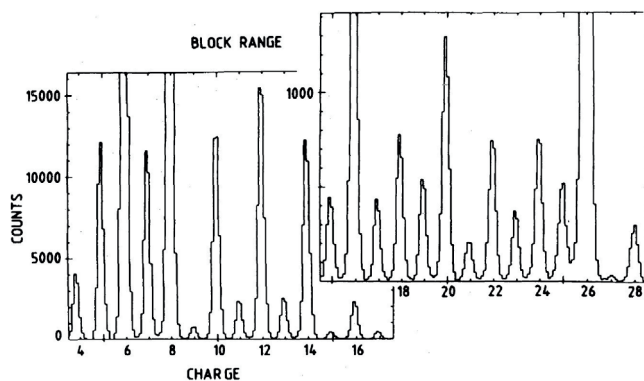
Fig. 1.10. Chemical measurements at ∼3 GeV/n for elements between Be and Ni performed by the C2 instrument onboard HEAO-3. Figure reproduced from Engelmann *et al.* (1990).

where P is the momentum of the particle and P_0 the threshold for Cherenkov emission. By using several counters, or by adding energy-loss measuring detectors, *e.g.* scintillators, one can measure both the charge and the momentum of the particle. They can be designed in large areas. The most accurate results so far on the chemical composition of cosmic rays up to ∼35 GeV/n have been obtained by the French-Danish experiment C2 onboard the HEAO-3 mission (Bouffard *et al.* 1982). This instrument combined five Cherenkov detectors of different thresholds with a precise hodoscope for measuring the trajectory of the particles; this latter information was used to derive the still unique measurements on the average isotopic mass of cosmic rays above 1 GeV/n (Ferrando *et al.* 1988). Figure 1.10 shows the unambiguous charge separation reached by this instrument for all elements from Be to Ni obtained by Engelmann *et al.* (1990).

Chapter 2

A PANORAMA OF OXYGEN IN THE UNIVERSE

2.1 The Sun and the solar system

2.1.1 Constraints from solar interior modelling and helioseismology

The Sun, as the closest star, has long been observed in details with extremely high precision and increasing accuracy. This has provided very strong constraints and insights both for astrophysics and for the physics of matter in conditions hard or even impossible to reach in terrestrial laboratories. In particular, the Sun is a benchmark for stellar structure and evolution theory. The solar mass and chemical composition are input parameters in solar models which at solar age should satisfy all available observational constraints. Any difference between a model and observation has to be understood either as due to an improper description of the physical processes governing the Sun or to erroneous measurements or analysis of observational data. The validation of the theoretical model of the Sun is a crucial and necessary step towards an accurate description of the internal structure and evolution of other stars with important returns for the understanding of the history and evolution of galaxies and cosmology.

2.1.1.1 Constructing a solar evolution sequence and the present solar interior model

The solution of the stellar internal structure equations, consisting of the equations of conservation of mass, momentum and energy and of the equation of energy transport, yields as a result the interior structure of a star once its mass and chemical composition have been fixed. These equations are usually written under the assumptions of spherical symmetry and hydrostatic equilibrium, and very often rotation and magnetic fields are neglected. The system of equations is complemented by boundary conditions in the stellar centre and at the surface where they are generally extracted from an atmosphere model calculated independently. The solutions of the equations provide the internal distribution of the mass, pressure, luminosity and temperature as a function of the radius, *i.e.* the distance to the stellar centre. The evolution of the star is drawn starting from an initial interior model – either on the pre-main sequence or on the zero age main sequence – by

calculating the temporal changes of the internal structure that result from the modification of the internal chemical composition due to nuclear reactions and/or mixing processes, and from the local gravitational expansion/contraction. The equations rely on physical parameters, the so-called input physics, which have to be provided by physicists. Microscopic physics entering the calculation of a stellar model include opacities, the equation of state, the nuclear reaction rates and microscopic diffusion of the chemical elements. The latter includes the internal diffusion due to gravitational settling, thermal gradients, concentration gradients and radiative forces. Macroscopic physics comprise the convective energy transport and possibly the transport of angular momentum and/or chemical elements resulting from convective overshooting, differential rotation, internal gravity waves and magnetic fields. For a recent overview of the theory of stellar structure and evolution we refer to the textbook by Maeder (2009) and references therein.

The solar interior model is obtained through the computation of a time-evolutionary sequence of a star of initial mass equal to one solar mass. This is pursued up to the age of the Sun with a set of input physics chosen as appropriately as possible. The solar model calibration process then consists in adjusting the unknown initial parameters of the evolutionary sequence of the Sun to reach, at solar age, the observed present luminosity, radius and surface metallicity $(Z/X)_s$. Here Z is the sum of the abundances of elements heavier than helium and X is the hydrogen mass fraction. The initial parameters of the model are mainly the initial helium abundance Y_0 in mass fraction, the initial global metallicity $(Z/X)_0$ and the mixing length parameter α entering the convection treatment. Once this calibration has been performed, the interior structure of the numerical model is examined and validated through the comparison with other available observational data, mainly helioseismic data, neutrino fluxes and surface abundance of the light elements (Li, Be). An overview of the solar model calibration can be found in Christensen-Dalsgaard (1982).

2.1.1.2   Constraining the solar model with observations

Global parameters of the Sun.   The global solar parameters − mass, radius, luminosity and age − are given in Table 2.1. They are known with a high precision (see *e.g.* the textbook by Stix 2004). The mass of the Sun, $M_\odot$, here taken from Lide (1994), is derived from planetary motions through Kepler's third law which provides the $GM_\odot$ product where G is the gravitational constant. The solar radius, $R_\odot$, here taken from Allen (1973), is obtained from the distance and angular diameter of the Sun. The latter is defined as the angular distance between the inflection points of the intensity profiles at two opposite limbs. The solar luminosity, $L_\odot$, given here comes from the mean solar irradiance measured by the Solar Maximum Mission (Willson *et al.* 1986). The solar age was derived by Chaussidon (2007) from the abundances and daughter products of radioactive nuclides in meteoritic material.

Table 2.1. Solar global parameters.

$M_\odot$ (g)	age (yr)	$R_\odot$ (cm)	$L_\odot$ (erg.s^{-1})
1.98919×10^{33}	4.567×10^9	6.9599×10^{10}	3.846×10^{33}

Chemical composition in the solar photosphere. The solar photospheric composition is still subject to uncertainties. Helium lines do not form in the mild temperatures prevailing in the solar photosphere which prevents the determination of the helium abundance from the spectrum. There is also an ongoing very constructive debate on the determination of the photospheric abundances of the heavier elements, in particular oxygen and neon (see Sect. 2.1.2). In the 1990s, the solar element mixture generally adopted by stellar modellers was the canonical mixture of Grevesse & Noels (1993, hereafter, GN93). At that time the model atmospheres used to extract the element abundances from the photospheric spectrum were one dimensional. In the beginning of the 2000s, the re-analysis of the solar spectrum in the light of three-dimensional, time-dependent, hydrodynamical model atmospheres, together with improved line transition probabilities and better physical description (NLTE corrections, effects of blends), led to a major revision of the solar photospheric abundances (see *e.g.* Asplund *et al.* 2009, hereafter, AGSS09). Remarkably, the abundances of C, N, O and Ne are lower in the AGSS09 revised solar mixture than in the GN93 mixture. In particular the ratio of the number of oxygen atoms with respect to hydrogen is decreased from $(O/H)_\odot = (7.41 \pm 1.30) \times 10^{-4}$ (GN93) to $(O/H)_\odot = (4.90 \pm 0.60) \times 10^{-4}$ (AGSS09) while the global metallicity is diminished by about 25% from $(Z/X) = 0.0244$ (GN93) to $(Z/X) = 0.0181$ (AGSS09). Independent evaluations by Caffau *et al.* (2008), also based on 3D model atmospheres, yield a higher value of the oxygen abundance $(O/H)_\odot = (5.75 \pm 1.01) \times 10^{-4}$ but still lower than the one in GN93. For thorough information on the subject the reader is referred to the discussion in Section 2.1.2.

Helioseismic inferences. The solar 5-minute oscillations were first detected with spectroheliographs by Evans & Michard (1962) and Leighton *et al.* (1962). Nowadays the frequencies, amplitudes and lifetimes of solar oscillations are measured through observations in Doppler velocity or in intensity by ground-based experiments (BiSON, GONG, LOWL IRIS, TON) or by space instruments (GOLF, VIRGO, SOI/MIDI). The maximum velocity amplitude of solar oscillations is about 15 cm s^{-1} while the relative change in intensity is 4×10^{-6}. The lifetimes of the modes can be of several months.

The properties of solar oscillations are described in details in many review papers and textbooks (see for instance Christensen-Dalsgaard 2002, for a recent review). The amplitudes of the oscillations are extremely small which allows one to treat them as small perturbations around a stationary equilibrium model, assumed to be a normal spherically symmetric solar evolution model. Furthermore, it can be shown that, except in the region of the Sun close to the surface, the oscillation

periods are much shorter than the timescale for energy exchange which allows the motion to be considered adiabatic. The solution of the equations of linear adiabatic stellar oscillations yields oscillation eigenmodes of frequency $\nu_{n,\ell,m}$. They consist of a radial part characterised by the radial order n (n is the number of nodes along the radius) and a surface pattern described by a spherical harmonic $Y_{\ell,m}$ where ℓ is the mode angular degree (ℓ is a measure of the number of wavelengths along the circumference) and m is the azimuthal order (number of nodes along the equator). Two important characteristic frequencies intervene in the problem in addition to the cutoff frequency. First, the acoustic Lamb frequency $S_\ell = [\ell(\ell+1)]^{\frac{1}{2}}(c/r)$ which is a measure of the compressibility of the medium and depends on the adiabatic sound speed $c = (\Gamma_1 P/\rho)^{\frac{1}{2}}$ where $\Gamma_1 = (\partial \ln P/\partial \ln \rho)_{\mathrm{ad}}$ is the first adiabatic coefficient and ρ the density. Second, the buoyancy or Brunt-Väissälä frequency N_{BV} given by $N_{\mathrm{BV}}^2 = g\left(\frac{1}{\Gamma_1}\frac{d\ln P}{dr} - \frac{d\ln \rho}{dr}\right)$ where g is the local gravity. N_{BV} is positive in a radiative region where it corresponds to the oscillation frequency of a perturbed fluid element while it is negative in convective regions. It is worth noticing that, for ideal gases, $c \propto (T/\mu)^{\frac{1}{2}}$ and $N_{\mathrm{BV}}^2 \simeq (g^2\rho/P)(\nabla_{\mathrm{ad}} - \nabla + \nabla_\mu)$ where ∇_{ad} and ∇ are the adiabatic and actual temperature gradient, respectively, μ is the mean molecular weight and ∇_μ is its gradient.

Different kinds of waves can propagate inside a star according to the value of the frequency: modes with frequencies higher than both S_ℓ and N_{BV} correspond to standing sound waves (acoustic p-modes), while modes with frequencies lower than both S_ℓ and N_{BV} correspond to standing gravity waves (g-modes). Other modes are evanescent. Most important, if rotation is neglected, the frequency of the modes can be expressed as a function solely of the density and sound speed. Therefore different frequency spectra are expected for stars of different mass, evolutionary stage and chemical composition. As an illustration Figure 2.1 shows the regions of propagation of p- and g-modes in the present solar interior.

In the solar case, the spatial resolution is very high which provides accurate frequencies for $\sim 10^5$ modes over a broad range of spherical harmonic degrees ℓ, from 0 to more than 1000. For many of the modes, the fractional frequency precision reaches levels of several parts in 10^6. Most of the observed modes are pressure (acoustic) modes excited stochastically in the solar convective envelope. As illustrated in Figure 2.2, solar oscillation waves propagate in cavities, the size of which depend on the degree ℓ of the mode. Modes are trapped between the solar surface where they are reflected due to decreasing density and an inner turning point located at a distance r_t from the centre given by $c(r_t)/r_t = 2\pi\nu_{n,\ell}[\ell(\ell+1)]^{-\frac{1}{2}}$. The broad range of ℓ modes accessible through observations allows one to scan a large part of the solar interior, from regions very close to the surface down to the location of their associated turning points. Modes of high degree ℓ provide information on the external layers while low degree modes probe the deep solar interior. With the present available data the whole region between $\sim 0.05\ R_\odot$ and $\sim 0.95\ R_\odot$ is scrutinised (see *e.g.* Basu & Antia 2008, and references therein).
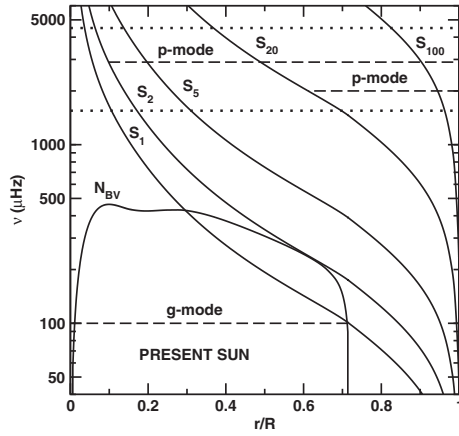
Fig. 2.1. Oscillation propagation diagram in a solar interior model. The frequency domain corresponding to solar-like oscillations (high degree p-modes) is in-between the dotted lines.
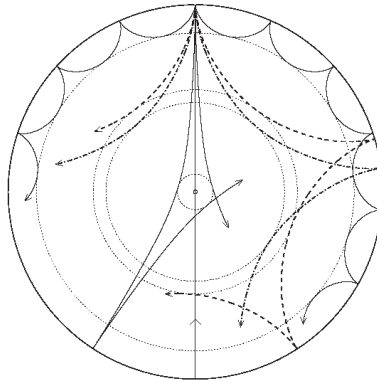
Fig. 2.2. Propagation of sound waves in the solar interior. In their way towards the centre, the wave paths are curved due to the increase of the sound speed with depth. Waves are refracted at their inner turning points, materialised by dotted circles. They then propagate back to the surface where they are reflected due to the rapid decrease of density. Figure reproduced from Christensen-Dalsgaard (2002).

Since a large set of extremely accurate frequencies are available, it is possible to perform an inverse analysis to resolve the structure and rotation of the interior of the Sun. Different inversion techniques have been designed (see *e.g.* Christensen-Dalsgaard 2002). Internal variation profiles have been derived for the adiabatic sound speed (accuracy of a few parts in 10^4), for the density (accuracy of a few parts in 10^3), and for the internal angular velocity $\Omega(r, \theta)$ where θ is the co-latitude.

Fig. 2.3. *Left:* continuous line, left vertical scale, is the variation of the sound speed in solar model *A* specified in Table 2.3. Dashed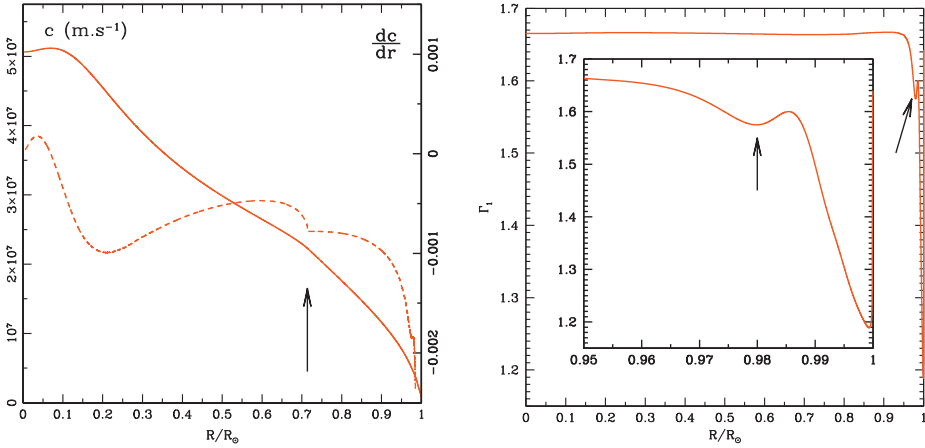 line, right scale is the corresponding variation of the sound speed gradient dc/dr. The arrow indicates the position of the basis of the convection zone. *Right:* variation of the Γ_1 adiabatic coefficient in model *A*. The insert is a zoom of the external layers. The arrows indicate the position of the helium dip, signature of the second ionisation of helium.

Internal profiles of the pressure and of Γ_1 which are directly related to the sound speed and density were also obtained.

Figure 2.3 (left panel) shows the internal profile of the sound speed and its radial derivative in the standard solar model *A* presented in the next subsection. A change of curvature is seen in the sound speed in the region between 0.70 and 0.75 $R_\odot$, which corresponds to the transition between the radiative and convective zones (hereafter cz). This signature is indeed also visible in the inverted solar sound speed profile which provides a precise inference of the radius at the basis of the convection zone R_{bcz} (see *e.g.* Basu & Antia 2008, and the data in Table 2.2). Other solar interior properties can be inferred from seismic data but depend on our knowledge of the plasma physics. Interestingly, the solar convection zone is mostly adiabatic, so that its structure depends solely on the equation of state (EoS) and on the chemical composition. The adiabatic coefficient Γ_1 estimated from the frequency inversion carries information on the helium abundance in the convective envelope Y_{cz}. In an ideal fully ionised gas $\Gamma_1 = 5/3$, but Γ_1 decreases in zones of partial ionisation. On the Γ_1-profile extracted from solar model *A* and shown in Figure 2.3, a dip is seen near 0.98 $R_\odot$. This dip is the signature of the second ionisation of helium, and its depth depends on the helium abundance in the zone under consideration. Since the convection zone is fully mixed on small timescales, the helium abundance in the ionisation zone reflects the abundance in the whole convective envelope. Different methods have been used to infer Y_{cz} (see *e.g.* Basu & Antia 2008, and references therein). Table 2.2 provides current values of R_{bcz} and Y_{cz} and their uncertainties as determined by Basu & Antia (2004).

Table 2.2. Solar convective envelope properties from helioseismology.

R_{bcz} $(R_\odot)$	Y_{cz}
0.7133 ± 0.0005	0.2485 ± 0.0034

Mean values obtained from the GONG and MDI observations. The error bars include systematic errors, including those stemming from the use of different EoS (see Basu & Antia 2004, for more information).

Table 2.3. Solar models obtained with different input mixtures and physics.

model	mixture	special inputs	Y_0	$(Z/X)_0$	Y_{cz}	R_{bcz} $(R_\odot)$
A	GN93	–	0.273	0.0278	0.244	0.714
B	GN93	no diffusion	0.266	0.0245	0.266	0.729
C	AGSS09	–	0.261	0.0203	0.232	0.727
D	AGS05	–	0.264	0.0196	0.233	0.730
E	GN93		0.276	0.0285	0.245	0.716
F	GN93	OP opacities	0.274	0.0285	0.244	0.713

Models A to D have been calculated with the Cesam2k code (Morel & Lebreton 2008) and models E and F with the CLÉS code (Scuflaire *et al.* 2008). Further details on the physics entering the calculations are given in the quoted papers. Unless specified the models take into account the microscopic diffusion of helium and heavy elements, including thermal, gravitational and chemical diffusion but excluding radiatively driven diffusion and are based on OPAL opacities and EoS (see text).

2.1.1.3   Results and caveats of solar model calculations

In the 1990s, standard solar models were mostly based on the canonical element mixture of GN93. The use of this mixture, together with updated microscopic physics, allowed one to build solar models in good agreement with both the helioseismological and the global solar observational constraints.

Model A presented in Table 2.3 is a calibrated standard solar model based on the GN93 solar mixture and on the Livermore opacities (OPAL95, Iglesias & Rogers 1996) and EoS (OPAL2005, see Rogers & Nayfonov 2002). It takes into account the microscopic diffusion of helium and heavy elements, including thermal, gravitational and chemical diffusion, but excludes radiatively driven diffusion (Michaud & Proffitt 1993). This model has been calculated with the Cesam2k stellar evolution code (Morel & Lebreton 2008), a code which has been compared to others and validated in the framework of the CoRoT ESTA comparison of stellar evolution and oscillation codes (Lebreton *et al.* 2008). In Figure 2.4 we show the differences between the sound speed profiles predicted by several solar models and the sound speed seismic determination of Basu *et al.* (2000). For model A and other similar models – not described here – produced by stellar modellers, the agreement between the predicted sound speed internal profile and the seismic findings are in the range $0.5-1\%$, while the convection zone depth and helium content reported in Table 2.3 agree well with the seismic data in Table 2.2. This remarkable – although not perfect – agreement has been a strong argument against
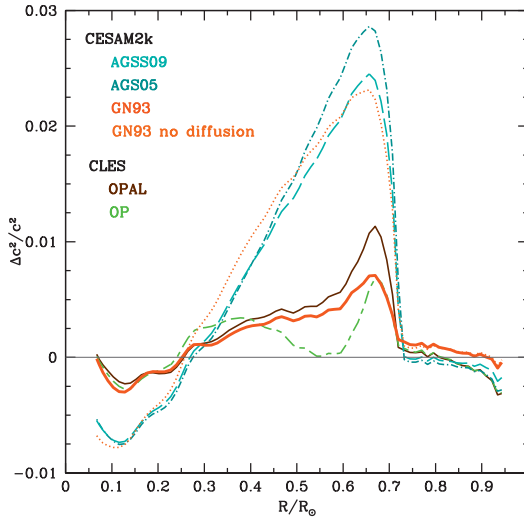
Fig. 2.4. Relative differences between the sound speed derived through inversion of oscillation frequencies by Basu *et al.* (2000) and the sound speed obtained in the solar models presented in Table 2.3: model *A* (thick continuous line), model *B* (dotted line), model *C* (dot-dashed line), model *D* (long dashed line), model *E* (thin continuous line), model *F* (long-dashed short-dashed line).

a stellar model origin for the so-called solar neutrino problem, which was finally understood as resulting from an inadequate understanding of the properties of the neutrino itself (see Avanzini 2011; Turck-Chièze *et al.* 2011, for recent results).

It is worth pointing out that it is the availability of helioseismic constraints that pressed solar modellers to consider the microscopic diffusion of chemical elements, in particular helium settling, mandatory input of solar model calculations (see *e.g.* Christensen-Dalsgaard *et al.* 1993). As an illustration we provide here results of model *B* which is similar to model *A* but without microscopic diffusion.

When confronted with the helioseismic inferences, this model is not acceptable, a major problem being that the predicted helium abundance in the convection zone is much higher.

The revision of the solar abundance mixture considerably darkened the picture of the nice agreement between the solar interior model and the observed oscillation frequencies and derived data. Models *C* and *D* have been calibrated with the same input physics as model *A* but with revised solar mixtures, *i.e.* the current AGSS09 mixture and the former AGS05 (Asplund 2005) mixture. As shown in Figure 2.4, in models *C* and *D*, the discrepancy in the sound speed already seen in model *A* just below the convection zone is strongly increased. Furthermore, the discrepant region now extends over the whole radiative zone and in the centre. Also, the agreement reached in model *A* with the seismic values of Y_{cz} and R_{bcz} is severely degraded. Remarkably, the disagreement in the sound speed is at the level of the

one obtained in models based on the GN93 mixture but ignoring the microscopic diffusion of helium and heavy elements, such as model B. The revision of the abundances of elements which are important contributors to the opacity of the plasma (such as O, Ne, Fe) is at the origin of the problem.

2.1.1.4 Can we satisfy seismic inferences in solar models based on the new mixture?

The disagreement in the sound speed is more noticeable in the radiative regions located just below the convective envelope between 0.4 and 0.7 $R_\odot$. This has naturally led to the questioning of the validity of the opacities in these regions. Opacities govern the radiative transport of energy, and their values impact both the structure of the radiative zone and the depth of the convective envelope. It has been estimated by Turcotte et $al.$ (1998) that in solar models based on the GN93 mixture, the main contribution to the opacity just below the convection zone is due to oxygen (35%), iron (20%), hydrogen (15%) and neon (13%), while in the central regions opacity is dominated by He, Fe and H (with contributions of 35, 27 and 23% respectively). With the new solar mixture, the opacity right below the convection zone is smaller by about 25%. If this mixture is indeed the correct one, one has to find compensations either in the opacities themselves or in other physical inputs of the models (see for instance Bahcall et $al.$ 2005; Montalbán et $al.$ 2004, and references therein).

According to Bahcall et $al.$ (2005), with the revised solar abundances the opacity should be increased by about 11% in the whole radiative region extending from 0.4 to 0.7 $R_\odot$. Subsequently, Christensen-Dalsgaard et $al.$ (2009) and Villante (2010) attempted to − artificially − adjust the solar model internal opacity to reproduce the helioseismic sound speed inference, and they both needed an opacity increase from $25 - 30\%$ beneath the convection zone to a few per cent in the solar core. As discussed by Badnell et $al.$ (2005) errors at this level are hardly supported by the comparisons of the two main sets of modern opacity data currently available, the OPAL opacities and those from the Opacity Project (OP, Badnell et $al.$ 2005). These opacity data show at the most differences of a few percent. As an illustration, we present in Table 2.3 two calibrated solar models, models E and F, both calculated with the old GN93 mixture but based on respectively the OPAL and OP opacities. These models have been obtained with the CLÉS code (Scuflaire et $al.$ 2008), a code which has also been validated in the CoRoT ESTA code comparison (Lebreton et $al.$ 2008). The comparison of models E and F shows that the OP data provide a better fit to the helioseismic sound speed in the outer radiative zone. However, in models using the revised solar mixture, the OP opacities would be unable to erase the whole discrepancy either in the radiative zone or in the centre. They would neither solve the problem encountered with Y_{cz} and R_{bcz} since these parameters are not that sensitive to the change from OPAL to OP (see $e.g.$ Basu & Antia 2008).

Uncertainties in the microscopic diffusion treatment and diffusion coefficients that would impact the chemical composition profiles – and therefore the opacities −

have also been invoked (see *e.g.* Bahcall *et al.* 2005; Montalbán *et al.* 2004). As pointed out by Guzik *et al.* (2005), several assumptions on the physics of the solar plasma are made to treat the diffusion of chemical elements in stellar models. Furthermore while the gravitational settling rates are rather secure, the thermal diffusion coefficients could still be in error by 30% (see Paquette *et al.* 1986). Also radiative forces are often neglected; however according to the detailed calculations of Turcotte *et al.* (1998) their impact on the opacities below the convective zone are rather moderate (0.5%) while the sound speed is affected at most by 0.06%. Guzik *et al.* (2005) investigated the effects of various diffusion treatments in solar models, and concluded that − improbably − high thermal diffusion coefficients are required to get a sound speed profile closer to the observations in models adopting the revised solar mixture. Also models based on such enhanced diffusion coefficients yield a helium abundance in the convective envelope significantly lower than the seismic finding.

Another approach has been followed by Delahaye & Pinsonneault (2006) who inferred the chemical composition of the Sun, in particular the $(O/H)_\odot$ ratio, by using the helioseismic values Y_{cz} and R_{bcz} to constrain solar interior models. By carefully examining the possible − known − uncertainties in solar models, including errors in the input physics and global parameters, they obtain an oxygen to hydrogen number ratio $(O/H)_\odot = (7.24 \pm 1.19) \times 10^{-4}$ compatible with the value in the GN93 mixture but far from that in the AGSS09 revised mixture. Delahaye & Pinsonneault conclude that the new solar abundances are severely disfavoured unless some non-standard physical effects alter the present view of the solar interior.

In addition to possibly erroneous opacities and diffusion velocities, other suggestions have been made to reconcile solar models based on the new abundances with helioseismic inferences. It has been suggested that the helioseismic helium abundance in the convection zone should be re-estimated and assessed, because it is sensitive to the equation of state used in the solar model computation and to the method of analysis. Also, the neon abundance has been incriminated but again the required abundance is improbably high, and it is impossible to reconcile the values of Y_{cz}, R_{bcz} and the sound speed and density profiles in models based on low oxygen and high neon abundances. Concerning opacities, interesting collaborative studies are in progress to examine and compare new theoretical and experimental opacity data from high-energy lasers and Z-pinches (see *e.g.* Turck-Chièze *et al.* 2011).

Last but not least, non-standard physical processes, *e.g.* internal gravity waves, overshooting, mass loss or accretion during the early solar history and magnetic fields, could also play a role but they have to be properly quantified and assessed, not to say that a proper theoretical description of some of them is still lacking. Some of them have been − unsuccessfully − tested in solar models (see for instance Montalbán *et al.* 2004; Castro *et al.* 2007; Guzik & Mussack 2010; Turck-Chièze *et al.* 2011, and references therein). In addition to the helioseismic constraints discussed here (helium abundance in and depth of the convective envelope, sound speed and density profiles), the new physical processes to be investigated should

also be able to account for the abundances of the light elements in the solar photosphere (Li, Be) and the solar internal rotation profile.

2.1.2   The solar atmosphere

In this section we ran into the awkward situation of not reaching consensus on the best procedure for the determination of the oxygen abundance in the solar atmosphere and on its ultimate best estimate. This reflects the present status of conflicting results obtained by different research groups. We would like to emphasise that the following primarily reflects the opinion of the main author of this section (NG), and is not shared in all details by others (HL). We are conscious that this is a somewhat unsatisfactory situation since one usually strives to supply the reader with a unique and hopefully authoritative view on a given subject. However, much of what is discussed is indeed not disputed, and conflicting opinions are present on a level which is perhaps of secondary importance for the typical reader. From this point of view we believe that the following discussion nevertheless manages to provide the reader with insight into the procedures and difficulties which one encounters when determining the atmospheric oxygen abundance of the Sun by means of spectroscopic methods.

2.1.2.1   The photosphere

The commonly adopted solar abundance of oxygen, derived from photospheric spectral lines, has recently experienced a significant downward revision by almost a factor of 2. We shall discuss the many reasons for this decrease, recommend a new value of the solar oxygen abundance, $A(O) = 8.69 \pm 0.05$ (Asplund *et al.* 2009), and examine the main implications of this new value.

Indicators of oxygen in the solar spectrum.   In spite of its very large abundance, there are only a handful of permitted O I lines in the solar photospheric spectrum which are sufficiently clean. However, three very low excitation forbidden lines at 6300, 6363 and 5577 Å are also present in the solar spectrum. Although very faint and blended, the first by a Ni I line, the second by two CN lines and the third by two C_2 lines, those lines have often been used in abundance studies. These forbidden lines, being very low excitation lines of a dominant species, namely O I, are not sensitive to departures from LTE. On the contrary, it is well known that the very high excitation permitted lines of O I suffer from rather large NLTE effects (see below).

Fortunately, the infrared spectrum and, especially, the infrared spectrum observed from space by the ATMOS experiment (Farmer & Norton 1992) shows an extremely large number of very clean absorption lines of the OH molecule in its ground state: pure rotation lines beyond 9 μm, vibration-rotation lines ($\Delta v = 1$) around 3 μm and eventually vibration-rotation lines of the first overtone ($\Delta v = 2$) lines around 1.6 μm. The latter lines are extremely faint (equivalent widths, EW, from 0.075 to 0.14 pm), hardly distinguishable from the noise. Asplund *et al.* (2004) did not consider these lines because of the difficulties in measuring them,

but Meléndez (2004) succeeded in using them as an O-abundance indicator (see below).

It has often been claimed that these molecular lines are not reliable indicators of the oxygen abundance because of their high temperature sensitivity. Asplund *et al.* (2011) have however shown that these OH lines are not more temperature-sensitive than the very high excitation permitted O I lines.

The infrared solar spectrum is also a gold mine as far as CO is concerned. An extremely large number of very clean vibration-rotation lines of CO are observed between 4.3 and 7.4 μm ($\Delta v = 1$) and between 2.3 and 2.9 μm ($\Delta v = 2$), together with lines of the isotopes. These lines have been used by Scott *et al.* (2006) and Ayres *et al.* (2006) to derive new abundances of C and O as well as the solar isotopic ratios.

We note that the lines of the electronic transitions (Asplund *et al.* 2005a) of OH in the blue solar spectrum (below 340 nm) cannot be used because they all suffer from severe blending problems.

Solar photospheric models. The new analyses of the solar chemical composition (Asplund *et al.* 2005a, 2009) and, in particular of the solar abundance of oxygen (Allende Prieto *et al.* 2001; Asplund *et al.* 2004; Asplund *et al.* 2011; Caffau *et al.* 2008) have been driven by the availability of three-dimensional, time-dependent, hydrodynamical models of the solar atmosphere (3D), successfully applied to the solar spectrum line formation (Asplund 2005; Asplund *et al.* 2005a; Caffau *et al.* 2008).

Various classic 1D models of the photosphere are also employed. The empirical model of Holweger & Müller (1974) (HM) has been used in a large number of solar abundance analyses for more than 30 years. In addition, theoretical models such as MARCS (Gustafsson *et al.* 2008) and Kurucz (see http://kurucz.harvard. edu) were also applied, particularly in stellar abundance analyses. When comparing stellar and solar results, data have to be obtained with the same type of model because we know that, among other dependencies, abundances might be very model dependent. A mean 3D model, 1DAV (sometimes also referred to as <3D>), has also been used occasionally; it is the result of averaging the 3D model mentioned above temporally and horizontally on surfaces of equal optical depth (Asplund *et al.* 2004; Asplund *et al.* 2011; Caffau *et al.* 2008; Steffen *et al.* 1995). Comparing 3D and 1DAV results, based on the same mean temperature structure, actually shows the role played by the heterogeneities.

The main characteristics of the 3D models are as follows (more details can be found in Stein & Nordlund 1998 and Nordlund *et al.* 2009 and references therein). The models are highly realistic, reproducing successfully a wide range of observational constraints. For the first time, the observed heterogeneous and ever changing nature of the photosphere (granulation) is successfully modelled. Also for the first time, the 3D models allow one to reproduce the solar line profiles as they are really observed in the solar spectrum: all the line profiles are asymmetric and the wavelengths of the line centres are shifted. These subtle characteristics in the line shapes result from the complex motions of matter in the photosphere. These

material motions themselves result from subtle overshooting of matter at the upper limit of the solar convection zone and propagating to high photospheric layers. Obviously, 1D models cannot reproduce these subtle but important properties of the line profiles, leading to unshifted, symmetric lines. Furthermore, the widths of the spectral lines are naturally predicted with the 3D models without invoking any fudge parameter such as micro- and macro-turbulence needed with 1D models. In addition, the new generation of 3D models reproduce in detail the observed centre-to-limb variation of the continuous intensity and the absolute intensity. 3D models are undoubtedly a great step forward in our modelling of the real nature of the solar photosphere (Asplund 2005; Caffau *et al.* 2008; Koesterke *et al.* 2008; Ludwig *et al.* 2009) (see also Sect. 1.2.2.1). Some examples of their realism will be shown hereafter.

The results. We hereafter describe the results recently obtained by different authors from the various indicators of the photospheric abundance of oxygen listed above. This detailed account illustrates the practical difficulties encountered in spectroscopic abundance studies.

The forbidden lines of O I. The [O I]λ6300 line is a faint (EW = 0.465 pm on disc-centre intensity spectra and 0.53 pm on disk-integrated flux spectra) but clear line. From the equivalent widths recently measured by different authors, we can estimate that the uncertainty of these measurements is very small, around 2 to 3%. This line is well known to be blended by a weak Ni I line. The transition probability of the latter line has been accurately measured by Johansson *et al.* (2003), $\log gf = -2.11 \pm 0.06$. Sophisticated analyses of this solar [O I] feature have been made recently based on equivalent widths and profile fittings, both on disc-centre intensity and flux spectra, with different 3D and 1D photospheric models (Allende Prieto 2008; Allende Prieto *et al.* 2001; Asplund *et al.* 2004; Asplund *et al.* 2011; Ayres 2008; Caffau *et al.* 2008; Scott *et al.* 2009). The main problem in all these analyses is the way the Ni I contribution is estimated as this explains the rather large differences in the results of the above mentioned works. Very recently, Scott *et al.* (2009) have shown, thanks to their new analysis of the Ni solar abundance, using many Ni I lines and different photospheric models, that the contribution of the Ni I line to the forbidden O I line can be estimated accurately and independently of the model atmosphere used: 0.173 pm in intensity and 0.191 pm in flux. This allowed Scott *et al.* (2009) and Asplund *et al.* (2011) to derive the O abundance from this line with a new 3D model, $A(\text{O}) = 8.64$. It is clear that Ni I contributes to about 37% to the observed line; neglecting this contribution easily explains why older solar O abundances derived from this line without the Ni I contribution led to very large values, around 8.9. We note that Caffau *et al.* (2008) found for this line a result of 8.68, 10% larger than the value mentioned above, with a somewhat different approach to estimate the Ni I blend by computing it from the Ni abundance recommended by Grevesse & Sauval (1998).

Recently, Centeno *et al.* (2008) analysed this blend in a sunspot. Because of the different polarisation of the [O I] and Ni I lines it is in principle possible to separate the Ni I contribution from that of [O I]. They concluded that the O abundance was rather large, $A(O) = 8.86$. However, Scott *et al.* (2009) have later clearly shown that a more adequate interpretation of the observations of Centeno *et al.* reduces the oxygen abundance to $A(O) = 8.66$.

Ayres (2008) also analysed this line with a single snapshot of the same 3D solar CO5BOLD model used by Caffau *et al.* (2008). He found a much larger abundance, $A(O) = 8.81$. However, he treated the Ni I contribution as a free parameter in his profile fittings, and concluded that the contribution of Ni I to the blend is much smaller.

The second [O I] line analysed, at 6366 Å, is even fainter than the first line discussed above (EW = 0.183 pm in flux spectra and 0.16 pm in disc-centre spectra). From recent measurements by Caffau *et al.* (2008) and Asplund *et al.* (2011), we estimate the uncertainty of these equivalent widths to be within 10%. However it is blended by two rather high excitation CN lines, Q2(25.5) 10-5 and P1(53.5) 8-3. The contributions of these two lines to the observed equivalent width cannot be predicted with accuracy because the transition probabilities of these lines are very uncertain. They have been derived empirically by Asplund *et al.* (2011) from other CN lines observed in the solar spectrum near the [O I] line. They amount to 0.063 pm for the flux and 0.05 pm for the intensity, with uncertainties of 30%. Caffau *et al.* (2008) used 0.05 and 0.03 pm respectively. The O abundance results of these two analyses are $A(O) = 8.78 \pm 0.05$ (Caffau *et al.*) and 8.70 ± 0.05 (Asplund *et al.*). This rather large difference of 0.08 dex is essentially due to the different CN contributions adopted by Caffau *et al.* and Asplund *et al.*. As an example, if the Caffau *et al.* results are normalised to the Asplund *et al.* CN contributions, their abundance result becomes $A(O) = 8.72$ compared with 8.70 for Asplund *et al.*; the small 0.02 dex difference arises from the different 3D models used by the two groups.

We also notice that the abundance correction for the blend by the two CN lines amounts to about -0.12 dex; a further correction of around -0.02 dex has to be applied for the use of a 3D model, compared with the result obtained with the 1D HM model. These corrections explain why neglecting them in some older oxygen abundance analyses led to abundance results around 8.9.

The third forbidden O I line at 5577 Å has recently been analysed by Meléndez *et al.* (2008). It is heavily blended by two C_2 lines and the [O I] line is only a minor contributor to the blend. Asplund *et al.* (2011) have shown that it is however possible to estimate the contributions of the C_2 lines, independently of the model atmosphere used, from neighbouring C_2 lines and from predictions made with abundances obtained from new analyses of the C_2 Swan bands. With these blends correctly taken into account, the new result from Asplund *et al.* with a new 3D model is $A(O) = 8.76$.

Summarising the O abundance results derived from the forbidden lines, we have $A(O) = 8.70 \pm 0.05$ from Asplund *et al.* (2011) (3 lines) and 8.73 ± 0.07 from Caffau *et al.* (2008) (2 lines). We also note that the abundances obtained from the

three [O I] lines show a spread from 8.64 to 8.70 and 8.76 in the work of Asplund *et al.*. This is due to the uncertainties in the equivalent width measurements of these faint lines combined with the rather large uncertainties of the blends.

The permitted lines of O I. Asplund *et al.* (2004) and Caffau *et al.* (2008) analysed a handful of high excitation permitted O I lines using their respective 3D models. They included the same 6 lines with the well-known IR triplet at 7771, 7774 and 7775 Å. Caffau *et al.* however added two more IR lines, and they analysed their lines in various spectra in flux and in intensity whereas Asplund *et al.* only used lines measured in flux spectra. Asplund *et al.* (2011) re-analysed the O I lines with a new 3D model and improved estimates of the departures from LTE. It has actually been well known for quite a long time that rather important departures from LTE affect these high excitation O I lines (Allende Prieto 2008; Allende Prieto *et al.* 2004; Asplund *et al.* 2004; Caffau *et al.* 2008; Kiselman & Nordlund 1995; Sedlmayr 1974; Shchukina *et al.* 2005). Recent numerical experiments show that the computed NLTE effects depend only very slightly on the model. However, one of the main problems is the efficiency of the collisions with neutral hydrogen atoms which are about 10^3 to 10^4 times more numerous than the electrons. Cross sections for these collisions are badly known and existing approximations might overestimate the cross sections by orders of magnitude. The question is: are these collisions really efficient and if so what is their impact? More details can be found in the papers cited above. Caffau *et al.* (2008) give NLTE corrections to the LTE derived abundances: they are very large, of order -0.28 to -0.21 dex for the strongest O I lines of the IR $\lambda7770$ triplet when using flux data and neglecting the collisions with the neutral hydrogen atoms. If these collisions are taken into account with the available cross sections, these corrections are much smaller, -0.16 to -0.12 dex for the same lines. For lines treated in the spectrum at the centre of the disc, the NLTE effects are smaller by 50 to 60%. Comparing the spread of the LTE 3D abundance results to the clustering of the same results in NLTE shows that the NLTE corrections are not only necessary but quite realistic. Very recently Pereira *et al.* (2009) succeeded in calibrating the effect of the collisions with H atoms from very accurate centre-to-limb observations of the O I lines. They confirmed that rather large NLTE effects are present, and concluded that these NLTE effects are better estimated with the available theoretical cross sections.

From the six permitted lines common to both works, the O abundance found by Asplund *et al.* (2004) is $A(O) = 8.64$ whereas the value of Caffau *et al.* (2008) is 25% larger, $A(O) = 8.74$. This last value is the unweighted mean of Caffau *et al.*. The discrepancy between these results is explained by the differences in treating the collisions with H atoms and the somewhat distinct NLTE corrections (0.04 dex), by the differences between the various 3D models and, more importantly, by the differences in the equivalent widths adopted for the lines. Actually the EWs measured by Caffau *et al.* (2008) are systematically larger than any other independent measurement. Asplund *et al.* (2011) carefully remeasured these EWs, and never succeeded in reproducing those by Caffau *et al.*. For the IR

$\lambda7770$ triplet, for example, they found EWs about 4% smaller than those of Caffau *et al.*. If we normalise the results of Caffau *et al.* (2008) as well as those of Asplund *et al.* (2004) for the new EWs, both works lead to oxygen abundances in excellent agreement, 8.71 and 8.70. Very recently Asplund *et al.* (2011) re-analysed these lines with a new 3D model and new NLTE corrections as mentioned above, and found $A(O) = 8.69 \pm 0.05$. We note however that Caffau *et al.* recommend a much larger value from their weighted mean result, 8.79.

Socas-Navarro & Norton (2007) constructed an empirical 3D model from spatially resolved spectro-polarimetric observations of spectral lines, and applied it to the analysis of simultaneous observations of the infrared O I $\lambda7770$ triplet. Their NLTE result is $A(O) = 8.63$.

The OH lines. Asplund *et al.* (2004) considered a large number of very clean and un-blended OH vibration-rotation and pure rotation lines in the infrared solar spectrum obtained from space by Farmer & Norton (1992). These lines, which have been revisited recently by Asplund *et al.* (2009) and Asplund *et al.* (2011) are expected to be formed in LTE (see the above mentioned paper for references). As already mentioned these lines are not more temperature sensitive than the high excitation O I lines. They are however formed in somewhat higher layers than the atomic lines.

The vibration-rotation lines of OH, which are formed at optical depths of about $\log \tau_{500} \sim -1.4$ for the 1D HM model, lead to a low abundance of oxygen, namely $A(O) = 8.69 \pm 0.03$ (Asplund *et al.* 2009) with a very small dispersion. We also note that the abundances derived from the different 1D models are quite different from the 3D result, because of the rather large temperature differences between the models in these layers. For example, the abundance derived with the frequently used 1D HM model is $A(O) = 8.86$, *i.e.* 0.17 dex larger than the 3D result.

The results for the purely rotational lines of OH, which are formed in higher layers between $\log \tau_{500} \sim -2$ and -1.6 for the HM model, show anomalous dependencies on the line intensities certainly related to the formation depth (Asplund *et al.* 2004; Asplund *et al.* 2011). These results on the abundance behaviour show that the realism of the 3D model begins to deteriorate towards the higher atmospheric layers (see next section). The stronger purely rotational lines of OH will therefore not be considered in the final result, only values obtained from a large number of fainter lines. The 3D abundance is $A(O) = 8.69 \pm 0.03$, in very good agreement with the findings from the other indicators and with a very small dispersion. Again for the same reasons as mentioned above, the value obtained with the 1D HM model, $A(O) = 8.83$, is 0.14 dex larger than the 3D outcome.

Meléndez (2004) succeeded in using the very faint vibration-rotation lines of the first overtone ($\Delta v = 2$) lines. Although extremely faint and therefore very difficult to measure with some accuracy, these OH lines are formed much deeper than the other OH lines. Actually, these very faint lines are observed around 1.6 μm where the continuous opacity reaches a minimum, *i.e.* at the deepest photospheric layers.

The 3D abundance, $A(O) = 8.57 \pm 0.06$, from Meléndez (2004) is also marginally in agreement with the other 3D values but with a much larger dispersion.

The CO lines. Scott *et al.* (2006) applied the 3D model to the analysis of the numerous vibration-rotation lines of the $\Delta v = 1$ and 2 sequences of CO observed in solar infrared spectra from space. The main characteristic of these CO lines is that they cover a very large range of optical depths of formation, from about $\log \tau_{500} \sim -1.5$ upwards. Because of its large dissociation energy, 11.108 eV, CO is the most sensitive temperature indicator: if we change the temperature by 1%, the number of CO molecules varies by about 25%. It is the best "thermometer" to test the realism of the models in a large optical depth range.

These lines have previously caused a great deal of trouble when analysed with 1D models (Ayres 2002; Grevesse & Sauval 1991; Grevesse *et al.* 1995) requiring much lower temperatures than those used in the available models.

Scott *et al.* (2006) find that the weak CO lines, formed in the deepest layers, lead to abundances consistent with the results from other indicators. For these lines, the combined carbon and oxygen abundances are in perfect agreement with the new low solar abundances of O and C obtained by Asplund *et al.* (2005, 2009); Asplund *et al.* (2004) using the 3D model: $A(O) = 8.69$ and $A(C) = 8.43$. As the strength of the CO lines depends on the product of the abundances of O and C, *i.e.* the sum of $A(O)$ and $A(C)$, we see from Scott *et al.* (2006) that the C+O abundances are larger than the 3D result when using 1D models: 0.45 dex larger with the HM model, 0.31 dex with the MARCS model and still 0.13 dex larger with the 1DAV model. These significant differences testify, if necessary, to the extreme temperature sensitivity of the CO lines, and show that even *the 1DAV model, the mean 3D model which has the same mean temperature structure as the 3D model, cannot replace the real 3D model* (see hereafter).

On the other hand, the strongest CO lines, which form in the highest layers, are however not well reproduced by the 3D model when the same low abundance derived from the other indicators already discussed is used. The problem with the strong CO lines formed in very high layers of the photosphere shows once again that, as already mentioned for the strong purely rotational lines of OH, the 3D model is less successful in these layers.

Ayres *et al.* (2006) also analysed the same CO lines leading to quite a different outcome. Their analysis used empirical 1D models only, and ends up with a high value of the oxygen abundance distinctively different from the low value found with a real 3D model. Their result is expected: Grevesse & Sauval (1991) and Grevesse *et al.* (1995) already found the same kind of behaviour of the CO lines using a specially constructed empirical model. It is likely that when using the best 1D model one will never succeed in simulating the effect of the inhomogeneities as shown by the large differences in abundance obtained when 3D results are compared with "mean" 3D 1DAV values. This is clear from the discussion of OH lines and the large differences between the 3D and 1DAV results. For CO, the differences 3D−1DAV are much larger than those for OH (Scott *et al.* 2006). All this is nicely confirmed in a recent paper by Koesterke *et al.* (2008). *Using the*

Table 2.4. A summary of the solar oxygen abundances from different indicators and model atmospheres as obtained by Asplund *et al.* (2009) and Asplund *et al.* (2011). Kurucz's 1D results are from Meléndez (2004). In col.7 (CAF) we report the 3D results of Caffau *et al.* (2008).

Indicator	3D	HM	MARCS	$1DAV$	Kurucz	CAF	$3D - HM$
[O I] ...	8.70 ± 0.05	8.73	8.69	8.70	8.79	8.74 ± 0.05	-0.03
O I	8.69 ± 0.05	8.69	8.62	8.73	8.67	8.79 ± 0.04	0.00
OH .... ($\Delta v = 0$)	8.69 ± 0.03	8.83	8.78	8.75	8.80	$-$	-0.14
OH .... ($\Delta v = 1$)	8.69 ± 0.03	8.86	8.75	8.74	8.82	$-$	-0.17

best 1D model actually misses one of the most important characteristics of the 3D models: they exhibit horizontal inhomogeneities and a thermal profile resulting from the realistic modelling of the competing effects of radiation and advection of matter. Only spectral lines of a major species, which are much less temperature sensitive, will be much less affected by the resulting 3D effects.

Result summary. Table 2.4 presents a summary of the solar photospheric abundances as derived from all the indicators of the solar oxygen obtained with two different 3D models and various 1D models often used in solar and stellar abundance analyses. Comments on the main characteristics of these results have already been made in the various sections here above. We however emphasise that if the NLTE and 3D-1D effects (and the effects of blends) differ significantly among the various indicators of the oxygen abundance, the resulting final abundances derived from these various indicators agree very well. We clearly see that very consistent results are only obtained when analysed with the 3D model. The situation is much less satisfactory with the 1D models which lead to very large dispersions of the results.

From the results reported in Table 2.4, *the solar abundance of oxygen recommended by Asplund et al. (2009) and Asplund et al. (2011) becomes $A(O) = 8.69 \pm 0.05$.* At this point we recall that Caffau *et al.* (2008) obtain a different value of $A(O) = 8.76 \pm 0.07$ in their independent analysis. While the discrepancy is small by the standards of stellar spectroscopy, it indicates the noticeable level of mainly systematic uncertainties inherent to spectroscopic abundance determinations.

It should again be stressed that the fairly large difference with previous results, which are based on classic 1D models, cannot be attributed to the use of 3D models alone. Actually, more realistic NLTE treatments also play a crucial role in addition to the adoption of more recent transition probabilities, better observations and a proper accounting of blends as well as a very demanding selection of the best lines.

2.1.2.2   The corona

Information on the solar oxygen abundance can also be derived from the analysis of UV and X-ray spectra of the solar corona, from γ-ray spectra of solar flares as well as from the solar wind and solar energetic particles collected with space instruments.

We know that the corona is an extremely heterogeneous and variable medium with regions having temperatures from a few hundred thousand K to many millions K. The solar upper layers actually show extremely complex structures with quiet and active regions of very different sizes, shapes and activity levels developing on diverse timescales. The chemical composition varies tremendously among these different coronal regions. Furthermore the ratio O/H is generally quite difficult to derive directly for the same coronal matter, and O is often the reference element to which other elements are compared (Bochsler 2007a; Feldman & Laming 2000; Feldman & Widing 2003, 2007; Raymond 2004; Reames 1999).

One of the main features of the coronal abundances is the well-known first ionisation potential (FIP) effect: elements with FIP lower than about 10 eV (*e.g.* Ca, Mg, Si, Fe, . . .) are overabundant in the corona relative to the photosphere whereas higher FIP elements (*e.g.* C, N, O, Ne, Ar, . . .) display photospheric-type abundances in the corona. This is a highly variable phenomenon. The FIP bias, ratio of coronal to photospheric abundances, can be very variable from one medium to the other with mean values of 2 to 3 (see *e.g.* Fig. 10 of Mewaldt *et al.* 2007). We note that the new abundances have allowed the revision of this FIP bias to lower values suggesting that some coronal features might actually show FIP factors lower than 1 (Grevesse *et al.* 2007).

As oxygen is basically the reference element, the lower abundance obtained from the analysis of the photospheric spectrum will have a direct impact on the coronal abundances. The most important one is undoubtedly on the abundance of neon which has decreased, from the Ne/O ratio, by the same amount as the new solar O abundance. From the mean Ne/O ratio observed in quiet sun matter showing no trace of the FIP effect, Ne/O = 0.175 (Young 2005), the new solar abundance of Ne is $A(\text{Ne}) = 7.93 \pm 0.09$, smaller than the previously recommended value of about 8.10.

That value of the ratio Ne/O in the various coronal layers has become a very hot field in recent years. A summary of these debates may be found in Grevesse *et al.* (2007) and in Asplund *et al.* (2009). It seems that the above mentioned ratio, Ne/O = 0.175, is the most widely found. This ratio should not vary because Ne and O are both high FIP elements in spite of a much higher FIP for Ne (21.6 eV) than for O (13.6 eV). We have to keep in mind that much smaller and much larger values than Ne/O = 0.15 are found in some peculiar solar coronal indicators (see hereafter). Two recent papers claim that higher abundances of O (and Ne) can be derived from coronal matter. Landi *et al.* (2007) succeeded in deriving the absolute abundance of neon, the Ne/H ratio, from the analysis of the UV spectrum of a solar flare. Actually they compared the intensity ratio of a Ne IX line to the free-free continuum radiation close to the neon line. They found a high value of

Ne, $A(\text{Ne}) = 8.11 \pm 0.12$, *i.e.* 0.18 dex larger than that given here above. With this abundance of Ne and Ne/O = 0.15, they derive a high abundance of oxygen, $A(\text{O}) = 8.93$. We have however to recall that variations of the Ne/O ratio by more than a factor of 2 are observed among various solar flares (Fludra & Schmelz 1995; Schmelz *et al.* 2005). We have also to recall that young and very active stars show the inverse FIP effect, *i.e.* elements with high FIP are enhanced compared to the low FIP elements (Güdel 2004). As both O and Ne are high FIP elements, with Ne being much higher than O and thus more susceptible to fractionation, we suggest that such an effect could possibly take place in the very active solar flares, and therefore explain the high Ne and O abundances obtained by Landi *et al.* (2007).

A second paper by Bochsler (2007b) also leads to a high abundance of oxygen. From the analysis of the very variable abundances in the solar wind, he derived photospheric values for O and Ne, $A(\text{O}) = 8.87 \pm 0.11$ and $A(\text{Ne}) = 7.96 \pm 0.13$. The abundances of He, Ne and O vary tremendously in the solar wind, but the variations of these three high FIP elements are well correlated. Bochsler explains these variations, actually depletions in the solar wind, by an inefficient Coulomb drag. He succeeds in correcting for this process and derives the values mentioned above. It is worth mentioning that the correction factors, that differ for each of these 3 elements (larger for He, smaller for O and even smaller for Ne), sensitively depend on the mean He abundance in the solar wind. Bochsler adopted a ratio He/H = 0.04, compared with He/H = 0.085 in the convection zone. This ratio actually varies from ∼0.0 to ∼0.08 but the majority of the data cluster between 0.01 and 0.05. If we adopt a ratio He/H = 0.03 in the solar wind, a value that is as reasonable as 0.04, the results of Bochsler (2007b) should be reduced by 0.11 dex and become $A(\text{O}) = 8.76 \pm 0.11$ and $A(\text{Ne}) = 7.85 \pm 0.13$. These last values are in better agreement with the values recommended here.

2.1.2.3 Some implications of the new low solar O abundance and comments

Solar metallicity.   Due to the decrease of the solar abundance of oxygen and of the other elements (Asplund *et al.* 2009) which contribute to the metallicity, Z, the new value of Z will decrease accordingly. *The present-day value is $Z = 0.0134$, much lower than the canonical value of $Z = 0.02$* and lower than the widely used $Z = 0.0189$ (Anders & Grevesse 1989) and $Z = 0.017$ (Grevesse & Noels 1993; Grevesse & Sauval 1998). The often used ratio Z/X, X being the hydrogen mass fraction, becomes $Z/X = 0.0181$; it is of course also lower than previously recommended values.

Protosolar oxygen.   The protosolar chemical composition is obtained from the present values by correcting for the slow diffusion of the chemical elements at the bottom of the convection zone. This correction of order 0.04 dex (Asplund *et al.* 2009) depends on the diffusion velocity. It is in agreement with the observed data for He when comparing the present helioseismological He abundance to the protosolar result derived from the calibration of solar standard models. With

that correction, the protosolar abundance of O becomes $A(O) = 8.75$, and the protosolar metallicity, $Z_0 = 0.0142$ with $Z_0/X_0 = 0.0199$.

The Sun, a normal star. Previous studies suggested that the Sun had too high a metallicity as compared to the solar neighbourhood. The new solar metallicity, in which oxygen contributes to 43%, shows that the Sun is now in agreement with the surrounding interstellar medium and nearby B-stars. The agreement between the Sun and these young stars is in itself puzzling because we would expect, from basic galactic chemical evolution, the solar oxygen abundance to be lower than that in these young objects. Perhaps the Galactic chemical evolution has been very slow during the last 4.5 Gyr.

Miscellaneous. As the stellar abundances are generally referred to the solar values, the new solar data will obviously alter the cosmic yardstick. This plays a non-negligible role in various fields of astrophysics like stellar modelling as a whole because decreasing the heavy element abundances leads to changes in the masses and ages of stars, but also in giant planets, T-Tauri models, Herbig Ae/Be, lithium depletion in pre-main sequence, gas/dust ratio in dense interstellar clouds, beat Cepheids, etc.

Standard solar models. Last but not least, the new solar abundances introduce a very serious problem in the standard solar model. As the heavy-element abundances, and especially O, C, Ne, Fe, etc., play a subtle and/or dominant role in various solar layers including the core, the region just below the convection zone and the convection zone itself, the lower abundances of these elements lead to serious problems when the predictions of the standard solar model are compared with helioseismological data (see Sect. 2.1.1).

2.1.2.4   Conclusions

The use of 3D models is without any doubt a great step forward in a more realistic description of the solar photospheric layers. 3D models are certainly to be improved in the future by a more adequate description of radiative transfer. Progress is also expected in the description and computation of the physical processes, *e.g.* NLTE and molecule formation, as long as more accurate atomic and molecular data become available.

Let us end with a quote from Asplund (2005): "*History has repeatedly shown us that improved modelling (and we could add improved atomic and molecular data as well as better description of the physical processes and also more demanding choice of the indicators of the abundances) not only reduces the uncertainties but in many cases also forces dramatic reinterpretations of observations. The recent downward revisions of the C, N and O photospheric abundances by almost a factor of 2 (Asplund et al. 2009) is a (the latest) clear testament to this.*"

2.1.3 Meteorites

As a complement to the oxygen composition of the Sun, the different classes, groups and subgroups of meteorites mentioned in Section 1.3.1 yield information about the history of the early solar system and of planetary formation, and possibly on the number of bodies (asteroids) that are represented in the meteoritic record. Of particular relevance here is that meteorites, or at least a special class of them (see below), have been at the focus of much effort devoted over the years to derive a meaningful set of elemental abundances representative of the composition of the bulk material from which the solar system formed some 4.6 Gyr ago. This bulk material is made of a well-mixed blend of many nucleosynthesis agents (Big Bang, single or binary non-exploding or exploding stars of different masses and initial compositions, interaction of stellar energetic particles with circumstellar material, interaction of Galactic cosmic rays with the interstellar medium) that have contributed to its composition over the approximate 10 Gyr elapsed between the formations of the Galaxy and of the SoS.

The latest detailed analysis of the bulk SoS composition is due to Lodders (2003). As in previous compilations, the selected elemental abundances are largely based on the analysis of a special class of rare meteorites, the CI1 carbonaceous chondrites, which are considered as the least-altered samples of primitive solar matter available at present. Other solar system materials from other origins may exhibit substantial deviations from the CI1 in their elemental compositions. This results from the physico-chemical processes that may have operated at different levels in different phases of the solar system material. In the following, the CI1 elemental abundances will be referred to as the "meteoritic" abundances. The solar photospheric abundances now come in quite good agreement with the CI1 data for a large variety of elements (Asplund *et al.* 2005; see also Sect. 2.1.2), and will be simply referred to in the following as the "photospheric" abundances. Some discrepancies between meteoritic and photospheric abundances may be attributed to spectroscopic or atomic data problems, to depletion in the Sun, or to the loss of volatile elements from meteorites. The abundances of the noble gases Ar, Kr and Xe, as well as of some specific elements like Hg, have still to rely on theoretical considerations. In the following, the elemental abundances at the time of formation of the solar system evaluated from the meteoritic and photospheric data will be referred to as the solar system elemental abundances.

The isotopic composition of the elements in the solar system is mostly based on the terrestrial data, except for H and the noble gases (Lodders 2003). Some adjustments are also applied for Sr, Nd, Hf, Os and Pb. The practice of using terrestrial isotopic data is justified by the fact that, in contrast to the elemental abundances, the isotopic patterns are considered not to be unaffected to any significant level by geological processes. Only some minor mass-dependent fractionation may operate, but some very limited mass-independent processes cannot be excluded. A notable exception to the high bulk isotopic homogeneity comes from the decay of relatively short-lived radio nuclides that existed in the early SoS, and decayed in early-formed solids in the solar nebula. Also interplanetary dust particles contain

isotopic signatures apparently caused by chemical processes. Additional isotopic "anomalies" are identified in certain meteorites. They are observed in quite a large suite of elements ranging from C to Nd (including the rare gases), and are now known to be carried by high-temperature inclusions (mainly Ca-Al-rich type, referred to as CAI inclusions) of primitive meteorites, as well as by various types of grains (*e.g.* Meyer & Zinner 2006 for a review). These grains are considered to be of circumstellar origin (this is why they are sometimes referred to as "stardust"), and have survived SoS incorporation. In contrast, the CAIs are formed from solar system material out of equilibrium with the rest of the solar nebula.

The isotopic anomalies in stardust or SoS inclusions contradict the canonical model of a homogeneous and gaseous protosolar nebula, and provide new clues to many astrophysical problems, such as the physics and chemistry of interstellar dust grains, the formation and growth of grains in the vicinity of objects with active nucleosynthesis, the circumstances under which stars (and in particular solar-system-type structures) can form, as well as the early history of the Sun (in the so-called "T-Tauri" phase) and of the solar-system solid bodies. Last but not least, they raise the question of their possible nucleosynthesis origin. If this is indeed the case, they offer the exciting perspective of comparing to observation the predicted signature of a very limited number of nucleosynthetic events, even possibly a single one. This situation is in marked contrast with the one encountered when trying to understand the bulk SoS composition, which results from the well-homogenised mixture of a large variety of nucleosynthesis events, and consequently requires the modelling of the chemical evolution of the Galaxy.

This section presents a brief review of the meteoritic elemental and isotopic (normal bulk and anomalous) compositions of oxygen. This element has a privileged status as it is the third most abundant element in the SoS, and the most abundant in the terrestrial planets. In spite of this large abundance, its SoS value is difficult to evaluate with high accuracy. This arises from special problems to determine its photospheric abundance from the solar spectrum (Sect. 2.1.2) and to its high volatility, leading to a strong O depletion in meteorites (see below).

In cosmochemical studies, the atomic abundance $N(\text{El})$ of an element El is classically normalised to $N(\text{Si}) = 10^6$ silicon atoms. This corresponds to $A(\text{Si}) = 7.51$ in the astronomical scale, where the abundances are measured with respect to the number of H atoms set to $A(\text{H}) = \log n(\text{H}) = 12$, so that

$$A(\text{O}) = \log \epsilon(\text{O}) = \log \left[n(\text{O})/n(\text{H}) \right] + 12. \tag{2.1}$$

The reported $A(\text{Si})$ value results from the lowering of the value 7.54 of Lodders (2003) by 0.03 dex, as recommended by Grevesse *et al.* (2007) following a re-evaluation of the photospheric Si abundance (see Sect. 2.1.2). The (present) photospheric or meteoritic abundances have to be corrected in order to obtain the SoS abundances representative of the bulk primitive solar nebula. As discussed by Lodders (2003), heavy-element fractionation in the Sun has altered with time its photospheric abundance. She proposes to relate the present abundance $A(\text{El})$ of

an element El heavier than He to the SoS value $A(\text{El})_0$ 4.6×10^9 years ago by

$$A(\text{El})_0 = A(\text{El}) + 0.074. \tag{2.2}$$

From the above, it results that the relation between astronomical and cosmochemical abundance scales is given by

$$A(\text{El})_0 = \log\ N(\text{El})_0 + 1.58. \tag{2.3}$$

The O isotopic composition in a sample is often measured in δ units defined as

$$\delta^{17,18}\text{O}_{\text{SMOW}} = [(^{17,18}\text{O}/^{16}\text{O})_{\text{sample}}/(^{17,18}\text{O}/^{16}\text{O})_{\text{SMOW}} - 1] \times 1000. \tag{2.4}$$

The δ's express deviations in part per mil of $^{17}\text{O}/^{16}\text{O}$ and $^{18}\text{O}/^{16}\text{O}$ from the standard mean ocean water (SMOW) values 0.0003829 and 0.0020052, respectively (McKeegan *et al.* 2001).

2.1.3.1   The meteoritic oxygen abundances and isotopic compositions

The nebular oxygen, along with hydrogen, carbon and nitrogen, have been only partially incorporated into forming SoS solid bodies. The O meteoritic abundances measured in the four known CI1 meteorites (Ivuna, Orgueil, Revelstoke and Tonk) that are massive enough for multiple chemical analysis (this is not the case for the fifth CI1 meteorite Alais) indicate that they represent only about 50% of the photospheric abundances (Lodders 2003). This relates directly to the rather low O condensation temperature ($T_C \approx 180$ K). In fact, about one fourth of the O is first removed from the nebular gas by inclusion into silicates and oxides before water ice condensates at 182 K. Some percentage of the remaining O is further bound in magnetite that forms from Fe metal at about 370 K[1]. As a result of the limited condensation of oxygen in meteorites, including CI1, the meteoritic abundance data cannot be used to estimate the SoS O content, which has consequently to be obtained only from photospheric analyses.

As far as the O isotopic composition is concerned, nearly all terrestrial samples concentrate along a single line of slope 0.52, referred to as the "terrestrial fractionation line (TFL)", on a three-isotope diagram of $\delta^{18}\text{O}$ *versus* $\delta^{17}\text{O}$ (see Fig. 2.5). This slope is interpreted in terms of the *mass-dependent fractionation* resulting from chemical processes in a homogeneous reservoir. Such a fractionation produces changes in $^{17}\text{O}/^{16}\text{O}$ about a factor of 2 smaller than those in $^{18}\text{O}/^{16}\text{O}$ because of the twice as small isotope mass difference in the former case. Lunar samples do not deviate in a detectable way from the TFL, while largely molten and homogenised material, like the one originating from Mars or Vesta, are located on fractionation lines that parallel the TFL (see Yurimoto 2007).

Much excitement in the cosmochemistry and astrophysics communities has been caused by the discovery by Clayton *et al.* (1973) of variations in a range of

---

[1] Note that most of the CI1 magnetite likely results from aqueous alteration, and not from nebular gas condensation (Hong & Fegley 1998).
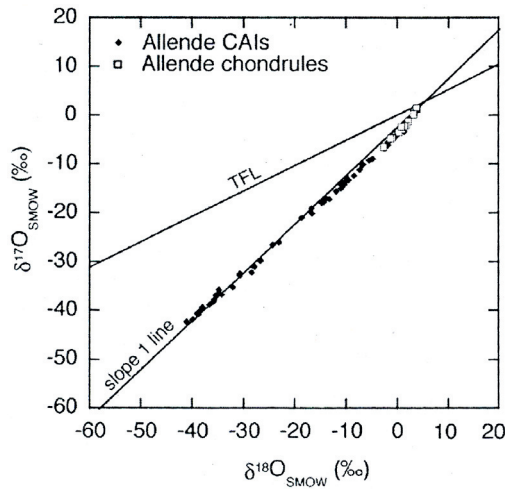
Fig. 2.5. Oxygen isotopic composition of the Allende meteorite CAIs and chondrules. The data reviewed by Clayton (1993) are seen to lie close to a line of slope unity, which differs markedly from the terrestrial fractionation line (TFL) of slope 0.52. More recent data do not modify the displayed pattern.

SoS materials of O isotopic compositions lying on a fractionation line with a slope deviating from that of the TFL. These oxygen components have been termed "isotopically anomalous", and are the result of *mass-independent fractionation* processes the very origin of which is considered as one of the most outstanding problems in cosmochemistry (McKeegan *et al.* 2001). The O isotopic anomalies in the components of the most primitive (*i.e.* least altered) meteorites (chondrites) and in differentiated meteorites from asteroids and Mars are reviewed in substantial detail by Yurimoto (2007). The summary of the situation presented below largely relies on their review, where many references can be found.

2.1.3.2 Bulk oxygen isotopic compositions of chondrites and achondrites

The bulk O isotopic compositions of chondrites show deviations from the TFL. With some exceptions, including the CI1s, most of them lie above or below this line. More precisely, chondrites in a single group define fractionation lines with slopes ranging from 0.5 to 1. This reflects mass-dependent fractionation (like aqueous alteration or thermal metamorphism) in the parent asteroids, or mass-independent effects in the various meteoritic components (see below).

The bulk O isotopic compositions of achondrites, as well as of rocks from the Moon or Mars, tend to be closer to the TFL than those of chondrites, some (like Moon samples) even lying on the TFL. Samples from extensively melted bodies define fractionation lines parallel to the TFL, while meteorites from only partly

melted asteroids that were not fully homogenised during melting define lines with steeper slopes than the TFL.

2.1.3.3   O isotopic anomalies in chondritic components

Chondrites are made of three major components which possibly formed at different times and/or locations in the SoS: (i) *refractory inclusions*, involving Ca-Al-rich inclusions (CAIs) and olivine aggregates (AOAs) made of individual grains of forsterite (Mg_2SiO_4), FeNi metal and small CAIs; (ii) *chondrules*, which are rounded objects whose main components are crystals of ferromagnesian olivine ($Mg_{2-x}Fe_xSiO_3$), pyroxene ($Mg_{1-x}Fe_xSiO_3$) ($0 < x < 1$) and FeNi metal, with interstitial glassy or micro-crystalline material. Some chondrules contain relict fragments of refractory inclusions and older chondrules, and are embedded in rims of igneous nature, or surrounded by fine-grained rims in primitive chondrites, and (iii) *a fine-grained matrix* made of mineral grains filling the interstices between refractory inclusions and chondrules. In primitive chondrites, the matrix is mostly composed of magnesian olivine and pyroxene crystals, and of amorphous ferromagnesian silicate particles. The matrices are chemically complementary to chondrules.

A question of substantial interest concerns the mechanism(s) and location(s) of formation of the chondritic components. The CAIs are generally thought to have formed from evaporation and condensation processes, with the subsequent melting and partial evaporation of some CAIs, referred to as igneous CAIs. The textures of most chondrules point to crystal growth from a rapidly cooling silicate melt. Relict fragments of refractory inclusions and older chondrules found in some chondrules, as well as their igneous or fine-grained rims suggest that chondrules result from various degrees of melting of dense aggregates of silicates, metal and sulphide grains during multiple transient heating events (*e.g.* shock waves) in the dusty inner (< 5 AU) solar nebula. As far as the matrix is concerned, it may result from extensive evaporation and re-condensation during chondrule formation.

The location of the CAI and chondrule formation is still debated. The so-called X-wind model puts their birth near the Sun, followed by their wind-blown radial transportation away from the Sun, where they assembled together with the matrix into the chondrite parent asteroids. An alternative model proposes that the chondrules and matrix formed very close to their accretion regions, and that the refractory inclusions formed closer to the proto-Sun.

The chondrite components generally display much larger deviations from the TFL than the bulk material. In primitive chondrites, the O isotopic compositions of CAIs, AOAs and chondrules differ markedly from the SMOW values. This is illustrated in Figure 2.5, where the values of $\delta^{17}O_{SMOW}$ and $\delta^{18}O_{SMOW}$ for the CAIs and chondrules of the carbonaceous chondrite Allende are seen to closely follow a line of slope unity, in contrast to the slope of 0.52 of the TFL. The deviations with respect to SMOW are commonly expressed as $\Delta^{17}O_{SMOW} = \delta^{17}O_{SMOW} - 0.52 \times \delta^{18}O_{SMOW}$. Recent data indicate that $\Delta^{17}O_{SMOW}$ covers a large range of values from less than -20 to $+5$ per mil. They also point to a ^{16}O richness of AOAs and most CAIs relative to chondrules within a chondrite group.

Some igneous CAIs complicate the picture, as they exhibit a ^{17,18}O enrichment comparable to the one observed in chondrules.

The variations in the O isotopic compositions of the chondrite refractory components are generally explained by the mixing in various proportions of SoS ^{16}O-rich and ^{17,18}O-rich reservoirs located in the inner solar nebula (*e.g.* Clayton 1993). The ^{16}O-rich reservoir has contributed substantially to the early SoS condensates, like the CAIs with $\Delta^{17}O_{SMOW} < -20$ per mil. The ^{17,18}O-rich reservoir has provided the heavy O-isotope excess in chondrules and in some other secondary chondrite minerals.

The chondrite matrix contains small amounts of silicate and oxide grains with grossly anomalous O isotopic compositions. These grains may be presolar stardust most of which are ^{16}O-poor (see below), or may be of solar venue. In the latter case, their anomalous isotopic composition would be the result of the irradiation of part of the circumsolar material by energetic particles accelerated during an active phase of the young Sun (see below).

2.1.3.4   Oxygen anomalies in stardust grains

In contrast to CAIs or other inclusions identified in meteorites, presolar grains first isolated in meteorites in 1987 have condensed in stellar outflows and have become part of the interstellar medium before finding their way into the SoS, and eventually surviving the processes of their trapping into meteorites. Presolar grains are also identified in interplanetary or cometary dust. These grains are referred to as "stardust" to distinguish them from the much more common interstellar dust particles that formed in other ways.

Stardust is identified by isotopic anomalies that are much larger than in all the other meteorite materials. These anomalies concern an extended variety of elements, and are too large to be explained by any physico-chemical fractionation process. They are instead classically attributed to nuclear reactions. Stardust grains largely consist of ordered crystalline structures made of high-temperature minerals. This structure is consistent with the condensation from cooling circumstellar gases. A large variety of stardust types have been identified so far, as reviewed by *e.g.* Meyer & Zinner (2006). Among them, oxide grains and some low-density graphite grains are of relevance here. The stardust oxides represent only a small fraction of all oxides found in meteorites. This is why they have been quite difficult to isolate and identify. They are found in the form of silicates, alumina (Al_2O_3)[2], spinel $(MgAl_2O_4)$ and hibonite $(CaAl_{12}O_{19})$.

Figure 2.6 shows the O isotopic composition for a variety of individual oxide and silicate grains. Four classes of these grains have been identified by Nittler *et al.* (1997) according to their O isotopic compositions. *Group 1 grains* have ^{17}O excesses and moderate ^{18}O depletions. *Group 2* grains have ^{17}O excesses and

---

[2]Presolar alumina grains have often been referred to as "corundum" as this is the stable form of Al_2O_3 on Earth. In contrast, Al_2O_3 has been found to exist in a variety of forms in presolar material.
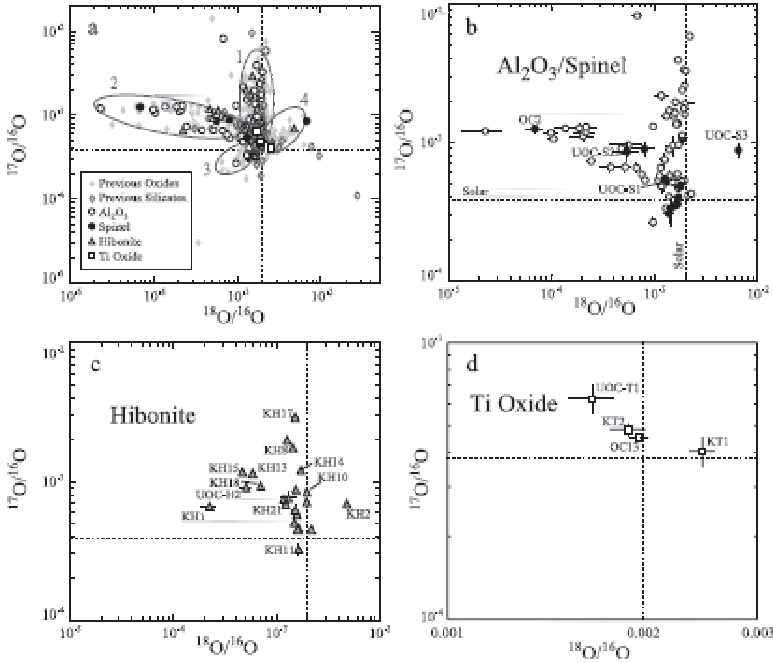
Fig. 2.6. Oxygen isotopic composition of stardust oxide and silicate grains. Panel **a** refers to data obtained prior to the work by Nittler *et al.* (2008) (where the original references to the earlier analyses are given). The other three panels refer to new data obtained by Nittler *et al.* (2008). The dotted lines show the SoS (assumed to be terrestrial) isotopic ratios (from Nittler *et al.* 2008).

large ^{18}O depletions. In addition, these grains are characterised by inferred high ^{26}Al/^{27}Al ratios. *Group 3* grains have close to solar or moderately lower than solar ^{17}O/^{16}O and ^{18}O/^{16}O ratios. *Group 4 grains* exhibit ^{17}O and ^{18}O enrichments. Among the ^{18}O-depleted grains, one shows an exceptionally high ^{17}O/^{16}O ≈ 0.014 ratio, and the other a remarkably low value of this ratio close to 3×10^{-5} (Fig. 2.6a). More recent data are also shown in Figure 2.6. Broadly speaking, they confirm the classification into four groups. They also show that there is some overlap of the groups, and that it is difficult in many cases to unambiguously associate a given grain with a specific group.

Among the graphite stardust, there is a class of low density $(1.6 - 2.05 \text{ g cm}^{-3})$ grains exhibiting large ^{18}O excesses with mostly close to SoS values of ^{17}O/^{18}O (Fig. 2.7a). This O composition is accompanied with other isotopic anomalies (^{18}O excesses correlated with ^{12}C/^{13}C ratios, ^{15}N excesses, high ^{26}Al/^{27}Al ratios, ^{28}Si excesses, but also large ^{29,30}Si excesses in some cases, excesses in some isotopes of elements heavier than Si; see Meyer & Zinner 2006 for details).
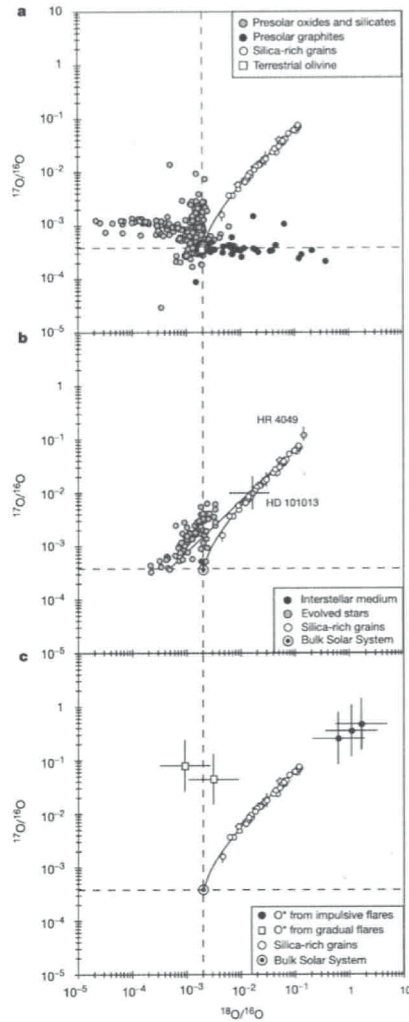
Fig. 2.7. Oxygen isotopic composition of anomalous silica-rich grains from Murchison compared with presolar oxide (see Fig. 2.6) and graphite grains (panel **a**), and with the interstellar medium or the photospheric abundances of evolved stars (panel **b**). Panel **c** compares the composition of the Si-rich grains with the predictions of a local irradiation model. The solid lines in panels **a** and **b** correspond to mixing lines between end members. Dashed lines represent bulk SoS (assumed to be terrestrial) ratios (from Aléon *et al.* 2005).

Recently, a class of abundant Si-rich grains with extreme ^{17}O and ^{18}O enrichments have been identified in the Murchison carbonaceous chondrite by Aléon *et al.* (2005). As seen in Figure 2.7, the measured O-isotopic compositions follow what could be interpreted as a mixing line between the SoS ratios and an extreme

end-member with $^{17}O/^{16}O$ and $^{18}O/^{16}O$ close to 0.1. Remarkably enough, $^{18}O/^{17}O$ is found to be close to the constant value of 1.65. In addition, the Si isotopic data are almost indistinguishable from normal. Aléon *et al.* (2005) note that their extreme ^{17}O and ^{18}O excesses are consistent with the abundances derived for the post-AGB star HR 4049, while the Ba-star HD 101 013 exhibits smaller excesses that are also compatible with the Si-rich grain data (Fig. 2.7b).

2.1.3.5 Origin of the SoS O isotopic anomalies in chondrite components

Three different mechanisms have been envisioned to explain the mass-independent fractionation leading to the O isotopic composition of chondrite components lying on the fractionation line with slope close to unity, as that displayed in Figure 2.5.

Nucleosynthesis origin. Following their discovery of an ^{16}O-rich component in meteorites, Clayton (1993) have proposed a stellar thermonuclear origin for this reservoir. This O isotope is indeed a classic product of He burning (see Chapter 3), especially in massive ($M \gtrsim 10\ M_\odot$) stars. In the terminology of galactic models for the evolution of the nuclide abundances, ^{16}O is of "primary" nature.

The thermonuclear synthesis of ^{17}O is primarily the result of proton captures on pre-existing ^{16}O, either in the non-explosive environments of low-mass red giant or AGB stars, or during nova outbursts, where it is produced as the unstable progenitor ^{17}F. The production of ^{18}O is mainly due to the incomplete transformation by α-particle captures of the ^{14}N resulting from H burning through the CNO cycles in the He-burning shell of exploding massive stars. The short explosion timescales may prevent ^{18}O to be too severely destroyed by $^{18}O\,(\alpha\,,\gamma)\,^{22}Ne$. Some ^{18}O synthesis could also take place in AGB stars. In contrast to ^{16}O, the production of ^{17}O and ^{18}O thus requires the presence of C, N and O, and depends on their initial abundances. They are referred to as "secondary" species.

In the course of the chemical evolution of the Galaxy, reservoirs with different proportions of ^{16}O and $^{17,18}O$ can appear, possibly leading to heterogeneities in the raw SoS material. More specifically, it has been proposed that the SoS dust component was ^{16}O-enriched relative to the larger dust reservoir.

A non-thermonuclear (loosely referred to as "spallation") origin of a ^{16}O-rich reservoir has also been examined by Lee (1978), who considers the irradiation of a portion of the circumsolar nebula by energetic particles from the proto-Sun. However, this mechanism is considered to be unlikely, as it would lead to correlated isotopic anomalies in other elements that are not observed.

Chemical mass-independent fractionation during the formation of solids. Some solids are known to have preserved mass-independent isotopic effects for periods ranging from about 10^8 to at least some 4×10^8 years. It has been proposed that reactions such as $O + SiO \rightarrow SiO_2$ could yield O isotopic anomalies in chondrite components, as SiO_2 has its symmetry modified if ^{16}O is replaced by ^{17}O or ^{18}O. It has been argued, however, that this reaction on SiO would be by far too slow in the inner solar nebula gas phase compared with $O + H_2 \rightarrow H_2O$,

but could instead be efficient in the formation of SiO_2 on the grain surface during CAI formation. Experiments would be welcome in order to help validating this model.

Photochemical self-shielding. Self-shielding in the UV photodissociation of CO is believed to be responsible for large C and O isotopic fractionation effects in molecular clouds. The first step in the dissociation of CO occurs through the excitation of a sufficiently long-lived state leading to narrow, isotopically separated absorption bands. As an example, the ^{12}CO and ^{13}CO absorption bands near 105.2 nm are separated by 45 cm^{-1} (Hashizume *et al.* 2000), which exceeds the Doppler width. The irradiation of a cloud by an UV continuum thus leads to a more rapid attenuation of the wavelength corresponding to ^{12}CO than to the less abundant ^{13}CO. As a consequence, the ^{12}CO in the interior of a cloud is fully dissociated well before ^{13}CO. At such a stage, ^{12}C is enhanced over ^{13}C. The same effect must be even stronger for oxygen, due to the fact that the $^{16}O/^{17,18}O$ ratios are larger than $^{12}C/^{13}C$. It is expected that self-shielding is in line with the slope-1 line displayed in Figure 2.5, even if it remains to be ascertained that the levels of fractionation of ^{17}O and ^{18}O are approximately equal, as required by the data shown in Figure 2.5.

Ultraviolet self-shielding may propagate to other O-bearing species than CO. This concerns the abundant atomic oxygen, as well as water ice which is likely to be enriched in ^{17}O and ^{18}O. For the protosolar nebular cloud, Yurimoto & Kuramoto (2004) adopt $\delta^{17,18}O = +120$ and -80 per mil for H_2O ice and CO, respectively.

As discussed in great detail by Yurimoto (2007), the O isotopic composition might vary with time and location in the solar nebula and during the disk evolution, leading today to intricate patterns that probe the complex history of the early SoS. The broad features of the different models that have been developed in order to understand the SoS O isotopic patterns are expected to be applicable to other protoplanetary disks and planetary systems. In this respect, a better understanding of our solar system would largely benefit from the study of other planetary systems, and vice versa. Further progress in this highly exciting field is expected from astronomical observations combined with modelling and precision geochemistry.

2.1.3.6   Origin of the stardust grains with isotopically anomalous oxygen

The origin of the anomalous ammonia, spinel, hibonite and TiO presolar grains (see above) has been discussed in many places, and has been re-assessed recently by Nittler *et al.* (2008). We limit ourselves here to a repetition of their conclusions in an abridged form.

(1) The O isotopic ratios of Groups 1, 2 and 3 (Fig. 2.6) are most consistent with an origin in low-mass red giants and AGB stars. Some Group 1 and Group 2 grains could possibly originate from red supergiants and Wolf-Rayet stars.

(2) The so-called "cool bottom processing" supposed to transport envelope material near the H-burning shell of AGB stars could account for the large ^{18}O depletions in Group 2 grains, and as well as for the high ^{26}Al/^{27}Al ratios observed in some cases. A range of temperatures at which the cool bottom processing operates is necessary to explain the data. Some Group 1 grains might have experienced this processing as well.

(3) A few grains have ^{17}O/^{16}O ratios that are too high to have the same origin as discussed in (1) and (2) above. Binary stars are invoked in these cases, allowing a pollution from a companion intermediate-mass star or nova outburst.

(4) Mass transfer in a binary star might also explain the composition of some hibonite grains. Others might require the consideration of galactic chemical evolution effects, with the constraint that AGB stars do not contribute significantly to the Mg isotope inventory.

(5) The ^{18}O-enriched Group 4 grains could result from the mixing of different layers of massive star explosions. It is even claimed that a single supernova might have been responsible for the Group 4 grains and for several Group 3 grains as well.

(6) Three of the identified TiO grains have O isotopic compositions compatible with an origin in a low-mass AGB star, while the origin of the fourth cannot be identified.

Regarding the low-density graphite grains loaded with O isotopic anomalies, they are generally considered to originate from Type II supernovae (Meyer & Zinner 2006, and references therein).

It has to be noted that other isotopic anomalies accompany the oxygen ones in the grains reported above. They are used to help constraining the possible origins of these grains.

From the summary above, one notes the high number of quite *ad hoc* assumptions that are needed in order to account for the observed anomalies. Some of them rely on very uncertain stellar or Galactic chemical evolution modelling. The general astrophysical plausibility of others remains to be demonstrated.

Finally, the extreme oxygen isotopic composition of the silica-rich grains reported in Figure 2.7 is extremely difficult, if not impossible, to reproduce by stellar thermonuclear models. It is explained instead (Aléon *et al.* 2005) in terms of a solar-flare type of irradiation of the circumsolar N, O and Ne gas by energetic protons, ^{3}He and ^{4}He. This model is seen in Figure 2.7 (panel **c**) to account well for the observations. Note that an irradiation model (with different particle fluencies) is also used to account for the presence in live form of the short-lived radioactivities ^{7}Be and ^{10}B in the early solar system (Chaussidon *et al.* 2006).

2.2   The Milky Way

The Milky Way, a Sbc-type spiral galaxy, has several physically distinct components: the disk, the bulge and a halo. We briefly describe each of them below.

The disk. The Milky Way disk contains most of the interstellar matter of our Galaxy. It is where present generations of stars are formed, and where the youngest populations of stars in the Galaxy are found. In the early 1980s, it was shown that the disk contains two distinct stellar components: the *thin* and the *thick* disk. Both components are supported by rotation. They are defined by their characteristic extent perpendicular to the Galactic plane (scale height) and kinematics, tracing their distinct formation and evolution. The thin and thick disks both have a radial exponential profile with respective scale-lengths of 4.5 and 3 kpc (*e.g.* Habing 1988; Ojha 2001). At the position of the Sun, the *thin disk* has a scale height of 225 ± 10 pc, a circular velocity of 243 ± 20 km s^{-1} (Caldwell & Ostriker 1981) and a low vertical velocity dispersion σ_W of 21 km s^{-1} (Veltz *et al.* 2008). The *thick disk* rotates more slowly, lagging by some 33 km s^{-1} behind the thin disk and with a higher vertical velocity dispersion σ_W of 45 km s^{-1}. At the position of the Sun, its scale height is 1048 ± 36 pc (Veltz *et al.* 2008). The thin disk is composed of gas (molecular clouds as well as H II regions, and stars with ages mostly younger than 5 Gyr, Nordström *et al.* 2004). The thick disk comprises mostly stars older than 10 Gyr (Bensby *et al.* 2004; Fuhrmann 1998). From the chemical point of view, the thin and thick disks are also distinct, the latter being more metal poor (with a mean metallicity of [Fe/H] ~ -0.6) than the former ([Fe/H] ~ -0.14, Nordström *et al.* 2004), although with overlapping metallicities.

The bulge. The inner few kiloparsecs of the galaxy are dominated by old stellar populations (> 10 Gyr, Ortolani *et al.* 1995; Zoccali *et al.* 2003) in the form of a prolate, boxy structure. Because of this highly prolate nature, the inner few kpc of the Milky Way bulge are sometimes referred to as the bar of the Milky Way. The bulge stellar populations, which are old and perhaps contain the first stars to have formed in the Universe, present metallicities ranging from [Fe/H] $= -1.2$ to $+0.5$ (Fulbright *et al.* 2006; Zoccali *et al.* 2008). The very inner zone, within 100 pc from the centre, is under the influence of the Milky Way central $2.6 \pm 0.2 \times 10^6 \, M_\odot$ black hole (Schödel *et al.* 2002). It comprises young stellar populations, gas and a nuclear bar. These inner regions are referred to as the *Galactic centre.*

The halo. The halo of the Milky Way is the largest and most massive component of the Galaxy. It is dominated by dark matter and comprises a predominantly very old (>12 Gyr) and metal poor ([M/H] < -1) stellar component, including globular clusters. The dark halo is very extended with half-mass radius around 150 kpc (*e.g.* Battaglia *et al.* 2005). The stellar halo is more concentrated and pressure supported. Recent findings by Carollo *et al.* (2007) indicate in fact two components to this stellar halo: a slightly flattened inner halo that dominates locally and only mildly rotates in a prograde direction (Chiba & Beers 2000, ~ 30 km s^{-1}), and a spherical outer halo dominating star counts beyond 15–20 kpc from the Galactic centre, counter-rotating by ~ -50 km s^{-1}(Carollo *et al.* 2007). The outer halo is also more metal poor than the inner halo ([Fe/H] ~ -2 *vs.* [Fe/H] ~ -1.6), and not as smooth.
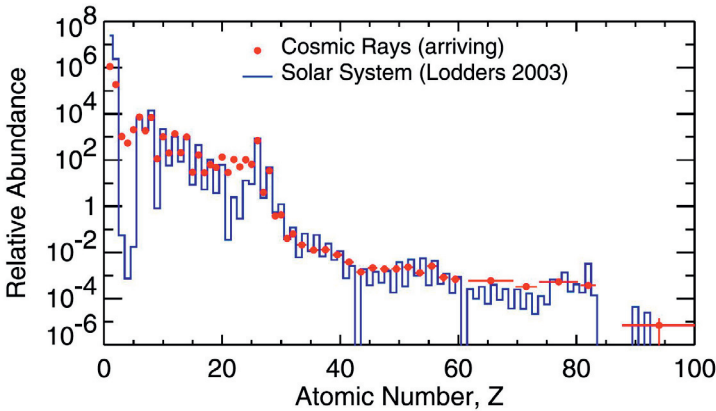
Fig. 2.8. Relative abundance in Galactic cosmic rays *versus* local abundances. Figure reproduced from Wiedenbeck (2007).

2.2.1 Solar vicinity

2.2.1.1 Cosmic rays

Abundances in Galactic cosmic rays, observed and at their source. Since the first measurements of the chemical composition, it has been clear that the composition of measured cosmic-ray fluxes is very similar to the Solar System composition, with a few noticeable exceptions such as the important sub–C (Li, Be, B) and sub–Fe (Sc to Mn) elements, as shown in Figure 2.8. The natural interpretation is that these elements are produced by nuclear spallation of the cosmic rays on interstellar matter (mainly hydrogen) when they propagate in the Galaxy. The measurement of the abundances of these elements, called "secondaries", with respect to their progenitors, called "primaries", provides a measure of the quantity of matter encountered. Models of propagation in, and leakage of, the Galaxy have been worked out to account successfully for the abundance of the elements, including that of radioactive isotopes which gives an estimate of the residence time of the cosmic rays in the Galaxy (see *e.g.* Berezinsky *et al.* 1990 for a full description of the cosmic-ray physics).

A last point of importance when dealing with cosmic-ray measurements is that the cosmic-ray flux depends on the solar activity, particularly at low energy, a phenomenon known as solar modulation (see *e.g.* Jokipii & Kota 2000; Potgieter 2008 for latest developments). In practice, this effect strongly decelerates the cosmic rays when they penetrate the Earth orbit from interstellar space, and gives all spectra the same shape below a few hundred MeV/n. This is shown in Figure 2.9, which displays the Galactic cosmic-ray oxygen spectrum measured with different levels of solar modulation. This makes the interstellar cosmic-ray spectrum at energies below ~ 500 MeV/n unreachable to measurements within the heliosphere.
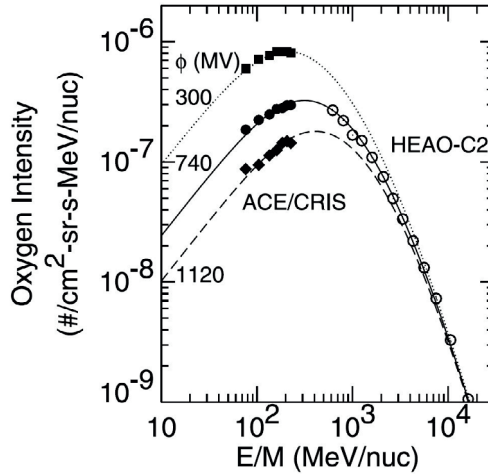
Fig. 2.9. Oxygen absolute spectrum as a function of solar modulation. The ACE/CRIS data correspond to different periods of measurement within the solar cycle. The solar modulation is parameterised by ϕ, the cosmic-ray flux being maximum at solar minimum (low ϕ). The solar modulation effect becomes negligible at energies larger than a few GeV/n. Figure reproduced from Wiedenbeck (2007).

These facts, with all others accumulated in several decades of observational and theoretical studies, form the cosmic-ray history paradigm believed to be valid for energies up to the knee. From "birth" to detection, the cosmic-ray history proceeds along the following steps:

- nucleosynthesis of the "primary" cosmic rays in star interiors (or during a supernova explosion);

- ejection and mixing with the interstellar medium (by stellar winds or supernova explosions) with possible condensation in grains;

- main acceleration presumably by supernova shocks;

- propagation in the Galaxy during which they form secondaries;

- interaction with the solar wind while they enter the heliosphere.

Two key findings derived from these models must be kept in mind when comparing cosmic-ray abundance with other material. First, cosmic rays represent a fresh material sample; their residence time in the Galaxy depends on the physics of the leakage from the Galaxy, being $\sim$30 Myr in the "leaky-box" model and $\sim 10^8$ yr in a purely diffusive model at $\sim$1 GeV/n (Ptuskin & Soutoul 1998). Second, because they propagate diffusively they sample the local material; at GeV/n energies, for

which we have the best measurements, cosmic rays reaching the Earth come from distances within ∼1 kpc.

A key question of cosmic-ray physics is to disentangle the different processes listed above in order to understand the propagation process itself, but ultimately to discern the composition of the cosmic rays at their source, one of the ways to identify this source. As demonstrated by the high statistics and broad energy range of the HEAO-3-C2 data, an important point is that all heavy ions have the same spectral shape at their source (Engelmann *et al.* 1990), so that it is indeed possible to derive "the" Galactic cosmic ray source abundance, independent of energy. In practice, the principle of the operation is to subtract from the observed flux of a given ion the secondary fraction produced by heavier elements during propagation. This secondary fraction is calculated by means of the propagation model and with nuclear cross-section data. Some elements, like B, are purely secondary, while some others are mostly primary. Obviously, the accuracy with which the primary abundance, or source abundance, is derived depends on the accuracy of the secondary production, which is at best of the order of ∼10 %. Thus, typically no reliable source abundance can be calculated for isotopes which have a secondary fraction around 90%.

Oxygen is essentially primary and, jointly with carbon, the most abundant element with $Z > 2$ in cosmic rays. However, its three stable isotopes do not share the same status. ^{16}O is mainly a primary isotope, while ^{17}O and ^{18}O are essentially secondaries. According to the latest calculations, no reliable source abundances can be derived for the heavy oxygen isotopes when all uncertainties are taken into account (Wiedenbeck 2007).

Figure 2.10 shows the abundances in the cosmic-ray source derived by Engelmann *et al.* (1990) compared to solar system abundances. The large error bars for some elements, *e.g.* P and Na, are due to the uncertainty in their (large) secondary fraction. In this figure the elements are ordered in terms of their first ionisation potential (FIP). Elements with a high FIP are clearly underabundant with respect to the solar system reference than elements with low FIP. Note that oxygen plays an important role in this plot due its high FIP and accurate source abundance determination. As a similar FIP bias is found in the solar wind, solar corona and solar energetic particles, this has led to the suggestion that cosmic rays originate mainly from coronal type material (Meyer 1985). In this model, the only clear isotopic anomaly in cosmic rays, that of ^{22}Ne, is explained by an *ad hoc* minor ejecta contribution from Wolf-Rayet stars. However difficulties in explaining outliers to the model, in particular the low abundances of H, He and N, have given more weight to an alternative model initially proposed by Epstein (1980). In this model, which has been fully developed by Meyer *et al.* (1997), cosmic rays are in fact grain destruction products. The correlation with FIP is in fact a correlation with volatility, as most elements with low FIPs are refractory and condense into grains in the interstellar medium. As shown by Ellison *et al.* (1997), because of their large mass to charge ratio, these grains are very efficiently accelerated in supernova shocks and, *via* sputtering, provide a source of highly energetic ions. Being suprathermal, these ions can then easily be further accelerated as cosmic
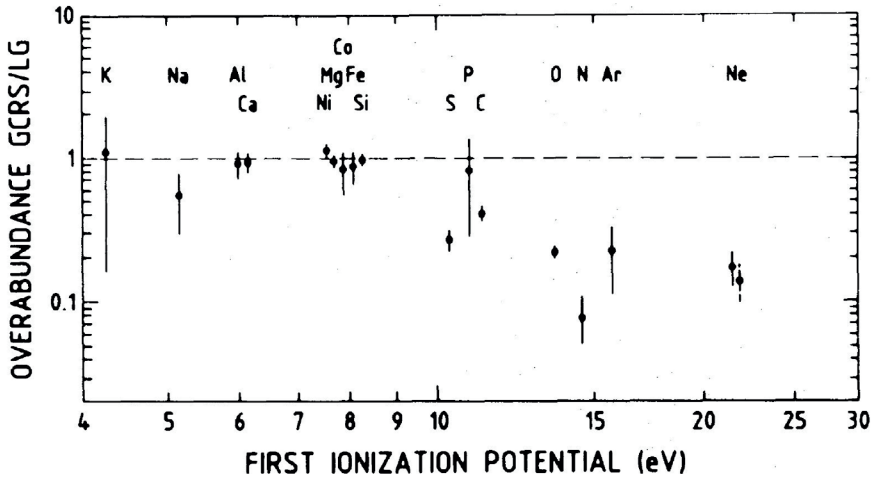
Fig. 2.10. Relative abundances in cosmic rays with respect to solar system, from HEAO-3-C2. Figure reproduced from Engelmann *et al.* (1990).

rays at relativistic energies by the same shock. The ^{22}Ne excess is explained in this model by a natural contribution of Wolf-Rayet stars, the supernovae accelerating their own pre-supernova material. As suggested by Higdon & Lingenfelter (2005), the most promising astrophysical site for cosmic-ray sources are superbubbles, where most of the core-collapse SNe and Wolf-Rayet stars reside. This would naturally explain both the ^{22}Ne isotopic anomaly and the abundances of C and O relative to refractory elements (Binns *et al.* 2005; Lingenfelter & Higdon 2007).

The anomalous cosmic-ray component. In addition to the Galactic component discussed in the previous section, a new energetic component was discovered for H, He, N, O and Ne during the early 1970s. It shows up as flux enhancements in the spectra below a few tens of MeV/n, not related to solar flares (see *e.g.* Klecker 1995). This component, with a spectral slope opposite the solid expectation from solar modulation physics and with strange abundances, was named anomalous cosmic rays. Figure 2.11 shows recent measurements of the oxygen ACR at different locations and times in the heliosphere. Very early after their discovery, Fisk *et al.* (1974) remarked that the elements detected were all with high FIP, and proposed that the anomalous cosmic rays are interstellar neutrals which freely drift in the heliosphere. They get ionised by UV radiation and charge exchange reactions with solar wind protons when they come close to the Sun. Once ionised, they are trapped in the solar wind and convected away to the outer heliosphere where they are thought to be accelerated to become the anomalous cosmic rays. A clear prediction, which revealed to be true, is that these ions are singly ionised.
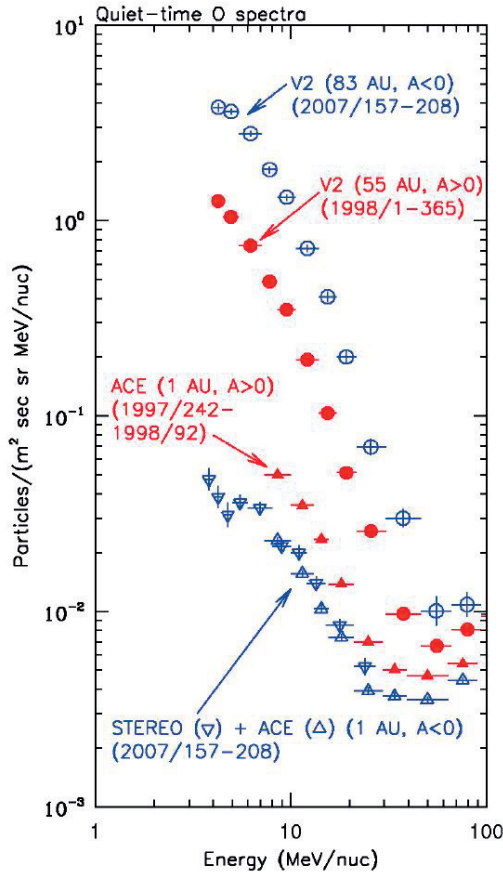
Fig. 2.11. Spectra of the oxygen anomalous cosmic-ray component, measured at different locations in the heliosphere. Figure reproduced from ACE News #110.

This population represents a very fresh sample of interstellar matter beyond the heliosphere, as only a few years separate their entry into the heliosphere as neutrals and the time they are observed as anomalous cosmic rays. Their observed chemical composition obviously depends on the composition and the ionisation state of the local interstellar medium, but also on the different processes they undergo, from ionisation to transport in the solar wind and acceleration (see Cummings & Stone 2007 for a recent review); as a matter of fact, the anomalous cosmic rays are used to improve the understanding of these processes. On the other hand, their isotopic composition does not suffer the above mentioned fractionation process, and thus represents a direct measurement of the isotopic composition of the local interstellar medium. Very accurate measurements have now been made, and have shown that the N and O isotopic compositions are consistent with solar system abundances (Leske 2000).

2.2.1.2   Diffuse interstellar medium

Pioneering measurements.   The first oxygen abundance measurements in the diffuse interstellar medium from absorption lines (Sect. 1.2.2.2) were published in the 1980s, from data of the *Copernicus* satellite. York *et al.* (1983) presented measurements on the sight lines of about 50 hot stars located typically several hundred parsecs away. The column densities from oxygen were obtained from the O I transitions at 1355.6 Å and the triplet at 988.7 Å, and they were compared to H^0 and H_2 column densities (molecular fraction could be of a few percent on such sight lines). Such a column density ratio $N(O^0)/N(H_{tot}) = N(O^0)/[N(H^0) + 2N(H_2)]$ is expected to be a good approximation of the oxygen abundance O/H, since the ionisation potential of neutral oxygen O^0 (13.618 eV) is slightly greater than that of H^0 (13.598 eV) and because O^0 and H^0 are strongly linked by charge exchange. H^+ and O^+ are expected to make negligible contributions to the total hydrogen and oxygen column densities in the gas probed here since it is mostly neutral. Atomic ionised states are thus neglected.

This first survey revealed an O/H ratio in the range of 40% to 70% of the solar value considered at that time, namely $(O/H)_\odot = 6.91 \times 10^{-4}$ (Trimble 1975; Ross & Aller 1976). This under-abundance compared to the Sun was (and still is) interpreted in terms of a depletion of a fraction of the interstellar oxygen atoms onto dust grains (see also de Boer 1981). Since the absorption lines are sensitive only to the gaseous species, all the atoms potentially in the solid phase are not probed; this is the main limit of this measurement method. However, as no systematic increase of the oxygen depletion with reddening was reported by York *et al.* (1983), it was concluded that dust grains are well mixed with the gas, and are quite independent of the radiation or density environment. The proportion of oxygen atoms in the solid phase was thus considered to be relatively constant. Keenan *et al.* (1985) also supported the conclusion of the homogeneity of oxygen depletion, based on the constancy of O/H as a function of $N(H_{tot})$. However, the dispersion of the O/H measurements was too large around the averaged value, even when considering the large error bars prevailing at that time. These error bars were mainly due to the saturation of the O I λ988.7 triplet and to the uncertainties associated with the weak O I λ1355.6 line. The reduction of the error bars was thus mandatory in order to progress in the study of interstellar oxygen.

Improving the accuracy with HST.   This became possible in the 1990s thanks to the Goddard High Resolution Spectrograph (GHRS) onboard the *Hubble Space Telescope* (HST). Meyer *et al.* (1998) claimed the *definitive* abundance of interstellar oxygen from GHRS measurements of the O I λ1355.6 line toward 13 lines of sight. This weak line was well detected thanks to the large throughput of the HST. The lines of sight of this survey are located between 130 and 1500 pc, and the H^0 column densities between $10^{20.1}$ and $10^{21.3}\,\mathrm{cm}^{-2}$. This survey revealed a homogeneous O/H ratio, with dispersion and error bars significantly reduced by comparison to the pioneering *Copernicus* measurements. The resulting abundance was $(O/H)_{ISM} = (3.19 \pm 0.14) \times 10^{-4}$; contrary to other species, it was found to
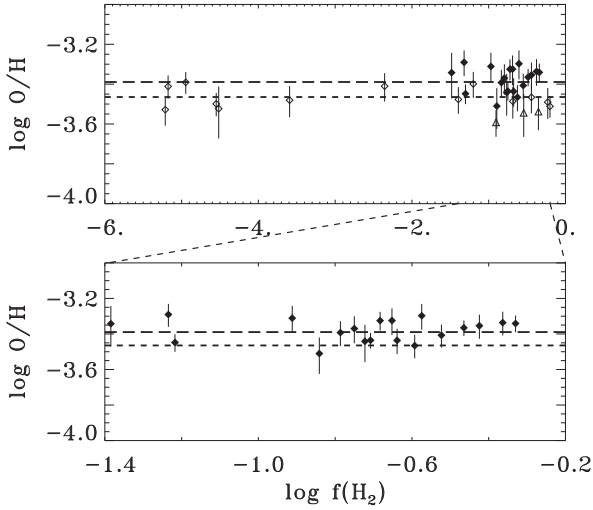
Fig. 2.12. O/H ratio as a function of the molecular fraction from HST observations (from André *et al.* 2003). Filled diamonds are measurements from André *et al.* (2003), open diamonds are from Meyer *et al.* (1998) and open triangles are from Cartledge *et al.* (2001). The dashed and long-dashed lines are the means of Meyer (2001) and André *et al.* (2003), respectively.

be independent of the total hydrogen averaged density or column density, as well of the molecular fraction (see Fig. 2.12, lower panel). The conclusion of negligible exchanges between gas and grains, at least for oxygen, was strengthened. Thus, the abundance of oxygen does not vary significantly in the local, diffuse interstellar medium. The solid or molecular reservoir of oxygen in the interstellar medium seems resilient enough to remain unchanged whatever the environments of the clouds are, at least in this range of densities.

Assuming various mixtures of oxides and silicates such as Fe_2O_3, $(Mg, Fe)SiO_3$ or $(Mg, Fe)_2SiO_4$, the abundance of interstellar oxygen tied up into dust grains was estimated to be O/H $\approx 1.8 \times 10^{-4}$. Thus, the interstellar total oxygen (*i.e.* gaseous plus solid) was estimated by Meyer *et al.* (1998) to be only about two thirds of the solar value, measured at that time by Grevesse & Noels (1993) at $(O/H)_\odot = (7.41 \pm 1.30) \times 10^{-4}$. Three different models were proposed to explain this apparent oxygen deficit in the local interstellar medium when compared to the Sun: a chemical enrichment by a local supernova; a recent, local infall of metal-poor extragalactic gas on the Galactic disk; and finally, a migration of the Sun from a more metal-rich area of the Galaxy where it formed to its current position.

However, two significant updates took place. First, Holweger (2001) and Allende Prieto *et al.* (2001) revised the solar abundance downward to about $(O/H)_\odot = 5.2 \times 10^{-4}$. Second, Welty *et al.* (1999) revised by almost 10% the oscillator strength value of the O I $\lambda1355.6$ line, which led to an increase of

the oxygen abundance from $(O/H)_{ISM} = (3.19 \pm 0.14) \times 10^{-4}$ to $(O/H)_{ISM} = (3.43 \pm 0.15) \times 10^{-4}$ (Meyer 2001). These two updates significantly reduced the disagreement between the interstellar and solar abundances of oxygen, and put less pressure on the models invoked to explain them.

Extending the range of probed media. Two new instruments allowed progress to be made for oxygen interstellar abundance in the late 1990s. First, a new spectrograph, STIS (Space Telescope Imaging Spectrograph), was installed onboard the HST. Its improved sensitivity allowed more distant, denser lines of sight to be probed since such targets have lower flux. Second, the *Far Ultraviolet Spectroscopic Explorer* (*FUSE*) was put in orbit. Its spectral range from 900 Å to 1200 Åallows numerous O^0, H^0 and H_2 lines to be observed.

A first extension was performed toward more distant and dense lines of sight. André *et al.* (2003) presented new measurements toward targets up to 5 kpc and $N(H_{tot})$ up to $10^{21.5}\,\mathrm{cm}^{-2}$. O^0 and O^+ column densities were measured from STIS observations (using $\lambda 1355.6$ Å and Ly-α), and H_2 from *FUSE* observations. From these diffuse interstellar measurements, they did not detect any gradient as a function of the Galactocentric distance, contrary to what was found from H^+ regions and B stars. Similarly to Meyer *et al.* (1998) in a less extended sample, André *et al.* (2003) found a homogeneous oxygen abundance (Fig. 2.12). However, the averaged ratio of André *et al.* (2003) is slightly larger than that of Meyer (2001): $(O/H)_{ISM} = (4.08 \pm 0.13) \times 10^{-4}$. This result was confirmed by Cartledge *et al.* (2004) on lines of sight with similar low densities as those of André *et al.* (2003), but on a slightly extended number of targets; Cartledge *et al.* (2004) found $(O/H)_{ISM} = (3.90 \pm 0.10) \times 10^{-4}$. It appears that lines of sight shorter than $\sim$800 pc (*i.e.* most of the sample from Meyer *et al.* 1998) have an O/H ratio typically $\sim$0.1 dex lower than those beyond $\sim$ 800 pc (*i.e.* most of the sample from André *et al.* 2003 and Cartledge *et al.* 2004). This oxygen deficit within a few hundred parsecs from the Sun might be the signature of a local infall of oxygen-poor material at this scale.

Cartledge *et al.* (2004) also reported that sight lines denser than $\sim$1.5 atoms per cm^3 exhibited a lower oxygen abundance, namely $(O/H)_{ISM} = (2.84 \pm 0.12) \times 10^{-4}$. This ratio is significantly lower than the one mentioned above, obtained on the low-density lines of sight. As first suggested by Cartledge *et al.* (2001), this might be the signature of enhanced oxygen depletion onto dust grains for denser interstellar clouds. Similar trends are seen in gas-phase abundances of other refractory elements. However, this difference ($\sim 4.0 \times 10^{-4} - 2.8 \times 10^{-4} \simeq 1.2 \times 10^{-4}$) is larger than the amount of oxygen expected to be locked into dust grains of classic composition. After a thorough reanalysis of abundances in the diffuse interstellar medium from literature data, Jenkins (2009) emphasised this point, and suggested that perhaps a fraction of oxygen could be locked in carbon or hydrogen compounds (or as O_2).

The second extension was performed in the Local Bubble (LB), *i.e.* a low-density cavity of size $\sim$100 pc in which the Solar System is embedded (see, *e.g.* Sfeir *et al.* 1999). *FUSE* gives access to the O I transitions stronger than $\lambda 1355.6$ Å
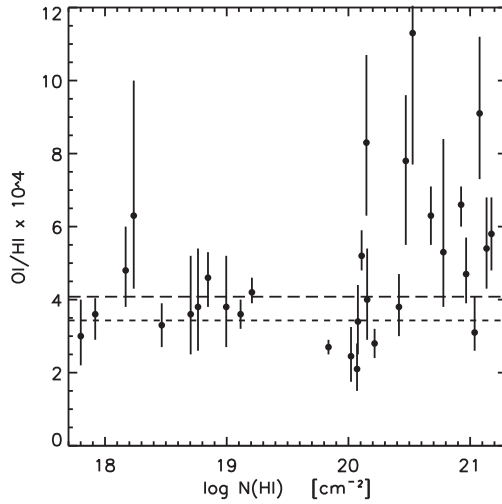
Fig. 2.13. O/H ratio as a function of H^0 column density, from *FUSE* observations. The dashed and long-dashed lines are the means of Meyer (2001) and André *et al.* (2003), respectively.

with a sensitivity about 10 000 times better than that of *Copernicus*. Lower O^0 column densities became thus detectable with *FUSE*. From measurements of 11 targets located within the Local Bubble with $N(H^0) < 10^{19.3}\,\text{cm}^{-2}$ Oliveira *et al.* (2005) reported $(O/H)_{LB} = (3.45 \pm 0.19) \times 10^{-4}$. This value is virtually identical to that obtained by Meyer (2001) beyond the Local Bubble, $(O/H)_{ISM} = (3.43 \pm 0.15) \times 10^{-4}$. The similarity of the oxygen abundance along low average density sight lines in the Local Bubble with that of denser sight lines beyond shows that there has not been significant infall of low-metallicity gas at the scale of the Local Bubble.

Finally, oxygen interstellar abundances were also measured recently with *FUSE* beyond the Local Bubble (see, *e.g.* Oliveira *et al.* 2006; Hébrard *et al.* 2005; Friedman *et al.* 2006; Oliveira & Hébrard 2006) using different O I transitions. The O/H values obtained (see Fig. 2.13) show more variations than in Meyer *et al.* (1998), André *et al.* (2003) or Cartledge *et al.* (2004) from λ1355.6 Å measurements only. This might be the signature of actual variations in the O/H ratio. However, some issues linked to saturation and/or oscillator strength values could be present (Hébrard *et al.* 2005; Friedman *et al.* 2006).

In summary, it is believed that the gas-phase abundance of oxygen in the diffuse interstellar medium is in the range $(3.4-4.1) \times 10^{-4}$. This O/H ratio is quite homogeneous, but is ~ 0.1 dex lower for sight lines below ~ 800 pc. This abundance is expected to be only $\sim 2/3$ of the total interstellar oxygen, the remaining $1/3$ being locked into dust grains in the solid phase. An increasing oxygen depletion seems to be observed toward the denser clouds. Significant variations of the $(O/H)_{ISM}$ ratio

were recently identified by *FUSE*; they need however to be confirmed in order to rule out possible systematic effects.

2.2.1.3 H II regions

The only H II region within $500\,\mathrm{pc}$ of the Sun for which the oxygen abundance has been determined is the Orion nebula (M 42), a bright object visible with the naked eye. Its hottest and most luminous ionising star, θ^1 Ori C, is of the O7 type; therefore it is able to produce O^+ and O^{++} ions in the nebula, a situation favourable for accurate oxygen abundance determinations.

The geometry of the Orion nebula is very far from the academic Strömgren sphere. The ionising stars irradiate a background molecular cloud, producing a flow of ionised gas towards the observer. While the overall morphology of the ionised nebula is rather simple and well described by a blister (Zuckerman 1973) or champagne flow (Tenorio-Tagle 1979), on small scales it reveals a complex structure with blobs and filaments (Ferland 2001; O'Dell 2001).

Abundances have been derived by means of both temperature-based empirical methods and photoionisation models, using optical data with increasing signal-to-noise ratios and spectral resolution. The photoionisation models were constrained with additional IR and UV data. Table 2.5 lists the oxygen abundance derived between 1991 and 2009 (in ppm units, *i.e.* $10^6 \times$ the number of oxygen particles with respect to hydrogen, as well as on the astronomical scale $A(\mathrm{O})$). The last columns summarise how the abundances were obtained. CEL indicates the use of collisionally excited lines of oxygen ions, ORL indicates the use of optical recombination lines. When the oxygen abundance was derived with an empirical, temperature-based method, the value of t^2 indicates the adopted temperature fluctuation according to the scheme of Peimbert & Costero (1969); $t^2 = 0$ indicates that temperature fluctuations were not considered. At first sight, the results shown in Table 2.5 may look discouraging. There is a difference of more than a factor of 2 between the smallest and largest values found for O/H in Orion. However, grouping the results according to the methods used reveals more consistency: the values obtained empirically without taking into account temperature fluctuations are the smallest; the values obtained using $t^2 \neq 0$ are the largest and the values derived from models in-between. Thus, the problem does not lie so much in the observation as in the interpretation. More on this discussion can be found in Sections 1.2.3.1 and 2.2.1.9.

A more recent study at a spatial resolution of $1\,\mathrm{arcsec}$ and summing up several hundreds of data points (Mesa-Delgado *et al.* 2008) indicates that the discrepancy between ORL and CEL abundances is systematic ($0.15 - 0.3\,\mathrm{dex}$) across the entire face of the nebula.

If one extends the definition of the solar vicinity and includes objects within $2\,\mathrm{kpc}$ from the Sun, there are a few more H II regions. Rodríguez & Delgado-Inglada (2011) have used the observations summarised in García-Rojas & Esteban (2007), and applied exactly the same methods and atomic data to derive the abundances in five of them. Using collisionally excited lines, the resulting average

Table 2.5. Determinations of the oxygen abundance in the Orion nebula.

O/H [ppm]	A(O)	references	domain	lines	method
400	8.60	Rubin *et al.* (1991, 1993)	O/IR	CEL	model
380	8.58	Baldwin *et al.* (1991)	O/IR/UV	CEL	model
310	8.49	Osterbrock *et al.* (1992)	O	CEL	$t^2 = 0$
281	8.45	Walter *et al.* (1992)	O	CEL	$t^2 = 0$
794	8.90	Walter *et al.* (1992)	O	CEL	$t^2 = 0.055$
300	8.48	Esteban *et al.* (1998)	O	CEL	$t^2 = 0$
440	8.64	Esteban *et al.* (1998)	O	CEL	$t^2 = 0.024$
281	8.45	Rodríguez (1999)	O	CEL	$t^2 = 0$
326	8.51	Deharveng *et al.* (2000)	O	CEL	$t^2 = 0$
324	8.51	Esteban *et al.* (2004)	O	CEL	$t^2 = 0$
468	8.67	Esteban *et al.* (2004)	O	CEL	$t^2 = 0.022$
513	8.71	Esteban *et al.* (2004)	O	ORL	
426	8.63	Esteban *et al.* (2004)	O	ORL (O^{++}), CEL (O^{+})	$t^2 = 0$
447	8.65	Esteban *et al.* (2004)	O	ORL (O^{++}), CEL (O^{+})	$t^2 = 0.022$
302	8.48	Blagrave *et al.* (2006)	O	CEL	$t^2 = 0$
332	8.52	Blagrave *et al.* (2006)	O	ORL (O^{++}), CEL (O^{+})	$t^2 = 0$
323	8.51	Mesa-Delgado *et al.* (2009)	O	CEL	$t^2 = 0$
389	8.59	Mesa-Delgado *et al.* (2009)	O	ORL	

oxygen abundance is A(O) $= 8.51$ with a dispersion of 0.04 dex and a typical intrinsic uncertainty (based on uncertainties in line intensities only) of 0.03 dex. Using recombination lines, the average oxygen abundance is A(O) $= 8.80$ with a dispersion of 0.08 dex and a typical intrinsic uncertainty of 0.04 dex.

2.2.1.4   Early B-type stars

The first systematic abundance studies of massive stars in young clusters and the field within a few kpc from the Sun were performed by Brown *et al.* (1986b,a), Kane *et al.* (1980) and Lennon & Dufton (1983) The method of analysis was fully based on Kurucz (1979) line-blanketed LTE stellar atmosphere models. Non-LTE line formation calculations for O II were not possible until Becker & Butler (1988) presented an extensive oxygen model atom. This allowed one to connect Kurucz's line-blanketed LTE models with non-LTE equivalent width calculations, an option that has since then been commonly considered for the stellar abundance analysis of B-dwarf stars in the solar neighbourhood for many years (*e.g.* Cunha & Lambert 1992, 1994; Daflon *et al.* 1999, 2001; Gies & Lambert 1992; Gummersbach *et al.* 1998; Kilian 1992; Nieva & Przybilla 2010; Nieva & Simón-Díaz 2011; Przybilla *et al.* 2008; Vrancken *et al.* 2000). Finally, with the advent of the new generation of stellar atmosphere codes at the end of the 1990s (Hillier & Miller 1998;

Table 2.6. Mean oxygen abundances in OB-associations in the solar neighbourhood derived by several authors in the last 20 years.

Author	Assoc.	$A(O)$	# stars	Stellar parameter determination	Codes
Ki92	Ori OB1	8.59±0.11	7	Spec. approach	Gold[1] (LTE) + DS[2] (NLTE)
	Sco-Cen	8.48±0.11	4		
CL94	Ori OB1	8.73±0.13	9	Phot. approach	ATLAS (LTE)
Gu98	Ori OB1	8.61±0.25	5	Spec. approach	ATLAS (LTE) + DS (NLTE)
DCB99	Cep OB2	8.61±0.11	8	Phot. approach	ATLAS (LTE)
Ro00	Cep OB3	8.79±0.25	6	Phot. approach	ATLAS (LTE)
Da01	Cep OB3	8.54±0.13	3	Phot. approach	ATLAS (LTE) + DS (NLTE)
	Cyg OB7	8.76±0.22	3		
	Lac OB1	8.67±0.16	5		
PNB08		8.76±0.03	6	Spec. approach	ATLAS (LTE) + DS (NLTE)
SD10	Ori OB1	8.73±0.04	13	Spec. approach	FASTWIND (NLTE)
NSD11	Ori OB1	8.77±0.03	13	Spec. approach	ATLAS (LTE) +DS (NLTE)

[1] LTE stellar atmosphere models computed by M. Gold (Diplomarbeit Universität München, 1984).

[2] DS: DETAIL + SURFACE (Butler & Gidding 1985; Giddings 1981)

References: GL92 (Gies & Lambert 1992), Ki92 (Kilian 1992), CL94 (Cunha & Lambert 1994), Gu98 (Gummersbach *et al.* 1998), DCB99 (Daflon *et al.* 1999), Ro00 (Rolleston *et al.* 2000), Da01 (Daflon *et al.* 2001), PNB08 (Przybilla *et al.* 2008), SD10 (Simón-Díaz 2010), NSD11 (Nieva & Simón-Díaz 2011).

Hubeny 1998; Santolaya-Rey *et al.* 1997), it was also possible to perform abundance analyses using fully line-blanketed, non-LTE computations. We should mention that analyses based on this last approach have been mainly centred in the study of B-type star abundances in other galaxies (see Sect. 2.3.2), and only scarcely applied to Galactic stars (Hunter *et al.* 2007; Simón-Díaz 2010; Simón-Díaz *et al.* 2006; Trundle *et al.* 2007).

Table 2.6 summarises the resulting mean abundances obtained by several authors in the last 20 years for various of the OB-associations located in the solar vicinity. The methods used for the determination of stellar parameters are also indicated (see Sect. 1.2.2.1 for a description of these methods). Note that we have separated the three recent studies by Przybilla *et al.* (2008), Simón-Díaz (2010) and Nieva & Simón-Díaz (2011). Before these works, all the studies seemed to point at the same conclusions: (i) a large scatter (up to 0.5 dex) in the derived abundances and (ii) mean values for the various associations and the global sample indicating lower abundances than the standard (Grevesse & Sauval 1998) set of solar abundances (see reviews by Herrero & Lennon 2004; Morel 2009). These results were not very encouraging, because the inhomogeneity of stellar abundances contradicted with the homogeneity in oxygen abundance found from studying the local diffuse interstellar medium (see Sect. 2.2.1.2). On the other hand, chemical evolution models of the Galaxy (*e.g.* Chiappini *et al.* 2003; Carigi *et al.* 2005) predict a small enrichment of the ISM in metals during the lifetime of the Sun

(*i.e.* because they are younger than the Sun, nearby OB-type stars are expected to be slightly metal-rich).

At that time, there was, however, some suspicion that the possible explanation for the large dispersion in the derived abundances could be associated to systematic effects due to a bad determination of the stellar parameters and/or to the assumptions in the abundance analysis (*e.g.* LTE in the line formation calculations, microturbulence, set of reliable lines). This suspicion has been recently confirmed by the studies of Przybilla *et al.* (2008) and Simón-Díaz (2010). These authors performed two thorough, independent abundance analyses of early B-type stars in the solar vicinity, paying special attention to those potential systematic errors that may affect the final results (see Nieva & Przybilla 2010 for a summary of the main sources of uncertainties).

The studies of Przybilla *et al.* (2008) and Simón-Díaz (2010) (complemented with Nieva & Przybilla 2010; Nieva & Simón-Díaz 2011) based their analyses on different codes (see Table 2.6), but led to similar conclusions about the dangers of using photometric indices for the determination of the stellar parameters prior to the abundance analysis and the importance of the identification of problematic lines. They stress that the best way to minimise systematic errors and eliminate spurious results is to perform a thorough self-consistent spectroscopic analysis (see Sect. 1.2.2.1) using a state-of-the-art stellar atmosphere[3] code and robust model atoms for non-LTE line-formation calculations. When this is done, a very narrow distribution of abundances is obtained (see Fig. 2.14, where results from Przybilla *et al.* 2008 and Simón-Díaz 2010 are compared with previous oxygen abundance determinations for stars in the solar neighbourhood and the Orion OB1 association). In addition, the new analyses indicate a mean oxygen abundance $\sim 0.10-0.15$ dex larger than previous estimates.

These new results, along with the recent determination of the protosolar oxygen abundance (see Sect. 2.1.2), have drastically changed our view about the chemical composition of early-B main sequence stars in the solar vicinity. Namely, oxygen abundances resulting from the analysis of B-type stars in the solar neighbourhood are homogeneous, and the mean abundances are coherent with the solar result (within the uncertainties associated with both studies).

2.2.1.5   Solar analogs

We have gathered data from two large samples of nearby dwarfs: Ecuvillon *et al.* (2006) and Luck *et al.* (2006) dealing with samples of 155 and 216 dwarfs, respectively. From these two samples, we selected stars with parameters close to solar, within [Fe/H] $\pm$ 0.10, $T_{\rm eff}$ $\pm$ 300 K, log g $\pm$ 0.5.

---

[3]In this sense, the study of Nieva & Simón-Díaz (2011) is especially interesting. These authors present a comparison of O and Si abundances for 13 early B-type stars in the Orion OB1 association, obtained by means of the stellar atmosphere codes FASTWIND and ATLAS+DETAIL/SURFACE. They find almost perfect agreement in the derived mean oxygen abundance, suggesting that the results are independent of the used codes (as long as a self-consistent spectroscopic analysis is performed from scratch).
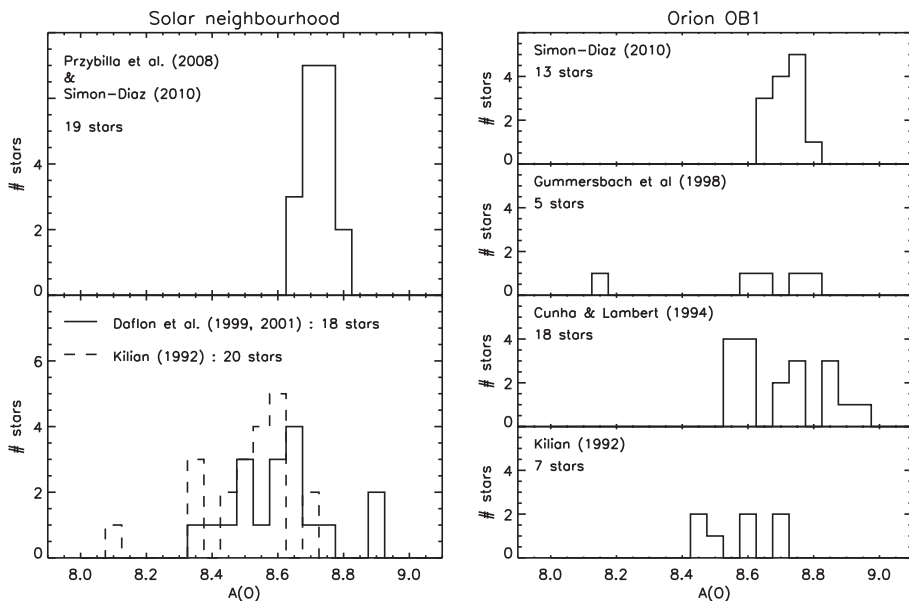
Fig. 2.14. Comparison of oxygen abundance determinations for early B-type stars in the solar neighbourhood (right panels) and the Orion OB1 association (left panels). Top panels show the histograms corresponding to recent results by Przybilla *et al.* (2008) and Simón-Díaz (2010). In both cases, the large dispersion found by previous works (lower panels) is considerably reduced. In addition, the derived mean oxygen abundance is now ∼0.10−0.15 dex larger.

Ecuvillon *et al.* (2006) derived oxygen abundances for 155 solar type stars, 96 of which are planet hosts. The oxygen abundances were derived from the [O I]λ6300 line, O I λ7774-7 permitted lines and UV OH lines. By considering the results from the most reliable line, [O I]λ6300, the oxygen abundances derived are compatible with the solar value. Luck *et al.* (2006) derived element abundances for 216 dwarfs of the solar neighbourhood. Planet hosts show a mean [O/Fe] = 0.01 ± 0.04 (average and standard error), which is compatible within the errors with solar analogs without detected planets, which show [O/Fe] = −0.04 ± 0.02. Considering the whole sample of solar analogs (with and without planets) the average [O/Fe] is −0.03 ± 0.02. Other work is not considered here as they were based on data with somewhat lower accuracy.

More recently, Meléndez *et al.* (2009) analysed data for 30 solar analogs, and the oxygen abundance derived from the permitted oxygen triplet lines for the 11 solar twins of the sample is [O/Fe] = −0.033 ± 0.011 dex (average and standard error). An independent analysis using another sample of 22 solar twins by Ramírez *et al.* (2009) found a similar result, [O/Fe] = −0.015 ± 0.006 dex.

Table 2.7. Oxygen abundances and star-to-star scatter in solar analog samples from: 1 Ecuvillon *et al.* (2006) (solar analogs); 2 Luck *et al.* (2006) (solar analogs); 3 Meléndez *et al.* (2009) (11 solar twins); 4 Ramírez *et al.* (2009) (22 solar twins). The absolute oxygen abundance values A(O) assume a solar oxygen abundance of A(O)$_\odot = 8.77$.

reference	[O/Fe]	A(O)
1	$+0.04\pm0.11$	8.81
2	-0.03 ± 0.11	8.74
3	-0.033 ± 0.035	8.74
4	-0.015 ± 0.028	8.75

The resulting mean oxygen abundances and standard deviations are shown in Table 2.7.

It is important to note that, so far, these different studies found no significant difference in oxygen abundances in stars with or without planets (Ecuvillon *et al.* 2006; Udry & Santos 2007).

2.2.1.6   Late type giants

The solar vicinity also contains late type giants with measured oxygen abundances. In late type giants, the only usable indicators are the forbidden [O I]λ6300, λ6363 lines. The Ni I line that blends into the λ6300 line is totally negligible in this type of stars where the low gravity tends to reinforce the oxygen forbidden line with respect to the neutral nickel line. One of the most recent analyses of red giant branch stars in the local volume can be found in Alves-Brito *et al.* (2010). For thin disk giants with metallicities within 0.15 dex from solar, it yields a mean A(O) = 8.67 with a dispersion of 0.075 using MARCS model atmospheres (A(O) = 8.68 with a dispersion of 0.089 using Kurucz). A larger sample of core helium-burning (red clump) giants was studied by Tautvaišienė *et al.* (2010) who derived oxygen abundances for a subset of 29 stars, 23 of which are within 0.15 dex of the solar metallicity, and found a mean A(O) = 8.63 ± 0.09 dex which compares very well with the local samples of solar analogs (see Table 2.7). There is therefore no strong difference (to the level of 0.1 dex) between the measured oxygen abundances of solar-type main-sequence stars and cool giants in field stars of the solar vicinity.

The comparison between unevolved and evolved cool stars can also be performed in a few nearby open clusters where both the main-sequence and red giant branches are observable. In M 67, the closest open cluster (at a distance of about 800 kpc) with nearly solar metallicity, the chemical composition of unevolved and evolved stars has been investigated by Randich *et al.* (2006). Their sample of unevolved stars has a mean oxygen abundance A(O)=8.68. For the sample of 9 giants, originally studied by Tautvaišiene *et al.* (2000), they find A(O) = 8.65.

In conclusion, in the solar vicinity and for cool stars with near solar metallicity, the oxygen abundances measured from unevolved stars and from red giants agree well. This indicates that the oxygen abundance in giants is not much altered by possible dredge-up of CNO cycled material from the star interior to its surface (see

Table 2.8. Determinations of the oxygen abundance in NGC 7027.

O/H [ppm]	$A(O)$	references	domain	lines	method
910	8.96	Aller (1954)	O	CEL	$t^2 = 0.0$
730	8.86	Péquignot *et al.* (1978)	O/IR/UV	CEL	model
700	8.85	Shields & Searle (1978)	O/IR/UV	CEL	model
420	8.62	Perinotto *et al.* (1980)	O/UV	CEL	$t^2 = 0.0$
300	8.48	Keyes *et al.* (1990)	O/UV	CEL	model
436	8.64	Middlemass (1990)	O/IR/UV	CEL	model
508	8.71	Kwitter & Henry (1996)	O/UV	CEL	model
410	8.61	Bernard Salas *et al.* (2001)	O/IR/UV	CEL	$t^2 = 0.0$
415	8.62	Kwitter *et al.* (2003)	O	CEL	$t^2 = 0.0$
457	8.66	Zhang *et al.* (2005)	O/IR/UV	CEL	$t^2 = 0.0$
270	8.43	Stanghellini *et al.* (2006)	O	CEL	$t^2 = 0.0$
660	8.82	Sterling *et al.* (2007)	O/IR/UV	CEL	model

Sect. 3.2.3). This adds confidence in using late type giants to measure the pristine oxygen abundance in distant stellar populations where the oxygen abundance cannot be derived from main sequence stars because they are too faint.

We should also mention Cepheids, which are late-type supergiants that evolved from intermediate-mass ($5-12\ M_\odot$) stars, and are thus a younger population than the late-type giants mentioned above. Due to their high luminosities, Cepheids can be also observed in nearby galaxies such as the Magellanic Clouds. Many studies have recently derived the oxygen abundances in Cepheids using the [O I] $\lambda6300$ line. From the compilation presented in Sect. 2.2.2.4, we selected all the Cepheids within 0.5 kpc of the Sun (46 objects), and obtain a mean $A(O) = 8.787 \pm 0.123$.

2.2.1.7   Planetary nebulae

It is instructive to first discuss the oxygen abundance in two bright, well-studied planetary nebulae located within 1 kpc from the Sun: NGC 7027 and IC 418.

NGC 7027 is the brightest planetary nebula (despite a 3.5 mag absorption by dust). It is a very high excitation nebula, with a central star of about $200\,000$ K and a rather high density (5×10^4 cm^{-3}). Table 2.8 lists the abundances derived for this object by various authors with the same layout as Table 2.5.

Except for the case of Aller (1954), empirical determinations tend to give lower oxygen abundances than models. The reason for that is not clear. Differences in observational values, atomic data and procedures may all play a role. Note that, for this high-excitation object, it is crucial to consider UV/IR data to allow a constraint on the highly ionised species of oxygen.

The degree of sophistication of the various models listed in the table differs significantly, as well as the model-fitting accuracy. In case of tailored modelling, when the final models fail to reproduce satisfactorily all the observed data, the abundances finally adopted are a matter of the author's personal choice.

Table 2.9. Determinations of the oxygen abundance in IC 418.

O/H [ppm]	A(O)	references	domain	lines	method
760	8.88	Torres-Peimbert & Peimbert (1977)	O	CEL	$t^2 = 0.035$
398	8.60	Barker (1978)	O	CEL	$t^2 = 0.0$
436	8.64	Aller & Czyzak (1983)	O	CEL	hybrid
275	8.44	Gutierrez-Moreno & Moreno (1988)	O	CEL	$t^2 = 0.0$
288	8.46	de Freitas Pacheco *et al.* (1992)	O	CEL	$t^2 = 0.0$
211	8.32	Hyung *et al.* (1994)	O/IR/UV	CEL	hybrid
153	8.18	Henry *et al.* (2000)	O/UV	CEL	model
139	8.14	Kwitter *et al.* (2003)	O	CEL	$t^2 = 0.0$
350	8.54	Pottasch *et al.* (2004)	O/IR	CEL	$t^2 = 0.0$
1660	9.22	Perinotto *et al.* (2004)	O	CEL	$t^2 = 0.0$
290	8.46	Sharpee *et al.* (2004)	O	CEL	$t^2 = 0.0$
500	8.70	Sharpee *et al.* (2004)	O	ORL	
371	8.57	Sterling *et al.* (2007)	O/IR/UV	CEL	model A
515	8.71	Sterling *et al.* (2007)	O/IR/UV	CEL	model B
398	8.60	Morisset & Georgiev (2009)	O/IR/UV	CEL	model

A final word of caution is that the more recent abundances are not necessarily the more reliable. This is particularly true in the specific case of NGC 7027. Discarding the two extreme values of Table 2.8, the oxygen abundance in NGC 7027 seems well established at A(O) $= 8.7 \pm 0.15$.

The second example concerns IC 418. This is also a bright and relatively dense ($n \sim 5 \times 10^4$ cm^{-3}) planetary nebula, but its central star has an effective temperature of $\sim 38\,000$ K only. This is *a priori* a good case for determining A(O) since only an optical spectrum is needed to observe all the oxygen ionisation stages present in the nebula. Yet, the values of A(O) shown in Table 2.9 are more dispersed than for NGC 7027, even when discarding the value from Perinotto *et al.* (2004) which is most likely an error. The value of Morisset & Georgiev (2009) is obtained from a very careful and sophisticated photoionisation modelling, in which the ionisation source is from a stellar model atmosphere that explains the observed stellar features. The density distribution of the nebula is chosen so as to reproduce the observed Hα surface brightness distribution. The intensities of optical, UV and IR lines are fitted within their respective error bars, taking into account of the size and position of the observing apertures. When examining in detail that paper and those of Sharpee *et al.* (2004) and Sterling *et al.* (2007), some questions subsist, but they do not drastically affect the final oxygen abundance. Reasonably, one can consider that, for IC 418, A(O) $= 8.6$ with an uncertainty of about 0.1 dex.

Note that, in NGC 7027, the oxygen abundance from recombination lines is larger than the one from CELs by a factor of 1.3 only (Zhang *et al.* 2005) while for IC 418, it is larger by a factor of 1.7 (Sharpee *et al.* 2004). These discrepancies are not among the largest found for planetary nebulae, yet they are significant and need explanation.

Relaxing the definition of the solar vicinity to distances within 2 kpc, there are a few more objects to consider (the exact number depends on the distances attributed to these objects, which can be uncertain). Rodríguez & Delgado-Inglada (2011) have derived in a homogeneous way the oxygen abundances in 7 planetary nebulae located within 2 kpc from the Sun (all the objects were chosen of low excitation to reduce uncertainties due to the ionisation correction, see Sect. 1.2.3.1). Using collisionally excited lines, the resulting average oxygen abundance is $A(\mathrm{O}) = 8.68$ with a dispersion of 0.09 dex. Using recombination lines, the average oxygen abundance is $A(\mathrm{O}) = 8.98$ with a dispersion of 0.13 dex. Although the intrinsic errors are estimated to be typically of $0.03-0.04$ dex, the consideration of Tables 2.8 and 2.9 warns that absolute uncertainties are probably of the order of 0.1 dex at least.

Apart from the RL-CEL abundance discrepancy, more important here than in the case of H II regions of the solar vicinity (see Sect. 2.2.1.3, but the statistics are admittedly low), one must recall that the oxygen observed in planetary nebulae may have been affected by nucleosynthesis in the progenitor star (see Sect. 3.2.3). This could partly explain the larger scatter of the oxygen abundance in planetary nebulae of the solar vicinity in comparison to that seen in H II regions (see a more complete discussion in Sect. 2.2.1.9).

2.2.1.8   Supernova remnants

The number of detailed spectroscopic X-ray studies of supernova remnants is insufficient to examine variations within the Galaxy of the oxygen abundance. We will thus review in this section the whole Galactic population of supernova remnants. As stated in Chapter 1, in young supernova remnants the vast majority of the X-ray emission arise from the shocked material ejected during the supernova explosion, and gives constraints on the nucleosynthesis products. In a latter phase of evolution (age > 1000 yr), the X-ray emission is dominated by the shocked ambient medium and provides insight into its abundance.

Supernova nucleosynthesis models predict that the ejecta of core-collapse supernovae, corresponding to massive main sequence stars, should contain an overabundance of the O-group elements relative to Si and heavier elements. Conversely, Type Ia supernovae, which arise from the carbon deflagration of a C+O white dwarf, are expected to produce predominantly Si, S, Ar, Ca and Fe. This difference in the nucleosynthesis products can be used to constrain the supernova type. Early optical supernova light curves provide the most efficient way to determine their type. However in our Galaxy, rare are the supernova events for which the light curve has been obtained. Among the 265 supernova remnants observed in our Galaxy (mostly in the radio, Green 2006), SN events have only been observed for eight of them (five are well-established and three are probable, Stephenson & Green 2005). For these historical supernovae, crude light curves have been registered. It is thus important to have ways to constrain, *a posteriori*, the type of the explosion through the determination of the abundance of the synthesised

heavy elements, in particular of oxygen which is a key element. This approach has been used to determine the supernova-remnant SN type in our Galaxy and in the Magellanic Clouds on the basis of X-ray spectra (Hughes *et al.* 1995).

Among supernova remnants, the rare oxygen-rich class is of specific interest with regards to oxygen emission. This class comprises a dozen objects with optical emission from fast-moving oxygen-rich knots associated to the ejecta, and generally interpreted as evidence of He-burning nucleosynthesis in the core of massive stars ($\geq 10\ M_\odot$, Blair *et al.* 2000). They are only three in our Galaxy (Park *et al.* 2007). These remnants originate from the core-collapse explosion of massive stars for which the composition of their ejecta, in terms of heavy elements, is dominated by oxygen. The mass of the progenitor can be constrained from the measurement of the total amount of ejected oxygen. Since X-rays provide an efficient way to observe highly ionised oxygen, a growing number of O-rich supernova remnants are detected by current X-ray satellites. Together with optical observation of the colder oxygen, and observations in X-rays of other synthesised elements (in particular iron), this improves our understanding of the ejecta in core-collapse supernova remnants. In our Galaxy, the members of this O-rich supernova-remnant category observed in X-rays are: Cas A (Lazendic *et al.* 2006), Puppis A and G292.0 + 1.8 (Park *et al.* 2007). They are also observed in the Small and Large Magellanic Clouds: 1E 0102.2-7219 (Sasaki *et al.* 2006), 0103−72.6 (Park *et al.* 2003), N132D (Borkowski *et al.* 2007) and B0049−73.6 (Hendrick *et al.* 2005). Finally, even in more distant galaxies like NGC 4449, it has been possible to observe O-rich supernova remnants in X-rays (Patnaude & Fesen 2003).

The oxygen lines can be observed in X-rays not only in O-rich core-collapse remnants but also in Type Ia although they are usually fainter. In Type Ia supernovae, the measurement of the oxygen abundance from X-ray lines is an important way to determine the composition of the ejected material. In the historical supernova SN 1006, the optical emission is very weak with only Balmer lines of hydrogen at the shock arising from the ionisation of neutral hydrogen immediately behind the shock. In X-rays, the thermal emission presents emission lines of oxygen (O VII and O VIII), as well as of Ne IX, Mg XI and Si XIII. Their over-solar abundances indicate that part of the emission arises from shocked ejecta rather than from shocked interstellar medium (Long *et al.* 2003).

2.2.1.9   Summary

We summarise here what we know of the oxygen abundance in the solar vicinity, and provide a short discussion outlining the points that require better understanding. Table 2.10 shows the average values of $A(\mathrm{O})$ derived for various categories of objects, together with the dispersion. References are taken from previous sections. We also indicate, for each entry, a typical value of the intrinsic uncertainty, $\Delta(A(\mathrm{O}))$, inherent to the method used to derive the abundance. A graphical form of the table is shown in Figure 2.15.

All the values of $A(\mathrm{O})$ are not expected to be identical (within the stated error bars); however, is the observed pattern in agreement with expectations? First of all, young stars (B-type stars) are anticipated to have a higher oxygen abundance

Table 2.10. Summary of oxygen abundances in the solar vicinity.

Objects	$A(O)$	References	$\Delta(A(O))$	Comments
Solar interior	8.86	Delahaye *et al.* (2006)	0.04	
Solar photosphere	8.69	Asplund *et al.* (2009)	0.05	
Solar photosphere	8.76	Caffau *et al.* (2006)	0.07	
Diffuse ISM	8.57 ± 0.04	this book Section 2.2.1.2	0.07	
H II regions	8.51 ± 0.04	Rodríguez & Delgado-Inglada (2011)	0.03	CEL method
H II regions	8.80 ± 0.08	Rodríguez & Delgado-Inglada (2011)	0.04	RL method
B-type stars	8.73 ± 0.04	Simón-Díaz (2010)	0.1	
B-type stars	8.76 ± 0.05	Nieva & Przybilla (2010)	0.1	
Solar analog planet hosts	8.86 ± 0.16	Ecuvillon *et al.* (2006)	0.1	from [O I] taking $A(O)_\odot = 8.74$
Solar analogs no known planet	8.81 ± 0.17	Ecuvillon *et al.* (2006)	0.1	from [O I] taking $A(O)_\odot = 8.74$
Solar analogs	8.75 ± 0.03	Ramirez *et al.* (2009)	0.1	from [O I] taking $A(O)_\odot = 8.77$
Late type giants	8.63 ± 0.09	Tautvaišienė *et al.* (2010)	0.1	from [O I] taking $A(O)_\odot = 8.83$
Late type giants	8.67 ± 0.08	Alves-Brito *et al.* (2010)	0.1	from [O I] taking $A(O)_\odot = 8.66$
Cepheids	8.79 ± 0.12	this book	0.1	from [O I] taking $A(O)_\odot = 8.79$
Planetary nebulae	8.68 ± 0.09	Rodríguez & Delgado-Inglada (2011)	0.03	CEL method
Planetary nebulae	8.98 ± 0.13	Rodríguez & Delgado-Inglada (2011)	0.04	RL method

than old stars (Sun and solar analogs, and late type giants), due to chemical enrichment of the gas out of which the stars are made. This is not what is seen. While one could argue that perhaps the Sun was born at a smaller Galactocentric radius than where it is located now, it is not possible to use this argument for the large sample of old stars observed. If one does not want to put the blame on systematic errors in the oxygen abundances in young or old stars, one must invoke, for example, a recent infall of low metallicity gas in the solar vicinity.

Do the abundances in the interstellar medium (diffuse interstellar medium and H II regions) confirm this view? The oxygen abundance in the diffuse ISM is lower than that of the B-type stars by 0.16 dex. This could be explained if 30% of the oxygen in the ISM were in a phase inaccessible to absorption line measurements. Surely depletion on dust grains is an important factor to take into account, but it seems that the observations require a larger depletion than can be accounted for by combination with Fe, Mg and Si into classic dust grains. A possibility is that oxygen in the lines of sight probed by interstellar line measurements is also partly in the form of ice.

H II regions provide an independent way to check this. However, depending on the method used to derive the oxygen abundance in them (collisionally excited lines *versus* recombination lines), the outcome is radically different: recombination lines give on average a value larger by 0.3 dex. If one takes the CEL values as representative of the gas-phase oxygen abundance, the problem seen when comparing diffuse medium and B-star abundances is exacerbated. Besides, while one could invoke the presence of ice in the neutral diffuse medium, this is not possible in the H II regions where it would be melted away. If we consider the RL abundances
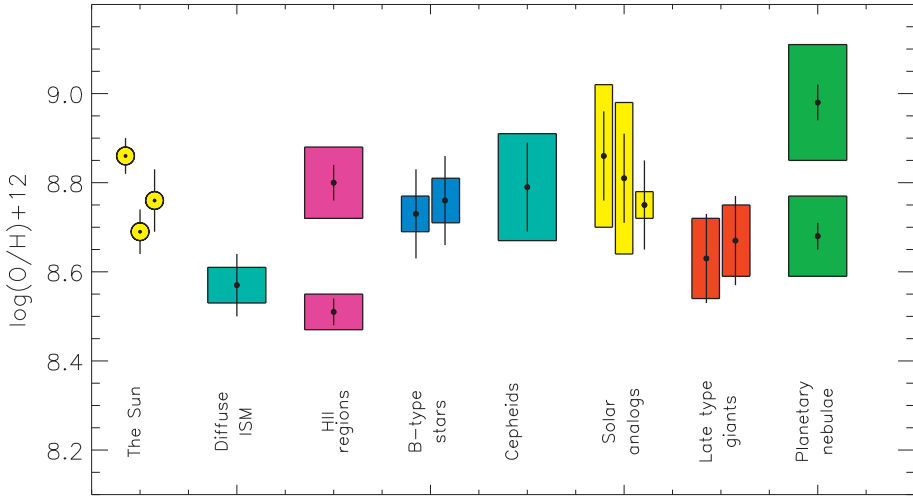
Fig. 2.15. The oxygen abundance in the solar vicinity for different types of objects and different methods, as indicated in the figure. The height of each rectangle corresponds to the observed dispersion. In the centre of each rectangle, there is a dot and an error bar, which gives the average value of $A(O)$ for the considered sample and the typical intrinsic uncertainty of the abundance determination in each object. References for the data used in this plot are indicated in Table 2.10.

as representative of the gas-phase oxygen abundances in H II regions, we would have to explain why it is higher by as much as .23 dex than the value observed in the diffuse ISM. To examine this question in more detail, Simón-Díaz & Stasińska (2011) performed a meticulous study of the chemical composition of the gas and B-type stars in the Orion star-forming region, eliminating the sources of dispersion that could be due to abundance gradients or incomplete mixing in the solar vicinity. They find that $A(O) = 8.74 \pm 0.04$ for the B-type stars, $A(O) = 8.51 \pm 0.02$ for the H II region from the collisionally excited lines and $A(O) = 8.65 \pm 0.03$ from the recombination lines. They also estimated the maximum amount of oxygen that could be depleted into silicates, olivines and oxides in the H II region, based on the abundances of Mg, Si and Fe measured in the stars. They find that this maximum depletion amounts to $22 - 25\%$ of the oxygen abundance estimated for the B-type stars. Taking this depletion into account, they conclude that the RL oxygen abundance in the nebula is compatible with the oxygen abundance in the stars, while the CEL oxygen abundance is not. However, this is not the end of the story, since they note that the abundances of the other elements (C, N, Ne) do not confirm the suggestion that the RL abundances are the correct ones. In addition, the temperatures measured in the nebula are not well reproduced by a tailored photoionisation model, whether it is constructed with CEL or RL abundances. So, unfortunately, the problem remains unsolved.

The comparison of the oxygen abundances between late type giants and solar analogs in the solar vicinity is important, since it is one of the only places where this can be carried out. At large distances, the abundances of oxygen in dwarfs cannot be measured, and one has to resort to abundances measured in evolved stars with the risk that they could be affected by nucleosynthesis in the stars themselves. The fact that late type giants and dwarfs give similar abundances in the solar vicinity asserts that, on average, the dredge-up effects on the abundances measured in giants should be negligible. Cepheids – which can also be observed at large distances due to their extremely high luminosities, and whose ages are intermediate between those of B stars and red giants – give an oxygen abundance which is intermediate between that of B stars and red giants. Taken at face value, this could be an indication of the epoch of a major infall of metal-poor material in the solar vicinity which was mentioned before. However, given the uncertainties, this would certainly be over-interpreting the data.

Planetary nebulae are also considered as probes of the oxygen abundance in galaxies. They are, in particular, the only direct probes of the oxygen abundance of distant galaxies that have stopped forming stars. Again, the solar vicinity is a good test place. Similarly to H II regions, planetary nebulae give very different CEL and RL results. The underlying reason for this is probably not the same (see García-Rojas & Esteban 2007; Henney & Stasińska 2010), but again one may wonder which of the two determinations actually gives a value of $A(O)$ that is representative of the real oxygen abundance. Taking into account depletion into dust grains, CEL abundances are compatible with the abundances from late-type stars, while the RL abundances are definitely not.

The above discussion must be of course kept in mind when comparing the results from chemical evolution models to observed abundances. We warn, however, that the comparison of abundances in other environments (see below) does not always lead to the same picture. It is not as yet clear how well we know the oxygen abundance in the solar vicinity, and therefore not obvious how to use oxygen abundance measurements as probes, despite the wealth of abundance indicators available.

Finally, let us recall that, from the studies of Ecuvillon *et al.* (2006) and Luck *et al.* (2006), planet hosting stars do not appear to have a significantly larger mean oxygen abundance than stars without planets.

2.2.2 *The Milky Way disk*

Abundance gradients in our Galaxy are more difficult to determine than in external galaxies, due to distance uncertainties (especially for planetary nebulae) and because many objects are highly obscured by dust lying close to the Galactic plane. On the other hand, it is worth deriving abundance gradients in the Milky Way because our Galaxy is a benchmark for chemical evolution models of galaxies. Only in the Milky Way we have direct access to abundance measurements from so many elements and sources, *e.g.* H II regions, planetary nebulae, individual B, F and G stars, etc., which all probe different epochs in the Milky Way history.

2.2.2.1 Open clusters

Open clusters are excellent probes to study the radial gradients of intermediate age stars because their ages and distances can be derived from colour-magnitude diagrams. Intermediate ages are defined as lying between 700 Myr and 9 Gyr (Friel 2006). Individual cool giant member stars can be analysed to derive the iron and oxygen abundances.

A metallicity gradient $\Delta[\text{Fe/H}]/\Delta\text{R}_{\text{GC}} = -0.06\,\text{dex kpc}^{-1}$ over Galactocentric distances of 7 to 16 kpc was derived by Friel *et al.* (2002) by considering 39 old open clusters. This gradient was confirmed by Salaris *et al.* (2004) and Jacobson *et al.* (2007), and Carraro *et al.* (2007) found that it is flattened in the outer parts of the Galaxy.

Concerning oxygen, very sparse abundance data are available in the literature for disk open clusters. Most of them can be found in Friel (2006), Yong *et al.* (2005) and Jacobson *et al.* (2007). Also Smiljanic *et al.* (2009) derived oxygen abundances from the forbidden [O I]λ630 line for 24 giants in 8 open clusters in the solar vicinity, and found a mean [O/Fe] of -0.06. In Table 2.11 all the data available on oxygen abundances in open clusters are listed. In Figure 2.16 the behaviour of [O/H] as a function of Galactocentric distance is shown, with different symbols corresponding to different age ranges. A gradient is apparent at Galactocentric distances between 5 and 15 kpc. The few oxygen abundance determinations for Galactocentric distances larger than 15 kpc indicate a higher value, close to solar. More oxygen abundance determinations would however be needed to fully use the potential of open clusters to measure the oxygen abundance gradient in the Galactic disk and its temporal variations.

2.2.2.2 H II regions

The first indication of an abundance gradient in the Milky Way disk came from the measurement of electron temperatures in H II regions through radio recombination lines (Churchwell & Walmsley 1975). Electron temperatures were found to increase with Galactocentric distances, indicating a decrease in the abundances of the most abundant coolants.

This interpretation was confirmed by the first study of abundances in Galactic H II regions as a function of Galactocentric distance (Peimbert *et al.* 1978). A few more studies on abundance gradients from Galactic H II regions followed. Table 2.12 presents a compilation of Galactic oxygen abundance gradients from H II regions in dex kpc^{-1}. Column 3 indicates the spanned range of Galactocentric distances in kpc. Column 4 gives the total number of objects used to derive the gradients. Note that the errors quoted for the gradients include only the scatter in the nominal values of the derived abundances about the best fit line. They do not take into account the uncertainties in the abundances and the possible errors on the Galactocentric distances, except in the case of the estimates by Rudolph *et al.* (2006).

Table 2.11. Oxygen abundances in open clusters.

cluster	Age (Gyr)	R_{GC} (kpc)	[Fe/H]	[O/Fe]	reference
NGC 1039	0.2	8.9	+0.07	−0.03	Friel (2006)
Pleiades	0.14	8.6	−0.03	+0.08	Friel (2006)
Hyades	0.8	8.5	+0.13	+0.02	Friel (2006)
Be 17	10	11.4	−0.11	−0.05	Friel (2006)
NGC 2112	2	9.2	−0.10	0.0	Friel (2006)
NGC 2243	5	10.7	−0.48	+0.03	Friel (2006)
Be 29	3.5	22.0	−0.44	+0.18	Friel (2006)
To 2	3	13.1	−0.4	−0.2	Friel (2006)
NGC 2360	1	9.3	+0.07	−0.1	Friel (2006)
Saurer 1	4	19.3	−0.38	+0.41*	Friel (2006)
Melotte 66	4	10.2	−0.38	+0.3	Friel (2006)
Melotte 71	1	10.0	−0.32	−0.16	Friel (2006)
NGC 2447	0.4	9.1	+0.03	−0.2	Friel (2006)
M 67	4	9.1	−0.03	0.0	Friel (2006)
M 67	4	9.1	−0.03	+0.2	Yong *et al.* (2005)
Cr 261	8	7.5	−0.22	−0.1	Friel (2006)
NGC 6791	9	8.1	+0.4	0.0	Friel (2006)
NGC 6791	9	8.1	+0.47	−0.31	Carretta *et al.* (2008)
NGC 6253	3	6.6	+0.46	−0.18	Carretta *et al.* (2008)
NGC 7789	1.5	9.4	−0.04	−0.07	Friel (2006)
Be 20	4.1	16.0	−0.59	+018	Yong *et al.* (2005)
Be 21	2.2	14.1	−0.54	−	Yong *et al.* (2005)
NGC 2141	2.5	11.8	−0.14	0.00	Yong *et al.* (2005)
Be 29	4.3	22.5	−0.54	+0.23	Yong *et al.* (2005)
Be 31	5.3	12.9	−0.53	+0.24	Yong *et al.* (2005)
NGC 7142	—	9.1	+0.08	+0.02	Jacobson *et al.* (2007)
NGC 6939	1-1.3	8.4	+0.00	−0.11	Jacobson *et al.* (2007)
IC 4756	0.7	7.2	+0.04	−0.05	Smiljanic *et al.* (2009)
NGC 2360	1	6.3	+0.04	−0.10	Smiljanic *et al.* (2009)
NGC 2447	0.5	6.5	−0.01	−0.14	Smiljanic *et al.* (2009)
NGC 3532	0.4	7.9	+0.04	−0.16	Smiljanic *et al.* (2009)
NGC 6281	0.3	8.5	+0.05	−0.12	Smiljanic *et al.* (2009)
NGC 6633	0.5	8.4	+0.08	−0.09	Smiljanic *et al.* (2009)

The only work that takes into account possible temperature fluctuations according to the scheme of Peimbert & Costero (1969) is that of Peimbert *et al.* (1978) where the largest gradient is found. But it contains only five objects. The only work using recombination lines rather than collisionally excited lines is that of Esteban & Peimbert (1995) and it finds a mild gradient. But it involves only six objects. Both works are unfortunately based on too few objects to provide a reliable estimate of the gradient.

It must be noted that, if temperature fluctuations do exist to such a level as to contaminate abundance determinations, they should be stronger at high metallicities. Indeed, many of the possible causes for temperature fluctuations (dust, stellar
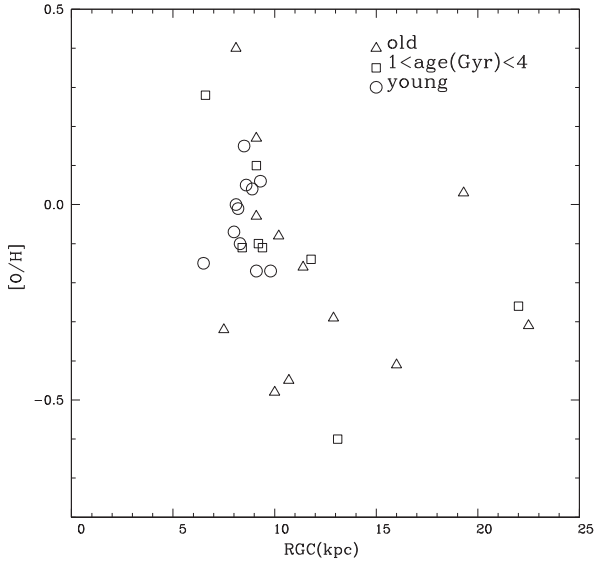
Fig. 2.16. [O/H] *vs.* Galactocentric distances R_{GC}(kpc) for the open clusters listed in Table 2.11.
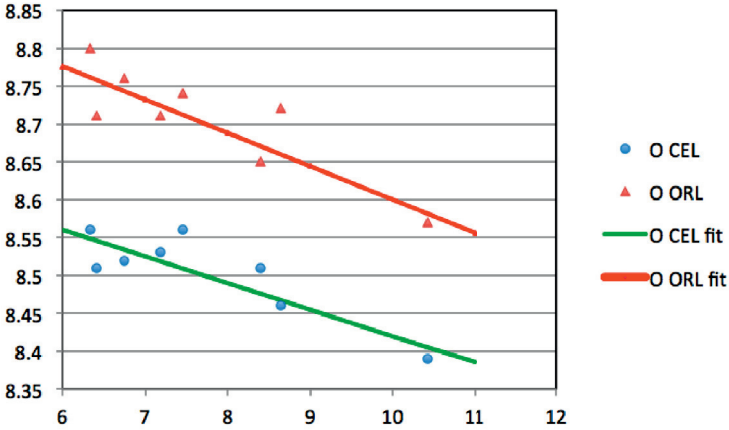

Fig. 2.17. Values of A(O) *vs.* Galactocentric radius in six H II regions. Triangles: values obtained from recombination line data by Esteban & Peimbert (1995). Circles: values obtained from collisionally excited lines for the same objects using the same spectra. Regression lines are shown for the two sets of abundances.

winds, supernovae) are likely to be more efficient at high metallicity. In addition, in such conditions, the temperature reacts more strongly to heating variations. Figure 2.17 shows the values of A(O) obtained by Esteban & Peimbert (1995) from recombination lines (triangles) as a function of Galactocentric distance, and

Table 2.12. Oxygen abundance gradient in the Milky Way disk from H II regions.

d log(O/H) / dR [dex kpc^{-1}]	A(O)$_0$	range [kpc]	number of objects	references
-0.13 ± 0.04	8.9	8–14	5	Peimbert *et al.* (1978)[a]
-0.067 ± 0.017	9.38 ± 0.04	4–14	35	Shaver *et al.* (1983)[b]
-0.064 ± 0.009	9.15 ± 0.06	0–12	34	Afflerbach *et al.* (1997)[c]
-0.040 ± 0.005	8.82 ± 0.05	5–15	34	Deharveng *et al.* (2000)[d]
-0.044 ± 0.010	9.04 ± 0.08	6–10	6	Esteban & Peimbert (1995)[e]
-0.035 ± 0.006	8.77 ± 0.05	6–10	6	Esteban & Peimbert (1995)[f]
-0.060 ± 0.010	9.19 ± 0.04	6–18	70	Rudolph *et al.* (2006)[g]
-0.041 ± 0.014	8.67 ± 0.05	0–15	68	Rudolph *et al.* (2006)[h]

[a] Optical spectroscopy, Te-based determinations, $t^2 = .035$.

[b] Optical spectroscopy, Te-based determinations, $t^2 = 0$, from their Equation 13a.

[c] O^{++}/H^+ from FIR data and radio continuum, photoionisation models to correct for O^+.

[d] Integrated optical fluxes, Te-based determinations, $t^2 = 0$, rediscussion of distances.

[e] Abundances from recombination lines.

[f] Abundances from collisionally excited lines, for the same objects as in [e].

[g] Optical spectroscopy from literature, abundances rederived in a consistent way (but see text), rediscussion of distances.

[h] Infrared and radio data from literature, abundances rederived in a consistent way, rediscussion of distances.

the values of $A(O)$ determined from collisionally excited lines from the original spectra used by these authors (circles). The regression lines for the two sets of data are also shown in the figure. We see that, contrary to expectations, the gradients are almost the same.

Rudolph *et al.* (2006) performed a thorough reanalysis of Milky Way H II regions, collecting the observations from the literature using both optical and infrared data, rederiving the abundances in a consistent way and rediscussing the distances. The estimated distance errors are of the order of 10% but the uncertainties in the abundances can be important, especially in the case of abundances derived from infrared data. However, the number of objects is sufficiently large to allow some conclusions. Rudolph *et al.* (2006) make the point that there is an intrinsic scatter of about 0.1–0.2 dex in the oxygen abundances at a given Galactocentric distance, implying that the interstellar medium might not be as well mixed as usually thought. They also note that there is an important offset between the abundances derived from optical data and those derived from infrared data, the latter being on average lower by about 0.25 dex. However, for some unknown reason, they disregard the data from Deharveng *et al.* (2000), which would precisely lead to an abundance pattern much similar to the one they obtain from infrared data. Note that the forbidden line abundances from the small sample of Esteban & Peimbert (1995) give results compatible with those of Deharveng *et al.* (2000).

Table 2.12 shows that there is a reasonable agreement on the value of the oxygen abundance gradient among the estimates of Deharveng *et al.* (2000),

Esteban & Peimbert (1995) and Rudolph *et al.* (2006) for infrared data. Interestingly, there is good agreement also for $A(O)_0$, the oxygen abundance extrapolated to the Galactic centre, between the value from Deharveng *et al.* (2000), the value obtained from collisionally excited lines for the H II regions studied by Esteban & Peimbert (1995) and that obtained by Rudolph *et al.* (2006) from infrared data. But it is too early to consider this agreement as a sign that the estimated value is correct. If temperature fluctuations are not important, one would not expect a difference between abundances derived from recombination lines and from optical collisionally excited lines; if they are important, one would expect a difference between the latter and abundances derived from infrared lines.

A possible flattening of abundance gradients in the outer disk has been reported by Fich & Silkey (1991) and Vilchez & Esteban (1996) but Deharveng *et al.* (2000) find no clear evidence for this.

Note that, in principle, one should account for the depletion of oxygen atoms in dust grains. If, as is sometimes argued, the dust-to-gas ratio is larger at high metallicity, the real ISM abundance gradient could be steeper than that derived from H II regions. This effect, however, is not expected to be large, since the maximum oxygen depletion is dictated by the abundances of Fe, Mg and Si, and is typically around 20%.

To conclude, it could be underlined that the data on Milky Way H II regions definitely indicate an abundance gradient. This gradient is gentle, of the order of $0.04\,\mathrm{dex\ kpc^{-1}}$. However, one would like to have a clearer idea of the abundance of oxygen in the innermost H II regions as well as of the abundance scatter at a given Galactocentric distance.

2.2.2.3   Young stars

In recent years, thanks to the development of proficient stellar atmosphere codes, it has become possible to use OB-type stars to derive abundance gradients in the Milky Way. Table 2.13 summarises the values obtained by different authors for the case of the oxygen gradient. It may be noticed that there seems to be no consensus between the different determinations. Even when the most recent determinations from the various groups are considered, the disagreement is noticeable (see highlighted values in Table 2.13).

The first studies of Gehren *et al.* (1985), Fitzsimmons *et al.* (1990), Kilian-Montenbruck *et al.* (1994) and Kaufer *et al.* (1994) suggested almost null oxygen gradients. However, these studies were affected by the pitfalls of using spatially and statistically restricted samples of stars (or abundance results from different studies, *viz.* Kaufer *et al.* 1994).

Smartt & Rolleston (1997) presented a compilation of results previously published by their group, extending the sample of Fitzsimmons *et al.* (1990) to 80 stars in 22 Galactic positions covering Galactocentric distances between 6 and 18 kpc. They were the first to report the detection of a significant Galactic oxygen abundance gradient using young early-type stars (-0.07 dex kpc^{-1}). Although the statistics and coverage in Galactocentric distances clearly improved in comparison

Table 2.13. Galactic oxygen gradient derived from B-type stars.

	Author	Range in R_g [kpc]	# stars	# assoc.	$\Delta A(O)/\Delta R$ [dex kpc^{-1}]	$A(O)_0$ [dex]
	G85	$8.5 - 17.0$	10		-0.012 ± 0.024	
	F90	$5.5 - 10.3$	20	4	-0.015 ± 0.014	
	KM94	$5.0 - 15.0$	38	4+loc	-0.021 ± 0.012	
	K94	$7.0 - 16.0$	16/55	10/20	-0.000 ± 0.009	
	SR97	$6.0 - 18.0$	80	22	-0.07 ± 0.01	
*	G98	$5.0 - 14.0$	16	10	-0.07 ± 0.02	9.16
*	R00	$6.0 - 18.0$	80	22	-0.067 ± 0.008	9.40
*	DC04	$4.7 - 13.2$	69	25	-0.031 ± 0.012	8.76
*	F11	$7.0 - 9.8$	35		-0.033 ± 0.005	

References: F90 (Fitzsimmons *et al.* 1990), SR97 (Smartt & Rolleston 1997), R00 (Rolleston *et al.* 2000), G85 (Gehren *et al.* 1985), KM94 (Kilian-Montenbruck *et al.* 1994), K94 (Kaufer *et al.* 1994), G98 (Gummersbach *et al.* 1998), DC04 (Daflon & Cunha 2004), F11 (Firnstein 2011).

to previous studies, two main deficiencies were present in this work. On the one hand, stellar parameters were not determined homogeneously in the whole sample of stars (see *e.g.* Rolleston *et al.* 1993, 1994); on the other hand, while the stellar parameter determination was based on LTE stellar atmospheres, the O II line spectra were analysed using the non-LTE calculations of Becker & Butler (1988) computed from non-LTE atmospheres. Both effects could introduce errors in the abundance gradient determination. To avoid these inconsistencies, Rolleston *et al.* (2000) reanalysed the whole data set presented in Smartt & Rolleston (1997) using fully coherent LTE techniques (*i.e.* LTE stellar atmospheres plus LTE line formation calculations) in order to determine the stellar parameters and abundance estimates. They confirmed the previous result by Smartt & Rolleston, deriving an oxygen abundance gradient of -0.067 ± 0.008 dex kpc^{-1}, and concluded that a full LTE analysis was sufficiently reliable for estimating the magnitude of the metal abundance gradients. However, they recognised that the absolute abundance values at any particular Galactocentric distance could be in error.

An independent determination of the oxygen abundance gradient was presented by Gummersbach *et al.* (1998). These authors analysed of a sample of 16 stars (also including some of the targets considered by Kaufer *et al.* 1994) using Kurucz ATLAS9 LTE atmospheres and Giddings-Butler DETAIL/SURFACE non-LTE line formation (hybrid approach, see Sect. 1.2.2.1) for both the stellar parameter and oxygen abundance determinations. The resulting gradient was in perfect agreement[4] with that determined by Smartt & Rolleston (1997) and later on by Rolleston *et al.* (2000); however, a systematic offset (~ 0.2 dex) between

---

[4]The comparison of results obtained by Kaufer *et al.* (1994) and Gummersbach *et al.* (1998) (see Table 2.13) serves to illustrate how the derived abundance gradient depends on
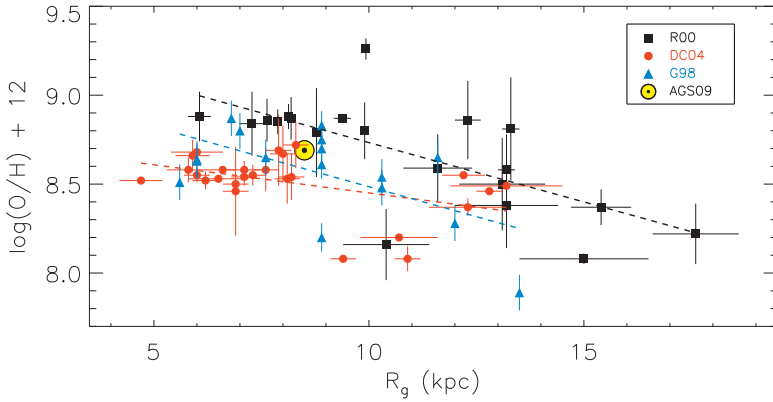
Fig. 2.18. Oxygen abundance gradients determined by Rolleston *et al.* (2000), Gummersbach *et al.* (1998) and Daflon & Cunha (2004) from the analysis of B-type stars in the Milky Way.

the absolute oxygen abundances derived by both studies at a given Galactocentric distance was found.

Daflon & Cunha (2004) revisited the subject, trying to eliminate some of the deficiencies present in previous studies. They observed, reduced and analysed homogeneously a large sample of stars (69 early B-type stars in 25 different locations along the Galactic disk). They followed a photometric approach for the stellar parameter determination (see Sect. 1.2.2.1), and complemented it with a hybrid non-LTE abundance analysis using ATLAS LTE stellar models and DE-TAIL/SURFACE non-LTE computations. Their analysis resulted in a flatter oxygen abundance gradient (-0.031 ± 0.012 dex kpc^{-1}), challenging previous results by Gummersbach *et al.* (1998) and Rolleston *et al.* (2000).

A comparison of results from these three studies is presented in Figure 2.18, where not only the derived oxygen abundance gradient is depicted, but also the points (including uncertainties in the oxygen abundance and in the distance) used by the various authors to compute the gradient. Apart from the differences in the slopes and the important offsets in the absolute oxygen abundances at certain Galactocentric distances, one can appreciate the enormous spread of the derived abundances in the three cases. For example, in the case of Daflon & Cunha, they obtained a scatter of ~ 0.20 dex in the mean derived abundances of five OB associations in the solar neighbourhood. Or even more dramatic, Gummersbach *et al.* (1998) derived a range in the oxygen abundance of individual stars in Orion OB1 of ~ 0.65 dex (almost of the same order as the range of abundances found in the whole Galactic sample).

the hypotheses considered in stellar atmosphere and line formation codes, even when the same observational data set and techniques to derive the stellar parameters and abundances are used.

Recent works by Przybilla *et al.* (2008) and Simón-Díaz (2010) have definitely shown that the oxygen abundance scatter previously found in B-type stars in the solar neighbourhood is a spurious result and the consequence of a bad characterisation of the abundance errors propagated from the uncertainties in the stellar parameter determination. In particular, both studies warned about the dangers in the use of photometric indices to establish the stellar parameters used in the abundance analysis (see Sects. 1.2.2.1 and 2.2.1.4).

This made clear the necessity of a revision of the oxygen abundance gradient based on self-consistent spectroscopic abundance analyses, an enterprise recently undertaken by Przybilla and collaborators. Preliminary analyses (Przybilla 2008) already indicated that the abundance scatter is dramatically reduced when typical systematic errors are eliminated. The final analysis (Firnstein 2011), based on 35 BA-supergiants, results in an oxygen gradient of -0.033 ± 0.005 dex kpc^{-1} (after correction for mixing with CNO-cycled material in the course of stellar evolution; N. Przybilla, priv. communication), and a solar neighbourhood oxygen abundance of 8.76 ± 0.05 dex.

2.2.2.4   Cepheids

Cepheid-type variable stars are another means of measuring the gradient along the Galactic thin disk. They are intermediate-mass ($5-12\ M_\odot$) stars that have evolved off the main sequence, and are crossing the instability strip during their evolution as supergiants. Because their pulsation period is directly linked to their intrinsic luminosity, the distance to individual Cepheids can be measured accurately once their period and apparent (dereddened) luminosity is known, which is very precious for measuring gradients along the Galactic disk. As massive evolved stars, they trace the gradient along the young Galactic disk. In recent years, several groups have re-examined the gradient along the Galactic disk using Cepheids as a tracer: Andrievsky *et al.* (2002b,c, 2004, 2005, 2002a); Kovtyukh *et al.* (2005b,a); Lemasle *et al.* (2007); Luck & Andrievsky ((2004); Luck *et al.* (2003, 2006); Mottini (2006), leading to accurate oxygen abundances. The oxygen photospheric atomic lines used in these studies are the [O I] lines at 6300 Å. We have compiled all these studies, leading to a total of 175 stars located between Galactocentric distances of 5 to 16 kpc (see Fig. 2.19), among which 104 have available K band apparent magnitudes from which the Galactocentric distance was derived, and an additional 71 had only V band photometry available (and whose distances may therefore suffer more from extinction effects). The oxygen gradient found from this combined sample is of -0.032 ± 0.007 dex kpc^{-1} for the total sample (-0.040 ± 0.009 dex kpc^{-1} when restricting the sample to stars whose distances were obtained from the K band). Andrievsky *et al.* (2004) and Lemasle *et al.* (2007) have noticed that the inner part of the disk seems to display a stronger gradient than the outer disk. Following this idea, we have isolated the outer disk, defined as $R_{GC} > 8$ kpc, and indeed find a slightly shallower gradient in the outer disk of -0.026 ± 0.008 dex kpc^{-1} for the total sample (-0.031 ± 0.012 dex kpc^{-1}
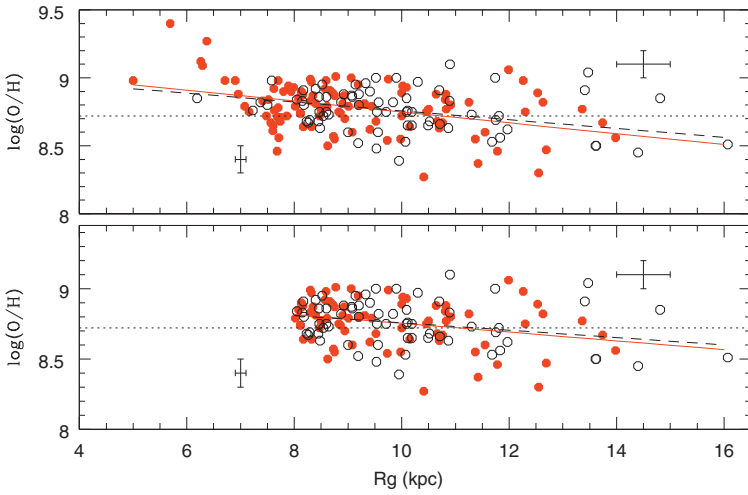
Fig. 2.19. Oxygen abundances as a function of Galactocentric distance for Galactic Cepheids (see text for the data source). The Galactocentric radii were computed using the K band (red filled circles) apparent luminosities for the Cepheids, while the black open circles were computed from the V band (when K band was not available). Two sets of gradients are reported as linear fits to the data: (*upper panel*) a global fit all along the Galactic disk from R_{GC} 5 to 16 kpc yields slightly stronger gradients (-0.032 ± 0.007 dex kpc^{-1} for the total sample or -0.040 ± 0.009 dex kpc^{-1} when restricting the sample to distances from the K band) than a fit restricted to the outer disk (*lower panel*) from R_{GC} 8 to 16 kpc (-0.026 ± 0.008 dex kpc^{-1} for the total sample or -0.031 ± 0.012 dex kpc^{-1} when restricting the sample to stars with K band distances).

when restricting the sample to stars with K band distances). Note that in all cases, the full and K selected samples yield compatible gradients (within error bars).

A word of caution must however be given in the interpretation of the oxygen gradients above, since oxygen in evolved intermediate and massive stars may be affected by internal mixing, CNO-cycled or even the deeper ON cycled material being dredged-up to the stellar surface. In this case, the surface carbon abundance is observed to be depleted compared to its original value, while nitrogen is correspondingly enhanced; oxygen can also be slightly depleted in the process. Indeed, Luck *et al.* (2006) show that carbon and oxygen abundances (in absolute abundances or relative to the star metallicity, [C/Fe] and [O/Fe]) are correlated, a behaviour that is suggestive of mixing processes.

2.2.2.5 Planetary nebulae

The progenitors of planetary nebulae are believed to have initial masses ranging from slightly above 1 $M_\odot$ to 4–5 $M_\odot$. This means that planetary nebulae are potentially very interesting tools for constraining the chemical evolution of the Milky Way disk, since they probe the oxygen abundance of the interstellar medium

over a whole range of epochs, and could, in principle, allow one to trace the evolution of the abundance gradient several Gyr back in time. There are, however, many unsolved issues which make such a use of planetary nebulae premature.

As argued in Section 1.2.3.1, although it is in principle easy to determine the oxygen abundance in planetary nebulae, the O/H ratios derived for some of the brightest best studied objects by various authors are more discordant than one would like. If for such cases differences between various determinations can amount to 0.2 dex, a typical error bar for most planetary nebulae would be at *least* ± 0.1 dex. In addition, there is the unsolved problem of "temperature fluctuations" and CEL-ORL abundance discrepancies (see Sects. 1.2.3.1 and 2.2.1.7) which is left aside in studies on the Galactic abundance gradients using planetary nebulae.

As in H ii regions, the abundance of oxygen derived in planetary nebulae involves only the gas phase, and ignores the possible depletion into dust grains, although this effect is not expected to be large (see Sect. 2.2.2.2). More worrisome in planetary nebulae is the fact that the oxygen abundance measured in the nebular envelopes may deviate from that in the parent molecular cloud due to nucleosynthesis and mixing during the progenitor evolution (see Sect. 3.2.3). This is expected for the most nitrogen-rich planetary nebulae in which some ON cycling might have occurred. This could also be a concern for the most metal-poor planetary nebulae, where the effects of hot bottom burning and third dredge-up might be significant.

The other big problem with planetary nebulae is that their distances are not well known. Distances to individual planetary nebulae can be measured using a large variety of methods, but the results are often discrepant. From a thorough literature search Bensby & Lundström (2001) found only 73 objects for which they considered the distances reliable. Most studies on planetary nebulae have to rely on statistical distances, which are obtained assuming that all the planetary nebulae share a given property. These statistical distances are calibrated on a sample of planetary nebulae for which individual distances are available. Presently, there is at least half a dozen different planetary-nebula statistical distance schemes (*e.g.* van de Steene & Zijlstra 1994; Bensby & Lundström 2001; Phillips 2002; Stanghellini *et al.* 2008), which vary in both the method and the calibration. Note that so far, statistical distances are obtained by assuming that planetary nebulae are a one-parameter family, while their properties depend at least on the mass of their progenitor star and on the time at which they are caught. It seems thus reasonable to consider that typical distance errors can amount to ±0.15 dex.

Table 2.14 summarises the results on abundance gradients using planetary nebulae obtained in the past 25 years. Since Faundez-Abans & Maciel (1986), who used a compilation of abundances from the literature, some effort has been made to perform a consistent derivation of abundances in entire samples. The situation is, however, far from ideal. The differences among the results are difficult to analyse since neither the samples nor the methods are the same.

The best study so far is that of Henry *et al.* (2010) who have built up a homogeneous sample of 124 objects observed, reduced and analysed with the same methods. Their sample has a long baseline, covering Galactocentric distances

Table 2.14. Oxygen abundance gradient in the Milky Way disk from planetary nebulae.

dA(O)/dR [dex kpc^{-1}]	A(O)$_0$	range [kpc]	number of objects	references
-0.094 ± 0.15	9.4	7–14	35	Faundez-Abans & Maciel (1986)[a]
-0.014 ± 0.016	8.92 ± 0.09	1–9	21	Koeppen *et al.* (1991)[b]
-0.031 ± 0.020	9.00 ± 0.10	1–11	15	Samland *et al.* (1992)[c]
-0.030 ± 0.010	8.79 ± 0.25		72	Amnuel (1993)[d]
-0.016 ± 0.01	8.8	1-14	~ 200	Pasquali & Perinotto (1993)[e]
-0.030 ± 0.007	8.92 ± 0.06	4–13	67	Maciel & Koppen (1994)[f]
-0.069 ± 0.006	9.25 ± 0.05	4–13	91	Maciel & Koppen (1994)[g]
-0.058 ± 0.008	8.84 ± 0.06	4–13	39	Maciel & Koppen (1994)[h]
-0.058 ± 0.007	9.13 ± 0.05	4–14	128	Maciel & Quireza (1999)[i]
-0.054 ± 0.018	9.16 ± 0.16	5–12	43	Martins & Viegas (2000)[j]
-0.037 ± 0.008	8.97 ± 0.07	2–13	79	Henry *et al.* (2004)[k]
-0.047 ± 0.007	9.25 ± 0.06	4–14	66	Maciel *et al.* (2005)[l]
-0.089 ± 0.003	9.34 ± 0.03	4–14	99	Maciel *et al.* (2005)[m]
-0.094 ± 0.010	9.05 ± 0.07	4–14	69	Maciel *et al.* (2005)[n]
-0.010	8.5	4–14	67	Stanghellini *et al.* (2006)[o]
-0.018 ± 0.011	?	2–14	70	Perinotto & Morbidelli (2006)[p]
-0.025 ± 0.012	?	2–14	70	Perinotto & Morbidelli (2006)[q]
-0.023 ± 0.009	?	2–14	24	Perinotto & Morbidelli (2006)[r]
-0.027 ± 0.012	?	2–14	21	Perinotto & Morbidelli (2006)[s]
-0.085	9.35	4–10	22	Pottasch & Bernard-Salas (2006)[t]
-0.035 ± 0.024	8.83 ± 0.19	2–17	14	Stanghellini & Haywood (2010)[u]
-0.023 ± 0.005	8.75 ± 0.05	2–17	80	Stanghellini & Haywood (2010)[v]
-0.011 ± 0.013	8.67 ± 0.09	2–17	22	Stanghellini & Haywood (2010)[w]
-0.023 ± 0.006	8.71 ± 0.06	2–17	145	Stanghellini & Haywood (2010)[x]
-0.061 ± 0.008	9.10 ± 0.07	1–21	48	Henry *et al.* (2010)[y]
-0.053 ± 0.010	9.05 ± 0.08	1–21	75	Henry *et al.* (2010)[z]
-0.058 ± 0.006	9.09 ± 0.05	1–21	124	Henry *et al.* (2010)[zz]

[a] Type II, abundances compiled from the literature. [b] Type II, homogeneous observational material and empirical abundance derivations. [c] Type II, homogeneous observational material an automated photoionisation model fitting. [d] Type In (according to his classification), abundances compiled from the literature. [e] Type II , abundances compiled from the literature. [f] Type I, abundances compiled from the literature. [g] Type II, abundances compiled from the literature. [h] Type III, abundances compiled from the literature. [i] Type II, abundances compiled from the literature. [j] Type II, homogeneous rederivation of abundances from compiled intensities. [k] mostly Type II, homogeneous data and abundance derivations. [l] data mostly from Maciel & Quireza (1999), 0–4 Gyr age group. [m] data mostly from Maciel & Quireza (1999), 4–5 Gyr age group. [n] data mostly from Maciel & Quireza (1999), 5–8 Gyr age group. [o] data from compilation, abundances recalculated in homogeneous way, all types. [p] set A, data from compilation, abundances recalculated in homogeneous way, Type II, distances from Zhang (1995). [q] set A, data from compilation, abundances recalculated in homogeneous way, Type II, distances from Cahn *et al.* (1992). [r] set A, data from compilation, abundances recalculated in homogeneous way, Type III, distances from Zhang (1995). [s] set A, data from compilation, abundances recalculated in homogeneous way, Type III, distances from Cahn *et al.* (1992). [t] mostly Type I, abundances using ISO data, the regression line does not include 4 oxygen-poor objects. [u] Type I bipolar excluded, compiled abundances. [v] Type II bipolar excluded, compiled abundances. [w] Type III bipolar excluded, compiled abundances. [x] all types bipolar excluded, compiled abundances. [y] Type I, homogeneous data and abundance calculation. [z] Type II, homogeneous data and abundance calculation. [zz] all types, homogeneous data and abundance calculation.
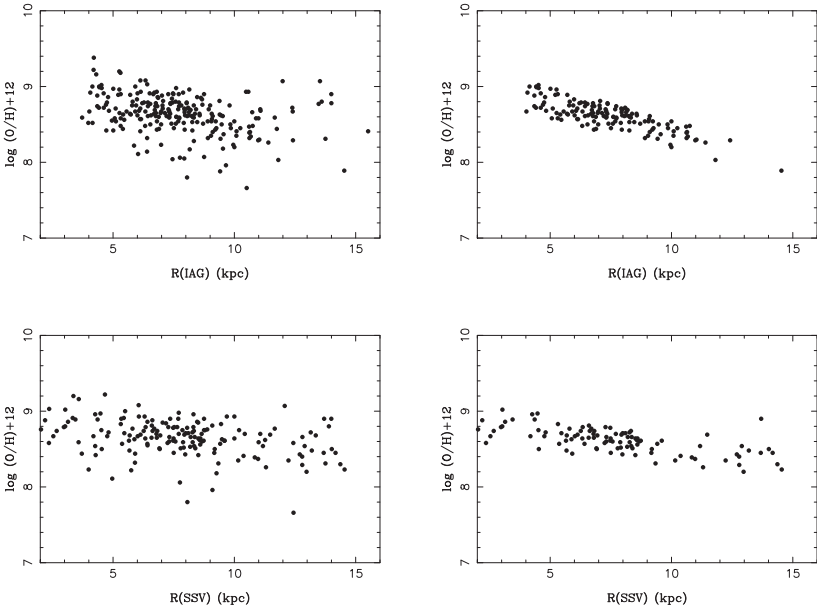
Fig. 2.20. The oxygen abundance in planetary nebulae of the Milky Way as a function of Galactocentric distance. *Top*: distances from the IAG/USP group. Bottom: distances from Stanghellini *et al.* (2008). *Left*: planetary nebulae with progenitors in the age range 2−10 Gyr. Right: planetary nebulae with progenitors in the age range 4−6 Gyr. Figure reproduced from Maciel & Costa (2009).

from 1 to 21 kpc. They have also carefully addressed the question of uncertainties in both oxygen abundances and radial distances.

The effect of distances is illustrated in Figure 2.20 where the top and bottom panels correspond to different statistical distance scales. Clearly the value of the gradient depends on the adopted distances.

Most studies conclude to a significant abundance gradient, but the quoted values are in the range between 0.01 and 0.09 dex kpc^{-1}. The most reliable value appears to be the one given by Henry *et al.* (2010), where the regression analysis accounting for uncertainties in both oxygen abundances and Galactocentric distances yields $A(O) = (9.09 \pm 0.05) - (0.058 \pm 0.006)R_g$ (R_g is the Galactocentric radius in kpc).

Since the progenitors of planetary nebulae span a wide range of ages, it is tempting to divide planetary nebulae into age groups. In a first attempt Maciel & Koppen (1994) simply used the planetary nebula classification of Peimbert (1978) who distinguishes Type I planetary nebulae (He and N-rich, which are likely the most massive ones and thus the youngest); Type II planetary nebulae (intermediate population) and Type III planetary nebulae (high velocity planetary nebulae, which actually should rather belong to the thick disk). They found that Type II

planetary nebulae show a steeper gradient than Type III (see Table 2.14). More recently, however, Perinotto & Morbidelli (2006) found no significant difference between Type II and Type III planetary nebula gradients and very shallow gradients. Adopting a different approach to assign planetary nebula ages, Maciel *et al.* (2005) found this time that oxygen gradients from planetary nebulae flatten in the course of galaxy evolution. Stanghellini & Haywood (2010), on the other hand, claim that the gradients steepen with time, although their result is not statistically significant. Henry *et al.* (2010) consider that there is no evidence so far for a steepening of the gradient with time. They make the point that progress on this question can be made only with improved distances and when understanding the natural scatter in oxygen abundances among planetary nebulae.

Concerning the radial variations of the abundance gradient in the Galaxy, Maciel & Quireza (1999) had suggested a flattening at large distances. This, however, is not confirmed by Henry *et al.* (2010). On the contrary, the latter see some evidence in their sample for a steepening of the gradient at Galactocentric distances larger than 10 kpc, but call for additional observations to confirm this trend. Much is expected on distances from the GAIA satellite to advance on this issue. However, a difficulty will remain: it is the fact that, at lower metallicities, stellar nucleosynthesis can modify the oxygen content of planetary nebulae significantly.

Although Henry *et al.* (2010) consider that it is too early to conclude that the gradient is anything but linear with a single slope across the entire disk, there is clear evidence that the gradient flattens towards the central parts of the Galaxy. Chiappini *et al.* (2009) have studied a large sample of planetary nebulae seen in the direction of the Galactic bulge, and identified a subsample of 44 objects which actually belong to the disk population and, in majority, lie within a few kpc from the Galactic centre. For this subsample they find $A(O) = 8.52 \pm 0.29$, which is significantly lower than the value of $A(O)_0 = 9.09 \pm 0.05$ taking the entire Henry *et al.* (2010) sample. Although Chiappini *et al.* (2009), unlike Henry *et al.* (2010), collected line intensities from the literature, they made a careful selection of the best data and applied uniform methods to derive abundances. Thus the difference found between their mean oxygen abundance and that extrapolated from Henry *et al.* (2010) is likely to be meaningful.

2.2.2.6   Summary of abundance gradients in the Milky Way

Table 2.15 gives a summary of recent determinations of oxygen abundance gradients in the Milky Way from various types of objects. The recommended references are marked with an asterisk. Figure 2.21 shows the results in graphical form. One can see that there is rather good agreement between the results from the preferred references. This might indicate that abundance gradient studies are improving since, for any type of object, there are non-negligible differences between values obtained by various authors over the past decade.

There are however a few worries. At any Galactocentric radius, Cepheids seem to extend to larger oxygen abundance values than the more massive B-type stars.

Table 2.15. Summary of oxygen abundance gradients in the Milky Way determined by using different types of objects.

Author	Object type	Range in Rg [kpc]	# objects	$\Delta \log A(O)$ [dex kpc^{-1}]	A(0)$_0$ [dex]
* Deharveng *et al.* (2000)	H II optical	$5-15$	34	-0.040 ± 0.005	8.82 ± 0.05
Esteban *et al.* (2005)	H II optical RL	$6-10$	6	-0.044 ± 0.010	9.04 ± 0.08
Esteban *et al.* (2005)	H II optical CEL	$6-10$	6	-0.035 ± 0.006	8.77 ± 0.05
Rudolf *et al.* (2006)	H II IR	$0-15$	68	-0.041 ± 0.014	8.77 ± 0.05
Pottasch & Bernard-Salas (2006)	PNe	$4-10$	18	-0.085	9.35
Stanghellini & Haywood (2010)	PNe	$2-17$	145	-0.023 ± 0.006	8.71 ± 0.06
* Henry *et al.* (2010)	PNe	$1-21$	124	-0.058 ± 0.006	9.09 ± 0.05
Gummersbach *et al.* (1998)	B-MS stars	$5-14$	16	-0.07 ± 0.02	9.158
Rolleston *et al.* (2000)	B-MS stars	$6.0-18.0$	80	-0.067 ± 0.008	9.401
Daflon & Cunha *et al.* (2004)	B-MS stars	$4.7-13.2$	69	-0.031 ± 0.012	8.767
* Firnstein (2011)	BA-Sgs	$5.5-11.0$	25	-0.033 ± 0.005	9.03
Lemasle *et al.* (2007)	Cepheids	$5-12$		-0.065 ± 0.013	9.19
* This book (Hill)	Cepheids	$5-16$	175	-0.032 ± 0.007	9.08 ± 0.06

H II regions oxygen abundances (from either optical or infrared forbidden lines) are lower than those of BA supergiants (corrected for stellar evolution effects) as determined by Firnstein (2011). The difference appears to be larger than what can be explained by depletion into dust grains. The other worry is that forbidden line oxygen abundances of planetary nebulae are larger than those in H II regions for Galactocentric distances up to about 10 kpc (except in the study of Stanghellini *et al.* 2010). This is contrary to what would be expected.

Most claims of steepening or flattening of the abundance gradients towards the centre or the outskirts of the Milky Way are premature. The only result that seems reliable is the flattening of the abundance gradient of planetary nebulae in the disk towards the centre of the Galaxy, as indicated by the comparison of the works by Chiappini *et al.* (2009) and Henry *et al.* (2010).

While many studies on abundance gradients emphasise the abundance scatter at a given Galactocentric distance, the extremely low dispersion found by Firnstein (2010) from a detailed study of BA supergiants is striking. Does this mean that, finally, the interstellar medium is really well mixed and that all the previous claims about dispersion were abused by uncertainties in distances or abundances?

2.2.2.7   Thick disk stars

Recent studies (Bensby *et al.* 2004) have allowed the chemical tagging of both thin and thick disk F, G and K main sequence stars in the solar vicinity. Thick disk stars are identified by their kinematics different from that of thin disk stars. The thick disk in the solar neighbourhood only makes up $\sim 4-15\%$ of the stellar density, but its stars bear the marks of their origin in their three-dimensional velocities: they stand out as stars with high orbital energies and slow rotation (since the thick disk has high velocity dispersions and lags behind the thin disk). For example, Bensby *et al.* (2004) define the probability of stars to belong to the thick disk in a Toomre diagram plotting the $\sqrt{V_W^2 + V_U^2}$ (or orbital energy perpendicular to the plane) *versus* the V_v velocity. The oxygen abundance in samples of hundreds of stars
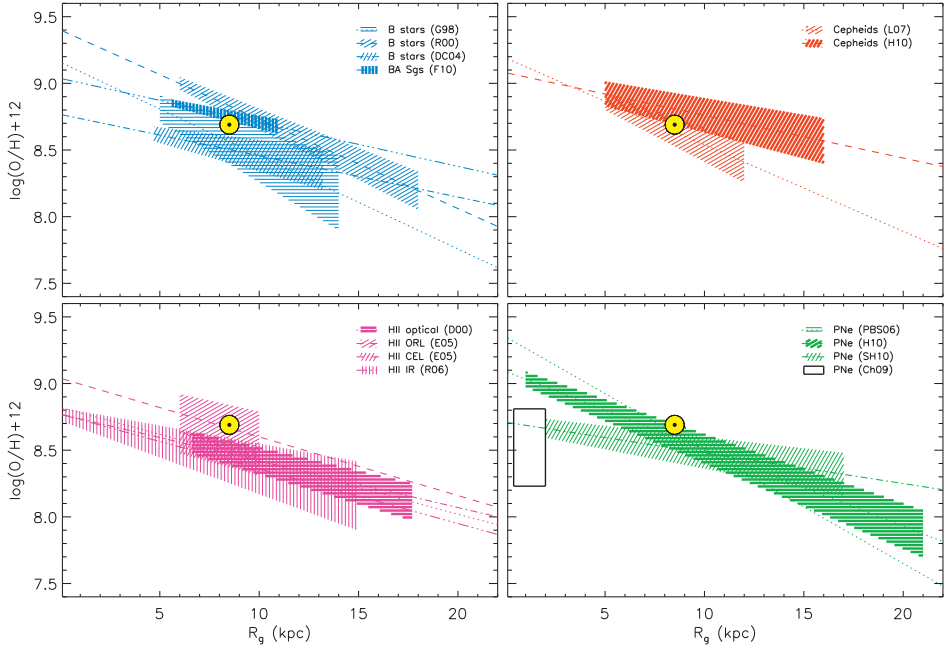
Fig. 2.21. Regression lines for the radial variation of $A(O)$ in the Milky Way. The object types and data sources are indicated in each panel. When available, error bars on the regression lines are indicated by hatched areas. In each panel, the preferred data are represented with heavier lines. The solar abundance $A(O)_\odot = 8.69$ is indicated in each panel for reference purposes. In the panel concerning planetary nebulae, the black rectangle indicates the distribution of $A(O)$ for inner disk planetary nebulae from Chiappini *et al.* (2009).

selected this way have been studied by Bensby *et al.* (2005); Reddy *et al.* (2006) and Ramírez *et al.* (2007), and a clear trend of oxygen excess (with respect to the stellar metallicity as traced by iron) is found for the vast majority of the sample, as demonstrated in Figure 2.22. In this figure, we have restricted the selected samples to always use the same oxygen indicator (see Sect. 1.2.2.1), the forbidden [O I]λ6300 line in the upper panel and the [O I]λ7700 triplet (corrected for NLTE) in the two lower panels. It is worth noting that the two indicators agree in the studies of Bensby *et al.* (2004) and Bensby *et al.* (2005) merely because they were defined in this way, the authors correcting the triplet oxygen abundances by an empirical factor (dependent on [Fe/H], $T_{\rm eff}$ and marginally on $\log g$), in addition to the NLTE correction factor. The latter is not a complete NLTE computation but a correction factor based on Gratton *et al.* (2000). For the Sun, this factor amounts to -0.05, but decreases for higher metallicities and increases for hotter temperatures. On the other hand, the Ramírez *et al.* (2007) and Reddy *et al.* (2003) oxygen abundances (of the same stars, analysed in the same way) yield
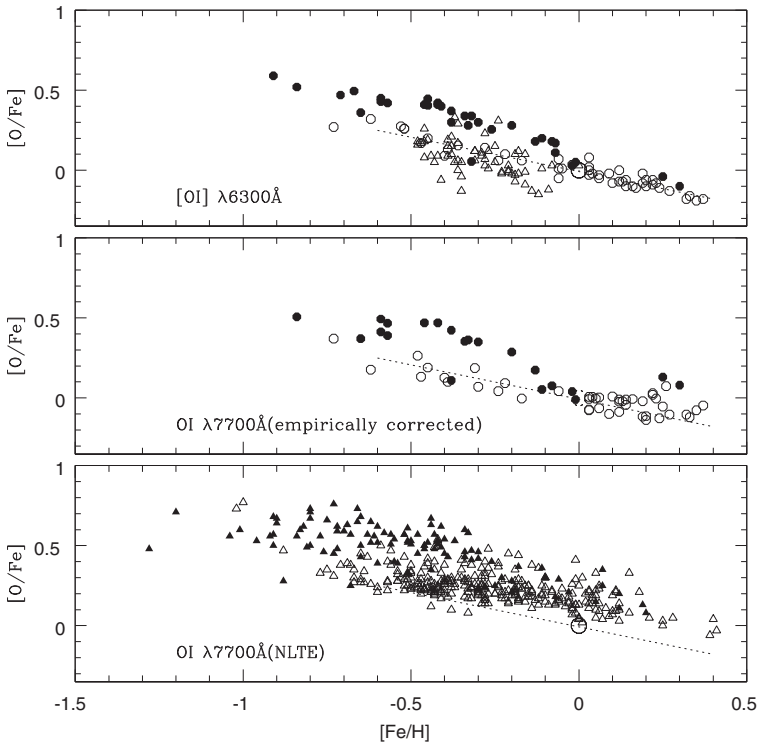
Fig. 2.22. Run of the oxygen excess [O/Fe] as a function of the star metallicity [Fe/H]. Thick disk: filled black triangles (Ramírez *et al.* 2007), filled black circles (Bensby *et al.* 2005). Thin disk: open black triangles (Ramírez *et al.* 2007), open black circles (Bensby *et al.* 2005). The dotted line depicts a regression through the thin disk points of Bensby *et al.* (2005).

different abundances from the [O I] than from the triplet lines, as illustrated by the square symbols in Figure 2.22 upper and lower panels were the thin disk stars follow a different trend (the dotted line is a simple regression through the thin disk points of Bensby *et al.* 2005). Furthermore, note that, in Ramírez *et al.* (2007), the O/Fe of thin disk stars is offset from the solar value by about 0.15 dex (median offset for stars with probabilities of belonging to the thin disk > 80%, within 0.1 dex of the solar metallicity) which may indicate a potential zero-value problem that could also affect thick disk stars. Bensby *et al.* (2004) and Bensby *et al.* (2005) demonstrate that the members of the thick disk more metal poor than [Fe/H] = −0.3 display a similar oxygen enhancement close to [Fe/H] = +0.45, whereas the metal-rich stars show a gradual decline of the oxygen excess with increasing metallicity, reaching a solar ratio around solar metallicity. They interpret this behaviour (called the *knee*) as the contribution of SN Ia supernovae to the chemical evolution of the thick disk for metallicities [Fe/H] > −0.3, bringing a large amount of iron and virtually no

oxygen to the gas, and hence decreasing the O/Fe ratio for subsequent generations of stars (see Chapter 4 for more discussion on chemical evolution interpretations).

Ramírez *et al.* (2007) on the other hand disagree with this interpretation, arguing against a *knee* and in favour of a shallow and gradual decline of [O/Fe] in the thick disk from about +0.5 to +0.4 in the $-0.8 < $ [Fe/H] $ < +0.3$ range. At higher metallicities, they argue that there is no hint of a *knee*, but rather that the (relatively few) stars with thick disk kinematics in that region show [O/Fe] ratios close to that of the thin disk. In fact they might not be genuine thick disk stars but rather thin disk stars with heated kinematics. In this case, the thick disk would have formed on a short timescale, shorter than the characteristic time for SN Ia to start contributing significantly to the chemical enrichment. The shallow decline of [O/Fe] would then only be due to mass-dependent yields of massive stars (see Chapters 3 and 4).

When compared to the oxygen excess in thin disk stars of the same metallicity, [O/Fe] is always larger in the thick disk stars, as illustrated in Figure 2.22, defining a distinct evolutionary path. This, together with the strongly overlapping metallicity distributions of these two populations, has been taken as a strong constraint on the thick disk formation scenario showing that the thin and thick disks are not directly related (thereby excluding the scenario of heating up an ancient thin disk into a thick disk with no new gas input). It is also striking that the thick disk [O/Fe] *vs.* [Fe/H] sequence is so narrow, making it hard to imagine that multiple low-mass mergers (à la Abadi *et al.* 2003) could make up such a well-defined sequence, all the more since the low-mass surviving galaxies have low [O/Fe] at these metallicities (Venn *et al.* 2004).

What has however been lately the subject of debate is the high metallicity extent of the thick disk, jeopardising the conclusion that SN Ia chemical enrichment takes place in the thick disk, and hence shortening its formation timescale. Mishenina (2004), based on a kinematical separation of a sample of 174 stars in the solar neighbourhood, argues that in fact the thick disk does not extend to solar metallicity but basically stops at [Fe/H] ~ -0.3, *i.e.* before the significant decrease in [O/Fe]. Bensby *et al.* (2007), on the other hand, conducted a survey of metal-rich and kinematically selected stars in the solar neighbourhood to address this precise point, and concluded that the thick disk indeed extends to solar and even supersolar metallicities (and low [O/Fe]), hinting at a formation timescale of up to 3 Gyr for the thick disk.

Another issue that has appeared even more recently is the possibility that what we call the thick disk, based on a kinematical selection in the solar neighbourhood, could simply be stars born at different Galactocentric radii that have migrated radially due to dynamical processes, thereby modifying their orbits to mimic a hotter component (Schönrich & Binney 2009; Sellwood & Binney 2002). In this scenario, a single disk component could give rise to an apparent dichotomy of kinematical and chemical properties (that we associate with the thin and thick disks) in the solar neighbourhood. To discriminate between such a scenario and the more classical thin and thick disk picture requires detailed chemical and dynamical studies of stars outside the solar neighbourhood, as well as sampling the

radial extent of the Milky Way disk. The measurement of [O/Fe] in these distant populations would be a discriminant factor.

2.2.3   The Milky Way bulge

Objects in the Galactic bulge are generally highly reddened due to extinction by intervening dust located in the spiral arms of the Galaxy. There are however a few windows where extinction is small, through which one can peep into the Galactic bulge and study its chemical composition and kinematics.

Like the bulges of other spiral galaxies, which are red, the bulge of our Galaxy is old, with an age of $10 - 12$ Gyr (Ortolani *et al.* 1995; Zoccali *et al.* 2003). Chemical abundance studies show that the bulge is metal rich with a metallicity distribution around $-1.2 \lesssim$ [Fe/H] $\lesssim +0.5$ (Fulbright *et al.* 2006; Zoccali *et al.* 2008).

Oxygen abundances in bulge objects can be derived from old stars and from planetary nebulae, and they are presented in the following.

2.2.3.1   Old stars

The O/Fe ratio.   The evolution of [O/Fe] as a function of metallicity is an important constraint for models of chemical evolution as this ratio ultimately probes the relative importance of Type II and Type Ia supernovae, which respectively yield the bulk of oxygen and iron.

At a given metallicity, [O/Fe] is enhanced in bulge field giants with respect to thin disk stars, as clearly shown by Figure 2.23 which reports the results from five groups. Zoccali *et al.* (2006) and Fulbright *et al.* (2007) used the forbidden [O I]λ6300 line while Cunha & Smith (2006), Rich & Origlia (2005) and Meléndez *et al.* (2008) used the infrared OH vibrational-rotational molecular transitions lines (note that the bulge giants in Meléndez *et al.* 2008 are taken from the Fulbright *et al.* 2006 sample). Whereas the [O I]λ6300 line shows some contamination by CN molecular lines, particularly in metal-rich stars, the use of OH lines relies on molecular dissociative equilibrium and on abundances of C and N (analysed through CN and CO lines). The agreement found for the different studies plotted in Figure 2.23 supports the robustness of this result.

On the other hand, concerning the comparison with the thick disk, different studies reach different conclusions. Based on the analysis of disk dwarf stars by Bensby *et al.* (2004), Zoccali *et al.* (2006) and Fulbright *et al.* (2007) find that the [O/Fe] ratio in bulge giants is enhanced with respect to the thick disk. On the other hand, from a detailed comparative analysis of infrared spectra of bulge and thick disk giants, Meléndez *et al.* (2008) find no chemical distinction between the bulge and the local thick disk.

A note on systematic errors.   It is important to realise that, as already mentioned in Section 1.2.2.1, the derived oxygen abundances depend on the choices of indicator, oscillator strength and oxygen abundance in the reference star. The
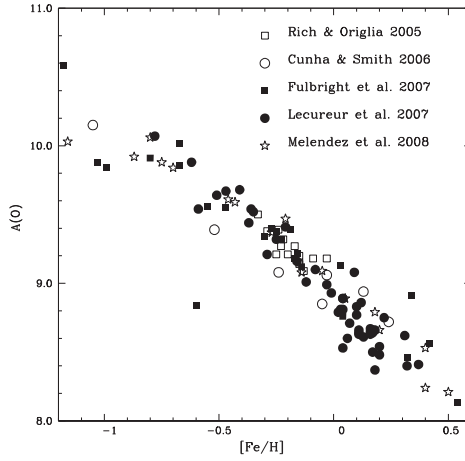
Fig. 2.23. [O/Fe] *vs.* [Fe/H] in field Galactic bulge giants. $A(O) = 8.74$ was adopted for the solar value as recommended by Allende-Prieto *et al.* (2001) for analyses using 1D model atmospheres.

important issue is the combination of oxygen abundance in the reference star and the $\log gf$ value.

Bensby *et al.* (2004) use for the [O I]λ6300 line a $\log gf = -9.819$ together with a solar oxygen abundance of $A(O) = 8.69$, and the same values were adopted by Zoccali *et al.* (2006) and Lecureur *et al.* (2007) for comparison purposes. The more conventional $\log gf = -9.717$ (Allende Prieto *et al.* 2001) would yield oxygen abundances lower by ~ 0.1 dex. Therefore, due to the $\log gf$ adopted, the Lecureur *et al.* sample could show an oxygen abundance higher by 0.1 dex. As a matter of fact, their absolute oxygen abundance for Arcturus is among the highest in Table 2.16 (although their [O/Fe] abundance relative to solar compares well with the other studies listed in this table).

In the derivation of the abundances in bulge giants Arcturus has been adopted as the reference star in all cases, except by Lecureur *et al.* (2007) who opted for μ Leo (but they give the parameters for Arcturus on their scale with respect to μ Leo). This allows one to check for offsets between the metallicity and oxygen abundance scales among the various studies. The $\log gf$ values of Fe I and Fe II lines – which are the lines used to derive the effective temperature, gravity, metallicity and microturbulence velocity – are fitted to Arcturus, and then used to derive stellar parameters of the sample bulge giants. For example, assuming [Fe/H] $= -0.50$ or -0.60 for Arcturus can give a 0.1 dex difference in $\log gf$ values of Fe I and Fe II, which can affect the final abundances by this much. In Table 2.16 we show the basic parameters and resulting iron and oxygen abundances obtained or adopted by these authors for Arcturus. It is clear that, while the iron abundances are similar within ± 0.06 dex in the Sun and 0.23 dex in Arcturus, for oxygen differences up to 0.31 dex in the Sun and 0.37 dex in Arcturus are seen. This is

Table 2.16. Parameters employed for Arcturus as reference star in bulge studies. References: 1 - Meléndez *et al.* 2003; 2 - Cunha & Smith 2006 (based on Smith *et al.* 2000 stellar parameters); 3 - Rich & Origlia 2005; 4 - Fulbright *et al.* 2006; 5 - Lecureur *et al.* 2007; 6 - Smith *et al.* 2002; 7 - Decin *et al.* 2003. Note: $A(X) = \epsilon(X) = \log(X/H)+12$.

T_{eff}	$\log g$	v_t	[Fe/H]	$A(O)_\odot$	$A(Fe)_\odot$	$A(O)$	$A(Fe)$	[O/Fe]	[O/H]	ref.	ind.
4275	1.55	1.65	−0.54	8.87	7.50	8.76	6.96	+0.43	−0.11	1	OH 1.5μ
4300	1.70	1.60	−0.49	8.77	7.45	8.49	6.96	+0.21	-0.28	2	OH 1.5μ
4250	1.50	1.50	−0.60	8.83	7.50	8.58	6.90	+0.35	−0.25	3	OH 1.5μ
4290	1.55	1.67	−0.50	8.69	7.45	8.67	6.95	+0.48	−0.02	4	[O I]
4300	1.50	1.50	−0.52	8.77	7.50	8.70	6.98	+0.45	−0.07	5	[O I]
4300	1.70	1.60	−0.72	8.77	7.50	8.39	6.78	+0.34	−0.38	6	OH 1.5μ
4350	1.50	1.70	−0.50	8.56	7.51	8.68	7.01	+0.62	+0.12	7	OH 3.6μ

mostly caused by differences in the oxygen indicator used, the assumed oscillator strengths and small differences in stellar parameters for Arcturus (which are rather homogeneous). When Arcturus is used as a reference star, only a fraction of these differences could possibly lead to a systematic difference in the oxygen abundance, whereas variations in stellar parameters would cause a spread around mean values and not systematic shifts. Similarly the assumed solar oxygen abundance creates systematic offsets: for the Sun, values of $A(O) = 8.77$ as recommended by Allende Prieto *et al.* (2001) for 1D model atmosphere calculations down to $A(O) = 8.66$ (Asplund *et al.* 2004) are presently used.

The oxygen abundance distribution.   All the samples of Galactic bulge stars with measured oxygen abundance comprise very few stars. In addition, all suffer from built-in metallicity biases (except the Lecureur *et al.* 2007; Zoccali *et al.* 2006 samples which were randomly picked on the bulge red giant branch and red clump).

On the other hand, abundances of iron and magnesium have been determined in larger samples of bulge giants. Using magnesium as a surrogate for oxygen, one can build a statistically more representative [O/H] distribution for bulge giants. Such a distribution is shown in Figure 2.24. The sample consists of 162 red clump giant stars in Baade's Window (Hill *et al.* 2010; Lecureur 2007), observed at high spectral resolution (R = 20 000) with the FLAMES/GIRAFFE spectrograph of the Very Large Telescope at the European Southern Observatory. To transform Mg/H into O/H, the anticorrelation between O/Mg and Mg/H was taken into account, as observed both in the bulge and the thin and thick disks by Lecureur *et al.* (2007), and Fulbright *et al.* (2007).

Figure 2.24 shows that the oxygen abundance distribution in bulge giants has a very strong peak at supersolar O/H, a sharp decrease at the higher abundances and a more extended oxygen-poor tail. This distribution is similar to the distribution of iron abundances found by Hill *et al.* (2010); Zoccali *et al.* (2008), but the peak in O/H is even narrower than that in Mg/H or Fe/H.
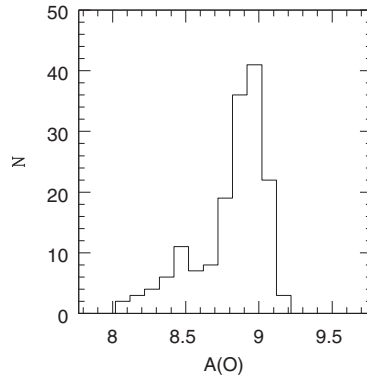
Fig. 2.24. [O/H] distribution in field Galactic bulge giants, using magnesium as a surrogate for oxygen.

Several caveats should however be mentioned with regards to this O/H distribution. First, the Mg/H to O/H transformation may suffer from some uncertainties. Second, it should be kept in mind that the sample considered here was selected to be red clump giants (core He-burning stars appearing on the red side of the horizontal branch), and there is therefore a built-in bias against stars more metal poor than [Fe/H] $\lesssim -1.2$ (or [O/H] $\lesssim -0.8$). Should the bulge contain a significant number of these metal-poor stars, they would have been missed in this sample. Finally, the sample can be perturbed by some stars actually belonging to the disk population but seen in projection on the bulge.

2.2.3.2   Planetary nebulae

As already mentioned, objects in the Galactic bulge are generally highly reddened, except in a few windows where extinction is small. Stellar abundance analyses in the bulge rely mostly on observations of giant stars in such windows (see Sect. 2.2.3.1). Planetary nebulae, due to their short lifetimes, are much less numerous, and one has to rely on observations covering the entire bulge in order to obtain meaningful statistics. Until the end of the 1990s, most of the planetary nebula spectra obtained for the bulge did not allow a determination of the electron temperature, as the weak [O III] $\lambda4363$ or [N II] $\lambda5755$ lines were not observed in these highly reddened objects. In such cases, as seen in Section 1.2.3.1, even tailored photoionisation modelling does not give a reliable oxygen abundance. The situation has now greatly improved.

Table 2.17 lists works which obtained temperature-based oxygen abundances in large samples of planetary nebulae in the direction of the Galactic bulge, giving the mean and dispersion of $A(O)$ of the various samples. In reality, the samples listed here are not exactly comparable, not only because of differences in data quality, but also because they were not selected in the same way. The sample of Escudero *et al.* (2004), for example, contains a larger proportion of planetary

Table 2.17. Mean oxygen abundances of planetary nebulae in the Galactic bulge.

mean $A(O)$	number of objects	references
8.48 ± 0.43	85	Stasińska *et al.* (1998)[a]
8.74 ± 0.15	30	Cuisinier *et al.* (2000)[b]
8.22 ± 0.43	45	Escudero & Costa (2001)[c]
8.44 ± 0.34	102	Górny *et al.* (2004)[d]
8.28 ± 0.39	52	Górny *et al.* (2004)[e]
8.63 ± 0.16	7	Exter *et al.* (2004)[f]
8.67 ± 0.18	38	Exter *et al.* (2004)[g]
8.70 ± 0.21	25	Wang & Liu (2007)[h]
8.86 ± 0.42	?	Milanova & Kholtygin (2009)[i]
8.41 ± 0.33	117	Chiappini *et al.* (2009)[j]
8.52 ± 0.29	44	Chiappini *et al.* (2009)[k]

[a] Compiled intensities, consistent abundance derivations.
[b] Homogeneous data set, consistent abundance derivations.
[c] Homogeneous data set, consistent abundance derivations.
[d] Proper bulge population, combined samples, consistent abundance derivations.
[e] Inner disk population, combined samples, consistent abundance derivations.
[f] Type I planetary nebulae, homogeneous data set, consistent abundance derivations.
[g] Type II planetary nebulae, homogeneous data set, consistent abundance derivations.
[h] Homogeneous high signal-to-noise data.
[i] Own empirical method, literature data.
[j] Proper bulge population, combined samples, only good quality data, consistent abundance derivations.
[k] Inner disk population, combined samples, only good quality data consistent abundance derivations.

nebulae that actually belong to the inner disk, while the sample of Cuisinier *et al.* (2000) mainly contains objects from the genuine bulge population. The sample by Wang & Liu (2007) is composed of very good quality data obtained with high resolution spectroscopy and long exposures. Unfortunately its size is small. The samples considered by Chiappini *et al.* (2009) are so far the best compromise between quality and quantity.

An important issue to consider, when dealing with the Galactic bulge population, is that objects seen in projection onto the bulge do not necessarily pertain physically to it. It is in fact possible to distinguish genuine bulge planetary nebulae from those actually located in the inner Galactic disk (see Górny *et al.* 2004 & Chiappini *et al.* 2009). The different kinematic properties of these two samples confirm that the contamination of one of these samples by the other is very small.

From Table 2.17 it appears that the genuine Galactic bulge population has a slightly larger mean and smaller dispersion in $A(O)$ than the inner disk. As a matter of fact, with such important dispersion, samples are better described by their median values and percentiles than by their mean and dispersion. In the case of the Chiappini *et al.* (2009) samples, the median, 25 and 75 percentiles are (8.57, 8.41, 8.71) for the 117 bulge planetary nebulae with best data, and (8.51, 8.30,
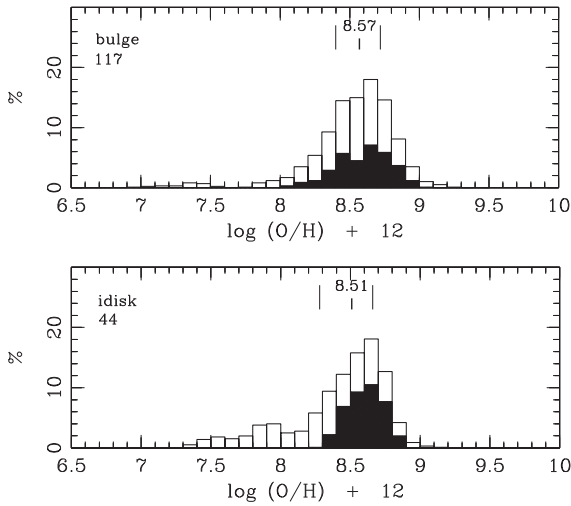
Fig. 2.25. Distribution of values of $A(O)$ for planetary nebulae belonging to the Galactic bulge (top) and to the inner disk (bottom) according to Chiappini *et al.* (2009). Objects with best data are represented in black. The positions of medians and quartiles are indicated.

8.66) for the 44 inner disk planetary nebulae with best data. Figure 2.25 shows the distribution of $A(O)$ in the proper bulge and in the internal-disk samples. Note that taking into account objects with less reliable abundances induces a long tail towards low values of $A(O)$, which almost disappears when retaining only the best data.

When discussing oxygen abundance distributions, possible biases due to sample selection must be considered. For example, is the sample biased towards lower values of the oxygen abundance because objects where the temperature cannot be measured have been removed? Chiappini *et al.* (2009) discuss this point and find that in their samples this does not occur.

Further questions are, what exactly does the oxygen abundances measure? Do they measure the abundances of the interstellar medium at the time when the progenitor was born? As discussed in Sections 3.2.3 and 2.2.2.5 the abundance of oxygen in planetary nebulae can be affected by ON cycling, or by hot bottom burning and dredge-up. In addition, oxygen can be depleted in dust grains perhaps up to 25% in the most extreme cases.

Finally, there is an even more subtle bias which has to do with the planetary nebula phenomenon itself: metallicity certainly plays a role in determining whether a star of given initial mass will produce a planetary nebula. The planetary nebula oxygen abundance distribution is therefore not necessarily illustrative of the oxygen abundance distributions of stars in the mass range that can lead to the planetary nebula phenomenon.

Some authors are trying to detect the presence of oxygen abundance gradients inside the bulge. For example, Escudero & Costa (2001) suggest the existence of a vertical abundance gradient in the bulge with lower O/H at high latitudes. This has probably to do with the fact that several populations of planetary nebulae are present in their sample.

2.2.3.3 Do planetary nebulae and stars tell the same story?

Both red giants and planetary nebulae are commonly used as abundance tracers of old stellar populations. However they may show different oxygen abundance distributions for several reasons.

- Biases in sample selection. For example, the most metal-rich stars may turn into the so-called "AGB-manqués" (O'Connell 1999) and never become planetary nebulae. The samples of red giants in which oxygen abundances have been measured are still small, and were not *a priori* selected to reflect the true bulge oxygen abundance distribution.

- Differences in progenitor mass range. *A priori*, planetary nebulae, which correspond to a more advanced phase in stellar evolution than red giants, should originate from stars of higher initial masses. However, if a significant fraction of planetary nebulae actually descend from interactive binaries, this is not necessarily true.

- In both objects, the initial oxygen abundance may have been modified by nucleosynthesis.

Figure 2.26 shows the oxygen abundance distribution for a sample of 42 red giant stars observed by Lecureur *et al.* (2007) in which the oxygen abundance was measured directly (and not using magnesium as a surrogate, as done in Fig. 2.24). Chiappini *et al.* (2009) argue that, despite its drawbacks, this sample should give a fair representation of the oxygen abundance distribution in bulge giants. This distribution is clearly different from that obtained in planetary nebulae as presented in Figure 2.25 (top), being shifted by about 0.3 dex towards higher values. Chiappini *et al.* (2009) analysed this question in detail, and came to the conclusion that the oxygen abundances in bulge planetary nebulae and giant stars do not convey the same story. However, they make the point that the observed discrepancy between both distributions could be due to systematic errors in the abundance derivations of either planetary nebulae or giant stars, or both.

Studies of microlensed dwarf stars, such as that of Bensby *et al.* (2010), could bring new light on this question if a large enough sample can be gathered.

2.2.4 The Milky Way halo

2.2.4.1 Field stars

As explained in Chapter 3 and already mentioned before, oxygen is uniquely produced in massive stars, tracing galaxy enrichment by Type II supernovae, while
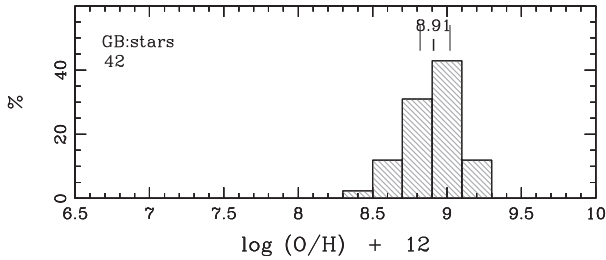
Fig. 2.26. Distribution of values of $A(O)$ for giant stars in the Galactic bulge (top). The positions of median and quartiles are indicated. Figure taken from Chiappini *et al.* (2009).

iron is also produced in Type Ia supernovae. The observed trends of Fe/O as a function of metallicity can thus help to understand the history of the region under study. Here, we present data concerning the stellar population of the Galactic halo, excluding the special case of globular clusters which is discussed in Section 2.2.4.3.

Since different oxygen abundance indicators (see Sect. 1.2.2.1) can give different oxygen abundances for a same star (*e.g.* Spite & Spite 1991), it is preferable to show a separate plot for each case. Note that, for each star, the best indicator is a function of the stellar parameters. In metal-poor stars, the low excitation potential forbidden lines at 6300 and 6363 Å are detected in giants and cool subdwarfs, but are essentially absent in turn-off stars. The O I permitted lines, among which the $\lambda 7770$ triplet is the strongest, appear in F–G dwarfs and subgiants, but they are faint in metal-poor K giants. The UV OH lines are strong in F-G-K stars while the IR OH lines are best detected in cool dwarfs.

In Figure 2.27 the values of [Fe/O] derived from high resolution and high signal-to-noise data are plotted, based on the oxygen forbidden line [O I]$\lambda 6300$ considered to be the most reliable oxygen abundance indicator. In Figure 2.28 we show the values of [Fe/O] for giants, subgiants and dwarfs, based on the UV OH lines. Note that the UV OH lines are the only detectable lines in very metal-poor dwarfs.

The IR OH lines have so far not been widely used as oxygen indicators. Meléndez *et al.* (2001) and Meléndez & Barbuy (2002) reported oxygen abundances from IR OH lines for 22 halo stars. Another 8 halo stars were studied by Balachandran *et al.* (2001). The [Fe/O] ratios derived from IR OH lines are in good agreement with those derived from the forbidden lines. However, a detailed analysis using NLTE, such as that described for the UV OH lines, is not yet available in the literature.

The O I permitted lines have been widely used, and they give high oxygen abundances at low metallicities, such as those found for example in Abia & Rebolo (1989). These lines are subject to strong NLTE effects, and the effects are stronger for increasingly metal-poor stars as has been demonstrated, for example, by Shchukina *et al.* (2005) and Meléndez *et al.* (2006).
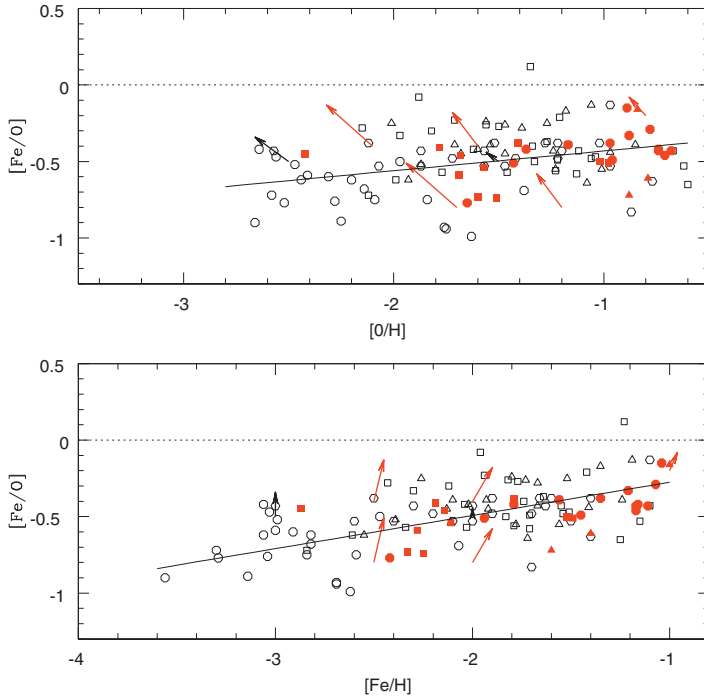
Fig. 2.27. [Fe/O] *vs.* [O/H] (top) and *vs.* [Fe/H] (bottom) in halo giants and subgiants, based on the forbidden oxygen line [O I]λ6300. Subgiants are represented in filled red symbols: triangles, Spite & Spite (1991); circles, Nissen *et al.* (2002); squares, García Pérez *et al.* (2006). Giants are represented by open symbols: hexagons, Barbuy (1988); triangles, Shetrone (1996); squares, Carretta *et al.* (2002); circles, Cayrel *et al.* (2004). Arrows indicate plausible 3D-modelling corrections, from Collet *et al.* (2005) for giants and Nissen *et al.* (2002) for subgiants. The black lines correspond to non-weighted regressions on all the points.

The most reliable and currently available data to study the [Fe/O] trends with metallicity in the Galactic halo are therefore those presented in Figures 2.27 and 2.28. Unfortunately, the number of stars analysed is still scarce. Large scheduled surveys, such as HERMES, will be able to increase the samples by orders of magnitude, allowing a deeper insight into the detailed history of the Galactic halo.

2.2.4.2   Planetary nebulae

Only a small number of planetary nebulae in the halo are known so far, less than 20, for an expected total of several thousands. Even if their number is growing due to serendipitous findings in large-scale surveys outside the Galactic plane, it will probably never allow good statistics. The few halo planetary nebulae that
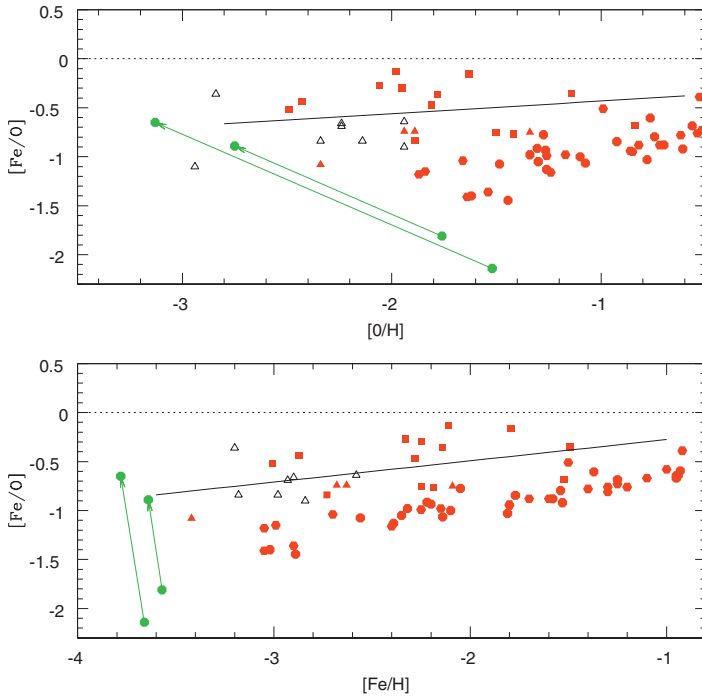
Fig. 2.28. [Fe/O] *vs.* [O/H] and [Fe/H] in halo giants, subgiants and dwarfs based on UV OH lines. Subgiants/Dwarfs are represented in filled red symbols: squares. García Pérez *et al.* (2006); hexagons, Israelian *et al.* (1998) and Israelian *et al.* (2001); circles, Boesgaard *et al.* (1999); triangles, Lai *et al.* (2008). Giants are represented in open black symbols: triangles, Lai *et al.* (2008). Green circles correspond to the binary star by González Hernández *et al.* (2008). The long green arrows indicate 3D-modelling corrections for this object. The black lines are the same as in Figure 2.27, illustrating the systematic difference between the two oxygen abundance indicators.

we have at hand span a wide range of oxygen abundances: until recently, the halo planetary nebula with the largest oxygen abundance was NGC 2242 with $A(O) = 8.19$, and the one with the lowest oxygen abundances was K 648 (located in the globular cluster M 15) with $A(O) = 7.61$ (Howard *et al.* 1997). Recently, another halo planetary nebula was discovered (SBS 1150 + 599A, also referred to as PNG 135.9 + 55.9 or TS 01) with a much lower oxygen abundance: $A(O) = 6.82 \pm 0.33$ (Stasińska *et al.* 2010), *i.e.* almost one hundredth of the solar value. In this case, however, it is clearly demonstrated that oxygen does not trace the chemical composition of the progenitor, as sulphur and argon abundances indicate a metallicity of about 1/30 solar. The extreme oxygen deficiency in this object can be explained by intense mixing on the AGB (Stasińska *et al.* 2010) due to the presence of a close companion. As a matter of fact, the study of the chemical composition of Galactic halo planetary nebulae is interesting to test models of

AGB nucleosynthesis at low metallicities rather than to help understanding the evolution of the halo.

2.2.4.3   Globular clusters

Globular clusters are fascinating objects nearly as old as the Universe, which give insight on a large variety of astrophysical issues. These large aggregates of stars can be used as cosmological tools. They bear witness to the formation and evolution of galaxies, and bring clues on the interactions and merging processes between galaxies. They represent unique laboratories for dynamical mechanisms that occur on timescales shorter than the Hubble time. Last but not least, they are invaluable laboratories to test the predictions of stellar evolution theory. However and despite their broad astrophysical importance, large uncertainties remain regarding their origin and formation processes as well as their early dynamical and chemical evolution. For all these reasons globular clusters have been extensively studied since the early 1950s. In particular they have been the subject of numerous spectroscopic chemical dissections which revealed striking anomalies in their light element contents and more specifically in their oxygen content.

We refer to Gratton *et al.* (2004), Sneden (2005), Charbonnel (2005) and Decressin (2007) for extended reviews on the observed abundance trends in globular clusters and only briefly recall the main points: (i) individual globular clusters appear to be fairly homogeneous as far as Fe and the iron peak elements (Ni, Cu) are concerned (with the notable exception of Ω Cen); (ii) they present very low scatter and the same trends as field stars for the neutron-capture elements (both *s*- and *r*-process; Ba, La, Eu) and the alpha elements (Si, Ca); (iii) they exhibit however large star-to-star abundance variations and specific patterns for the lighter elements C, N, O, Na, Mg, Al, Li and F that are not shared by their field counterparts and are thus called "abundance anomalies".

Among these anomalous patterns, the best documented one is the anticorrelation between O and Na abundances (see Drake *et al.* 1992; Pilachoswki 1989; Sneden *et al.* 1991 for the earlier studies and Carretta *et al.* 2009 for more recent data). Figure 2.29 shows the O-Na anticorrelation in the homogeneous and extended VLT survey by Carretta *et al.* (2009) for a unique sample of 1958 stars in 19 Galactic globular clusters. This is the largest database of this kind to date. It spans a large range in globular cluster metallicity ([Fe/H] from -2.4 to -0.4 dex) and global physical properties such as total cluster mass, concentration, density and horizontal branch morphology. Additionally the sampled globular clusters belong to both the disk and halo populations. The O-Na anticorrelation can be considered as "universal" as far as Galactic globular clusters are concerned, since it has been found in all the objects where it has been so far looked for. It is now even accepted as the decisive observational criterion defining *bona fide* globular clusters (Carretta *et al.* 2010). Most importantly, and thanks to the advent of 8-10 m class telescopes, the O-Na anticorrelation in globular clusters can be observed both among bright red giants and unevolved stars, *i.e.* turn-off and sub giants (Carretta *et al.* 2004a; Gratton *et al.* 2001; Ramirez & Cohen 2002).
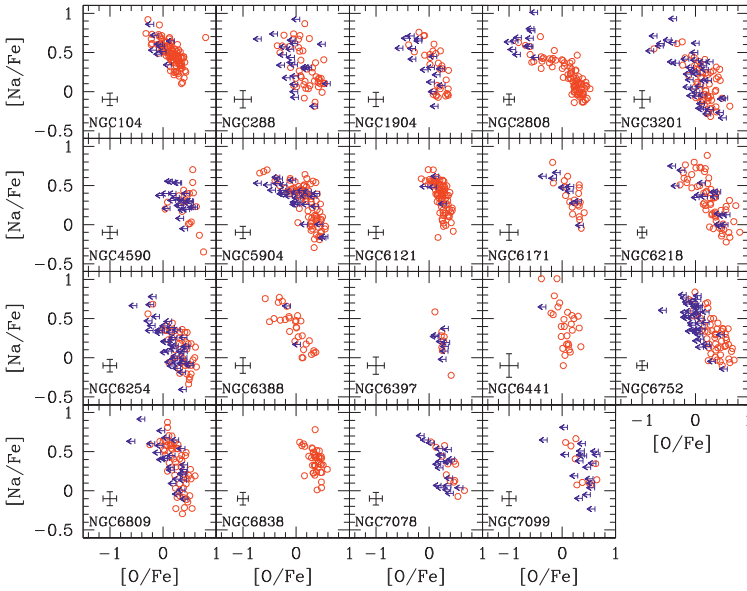
Fig. 2.29. The O-Na anticorrelation observed in 19 Galactic globular clusters by Carretta and collaborators. The Na and O abundances were obtained from GIRAFFE and UVES spectra. Upper limits in O abundances are shown as arrows, detections are indicated as open circles. Figure reproduced from Carretta *et al.* (2009).

In addition and whenever all the necessary data are available, N is found to be anticorrelated with O which positively correlates with C, and the sum C+N+O appears to be constant within observational errors (Carrett a *et al.* 2005; Dickens *et al.* 1991; Ivans *et al.* 1999; Smith *et al.* 1996, 2005; Yong *et al.* 2009, 2008). Last but not least, variations in Al and Mg, again correlated with each other, have been discovered (*e.g.* Ivans *et al.* 1999; Lind *et al.* 2011; Ramirez & Cohen 2002; Shetrone 1996). The sum Mg+Al is also found to be constant in several clusters (Shetrone 1996), and observations in NGC 6752, M 13 and M 71 show that Mg depletion is due to the burning of ^{24}Mg (Yong *et al.* 2006, 2005, 2003).

As an illustration we show in Figure 2.30 the abundance patterns in NGC 6752, which is to date one of the best studied globular clusters as far as its chemical properties are concerned. The largest O values are similar to those of field halo stars of the same metallicity as NGC 6752 ([Fe/H] = −1.5); we can thus assume that this is the original O abundance of the intra-cluster gas. This is also true for the corresponding values of Na, Al and Mg. We can consider then that all abundances corresponding to the highest O values (as indicated by open circles in Fig. 2.30) are the initial ones, and that abundances at the other extreme (indicated by open squares) correspond to the most extremely processed material. Pasquini *et al.* (2005) reported observations of Li in 9 turn-off stars of NGC 6752 with
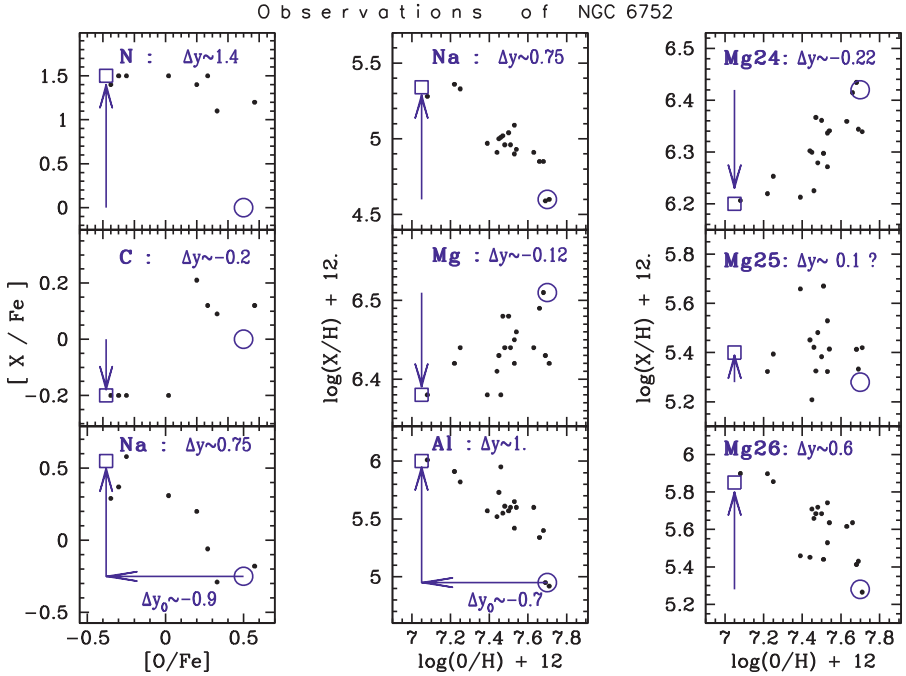
Fig. 2.30. Abundances of C, N, Na, Mg, Al and Mg isotopes in stars of NGC 6752, as a function of the corresponding oxygen abundance. Observations (filled symbols) in the *left column* (plotted as a function of [O/Fe]) are from Carretta *et al.* (2005) for turn-off stars, and in the other two columns (plotted as a function of O/H) from Yong *et al.* (2003) for bright giant stars. In all figures, the estimated initial abundances of the gas from which the cluster was formed are indicated by an open circle (*i.e.* it is assumed that they have the same composition as field halo stars of the same metallicity [Fe/H] = −1.5, with, *e.g.* [O/Fe] = 0.5, [C/Fe] = 0, etc.). The most extreme abundances observed at present in NGC 6752 are indicated by open squares. Arrows indicate the magnitude and direction of the abundance spread, which is also given by Δy (in dex, where $y = \log(\text{abundance})$) in each panel; Δy_O in the bottom panels indicates the corresponding variation of oxygen abundance, larger in the case of Carretta *et al.* (2005) (∼0.9 dex) than in the case of Yong *et al.* (2003) (∼0.7 dex). In the former case the authors have indeed tried to enhance the chance of including extreme cases by selecting stars with potentially strong and weak CN bands using the Strömgren c_1 index. Figure reproduced from Prantzos *et al.* (2007).

UVES, and found that Li is correlated with O and anticorrelated with Na. Stars with "original" O (high) and Na (low) have a Li content similar to low-metallicity stars in the halo field, *i.e.* $A(\text{Li}) = \log(\text{Li/H}) + 12 \sim 2.3$. Stars with "extreme" abundances (lowest O and highest Na) are not devoid of Li but have a significant amount of $A(\text{Li}) \sim 2$ (see also *e.g.* Lind *et al.* 2009).

The abundance anomalies of oxygen and other chemical elements that have been presented here constitute serious challenges for theories of globular cluster evolution. These are discussed in Section 4.3.5.

2.3   The local Universe

It is interesting to note that the first published spectra of extragalactic H II regions containing all the necessary information to derive the oxygen abundance (Feast 1961; Sargent & Searle 1970) were not used for that purpose. Searle (1971) was the first to interpret the spectra of giant H II regions in spiral galaxies in terms of oxygen abundance gradients. A year later, Searle & Sargent (1972) determined the oxygen abundance in two dwarf blue galaxies, II ZW 40 and I ZW 18, the latter holding the record of the most oxygen-poor galaxy known for over two decades. In that same paper, Searle & Sargent (1972) laid the basis for the interpretation of the oxygen abundance in galaxies in terms of their star formation histories. Since then, the field of abundance determinations in external galaxies has exploded. While the first papers used only giant H II regions as abundance probes of their home galaxies, later studies extended to luminous stars and planetary nebulae. In this section, we present a brief summary of our present knowledge of the oxygen abundance as obtained by various indicators in a selection of objects. We first concentrate on the Magellanic Clouds, a pair of irregular galaxies and the closest ones where oxygen abundances have been determined systematically from H II regions, young and old stars and planetary nebulae. We then present the state of our knowledge on a selection of nearby spiral galaxies. After a short comment on the oxygen abundance determination in galaxies that stopped forming stars, we turn to a more global aspect that encompasses galaxies of all morphological types: the mass-metallicity relation. We end up this brief panorama with the most distant galaxies and comment on the evolution of the mass-metallicity relation with redshift.

2.3.1   The Magellanic Clouds

The Magellanic Clouds, located at a distance of ∼50 kpc, were long considered the closest galaxies to the Milky Way, and they are the most massive galaxies among the Milky Way satellites. Therefore, they have been studied in ample detail. Being two irregular galaxies, of much smaller mass than the Milky Way, they offer easy probes of a different formation and evolution than witnessed in our own galaxy.

The first estimates of the oxygen abundance in the Magellanic Clouds came from studies of H II regions in the mid 1970s. These studies already led to the discovery of significant abundance differences between the Large Magellanic Cloud (LMC), the Small Magellanic Cloud (SMC) and the Galaxy (see Dufour 1984, and references therein). The values recommended by Dufour in his review concerning the chemical composition of H II regions in the Magellanic Clouds at that epoch were $A(\mathrm{O}) = 8.02$ dex (SMC) and $A(\mathrm{O}) = 8.43$ dex (LMC). All these

Table 2.18. Summary of oxygen abundances in the LMC.

	References	$A(O)$	Notes
	H II regions		
*	This book (Stasińska)	8.33±0.13	19 H II regions; CEL $t^2 = 0$
	Garnett (1999)	8.4	about 20 H II regions; CEL $t^2 = 0$
	Russell & Dopita (1990)	8.37±0.22	4 H II regions; models
	Dufour (1984)	8.43±0.08	H II regions (see text)
	B-type stars (Main Sequence and Supergiants)		
*	Trundle *et al.* (2007)	8.40±0.18	NGC2004, 23 B-Sgs
*	Hunter *et al.* (2007)	8.33±0.08	N11, 30 stars mostly B-Sgs
*	Korn *et al.* (2002)	8.37±0.06	NGC2004, 4 B-MS
	F-G-K Supergiants & Cepheids		
*	Andrievsky *et al.* (2001)	8.51±0.08	9 F-Sgs
	Luck *et al.* (1998)	8.39±0.17	7 Cepheids
	Luck & Lambert (1992)	8.68±0.30	9 Cepheids
	RGB stars		
	Mucciarelli *et al.* (2011)	8.44±0.06	14 RGBs in NGC 1866
*	Mucciarelli *et al.* (2011)	8.20±0.20	7 RGBs in the field
	Pompéia *et al.* (2008)	8.27±0.14	7 RGBs in the field
	Smith *et al.* (2002)	8.16±0.17	12 RGBs in the field
	Supernova remnants		
	Russell & Dopita (1990)	8.25	3 SNRs; models
	Planetary nebulae		
*	This book (Stasińska)	8.19±0.30	87 PNe
	Maciel, Costa, & Idiart (2009)	8.40±0.20	23 PNe
	Wang & Liu (2008)	8.3±0.33	120 PNe; CEL $t^2 = 0$
	Leisy & Dennefeld (2006)	8.26±0.35	120 PNe
	Stasińska *et al.* (1998)	8.10±0.25	108 PNe

determinations were obtained by means of the direct, temperature-based method assuming no temperature fluctuations (see Sect. 1.2.3.1). Russell & Dopita (1990) obtained and analysed the spectra of several bright H II regions in both Clouds, fitting them with the multipurpose code MAPPINGS (which is able to produce photoionisation and shock models). Their results (see Tables 2.18 and 2.19) are in substantial agreement with previous studies of H II regions. Garnett (1999) presented an update of oxygen abundances in Magellanic Clouds H II regions, re-analysing all the spectra available so far. A similar analysis was done for this book, with the same atomic data as used for planetary nebulae (see below). In a few bright H II regions in the Magellanic Clouds (30 Dor or N11B in the LMC, N 66 and NGC 346 in the SMC), deep spectra allowed the determination of the oxygen abundance from recombination lines (Peimbert *et al.* 2000; Tsamis *et al.* 2003). The resulting values were larger than those derived from collisionally excited lines by about 0.3 dex, so there is the same RL/CEL abundance discrepancy as seen in Galactic H II regions.

Table 2.19. Summary of oxygen abundances in the SMC.

	References	$A(O)$	Notes
	H II regions		
*	This book (Stasińska)	8.00±0.19	19 H II regions; CEL $t^2 = 0$
	Garnett (1999)	8.0	about H II regions; CEL $t^2 = 0$
	Russell & Dopita (1990)	8.13 ± 0.10	6 H II regions; models
	Dufour (1984)	8.02 ± 0.08	H II regions; model grids
	B-type stars (Main Sequence and Supergiants)		
*	Hunter *et al.* (2007)	8.06 ± 0.10	NGC 346: 10 MS, 4 B-Sgs
*	Trundle *et al.* (2007)	7.90 ± 0.19	NGC 330: 5 MS, 15 B-Sgs
	A-type Supergiants		
	Venn (1999)	8.14 ± 0.10	9 A
	F-G-K Supergiants & Cepheids		
	Hill (1999)	7.72 ± 0.19	6 K-Sgs in NGC330
	Luck *et al.* (1998)	7.87–8.14	7 Cepheids
*	Hill *et al.* (1997)	8.14 ± 0.12	6 K-Sgs in the field
	Luck & Lambert (1992)	8.21 ± 0.19	8 Cepheids
	Supernova remnants		
	Russell & Dopita (1990)	7.93	2 SNRs; models
	Planetary nebulae		
*	This book (Stasińska)	7.93 ± 0.31	28 PNe; CEL $t^2 = 0$
	Maciel, Costa, & Idiart (2009)	7.89 ± 0.44	46 PNe; CEL $t^2 = 0$
	Wang & Liu (2008)	8.1 ± 0.30	37 PNe; CEL $t^2 = 0$
	Leisy & Dennefeld (2006)	7.74 ± 0.50	61 PNe; CEL $t^2 = 0$
	Stasińska *et al.* (1998)	7.74 ± 0.39	49 PNe; CEL $t^2 = 0$

Russell & Dopita (1990) obtained spectra of a few supernova remnants together with their H II regions. They analysed them with the multipurpose MAPPINGS code. The sample is small, but the oxygen abundances are roughly consistent with those of their H II regions.

The determination of reliable stellar oxygen abundances in the Magellanic Clouds started in the late 1980s. The proximity of these two galaxies makes it possible to observe individual B-type stars (both main sequence objects and supergiants) and A-K supergiants (also including Cepheids).

In the case of cool stellar objects, the determination of chemical abundances in Magellanic Cloud stars reached a satisfactory state only after Spite *et al.* (1989). Previous analyses were highly unreliable, with very different abundances derived for the same stars by independent investigators (up to 0.7 dex). After the first reliable determination of oxygen abundance in 3 F-Sgs in the SMC by Spite *et al.* (1989), several authors analysed small samples of F-K supergiants and Cepheids (*e.g.* Andrievsky *et al.* 2001; Hill 1999; Hill *et al.* 1995, 1997; Luck & Lambert 1992; Luck *et al.* 1998). Oxygen abundances in red giant branch stars, either in clusters or in the field, have also been obtained (*e.g.* Smith *et al.* 2002; Pompéia *et al.* 2008;

Mucciarelli *et al.* 2011). A summary of these and other results can be found in Tables 2.18 and 2.19 [5].

Early in the 1990s, the research group at Queen's University Belfast studying massive stars began a program to determine the chemical composition of B-type stars in the Magellanic Clouds. The results were published in many papers (Dufton *et al.* 1990; Dufton *et al.* 2000; Dufton *et al.* 2005; Lennon *et al.* 1990; Lennon *et al.* 1991; Lennon *et al.* 1996; Lennon *et al.* 2003; Rolleston *et al.* 1993; Rolleston *et al.* 1996; Rolleston *et al.* 1999; Rolleston *et al.* 2002; Trundle *et al.* 2004; Trundle & Lennon 2005; Lee *et al.* 2005) while, in parallel, stellar atmosphere codes for massive stars were improving. This work culminated after almost 20 years with the "VLT-FLAMES Survey of Massive Stars" (P.I. S. Smartt, see Evans *et al.* 2008, for a description of the program and main results). This large program using the Very Large Telescopes at the European Southern Observatory collected the largest homogeneous sample of Magellanic Cloud B-type stars studied to date. The observations were centred in two young clusters (N11, NGC 346) and two old clusters (NGC 2004, NGC 330) in the LMC and SMC, respectively. The stars were analysed homogeneously with the NLTE plane-parallel code TLUSTY. The main results on the abundance analysis can be found in Hunter *et al.* (2007) and Trundle *et al.* (2007), and those corresponding to oxygen abundances are summarised in Tables 2.18 and 2.19. The oxygen abundances derived from the study of the two clusters in each galaxy are, within the errors, in good agreement. These results, which can be considered our best knowledge of oxygen abundances in B-type stars in the Magellanic Clouds to date, led to characteristic values for the oxygen abundance in the LCM and SMC of 8.35 ± 0.17 and 8.00 ± 0.11 dex, respectively.

There have been numerous systematic studies on the chemical composition of planetary nebulae in the Magellanic Clouds; actually, many more than on H ii regions. The first systematic studies were undertaken by various groups: Aller *et al.* (1987); Dopita *et al.* (1985); Monk *et al.* (1988); Webster (1988). The observations are difficult since, as in the case of H ii regions, the sky and surrounding diffuse emission must be subtracted properly. Sky subtraction is probably the main cause of differences in values obtained by different observers. The data set of Leisy & Dennefeld (2006) contains their own observations and a careful compilation of previous observations. Maciel, Costa, & Idiart (2009) have gathered a sample based on the observations of their own group, and analysed them in a homogeneous way. However, the observations were obtained with a smaller telescope. Finally, using the line intensities of the better observed objects from the Leisy & Dennefeld (2006) data base, abundances have been re-derived by Wang & Liu (2008) as well as by Stasińska (this book). For the latter, only the best observational data were selected, and the abundance determinations were carried out with the same atomic data as for the H ii regions, using the ionisation correction factors of Kingsburgh

---

[5]We exclude from the table results concerning old clusters, which present the same trends as the globular clusters in the Milky Way (see Sect. 2.2.4.3).
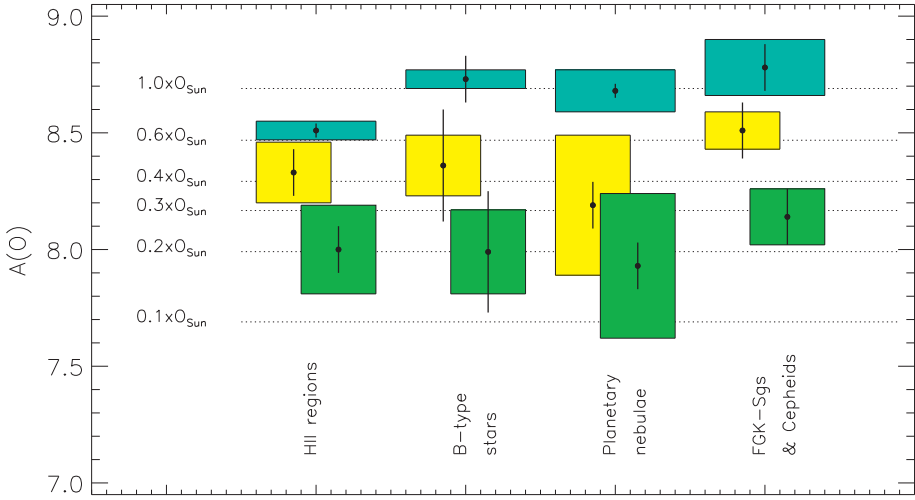
Fig. 2.31. The oxygen abundance in the SMC, the LMC and the solar vicinity as derived from different types of objects. The height of each rectangle corresponds to the observed dispersion. The vertical black line inside each rectangle represents the estimated uncertainty intrinsic to the method of abundance derivation. The data used in this plot are from those references marked with an asterisk in Tables 2.18 and 2.19. Horizontal, dotted lines indicate oxygen abundances with respect to the solar value (taking $A(O)_\odot = 8.69$).

& Barlow (1994). The resulting mean and dispersion are reported in Tables 2.18 and 2.19 together with the values from the other authors. Note that Milanova & Kholtygin (2009) also give average oxygen abundances in planetary nebulae of the Magellanic Clouds: 8.32 ± 0.55 and 8.30 ± 0.21 dex for the LMC and SMC, respectively. They were determined with a different empirical method designed by the authors, not yet fully evaluated (see Sect.1.2.3.1), and are significantly different from those of the remaining authors.

In Figure 2.31 we plot the ranges of oxygen abundances derived from each family of objects for the SMC and the LMC. The results for the solar vicinity from Sect. 2.2.1.9 are also included for reference. As has been known for decades, the LMC and SMC abundances are approximately half and a quarter solar, respectively. In detail, there are however several points worth noticing.

- The discrepancy between the abundances in H II regions and B-type stars is apparent only in the solar vicinity. Does this mean that it is due to a larger depletion of oxygen into dust in the more metal-rich environment of the solar vicinity? Or, does this mean that the bias in abundance determination from collisionally excited lines disappears at lower metallicities? None of the two interpretations seems to be correct. As shown by Simón-Díaz & Stasińska (2011), there are not enough metals available to sufficiently deplete oxygen to bring H II region and young star determinations into agreement. On the

other hand, oxygen recombination lines observed in a few Magellanic Cloud
H II regions lead to the same discrepancies between abundances derived
from recombination and from collisionally excited lines as found in the solar
vicinity (Tsamis *et al.* 2003).

- The spread in oxygen abundances is much larger in the Magellanic Clouds
  than in the Solar vicinity, except for the case of Cepheids. This could perhaps
  be an artefact due to the smaller number of objects considered in the solar
  vicinity than in the Clouds, but this question deserves further attention.

- The spread in oxygen abundances is very similar for B-type stars and H II
  regions in all three cases. This is reassuring, but again, one has to keep in
  mind that the samples are not very large.

Is there an abundance gradient in the Magellanic Clouds? From their study of H II
regions, Pagel *et al.* (1978) obtained for $A(O)$ a slope of 0.03 ± 0.02 dex kpc^{-1},
which is hardly significant, and they found no gradient at all for the SMC. However,
studies of asymptotic giant branch stars or RR Lyrae stars, which probe past
epochs, seem to indicate a slight metallicity gradient in the LMC as discussed by
Feast *et al.* (2010). The most likely reason for this seems to be that the proportion
of older stars increases in the outer regions of the LMC.

2.3.2   Abundance gradients in spiral galaxies

In this section we only discuss the abundance distribution of oxygen. The relation
between mass and metallicity of galaxies is discussed in a more general context
in the next section. Searle (1971), Shields (1974) and Smith (1975) demonstrated
many years ago the presence of radial abundance gradients in the disks of spiral
galaxies – as derived from H II regions – with the maximum oxygen abundance
occurring at their centres. This fundamental property of spiral galaxies has been
confirmed by many studies not only of H II regions, but also of supernova remnants,
planetary nebulae and stars.

The main source of information on abundance distributions in spiral galaxies
is the analysis of the emission line spectra of H II regions. Vila-Costas & Edmunds
(1992) provided the first global view on the relation between abundance gradients
and the physical properties of spiral galaxies. In order to compare the gradients
of different galaxies, a length scale must be chosen. The R_{25} radius, defined as
the length of the major axis out to a blue surface brightness level of 25 mag
arcsec^{-2} corrected for extinction and galactic inclination, gave good results and
has been adopted ever since. Vila-Costas & Edmunds (1992) analysed data for
30 galaxies and found that barred galaxies have shallower gradients. Among non-
barred spirals, there is a correlation of gradient slope with morphological type.
This study was based on a compilation of data from the literature. Zaritsky *et al.*
(1994) extended it by obtaining new observations of 159 H II regions to reach a
merged total sample of 42 galaxies. They concluded that the slope of the gradients
is only marginally correlated with galaxy morphological type. On the other hand,

they found suggestive evidence that the presence of bars induces flatter gradients. They also defined a characteristic oxygen abundance for each galaxy as being the abundance at $R/R_{25} = 0.4$, a definition which is robust against abundance gradients and does not require extrapolation. They find that the characteristic abundance is strongly correlated with the galaxy Hubble type and luminosity.

However, those conclusions rely on strong line methods to derive abundances, and these are uncertain and subject to biases (see Chapter 1). Direct, temperature-based methods would be much more appropriate to discuss abundance gradients. Unfortunately, auroral lines allowing the determination of the electron temperature are not detected in the majority of H II regions in spiral galaxies[6]. Even in the case of detection, as shown by Stasińska (2005), biases may occur at high metallicities. In addition, there is still the unsolved problem of temperature fluctuation and abundance discrepancies between forbidden and recombination lines. A comparison of H II region results with those obtained by studying other abundance indicators (supernova remnants, stars, planetary nebulae) is therefore crucial.

Supernova remnants were the first candidates to be considered. Unlike H II regions, the conditions in the post-shock gas of SNRs are such that the high-excitation emission line [O III] λ4363 is easier to detect. Their study seemed most promising in the early 1980s (Blair *et al.* 1982; Dopita *et al.* 1980). However, the derived abundances were based on first-generation shock models and were never updated. Larger collections of suitable spectra from SNRs were not obtained either. Finally, the contamination by stellar ejecta is an issue to be discussed in detail when this field is revived.

The use of planetary nebulae to study abundance gradients in spiral galaxies began with the work of Jacoby & Ford (1986), followed by several investigations on M 33 (Bresolin *et al.* 2010; Magrini *et al.* 2004, 2009). Planetary nebulae have the advantage over H II regions that their oxygen abundance results are not biased at high metallicities as argued by Stasińska (2005); however, they have their own problems (see Sect. 2.2.2.5).

B- and A-type supergiants have become very important oxygen abundance indicators in spiral galaxies, yielding invaluable information about the stellar chemical composition (and the present-day chemical properties of the ISM) in these galaxies. Three features make these stellar objects perfect candidates to complement (and even to go beyond) oxygen abundance determinations based on the analysis of H II regions. First, blue supergiants are among the most luminous stellar objects, and hence can be observed at very large distances. In addition, the derived oxygen abundance is not affected by dust depletion as in the case of H II determinations. Finally, stellar abundances are not only unaffected by bias at high metallicities, but in this case the metal lines are stronger and hence easier to detect and measure. Thanks to the development of stellar atmosphere codes for massive stars and the availability of medium (4 m) and large size (8−10 m) telescopes, the number of

---

[6]This situation is changing with the availability of the 8−10 m telescopes and will improve enormously with the future generation of Extremely Large Telescopes.

studies of B- and A-type supergiants in spiral galaxies from the Local Group (*e.g.* Monteverde *et al.* 2000; Trundle *et al.* 2002; Urbaneja *et al.* 2005; Venn *et al.* 2000) and far beyond (*e.g.* Bresolin *et al.* 2002, 2001; Kudritzki *et al.* 2008; Urbaneja *et al.* 2005b) has increased continuously since the first investigations on M 33 by McCarthy *et al.* (1995) and Monteverde *et al.* (1997).

Below, we individually comment on the oxygen abundance distribution of the spiral galaxies which have been studied most extensively and using various indicators.

2.3.2.1   M 33

This is the third largest member of the Local Group. It is a late-type spiral galaxy. Although of type SAc, its spiral arms are somewhat ill-defined and knotty. It was one of the first galaxies in which a radial abundance gradient was recognised (Searle 1971). Due to its modest distance (810 kpc) and almost face-on orientation, it is the spiral galaxy with the largest amount of data available to study the distribution of oxygen abundances across its face. In particular, it is the galaxy with the largest homogeneous sample of H II regions where the [O III] $\lambda4363$ line could be measured, allowing a direct, temperature-based determination of the oxygen abundance for 61 objects (Rosolowsky & Simon 2008). Surprisingly, these authors found an intrinsic oxygen-abundance scatter of ~ 0.11 dex at a given radius (see top panel of Fig. 2.32), implying that the interstellar medium would not be well mixed. Another consequence is that any determination of the abundance gradient must be very uncertain if based on a small object sample. For example, the first studies of H II regions in M 33 indicated a steep oxygen gradient (*e.g.* Garnett *et al.* 1997; Kwitter & Aller 1981; Smith 1975; Vilchez *et al.* 1988) of the order -0.11 dex kpc^{-1}, while more recent determinations converge to a much shallower gradient (Crockett *et al.* 2006; Magrini *et al.* 2007b). To test the hypothesis of azimuthal abundance variations suggested by Rosolowsky & Simon (2008), Bresolin (2011) obtained deep spectroscopy of 25 H II regions in the inner 2 kpc of M 33. He found a scatter of 0.06 dex in oxygen abundance, much smaller than the value of 0.21 found by Rosolowsky & Simon (2008) in the same region (see a comparison of their results in Fig. 2.32). He attributed this lower scatter to his more accurate measurements of the weak [O III] $\lambda4363$ line. He then computed a new radial oxygen gradient for M 33, merging his data with those from Rosolowsky & Simon (2008) where [O III] $\lambda4363$ has a good signal-to-noise ratio. The result is shown in Table 2.20. Concerning the suggestion by Magrini *et al.* (2007b) about the presence of two slopes for the gradient of M 33, being steeper in the inner region (-0.19 dex kpc^{-1}) and shallower in the outer region (-0.038 dex kpc^{-1}), this is obtained by averaging results from various abundance indicators but could be totally spurious.

For M 33, the oxygen abundance gradient has also been derived from planetary nebulae. Magrini *et al.* (2003) pioneered these studies with a first sample of 3 objects with measured [O III] $\lambda4363$. Magrini *et al.* (2004) extended the sample of planetary nebulae with derived abundances to 11 objects, by using a photoionisation model "to overcome the lack of direct information on the electron
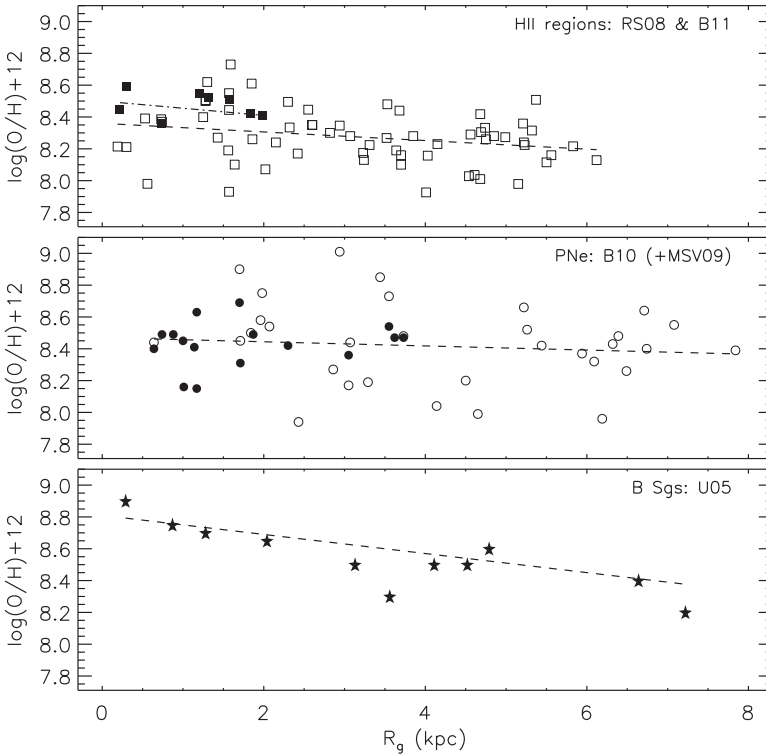
Fig. 2.32. O/H values in H II regions, planetary nebulae and B Supergiants as a function of galactocentric distance in M 33 as found by the most recent studies for each type of object. Top: measurements and gradients derived by Rosolowsky & Simon (2008, open squares) and Bresolin (2011, filled squares). Middle: gradient derived by Bresolin *et al.* (2010) by using his own determinations (filled circles) and best data from Magrini *et al.* (2009, open circles). Bottom: stellar abundances from Urbaneja *et al.* (2005b).

temperature". As explained in Section 1.2.3.1 this is expecting too much from photoionisation models and may lead to disastrous results. Magrini *et al.* (2009) presented a large sample of planetary nebulae deriving the oxygen abundance for 93 of them and obtaining a gradient of -0.031 ± 0.013 dex kpc^{-1}. Note however that, in this sample, a direct measurement of the electron temperature is possible for only about one third of the objects, and the authors – dangerously – used an empirical calibration to estimate the electron temperature. Bresolin *et al.* (2010) obtained deep spectra of 16 planetary nebulae in the inner zones of M 33, and managed to measure the intensity of [O III] $\lambda 4363$ in all of them. Note that their data were obtained with slit spectroscopy, allowing a proper sky subtraction – which is crucial in such studies – while the data of Magrini *et al.* (2009) were obtained through fibres. Unfortunately, the data by Bresolin *et al.* (2010) do not cover the entire range of galactocentric distances in M 33. The best estimate so far

Table 2.20. Radial variation of oxygen abundances in M 33 for various types of objects.

[kpc]	Range in Rg [kpc]	# objects	$\Delta \log A(O)$ [dex kpc^{-1}]	$A(0)_0$ [dex]
H II regions				
* Bresolin (2011)	0 − 8	~ 40	-0.045 ± 0.006	8.50 ± 0.02
Magrini *et al.* (2010)	0 − 8	103	-0.037 ± 0.009	8.47 ± 0.04
Rosolowsky & Simon (2008)	0 − 6.1	61	-0.027 ± 0.012	8.36 ± 0.04
Magrini *et al.* (2007b)	0 − 8	14	-0.054 ± 0.011	8.53 ± 0.05
Planetary nebulae				
* Bresolin *et al.* (2010)	0.5 − 4.7	48	-0.013 ± 0.016	8.47 ± 0.07
Magrini *et al.* (2009)	0.5 − 8.0	91	-0.031 ± 0.013	8.44 ± 0.06
B supergiants				
* Urbaneja *et al.* (2005b)	0 − 7.5	11	-0.06 ± 0.02	8.81 ± 0.007

of the radial distribution of the oxygen abundance in M 33 from planetary nebulae is obtained by combining the spectral data from Bresolin *et al.* (2010) with the subsample from Magrini *et al.* (2009) with measured [O III] $\lambda 4363$ intensities, and deriving the abundances in a consistent way. The result is shown in Figure 2.32 (middle). The obtained value of the gradient is -0.013 ± 0.016 dex kpc^{-1}, much lower than that found by Magrini *et al.* (2009) but still with substantial dispersion. Note that this dispersion is much larger than found by Bresolin (2011) from H II regions. In principle, one could expect a larger dispersion in planetary nebulae since they probe an extended age range. However, it is not excluded that errors might be larger than expected.

M 33 was also the first spiral galaxy (other than the Milky Way) for which an oxygen abundance gradient was determined from stars. The preliminary results presented in Monteverde *et al.* (1997) – they derived oxygen abundances from only one line – were confirmed with a more accurate study by Monteverde & Herrero (1998) and Monteverde *et al.* (2000). They obtained an oxygen gradient of -0.20 ± 0.07 dex kpc^{-1}. In a more recent study, Urbaneja *et al.* (2005b) increased the sample of analysed stars to 11 and used modern stellar atmosphere codes; this resulted in a shallower gradient, -0.06 ± 0.02 dex kpc^{-1} (see bottom panel of Fig. 2.32).

Finally, the oxygen abundance gradient in M 33 was also derived from the analysis of optical spectra of SNRs by Blair & Kirshner (1985) who found a value of -0.035 dex kpc^{-1}. Recently a completely new way to estimate the abundance gradient in M 33 was proposed, using the observed periods of Cepheids (Beaulieu *et al.* 2006). However, the result based on only 5 Cepheids was of -0.2 dex kpc^{-1} in metallicity which the authors translated to -0.16 dex kpc^{-1} in oxygen abundance.

Table 2.20 summarises the most recent and best data on the oxygen abundance distribution in M 33. For planetary nebulae and H II regions, all the determinations are temperature-based. The recommended references are marked with an asterisk.

2.3.2.2   M 101

This is a grand design face-on spiral galaxy of type SAB(rs)cd, located at a distance of 7.5 Mpc. It is the other spiral galaxy used by Searle (1971) and Smith (1975) to establish the presence of an abundance gradient in spirals. Many spectroscopic studies of H II regions in the disk of M 101 have been carried out (*e.g.* Garnett & Kennicutt 1994; Kennicutt & Garnett 1996; Kinkel & Rosa 1994; McCall *et al.* 1985; Rayo *et al.* 1982; Shields & Searle 1978; Torres-Peimbert *et al.* 1989; van Zee *et al.* 1998, among others), each based on electron temperature measurements of 1–5 bright H II regions. The most comprehensive determination of the oxygen abundance gradient was obtained by Kennicutt *et al.* (2003) who used 20 H II regions with a detected [O III] $\lambda 4363$ line (-0.027 dex kpc^{-1}, with a central extrapolated value 8.76 ± 0.06 dex). For the innermost H II regions, no determination of the electron temperature was available until the observations of Bresolin *et al.* (2007) who extended the set of direct abundance measurement to 3 kpc from the centre of the galaxy. Adding his new data for the innermost objects to the sample of Kennicutt *et al.* (2003) with measured electron temperatures, Bresolin *et al.* (2007) finds for a total of 22 objects: $A(\mathrm{O}) = (8.75 \pm 0.05) - (0.90 \pm 0.07) R/R_{25}$, where $R_{25} (= 33.3$ kpc) is the isophotal radius.

Note that the measurement of the Balmer discontinuity or of oxygen recombination lines in a few H II regions in M 101 allows the determination of the temperature fluctuation parameter t^2 (see Sect. 1.2.3.1), yielding values of t^2 ranging from 0.04 to 0.07 (Bresolin *et al.* 2007; Esteban *et al.* 2002). Therefore, in M 101 as in Milky Way H II regions (and probably in any spiral galaxy as well), one is facing the problem that abundances derived from collisionally excited lines might need correction.

While M 101 is a milestone for abundance gradients in spiral galaxies, due to the wealth of bright H II regions it contains, its large distance has prevented so far the use of planetary nebulae or stars for abundance derivation.

2.3.2.3   M 31

This galaxy, also known as Andromeda, is the largest galaxy of the Local Group and the closest spiral, at a distance of 790 kpc. It is of type SA(s)b. Despite its proximity, our knowledge of its chemical properties is more imprecise in comparison with M 33 or even other more distant spiral galaxies (M 101, NGC 300). M 31 is inclined by 77 degrees, making the effects of extinction stronger than in face-on galaxies. Bright, large H II regions are scarce in M 31, and additionally, those observed have usually low excitation. As a consequence, the [O III] $\lambda 4363$ line used to estimate the electron temperature is too weak to be detected, and hence empirical calibrations must be used to estimate the abundances. Few spectroscopic studies of H II regions have been conducted since the pioneering studies of Dennefeld & Kunth (1981) and Blair *et al.* (1982). The most recent result is that of Galarza *et al.* (1999) who, from observations of about 20 H II regions in the disk at galactocentric distances between 0 and 15 kpc, found a gradient of -0.06 ± 0.03 dex kpc^{-1}

based on the O_{23} index as calibrated by Edmunds & Pagel (1984). As emphasised in Sect. 1.2.3.1, the oxygen abundances obtained from such indices vary with the choice of calibration. In addition, it may lead to systematic biases, so the obtained gradients are uncertain.

Spectra for a few supernova remnants have been obtained (Dennefeld & Kunth 1981; Blair *et al.* 1982). With the help of a grid of shock models Dopita *et al.* (1984) defined a "metallicity index" with which they obtained an abundance gradient of $-0.05 \pm 0.02\,\mathrm{dex\,kpc^{-1}}$ from 10 supernova remnants of the Blair *et al.* (1982) sample. Unfortunately, this study was never updated with more recent shock models.

So far available studies on planetary nebulae in M 31 do not tell much about abundance gradients in this galaxy as they rather concentrate on the bulge (Jacoby & Ciardullo 1999; Stasińska *et al.* 1998). However, several campaigns of spectroscopic observations of planetary nebulae in the disk of M 31 are announced, so the situation could change rapidly.

Studies of BA-Sgs in M 31 are of great importance, because they allow us to have an independent measurement of present-day oxygen abundances to be compared with results from the analysis of H II regions through empirical calibrations. Trundle *et al.* (2002) presented the analysis of seven B-Sgs lying in four OB-associations. A comparison of the stellar oxygen abundance gradient – also including previous results of Venn *et al.* (2000) and Smartt *et al.* (2001) – with that of nebular results shows an offset of $0.15-0.4$ dex between the two methods which is critically dependent on the empirical calibration adopted for the R_{23} in the nebular case. Trundle *et al.* (2002) did not find any evidence of a significant abundance gradient in the range $5-12\,\mathrm{kpc}$; however, they emphasise that the number of data points is very restricted to be able to draw a firm conclusion on this issue. More importantly, the stellar analysis by Trundle *et al.* (2002) suggests that the inner part of M 31 is not as metal rich as proposed by certain studies of H II regions (which, as emphasised above, are nonetheless very uncertain).

Figure 2.33 shows the state of the art regarding the oxygen abundance distribution in M 31 as obtained from supergiants and H II regions. For the latter, we have considered the line intensities of the H II regions observed by Galarza *et al.* (1999) and classified as "bright compact", which are the most suitable for abundance determinations. We have converted them into oxygen abundances using various strong line indicators: N_2 and O_3N_2, as calibrated by Pettini & Pagel (2004), O_3N_2 as calibrated by Bresolin *et al.* (2007) and the P index as calibrated by Pilyugin & Thuan (2005). The regressions obtained for these data are given in Table 2.21. The only indicator that gives a gradient is O_3N_2. However, none of the H II indicators agree[7]. Therefore it is not currently possible to conclude on the presence of an abundance gradient in M 31, even less to propose a value for it.

---

[7]This illustrates how misleading it can be to use strong line methods to derive abundance gradients in galaxies.
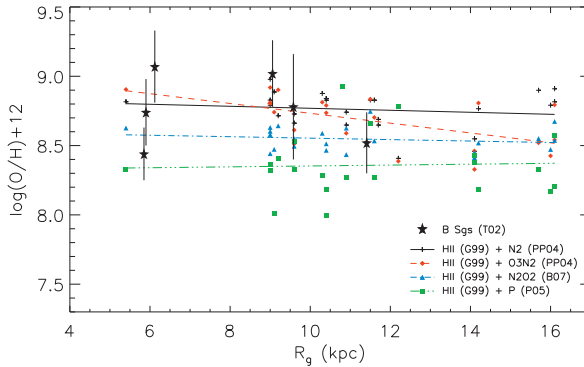
Fig. 2.33. O/H values in H II regions and B Supergiants as a function of galactocentric distance in M 31. For the stars, the data are from Trundle *et al.* (2002). For the H II regions, the line intensities were taken from Galarza *et al.* (1999) and converted into oxygen abundances using various strong-line indices, as indicated in the plot. The regression lines are plotted for each data set.

Table 2.21. Oxygen abundance gradients in M 31.

	Range in Rg [kpc]	# objects	$\Delta \log A(O)$ [dex kpc^{-1}]	$A(0)_0$ [dex]
H II regions				
N_2, calib. Pettini & Pagel (2004)	$5.5 - 16$	26	-0.007 ± 0.010	8.84 ± 0.12
O_3N_2, calib. Pettini & Pagel (2004)	$5.5 - 16$	22	-0.035 ± 0.011	9.09 ± 0.13
N_2O_2, calib. Bresolin *et al.* (2007)	$5.5 - 16$	22	-0.005 ± 0.006	8.61 ± 0.07
P, calib. Pilyugin & Thuan (2005)	$5.5 - 16$	23	0.003 ± 0.017	8.32 ± 0.20
B supergiants				
Trundle *et al.* (2002)	$6 - 12$	6	-0.006 ± 0.020	?

A systematic study of H II regions as well as of BA-Sgs in M 31 with the present generation of very large telescopes would be needed to obtain a reliable estimate of the oxygen abundance gradient in this galaxy.

2.3.2.4 NGC 300

This is a Scd galaxy located in the Sculptor Group at a distance of 1.9 Mpc, and with a (relatively small) inclination of 40 degrees. The census of its observational properties is growing rapidly.

Until very recently, the most comprehensive study of the oxygen abundance in the interstellar medium of NGC 300 was carried out by Deharveng *et al.* (1988). The [O III] $\lambda 4363$ line could be measured in only two H II regions so the abundance gradient had to be derived from strong line methods. Using the O_{23} calibration proposed by Dopita & Evans (1986), Deharveng *et al.* (1988) obtained the first estimate of the oxygen abundance gradient in NGC 300, based on about 20 H II
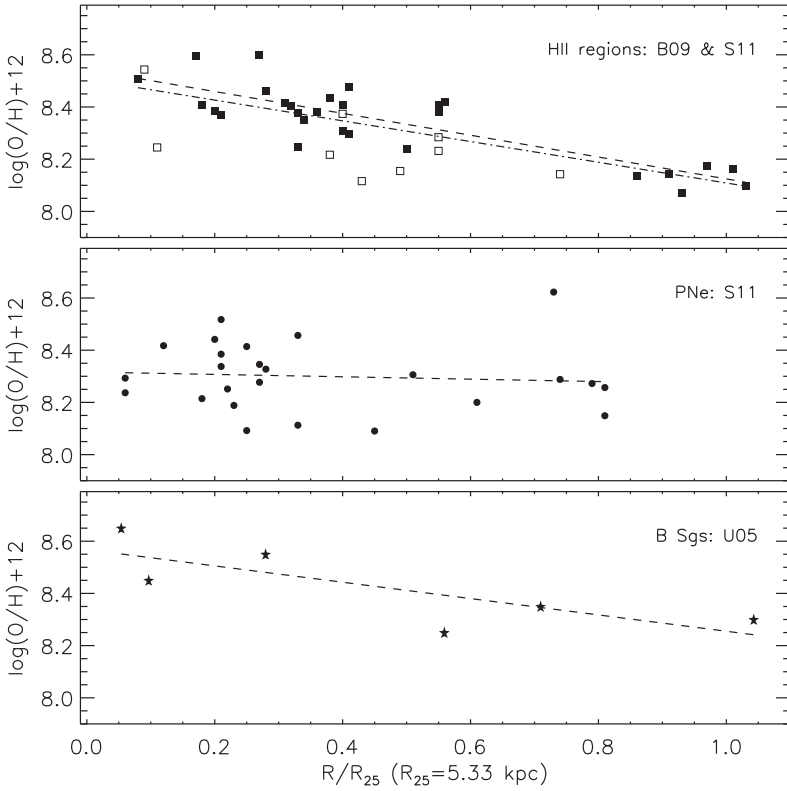
Fig. 2.34. O/H values in H II regions (top), planetary nebulae (middle) and B supergiants (bottom) as a function of galactocentric distance in NGC 300 as found by the most recent studies for each type of object. See Table 2.22 for references. Giant H II regions are represented with filled squares, compact H II regions with open squares.

regions. A linear regression to their data points gives $A(O) = (8.95 \pm 0.04) - (0.11 \pm 0.02)R/R_{25}$, where $R_{25} = 5.33$ kpc.

Bresolin *et al.* (2009) obtained deep spectra of giant H II regions in this galaxy, and derived an oxygen abundance gradient based solely on the temperature-based method. A linear regression to their 27 data points gives $A(O) = (8.57 \pm 0.02) - (0.077 \pm 0.006)$ dex kpc^{-1}. Note that the gradient is more moderate but much better defined than when using the data of Deharveng *et al.* (1988).

Peña (2010) observed compact H II regions and planetary nebulae in NGC 300, and managed to measure the temperature in 10 compact H II regions and 27 planetary nebulae, out of which oxygen abundances can be derived (Stasińska *et al.* 2011, in preparation). The oxygen abundances of these objects are plotted in Figure 2.34 as a function of galactocentric radius, together with the values for the giant H II regions from Bresolin *et al.* (2009). It may be appreciated that the

Table 2.22. Radial variation of oxygen abundances in NGC 300 for various types of objects.

[kpc]	Range in Rg	# objects	$\Delta \log A(O)$ [dex kpc^{-1}]	$A(0)_0$ [dex]
H II regions				
Stasińska *et al.* (this book)	0–6	37	-0.075 ± 0.009	8.51 ± 0.03
* Bresolin *et al.* (2009)	0–6	27	-0.077 ± 0.006	8.57 ± 0.02
planetary nebulae				
* Stasińska *et al.* (this book)	0–6	25	-0.008 ± 0.020	8.32 ± 0.04
B supergiants				
* Urbaneja *et al.* (2005)	0–6	6	-0.055 ± 0.045	8.58 ± 0.13

compact H II regions tend to have slightly smaller abundance values than the giant H II regions at the same galactocentric distance. Merging them with the sample of Bresolin *et al.* (2009) leads to virtually the same gradient but a larger dispersion. This reminds us of the result by Bresolin (2011) about reducing the azimuthal abundance scatter when considering only the objects with the best spectra. Regarding planetary nebulae, as Figure 2.34 shows, there is an important scatter and no significant gradient.

Urbaneja *et al.* (2005) carried out a detailed spectral analysis of six early B-type supergiants with galactocentric distances extending to 7 kpc and determined their oxygen abundances. A linear fit to their results gives: $A(O) = (8.58 \pm 0.13) - (0.055 \pm 0.045)$ dex kpc^{-1}. This is fully compatible with the data of giant H II regions, but obviously, the result would be more conclusive with a larger number of B stars.

Note that this apparent agreement between young star and H II region abundances is similar to what is seen in the Magellanic Clouds and different from what occurs in the solar vicinity and M 33. In the latter two cases, oxygen abundances from young stars tend to be higher than those derived from collisionally excited lines, even taking into account depletion into dust grains in H II regions. There is no explanation so far for this fact.

Table 2.22 summarises our present knowledge on the oxygen abundance distribution in NGC 300. The recommended references are marked with an asterisk.

Figure 2.35 represents in graphical form a summary of the radial variations of the oxygen abundance in M 33, NGC 300 and M 101 as derived from different indicators.

2.3.3 Galaxies that stopped forming stars

In galaxies that stopped forming stars, the best oxygen abundance tracers, namely H II regions and blue supergiants, are absent. Until recently, the only way to estimate the metallicity was using strong stellar absorption line features in integrated spectra (such as the Lick indexes, see Burstein *et al.* 1984). However, as shown by *e.g.* Buzzoni (2002), these features are also dependent on other properties of the
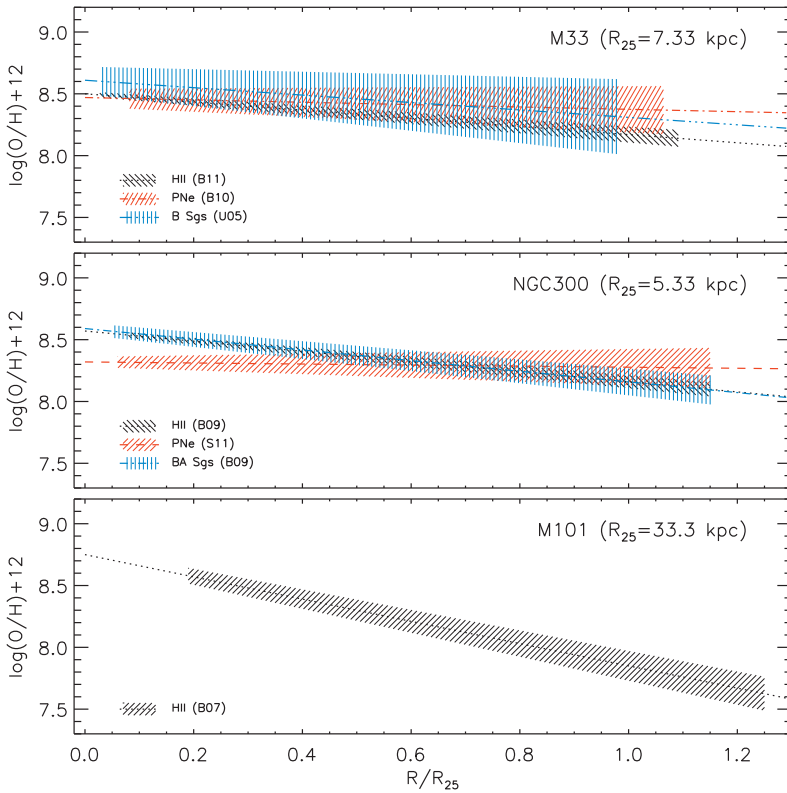
Fig. 2.35. Summary of the radial variations of the oxygen abundance for M 33, NGC 300 and M 101. See Tables 2.20 and 2.22 for references in the case of M 33 and NGC 300, respectively.

stellar populations such as their age or the stellar initial mass function. In addition, while the "metallicity" of a star generally refers to its iron abundance, the absorption line indices measured in stellar populations depend on the abundances of other elements, which are known not to vary in lockstep with iron. While stellar population models of absorption line indices with variable element abundance ratios are now available (Thomas *et al.* 2011), it would still be extremely valuable to measure directly the abundance of oxygen in individual objects of such galaxies. Planetary nebulae offer such possibilities.

Richer & McCall (2008) have obtained temperature-based oxygen abundances in several dwarf elliptical galaxies. As discussed elsewhere in this book (*e.g.* Chapter 3), there is always the worry with planetary nebulae that the oxygen abundances may not represent the chemical composition of the gas out of which the progenitors were formed. By considering various abundance ratios, Richer & McCall (2008) have shown that, in these galaxies, there are a few planetary nebulae which appear to have dredged up oxygen, but they are exceptions.

Walsh *et al.* (1999) and Méndez *et al.* (2005) have obtained spectra of planetary nebulae in Cen A (the nearest giant elliptical galaxy located at 3.5 Mpc) and NGC 4697 (a flattened elliptical galaxy at 11 Mpc), respectively. The crucial [O III] $\lambda 4363$ line could not be detected however, so the derived oxygen abundances are uncertain. But with the next generation of very large telescopes, it should be possible to obtain reliable oxygen abundances from planetary nebulae in at least a few giant elliptical galaxies.

2.3.4   The mass-metallicity relation of galaxies

The first mention of the existence of a relation between the mass of a galaxy and its metallicity (hereafter $M - Z$) was in a study of Lequeux *et al.* (1979) on 7 irregular and blue compact galaxies, in which the chemical composition was derived from the emission lines produced by ionised gas. As always in such studies, it is the oxygen abundance which represents the "metallicity". This relation is fundamental to understand the chemical evolution of galaxies and many scenarios have been proposed to explain it (see Chapter 4). It has been established for ever growing samples of galaxies, although usually the galaxy luminosities were considered rather than their masses, the latter being more difficult to obtain.

The work by Tremonti *et al.* (2004) represents a major quantitative jump as well as an important improvement in the derivation of the galaxy masses, and has become a reference. It is based on about 53 000 star-forming galaxies at $z \lesssim 0.1$ from the Sloan Digital Sky Survey (`http://www.sdss.org`), a massive survey whose final product includes spectra in the $3800-9200$ Å wavelength range for about 900 000 galaxies. These spectra allow the determination of the stellar masses of galaxies by using spectral synthesis techniques, in which the observed continua are compared to theoretical templates of known stellar masses. In the work by Tremonti *et al.* (2004), the gas-phase oxygen abundances were obtained by simultaneous fits of all the most prominent emission lines with a grid of photoionisation models by Charlot & Longhetti (2001) designed for the interpretation of integrated galaxy spectra. Figure 2.36 shows the resulting mass-metallicity relation. The relation is prominent with a slight levelling-off at the highest masses. It is often thought that the abundance analysis of Tremonti *et al.* (2004) is the best that can be done, since it is sophisticated and relies on a large grid of photoionisation models. However, it has been shown by Yin *et al.* (2007) that there is an offset between the O/H values derived by this approach and the temperature-based method. This offset is due to fact that, in real galaxies, the nitrogen abundance varies with metallicity in a manner not well accounted for by the grid of photoionisation models that were used, and by the fact that all the strong lines were fitted simultaneously by a chi-square procedure, and thus an incorrect N/O has an impact on the derived O/H.

Lee *et al.* (2006) have extended the mass-metallicity relation by 2.5 decades downwards in stellar mass, using near infrared photometry to determine the galaxy masses (see Fig. 2.37). In this case, all the metallicities (*i.e.* oxygen abundances) were derived from the direct, temperature-based method using the [O III] $\lambda 4363$
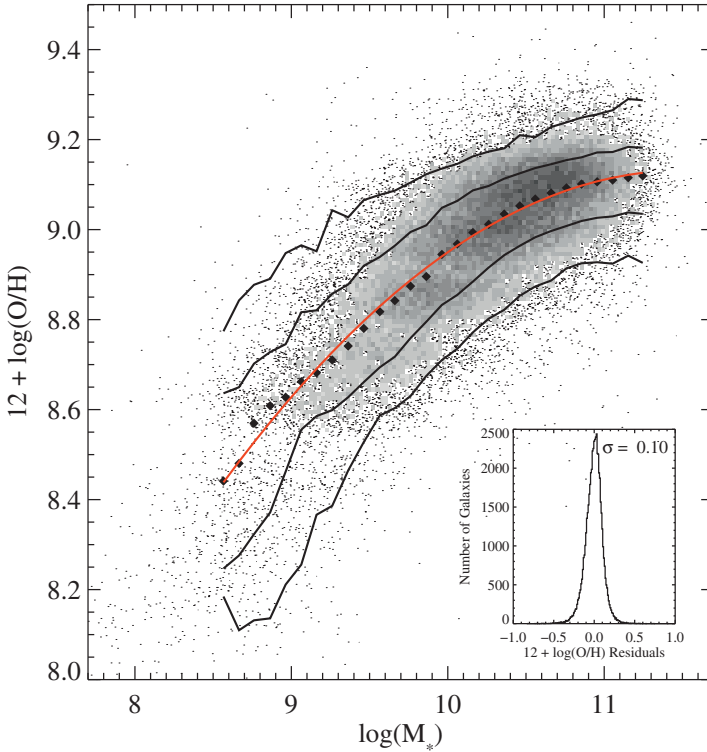
Fig. 2.36. Relation between stellar mass, in units of solar masses, and gas-phase oxygen abundance for 53 400 star-forming galaxies in the SDSS. The large black filled diamonds represent the median in bins of 0.1 dex in mass that include at least 100 data points. The solid lines are the contours that enclose 68% and 95% of the data. The red line shows a polynomial fit to the data. The inset plot shows the residuals of the fit. (Figure reproduced from Tremonti *et al.* 2004.)

line. The fit they obtain is given by

$$12 + \log(\text{O/H}) = (5.65 \pm 0.23) + (0.298 \pm 0.030) \log M_\star, \tag{2.5}$$

where $M_\star$ represents the stellar mass of a galaxy, *i.e.* the integrated mass of all the stars in units of solar masses. From this figure, it appears that the slope of the mass-metallicity relation is not the same for low galaxy masses as for high masses. However, such a conclusion is premature, given that the metallicities have been obtained with very distinct approaches.

Kewley & Ellison (2008) have shown that the mass-metallicity relation has very different shapes according to how the metallicities are derived. Figure 2.38 shows the mass-metallicity relation they find for the same sample of 27 730 local star-forming galaxies from the SDSS, using ten different metallicity indicators. The
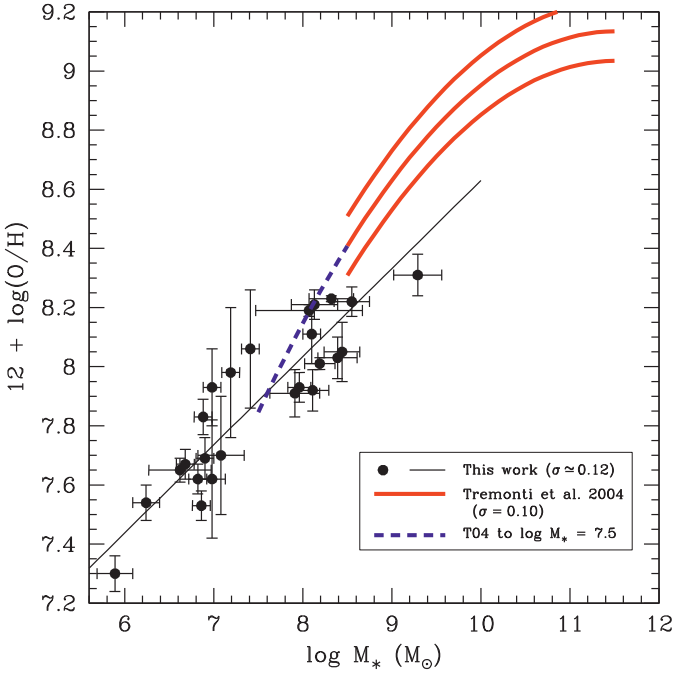
Fig. 2.37. The mass-metallicity relation expanded to low-mass galaxies. The thick curves represent the polynomial fit of Tremonti *et al.* (2004) and the $\pm 1\sigma$ curves. (Figure reproduced from Lee *et al.* 2006.)

result of Tremonti *et al.* (2004) is shown in the upper left panel. Note that, in the lowest right panel, where the oxygen abundances have been derived using the direct temperature-based method, there are few points (few galaxies in the SDSS have the [O III] $\lambda 4363$ line measured) and a large dispersion. This dispersion is probably due to the fact that many of those objects are actually giant H II regions in large galaxies and not *bona fide* galaxies. In all the remaining panels, the abundances have been obtained using a strong line index. Kewley & Ellison (2008) point out that it is essential to use the same metallicity calibrations when comparing different $M - Z$ relations. In the light of the analysis by Stasińska (2010) which is mentioned in Chapter 1, the problem is even more complicated. If a given sample of objects has different structural properties than that used to calibrate the metallicity indicators, the abundances will be biased and may lead to spurious conclusions. In the case of massive galaxies, the considered spectra are taken through a fibre, which will sample the central parts of galaxies if the angular dimension of the galaxy is large. If the angular sizes are small and the galaxies are massive, the spectra correspond to the integrated flux from H II regions of possibly different metallicities and from diffuse emission in the galaxies. Also, if the sample of supposed star-forming galaxies contains galaxies with active nuclei
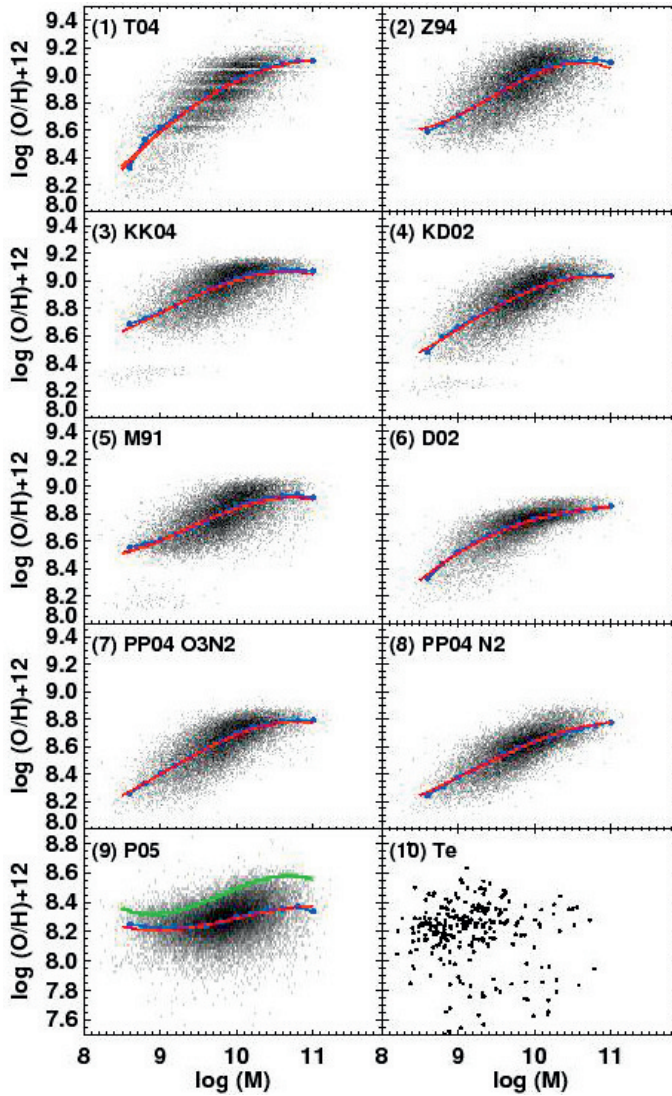
Fig. 2.38. The mass-metallicity relation for star-forming SDSS galaxies using various abundance indicators. (Figure reproduced from Kewley & Ellison 2008.)

(the criteria for separating both kinds of galaxies are different in Kewley *et al.* 2001, Kauffmann *et al.* 2003 and Stasińska *et al.* 2006), the oxygen abundance derived for galaxies with active nuclei will be biased as compared to the abundance for a purely star-forming galaxy.

To conclude, while there is no doubt that a strong $M - Z$ correlation exists, extending over five decades in stellar masses, the exact form of this correlation

is not well known. When going to higher redshifts (see next section) and trying to establish a possible redshift evolution of the $M - Z$ relation, the abundance calibrations must be discussed in detail: it is not necessarily sufficient to use the same calibrations for samples at different redshift. One must make sure that the physical conditions in the emission-line nebulae (ionising radiation field, gas density distribution) are similar, or account for any systematic difference.

2.3.5   The hot gas in clusters of galaxies

Due to the fact that X-ray observations can only be performed outside the Earth's atmosphere and to the faintness of extragalactic sources, clusters of galaxies were detected in X-rays only a few decades ago. The first detection of a cluster of galaxies in X-rays was made from a balloon flight by Boldt *et al.* (1966), who identified a diffuse source with the Coma cluster. Felten *et al.* (1966) showed that this X-ray emission could not be due to the superposition of the X-ray emissions from all the galaxies belonging to Coma, because they would have had to be in average 10^4 times brighter at 25 keV than our own Galaxy. These authors therefore suggested that the X-ray emission was due to thermal bremsstrahlung from the hot (2×10^8 K) intergalactic medium, and this is now the universally adopted mechanism to account for most of the X-ray emission, at least in the range between 0.5 and about 20 keV. This mechanism accounts naturally for the presence of emission lines in the X-ray spectra of clusters, and in particular of oxygen lines around $0.5 - 0.8$ keV.

The first X-ray spectra of clusters were very coarse (see *e.g.* Boldt *et al.* 1966 and Gursky *et al.* 1971). However, a few years later, the Ariel 5 satellite allowed the detection of iron line emission around 7 keV for the first time in the spectrum of the Perseus cluster (Mitchell *et al.* 1976) and the comparison of the iron abundance thus measured with the fraction of metals injected into the ICM by supernova-driven winds, calculated by Larson (1975). At the end of the 1970s, it became possible to measure the abundance of elements other than iron in the ICM. For example, based on high resolution X-ray spectroscopy with the Einstein Observatory, Canizares *et al.* (1979) detected K-alpha line emission from hydrogenic oxygen (O VIII) in the spectrum of M 87, the giant elliptical galaxy at the centre of the Virgo cluster. Note, however, that this emission was due to an individual galaxy and not to the diffuse intracluster medium.

Accurate measurements of element abundances other than iron in the ICM only became possible after the launch of ASCA in 1993. With this satellite, Fukazawa *et al.* (1994) were able to compute for the Centaurus cluster the variations of the equivalent widths of the emission lines due to various elements (including oxygen) as a function of distance to the cluster centre; they also derived the variations of metal abundance with radius (note however that the metallicity is obviously dominated by the iron abundance), and showed that the metal abundance increased towards the centre in cooling core clusters. A recent and detailed review of the observations of metals in the ICM can be found in Werner *et al.* (2008). We hereafter concentrate on recent observations of oxygen and their interpretation.
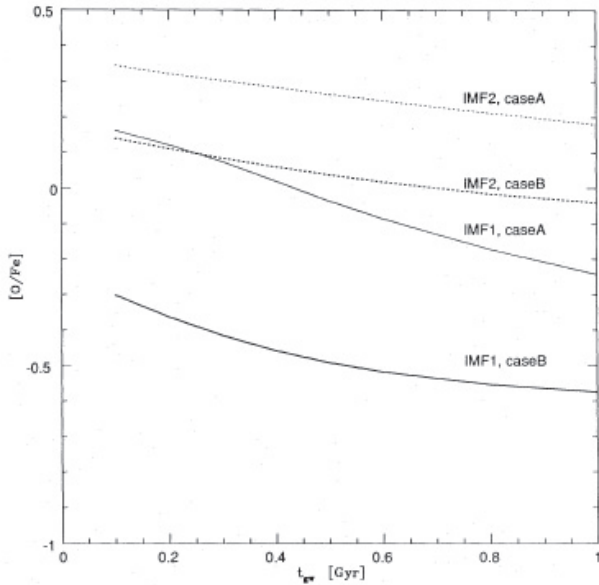
Fig. 2.39. Variation of the oxygen to iron ratio in the IGM as a function of the time when the galactic wind occurs (t_{gw}) for various models. The solid and dotted lines represent two different IMFs for $M_G = 10^{12}$ $M_\odot$, respectively. The thick and thin lines correspond to case A and case B, respectively. Taken from Figure 9 of Mihara & Takahara (1994).

The origin of metal (predominantly iron) enrichment of the ICM was discussed by a number of authors such as Arnaud *et al.* (1992) or Mihara & Takahara (1994). The latter estimated the iron and oxygen production in clusters; in their Figure 9 (reproduced here in Fig. 2.39), they show for several models the variation of the [O/Fe] abundance as a function of the time when the galactic wind occurs. [O/Fe] is found to decrease with time, because the amount of iron produced by Type Ia supernovae increases with time while the amount of oxygen remains constant. Mushotzky *et al.* (1996) accurately estimated the abundances of several elements in four clusters and found the [O/Fe] ratio to be consistent with an origin in core-collapse supernovae (also called Type II supernovae).

Abundance studies with ASCA and BeppoSAX have led to the general picture of an early homogeneous metal enrichment of the ICM by Type II supernovae, producing α-elements in the proto-cluster phase followed by a subsequent more centrally peaked enrichment by Type Ia supernovae.

With the launching of XMM-Newton and Chandra, the determinations of heavy element abundances became more accurate, as shown *e.g.* by Tamura *et al.* (2004) for a sample of 19 clusters observed with the Reflection Grating Spectrometers (RGS) and European Photon Imaging Camera (EPIC) of XMM-Newton. An example of spectral fitting is shown in Figure 2.40 for the cluster Abell 262.
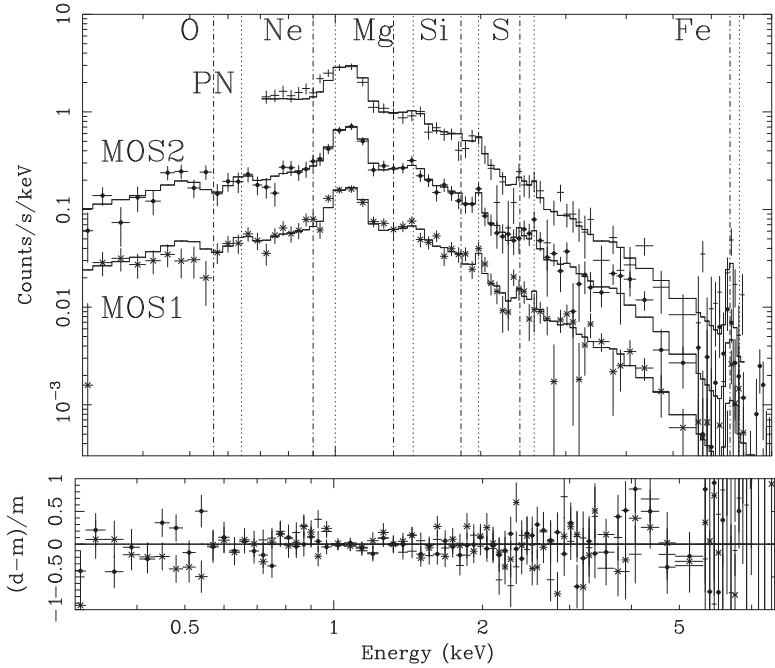
Fig. 2.40. XMM-Newton spectra of the cluster Abell 262 between $1'$ and $2'$ in projected radius. The MOS1 and pn spectra are multiplied by factors of 0.25 and 2, respectively. The model is shown as a histogram. Expected line positions for H- and He-like ions are indicated by vertical lines. The bottom panel shows the fit residuals. The oxygen and iron abundances in this case are 0.5 and 0.7 times solar, respectively. Taken from Tamura *et al.* (2004).

With XMM-Newton, it also became possible to draw radial profiles for individual elements (see Fig. 2.41).

However, although the quality of the X-ray data had improved drastically since the beginning of X-ray observations, it also became clear that several sources of uncertainty were not negligible when computing heavy element abundances and in particular oxygen abundances.

First, the assumption of a single temperature for the ICM is probably too simplistic, and induces errors in the determination of heavy element abundances. This was first pointed out by Buote (2000) for groups from ASCA data. In the case of oxygen, Matsushita *et al.* (2007a) found an increase in abundance from single- to two- to multi-temperature models.

Second, metals may not be (and in fact are not in most cases) homogeneously distributed throughout the cluster. Besides, the distribution of metals is not even necessarily spherically symmetric, and therefore even radial profiles are not really correct, since they may average regions with very different metal abundances. Projection effects are particularly important, since clusters are obviously 3D objects.
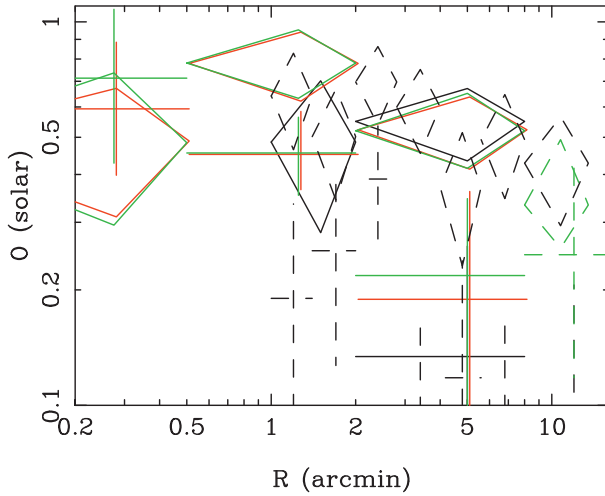
Fig. 2.41. Radial profile of the oxygen abundance in the Centaurus cluster. Dotted and solid lines correspond to the results of the projected and de-projected spectra respectively. The results from the EMOS are shown with diamonds and those from the EPN with crosses. Taken from Figure 3 of Matsushita *et al.* (2007a).

When a spectrum is obtained, it is built up by the sum of the spectra emitted by all the "layers" along the line of sight. It is therefore necessary to de-project spectra when making a spatial analysis, and this obviously requires hypotheses and introduces errors. With XMM-Newton and Chandra, it is now possible to draw not only profiles but metallicity maps. However, due to the limited number of photons detected in X-rays, even with very long exposure times, it is not viable with the present satellites to draw maps of single-element distributions (except iron). Interestingly, temperature and metallicity maps have shown that even clusters which appear relaxed in X-rays when their intensity maps are considered may have very disturbed temperature and metallicity maps, implying that one or several mergers have taken place in the last few Gyr. The metallicity map of Abell 85 is shown in Figure 2.42; its interpretation, together with that of the corresponding temperature map, was that Abell 85 has undergone at least one merger coming from the north-west, and is presently experiencing a second merger (Durret *et al.* 2005). The oxygen abundance in the central region of this cluster was found to be about 0.4 times solar.

Third, another source of error in oxygen abundances is due to the contribution of Galactic O VIII emission, which must be subtracted when estimating cluster oxygen abundances; this can obviously be a problem, especially for low redshift objects.

Fourth, oxygen lines are at low energies (below 1 keV) where instrument calibrations are not very accurate, and this is another source of uncertainty in oxygen abundance measurements.
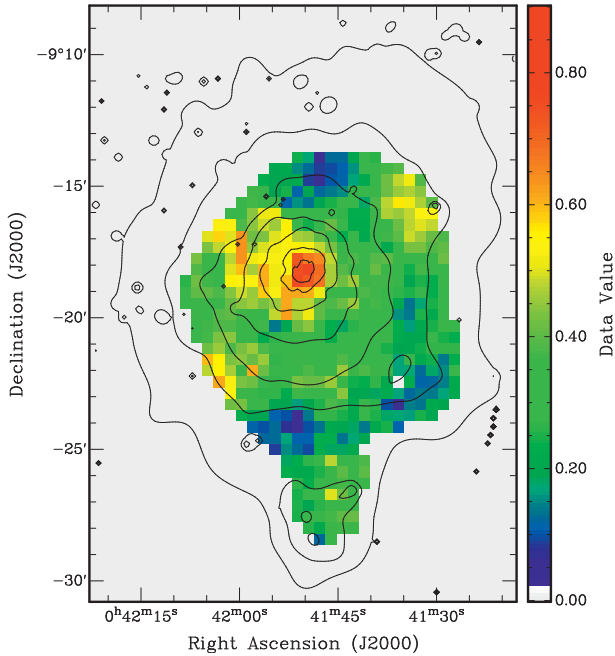
Fig. 2.42. Metallicity map of the Abell 85 cluster. XMM-Newton X-ray intensity contours in the [0.5−8.0] keV band are superimposed. The scale is in solar units. Taken from Durret *et al.* (2005).

Note that it was the RGS on XMM-Newton which made the classic cooling flow model collapse, since the intensities of emission lines at low energy detected by the RGS were found to be much smaller than those predicted by the standard cooling flow model (Peterson *et al.* 2003, 2001). A high quality RGS spectrum of the Centaurus cluster is shown in Figure 2.43 (Takahashi *et al.* 2009).

With its even higher energy resolution below 1 keV and its low background, the Suzaku satellite allows even better overall heavy element abundance determinations (its poor spatial resolution does not allow a radial analysis). However, contamination of the optical blocking filter can result in a ∼20% systematic error on the oxygen abundance (Matsushita *et al.* 2007b). This is in any case a rather small uncertainty compared to those obtained for oxygen with other instruments.

It is interesting to note that the oxygen abundances estimated in the IGM of the Centaurus and Fornax clusters are consistent with those estimated from optical spectroscopy of the central cD galaxy (Matsushita *et al.* 2007a,b).

The next generation X-ray telescopes should allow the derivation of the oxygen abundance in the IGM with a much better precision, and perhaps even the drawing of the oxygen spatial distribution. However, astronomers will have to wait some time for such satellites to be launched.
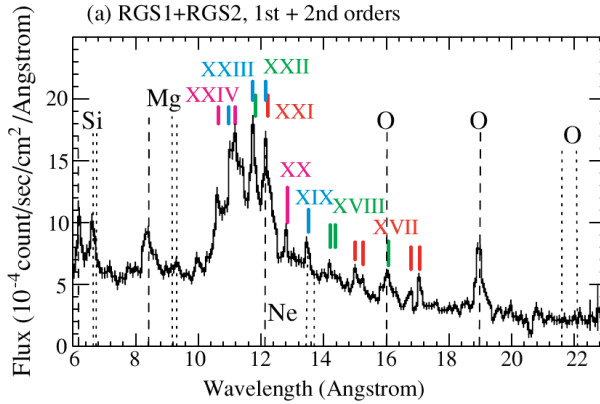
Fig. 2.43. RGS spectrum of the Centaurus cluster. The positions of the H- and He-like K lines of several major elements are indicated with dashed and dotted lines, respectively. The colour tick marks indicate Fe L lines of various ionisation states. Taken from Figure 9a of Takahashi *et al.* (2009).

2.4   The high-redshift Universe

Studies of element abundances beyond the galaxies of the Local Group have experienced a remarkable data-flow acceleration in the last few years. We have witnessed wholesale abundance determinations in tens of thousands of galaxies from large scale surveys such as the 2dF galaxy redshift survey and the Sloan Digital Sky Survey (SDSS). Chemical abundance studies have also been increasingly extended to high redshifts, charting the progress of stellar nucleosynthesis over most of the age of the Universe.

2.4.1   Oxygen abundance in galaxies up to $z \simeq 1$

The metallicity[8] of large galaxy samples with $0.3 < z < 1$ has now been obtained (*e.g.* Kobulnicky & Kewley 2004; Kobulnicky *et al.* 2003; Liang *et al.* 2004; Lilly *et al.* 2003; Savaglio *et al.* 2005). Figure 2.44 shows $12 + \log{(\mathrm{O/H})}$ as a function of redshift for the Gemini Deep Deep Survey (GDDS), the Canada-France Redshift Survey (CFRS) and the Team Keck Redshift Survey (TKRS). The mean metallicity of all 261 galaxies, as derived from the R_{23} index using the calibration by Kobulnicky & Kewley (2004), is $12 + \log{(\mathrm{O/H})} = 8.72 \pm 0.17$, *i.e.* roughly solar. No metallicity-redshift evolution is observed in the line emitters, although the probed redshift range ($0.3 < z < 1$) corresponds to a time interval of 4.3 Gyr. However, galaxies in Figure 2.44 include all masses, and therefore the presence of

---

[8]In this section, "metallicity" refers to the "oxygen abundance" as is common practice in this field.
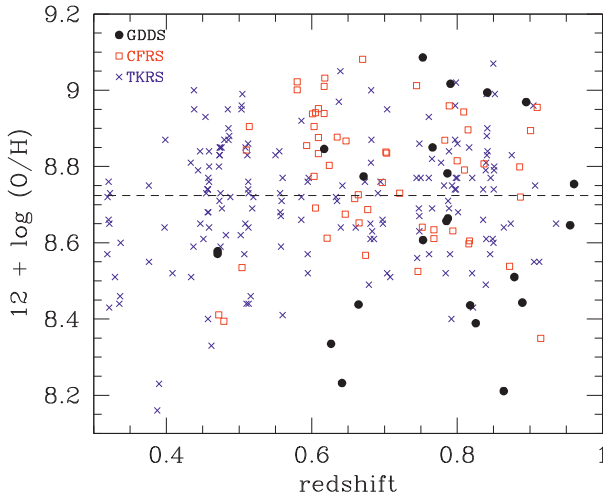
Fig. 2.44. Oxygen abundance as a function of redshift for GDDS (filled circles), CFRS (open squares) and TKRS (crosses) galaxies, as derived using the R_{23} index with the calibration by Kobulnicky & Kewley (2004). The mean total metallicity (dashed line) is $12 + (O/H) = 8.72 \pm 0.17$, *i.e.* roughly solar. No significant redshift evolution is observed for the total sample of 261 galaxies from $z = 0.32$ to 0.96, corresponding to a time interval of 4.3 Gyr. Figure reproduced from Savaglio *et al.* (2005).

a mass-metallicity relation at these redshifts may obscure any redshift evolution of the metallicity[9].

The metallicity and the mass of galaxies are strongly correlated in the local Universe (see Sect. 2.3.4). More massive galaxies have higher metallicities than less massive galaxies. This mass-metallicity, $(M - Z)$, relation has been detected at high redshift only recently. Measurements of the stellar mass require deep optical/near-infrared photometry of faint targets, and this is not easy to obtain for a sufficiently large sample for which the metallicity is also known. To explore any redshift evolution, the luminosity can be used instead as a mass proxy although it is more difficult to interpret physically. Using oxygen abundances derived with their own calibration of the R_{23} index in 177 galaxies from the GOODS-N survey, Kobulnicky & Kewley (2004) found that the luminosity-metallicity, $(L - Z)$, evolves with redshift, with the highest redshift galaxies lying systematically to the bright/metal-rich side of the overall $L - Z$ relation. Given the redshift evolution of the $L - Z$ relation, does the $M - Z$ relation also evolve with time?

Savaglio *et al.* (2005) estimated the masses of 69 galaxies in the GDDS and CFRS samples by fitting a stellar population synthesis model to the observed

---

[9]In addition, one should remember that the average properties of line emitters might change systematically with redshift, so that abundances derived from the R_{23} index might be biased in a way that is correlated with redshift. This question needs further investigation.
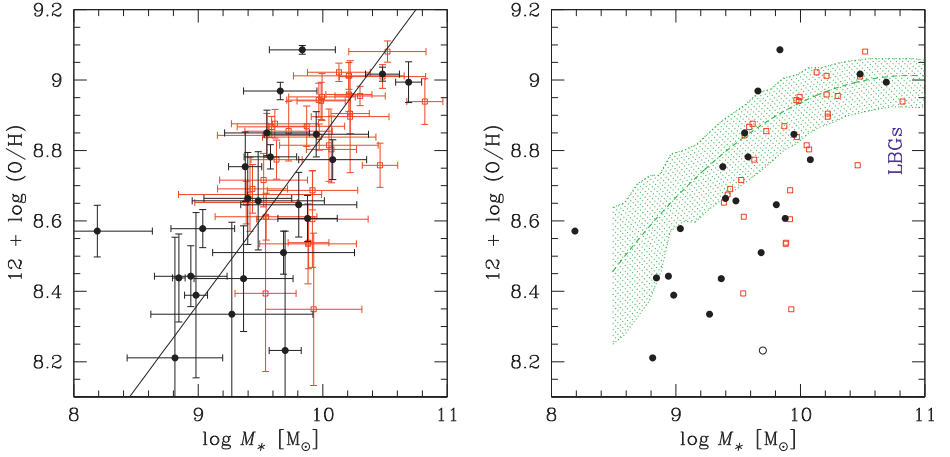
Fig. 2.45. *Left:* metallicity as a function of stellar mass for GDDS (filled circles) and CFRS (open squares). The straight line is the linear bisector fit. The correlation is significant at more than 6 σ. *Right:* the points are as in the left panel, but error bars are omitted. The short-dashed line and hatched area indicate the "converted" (see text) polynomial fit and ± 1 σ dispersion, respectively, derived for the SDSS $z \sim 0.1$ galaxies (Tremonti *et al.* 2004). Most of the $z \sim 0.69$ galaxies are distributed below the SDSS fit. The position of Lyman Break galaxies at $z \sim 2.2$ after correcting from the $N2$ to the R_{23} calibrator is also shown. Figures adapted from Savaglio *et al.* (2005).

continuum energy distribution. For 56 of them at a median redshift of $z = 0.69$, they also determined the metallicity using the R_{23} index as calibrated by Kobulnicky & Kewley (2004). The stellar mass and metallicity distributions are strongly correlated at the level of 6.3 σ, as shown in Figure 2.45 (left panel). The linear best-fit gives: $12 + \log(\text{O/H}) = (0.478 \pm 0.058) \log M_\star + (4.062 \pm 0.579)$. This result is compared with the $M - Z$ relation found by Tremonti *et al.* (2004) for the 53 000 SDSS galaxies at $z \sim 0.1$. For the sake of consistency, their relation has been converted to match the IMF and the metallicity calibrator used by Savaglio *et al.* (2005). The "converted" $M - Z$ relation is: $12 + \log(\text{O/H}) = -2.4412 + 2.1026 \log M_\star - 0.09649 \log^2 M_\star$. In Figure 2.45 (right panel), it can be seen that most of the $z = 0.69$ galaxies are distributed below the $z \sim 0.1$ relation, and preferentially these are galaxies with $M_\star < 10^{10}$ $M_\odot$. This suggests that massive galaxies reach higher metallicities much earlier than low-mass galaxies. In other words, the mass-metallicity relation appears to evolve from steep at high redshifts to flatter at low redshifts.

2.4.2 *Oxygen abundances in galaxies beyond $z \simeq 1$*

Oxygen abundance measurements in galaxies beyond $z \simeq 1$ have been mostly obtained in the so-called Lyman break galaxies. These are characterised by a

break in their ultraviolet continuum due to the Lyman limit from the intergalactic and interstellar H I absorption below 912 Å. They are hence easily detected using well-defined colour selection criteria. The combination of this very efficient selection technique of star-forming galaxies at high redshifts and the considerable improvement of spectrographs on 8–10 m class telescopes, both in sensitivity and wavelength coverage extended toward the near-infrared domain, has led to a dramatic increase of metallicity determinations at high redshifts in the last decade.

Erb *et al.* (2006a,b) used the near-infrared spectrograph NIRSPEC on the Keck II telescope to record the spectral region encompassing the Hα emission line in the K band, and constructed composite spectra of sufficiently high signal-to-noise ratio to allow the weaker [N II] emission lines to be measured in $z \sim 2.2$ star-forming galaxies. The application of the $N2$ index calibration of Pettini & Pagel (2004) then yields average oxygen abundance values for different subsets of these galaxies. Maiolino *et al.* (2008) and Mannucci *et al.* (2009) used the integral field spectrograph SINFONI on the Very Large Telescope (VLT) to determine the gas metallicities of galaxies at $3 < z < 3.7$, by means of a combination of strong line diagnostics based on Hβ, [O II], [O III] and [Ne III]. The stellar masses were derived by fitting the galaxy spectral energy distribution.

It turns out that many of the star-forming galaxies at $z \sim 2.2$ have already gained near-solar metallicities. This conclusion has been reached independently by several groups, applying a variety of abundance diagnostics to galaxies selected by different techniques, including near-infrared and sub-millimetre selections (*e.g.* de Mello *et al.* 2004; Mehlert *et al.* 2002; Savaglio *et al.* 2004; Swinbank *et al.* 2004). In all these cases, however, we are dealing with relatively bright objects, that is more luminous[10] than $L_\star$. Although no clear luminosity-metallicity relation is observed in these galaxies (Erb *et al.* 2006a), it is still very likely that galaxies less luminous than $L_\star$ are in general less chemically enriched. For instance, the sub-$L_\star$ damped Lyα galaxies, also observed at $z \sim 2$, have metallicities between 1/100 and 1/10 solar (see below).

In the left-hand panel of Figure 2.46, we plot the mean metallicity, averaged over 14 to 15 galaxies at $z \sim 2.2$ in each mass bin, against their mean stellar mass (large filled circles, Erb *et al.* 2006a). In the right-hand panel, we show the metallicities as a function of the stellar mass of individual galaxies at $3 < z < 3.7$ from Maiolino *et al.* (2008, empty circles) and Mannucci *et al.* (2009, filled circles). We can observe that, for both samples of galaxies at $z \sim 2.2$ and $3 < z < 3.7$, there is a monotonic increase in metallicity with stellar mass. Can this be due to a spurious effect? The main uncertainty we may think of is that the masses in the lowest mass range are underestimated, because the faint old stellar populations are not properly taken into account. However, this would even steepen the observed correlation, as the lowest mass bins would move to the right by $0.3 - 0.5$ dex.

---

[10]$L_\star$ is the luminosity of a "typical galaxy" and is equal to $L_\star \simeq 1.8 \times 10^{11} L_\odot$. It corresponds to a star formation rate of SFR $\simeq 18 \ M_\odot \ \mathrm{yr}^{-1}$ (Reddy *et al.* 2010).
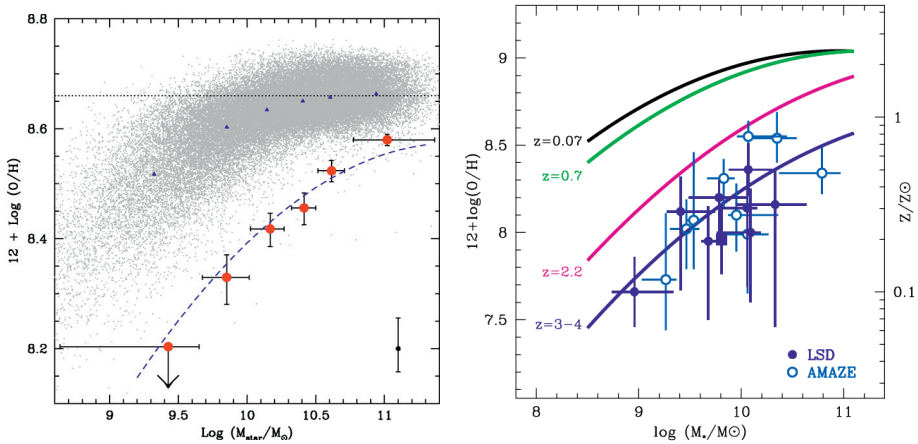
Fig. 2.46. *Left:* observed relation between stellar mass and oxygen abundance in Lyman break galaxies at $z \sim 2.2$, shown by the filled circles. Each point represents the average value of 14 to 15 galaxies, with the metallicity estimated from the [N II]/Hα ratio of their composite spectrum. The small grey dots are the metallicities of the 53 000 SDSS $z \sim 0.1$ galaxies of Tremonti *et al.* (2004) also determined using the $N2$ index, and the filled triangles represent the mean metallicity of the SDSS galaxies in the same mass bins as those used for the $z \sim 2.2$ galaxies. The dashed line is the best-fit mass-metallicity relation of Tremonti *et al.* (2004), shifted downward by 0.56 dex to fit the high-redshift galaxies. Figure reproduced from Erb *et al.* (2006a). *Right:* evolution of the mass-metallicity relation from $z \sim 0.07$ (Kewley & Ellison 2008), $z \sim 0.7$ (Savaglio *et al.* 2005), $z \sim 2.2$ (left-hand panel) to $z \sim 3.5$ (Maiolino *et al.* 2008; Mannucci *et al.* 2009). Figure reproduced from Mannucci *et al.* (2009).

We then compare (Fig. 2.46) the observed mass-metallicity relations at high redshifts with each other and with the best fits derived for samples of galaxies at lower redshifts, $z \sim 0.07$ and $z \sim 0.7$ (already discussed in the above section). This comparison clearly shows an evolution of the mass-metallicity relation through cosmic epochs. This evolution should, however, *not* be seen as an evolutionary sequence of individual objects, but as the evolution of the mass-metallicity relation of galaxies dominating the star formation density at each epoch. Indeed, at each redshift the various surveys are sampling different classes of star-forming galaxies, which are not necessarily each other's progenitors.

It is interesting to underline the following two aspects. *First*, we consider the metallicities at a mass of $M_\star \sim 10^{10}\ M_\odot$. It is worth noting that the metallicity at $z \sim 2.2$ is lower by a factor of about 2.5 with respect to local galaxies. Although significant, such metallicity decrease is modest if one considers that from $z = 0$ to $z = 2.2$ the elapsed time is about 75% of the age of the Universe. This is consistent with the shallow metallicity-redshift evolution deduced by Kobulnicky & Kewley (2004) for galaxies at $0.3 < z < 1$. From $z \sim 2.2$ to $z \sim 3.5$, the average metallicity

decreases by another factor of about 2.5. However, the latter evolution is much stronger and faster, since it occurs on a much shorter timescale of only ∼1 Gyr. *Second*, there is indication for a differential mass-dependent evolution of the metallicity. In particular, the metallicity evolution in low-mass systems appears stronger than in massive galaxies. A detailed investigation of differential selection effects as a function of stellar mass is required to rule out that observational biases are not affecting the slope of the mass-metallicity relation at each epoch. However, if confirmed, such mass-dependent evolution of the metallicity can be regarded as the "chemical" version of galaxy downsizing: high-mass galaxies reach high metallicities at high redshift on short timescales, while low-mass galaxies enrich their ISM over a prolonged period of time that extends to the current epoch (Maiolino *et al.* 2008).

As previously mentioned in Section 1.2.3.1, abundances derived from various strong emission line methods may be heavily biased, which has not yet been fully analysed. As a consequence, despite careful cross-calibration of the different strong line diagnostics used in different redshift surveys, the exact redshift evolution of the mass-metallicity relation could be somewhat different from the one currently derived, but it is very likely that the general trend is correct. This trend is further confirmed by the work of Vale Asari *et al.* (2009) which shows a similar *stellar* mass-metallicity evolution from the fossil record of local galaxies.

Mannucci *et al.* (2010) have investigated the dependence of gas-phase metallicity $12 + \log(O/H)$ on stellar mass and star formation rate (SFR) for the same samples of galaxies between $z = 0$ and $z \sim 3.5$. They found that in the local Universe the metallicity is closely related to stellar mass and SFR. Local SDSS galaxies, indeed, define a tight surface in this 3D space, *the fundamental metallicity relation*, with a small residual dispersion of ∼0.05 dex in metallicity, *i.e.* ∼12%. The overall shape of the fundamental metallicity relation is debatable as it may depend on several details, but the main properties of the fundamental metallicity relation appear to be very robust. At low stellar mass, metallicity decreases sharply with increasing SFR, while at high stellar mass, it does not depend on SFR. The mass-metallicity relation discussed above, together with the luminosity-metallicity and velocity-metallicity relations, is in fact a particular projection of this fundamental relation into one plane, and neglecting the dependence of metallicity on SFR results in the doubling of the observed dispersion.

High-redshift galaxies up to $z \sim 2.5$ are found to follow the same fundamental metallicity relation defined by local galaxies, with no indication of evolution even if they have, on average, higher SFRs because of selection effects. At $z > 2.5$, the statistics and several potential biases strongly affect the conclusions. This suggests that the same physical processes seem to be in place in the local Universe and up to at least $z \sim 2.5$. Distant galaxies, however, show a larger dispersion than local SDSS galaxies, namely between 0.2 and 0.3 dex. This is at least partly due to the higher uncertainties in the estimates of both their metallicity and SFR. Hence, the observed evolution of the mass-metallicity relation appears to arise from the increase of the average SFR with redshift, which results in the sampling of different parts of the same fundamental metallicity relation at different redshifts.

Mannucci *et al.* (2010) have introduced the new quantity $\mu_\alpha = \log(M_\star) - \alpha \log(\text{SFR})$ with $\alpha = 0.32$, which defines a projection of the fundamental metallicity relation. The same quantity also cancels out any redshift evolution up to $z \sim 2.5$, *i.e.* all galaxies follow the same relation between $\mu_{0.32}$ and metallicity: $12 + \log(\text{O/H}) = 8.90 + 0.39x - 0.20x^2 - 0.077x^3 + 0.064x^4$, where $x = \mu_{0.32} - 10$.

2.4.3   Oxygen abundances in QSO absorption line systems and GRB hosts

Galaxies that cross quasar (QSO) sight lines produce a characteristic damped Lyα absorption line which is easily recognised in the QSO spectra. These so-called damped Lyα systems (DLAs) have typical H I column densities larger than $N(\text{H I}) = 2 \times 10^{20}\,\text{cm}^{-2}$, and allow one to probe the metallicity of the most distant galaxies. Gamma-ray burst (GRB)[11] hosts are galaxies where the event has recently occurred, "illuminating" (for a short time) an otherwise unnoticed galaxy. At peak emission, GRBs are more luminous than QSOs, and offer the best approach to probe the chemical composition of galaxies at very high redshifts ($z \gtrsim 6$)); furthermore, after the GRB has faded, it is possible to study in detail the host galaxy (in the case of DLA galaxies, this is extremely difficult because of the background brightness of the QSOs).

Abundance measurements are now available for over two hundred damped Lyα systems and one hundred sub-DLAs at redshifts between $z = 0$ and 5. Sub-DLAs are QSO absorption line systems with H I column densities between $N(\text{H I}) = 10^{19}\,\text{cm}^{-2}$ and the DLA threshold. The derived abundance measurements refer mainly to those inferred from iron and silicon. Fewer oxygen abundance measurements have been reported up to now (see Molaro *et al.* 2000; Petitjean *et al.* 2008; Pettini *et al.* 2002) because of the saturation of the O I λ1302 absorption line – the only strong O I line accessible redwards of the Lyα forest – in most objects. High resolution and high signal-to-noise ratio spectra bluewards of the Lyα absorption line are needed to detect the weaker O I transitions that fall in the Lyα forest. Figure 2.47 shows the derived oxygen abundances as a function of redshift. The large dispersion of [O/H] values, which reaches 2 dex, may be noticed.

In QSO absorption line studies, [Fe/H] is usually used as a metallicity indicator. Figure 2.48 (left panel) shows the [O/Fe] abundance ratio *versus* the oxygen abundance [O/H] for DLAs. In principle, this ratio should be corrected for metal depletion into dust grains. However, this correction is known to be negligible when [O/H] < −1.2 (Dessauges-Zavadsky *et al.* 2006; Prochaska & Wolfe 2002; Wolfe *et al.* 2005). To support this hypothesis, we plot in Figure 2.48 (right panel) the abundance ratio [S/Fe] *versus* the sulphur abundance [S/H]. This figure suggests that [S/Fe] decreases with decreasing [S/H], and reaches a plateau for [S/H] values below −1.2. This behaviour is interpreted as a consequence of the largest depletion of iron into dust grains when [S/H] > −1.2. Interestingly, all the systems with oxygen measurements (except two) have precisely metallicities [O/H] < −1.2. This

---

[11]GRBs are believed to be associated with the death of massive metal-poor stars or with mergers of neutron stars or black holes.
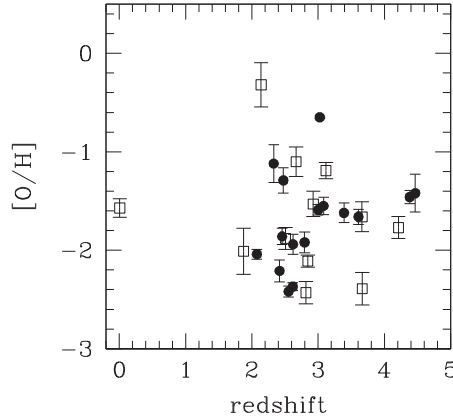
Fig. 2.47. Oxygen abundances [O/H] measured in DLA (filled circles) and sub-DLA (open squares) systems plotted as a function of redshift. A large dispersion in [O/H] values is observed reaching 2 dex. Data obtained from the compilation by Dessauges-Zavadsky and using the solar values of Asplund *et al.* (2009).
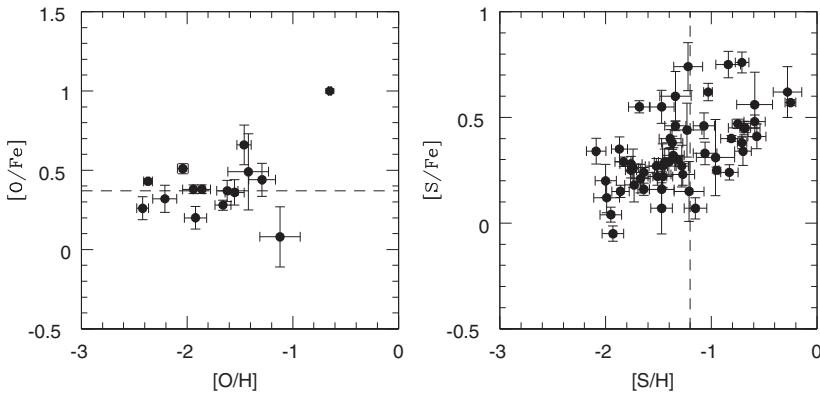
Fig. 2.48. *Left:* [O/Fe] abundance ratios plotted *versus* the O abundances [O/H]. All the oxygen measurements in DLAs (except two) are confined to [O/H] < −1.2, and have pretty constant [O/Fe] ratios with a mean value of 0.37 ± 0.14 (dashed line). *Right:* [S/Fe] abundance ratios plotted *versus* the S abundances [S/H]. This plot illustrates the iron depletion into dust grains when [S/H] > −1.2 (limit represented by the dashed line). This effect is highlighted by the departure and the sharp increase of the [S/Fe] ratios from the plateau observed at [S/H] < −1.2. Data obtained from the compilation by Dessauges-Zavadsky and using the solar values of Asplund *et al.* (2009).

reflects a bias against systems with [O/H] > −1 where most of the O I transitions are saturated. The measured [O/Fe] ratios are distinctly constant with a relatively small scatter over the [O/H] range. The mean value at [O/H] < −1.2 is
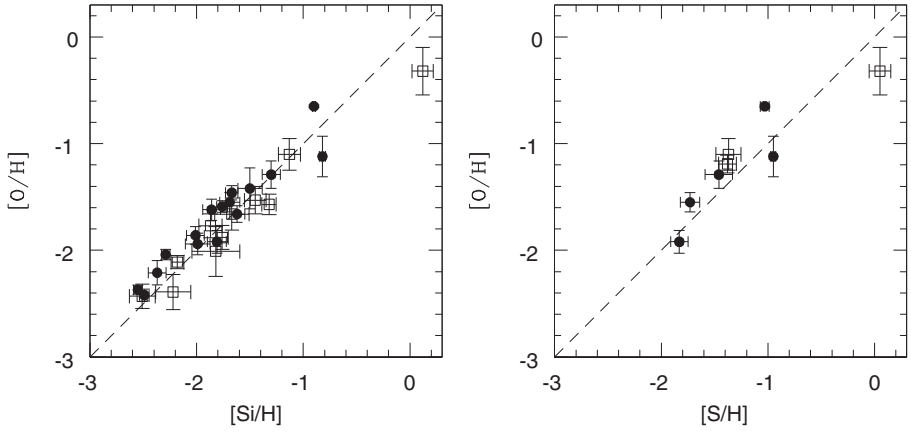
Fig. 2.49. O abundance *versus* Si abundance (left panel) and *versus* S abundance (right panel). The dashed lines represent the [O/H]–[Si/H] and [O/H]–[S/H] correlations. We can observe that the abundances of the three α-elements correlate very well, and Si and S can be used as proxies for O. Data obtained from the compilation by Dessauges-Zavadsky and using the solar values of Asplund *et al.* (2009).

[O/Fe] $= 0.37 \pm 0.14$. The small scatter probably reflects similar nucleosynthesis histories and/or efficient mixing of the gas in the systems. Over the same range of metallicities as measured in DLAs, the [O/Fe] ratio is found to be equal to 0.7 dex in metal-poor Milky Way halo stars if the measurements are not corrected for 3D radiative hydrodynamical effects, and to 0.47 dex, if corrected (Cayrel *et al.* 2004).

As the abundance of oxygen is difficult to measure in DLAs and sub-DLAs, the abundance of silicon or sulphur, two other α-elements produced by Type II supernovae, is often used as a proxy. We plot in Figure 2.49 the [O/H] abundance *versus* the [Si/H] and [S/H] abundances. It is apparent that the abundances of the three elements correlate very well.

In Figure 2.50 we show the metallicity evolution of DLAs/sub-DLAs (open squares) and GRB host galaxies (filled symbols). It can be observed that QSO absorption line systems do exhibit a statistically significant evolution in metallicity with time, despite a large scatter, but still relatively modest with a slope of $\Delta \log Z / \Delta z = -0.35 \pm 0.03$ (see the dashed line). Moreover, it is interesting to point out that there is no DLA with $12 + \log{(O/H)} < 6$. This metallicity "floor" has important implications regarding the presence of primordial (zero metallicity) gas within galaxies. If primordial gas with significant surface density and large cross section exists in high-redshift galaxies, then it is always surrounded by metal-enriched gas yielding a mass-weighted metallicity exceeding 1/1000 solar. Alternatively, primordial gas may not exist in the neutral gas phase within high-redshift galaxies.

Figure 2.50 indicates that GRB host galaxies at $z > 2$ tend to be on average more metal rich than QSO absorption line systems by about a factor of 5. On the
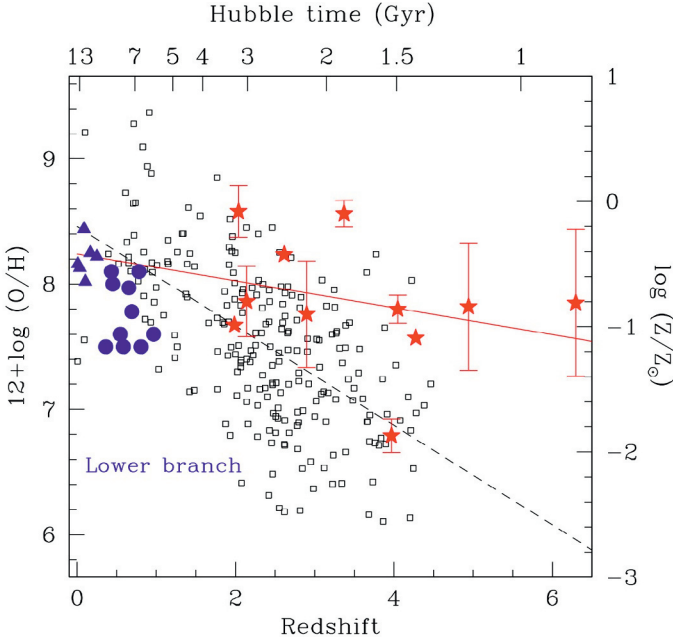
Fig. 2.50. Oxygen abundance as a function of redshift (lower x-axis) or Hubble time (upper x-axis). Filled circles are GRB host abundances determined with the R_{23} index, when choosing the lower branch solution (see Savaglio *et al.* 2009, for a description of the calibration used). Filled triangles are GRB host abundances determined with the T_e-base method or with the $O3N2$ index calibrated by Pettini & Pagel (2004). Filled stars are the GRB host abundances, derived from the absorption lines detected in the afterglow spectra. Open squares correspond to DLA oxygen abundances measured in QSO spectra. The solid and dashed lines represent the linear correlations for GRB hosts and DLAs, respectively. The GRB host galaxies clearly have larger oxygen abundances than DLAs, but have a flatter metallicity evolution. Figure reproduced from Savaglio *et al.* (2009).

other hand, their redshift evolution is much flatter with a slope of $\Delta \log Z / \Delta z = -0.18 \pm 0.10$ (see the solid line in Fig. 2.50). GRB host galaxies also exhibit very large H I column densities, even larger than DLAs, with a median value of $\log N(\text{H I}) = 21.7$, as measured from the damped Lyα profile imprinted on the GRB afterglow sight line (Prochaska *et al.* 2007). To explain this difference in both the metallicity and H I column density between DLAs and GRB hosts, we can invoke two possible scenarios. One is that the DLAs and GRB hosts trace the same population of galaxies, but show different properties because of different sight line geometries: the GRB sight lines originate within the host galaxy and very certainly within a young star-forming region. On the other hand the QSO sight lines pass randomly through the galaxy and statistically more often through the outer regions because of the higher cross sections, and hence have lower metallicities (due to
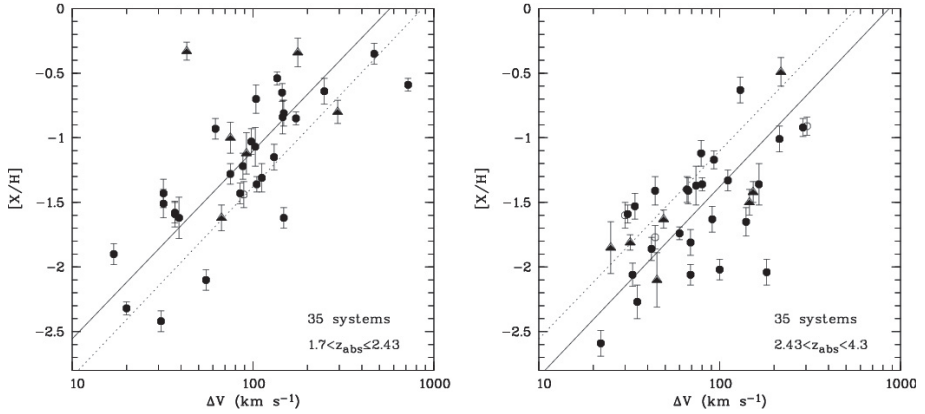
Fig. 2.51. Average metallicity, [X/H] (with X referring to Zn, S or Si), of 70 DLA (filled circles) or sub-DLA (filled triangles) systems *versus* the velocity width of their low-ionisation line profiles, ΔV, displayed on a logarithmic scale. A positive correlation between the two quantities is detected. The existence of this correlation, over more than a factor of 100 spread in metallicity, is very likely the consequence of an underlying mass-metallicity relation for galaxies responsible for DLA absorption lines. Moreover, when considering two sub-samples of systems with $1.7 < z < 2.43$ (left panel) and with $2.43 < z < 4.3$ (right panel), we observe a redshift evolution of the velocity-metallicity relation, as shown by the linear least-square bisector fits to each sub-sample (solid lines in the corresponding panels; the dotted lines are fits to the other sub-sample). Figure reproduced from Ledoux *et al.* (2006).

metallicity gradient within the galaxies) and lower H I column densities. The other possibility is that the DLAs and GRB hosts belong to two different classes of high-redshift galaxies: DLAs, because of their low metallicities, probably preferentially probe low-mass galaxies according to the mass-metallicity relation (see above), while GRB hosts might be associated with more massive galaxies. In comparison to the star-forming galaxies detected at $z \sim 2.2$, the GRB host galaxies with their average metallicity $12 + \log(\mathrm{O/H}) \simeq 8.2$ at $z \sim 2$ already tend to resemble the star-forming galaxies at the low-mass end, $M_\star < 3 \times 10^9 \ M_\odot$ (see Fig. 2.46).

2.4.4   Mass-metallicity relation in QSO absorption line systems

Using a sample of 70 DLAs/sub-DLAs with neutral hydrogen column densities $\log N(\mathrm{H\,I}) > 20 \ \mathrm{cm}^{-2}$ and redshifts in the range $1.7 < z < 4.3$, Ledoux *et al.* (2006) have shown that there is a clear correlation between metallicities [X/H], derived from Zn abundances when available or Si and S abundances, and velocity widths of the low-ionisation line profiles ΔV (see Fig. 2.51). Scatter in the data points is expected due to random impact parameters through the absorbing galaxies, and indeed, the scatter observed in Figure 2.51 is much larger than the metallicity measurement uncertainties. Negative radial gradients in metallicity, like those

observed in the disks of large nearby spirals, could also contribute to the scatter. However, this effect is probably not very important. For instance, Chen *et al.* (2005) derived a metallicity gradient of only -0.041 ± 0.012 dex kpc^{-1} from the galactic centre to 30 kpc radius from a sample of six $z < 0.65$ galaxy-DLA pairs.

Such a velocity-metallicity correlation, over more than a factor of 100 spread in metallicity, is thought to be the consequence of an underlying mass-metallicity relation for the galaxies responsible for DLA absorption lines. While peculiar ejection of hot gas should primarily affect the kinematics of high-ionisation lines, such as C IV and Si IV, the measurements of line profile velocity widths based here on low-ionisation lines should, instead, be dominated by motions on a galactic scale governed, or induced, by gravity. Indeed, for disk galaxies, the rotation velocity is a direct measure of their total mass. Lines of sight that do not pass through the centre of the galaxy will not trace the full depth of the potential well, and therefore, will tend to show smaller velocity dispersions than the rotation velocity (see the models by Prochaska & Wolfe 1997; Wolfe & Prochaska 1998). Hence, for random lines of sight through a large sample of disk galaxies, there should be a mean relationship between mass and profile velocity width, albeit with a large scatter induced by the range of impact parameters and inclination angles probed by the observations. Gas infall/outflow or galaxy sub-clump merging will also produce kinematically broadened line profiles with velocity widths scaling as the infall/outflow velocities, which again scale as the depth of the combined potential well of galaxies or mergers. Simulations have shown that, in that case, the line profile velocity width is a good indicator of the circular velocity of the underlying dark-matter halo with $\Delta V \sim 0.6 v_c$ (Haehnelt *et al.* 1998a; Maller *et al.* 2001; Nulsen *et al.* 1998).

For these reasons, it is assumed that the dynamical mass of DLA galaxies is the dominant factor setting up the observed DLA velocity-metallicity correlation. In addition, a redshift evolution is observed in this velocity-metallicity correlation as depicted in Figure 2.51. Indeed, the median redshift of the Ledoux *et al.* (2006) sample is $z_{med} = 2.43$, and it is shown that the two sub-samples of systems with, respectively, $z > 2.43$ and $z < 2.43$ differ significantly. Both the median DLA metallicity and median DLA velocity width increase with decreasing redshift. This suggests that galaxy haloes of a given mass are becoming more metal-rich with time. This result is consistent with the evolution of the mass-metallicity relation through the cosmic epoch observed for UV-selected star-forming galaxies over $z \sim 2.2$ to $z \sim 3.5$ (see Fig. 2.46).

Moreover, assuming a simple linear scaling of the galaxy luminosity with the mass of the dark matter halo, *i.e.* $m_R = -7.5 \log(v_c/200 \text{ km s}^{-1}) + m_R^0$, where m_R is the galaxy apparent R-band magnitude and $m_R^0 = 26.6$ for the Λ-CDM cosmological model (Haehnelt *et al.* 1998b, 2000), we can deduce the luminosity-metallicity relation. As a consequence, the spread in DLA metallicity of more than two orders of magnitude could reflect a spread in DLA galaxy luminosity of more than ten magnitudes. Interestingly, the slope of this DLA luminosity-metallicity relation is consistent with that derived by Tremonti *et al.* (2004) for the luminosity-metallicity relation for $z \sim 0.1$ galaxies from the SDSS.

Chapter 3

OXYGEN PRODUCTION AND DESTRUCTION

In this chapter, we first introduce the nuclear processes by which oxygen isotopes can be synthesised and destroyed. We then describe the main astrophysical sites where these reactions may occur, with special emphasis on massive stars and low/intermediate mass stars.

3.1 Oxygen and nuclear physics

Over the last decades, much experimental and theoretical work has led to the improvement of our knowledge of the rates of many thermonuclear reactions of astrophysical interest. In this section, we present an update of the NACRE[1] compilation (Angulo *et al.* 1999) for the charged-particle induced reactions involving the stable oxygen isotopes in their entrance or exit channels, or leading in their exit channels to unstable isobars that decay to stable oxygen isotopes. The reader is referred to NACRE for the rates that do not need to be revised since the publication of this compilation. We then briefly discuss the impact of the uncertainties in these nuclear reactions on the oxygen abundance predictions. Of course, other reactions than those considered here may influence indirectly the oxygen production, but they will not be further discussed.

3.1.1 Some generalities about thermonuclear reaction rates in astrophysical conditions

As it is well known, the nuclear reaction rates in astrophysical plasmas are obtained by integrating the reaction cross sections σ over a Maxwell-Boltzmann distribution of the relative energies E of the reaction partners. They are classically expressed as an average of the product of σ times the relative velocity v defined as

$$N_A \langle \sigma v \rangle = N_A \frac{(8/\pi)^{1/2}}{\mu^{1/2}(k_B T)^{3/2}} \int \sigma(E) \, E \exp\left(-\frac{E}{k_B T}\right) dE, \qquad (3.1)$$

where N_A, k_B, μ and T are the Avogadro number, Boltzmann constant, reduced mass and temperature. For charged-particle induced reactions, the astrophysical

---

[1]Nuclear Astrophysics Compilation of REaction rates. The update dates back to october 2009.

S-factor is conveniently used instead of the cross section to compensate for the rapid variation of the cross section with E below the Coulomb barrier. It is defined as

$$S(E) \quad = \quad E \exp(2\pi\eta)\,\sigma(E), \tag{3.2}$$

where $\eta = Z_1 Z_2 e^2/\hbar v$ is the Sommerfeld parameter, Z_1 and Z_2 being the charge numbers of the interacting nuclei.

In NACRE, Equation (3.1) is integrated numerically for the non-resonant and broad resonance contributions to the rates. The narrow resonances are treated separately. If they are approximated by Breit-Wigner forms, their contributions to the rates are functions of temperature, resonance strengths and widths. The reader is referred to Angulo *et al.* (1999) for details, as well as for an original analytic approximation of the rates.

A major experimental challenge in the evaluation of the rates lies in the identification of narrow resonances at the largely sub-Coulomb energies of astrophysical interest (the so-called Gamow window). Another difficulty concerns the extrapolation of the non-resonance contribution (*i.e.* is the S-factor) to these low energies, where direct experimental data are not available except in a few cases. The extrapolation techniques documented in NACRE may vary from one reaction to the other. In some cases, a simple constant value is adopted. In others, the extrapolations are based on an R-matrix fit or on the direct capture model. For extrapolations at the energies that are relevant to high temperatures (typically $T \gtrsim 3 \times 10^9$ K for the reactions considered here), Hauser-Feshbach model calculations are used.

For NACRE it has been a key goal to evaluate the rate uncertainties as a function of temperature. As a result, recommended ("adopted"), lower and upper limits of the rates are provided for the reactions under consideration, and all these rates are available in extended tabular form (whose use in stellar modelling is highly recommended) at the website `http://www.astro.ulb.ac.be`.

3.1.2 Main reactions

3.1.2.1 $\quad ^{15}\mathrm{N}\,(\mathrm{p}\,,\gamma)\,^{16}\mathrm{O}$

The $^{15}\mathrm{N}(\mathrm{p},\gamma)^{16}\mathrm{O}$ reaction is responsible for the break-out from the cold mode of the CN cycle (labelled I in Fig. 3.1), which is in general the main energy provider in the CNO burning. As $^{15}\mathrm{N}(\mathrm{p},\alpha)^{12}\mathrm{C}$ is faster than $^{15}\mathrm{N}(\mathrm{p},\gamma)^{16}\mathrm{O}$ (see NACRE), this leaking from the CN cycle is weak, so that the $^{15}\mathrm{N}$ radiative proton captures cannot drastically affect the oxygen abundances. For compilation purposes, we however provide an update of the NACRE $^{15}\mathrm{N}\,(\mathrm{p}\,,\gamma)\,^{16}\mathrm{O}$ rate. It is based on a new low-energy extrapolation of the S-factor proposed by Mukhamedzanov *et al.* (2008) who apply the asymptotic normalisation constant (ANC) method to new indirect measurements (no additional direct capture measurements have been made available since NACRE).

The ANC method relies on the assumption that the nuclear reactions at low energies are independent of the nuclear structure in the internal region, and are
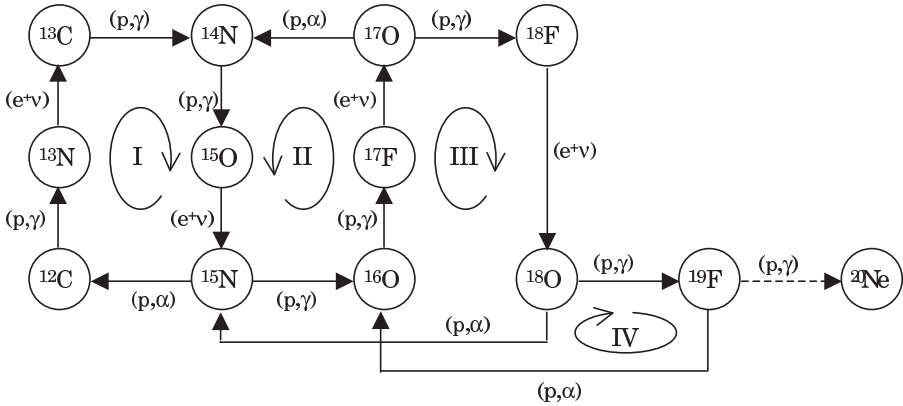
Fig. 3.1. Reactions involved in the cold CNO mode of hydrogen burning. This mode refers to situations in which the β-decay lifetimes of unstable nuclides are shorter than their lifetimes against charged particle captures. Hot modes apply in the reverse situation, and can develop mainly in explosive scenarios.

dominated instead by the wave function in the peripheral region. Mukhamedzanov *et al.* (2008) investigated the proton transfer reaction ^{15}N(^{3}He,d)^{16}O, and extracted the ANCs of the ground and excited states of ^{16}O by fitting the observed angular distribution data within the DWBA approximation. The derived ANCs are proportional to the non-resonant direct capture cross section. For the resonance parameters, Mukhamedzanov *et al.* (2008) re-evaluated the proton and α-particle widths by fitting the ^{15}N(p,α)^{12}C reaction rate that largely dominates ^{15}N$\,(p\,,\gamma)\,^{16}$O at the low energies considered.

Figure 3.2 shows the S-factor for ^{15}N(p,γ)^{16}O obtained from the combined use of the R-matrix and ANC methods, and with the revised proton and α-particle widths. The total S-factor at zero energy is predicted to be $S(0) = 36 \pm 6$ keV b, and the zero-energy S-factor for the non-resonant direct capture to the ground state is 0.86 keV b, which is 9 times smaller than that estimated by Rolfs & Rodney (1974). It should be noted that the ANC method relies on the reproduction of the angular distribution data derived from an indirect measurement, and thus provides only model-dependent reaction rates. We consider that the procedure adopted by Mukhamedzanov *et al.* (2008) is suitable for the ^{15}N radiative capture.

The reaction rates calculated with the revised S-factor of Figure 3.2 are listed in Table 3.1. Below $T_9 = 0.15$, they are approximately half of the NACRE rates. As a consequence, the break-out from the CN cycle (cycle I) to the ON cycle (cycle II) is even smaller than previously expected.

3.1.2.2 ^{17}O$\,(p\,,\alpha)\,^{14}$N and ^{17}O$\,(p\,,\gamma)\,^{18}$F

Figure 3.1 shows that ^{17}O(p,α)^{14}N closes cycle II of the CNO cycle, while a break-out to cycle III is allowed by ^{17}O$\,(p\,,\gamma)\,^{18}$F . The relative rates of these two
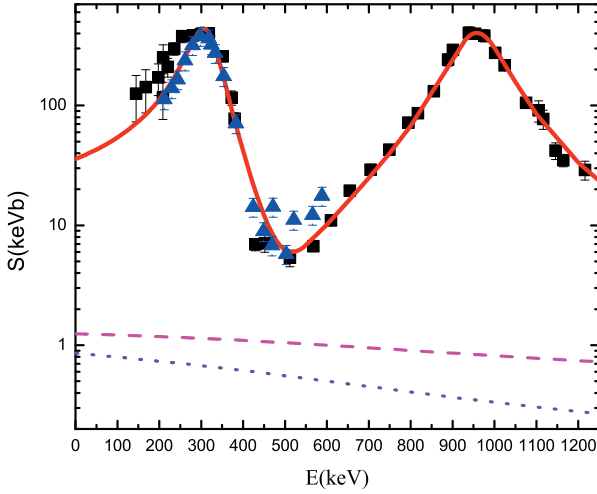
Fig. 3.2. The ^{15}N(p,γ)^{16}O S-factor. The experimental data are from Rolfs & Rodney (1974) and Hebbard (1960). The solid curve is obtained from the combination of the R-matrix and ANC methods (see text). The dashed curve is the total non-resonant capture S-factor obtained from the sum of the non-resonant component of eight bound states. The dotted curve is the non-resonant component for the ground state transition (from Mukhamedzanov *et al.* 2008).

^{17}O destruction channels are thus relevant in the calculation of the CNO yields of ^{17}O and ^{18}O.

For $0.02 < T_9 < 0.1$, the ^{17}O(p,α)^{14}N rates are dominated by the 1^- $E_r = 65.1$ keV resonance in ^{18}F (excitation energy $E_x = 5.6716$ MeV). Its properties have been analysed in several experiments (see *e.g.* NACRE). In contrast, the characteristics of the 2^- resonance at $E_r = 183.3$ keV (excitation energy $E_x = 5.7898$ MeV) remained poorly known at the time of the NACRE compilation, compilation with large concomitant uncertainties in the rates, especially in the $0.1 \lesssim T_9 \lesssim 0.4$ temperature range of interest in classical novae.

Recent studies of the 2^- resonance have led to an improvement of the situation. Fox *et al.* (2005, 2004) derive for this resonance the strength $\omega\gamma_{p\gamma} = (1.2 \pm 0.2) \times 10^{-6}$ eV. Chafa *et al.* (2007) (see also Chafa *et al.* 2005, 2006) report the values $\omega\gamma_{p\gamma} = (2.2 \pm 0.4) \times 10^{-6}$ eV and $\omega\gamma_{p\alpha} = (1.6 \pm 0.2) \times 10^{-3}$ eV. The latter result is confirmed by Newton *et al.* (2007) who obtain $\omega\gamma_{p\alpha} = (1.66 \pm 0.17) \times 10^{-3}$ eV.

Here we adopt the rates for ^{17}O(p,α)^{14}N and for ^{17}O(p,γ)^{18} from Chafa *et al.* (2007) as the revised reaction rates. In addition to the 1^- and 2^- resonances reported above, these rates are calculated by taking into account the level at $E_r = -3.12$ keV (^{18}F level at $E_x = 5.6034$ MeV) for which a new resonance strength is also reported by Chafa *et al.* (2007). The contribution from 15 levels at higher energies already considered in NACRE is also included. In addition to this resonant contribution, the direct capture process can affect the ^{17}O(p,γ)^{18}F rate.

Table 3.1. The ^{15}N$(p,\gamma)^{16}$O rates calculated with the S-factors of Mukhamedzanov *et al.* (2008). The NACRE values are provided for comparison. Here and in all the following tables, the rates are in units of cm^3/(mol s).

T_9	$N_A\langle\sigma v\rangle$	NACRE	T_9	$N_A\langle\sigma v\rangle$	NACRE
0.007	4.39E−25	7.01E−25	0.100	2.23E−05	4.23E−05
0.008	1.29E−23	2.08E−23	0.110	6.10E−05	1.15E−04
0.009	2.24E−22	3.67E−22	0.120	1.49E−04	2.78E−04
0.010	2.62E−21	4.33E−21	0.130	3.34E−04	6.16E−04
0.011	2.24E−20	3.75E−20	0.140	6.95E−04	1.27E−03
0.012	1.50E−19	2.54E−19	0.150	1.36E−03	2.46E−03
0.013	8.25E−19	1.40E−18	0.160	2.53E−03	4.53E−03
0.014	3.83E−18	6.55E−18	0.180	7.74E−03	1.35E−02
0.015	1.54E−17	2.66E−17	0.200	2.07E−02	3.52E−02
0.016	5.52E−17	9.56E−17	0.250	1.55E−01	2.44E−01
0.018	5.26E−16	9.22E−16	0.300	7.19E−01	1.05E+00
0.020	3.67E−15	6.50E−15	0.350	2.33E+00	3.17E+00
0.025	1.80E−13	3.25E−13	0.400	5.80E+00	7.48E+00
0.030	3.51E−12	6.41E−12	0.450	1.20E+01	1.49E+01
0.040	2.66E−10	4.96E−10	0.500	2.14E+01	2.58E+01
0.050	5.78E−09	1.09E−08	0.600	5.11E+01	5.90E+01
0.060	6.08E−08	1.16E−07	0.700	9.50E+01	1.07E+02
0.070	4.00E−07	7.64E−07	0.800	1.53E+02	1.68E+02
0.080	1.90E−06	3.63E−06	0.900	2.27E+02	2.46E+02
0.090	7.11E−06	1.36E−05	1.000	3.25E+02	3.50E+02

The low-energy S-factor as revised by Chafa *et al.* (2007) is given by $S_{DC}(E) = 6.2 + 1.61E - 0.169E^2$ keV b, where E is in MeV.

The new reaction rates are listed in Tables 3.2 and 3.3. The errors are estimated from a Monte Carlo analysis. The ratio of the new ^{17}O(p,α)^{14}N rates to those in NACRE is shown in Figure 3.3. The difference for $T_9 < 0.02$ is mainly due to the lower value of the single-particle width of the subthreshold level at $E_x = 5.603$ MeV. For $0.1 < T_9 < 0.4$, the reaction rates increase because of the new data for the 183.3 keV resonance. With the S_{DC}-factor of Chafa *et al.* (2007), the direct capture process affects the rates for $T_9 < 0.8$.

For ^{17}O(p,γ)^{18}F, the revised rates are in agreement with NACRE above $T_9 = 0.4$, as shown in Figure 3.4. For $0.1 < T_9 < 0.4$, the new rates are smaller than the NACRE values by up to a factor of about 5. This deviation comes from the new data for the 183.3 keV resonance.

3.1.2.3 ^{18}O$(p,\alpha)^{15}$N

According to the NACRE rates, the burning of ^{18}O predominantly proceeds through ^{18}O(p,α)^{15}N in the $T_9 \lesssim 0.02$ and $T_9 \gtrsim 0.7$ regions, leading to the closure of cycle III as shown in Figure 3.1. However, for $0.02 \lesssim T_9 \lesssim 0.7$, ^{18}O(p,$\gamma$)^{19}F is responsible for a leak out of cycle III.

Table 3.2. The $^{17}\mathrm{O}\,(\mathrm{p}\,,\alpha)\,^{14}\mathrm{N}$ rates from Chafa *et al.* (2007).

T_9	Lower	Rate	Upper	T_9	Lower	Rate	Upper
0.01	4.02E−25	4.97E−25	5.92E−25	0.13	4.35E−4	4.96E−4	5.57E−4
0.011	4.27E−24	5.23E−24	6.18E−24	0.14	1.18E−3	1.35E−3	1.52E−3
0.012	3.50E−23	4.24E−23	4.99E−23	0.15	2.85E−3	3.27E−3	3.69E−3
0.013	2.31E−22	2.79E−22	3.26E−22	0.16	6.19E−3	7.12E−3	8.04E−3
0.014	1.29E−21	1.54E−21	1.80E−21	0.18	2.25E−2	2.59E−2	2.92E−2
0.015	6.23E−21	7.44E−21	8.65E−21	0.2	6.25E−2	7.18E−2	8.11E−2
0.016	2.75E−20	3.26E−20	3.77E−20	0.25	3.84E−1	4.39E−1	4.94E−1
0.018	5.12E−19	6.19E−19	7.26E−19	0.3	1.48E+0	1.65E+0	1.82E+0
0.02	1.11E−17	1.53E−17	1.94E−17	0.35	6.02E+0	6.50E+0	6.97E+0
0.025	1.10E−14	1.54E−14	1.99E−14	0.4	2.56E+1	2.75E+1	2.94E+1
0.03	1.30E−12	1.76E−12	2.22E−12	0.45	9.28E+1	9.99E+1	1.07E+2
0.04	4.77E−10	6.14E−10	7.52E−10	0.5	2.73E+2	2.95E+2	3.16E+2
0.05	1.52E−8	1.92E−8	2.32E−8	0.6	1.42E+3	1.53E+3	1.63E+3
0.06	1.46E−7	1.81E−7	2.17E−7	0.7	4.64E+3	4.96E+3	5.28E+3
0.07	7.09E−7	8.73E−7	1.04E−6	0.8	1.12E+4	1.20E+4	1.27E+4
0.08	2.28E−6	2.79E−6	3.30E−6	0.9	2.24E+4	2.38E+4	2.51E+4
0.09	5.96E−6	7.16E−6	8.36E−6	1.0	3.91E+4	4.12E+4	4.34E+4
0.1	1.56E−5	1.80E−5	2.05E−5	1.25	1.09E+5	1.14E+5	1.19E+5
0.11	4.62E−5	5.20E−5	5.77E−5	1.5	2.29E+5	2.38E+5	2.47E+5
0.12	1.45E−4	1.64E−4	1.83E−4				

Table 3.3. The $^{17}\mathrm{O}\,(\mathrm{p}\,,\gamma)\,^{18}\mathrm{F}$ rates from Chafa *et al.* (2007).

T_9	Lower	Rate	Upper	T_9	Lower	Rate	Upper
0.01	2.37E−25	4.55E−25	6.73E−25	0.13	1.84E−6	2.79E−6	3.74E−6
0.011	2.52E−24	4.84E−24	7.15E−24	0.14	4.25E−6	6.29E−6	8.33E−6
0.012	2.04E−23	3.91E−23	5.79E−23	0.15	9.16E−6	1.32E−5	1.73E−5
0.013	1.32E−22	2.54E−22	3.76E−22	0.16	1.84E−5	2.61E−5	3.38E−5
0.014	7.14E−22	1.37E−21	2.03E−21	0.18	6.13E−5	8.50E−5	1.09E−4
0.015	3.30E−21	6.34E−21	9.37E−21	0.2	1.66E−4	2.27E−4	2.89E−4
0.016	1.34E−20	2.57E−20	3.80E−20	0.25	1.07E−3	1.48E−3	1.89E−3
0.018	1.60E−19	3.07E−19	4.53E−19	0.3	4.24E−3	5.98E−3	7.71E−3
0.02	1.39E−18	2.62E−18	3.85E−18	0.35	1.53E−2	2.08E−2	2.62E−2
0.025	1.47E−16	2.37E−16	3.26E−16	0.4	5.73E−2	7.20E−2	8.67E−2
0.03	8.02E−15	1.08E−14	1.36E−14	0.45	2.01E−1	2.38E−1	2.75E−1
0.04	2.10E−12	2.66E−12	3.23E−12	0.5	6.02E−1	6.95E−1	7.89E−1
0.05	6.55E−11	8.19E−11	9.83E−11	0.6	3.41E+0	3.88E+0	4.35E+0
0.06	6.66E−10	8.27E−10	9.89E−10	0.7	1.21E+1	1.37E+1	1.53E+1
0.07	3.60E−9	4.55E−9	5.50E−9	0.8	3.14E+1	3.55E+1	3.95E+1
0.08	1.35E−8	1.78E−8	2.22E−8	0.9	6.57E+1	7.38E+1	8.19E+1
0.09	4.09E−8	5.77E−8	7.44E−8	1.0	1.18E+2	1.32E+2	1.45E+2
0.1	1.12E−7	1.68E−7	2.23E−7	1.25	3.26E+2	3.64E+2	4.03E+2
0.11	2.95E−7	4.54E−7	6.13E−7	1.5	6.34E+2	6.98E+2	7.62E+2
0.12	7.53E−7	1.16E−6	1.57E−6				
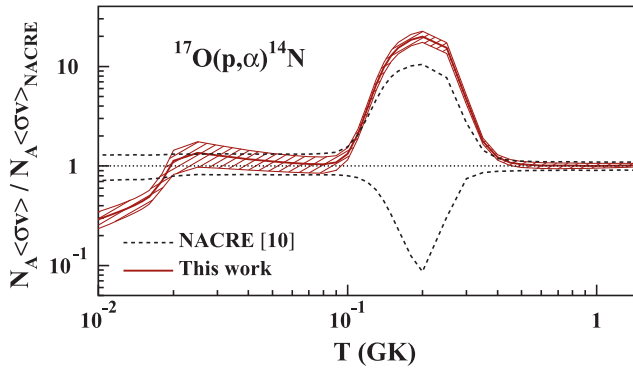
Fig. 3.3. Ratio of the Chafa *et al.* (2007) (labelled "This work") and NACRE rates for $^{17}O(p,\alpha)^{14}N$. The hatched area represents the uncertainties in the reaction rates. $T(GK)$ is the temperature in 10^9 K (generally expressed as T_9). Figure adopted from Chafa *et al.* (2007).
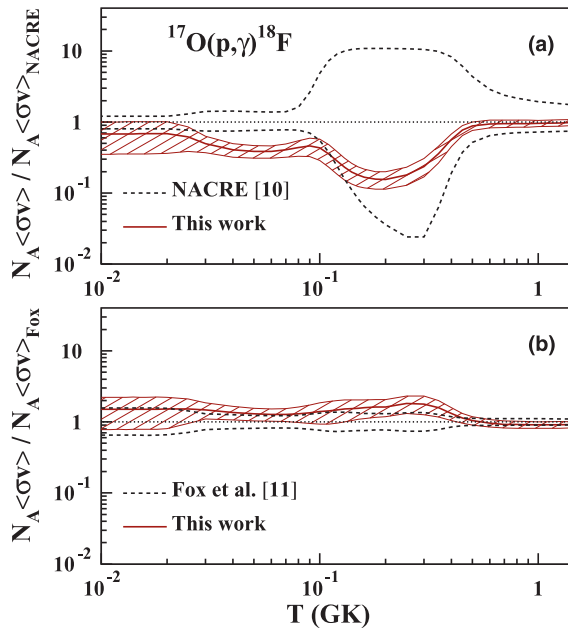
Fig. 3.4. Ratio of the Chafa *et al.* (2007) (labelled "This work") to **(a)** the NACRE rates, and **(b)** the rates of Fox *et al.* (2005) for $^{17}O(p,\gamma)^{18}F$. The hatched areas represent the uncertainties in the reaction rates. Figure adopted from Chafa *et al.* (2007).

The narrow resonances at 20 and 143.5 keV and the broad one at 656 keV in ^{19}F dominate the $^{18}O(p,\alpha)^{15}N$ NACRE rates. In fact the 656 keV resonance gives

Table 3.4. Revised ^{18}O$(p, \alpha)^{15}$N rates based on the experiments of La Cognata *et al.* (2008) (referred to as LA08).

T_9	LA08	NACRE	T_9	LA08	NACRE
0.007	1.09E−24	8.32E−25	0.018	1.75E−15	1.71E−15
0.008	5.48E−23	4.13E−23	0.02	1.41E−14	1.40E−14
0.009	1.17E−21	8.85E−22	0.025	9.95E−13	9.94E−13
0.01	1.37E−20	1.05E−20	0.03	2.61E−11	2.61E−11
0.011	1.06E−19	8.34E−20	0.04	3.07E−09	3.07E−09
0.012	6.16E−19	5.00E−19	0.05	1.01E−07	1.01E−07
0.013	2.94E−18	2.48E−18	0.06	2.92E−06	2.91E−06
0.014	1.23E−17	1.08E−17	0.07	7.94E−05	7.93E−05
0.015	4.71E−17	4.31E−17	0.08	1.17E−03	1.17E−03
0.016	1.68E−16	1.58E−16	0.09	9.63E−03	9.63E−03

a strong contribution in the entire temperature range considered in NACRE. The 143.5 keV resonance was reported by NACRE to be fairly well known. In contrast, uncertainties remained in the 20 keV resonance properties, with concomitant uncertainties in the rate. This was mainly due to the adoption of the resonance strength predicted by the DWBA analysis of the proton transfer reactions and from direct capture measurements. In addition, a resonance at 90 keV had an unknown J^π value, so that its contribution to the rate could not be ascertained.

To reduce the uncertainties in the reaction rates, the 20 and 90 keV resonances have been investigated by means of the Trojan horse method (La Cognata *et al.* 2008), which is an indirect technique to evaluate cross sections at energies well below the Coulomb barrier. The strengths of the 20 and 90 keV resonances derived in such a way are $\omega\gamma = 8.3^{+3.8}_{-2.6} \times 10^{-19}$ eV and $(1.76 \pm 0.33) \times 10^{-7}$ eV, respectively. The rates provided in Table 3.4 are obtained by updating the NACRE predictions with these new resonance strengths. This leads to a marginal increase of the original NACRE rates, but also to a significant reduction of the uncertainties around $T_9 = 0.01$, as shown in Figure 3.5.

3.1.2.4 ^{12}C$(\alpha, \gamma)^{16}$O

This reaction is classically considered as one of the most important in stellar physics. It influences the structure and nucleosynthesis of the stars during their central He-burning phase, as well as during the subsequent nuclear burning stages in massive stars up to their final (supernova) fate. No wonder then that the radiative capture of α-particles by ^{12}C at energies of astrophysical relevance (around a centre-of-mass energy of about 300 keV for hydrostatic He-burning conditions) has been one of the most studied reactions. Both direct and indirect techniques have been applied to measure the cross sections or the quantities entering their estimate. In recent years, precise measurements of γ-ray angular distributions and of cascade transitions have also accumulated (Assunção *et al.* 2006; Hammer *et al.* 2005; Kunz *et al.* 2001; Matei *et al.* 2006; Roters *et al.* 1999; Tischhauser *et al.* 2002). In spite of all these efforts, uncertainties that are generally considered to
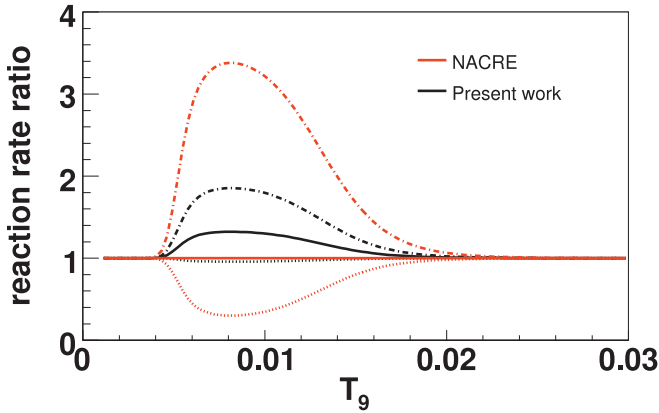
Fig. 3.5. Ratio of the La Cognata *et al.* (2008; labelled "Present work") and NACRE rates for ^{18}O(p,α)^{15}N. The ratio of the upper and lower limits of the two sets of rates to the recommended values are also shown by dot-dashed and dotted curves, respectively. Original figure from La Cognata *et al.* (2008).

be too large for astrophysics purposes remain in the stellar rates. This situation results from the fact that the cross section is so small (approximately 10^{-17} b) in stellar conditions that it will remain unreachable to direct measurement in the foreseeable future. Consequently, extrapolations from higher energies to the relevant Gamow window cannot be avoided. Their reliability is hampered by the special structural features of the ^{16}O nuclear levels, leading to various contributions to the S-factor (for a review, see *e.g.* Buchmann 2006).

The NACRE rates are not discussed here. We just review the post-NACRE information in some detail. In recent years, new experimental data have become available. They have been analysed extensively with the R-matrix method. Representative results are given by Kunz *et al.* (2002, 2001). The resulting reaction rates are based on γ-ray angular distribution measurements, and on a systematic description of the radiative capture data, elastic scattering data and α-particle spectrum of the β-delayed α-decay of ^{16}N. The derived rates are listed in Table 3.5. Following Kunz *et al.* (2002) they can be approximated by

$$
\begin{aligned}
N_A\langle\sigma v\rangle &= \frac{1.21 \times 10^8}{T_9^2(1 + 6.06 \times 10^{-2}T_9^{-2/3})^2}\exp\left[-\frac{32.12}{T_9^{1/3}} - \left(\frac{T_9}{1.7}\right)^2\right] \\
&+ \frac{7.4 \times 10^8}{T_9^2(1 + 0.47T_9^{-2/3})^2}\exp\left(-\frac{32.12}{T_9^{1/3}}\right) \\
&+ \frac{1.53 \times 10^4}{T_9^{2/3}}(1 + 2 \times 10^6 T_9^{1/3})\exp\left(-\frac{38.534}{T_9^{1/3}}\right).
\end{aligned}
\tag{3.3}
$$

Table 3.5. Lower limits, recommended values and upper limits of the rates of $^{12}\text{C}\,(\alpha\,,\gamma)\,^{16}\text{O}$ from the R-matrix analysis of Kunz $et\ al.$ (2002).

T_9	lower	$N_A\langle\sigma v\rangle$	upper
0.04	5.89E−31	8.36E−31	1.11E−30
0.05	3.65E−28	5.20E−28	6.93E−28
0.06	4.90E−26	6.90E−26	9.30E−26
0.07	2.39E−24	3.42E−24	4.57E−24
0.08	5.90E−23	8.40E−23	1.13E−22
0.09	8.80E−22	1.26E−21	1.69E−21
0.10	9.00E−21	1.29E−20	1.73E−20
0.11	6.80E−20	9.80E−20	1.32E−19
0.12	4.11E−19	5.92E−19	7.96E−19
0.13	2.04E−18	2.93E−18	3.95E−18
0.14	8.60E−18	1.24E−17	1.67E−17
0.15	3.18E−17	4.58E−17	6.18E−17
0.16	1.05E−16	1.51E−16	2.04E−16
0.18	8.60E−16	1.24E−15	1.68E−15
0.20	5.25E−15	7.58E−15	1.02E−14
0.25	1.93E−13	2.79E−13	3.79E−13
0.30	2.96E−12	4.28E−12	5.83E−12
0.35	2.60E−11	3.75E−11	5.11E−11
0.40	1.54E−10	2.22E−10	3.03E−10
0.45	6.90E−10	9.90E−10	1.35E−09
0.50	2.50E−09	3.59E−09	4.91E−09
0.60	2.06E−08	2.95E−08	4.04E−08
0.70	1.10E−07	1.57E−07	2.15E−07
0.80	4.36E−07	6.19E−07	8.48E−07
0.90	1.39E−06	1.97E−06	2.70E−06
1.00	3.78E−06	5.32E−06	7.29E−06
1.25	2.85E−05	3.95E−05	5.40E−05
1.50	1.40E−04	1.91E−04	2.59E−04
1.75	5.38E−04	7.20E−04	9.63E−04
2.00	1.75E−03	2.29E−03	3.00E−03
2.50	1.23E−02	1.54E−02	1.95E−02
3.00	5.55E−02	6.81E−02	8.33E−02
3.50	1.66E−01	2.21E−01	2.66E−01
4.00	4.82E−01	5.86E−01	6.98E−01
5.00	2.41E+00	2.91E+00	3.44E+00
6.00	7.63E+00	1.07E+01	1.26E+01
7.00	2.56E+01	3.08E+01	3.61E+01
8.00	5.88E+01	7.08E+01	8.30E+01
9.00	1.14E+02	1.37E+02	1.61E+02
10.00	1.93E+02	2.32E+02	2.72E+02

Figure 3.6 compares the rates of Kunz $et\ al.$ (2002) with those proposed by Caughlan & Fowler (1988) (CF88), NACRE (recommended values) and Buchmann (1996). Note in particular that the CF88 and NACRE rates exhibit a different temperature dependence than the ones of Kunz $et\ al.$
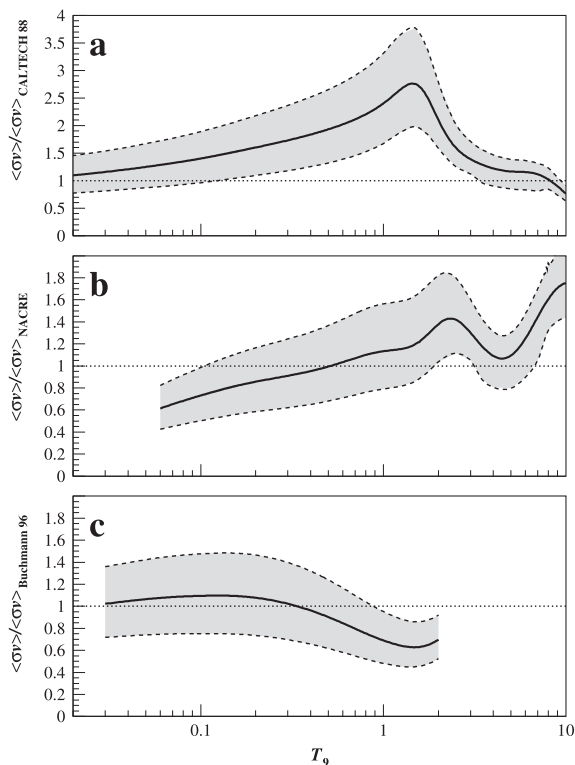
Fig. 3.6. Ratios of the rates for ^{12}C$(\alpha,\gamma)^{16}$O proposed by Kunz *et al.* (2002) and Caughlan & Fowler (1988) (CF88; panel **a**), NACRE recommended rates (panel **b**) (the contribution of cascade transitions is neglected; see *e.g.* Buchmann 2006 for a discussion of these transitions) and Buchmann (1996) (panel **c**). The solid curves are obtained with the recommended values of Table 3.5, and the shaded area are bounded by the ratios calculated with the lower and upper limits listed in this table. Original figure from Kunz *et al.* (2002).

A recent re-evaluation of the ^{12}C$(\alpha,\gamma)^{16}$O rate based on the direct capture model (potential model) has been carried out by Katsuma (2008). Some rate values are listed in Table 3.6. They are compared in Figure 3.7 to the NACRE data. The two sets of predictions deviate from each other especially at $T_9 \gtrsim 0.5$, where the higher rates obtained with the potential model are due to the inclusion of the contribution from cascade transitions to ^{16}O excited states that are neglected in NACRE. In contrast, any possible contribution from narrow resonances is neglected in the potential model rates, while they are included in NACRE. Comparing Figure 3.7 with Figure 3.6, the potential and R-matrix predictions show similar trends of the temperature dependence of the rates. However, the enhancement around $T_9 = 1$–2 compared to NACRE is much stronger in the potential than

Table 3.6. The $^{12}\text{C}\,(\alpha,\gamma)\,^{16}\text{O}$ rates calculated by Katsuma (2008) [KA08] with a potential model including the contribution of cascade transitions. The recommended NACRE rates are listed for comparison.

T_9	[KA08]	NACRE	T_9	[KA08]	NACRE
0.06	6.25E–26	1.02E–25	0.35	4.31E–11	4.03E–11
0.07	3.18E–24	4.98E–24	0.40	2.60E–10	2.31E–10
0.08	8.07E–23	1.22E–22	0.45	1.18E–09	1.00E–09
0.09	1.23E–21	1.80E–21	0.50	4.32E–09	3.52E–09
0.10	1.29E–20	1.81E–20	0.60	3.66E–08	2.75E–08
0.11	9.91E–20	1.35E–19	0.70	2.01E–07	1.40E–07
0.12	6.02E–19	7.98E–19	0.80	8.14E–07	5.36E–07
0.13	3.02E–18	3.89E–18	0.90	2.66E–06	1.66E–06
0.14	1.29E–17	1.61E–17	1.00	7.42E–06	4.41E–06
0.15	4.80E–17	5.86E–17	1.25	5.96E–05	3.19E–05
0.16	1.60E–16	1.91E–16	1.50	3.13E–04	1.53E–04
0.18	1.32E–15	1.53E–15	1.75	1.26E–03	5.76E–04
0.20	8.20E–15	9.11E–15	2.00	4.19E–03	1.84E–03
0.25	3.09E–13	3.21E–13	2.50	2.85E–02	1.27E–02
0.30	4.84E–12	4.75E–12	3.00	1.19E–01	5.81E–02

in the R-matrix case. Further experiments in the energy range $E_{\text{c.m.}} = 3$–8 MeV are in fact required to ascertain the reaction rate at $T_9 > 1$ (Kunz *et al.* 2002).
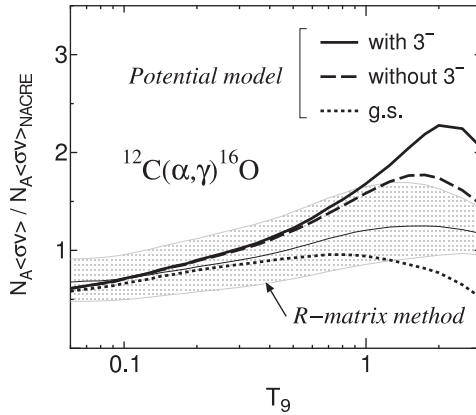
Fig. 3.7. Ratios of the rates of $^{12}\text{C}\,(\alpha,\gamma)\,^{16}\text{O}$ calculated by Katsuma (2008) with a potential model to the NACRE rates. The solid, dashed and dotted lines are obtained with the use of the NACRE recommended rates, and with the inclusion of different transitions in the potential model, as indicated in the figure; the solid line refers to the rates of Table 3.6. The shaded band corresponds to the adoption of the rates of Table 3.6 and of the upper and lower limits of the NACRE rates. The label "R-matrix method" refers to the results of Kunz *et al.* (2002).
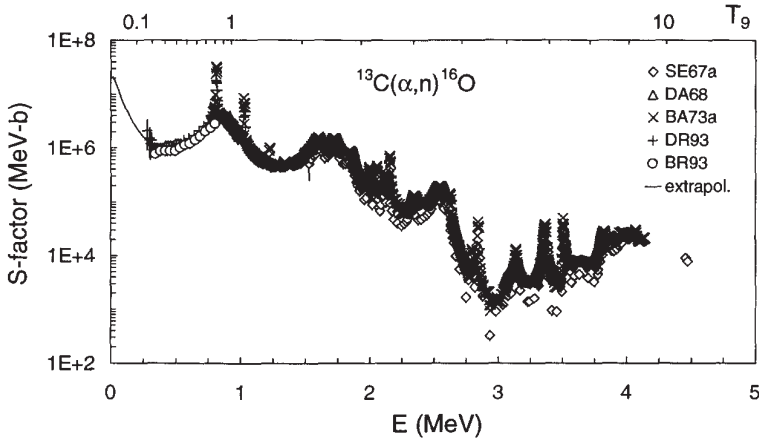
Fig. 3.8. S-factor for $^{13}\mathrm{C}\,(\alpha\,,\mathrm{n})\,^{16}\mathrm{O}$.

3.1.2.5 $^{13}\mathrm{C}\,(\alpha\,,\mathrm{n})\,^{16}\mathrm{O}$

About half of all heavy nuclides in the Universe are produced by the s-process, which involves a sequence of slow neutron captures and β-decays. The $^{13}\mathrm{C}(\alpha,\mathrm{n})^{16}\mathrm{O}$ reaction is considered to be the main neutron source for the s-process in asymptotic giant branch (AGB) stars. The knowledge of its rate is thus necessary in order to evaluate the s-process efficiency in these stellar conditions.

At present, the direct measurements of the $^{13}\mathrm{C}(\alpha,\mathrm{n})^{16}\mathrm{O}$ rate have been limited to incident energies $E_{\mathrm{c.m.}} > 280$ keV (Drotleff *et al.* 1993)[2]. This is in excess of the Gamow peak energy which is around 200 keV at temperatures $T_9 = 0.1$ close to those typical for the operation of the s-process in AGB stars.

The NACRE $^{13}\mathrm{C}(\alpha,\mathrm{n})^{16}\mathrm{O}$ S-factor is shown in Figure 3.8. For $T_9 < 4$, it is based on experimental cross sections in the $E_{\mathrm{c.m.}} = 0.28 – 4.47$ MeV range. Below $E_{\mathrm{c.m.}} = 0.28$ MeV, the S-factor extrapolation is obtained with the assumed contribution from the $1/2^+$ subthreshold state at the excitation energy $E_x = 6.356$ MeV in $^{17}\mathrm{O}$. This state is considered to originate from the $\alpha+^{13}\mathrm{C}$ cluster structure with relative angular momentum $l = 1$ (Descouvemont 1987; Dufour & Descouvemont 2001). In NACRE, this structure is assumed to be well developed (*i.e.* to have a large α-particle spectroscopic factor S_α). In these conditions, the subthreshold state strongly influences the low-energy S-factor, and consequently the AGB star s-process efficiency.

In order to investigate the $\alpha+^{13}\mathrm{C}$ component in the subthreshold state, indirect measurements of the $^{13}\mathrm{C}(^6\mathrm{Li},\mathrm{d})^{17}\mathrm{O}$ and $^{13}\mathrm{C}(^7\mathrm{Li},\mathrm{t})^{17}\mathrm{O}$ reactions have been performed by Kubono *et al.* (2003). From the analysis of their data with the help

---

[2]Note the recent direct measurement by Harissopulos *et al.* (2005) of the absolute cross section in the $E_\alpha = 0.8$ to 8.0 MeV range with an overall accuracy of 4%.
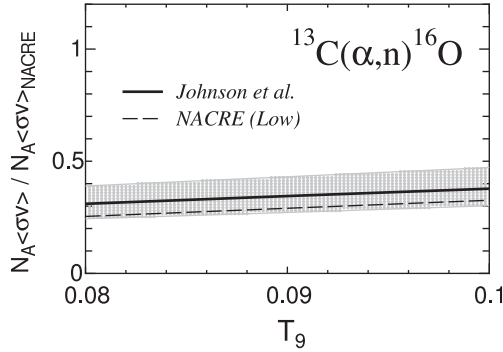
Fig. 3.9. Ratio of the ^{13}C(α, n) ^{16}O adopted rates obtained by the ANC method (Johnson *et al.* 2006) to the adopted NACRE ones (solid line). The dashed line corresponds to the ratio of the lower limit to the adopted NACRE rates. The shaded area shows the region between the ratios of the lower and upper limits of the rates of Johnson *et al.* (2006) to the adopted NACRE rates.

of the distorted waves Born approximation (DWBA), they have predicted $S_\alpha = 0.01$ for this state. Compared to NACRE, this leads to a much reduced contribution of the subthreshold state to the ^{13}C$(\alpha,n)^{16}$O rate, and thus to a lowering of the efficiency of the ^{13}C neutron source.

The conclusions of Kubono *et al.* (2003) have been challenged by Keeley *et al.* (2003) who have re-analysed the same experimental data using the DWBA model complemented with the coupled reaction channel (CRC) model. The resulting $S_\alpha \approx 0.4$ is by far larger than the value reported by Kubono *et al.* (2003). A new measurement of ^{13}C$(^7$Li,t$)^{17}$O has been performed recently by Pellegriti *et al.* (2008) and analysed with the DWBA model. The resulting S_α, equal to 0.29 ± 0.11, is marginally in agreement with the value reported by Keeley *et al.* (2003).

The contribution from the subthreshold state has also been evaluated with the ANC method by Johnson *et al.* (2006) based on the low-energy differential cross section of ^{13}C$(^6$Li,d$)^{17}$O$(1/2^+)$ measured in inverse kinematics. They derive the value $S = (2.5\pm0.7)\times10^6$ MeV b for the low-energy astrophysical S factor, which is 10 times smaller than the one $(2.30\times10^7$ MeV b) adopted in NACRE. This leads to a reaction rate that is 3 times smaller than NACRE in the $T_9 = 0.08-0.1$ range, as shown in Figure 3.9. In fact, the adopted rates predicted by the ANC method correspond approximately to the lower limit of the NACRE rates (Table 3.7).

In summary, the ^{13}C$(\alpha,n)^{16}$O rates are still quite uncertain in astrophysically relevant conditions. All the results obtained from the recent indirect measurements suggest, however, that the reaction rates in the $T_9 = 0.08 - 0.1$ range of relevance to the s-process are smaller than those adopted by NACRE. This relates to the fact that the α-particle spectroscopic factor of the subthreshold $1/2^+$ state seems to be $S_\alpha < 0.4$, which implies that the $\alpha+^{13}$C cluster structure may be less well developed than assumed in NACRE.

Table 3.7. Rates of $^{13}\text{C}\,(\alpha\,,\text{n})\,^{16}\text{O}$ predicted by the ANC method (Johnson *et al.* 2006) and reported in NACRE. For each temperature, the rates are obtained by multiplying the entries by $10^{\exp}$ (from Johnson *et al.* 2006).

T_9	Johnson et al.			NACRE			exp
	Low	Adopt	High	Low	Adopt	High	
0.08	1.17	1.49	1.87	1.22	4.80	5.80	-16
0.09	1.90	2.41	3.01	2.03	6.99	8.45	-15
0.10	2.11	2.64	3.30	2.28	6.99	8.49	-14

Table 3.8. Adopted energies and strengths of the resonances contributing to $^{14}\text{N}\,(\alpha\,,\gamma)\,^{18}\text{F}$ (from Görres *et al.* 2000).

E_r(MeV)	J^π	$\omega\gamma$ (eV)
0.237	4^+	2.6×10^{-17}
0.446	1^-	46×10^{-6}
0.883	4^+	21.1×10^{-3}
1.088	3	7×10^{-3}
1.189	1^-	1.3
1.258	1^-	0.44

Table 3.9. The $^{14}\text{N}\,(\alpha\,,\gamma)\,^{18}\text{F}$ rates. They are obtained from the adoption of the resonance energies and strengths listed in Table 3.8. The direct capture component $N_A\langle\sigma v\rangle_{\text{DC}} = 1.01 \times 10^9 T_9^{-2/3}\exp(-36.023T_9^{-1/3})$ (Görres *et al.* 2000) is added to the resonant contribution.

T_9	$N_A\langle\sigma v\rangle$	T_9	$N_A\langle\sigma v\rangle$	T_9	$N_A\langle\sigma v\rangle$
0.07	4.06E$-$28	0.16	1.80E$-$13	0.60	5.56E$-$04
0.08	4.50E$-$26	0.18	5.49E$-$12	0.70	1.99E$-$03
0.09	6.56E$-$24	0.20	8.32E$-$11	0.80	6.95E$-$03
0.10	1.38E$-$21	0.25	1.05E$-$08	0.90	2.36E$-$02
0.11	1.30E$-$19	0.30	2.53E$-$07	1.00	7.17E$-$02
0.12	5.76E$-$18	0.35	2.36E$-$06	1.25	6.31E$-$01
0.13	1.41E$-$16	0.40	1.23E$-$05	1.50	2.80E$+$00
0.14	2.17E$-$15	0.45	4.35E$-$05	1.75	8.02E$+$00
0.15	2.30E$-$14	0.50	1.19E$-$04	2.00	1.74E$+$01

3.1.2.6 $^{14}\text{N}\,(\alpha\,,\gamma)\,^{18}\text{F}$

During He burning, the ^{14}N abundantly produced by the CNO cycles is converted into ^{18}O via $^{14}\text{N}(\alpha,\gamma)^{18}\text{F}(\text{e}^+\nu)^{18}\text{O}$. Following NACRE, resonances located at $E_r = 0.237, 0.435, 0.883, 1.088, 1.189$ and 1.258 MeV contribute significantly to the rate of $^{14}\text{N}(\alpha,\gamma)^{18}\text{F}$ below $T_9 = 2$. This resonance contribution has been re-investigated by Görres *et al.* (2000). Their adopted resonances and strengths are listed in Table 3.8. We use these data to calculate the reaction rates of Table 3.9. The rates in the $T_9 = 0.1 - 0.5$ range are dominated by the narrow 1^- resonance at
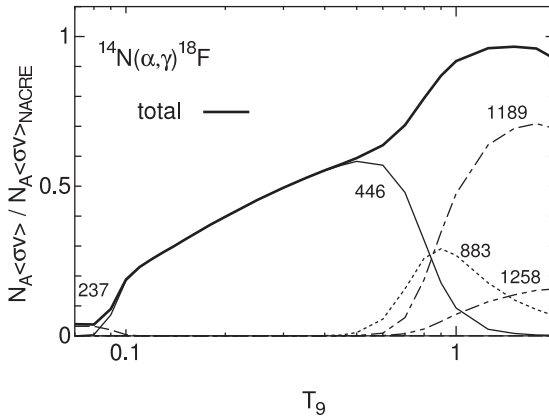
Fig. 3.10. Ratio of the rates derived from Görres *et al.* (see Table 3.9) to the adopted NACRE ones for $^{14}\text{N}(\alpha,\gamma)^{18}\text{F}$. The bold solid curve refers to the total reaction rates, while the curves labelled with a resonance energy (in keV) correspond to the contribution of individual resonances.

$E_r = 446$ keV. In contrast, the resonances above $E_r = 1.373$ MeV (see NACRE) have no impact on the rates below $T_9 = 2$, and are neglected here. The non-resonant direct capture component proposed by Görres *et al.* (2000) is added to the resonance contribution. It is influential only in the approximate $T_9 = 0.1 - 0.5$ range.

Figure 3.10 shows the ratio of the new rates to the adopted NACRE ones. The new rates are seen to be $2-5$ times smaller in the $T_9 = 0.1 - 0.5$ range. This change comes mainly from the revised energies and strengths of the lowest two resonances.

3.1.2.7 $^{18}\text{O}(\alpha,\gamma)^{22}\text{Ne}$

The burning of ^{14}N into ^{18}O (Sect. 3.1.2.6) is followed by $^{18}\text{O}(\alpha,\gamma)^{22}\text{Ne}$. This opens the possibility of neutron production by $^{22}\text{Ne}(\alpha,\text{n})^{25}\text{Mg}$, which is considered to be responsible for the s-process in massive stars.

Below $T_9 = 1$, the $^{18}\text{O}(\alpha,\gamma)^{22}\text{Ne}$ rate is dominated by the contribution of resonances. In particular, the rate at temperatures close to typical s-process ones ($T_9 \lesssim 0.3$) is dominated by resonances with energies below 490 keV. Dababneh *et al.* (2003) have conducted a post-NACRE re-investigation of the low energy resonances, and their measurements lead to the reaction rates listed in Table 3.10. These rates are slightly reduced compared to NACRE at $T_9 = 0.1 - 0.3$ (see also Fig. 3.11), and the uncertainties are appreciably reduced. For $T_9 \leq 6$, the

Table 3.10. The $^{18}\mathrm{O}(\alpha,\gamma)\,^{22}\mathrm{Ne}$ adopted rates from Dababneh *et al.* (2003) and from NACRE.

T_9	DA03	NACRE	T_9	DA03	NACRE
0.07	1.53E−24	1.53E−24	0.25	2.55E−09	2.95E−09
0.08	5.07E−23	5.08E−23	0.3	6.70E−08	7.33E−08
0.09	8.86E−22	9.20E−22	0.35	8.86E−07	9.38E−06
0.1	2.32E−20	2.73E−20	0.4	6.86E−06	7.16E−06
0.11	8.83E−19	1.09E−18	0.45	3.50E−05	3.63E−05
0.12	2.19E−17	2.72E−17	0.5	1.30E−04	1.35E−04
0.13	3.38E−16	4.20E−16	0.6	9.44E−04	9.74E−04
0.14	3.51E−15	4.36E−15	0.7	4. E−03	3.94E−03
0.15	2.65E−14	3.29E−14	0.8	1.1 E−02	1.11E−02
0.16	1.55E−13	1.92E−13	0.9	2.4 E−02	2.46E−02
0.18	2.94E−12	3.62E−12	1.	4.5 E−02	4.63E−02
0.2	3.11E−11	3.79E−11			
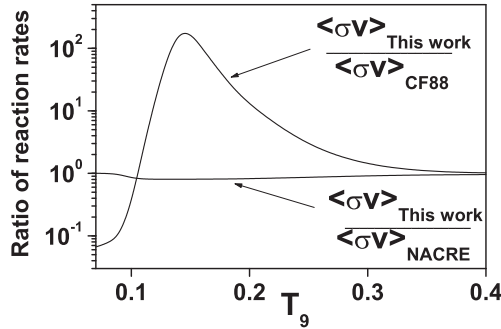
Fig. 3.11. Ratio of the Dababneh *et al.* (2003) ("This work") and NACRE adopted rates for $^{18}\mathrm{O}(\alpha,\gamma)^{22}\mathrm{Ne}$. The ratio of the Dababneh *et al.* (2003) and Caughlan & Fowler (1988) [CF88] rates is also shown. Figure from Dababneh *et al.* (2003).

Dababneh *et al.* (2003) $^{18}\mathrm{O}(\alpha,\gamma)^{22}\mathrm{Ne}$ rate can be approximated by

$$
\begin{aligned}
N_A\langle\sigma v\rangle =\ & 1.95\times10^{-13}T_9^{-3/2}\exp(-2.069/T_9) \\
& +1.248\times10^{-2}T_9^{-3/2}\exp(-4.462/T_9) \\
& +1.845\times10^{-2}T_9^{-3/2}\exp(-5.373/T_9) \\
& +5.95T_9^{-3/2}\exp(-6.285/T_9)+12.74T_9^{-3/2}\exp(-7.119/T_9) \\
& +31.19T_9^{-3/2}\exp(-7.287/T_9) \\
& +3.22\times10^5T_9^{-1/2}\exp(-21.801/T_9).
\end{aligned}
\tag{3.4}
$$

3.1.3 Other charged-particle reactions involving stable oxygen isotopes

As already emphasised in the introduction of this section, several charged-particle induced reactions which involve the stable oxygen isotopes directly or through the decay of an unstable isobar are not discussed here, as their rates have not been revised since the publication of NACRE. The reader is referred to Angulo *et al.* (1999) and to the website `http://www.astro.ulb.ac.be` for detailed information on the rates of the reactions $^{16}O\,(p\,,\gamma)\,^{17}F$, $^{14}N\,(\alpha\,,n)\,^{17}F$, $^{16}O\,(\alpha\,,\gamma)\,^{20}Ne$, $^{17}O\,(\alpha\,,n)\,^{20}Ne$, $^{18}O\,(\alpha\,,n)\,^{21}Ne$, $^{19}F\,(p\,,\alpha)\,^{16}O$ and $^{20}Ne\,(p\,,\alpha)\,^{17}F$.

3.1.4 A brief analysis of the impact of nuclear uncertainties on the stellar oxygen yields

As it is well known, the cold CNO cycles produce ^4He, while almost the entire initial C, N and O content of the H-burning zones turns into ^{14}N as a result of the relative slowness of $^{14}N\,(p\,,\gamma)\,^{15}O$ with respect to the other relevant reactions. These cycles also modify the isotopic composition of the residual oxygen.

The cold CNO cycles comprise branching points at ^{15}N, ^{17}O and ^{18}O (see Fig. 3.1). In terms of the NACRE rates, their main characteristics may be very briefly summarised as follows: (i) at $T_6 = 25$ (T_6 is the temperature expressed in 10^6 K), $^{15}N\,(p\,,\alpha)\,^{12}C$ is 1000 times faster than $^{15}N\,(p\,,\gamma)\,^{16}O$, and the CN cycle reaches equilibrium already before 10^{-3} of the initial protons have been burned; (ii) $^{17}O\,(p\,,\alpha)\,^{14}N$ and $^{17}O\,(p\,,\gamma)\,^{18}F$ are the competing ^{17}O destruction reactions and (iii) $^{18}O\,(p\,,\gamma)\,^{19}F$ and $^{18}O\,(p\,,\alpha)\,^{15}N$ compete to destroy ^{18}O. At the relevant temperatures, NACRE predicts that $^{18}O\,(p\,,\gamma)\,^{19}F$ is roughly 1000 times slower than $^{18}O\,(p\,,\alpha)\,^{15}N$. Finally, let us note that any important leakage out of the CNO cycles to ^{20}Ne is prevented by the fact that $^{19}F\,(p\,,\alpha)\,^{16}O$ is always much faster than $^{19}F\,(p\,,\gamma)\,^{20}F$. Certainly, at least some of the features mentioned above may be affected to some extent by standing uncertainties in some key rates.

The impact of the reaction rate uncertainties on the CNO yields has been analysed in the framework of parameterised astrophysics conditions or of realistic stellar models. We just illustrate some results from selected studies. Figure 3.12 shows the abundances of the O isotopes obtained under the assumption of constant H-burning density $\rho = 100$ g cm^{-3} and at two different constant temperatures, $T_6 = 25$ and 55. The curves are constructed by combining, in every possible way, the NACRE lower and upper limits of all the relevant reaction rates. One "reference" abundance calculation is also performed with all the recommended NACRE rates. The initial abundances are the solar values of Anders & Grevesse (1989). In spite of its highly simplistic nature, this analysis provides results that are of reasonable qualitative value, as testified by comparison with detailed stellar model predictions.

Figure 3.12 confirms the well-known drastic dependence of the O isotopic composition on the burning temperature. In particular, ^{17}O is produced at $T_6 \lesssim 25$, but is destroyed at higher temperatures. This has the important consequence that
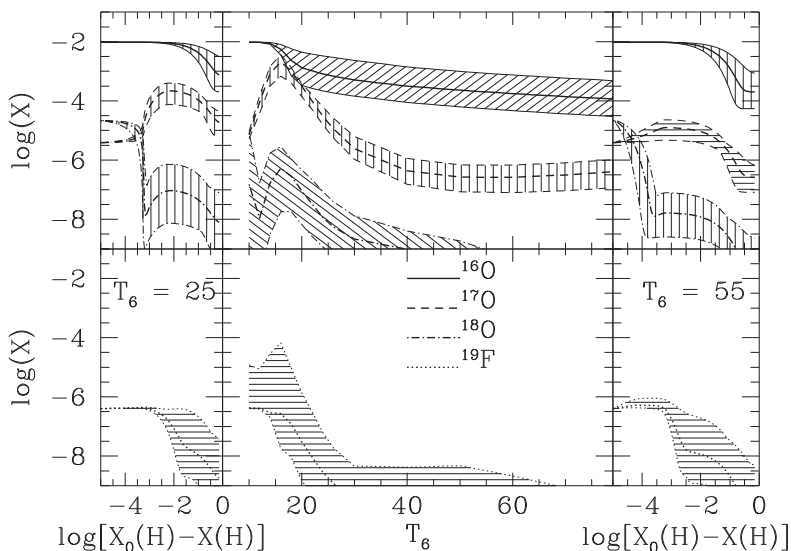
Fig. 3.12. *Left and right panels:* time variations of the mass fractions of the stable O isotopes versus the amount of hydrogen burned at constant density $\rho = 100$ g cm^{-3} and constant temperatures $T_6 = 25$ and 55. The H mass fraction is labelled $X(H)$, with the subscript 0 referring to its initial value. Data for ^{19}F are included. *Middle panel:* mass fractions of the same nuclides at H exhaustion $[X(H)=10^{-5}]$ as a function of T_6. The shaded areas delineate the uncertainties resulting from the NACRE reaction rates. Figure from Arnould *et al.* (2003).

the amount of ^{17}O emerging from the CNO cycles, and eventually transported to the stellar surface, is a steep function of the stellar mass. This conclusion could get some support from the observation of a large spread in the oxygen isotopic ratios at the surface of red giant stars of somewhat different masses. Figure 3.12 also demonstrates that the oxygen isotopic composition cannot as yet be fully reliably predicted at a given temperature as a result of the cumulative uncertainties associated with the different production and destruction rates. This situation prevents a fully meaningful comparison to be made with spectroscopic data, and even more so, any firm conclusion to be drawn from models for the chemical evolution of galaxies. Figure 3.12 is complemented with Table 3.11 which illustrates uncertainties of purely nuclear origins associated to the operation of the CNO cycles in various detailed model stars at different stages of their evolution. Of course, the results displayed in Figure 3.12 and in Table 3.11 must be updated with the adoption of the revised rates discussed above. The conclusions are not likely to be drastically different from those mentioned above.

An extended sensitivity analysis of the nova properties and yields to reaction rate uncertainties has also been conducted over the last decade (Starrfield *et al.* 2009, and references therein). These explosions involve the hot pp, CNO and NeNa or MgAl chains of H burning, in which proton captures by unstable nuclides
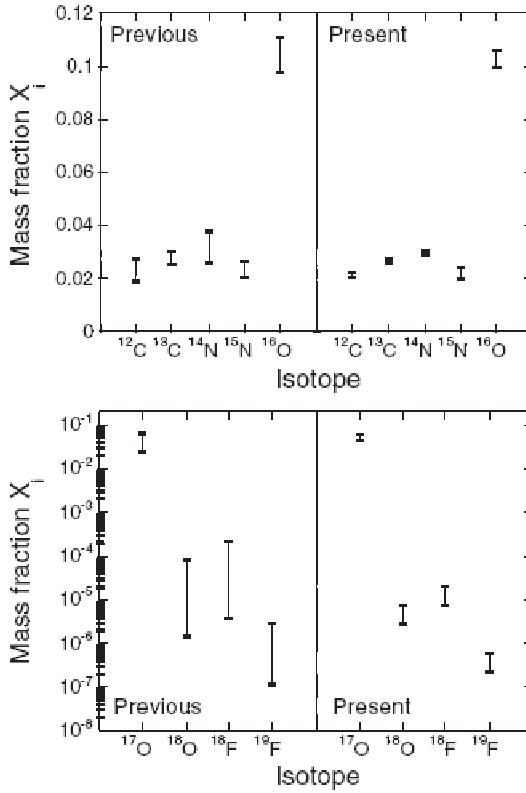
Fig. 3.13. Variations of the predicted C, N and O isotopic mass fractions in the ejecta of a specific nova model. The abundances in the left panels result from the use of the recommended NACRE $^{17}O\,(p\,,\gamma)\,^{18}F$ and $^{17}O\,(p\,,\alpha)\,^{14}N$ rates. Those on the right are predicted with the rates of Fox *et al.* (2004). Figure adopted from Fox *et al.* (2004).

compete with β-decays. The hot CNO also involves reactions making up the cold mode (see Fig. 3.1) such as $^{17}O\,(p\,,\gamma)\,^{18}F$, $^{17}O\,(p\,,\alpha)\,^{14}N$ and $^{18}F\,(p\,,\alpha)\,^{15}O$. Figure 3.13 shows the changes in the abundances of the oxygen isotopes from a specific nova model that result from the use of the ^{17}O proton capture rates from Fox *et al.* (2004) instead of the NACRE values (see Sect. 3.1.2.2). This may not be, however, the last word about the ^{17}O nova yields, since using their own rates Chafa *et al.* (2005) obtain abundances closer to those derived using the NACRE rates than to those derived using Fox *et al.* (2004) rates.

3.1.5   Neutron captures involving oxygen isotopes

Stellar radiative neutron capture rates by ^{15}N, ^{16}O and ^{18}O can be found in the compilation by Bao *et al.* (2000). For ^{17}O, only an estimate by Wagoner (1969) is

Table 3.11. Oxygen isotopic composition at the surface of stars of initial solar content and with different masses M after convective transport of part of the central H-burning ashes. The isotopic ratios and the quoted uncertainties result from the use of the recommended NACRE rates of H burning through the CNO mode, and of their lower and upper limits provided by NACRE. Table from Stoesz & Herwig (2003).

$M(M_\odot)$	$^{16}O/^{17}O$	$^{16}O/^{18}O$
1.0	2410^{+13}_{-16}	469^{+46}_{-12}
1.5	1260^{+180}_{-130}	545^{+70}_{-20}
2.0	115^{+38}_{-20}	565^{+95}_{-20}
Initial	2465	442

available. As shown by Rayet & Hashimoto (2000), ^{16}O can become an important neutron poison in stars with low enough metallicity where it reduces the efficiency of the s-process.

3.1.6 Conclusions

Since the NACRE compilation, much effort has been put into the improvement of our knowledge of the rates of a variety of reactions involved in the stellar production or destruction of the stable oxygen isotopes. In spite of some progress, nuclear uncertainties remain which add up to those of purely astrophysical origin. To some extent, this situation hampers both a fully reliable comparison with relevant spectroscopic information and a quantitative evaluation of the merits of the different model stars.

3.2 Stellar nucleosynthesis

3.2.1 Stellar evolution in a nutshell

During the longest part of their lives, stars are in hydrostatic equilibrium. A star element in equilibrium undergoes a gravitational force balanced by a pressure gradient. In a normal star, pressure depends on temperature, and therefore the existence of a pressure gradient implies the buildup of a temperature gradient. The higher the temperature, the greater the quantity of energy contained per unit volume in the radiation field. Since the central parts are hotter than the outer ones due to the temperature gradient resulting from hydrostatic equilibrium, energy flows outwards from the inner parts of the star, and thus the star loses energy continually. Interestingly, the more efficiently the energy is evacuated from the central regions where it is produced, the hotter these central regions become! Indeed, if the central regions lose energy, the temperature gradient will become weaker and they will slowly contract, becoming warmer! Stars (made of perfect gas) are thus systems with a global negative specific heat.

Stars evolve because they continually lose energy to maintain hydrostatic equilibrium or, in other words, to balance the gravitational force. Note that these

logical deductions do not involve any particular source of energy. Luminosity is a direct consequence of hydrostatic equilibrium and not of the nuclear reactions that occur in the stellar interior. Of course nuclear reactions are important and we are going to see how below.

3.2.1.1   The main energy reservoirs

The energy which flows from the stellar interior and is lost at the surface has of course to be extracted in one way or another from the stellar material. These mechanisms of energy extraction are responsible for the evolution of the star.

There are actually two main sources of energy in a star. First, a star can extract energy from the gravitational potential through a global (macroscopic) contraction. Second, a star can also release energy by the thermonuclear reactions which take place in its central regions where the temperature and density are adequate for such processes to occur (microscopic contractions).

These two processes for producing energy have different characteristic time-scales. If the Sun had only the gravitational energy source, its lifetime would be of the order of a few tens of million years, instead a simple estimate gives a lifetime of ten billion years when nuclear sources are taken into account. Only the latter value is in agreement with what we know about the past history of the Earth and the apparition of life on its surface. Therefore the presence of the nuclear source is important not to explain the luminosity of stars (stars could shine even without hosting nuclear active regions), but to explain why they can shine *for very long periods of time.* Besides this energetic aspect, nuclear reactions are of course the processes through which chemical elements are synthesised in stellar interiors, and play a key role in the long chain of events that occur from the Big Bang to the apparition of living bodies.

The evolution of a star can be viewed as a succession of phases whereby the energy is mainly produced by either nuclear reactions or contraction. When the star has burned all the nuclear fuel available in its central regions, in order to maintain the luminosity required by the hydrostatic equilibrium, it has to produce energy via contraction until new central conditions are reached that are adequate for the ignition of new nuclear reactions. This succession of contraction periods will increase both the central temperature and density as can be seen in Figure 3.14. At a given point (which depends mainly on the initial mass of the star), the central regions can become sensitive to degeneracy effects.

3.2.1.2   Perfect gas and degenerate gas

Let us recall that degeneracy pressure results from Pauli Exclusion Principle: only two fermions of spin one-half, *e.g.* electrons, neutrons or neutrinos, may occupy the same spatial quantum state. Two particles are in two different quantum states if the product of their differences in position Δx and momentum Δp is superior to the Planck constant. An increase of the density restricts the domain for the positions and thus reduces Δx. The Exclusion Principle implies therefore that certain particles will acquire very large impulses, much greater than they would
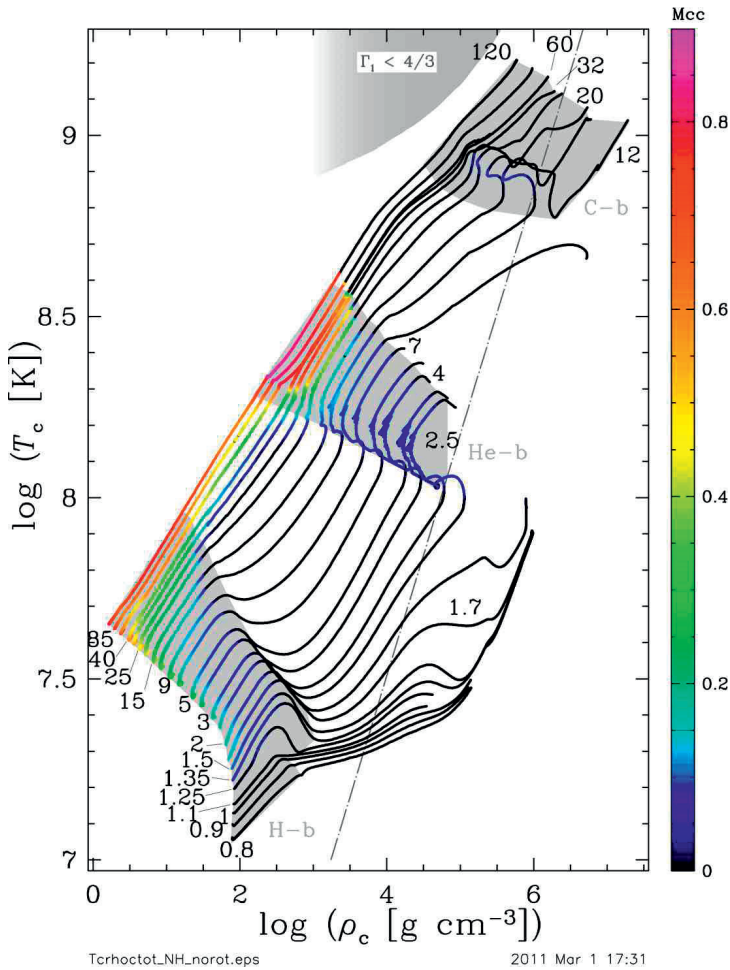
Fig. 3.14. Evolutionary tracks for rotating stellar models at a metallicity $Z = 0.014$ in the log T_c–log ρ_c plane. Grey zones along the tracks indicate the positions of stars during the core H-, He- and C-burning phases. The region of pair instability is indicated by $\Gamma_1 < 4/3$. The line where the Fermi energy of the electron is equal 2 kT is indicated (long dashed-dotted line). The colours specify the mass fraction of the convective cores. Figure from Ekström *et al.* (2011).

by thermal agitation. These particles with large velocities exert a pressure that is not thermal in origin and depends only on density.

Depending on whether the stellar material is degenerate or not, the two main sources of energy, contraction and nuclear reactions, have very different behaviours. In non-degenerate conditions, nuclear reactions are stable and contraction implies

an increase of the central temperature. In degenerate conditions, nuclear reactions are explosive and contraction may produce a cooling of the medium.

Let us first consider a uniform contraction of a mass M. For such case a variation in radius ΔR corresponds to variations in pressure ΔP and density $\Delta \rho$ so that we have the following relations:

$$\frac{\Delta P}{P} = -4\frac{\Delta R}{R}, \quad \text{and} \quad \frac{\Delta \rho}{\rho} = -3\frac{\Delta R}{R}.$$

The first equality is deduced from the hydrostatic equilibrium equation and the second from the continuity equation. From these two relations, we can write

$$\Delta \ln P = \frac{4}{3}\Delta \ln \rho.$$

Let us now express the equation of state as

$$\Delta \ln \rho = \alpha\Delta \ln P - \delta\Delta \ln T,$$

where α and δ are defined by $\alpha = \left(\frac{\partial \ln \rho}{\partial \ln P}\right)_{T,\mu}$ and $\delta = -\left(\frac{\partial \ln \rho}{\partial \ln T}\right)_{P,\mu}$, and where μ, the mean molecular weight, is supposed to remain constant. From these two relations, by eliminating ΔP, one obtains the following relation between a variation in log T and log ρ:

$$\Delta \ln T = \left(\frac{4\alpha - 3}{3\delta}\right)\Delta \ln \rho. \tag{3.5}$$

For a perfect gas law we have $\alpha = \delta = 1$. Therefore an increase of, for instance, 3% in density implies an increases of 1% in temperature.

On the other hand, if the gas is completely degenerate and non-relativistic, the relation between the degenerate electronic gas pressure and density is given by

$$P \propto \rho^{5/3}. \tag{3.6}$$

In the log T_c versus log ρ_c diagram, where T_c is the central temperature and ρ_c is the central density, the region where the perfect gas electron pressure equals that of the degenerate gas is a line with slope 2/3. The track of a slowly contracting star in the log T_c–log ρ_c diagram is a straight line with slope 1/3 (see Eq. (3.5) with $\alpha = \delta = 1$). Thus eventually a star will cross the frontier between the perfect and degenerate gas. For a degenerate, non-relativistic gas, $\alpha = 3/5$ and $\delta = 0$. In this case, Equation (3.5) is no longer valid, but if during the course of evolution when the central conditions shift from the non-degenerate to the degenerate regime α becomes less than 3/4 before δ is equal to zero, a contraction can then produce cooling! This can be understood as due to the fact that, in order to allow electrons to occupy still higher energy states, some energy has to be extracted from the non-degenerate nuclei which, as a consequence, cool down.

3.2.1.3   Evolution under non-degenerate and degenerate conditions

Let us first consider non-degenerate conditions. Let us imagine that for whatever reason an excess of energy is produced in the centre of the star. This will produce the heating of matter. When the perfect gas law prevails, an increase of temperature will produce an increase of pressure and therefore an expansion. This implies an increase of the potential energy and, through the virial theorem, a decrease of the internal energy. Therefore the temperature decreases as well as the nuclear reaction rates. We see that, in perfect gas conditions, there is a negative feedback which stops the runaway. The nuclear reactions are stable when the perfect gas law prevails.

When matter is degenerate, the behaviour is quite different. The excess of energy produced at the centre, which implies a temperature increase, no longer provokes an expansion, since there is no longer a coupling between pressure and temperature. The nuclear reaction rates increase, new excesses of energy are produced, a flash or an explosion occurs. The nuclear reactions are unstable in degenerate matter. This process is responsible for the explosion of Type Ia supernovae. It triggers also what is called the helium flash at the tip of the red giant branch (RGB) for stars with masses below about 1.8 $M_\odot$ (at solar metallicity).

3.2.1.4   The five mass ranges

The different behaviours of both contraction and nuclear reaction rates in perfect gas and degenerate regimes are the main causes for the variety of evolution paths followed by stars of different initial masses. Schematically five mass ranges can be considered (Maeder 2009).

(1) *Substellar objects.* This range corresponds to objects that during their contraction phase enter the degenerate regime before hydrogen ignition. Further contraction cools the central regions as explained above, and thus these central regions never reach the appropriate conditions for hydrogen ignition. These objects become the so-called brown dwarfs. According to Baraffe (2002) the stellar/substellar transition occurs for a mass around 0.075 $M_\odot$. Note that in objects more massive than 0.012 $M_\odot$ (Chabrier *et al.* 2000; Saumon *et al.* 1996) deuterium burning occurs.

(2) *The very low-mass stars.* This range corresponds to stars which go only through the hydrogen-burning phase (progenitors of helium white dwarfs). These stars have initial masses between 0.075 and 0.5 $M_\odot$. Note that single stars in this mass range have main-sequence lifetimes greater than the age of the Universe. Thus the observed helium white dwarfs probably originate from more massive progenitors in close binary systems (Benvenuto & De Vito 2004) and not from single low-mass stars.

(3) *The low-mass stars.* Stars with masses between 0.5 and 1.7–2.5 $M_\odot$ evolve only through the hydrogen- and helium-burning phase (progenitors of carbon-oxygen white dwarfs). Helium ignition occurs in degenerate conditions. This

produces what is called a helium flash. This process is not destructive for the star. It releases in a short time sufficient energy to remove degeneracy in the central regions. After the helium-flash, core helium burning continues smoothly in non-degenerate conditions until the production of a carbon-oxygen white dwarf in the central region. The envelope is ejected by mass loss occurring along the red giant and asymptotic giant branches.

(4) *The intermediate-mass stars.* Stars in this range ignite helium in non-degenerate conditions (no helium flash). Their end stellar state is either carbon-oxygen white dwarfs (*i.e.* same as the low-mass stars) or oxygen-neon white dwarfs, if carbon burning can occur in the core. They have initial masses between 0.5 and about 8 $M_\odot$. The upper limit is still quite difficult to obtain from models due to uncertainties in the sizes of the convective cores and mass loss (Siess 2007). There may be some other possible final fates such as the complete disruption of the star due to carbon burning in degenerate conditions or production of a neutron star by collapse of the core before neon ignition due to electron captures (Maeder 2009). The value of 8 $M_\odot$ quoted here is obtained from observations of white dwarfs in stellar clusters which allow one to deduce the initial masses of the stars having given birth to the white dwarfs. Relations between the mass of the white dwarf and the initial mass of the progenitor can be derived, in particular the initial mass of stars giving birth to white dwarfs just below the Chandrasekhar mass. Let us note that this method is not free from any theoretical input since the deduction of the initial mass of the white dwarf progenitors is deduced from stellar models (Kalirai *et al.* 2008)!

(5) *Massive stars.* This range corresponds to all stars that can evolve beyond the carbon-burning phase until the formation of an iron core (progenitors of neutron stars and black holes), or until the pair instability is encountered (in general during oxygen burning) and the star explodes (Heger *et al.* 2003). Generally massive stars have initial masses greater than about 8 $M_\odot$ (Maeder & Meynet 1989). These stars are the main source of oxygen (^{16}O) in the Universe.

Most of this oxygen is produced during the core He-burning phase (non-explosive nucleosynthesis), and in general the explosive nucleosynthesis does not affect significantly the yields of oxygen isotopes (see Sect. 3.2.15).

Classical novae occur in binary systems consisting of a carbon-oxygen or oxygen-neon-magnesium white dwarf accreting hydrogen-rich matter from a main-sequence companion. Sporadically, a thermonuclear runaway leads to the synthesis of new isotopes and to the ejection of material from the surface of the accreting white dwarf. Concerning the oxygen isotopes, hydrodynamical models of novae show that these objects do not contribute to the synthesis of ^{16}O and ^{18}O, but could contribute in making ^{17}O (José *et al.* 1998; Starrfield *et al.* 2009, 1974).

Table 3.12. Model characteristics. The star ages in Myr at the end of the first three nuclear phases are indicated. For the last three, the duration of the considered phase is indicated in years. The third column gives the actual mass of the star at the considered evolutionary stage. The central temperature and density are given in columns 4 and 5. The quantities q_{cc} and q_{env} correspond to the fraction of the mass encompassed respectively in the convective core and in the convective envelope. The last two columns indicate the ratios of nitrogen to carbon and of nitrogen to oxygen at the surface (ratios of mass fractions).

Phase	Age [Myr]	Mass $M_\odot$	$\log T_c$	$\log \rho_c$	q_{cc}	q_{env}	N/C	N/O
End H	6.60	24.20	7.875	1.518	0.090	0.000	0.31	0.11
End He	7.30	16.17	8.539	3.554	0.013	0.000	16.2	2.21
End C	7.32	16.00	9.127	6.563	0.000	0.464	19.1	2.38
End Ne	+50.4y	16.00	9.218	6.594	0.000	0.464	19.1	2.38
End O	+0.3 y	16.00	9.411	7.374	0.000	0.166	19.1	2.38
End Si	+0.1 y	16.00	9.787	8.638	0.001	0.062	19.1	2.38

3.2.2   Massive stars

3.2.2.1   A reference case: a 25 $M_\odot$ star

We have plotted in Figures 3.15 to 3.17 the chemical structure of a 25 $M_\odot$ star at various stages during its evolution (Hirschi *et al.* 2004). The metallicity is $Z = 0.02$ and the effects of rotation are not included. Several model characteristics are presented in Table 3.12.

Abundance profiles at the end of the main sequence

During the main-sequence phase, the abundance of ^{16}O is decreased in the central region as a consequence of the CNO cycle. At the end of the core H-burning phase, its abundance in the central region is about a factor of 30 lower than the initial value (see top panel of Fig. 3.15). In the outer part of the star (for $M_r/M_\odot > 15$), its abundance has not been changed. In the zone comprised between ~ 8 $M_\odot$ and 15 $M_\odot$, the abundance of oxygen increases in steps from the central value to that in the envelope. These steps result from various intermediate convective zones which appear above the core during the main-sequence phase. The situation for ^{17}O is somewhat different. In the same manner as ^{16}O, ^{17}O is destroyed in the central region and has kept its initial abundance in the envelope. However it is produced in the region comprised between 11 and 15 $M_\odot$. This arises from the fact that in the CNO cycle, this isotope is produced at temperatures below about 25 million degrees while it is destroyed at higher temperatures; hence its maximum abundance in regions of partial H burning. The last stable isotope of oxygen ^{18}O
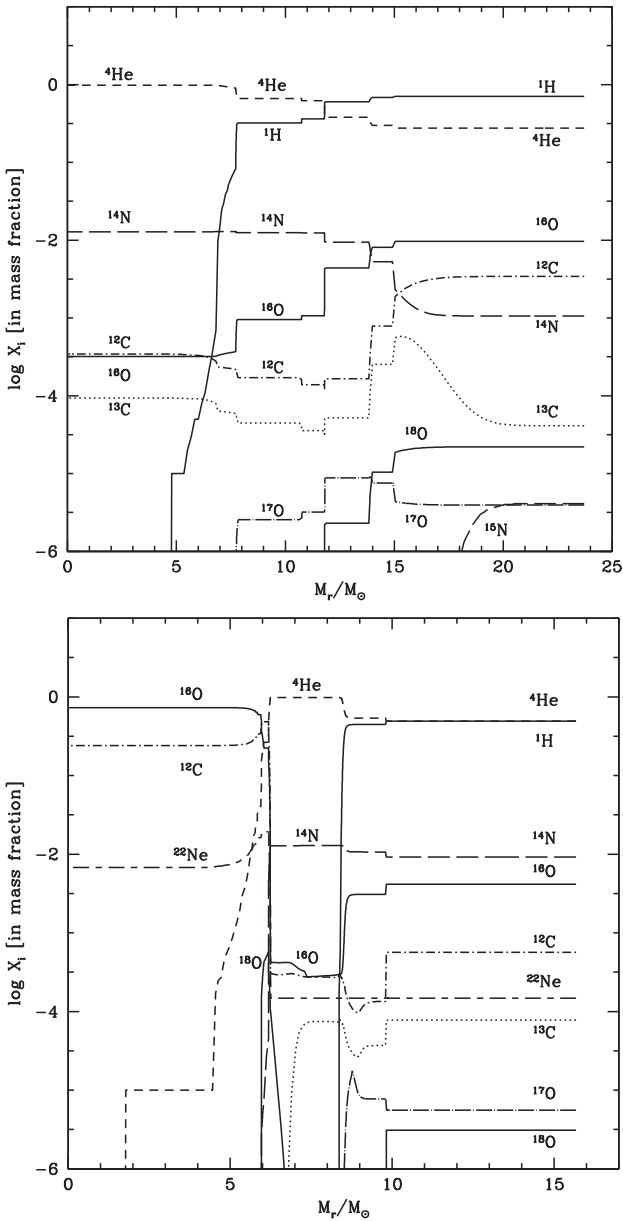
Fig. 3.15. Variations of the abundances (logarithm of the mass fraction) of some elements as a function of the mass (in solar units) inside a $Z = 0.02$ stellar model with an initial mass of 25 $M_\odot$. *Top:* at the end of the core H-burning phase. At this stage, the surface abundances have kept their initial values. *Bottom:* same as top figure but at the end of the core He-burning phase. The total mass is now 16 $M_\odot$ because of the effect of stellar winds.
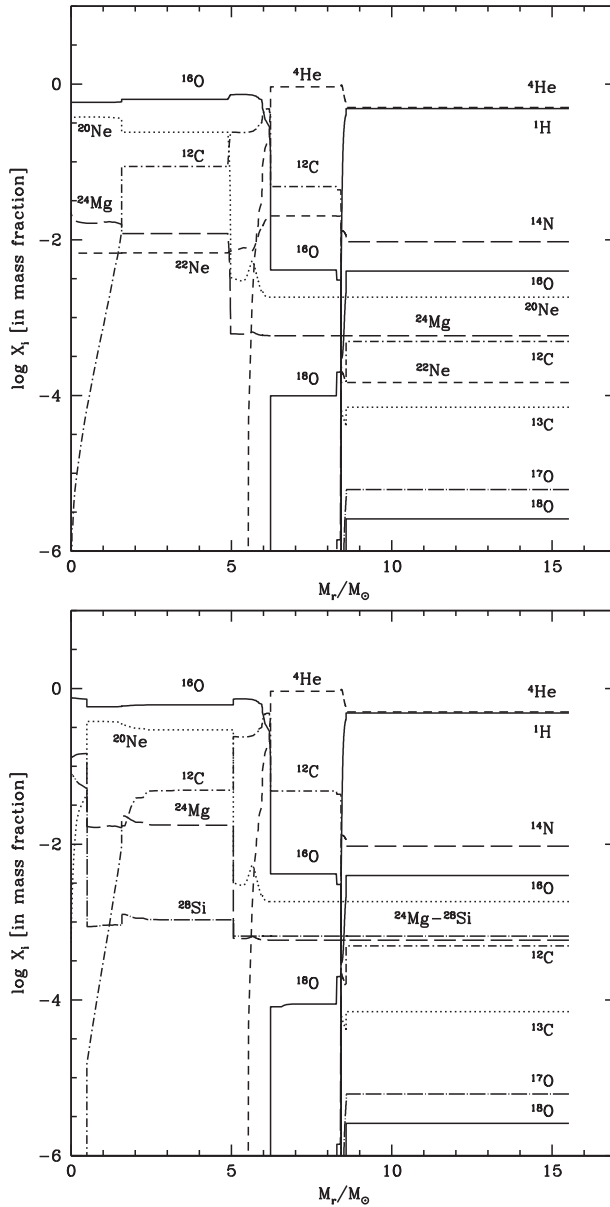
Fig. 3.16. *Top*: same as in Figure 3.15 at the end of the core C-burning phase. *Bottom*: same as in Figure 3.15 at the end of the core Ne-photodisintegration phase.

is completely destroyed in the central regions. As for ^{16}O and in contrast to ^{17}O, there is no region in the star where this element has been produced at this stage of the evolution.
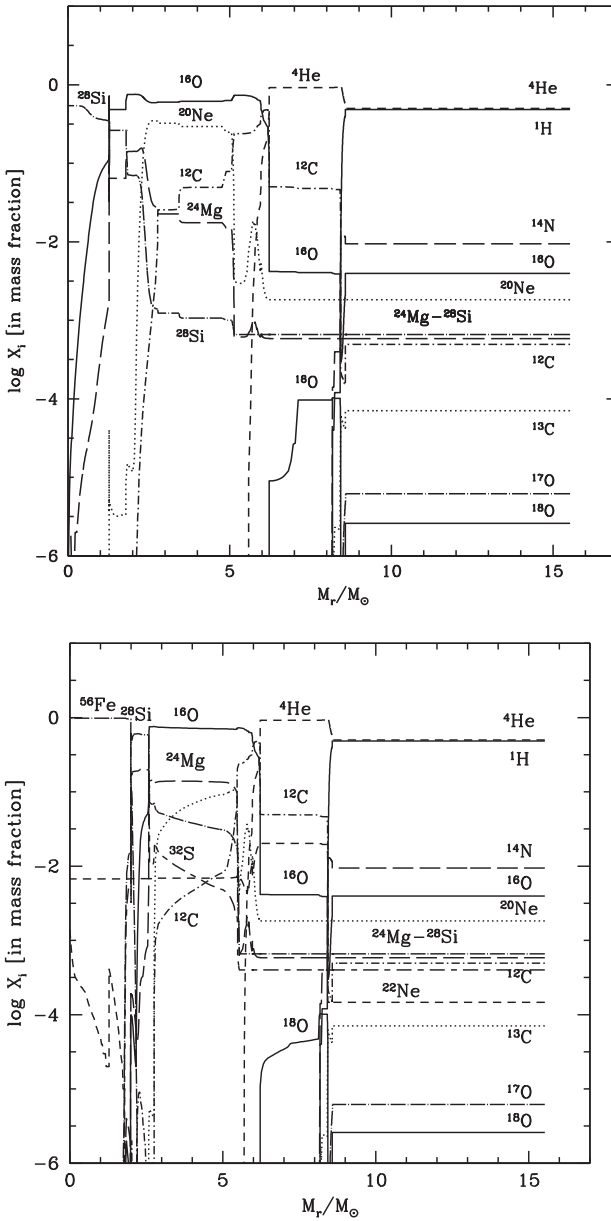
Fig. 3.17. *Top*: same as in Figure 3.15 at the end of the core O-burning phase. *Bottom*: same as in Figure 3.15 at the end of the core Si-burning phase.

Thus at the end of the main sequence phase, the ^{16}O content of the star has decreased. Initially the integrated mass of ^{16}O in the star was about 0.24 $M_\odot$.

At the end of the main sequence phase, it is equal to 0.11 $M_\odot$. A very small part, 0.008 $M_\odot$, has been lost by stellar wind. Most of the decrease of the ^{16}O abundance is due to its transformation into ^{14}N through the CNO cycle. The integrated mass of ^{17}O has also decreased. The decrease is however much weaker than for ^{16}O going down from 10^{-4} to 8×10^{-5} $M_\odot$. The integrated mass of ^{18}O has decreased from 5.5×10^{-4} to 2.2×10^{-4} $M_\odot$.

Abundance profiles at the end of the core He-burning phase

The core He-burning phase is the main phase of ^{16}O production.

The chemical structure of the star at the end of the core He-burning phase is shown in the bottom panel of Figure 3.15. The core He-burning phase has a lifetime of 0.7 Myr. This corresponds to 10.6% of the core H-burning phase lifetime. In the central region, helium has been transformed into ^{12}C and ^{16}O through the 3α reaction followed by ^{12}C$(\alpha, \gamma)^{16}$O. Outside the core, the abundance of ^{16}O is still inferior to its initial value. In the H-burning shell, this is of course a consequence of the CNO cycle. Two zones can be recognised in this region. In the inner one, which extends from 6 to 8.3 $M_\odot$, complete H burning occurs. In the outer one, which extends from 8.3 to 9.7 $M_\odot$, H burning is only partial and a much higher ^{16}O abundance is obtained. Outside the H-burning shell, there is a decrease of the ^{16}O abundance by more than a factor of 2 with respect to the initial value due to dredge-up. The ^{17}O isotope is completely destroyed in the core. It is also destroyed in the inner H-burning shell and produced in small amounts in the outer H-burning shell. At the surface, the abundance of ^{17}O has increased from 4 to 6×10^{-6} due to dredge-up. At the very beginning of the core He-burning phase, the chain of reactions

$$^{14}\text{N}(\alpha, \gamma)^{18}\text{F}(\beta, \nu)^{18}\text{O}(\alpha, \gamma)^{22}\text{Ne}$$
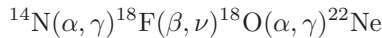
transforms ^{14}N into ^{22}Ne via ^{18}O. In the nascent He-burning shell, the transformation is not complete producing a steep rise in ^{18}O. In the whole region processed by H-burning, ^{18}O is destroyed. At the surface, due to dredge-up, the ^{18}O abundance has decreased from 22 to 3×10^{-6}.

At the end of this phase, the integrated mass of ^{16}O in the star reaches a value of 4.4 $M_\odot$. This means that the mass of oxygen has increased by more than a factor 18 with respect to its initial value. For ^{17}O the situation has not drastically changed with respect the one reached at the end of the core H-burning phase, while for ^{18}O, despite the peak in the He-burning shell, the integrated mass has decreased.

Abundance profiles at the end of the core C-burning phase

At the end of the C-burning phase (see top panel of Fig. 3.16), the abundance of ^{16}O in the inner 1.5 $M_\odot$ of the star has slightly decreased. The core remains radiative during the C-burning phase as a consequence of the high neutrino flux. Indeed the neutrinos are very efficient in evacuating the energy produced in the

core, and prevent the apparition of a convective zone in the central region. Between 1.5 and 5 $M_\odot$, one can see the abundances resulting from the activity of the C-burning shell. Again the abundance of ^{16}O is slightly decreased with respect to the value reached at the end of the core He-burning phase. Between 5 and 6 $M_\odot$, one can see a region where the abundances of ^{16}O and ^{12}C have remained unchanged since the end of the core He-burning phase. The activity of the He-burning reaction extends from 6 to about 8.5 $M_\odot$. In that region, important changes have taken place: a small quantity of helium has been transformed into ^{12}C and ^{16}O, while ^{14}N has been transformed partly in ^{18}O and partly in ^{22}Ne. Between this He-burning zone and the envelope, there is a very thin H-burning shell characterised by a decrease of ^{12}C and ^{16}O abundances and an increase of the ^{14}N abundance. The abundances in the envelope do not show great changes with respect to the situation reached at the end of the core He-burning phase.

At the end of this phase, the integrated mass of ^{16}O is 3.9 $M_\odot$, slightly less than at the end of the previous phase. This is mainly due to the destruction of ^{16}O in the central region and, to a lesser extent, to mass loss (see below for more details). The integrated mass of ^{17}O has not changed significantly, while that of ^{18}O has nearly doubled due to nuclear processes in the He-burning shell.

Abundance profiles at the end of the Ne-photodisintegration phase

The abundances at the end of the Ne-photodisintegration phase are shown in the bottom panel of Figure 3.16. The abundances of all the oxygen isotopes are little affected, and therefore, their integrated masses are not significantly changed with respect to the values obtained at the end of the core C-burning phase.

Abundance profiles at the end of the core O-burning phase

The abundance profiles at the end of the core O-burning phase are shown in the top panel of Figure 3.17. Core O-burning has depleted oxygen in the inner 1 $M_\odot$. Between 1 and 5 $M_\odot$, the abundance profiles result from various shell burnings. Going from the centre outwards (inside out), results from the nuclear activity of the O-, Ne- and C-burning shells can be seen. Beyond 5 $M_\odot$, no significant changes have occurred. The only noticeable ones are the abundance decreases of ^{18}O and ^{17}O between 6.2 and 7 $M_\odot$. This is due to the increased temperature in this region when the central parts of the star contract.

As a result of its destruction in the core, the integrated mass of ^{16}O has been lowered from 3.9 to 3.1 $M_\odot$. The mass of ^{17}O has not changed significantly, while that of ^{18}O continues to decrease.

Abundance profiles at the end of the core Si-burning phase

They are shown in the bottom panel of Figure 3.17. ^{16}O has now been completely destroyed in the inner 2.5 $M_\odot$. Beyond these 2.5 $M_\odot$, the abundances of all the oxygen isotopes are unchanged.
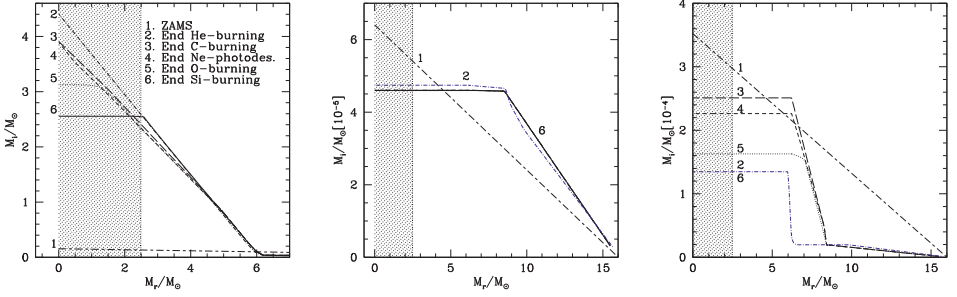
Fig. 3.18. *Left:* ^{16}O mass ejected at a specific evolutionary stage if the whole mass above M_r were ejected. The ordinate corresponds to the integration of the mass of ^{16}O performed from the value of M_r indicated on the abscissas up to the surface. This means that the ordinate corresponding to the abscissa 0 is equal to the total quantity of ^{16}O inside the star at the corresponding stage. Note that for all the models considered here the actual total mass of the star does not change much and is around 16 $M_\odot$ (see text). This implies that the variations of the integrated quantities are due to nuclear processes occurring in the star and not to loss of mass through the effect of stellar winds. The inner 2.5 $M_\odot$ are hatched to indicate that this part of the star will probably remain locked in a compact remnant (neutron star or black hole). *Middle:* same as left panel for ^{17}O. Note that curves 3, 4 and 5 are identical to curve 6. *Right:* same as left panel for ^{18}O.

At this stage the total mass of ^{16}O in the star is 2.6 $M_\odot$, and that of ^{17}O and of ^{18}O are respectively of 46×10^{-6} and 12×10^{-5} $M_\odot$.

So, when are the oxygen isotopes produced?

In the left panel of Figure 3.18 we show the total quantity of ^{16}O which would be ejected if, at a specific evolutionary stage, the whole mass above M_r were ejected. For instance, if at the end of the core helium-burning phase the whole envelope above 2.5 $M_\odot$ were ejected, then a total quantity of about 2.6 $M_\odot$ of oxygen would be ejected. In other words the quantity plotted on the vertical axis is obtained using the expression

$$M_i(M_r) = \int_{M_r}^{M} X_i(m_r) \mathrm{d}m_r,$$

with M being the actual star mass at the evolutionary stage under consideration and $X_i(m_r)$ the oxygen mass fraction in the model at that stage and at the Lagrangian mass coordinate, m_r. Note that the curve labelled ZAMS is obtained simply by using for $X_i(m_r)$ a constant value equal to the initial abundance of the considered isotope. We performed the integration only over the central 16 $M_\odot$ of our 25 $M_\odot$ model. The value of 16 $M_\odot$ corresponds to the final mass of the star at the pre-supernova stage. This mass results from the effects of stellar winds occurring during the whole stellar lifetime. Restricting the integration over 16 $M_\odot$

allows the comparison of quantities integrated over the same part of the star at all the evolutionary stages.

Two interesting features are brought to light from such a plot: first, it shows the effect of the different nuclear phases on the integrated masses of ^{16}O; second, it allows one to see how the ejected mass would change for different mass cuts (in that case curve number 6 corresponding to the pre-supernova stage must be considered).

Looking at the left panel of Figure 3.18, a few interesting points may be underlined:

- The mass of ^{16}O in the layers outside the hatched zone, *i.e.* outside the zone which may remain locked in the stellar remnant, does not change much after the end of the core C-burning stage. Even after the core He-burning phase, the mass of ^{16}O in this region is almost the one obtained at the pre-supernova stage.

- One notes that the region which will contribute to the ^{16}O production is comprised between 2.5 and 6 $M_\odot$.

- If the cutoff between the remnant and ejecta masses were smaller than the mass considered here (2.5 $M_\odot$), the ^{16}O yields would be little affected. This is because in these inner regions ^{16}O is mostly destroyed.

The integrated masses of ^{17}O and ^{18}O are shown in the middle and right panels of Figure 3.18. We can note the following points.

- At the end of the core He-burning phase, the star already has the ^{17}O mass which will be present at the pre-supernova stage. This is not the case for ^{18}O.

- ^{17}O is produced in the H-burning zones (outside $M_r = 8.5\ M_\odot$).

- ^{18}O is created in the partial He-burning regions. A slight excess of this isotope is observed in the region around 6 $M_\odot$ at the end of core C-burning phase, but this excess of ^{18}O is then destroyed during the subsequent evolutionary stages.

- At the pre-supernova stage, the masses for both isotopes are smaller than those initially present.

Before discussing how the present results vary as a function of initial mass, metallicity and rotation, and how other physical ingredients may also impact them, let us just say a few words about the effect of mass loss on this particular model. As can be seen from Table 3.12, most of the mass loss occurs during the core He-burning stage (loss of 8 $M_\odot$). During that stage, due to dredge-up, matter
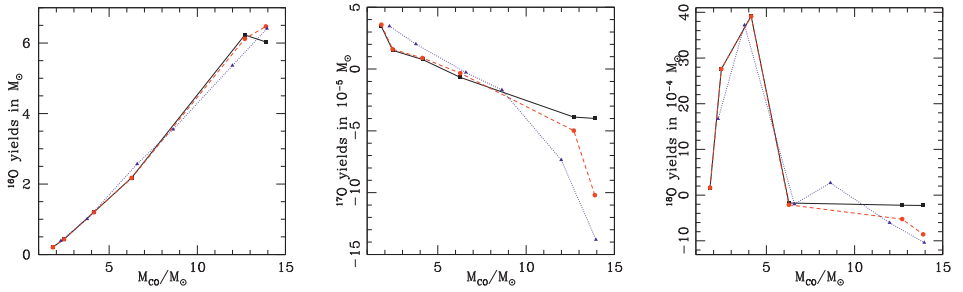
Fig. 3.19. *Left:* the solid lines shows the yields of ^{16}O in the ejecta of the supernova as a function of the CO core mass (models from Hirschi *et al.* 2004). The initial masses corresponding to each dot from left to right are 12, 15, 20, 25, 40 and 60 $M_\odot$ respectively (solar metallicity, non-rotating models). The dashed line shows the complete yields, *i.e.* the yields of the supernova and of the stellar winds. The dotted line shows the complete yields for rotating models with $v_{\mathrm{ini}} = 300$ km s^{-1}. *Middle:* same as left panel for ^{17}O. *Right:* same as left panel for ^{18}O.

is depleted in ^{16}O and ^{18}O but slightly enriched in ^{17}O. For ^{16}O the contribution of the wind is completely negligible. Indeed the wind yield[3] for this isotope, namely -1.07×10^{-2} $M_\odot$, has an absolute value which amounts to only 5×10^{-3} of the yield in the supernova ejecta (2.18 $M_\odot$). For the other two isotopes, wind and supernova yields are of the same order (^{17}O: wind $+3.4 \times 10^{-6}$, supernova -6.7×10^{-6}; ^{18}O: wind -3.88×10^{-5}, supernova -17.4×10^{-5} in solar masses). Thus in that case winds do affect the final total yield (wind and supernova), but of course it remains to be seen to which extent a 25 $M_\odot$ star contributes to the destruction or production of these two isotopes. As we shall see this is probably not the case.

3.2.2.2 Effects of mass, metallicity, rotation, etc.

Mass. How does the situation change when the initial mass varies? For masses lower than 25 $M_\odot$, at standard metallicity ($Z = 0.02$), the main thing affecting the ^{16}O yields is the mass of the CO core which decreases when the initial mass decreases. In the left panel of Figure 3.19, we show the ^{16}O yields as a function of the mass of the CO core at the pre-supernova stage[4]. We see that at least for $M \leq 25$ $M_\odot$ the relation is not far from linear. For the larger masses, the situation is less clear due to the action of the stellar winds which may peel off the CO core,

---

[3]The yield of an element is the difference between its mass in the ejecta at the time of the ejection and its mass initially present in the same portion of the star. Yields may be negative when the element is destroyed by the star.

[4]Note that the mass of the CO core at the end of the core C-burning stage is already very close to the value obtained at the pre-supernova stage.

and thus decrease the quantity of ^{16}O at the time of the pre-supernova (see below for a more detailed discussion of this point).

The ^{17}O yield decreases when the initial mass increases, becoming even negative for stars with $M \geq 25\ M_\odot$ as can be seen in the middle panel of Figure 3.19. This reflects the fact that ^{17}O is produced in H-burning regions with temperatures lower than a given limit. For ^{18}O (see the right panel of Fig. 3.19) the situation is more complicated in the sense that the yield of this isotope first increases with mass until a maximum is reached around 20 $M_\odot$, then it decreases becoming negative for stellar models with higher initial mass. This behaviour results from the fact that ^{18}O is what we might tentatively call a "transitory element" in a chain of reactions. This means that its peak abundance will be reached for a relatively narrow domain of temperatures. Indeed the temperatures have to be high enough to allow the chain to synthesise it but low enough to prevent its destruction.

It is interesting to compare the yields of ^{17}O and ^{18}O in massive stars with those obtained by Marigo (2001) for intermediate mass stars. Marigo (2001) shows that ^{17}O may be produced in intermediate mass stars with initial masses above about 4 $M_\odot$ with yields of the order of a few $10^{-3}\ M_\odot$. This is well above what the massive stars in the range between 12 and 20 $M_\odot$ can do. Above 20 $M_\odot$, ^{17}O is destroyed but at a level which probably remains negligible with respect to what is produced in intermediate mass stars. Thus for ^{17}O intermediate mass stars appear as a much more promising source than massive stars.

The contrary occurs for ^{18}O. Indeed, according to Marigo (2001), this element is destroyed in intermediate mass stars with initial masses above about 4 $M_\odot$. As can be seen in the right panel of Figure 3.19, it is produced in the 15 and 20 $M_\odot$ models.

Metallicity.   When one discusses the effects of a change of the initial metallicity on the yields of a given element, it is useful to first discern if the isotope considered is a primary or a secondary element. By primary element we mean an element which would be produced in about the same quantity in a Population III star as in a Population I star, *i.e.* an element whose yield does not depend much on the initial metallicity of the star. Secondary elements, on the contrary, are those whose yields crucially depend on the initial abundance in heavy elements of the star. Their yields are thus very different in Population III and Population I stars. It is well known that ^{16}O is in that respect a primary element. This comes from the fact that it is produced from helium in the core helium-burning phase. Whatever the initial metallicity the core, it becomes almost pure helium by the end of the core H-burning phase. Of course there is still a metallicity dependence due to the fact that the physical conditions, such as temperature and density, are different depending on the initial metallicity of the star, but these effects are of second order importance. The production of the other two oxygen isotopes depends on the initial CNO content of the star. For instance ^{18}O results from the transformation of the ^{14}N produced during the core H-burning phase, whose abundance is equivalent to the initial value of the sum of the CNO elements. However since their production occurs only for relatively narrow physical

Table 3.13. Yield comparisons for 20 $M_\odot$ non-rotating and rotating stellar models at various metallicities. The yields are in solar masses. Data from Hirschi (2007).

Initial Z	Y(^{16}O)	Y(^{17}O)	Y(^{18}O)	Y(^{16}O)	Y(^{17}O)	Y(^{18}O)
		$v = 0$			$v = 300$ km s^{-1}	
10^{-3}	1.46	–5.5e–7	–1.1e–5	2.70	4.85e–7	–1.89e–5
10^{-5}	1.50	3.1e–7	–9.4e–8	2.37	3.40e–7	5.27e–7
10^{-8}	1.20	1.9e–7	–2.2e–10	1.96	1.70e–8	2.14e–7

conditions, their yields in the global ejecta may not present any clear trend with metallicity. This is what occurs in massive stars.

Let us compare the yields of three non-rotating 20 $M_\odot$ models computed with the same physical ingredients except for different initial abundances. The yields are shown in Table 3.13. The yields of ^{16}O are almost constant, while those of ^{17}O and ^{18}O vary significantly. Moreover, no clear trend with metallicity is noticed thus illustrating the point discussed above.

Overshooting. The size of the convective cores is poorly known from *ab initio* physical principles. This is a very important quantity since it affects the lifetime and the nucleosynthesis of a given star. In stellar models, the limit of the convective core is determined through criteria which may vary from one author to another. A typical approach to compute the size of the convective core is to determine the point within the star where the convective cells have zero velocity. Overshooting increases the size of the convective cores, and as a result, a star of a given initial mass with overshooting will have a behaviour roughly similar to that of a star of higher initial mass without it. It is difficult to be more quantitative here since, in order to study this effect, a series of models with exactly the same physical ingredients should be computed for different values of the overshooting parameter. Let us just give an example: the ejected mass of ^{16}O in a 20 $M_\odot$ stellar model without overshooting is 2.0 $M_\odot$ while it is 3.1 $M_\odot$ in the same model when a moderate overshooting (of 0.25 H_p) is taken into account (Meynet 1990). Thus the effect is quite important.

The reaction ^{12}C$(\alpha, \gamma)^{16}$O. In the list of important nuclear reaction rates in astrophysics, ^{12}C$(\alpha, \gamma)^{16}$O appears in the top rank as reflected by the abundant literature on the subject. It affects not only the quantities of carbon and oxygen synthesised by the star, but has an impact on many other stellar model outputs, *e.g.* the formation of blue loop during the core helium-burning phase of massive stars or the nature of the stellar remnant at the end of the evolution (see for instance the text by Woosley in Hauck *et al.* 1986). There is still some uncertainty pertaining to this yield which amounts to about a factor of 2. Recently, Tur *et al.* (2007) have studied the impact of a rate change for this reaction on the production of the ^{16}O and ^{18}O isotopes (see their Fig. 3).

Mass loss. Mass loss intensity is a key quantity in stellar evolution. It affects the tracks in the HR diagram, lifetimes, surface abundances, chemical yields, pre-supernova status, the nature of the remnant, the mechanical energy released in the interstellar medium, the hardness of the radiation field, etc.

The main mass-loss trigger is radiation pressure. Quoting Eddington (1926), "*the radiation observed to be emitted must work its way through the star, and if there were too much obstruction it would blow up the star.*" Note that although it was already realised in the 1920s that radiation pressure might produce mass loss, it is only in the late 1960s, when sensitive UV diagnostics of mass loss from O stars became available, that the effects of mass loss on the evolution of stars were really considered.

Radiation triggers mass loss through the line opacities in hot stars. It may also power strong mass loss through the continuum opacity when the star is near the Eddington limit. For cool stars, radiation pressure is exerted on dust grains. Note that other mechanisms such as pulsations, mass transfer in close binary systems or rotation near the critical limit may also trigger mass loss episodes.

For hot stars, typical values for the terminal wind velocity v_∞ are of the order of 3 times the escape velocity, *i.e.* about $2000-3000$ km s^{-1}, and mass loss rates are between $10^{-8}-10^{-4}$ $M_\odot$ per year. Luminous Blue Variable (LBV) stars during outbursts show mass loss rates as high as $10^{-4} - 10^{-1}$ $M_\odot$ per year (Lamers & Cassinelli 1999).

According to recent estimates, the mass loss rate $\dot{M}$ varies with luminosity L as

$$\dot{M} \sim L^{1.7} . \tag{3.7}$$

With the mass-luminosity relation for massive stars

$$L \sim M^2, \tag{3.8}$$

this gives

$$\dot{M} \sim M^{3.4} . \tag{3.9}$$

For massive stars, the main-sequence lifetime, t_{MS}, scales as

$$t_{\mathrm{MS}} \sim M^{-0.6} , \tag{3.10}$$

the amount ΔM of mass lost during the main sequence is then

$$\Delta M \sim M^{2.8} \tag{3.11}$$

and the relative mass lost is

$$\frac{\Delta M}{M} \sim M^{1.8} . \tag{3.12}$$

Thus, not only the *total* amount of mass lost grows strongly with the stellar mass, but also the *relative* amount, which illustrates the importance of this effect.

In addition to the intensity of the stellar winds for different evolutionary phases, one needs to know how the winds vary with the metallicity. This is a key effect in order to understand the massive-star populations observed in regions of different metallicities. It has also an important impact on the yields expected from stellar models at various metallicities.

Current wisdom considers that very metal-poor stars lose only very small amounts of mass through radiatively driven stellar winds. This comes from the fact that, when the metallicity is low, the number of strong absorbing lines is small, and thus the coupling between the radiative forces and matter is weak. Wind models impose a scaling relation of the type

$$\dot{M}(Z) = \left(\frac{Z}{Z_\odot} \right)^\alpha \dot{M}(Z_\odot), \tag{3.13}$$

where $\dot{M}(Z)$ is the mass loss rate when the metallicity is equal to Z and $\dot{M}(Z_\odot)$ is the mass loss rate for the solar metallicity, Z being the mass fraction of heavy elements. In the metallicity range from $1/30$ to 3.0 times solar, the value of α is between 0.5 and 0.8 according to stellar wind models (Kudritzki *et al.* 1987; Leitherer *et al.* 1992; Vink *et al.* 2001). Such a scaling law implies for instance that a non-rotating 60 $M_\odot$ star with $Z = 0.02$ ends its stellar life with a final mass of 14.6 $M_\odot$, while the same model with a metallicity of $Z = 10^{-5}$ ends its life with a mass of 59.57 $M_\odot$ (*cf.* models of Meynet & Maeder 2005 and Meynet *et al.* 2006 with $\alpha = 0.5$).

Thus the 60 $M_\odot$ star with $Z = 10^{-5}$ will be expected to give birth to a black hole. In that case nearly all (if not all) the stellar mass may disappear in the remnant preventing the star from enriching the interstellar medium with new synthesised elements (see however the case of Nova Scorpii, González Hernández *et al.* 2009 in Sect. 3.2.2.4). The metal-rich model, on the other hand, will probably leave a neutron star, and contribute to the enrichment of the interstellar medium through both the winds and the supernova ejecta.

A star that loses a lot of material through stellar winds may enrich the interstellar medium in a different manner to a star that retains most of its mass until the supernova explosion. As Maeder (1992) pointed out, when the stellar winds are strong, material partially processed by the nuclear reactions is released, favouring some species (*e.g.* helium and carbon which would be partially destroyed if locked in the star) and disfavouring others (*e.g.* oxygen which would be produced by further transformation of the species which are wind-ejected). Thus the effect of mass loss on ^{16}O are clear: an increase of mass loss will tend to reduce the ^{16}O yield. As a numerical example we can compare the ^{16}O yields obtained from massive star models computed by Maeder (1992) with normal and twice the normal mass loss rate for $Z = 0.02$ (see Fig. 3.20). We see that differences are important for stars more massive than 25 $M_\odot$: the yields of ^{16}O are multiplied by factors between 2 and 4 for stars in the mass range between 40 and 85 $M_\odot$ when low mass loss rates are used. In the case of the 120 $M_\odot$ star, the yield increase is even more spectacular. Let us estimate the effect on the yields for a generation of massive stars. With a Salpeter initial mass function (IMF, see Chapter 4), when N stars
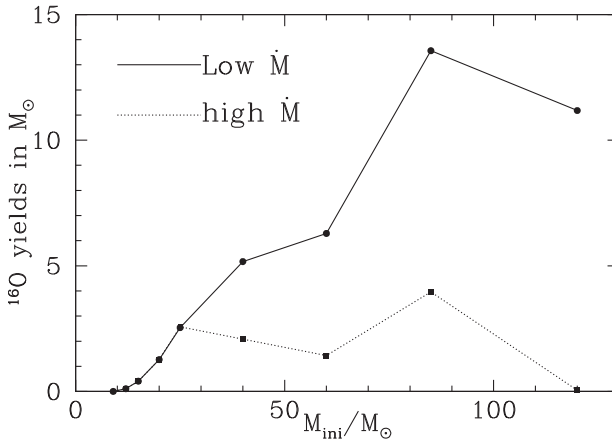
Fig. 3.20. Yields of ^{16}O from the models of Maeder (1992) computed with a high and a low mass loss rate.

are formed there are $0.8N$ stars with masses between 8 and 25 $M_\odot$ and $0.2N$ stars with masses between 25 and 120 $M_\odot$. Looking at the case with the high mass loss rates in Figure 3.20, we can assume, just for order-of-magnitude estimates, that the yields for stars with $M > 25$ $M_\odot$ have the same value Y_O for all masses. In the lower mass range let us take a typical yield equal to $Y_O/2$. Thus in the case of high mass loss rate the whole massive star population would release a mass M_O of newly synthesised oxygen equal to $(0.8Y_O/2 + 0.2Y_O)N = 0.6Y_O N$. When the low mass loss rates are used, the yields of stars between 8 and 25 $M_\odot$ are not changed, while those of stars with $M > 25M_\odot$ are increased. Let us suppose that they are increased by a factor 4 which is clearly an overestimate (except for the 120 $M_\odot$ case). Then the yield for a whole massive star population would be proportional to $(0.8Y_O/2 + 4 \times 0.2Y_O)N = 1.2Y_O N$. Thus, here, lowering the mass loss rates doubles the contribution of massive stars to ^{16}O production. This is of course not negligible (although let us recall that this is clearly an overestimate).

The reduction of the oxygen yield by mass loss will occur at high metallicity where the stellar winds are stronger. Now, since the new element fraction ejected by a stellar generation is the same, the mass which is not ejected in the form of new oxygen must be ejected in the form of another element. Which is this element? The yields of helium, carbon and oxygen are shown in Figure 3.21. Comparing column 1 (very weak mass loss) with column 5 (very strong mass loss), one sees that the deficit of oxygen in the high mass loss regime is more than compensated by a large increase in the yields of helium and carbon.

Rotation.   It has been known for a long time that stars rotate. The first known detailed account of the Sun rotation dates back to the time of Galileo Galilei at the beginning of the 17th century. Nowadays our knowledge of the star rotation
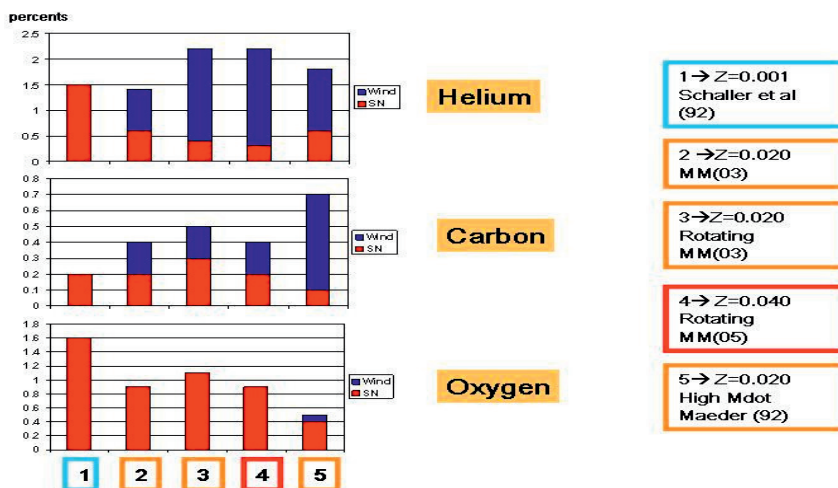
Fig. 3.21. Mass fraction in a generation of stars initially more massive than 8 $M_\odot$ ejected in the form of new helium, carbon and oxygen. A Salpeter IMF has been used. Various stellar models are compared: the labels MM03 and MM05 are for Meynet & Maeder (2003) and Meynet & Maeder (2005), respectively.

is mainly based on Doppler widening of absorption lines. Very recently, interferometric techniques have revealed the shape of some stars strongly deformed by fast rotation as Achernar (Domiciano de Souza *et al.* 2003; Carciofi *et al.* 2008) or the variation of the effective temperature with the latitude (Zhao *et al.* 2009).

Recent works have provided new estimates of the rotation velocity of B-type stars. Dufton *et al.* (2006) have measured the rotation of stars in two Galactic clusters – NGC 3293 and NGC 4755 – whose ages are comprised between 10 and 15 Myr. For stars with masses between 3 and 12 $M_\odot$, they find that the velocity distribution peaks at 250 km s^{-1} accounting for a random distribution of the inclination[5]. Similar results have been obtained by Huang & Gies (2006a, 2006b). These authors also show that the average velocity of stars with masses between 8.5 and 16 $M_\odot$ remains more or less constant when the surface polar gravity decreases, *i.e.* when evolution proceeds. On the other hand, for masses between 2.5 and 8.5 $M_\odot$ the velocity decreases with decreasing polar gravity, indicating that, in this mass range, some breaking mechanism is active which does not work in the higher mass range (magnetic breaking?). Binary systems appear to experience more spin down than single stars.

Huang & Gies (2006a) have also observed that for the more massive stars of their sample (masses between 8.5 and 16 $M_\odot$) there is an increase of the helium mass fraction at the surface of the star when the polar gravity decreases. The

---

[5]In that case, one passes from the $v \sin i$ values to the v values by multiplying $v \sin i$ by $4/\pi = 1.27$. This is true only on average.

increase of Y, the helium mass fraction, amounts to $23 \pm 13\%$, between the zero- and terminal-age main sequences (*i.e.* if $Y = 0.25$ on the zero-age main sequence, it reaches values as high as 0.31 on the terminal-age main sequence). Such helium enrichments at the surface have also been observed by Lyubimkov *et al.* (2004).

Does the velocity distribution vary as a function of metallicity? This question is still debated. For instance Keller (2004) measured the rotational velocities of 100 main sequence early B-type stars in clusters of the LMC, and compared them with those of early B-type stars in clusters of the solar neighbourhood. He found that the LMC stars are faster rotators than the Galactic ones: the mean value of $v \sin i$ is 116 km s^{-1} for the Galactic stars and 146 km s^{-1} for the LMC stars. On the other hand, Penny *et al.* (2004) found no difference between the velocities of O-type stars in the Magellanic Clouds and in the Galaxy. Numerous surveys are now being undertaken with the aim of providing further constraints on this topic, *e.g.* the VLT-Flames survey. The fact that the fraction of Be stars among B stars increases with decreasing metallicity (Be stars being stars near the break-up limit) may favour the situation where the distribution of initial rotations contains more fast rotators at low metallicity.

Rotation triggers many instabilities in stellar interiors. In turn these instabilities drive the transport of chemical species and of angular momentum in radiative zones. Typically on the main sequence, rotational diffusion will continually refuel the core in hydrogen, slowing down its mass decrease. At the end of the core H-burning phase this will produce a more massive He core. The latter, in turn, will give birth to a more massive CO core. It may be easily deduced from the above line of reasoning that a rotating star will produce more ^{16}O than a non-rotating one.

In Table 3.13 we can see the effects of rotation on the yields of the three oxygen isotopes. For ^{16}O, as emphasised above, the yields are increased by rotation (see also upper panel of Fig. 3.24). We note however that the increase is more important for the model at $Z = 10^{-3}$ than for models at lower metallicities. For the other two isotopes, it is difficult to deduce any general behaviour from these data. We can just note that ^{18}O production is favoured in rotating models for metallicities below 10^{-5}. This is related to the fact that in these models a strong peak of primary nitrogen is produced in the H-burning shell. Nitrogen from this peak diffuses into regions of lower nitrogen abundance, in particular in the He core where it is transformed into primary ^{18}O and ^{22}Ne.

Interestingly, in plots of the yields *versus* the CO-core mass, models with and without rotation produce very similar curves (see Fig. 3.19). This illustrates well the fact that the size of the CO core is the determining factor. Of course rotation will change the correspondence between a given CO core mass and the initial mass.

Figure 3.22 shows the chemical yields from models with and without rotation (Hirschi *et al.* 2005) at $Z = 0.020$. Figure 3.23 shows these yields multiplied by the stellar initial mass function (IMF). The main conclusion is that, below an initial mass of 30 $M_\odot$, the cores are larger and thus the production of α–elements is enhanced. Typically a rotating 20 $M_\odot$ model will have more or less the same nucleosynthetic contribution as a non-rotating 30 $M_\odot$ stellar model. This is true
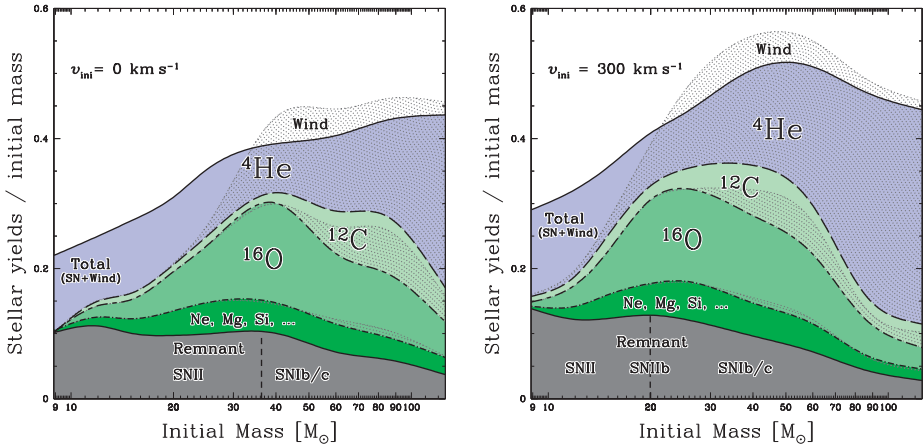
Fig. 3.22. Stellar yields. *Top panel*: models without rotation. *Bottom panel*: models with $v_{\rm ini} = 300$ km s^{-1} (Hirschi *et al.* 2005). To illustrate how to read this figure, let us consider the case of the 60 $M_\odot$ star without rotation. In that case, the mass in solar masses of new helium synthesised by the star is the length of the ^{4}He area at the 60 $M_\odot$ abscissa $(0.4 - 0.28 = 0.12)$ multiplied by the initial mass of the star (here 60). This gives about 7.2 $M_\odot$ of new helium produced by the star. The dotted areas correspond to the yields ejected by stellar winds only. Note that the total yield (wind and supernova) may be inferior to the yields ejected by winds in case the considered element is destroyed in the layers ejected at the time of the supernova explosion.
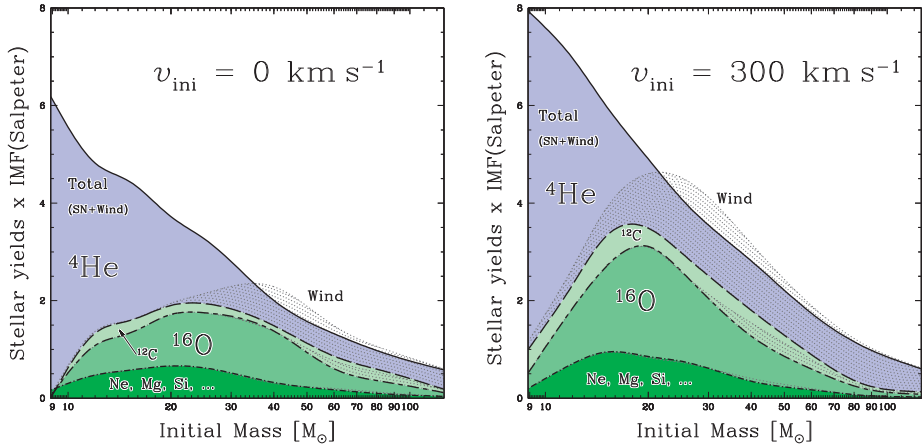
Fig. 3.23. IMF-weighted yields. *Top panel*: models without rotation. *Bottom panel*: models with $v_{\rm ini} = 300$ km s^{-1} (Hirschi *et al.* 2005).

for velocities during the main sequence phase equal to the peak value of the velocity distribution. Above 30 $M_\odot$, mass loss is the dominant effect and more He is ejected

before being further processed, while the size of the core is only slightly reduced. When accounting for the weighting by the IMF, the production of oxygen and of α–elements is globally enhanced as illustrated by Figure 3.23, while the effect on the He–production in massive stars remains limited.

3.2.2.3   Yields

In Figure 3.24, yields from different authors for the three stable isotopes of oxygen are shown as a function of the initial mass. All the models are computed for a metallicity $Z = 0.02$. In the important mass range between 10 and 30 $M_\odot$ the ^{16}O yields from the various authors agree well, while above this mass range great discrepancies are present. For the other two isotopes, large differences are found for the whole mass range considered in Figure 3.24.

3.2.2.4   Observational probes

Let us first begin by recalling a few observations supporting the now well-accepted fact that stars are indeed the sources of new synthesised elements. Historically one of the first observational hints that indeed stars were building new elements came from the detection of technetium at the surface of a red giant star (Merrill 1952). This radioactive element has indeed a disintegration lifetime (2.13×10^5 y) much shorter than the lifetime of the star in which it was observed. This clearly indicated that the origin of this element was related to processes occurring in the star itself. Today gamma-ray line observations allow the detection of gamma rays coming from the disintegration of radioactive elements. Up until now, five isotopes have been detected in this way: ^{26}Al (mean lifetime 1.04×10^6 y) and ^{60}Fe (2.2×10^6 y) have been detected as a diffuse emission in the Galactic disk, their abundances reflecting the global recent nucleosynthetic activity in the Galactic disk in the last million years; the emissions arising from the decay of ^{44}Ti (89 y) ^{56}Co (0.31 y) and ^{57}Co (1.1 y) have been observed from point sources linked to young supernova remnants (Ti in Cas A, isotopes of Co in SN1987A) constraining the yield of individual events (see *e.g.* the review by Leising & Diehl 2009).

The observation of surface abundances of non-radioactive elements is also an efficient probe for studying stellar evolution and checking the internal nuclear processes. Certainly one of the first findings supporting the view that massive stars are important oxygen producers is the observation that, in very metal-poor halo stars, the [O/Fe] ratio is higher (by about a factor of 3) than that measured in stars with solar metallicity. This trend is attributed to the fact that in the very early time of the chemical enrichment of the Galaxy only the short-lived massive stars contribute. The fact that stars born in such an early time have an oxygen excess is an indication that the massive stars do produce great quantities of it (see Chapter 4).

Another argument is the fact that some stars, called Wolf-Rayet (WR) stars, offer the wonderful opportunity to look at what happens in their core. How is
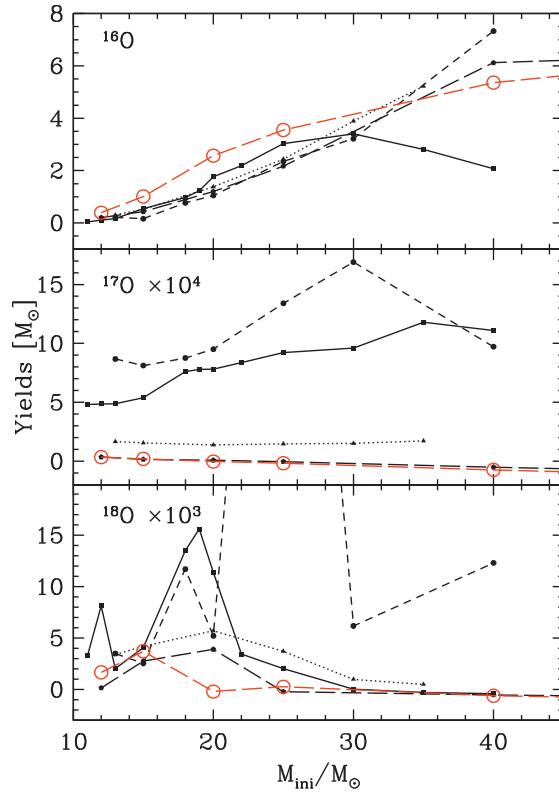
Fig. 3.24. Yields in ^{16}O, ^{17}O and ^{18}O for different initial models at a metallicity $Z =$ 0.02: the continuous curves with black squares corresponds to the yields from Woosley & Weaver (1995); the dotted lines with black triangles present the results from Chieffi & Limongi (2004); the dashed lines with black circles, those of Nomoto *et al.* (2006); the long dashed lines with black pentagons show the yields obtained by Hirschi *et al.* (2005) from non-rotating models; and the long dashed curve with large empty circles the yields from the same authors obtained from rotating models with $v_{ini} = 300 \, \mathrm{km \, s^{-1}}$. The yields are given in solar masses. The yields in ^{17}O and ^{18}O have been respectively multiplied by 10^4 and 10^3. Note that the results of Hirschi *et al.* (2005) correspond to yields obtained from pre-supernova models, *i.e.* the explosive nucleosynthesis is not accounted for. The other references account for the changes due to explosive nucleosynthesis. Note that for the isotopes considered here, the effect of the explosive nucleosynthesis is believed to be very modest.

this possible? Thanks to heavy mass loss and internal mixing processes, elements produced in the central regions appear at the surface thus offering an opportunity to check the nuclear processes occurring in stellar interiors (see the review on WR stars by Crowther 2007).

Wolf-Rayet stars occupy the upper left-hand corner of the HR diagram and thus they are hot and luminous stars (see *e.g.* Hamann *et al.* 2006). At solar metallicity, they originate from stars more massive than about 25 $M_\odot$ that have lost their initial H–rich envelope by stellar winds or through a Roche lobe overflow in a close binary system. The stars enter the WR phase as WN stars, whose surface abundances are representative of equilibrium CNO processed material. If the peeling off continues, the star may enter the WC/WO phase, during which the He–burning products appear at the surface. In our Galaxy, van der Hucht (2001, 2006) identifies 298 WR stars (171 WN, 10 WN/WC, 113 WC and 4 WO), of which 24 (8%) are in the open cluster Westerlund 1 and 60 (20%) are in open clusters near the Galactic Centre. One estimates that their total number in our Galaxy is as high as a few thousands.

The observed surface abundances during the WN phase correspond to CNO equilibrium values, while those observed during the WC/WO phase well correspond to the apparition at the surface of He-burning products (Crowther 2007). Oxygen diagnostics in WC stars lie in the near UV and are thus difficult to observe from the ground. Thanks to space-based spectroscopy, Crowther *et al.* (2002) derived an oxygen mass fraction of 5–10% in WC stars. Such a high oxygen value (let us recall that at solar metallicity oxygen has a mass fraction of at most 1%) beautifully supports the view that indeed oxygen is a product of helium burning.

Although a little aside from the subject of oxygen nucleosynthesis, it is interesting to mention the following: WC stars offer a neat and original way to measure the initial CNO abundance. At first sight, this assertion looks quite strange. How can material heavily processed by at least two nuclear phases (H- and He-burning reactions) still provide information on initial conditions? The reason is that during the core H-burning phase CNO are transformed into N; therefore, N at this stage is a measure of the initial CNO content. During the core He-burning phase, this N is converted into ^{22}Ne, and when the He core is naked, the measure of the neon abundance then gives access to the initial CNO content of the star.

The high overabundance of ^{22}Ne at the surface of the WC star predicted by He-burning reactions is well confirmed by observations (see *e.g.* Ignace *et al.* 2007). But comparisons between the observed Ne/He ratio at the surface of WC stars with models computed with $Z = 0.02$ show that the latter overpredict the Ne abundance, while models starting with $Z = 0.014$ give a much better fit as can be seen in Figure 3.25. This is an indirect argument that the solar abundances of Asplund *et al.* (2004) represent much better the metallicity of the solar vicinity than previous estimates (see Chapter 2).

Let us note that this overabundance of ^{22}Ne at the surface of WC stars is not only an important confirmation of the nuclear reaction chains occurring during He-burning, but it is also related to the question of the origin of the material accelerated into Galactic cosmic rays (see recent measurements of the ^{22}Ne/^{20}Ne ratio in cosmic rays in Binns *et al.* 2005) and to the weak *s*-process in massive stars since ^{22}Ne is the source of neutrons in these stars.

Let us end this section by mentioning an interesting approach to constrain the chemical composition of core-collapse supernova ejecta (very rich in oxygen).
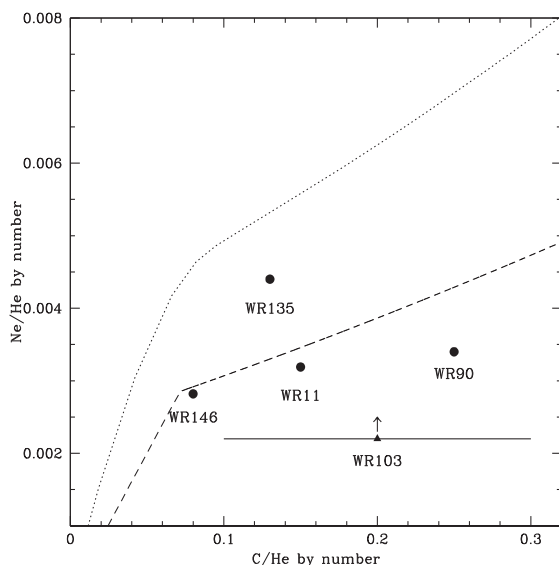
Fig. 3.25. The black points show the Ne and C abundances observed at the surface of WC stars by Dessart *et al.* (2000; filled circles) and by Crowther *et al.* (2006; filled triangles). The dotted line shows the prediction for a 60 $M_\odot$ stellar model with $Z = 0.020$ of Meynet & Maeder (2003) and the dashed line for a 60 $M_\odot$ stellar model with $Z = 0.014$.

When a core collapse occurs in a binary system, there is a chance that part of the ejecta will be intercepted by the companion. In that case the companion may present surface abundances different from those of nearby stars. At the present time three such cases have been observed (see *e.g.* González Hernández *et al.* 2009). For instance large overabundances (factors between 6 to 10 with respect to solar values) of oxygen, magnesium, silicon and sulphur have been observed in the atmosphere of the star orbiting a probable black hole, Nova Scorpii 1994. This is the first observational evidence of a supernova event being associated to the birth of a black hole. This also indicates that not all the mass is swallowed by the black hole, but a fraction of it participates in the chemical enrichment of the surroundings. Finally this observation also supports the view that at the time of the supernova event large quantities of oxygen are ejected into the interstellar medium.

3.2.2.5 Core-collapse supernovae

What are the effects of explosive nucleosynthesis on the yields of the oxygen isotopes? To answer this question we may compare the yields obtained at the pre-supernova stage with those obtained after the passage of the shock wave in the outer layer when the star explodes as a supernova. Woosley & Weaver (1995) provide such numbers for a 25 $M_\odot$ star at solar metallicity. The ejected masses before the explosive nucleosynthesis are 3.45 $M_\odot$ for ^{16}O, 1.01×10^{-3} $M_\odot$ for ^{17}O

and 2.72×10^{-3} $M_\odot$ for ^{18}O, and 3.25 $M_\odot$ for ^{16}O, $1.01\times^{-3}$ $M_\odot$ for ^{17}O and 2.52×10^{-3} $M_\odot$ for ^{18}O after the explosion. Thus the effects of the explosive nucleosynthesis are very modest (at least for this stellar mass). They are larger for elements produced in the regions lying closer to the centre, as expected, since it is in these regions that the higher values of temperature and density are reached.

The most important effect of supernova explosion on the yields is actually through the mass cut, *i.e.* the dividing line between the mass which will remain locked in the compact remnant and that ejected at the time of the supernova event. As already outlined above, in the case of the 25 $M_\odot$ star discussed in Section 3.2.2.1, if the mass cut is below 2.5 $M_\odot$, the yields of ^{16}O are little affected (see Fig. 3.18). If the mass cut is above 2.5 $M_\odot$, then its exact value has important consequences: the mass of ^{16}O ejected decreases with increasing mass cut by about 0.07 $M_\odot$ per tenth of solar mass.

3.2.2.6   Pair-instability supernovae

Very massive stars which form a helium core of about 40 $M_\odot$ or larger experience the electron-positron pair instability (Barkat *et al.* 1967; Bond *et al.* 1984). Physically this instability comes from the fact that, in the advanced phases of the evolution, photons have sufficient energy to produce electron-positron pairs. In these very massive stars, the hydrostatic equilibrium is mostly sustained by the radiative pressure gradient. Since the process of pair formation removes important agents sustaining the star (*i.e.* photons), it contributes to make the star unstable with respect to contraction: the star rapidly collapses. The acceleration of the nuclear energy reaction rates due to neon, oxygen and silicon burning may then turn the collapse into an explosion.

For helium core masses between 40 and 63 $M_\odot$, the energy released is not sufficient to disrupt the star and the star becomes pulsationally unstable (Heger & Woosley 2005). The envelope and part of the He core are ejected, and a black hole is formed. For helium core masses between 63 and 130 $M_\odot$, the released energy is enough to completely disrupt the stars. Above 130 $M_\odot$, photodisintegration in the cores lead to black-hole formation.

Pair-instability supernovae only occur if the progenitor star can retain sufficient mass at the end of its evolution to encounter the instability described above. This is the reason why these events are believed to take place only in very metal-poor stars where line driven winds are very weak. For instance it was expected to see the signature of pair-instability supernovae in the very iron poor stars observed in the halo; however no such signature has yet been found (Cayrel *et al.* 2004).

Recently the observation of very luminous supernovae presenting many observed characteristics compatible with pair-instability supernovae suggested that in the present-day Universe such events may occur. However recent near-infrared observations of the SN 2006gy, for instance, show that the luminosity curve presents a late-time decline which is not in agreement with the various pair-instability supernova models (Miller *et al.* 2010).

Thus at the moment, although the physics of such explosions is well understood and their nucleosynthetic outputs well described, any direct link with observed features remains elusive. It is thus difficult to quantitatively estimate the importance of such events in the synthesis of oxygen. At the moment it seems that their main contribution was in the very early Universe, although even at that time stars may have lost high amounts of mass due to fast rotation (Ekstroem *et al.* 2008) and thus avoided the pair instability. Yields from pair-instability supernova models can be found in Heger & Woosley (2005).

3.2.3   Low- and intermediate-mass stars

Low- and intermediate-mass stars finish their lives as carbon-oxygen white dwarfs. Their initial masses are typically between 0.5 $M_\odot$ (less massive stars burn only hydrogen and end up as helium white dwarfs) and $6-8$ $M_\odot$ (more massive stars go through all the nuclear phases beyond helium burning as discussed in Sect. 3.2.2). After having gone through the central hydrogen-burning phase that is referred to as the main sequence, these objects undergo a short period of shell hydrogen burning on the red giant branch followed by core helium burning on the so-called clump[6]. When the helium fuel is consumed in the central region, low- and intermediate-mass stars evolve to the asymptotic giant branch (hereafter AGB). The electron-degenerate core of carbon and oxygen, which is the product of helium burning, is then surrounded by a helium-burning shell and a more external hydrogen-burning shell. From this time on, recurrent thermal pulses take place in the helium-burning shell. This is the so-called the TP-AGB phase, which provides a rich and unique nucleosynthesis. Moreover, recurrent dredge-up events (third dredge-up) enrich the stellar surface with the freshly synthesised nuclides that are then ejected into the interstellar medium through the strong winds (prior to the TP-AGB, the surface composition of the stars has also been altered by the first and possibly second dredge-up events). Through these mechanisms, low- and intermediate-mass stars thus play a crucial role in the chemical evolution of galaxies. Let us now have a closer look at their contribution to the oxygen isotopes.

3.2.3.1   A reference case: a 5 $M_\odot$ star

We focus first on a reference object, a 5 $M_\odot$ star with metallicity [Fe/H] $= -1.56$ (from Decressin *et al.* 2009). In this model the effects of rotation are not included.

Abundance profiles at the end of the main sequence

Figure 3.26 (top) shows the abundance profiles of different chemical species inside the star at the end of the main sequence. In regions deeper than $\mathrm{M}_r/M_\odot \sim 3$,

---

[6]Low- and intermediate-mass stars respectively ignite central helium burning in electron-degenerate and non-degenerate cores. The mass limit is approximately 2–2.2 $M_\odot$ and depends on the initial stellar metallicity.
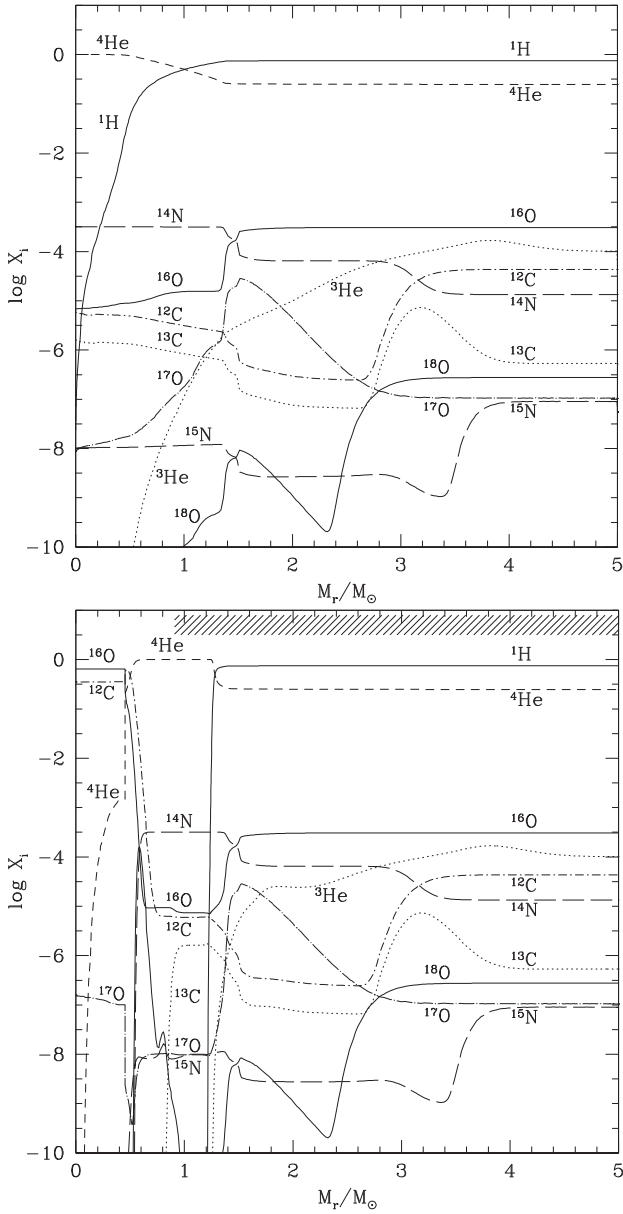
Fig. 3.26. Abundance profiles (in mass fraction) of chemical elements as a function of depth (reduced mass in solar units) inside the reference 5 $M_\odot$, [Fe/H] $= -1.56$ model. *Top*: at the end of the main sequence. *Bottom*: at the end of the core He-burning phase. The hatched area indicates the maximum extent of the convective envelope during the dredge-up episode that occurs early on the AGB.

the oxygen isotopes are affected by the ON cycle, ^{16}O and ^{18}O being destroyed by p-captures and α-decay, while ^{17}O is produced at a high rate. In the most central regions where the CNO cycle has reached equilibrium the three oxygen isotopes are depleted.

Abundance profiles at the end of core He burning and dredge-up

Figure 3.26 (bottom) shows the chemical structure of the star at the end of central helium burning. In the core ($M_r/M_\odot < 0.45$), helium has been transformed into ^{12}C and ^{16}O through 3α and ^{12}C$(\alpha,\gamma)^{16}$O reactions. At the edge of the core ($0.45 < M_r/M_\odot < 1.5$) the three oxygen isotopes are depleted due to hydrogen burning through the CNO cycle in a shell. In the most external regions ($M_r/M_\odot > 1.5$) the abundance profiles have not been modified since the end of the main sequence.

Following core He exhaustion, the star starts ascending the AGB, and its convective envelope deepens down to the nuclearly processed regions as indicated by the hatched area in Figure 3.26 (bottom). This is the so-called second dredge-up[7] that leads to changes in the stellar surface abundances. In the model presented here, ^{16}O/^{17}O then decreases by a factor of $\sim$26 (the convective envelope totally engulfs the ^{17}O peak) while ^{16}O/^{18}O increases by a factor of $\sim$1.6. The fresh ^{16}O produced in the core is not affected by the dredge-up and remains trapped into the degenerate core of the future white dwarf. Finally, let us note that during the dredge-up episode on the early-AGB the sum C+N+O at the surface of this standard (non-rotating) model remains constant, since only H-burning products are conveyed to the surface.

TP-AGB phase

Later on helium and hydrogen burnings ignite inside two thin layers surrounding the contracting degenerate carbon-oxygen core. These burning shells become thinner, hotter and closer to each other with time, and their ashes increase the core mass. Soon a first thermal instability (or thermal pulse) occurs in the helium-burning shell, which marks the beginning of the TP-AGB. This evolution phase is characterised by long periods of quiescent H-shell burning (or inter-pulses), interrupted by recurrent thermal pulses of the helium-burning shell. The enormous quantity of energy produced by each pulse powers a convective pocket that engulfs the ashes of the hydrogen-burning shell causing its momentary extinction. When the thermal pulse dies down, the stellar convective envelope moves inward in mass and eventually reaches the region previously mixed by the convective pocket. This is known as the third dredge-up, which conveys the products of partial helium burning to the surface. Following each thermal pulse the hydrogen-burning shell

---

[7]For stars less massive than 2–2.5 $M_\odot$, a first dredge-up episode already occurs at the tip of the red giant branch, see Section 3.2.3.2.

reignites and the star enters a new inter-pulse period. The cycle inter-pulse – thermal pulse – third dredge-up occurs several times on the TP-AGB, depending on the initial mass and composition of the star. It ends up when the stellar envelope has been entirely ejected by the important mass loss that the star undergoes at this stage of its evolution. In the most massive AGB stars such as the reference model discussed here, the convective envelope dips into the regions of H burning, leading to nuclear processing at the base of the envelope. This is the so-called hot bottom burning, which leads to modification of the surface abundance when the temperature at the base of the convective envelope exceeds $\sim$50 million K. As first investigated by Boothroyd et $al.$ (1993), hot bottom burning can efficiently reduce the ^{12}C/^{16}O ratio at the stellar surface and, if it is strong enough, it possibly prevents the formation of C stars. During the TP-AGB, three different nucleosynthesis sites thus have to be distinguished: the burning shells, the convective region where the thermal pulse develops and the base of the convective envelope.

Figure 3.27 shows the abundance profiles of key elements in the tiny region of nuclear activity ($i.e.$, helium- and hydrogen-burning shells) in our reference model (initial mass of 5 $M_\odot$ and [Fe/H] $= -1.56$) at the end of the inter-pulse phase after the 14th thermal pulse. The nuclear energy supplied by the helium-burning shell comes from the 3α ($\sim$70%) and ^{12}C(α, γ) ($\sim$29%) reactions. The helium-burning shell produces ^{12}C and, to a lower extent, ^{16}O, while during the previous central He-burning stage the ^{16}O production was preponderant. In addition ^{16}O, ^{17}O and ^{18}O are partially destroyed in the hydrogen-burning shell.

During the next thermal pulse part of the inter-shell region is engulfed by the convective tongue. ^{17}O, which is not produced inside thermal pulses, is then destroyed mainly through ^{17}O$(\alpha,$n$)$ and ^{17}O(α, γ), the first reaction being at least ten times faster than the second and weakly contributing to neutron production inside the thermal pulses. ^{17}O destruction already operates from the first thermal pulses on, whatever the initial stellar mass and metallicity. In subsequent thermal pulses, the ^{17}O mass fraction stabilises around 4 to 8×10^{-10}, which represents a balance between the amount of ^{17}O removed from the inter-shell region and that destroyed by the thermal pulse.

On the other hand ^{18}O is produced inside the thermal pulse via the ^{14}N$(\alpha, \gamma)^{18}$F reaction and the rapid ^{18}F $\beta-$decay to ^{18}O which significantly contributes to the thermal pulse energetics. This isotope is destroyed by three reactions: ^{18}O(α, γ), ^{18}O$(\alpha,$n$)$ and ^{18}O(p,$\alpha)^{15}$N in order of decreasing nuclear timescales (although the third reaction can become faster than the first one when significant amounts of protons are produced). Since the convective tongues heat up during the TP-AGB, ^{18}O destruction becomes more and more efficient from pulse to pulse.

We can now identify which specific nuclear region contributes to change the abundance of each oxygen isotope inside a TP-AGB star. ^{16}O is depleted in the inter-shell region, but is produced inside the thermal pulses. During third dredge-up events, its surface abundance increases very slightly. ^{17}O is always considerably depleted in both the inter-shell and thermal pulse regions, so that the third dredge-up decreases its surface abundance. Finally, at the end of full amplitude thermal pulses, ^{18}O has a lower abundance than within the convective envelope.
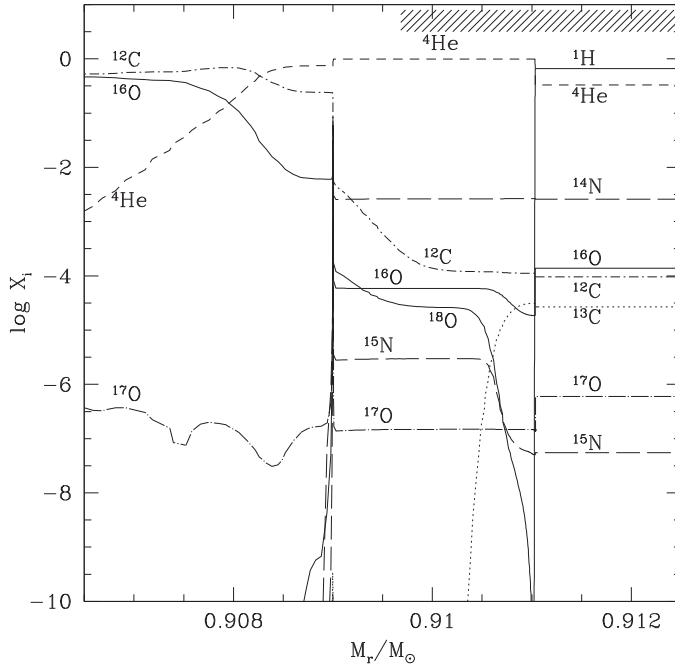
Fig. 3.27. Abundance profiles in the internal zone of the reference AGB star (initial mass of 5 $M_\odot$, [Fe/H] $= -1.56$) at the end of the inter-pulse phase just before the occurrence of the 15th thermal pulse. At that stage the total mass of the star is 3.53 $M_\odot$. The helium-burning region extends from $M_r/M_\odot \sim 0.904$ up to ~ 0.909, and is surrounded by the inter-shell region that contains the ashes of shell hydrogen burning. The temperature at the base of the convective envelope (located at $M_r/M_\odot \sim 0.911$) is $\sim 89 \times 10^6$ K, so that hot bottom burning is efficient at that stage. The hatched area on top indicates the maximum extent of the convective envelope during the next dredge-up episode. During the forthcoming 15th pulse, the convective tongue will extent up to $M_r/M_\odot \sim 0.911$.

Its abundance thus drastically decreases from third dredge-up to third dredge-up. Consequently, both $^{16}O/^{17}O$ and $^{16}O/^{18}O$ surface isotopic ratios increase during each third dredge-up episode. On the other hand if hot bottom burning occurs, the operation of the ON cycle in the convective envelope increases the amount of ^{17}O at the expense of ^{16}O, and substantially destroys ^{18}O at the stellar surface. So in massive AGB stars, such as the reference case presented here, $^{16}O/^{17}O$ can decrease after each thermal pulse while $^{16}O/^{18}O$ increases much more than in lower-mass stars that do not experience hot bottom burning.

Figure 3.28 presents the evolution of the surface abundances and isotopic ratios until the end of the TP-AGB phase in the reference model. The abscissa is the total stellar mass, which decreases due to strong mass loss on the TP-AGB and
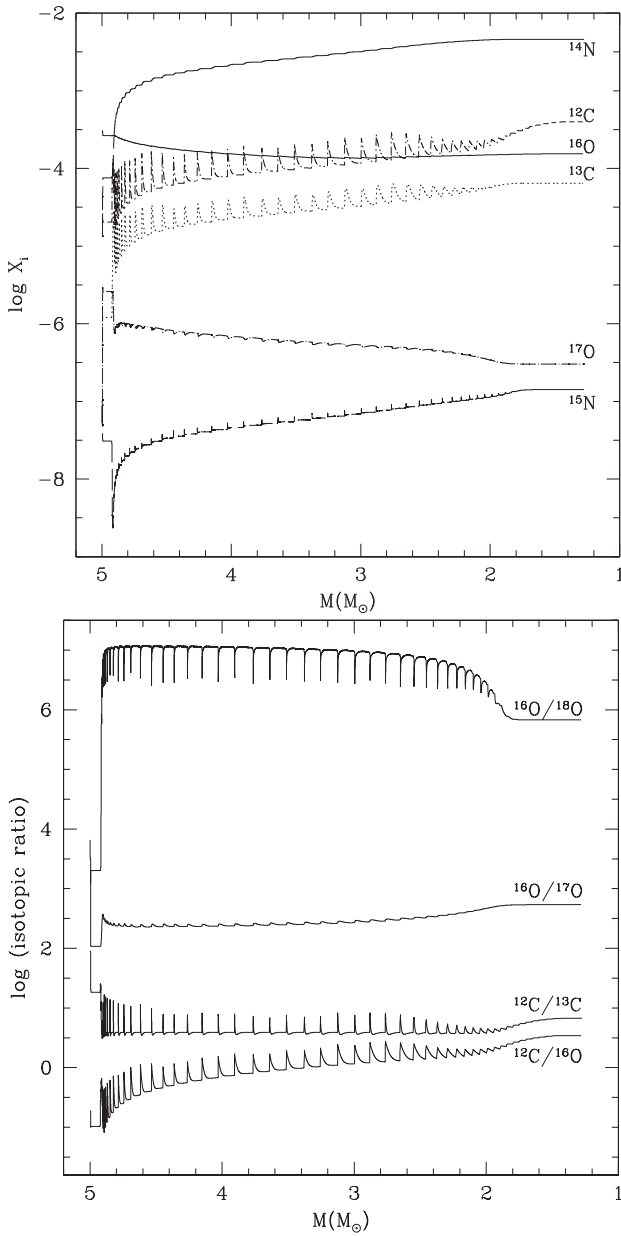
Fig. 3.28. *Bottom*: evolution of the surface abundances (logarithm of the mass fraction) of some elements as a function of remaining total stellar mass (in solar units) for our reference model (initial mass of 5 $M_\odot$ and [Fe/H] = −1.56). *Top*: same for isotopic ratios.

depicts time. Peaks on the tracks indicate the occurrence of successive thermal pulses and of associated third dredge-up and hot bottom burning episodes.

3.2.3.2 Effects of mass, metallicity, rotation, etc.

Mass and metallicity. The chemical profiles inside a star at a given evolutionary phase depend both on stellar mass and metallicity, as shown at the end of central hydrogen and helium burning in Figure 3.29 (2.5 $M_\odot$, [Fe/H] = −1.56) and Figure 3.30 (5 $M_\odot$, solar metallicity), which can be compared to Figure 3.26 (5 $M_\odot$, [Fe/H] = −1.56, reference model). The more massive a star at a given metallicity, or the less metallic a star at a given initial mass, the larger the temperature, pressure and density at a given depth, which induces a shift of the chemical profiles towards a more external region in terms of M_r/M_*.

In the case of low-mass stars (M ≤ 2 − 2.2 $M_\odot$) that ignite central He burning via a flash in the degenerate core at the tip of the red giant branch, a first dredge-up already modifies the surface abundances at the base of the red giant branch. The convective envelope expands inwards, and reaches the regions that have been previously nuclearly processed (*i.e.* both during central and thick shell H burnings), its maximum expansion decreasing with increasing initial stellar mass (Boothroyd & Sackmann 1999; Charbonnel 1994; El Eid 1994). The first dredge-up leads to an increase of the surface abundance of ^{17}O and a decrease of ^{16}O and ^{18}O, the amplitudes of which depend on the initial stellar mass as shown in Figure 3.31. For initial stellar masses lower than 2.5 $M_\odot$, the predicted post dredge-up ^{16}O/^{18}O ratio slightly increases with respect to its initial value (by up to ∼30 − 40%), while the post dredge-up ^{16}O/^{17}O ratio is substantially diminished from its initial value. This depends crucially on the maximum depth reached by the convective envelope, *i.e.* on how far the ^{17}O peak is engulfed by the convective envelope.

Thermohaline mixing. Numerous observations provide compelling evidence of a non-canonical mixing process that occurs when low-mass stars reach the so-called bump in luminosity on the red giant branch. At that phase, indeed, the surface carbon isotopic ratio drops, together with the abundances of lithium and carbon, while that of nitrogen increases slightly (see references in Charbonnel & Lagarde 2010). Thermohaline mixing has recently been identified as the mechanism that governs the photospheric composition of low-mass bright giants (Charbonnel & Zahn 2007). In these stars, this double-diffusive instability is induced by the molecular weight inversion created by the ^{3}He(^{3}He,2p)^{4}He reaction in the external wing of the hydrogen-burning shell. Among the oxygen isotopes, only ^{18}O is affected by this mechanism, which leads to a slight increase of the ^{16}O/^{18}O surface ratio compared to the post dredge-up value, while the ^{16}O/^{17}O ratio does not change (Charbonnel & Lagarde 2010).

Rotation. We show in Figure 3.32 the abundance profiles at the end of central hydrogen and helium burning for a 5 $M_\odot$, [Fe/H] = −1.56 model computed taking into account the effects of rotation as described within the formalism developed by
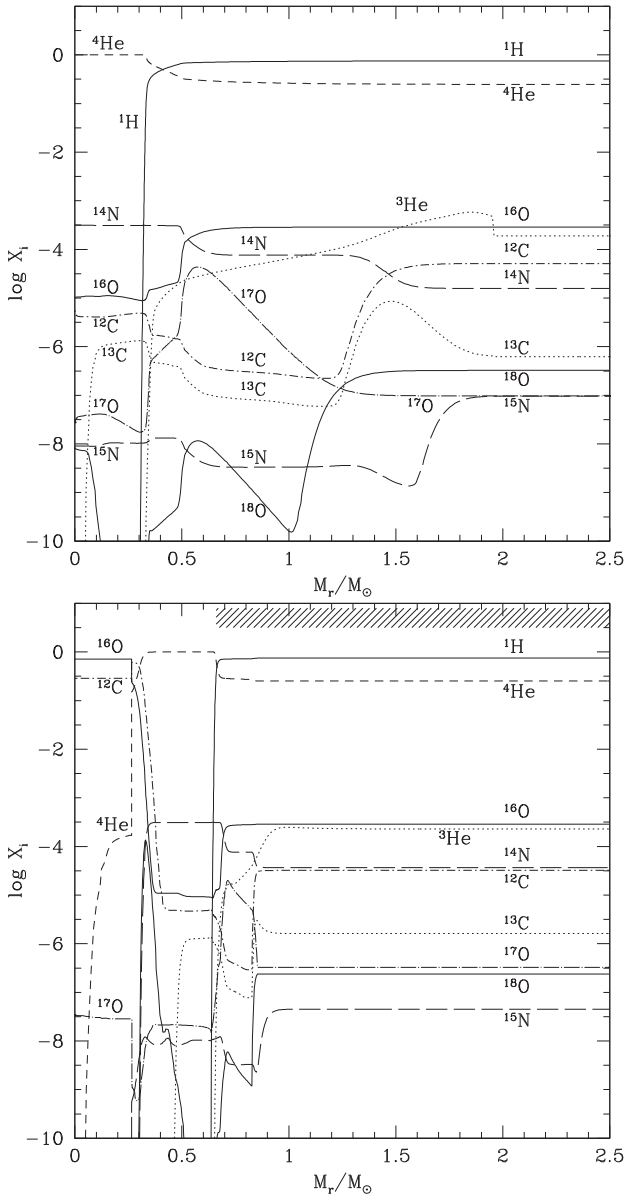
Fig. 3.29. Same as Figure 3.26 for a star with an initial mass of $2.5\,M_\odot$ and $[\text{Fe/H}] = -1.56$.

Zahn (1992) and Maeder & Zahn (1998) (see Sect. 3.2.2 and Decressin *et al.* 2009, for more details). The initial rotation velocity on the zero-age main sequence for
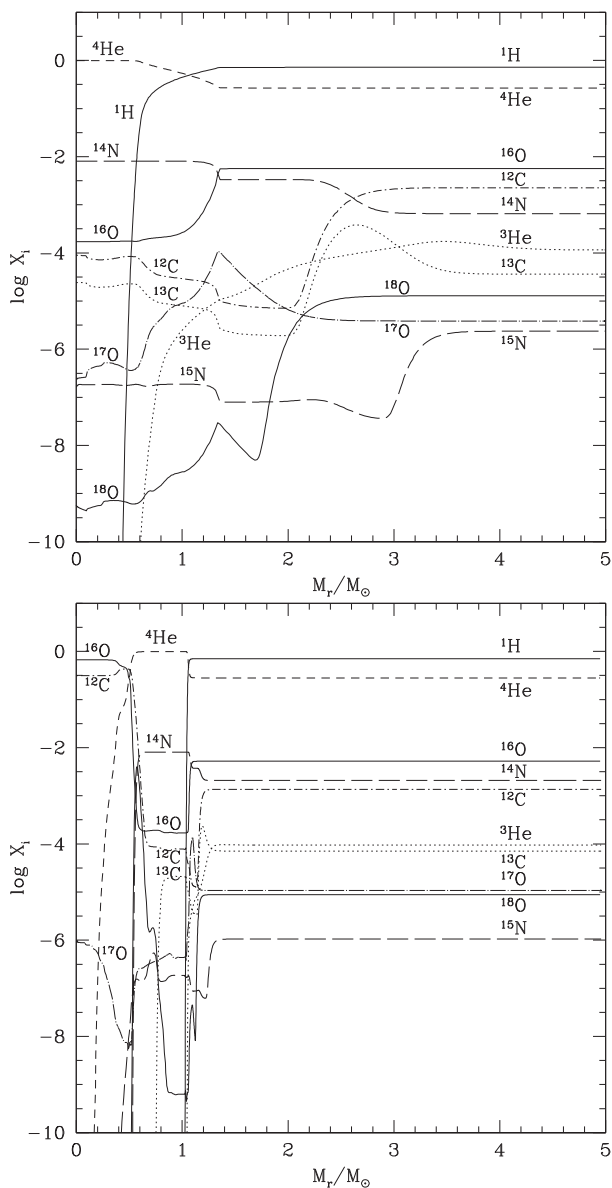
Fig. 3.30. Same as Figure 3.26 for a star with an initial mass of 5 $M_\odot$ at solar metallicity. At the end of central He burning (bottom) the convective envelope has already started deepening in mass and homogenising the external layers down to $M_r/M_\odot \sim 1.2$.

this model is 300 km s^{-1}. Rotation-induced mixing strongly modifies the internal chemical structure compared to the standard case (compare Figs. 3.26 and 3.32).
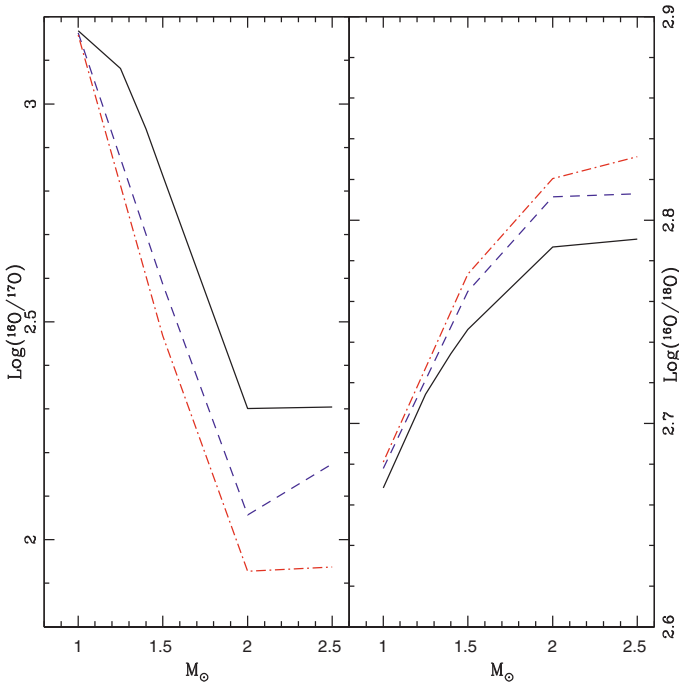
Fig. 3.31. Theoretical predictions for the surface oxygen isotopic ratios at the end of the first dredge-up as a function of the initial stellar mass for various metallicities (solar, solid line; [Fe/H] = −0.56, dashed line; [Fe/H] = −0.86, dashed-dot line). Models from Lagarde *et al.* (2011).

In the rotating model at the end of central helium burning, the abundance gradients are smoothed out in the radiative envelope (*i.e.* the region between the helium-rich region, or helium buffer, and the base of the convective envelope) compared to the standard case: ^{14}N produced in the internal H-burning layers diffuses outwards, while the ^{12}C and ^{16}O present in the envelope are transported inwards. As a consequence during the whole central He-burning phase, rotation-induced mixing produces a continuous (although modest) increase in ^{14}N concomitant to a decrease of ^{12}C and ^{16}O at the stellar surface (remember that in the standard reference model presented in Sect. 3.2.3.1, the surface composition is modified by the second dredge-up only). At the same time, the products of central helium burning, namely ^{12}C and ^{16}O, are transported from the core into the helium buffer (*i.e.* the region where helium is the dominant species, between ∼0.6 and 1.4 $M_\odot$) due mainly to shear turbulence. However the large mean molecular weight gradient existing at the base of the hydrogen-burning shell prevents the transport of primary C, N and O from the helium buffer into the hydrogen-burning shell, and hence to the surface. At the same time, hydrogen is transported from the convective envelope inwards and is rapidly captured by ^{12}C and ^{16}O nuclei through CNO
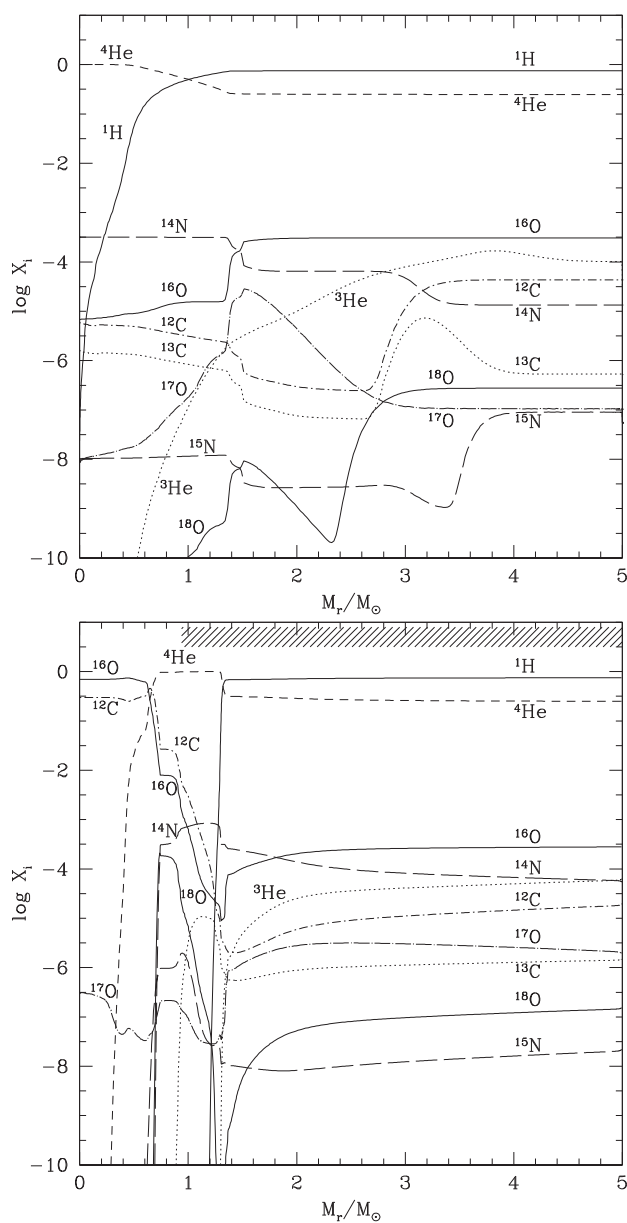
Fig. 3.32. Same as Figure 3.26 for a star with an initial mass of 5 $M_\odot$ and [Fe/H] = -1.56 computed with rotation (initial rotation velocity of 300 km s^{-1}).

burning at high temperature, leading to the production of a peak of primary ^{14}N at the base of the hydrogen-burning shell as can be seen in Figure 3.32 (right).
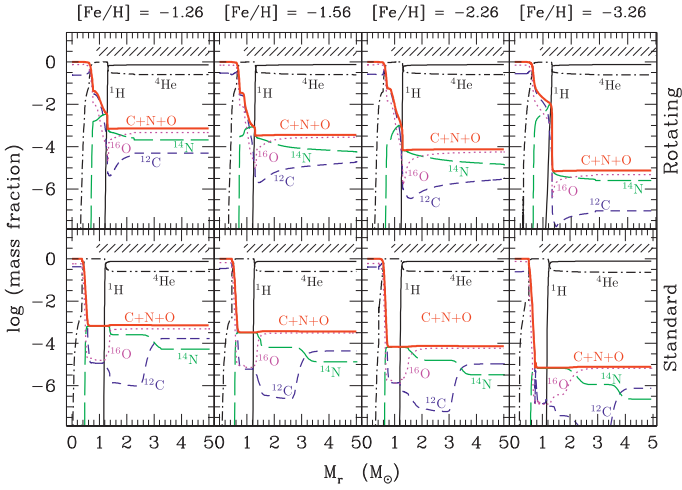
Fig. 3.33. Abundance profiles at the end of central He burning in rotating (top) and standard (bottom) 5 $M_\odot$ models at various metallicities as indicated. The elements shown are ^{1}H (full line), ^{4}He (dotted-dashed), ^{12}C (short-dashed), ^{14}N (long-dashed), ^{16}O (dotted) and C+N+O (thick). The hatched area on top of each panel indicates the maximum extent of the convective envelope during the second dredge-up. Figure from Decressin *et al.* (2009).

The resulting chemical profiles at the end of central helium burning thus differ significantly from those obtained in the standard reference case, where ^{14}N is only produced in the hydrogen-burning shell from the ^{12}C and ^{16}O originally present in the star and, therefore, of secondary origin (Meynet & Maeder 2002). During the second dredge-up, the convective envelope of the 5 $M_\odot$ rotating model reaches the polluted helium buffer (hatched area in Fig. 3.32), producing a large surface abundance increase in ^{4}He and in primary ^{12}C, ^{14}N and ^{16}O. As a consequence there is an increase in the total C+N+O and overall metallicity in the envelope and thus at the stellar surface.

The impact of rotation on stellar properties and yields is known to depend strongly on metallicity (see *e.g.* Meynet & Maeder 2002). The metallicity dependence for rotating 5 $M_\odot$ stars is depicted in Figure 3.33. As discussed previously, the C+N+O profile outside the CO core is constant (*i.e.* it neither changes with time nor with depth in these layers with respect to its initial value) in the standard models, while it strongly increases in the helium buffer below the hydrogen-burning shell in the rotating models. This C+N+O step is higher in rotating stars with lower metallicity, which results in a stronger C+N+O surface enhancement after the second dredge-up in the most metal-poor stars as shown in Figure 3.34. At [Fe/H]= -2.26, the envelope (and thus the wind) of all stars more massive than $\sim$5 $M_\odot$ undergoes a C+N+O increase of one to two orders of magnitude, while an increase of a factor of 5 is obtained at [Fe/H]= -1.26. When metallicity becomes
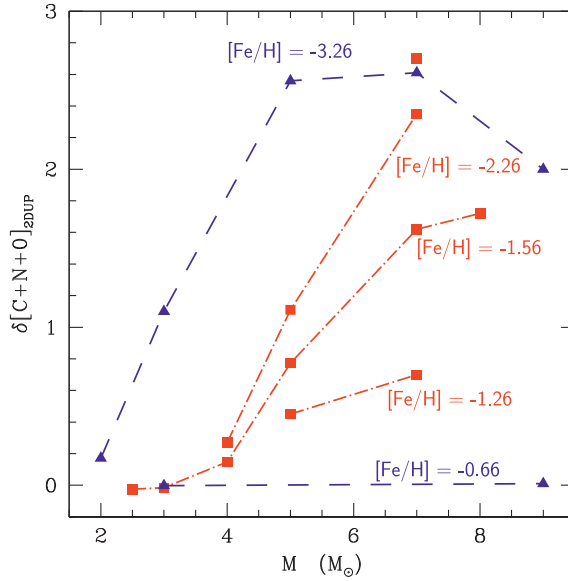
Fig. 3.34. Surface C+N+O increase index ($\delta[C+N+O]_{2DUP} = [(C+N+O)/Fe]_{2DUP}$- $[(C+N+O)/Fe]_{ini}$) at the end of the second dredge-up for rotating stars of various initial masses and metallicities. Figure from Decressin *et al.* (2009).

Table 3.14. Surface abundance variations after the completion of the second dredge-up with respect to the initial composition for the models with initial value of $[Fe/H] = -1.56$. See Decressin *et al.* (2009) for more details.

	$2.5\ M_\odot$	$3\ M_\odot$	$4\ M_\odot$	$5\ M_\odot$	$7\ M_\odot$	$8\ M_\odot$
			Standard models			
He	0.26	0.26	0.29	0.32	0.36	0.36
$\delta[C/Fe]$	-0.20	-0.25	-0.29	-0.31	-0.30	-0.34
$\delta[N/Fe]$	0.44	0.48	0.60	0.75	0.79	0.81
$\delta[O/Fe]$	-0.01	-0.01	-0.03	-0.06	-0.10	-0.11
$\delta[CNO/Fe]$	0.00	0.00	0.00	0.00	0.00	0.00
			Rotating models			
He	0.29	0.29	0.32	0.34	0.35	0.36
$\delta[C/Fe]$	-1.12	-0.86	-0.20	1.44	2.14	2.16
$\delta[N/Fe]$	1.23	1.12	1.13	1.24	1.19	1.09
$\delta[O/Fe]$	-0.65	-0.36	-0.01	0.18	1.46	1.55
$\delta[CNO/Fe]$	0.00	0.00	0.15	0.78	1.62	1.71

higher than $[Fe/H] \sim -1$, rotation-induced mixing increases the total C+N+O by less than a factor of $2 - 3$. The effect is null for more metal-rich stars.

Table 3.14 summarises the abundance variations after the second dredge-up in all the standard and rotating models of Decressin *et al.* (2009) at $[Fe/H] = -1.56$.

The main signature of rotational mixing at the surface of massive early-AGB stars ($M \geq 4\ M_\odot$) is a strong increase in He-burning products, *i.e.* primary CNO. The total increase of C+N+O at the surface of rotating models depends mainly on the depth reached by the convective envelope during the second dredge-up; a stronger variation is thus predicted with increasing stellar mass.

3.2.3.3   Yields

As far as oxygen isotopes are concerned, low- and intermediate-mass stars at the end of their existence are net producers of ^{17}O, and partially destroy ^{16}O and ^{18}O. Although both the evolution of these stars and their nucleosynthesis are very well understood, the quantitative determination of reliable yields is still unreliable today. This is due to several uncertainties in the input physics of the stellar models, in particular in the mass loss rates that are crucial as far as the competition between the third dredge-up and hot bottom burning is concerned, but also in the treatment of internal transport processes of chemicals (convection, overshooting, rotation-induced mixing, thermohaline instability, etc.) during the TP-AGB phase and even during earlier evolution phases.

In view of the uncertainties we decide to show here only the results of the most recent computations published to date in the literature, that is the standard (*i.e.* non-rotating) models for stars of various initial masses and metallicities by Karakas (2010). Figures 3.35 and 3.36 present for each O isotope the corresponding production factor (defined as $\log_{10}[<X(i)>/X_0(i)]$, where $<X(i)>$ is the average mass fraction of species i in the wind and $X_0(i)$ its initial mass fraction). We refer to this paper for more details and comparisons with other studies.

3.2.3.4   Observational probes

The theoretical oxygen isotope ratios can be compared with those observed in evolved stars (Harris & Lambert 1984a,b; Harris *et al.* 1985b, 1987, 1985a, 1988), in interstellar grains (Nittler *et al.* 1994)[8] and in meteorites (Huss *et al.* 1994). Note however that the few measurements that were made only for field giants have large observational errors that prevent a thorough comparison with model predictions, and do not allow a clear investigation of the dependence of these ratios with the stellar mass.

Figure 3.37 shows the comparison for stars with masses below $\sim 3\ M_\odot$. The data are from Harris & Lambert (1984a), Harris *et al.* (1988), and the models from Charbonnel & Lagarde (2010) account for rotation-induced mixing and thermohaline convection (see the labels in the figure caption). In the $^{16}O/^{17}O$ *vs.* $^{16}O/^{18}O$ plane, the post-dredge-up stellar observations lie along a roughly vertical band consistent with the theoretical predictions of first dredge-up in stars with initial oxygen isotope ratios very close to the solar values. As discussed

---

[8]Most grains form during high-mass-loss episodes of AGB stars, namely near the tip of the AGB.
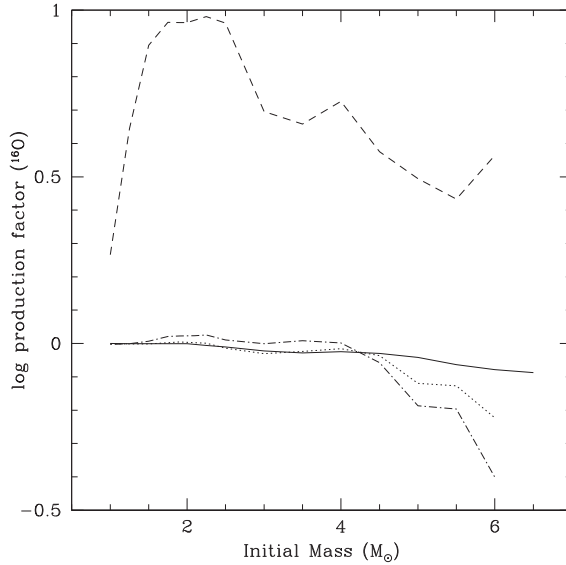
Fig. 3.35. Production factor (defined as $\log_{10}[<X(i)>/X_0(i)]$, where $<X(i)>$ is the average mass fraction of species i in the wind and $X_0(i)$ its initial mass fraction) of ^{16}O as a function of initial mass for various metallicities ($Z = 0.02$, solid line; $Z = 0.008$, dotted line; $Z = 0.004$, dot-dashed line; $Z = 0.0001$, long dashed line). The large production factor in the lowest metallicity models results from the contribution of deep third dredge-up bringing a bit of ^{16}O into an envelope with very little ^{16}O to begin with. The overall contribution of these stars to ^{16}O production should be small though, but could have important consequences when observing O in low metallicity planetary nebulae (see Karakas & Lugaro 2010). Models from Karakas (2010).

in Section 3.2.3.2, thermohaline convection on the red giant branch affects only slightly the ^{16}O/^{18}O ratio in low-mass stars, and leaves ^{16}O/^{17}O unaffected. On the other hand, rotation-induced mixing lowers the ^{16}O/^{17}O and helps accounting for the lowest ^{16}O/^{18}O values of the sample stars. Given the large observational uncertainties, the predictions are reasonably consistent with the O isotopic ratios measured in red giant stars. Also, the data for AGB stars with ^{12}C/^{13}C near the CN-cycle equilibrium value (not shown here) have oxygen isotope ratios consistent with theoretical predictions for intermediate-mass stars undergoing hot bottom burning.

However in the ^{16}O/^{17}O *vs.* ^{16}O/^{18}O plane, the oxygen isotope ratios observed in AGB stars as well as in some of the pre-solar oxide grains (Nittler *et al.* 1994) are in a region inaccessible to both the first dredge-up or hot bottom burning (see *e.g.* Fig. 7 in Boothroyd & Sackmann 1999). Cool carbon stars (the so-called J-type stars) show rather low ^{16}O/^{17}O isotopic ratios while only upper limits have been found for the ^{16}O/^{18}O ratio. Most of the other AGB stars present ^{16}O/^{17}O
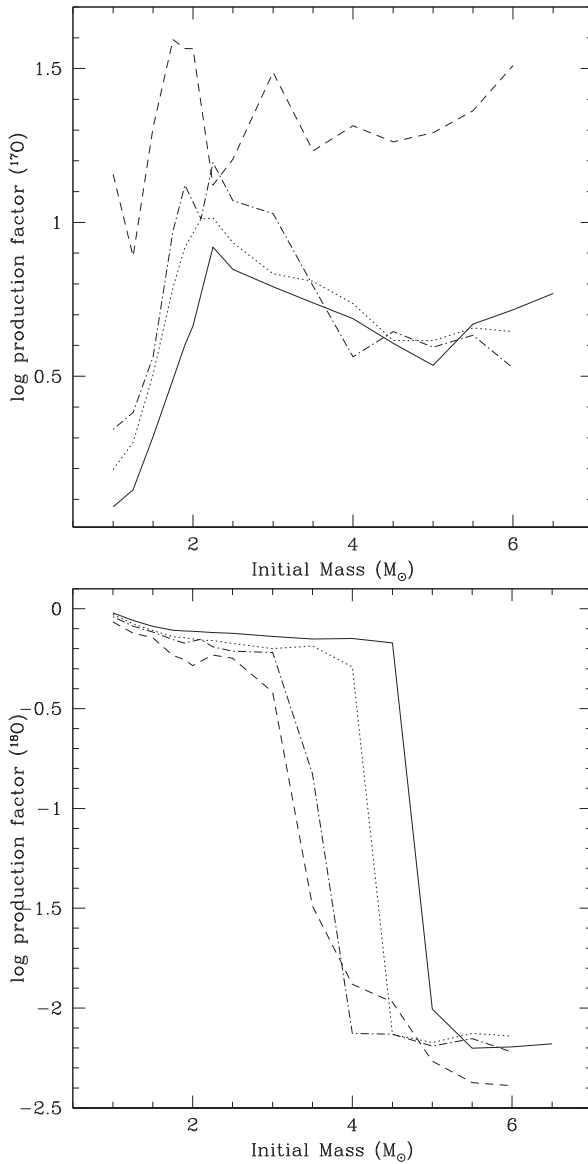
Fig. 3.36. Same as Figure 3.35 for ^{17}O and ^{18}O.

ratios between 300 and 4000 and ^{16}O/^{18}O ratios between 500 and 5000. Stars with rather high ^{16}O/^{17}O ratios are difficult to explain with intermediate-mass AGB models (see *e.g.* Boothroyd *et al.* 1995). Let us however emphasise that part of the discrepancy may be due to the important uncertainties that remain concerning the nuclear cross sections of proton captures on ^{17}O.
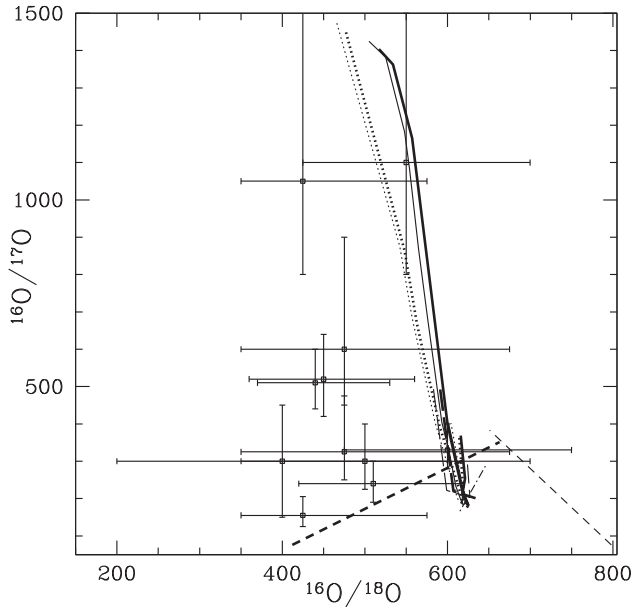
Fig. 3.37. $^{16}O/^{17}O$ *vs.* $^{16}O/^{18}O$ observed by Harris & Lambert (1984a); Harris *et al.* (1988) for red giant stars in the 1–3 $M_\odot$ range. The lines are predictions for solar metallicity models by Charbonnel & Lagarde (2010). Theoretical predictions are shown at the tip of the RGB and after completion of the second dredge-up (thin and thick continuous lines respectively). Standard models (neither thermohaline nor rotation-induced mixing) are shown as dotted lines, models with thermohaline mixing only (no rotation) as solid lines and models with thermohaline and rotation-induced mixing for different initial rotation velocities as long-dashed, dot-dashed and dashed lines. Figure from Charbonnel & Lagarde (2010).

On that question grain data are more precise than stellar data. Indeed, while many of the grain data are consistent with dredge-up in stars of near-solar metallicity, roughly a dozen grains show ^{18}O depletion by factors ≥ 3, and several of these have ^{17}O abundances a factor of 2 lower than would be expected by AGB stars undergoing hot bottom burning. In view of the relatively large $^{12}C/^{13}C$ ratios observed in most of these AGB stars, the non-canonical mixing that could lead to the observed patterns is suspected to occur on the RGB rather than on the AGB (see Sect. 2.2.3.2).

Finally, another very interesting way to constrain stellar evolution models of AGB stars is to compare the predicted surface isotopic ratios with those determined in primitive meteorites (mainly through grains included inside carbon rich chondrites). For example, measurements of the O isotopic ratios have been made on a ~3 μm Al_2O_3 grain of the Bishunpur LL3.1 chondrite by Huss *et al.* (1994). The derived ratios, $^{16}O/^{17}O = 385 \pm 5$ and $^{16}O/^{18}O = 853 \pm 30$, are in perfect agreement with ratios corresponding to a 3–4 $M_\odot$ AGB star of nearly solar

metallicity. This is of course in favour of the presence, when the Solar System was formed, of one or a few AGB stars in its surroundings. Such grains are indeed well known to be formed in the cool atmosphere of evolved AGB stars (*i.e.* when mass loss rates become rather high).

3.2.4   Binary stars

Many massive stars belong to multiple systems (Zinnecker 2008), a subset of which will go through mass transfer episodes. In such cases, the evolution of the massive star will be modified with respect to that it would have had in isolation. Also, before any mass transfer event actually occurs, tidal forces in close binary systems probably trigger instabilities inside the star that modify its structure.

A lot of work remains to be done in this area of research, and also the range of parameters to be explored is much more extended than in a single star evolutionary scenario. In addition to mass, metallicity and rotation which are, among others, very important properties of single stars, mass ratios and orbital periods are needed to specify the evolution of a binary system.

At present chemical evolution models of galaxies account for binary scenarios only through Type Ia supernovae. Therefore, it is difficult to assess the importance of close binary evolution in the synthesis of oxygen. Langer (2003) provides an interesting discussion of this question. He first makes a very general comment on the importance of a given star population in the synthesis of a peculiar element. If that population represents a fraction f of the whole stellar population, in order to contribute in a significant way to the synthesis of that element, the respective yield in that population needs to be larger by a factor $1/f$ than the corresponding single star yield. Applied to binary systems, if we take $f = 0.5$ (clearly an over-estimate since not all binary systems have components that will undergo a mass transfer episode), then the yield would be enhanced by about a factor of 2 (here an underestimate) with respect to the single star scenario for binary evolution to have a significant impact.

Regarding ^{16}O, although in some peculiar situations the enhancement factor can indeed be greater than a factor of 2, it seems reasonable to think that close binary evolution will not significantly distort the single star scenario as far as chemical evolution is concerned (Langer 2003). For the other two isotopes, the situation may be different, but remains difficult to be assessed in a quantitative way.

3.3   Final comments

Let us end this chapter emphasising two important aspects.

1. Massive stars are the sources of ^{16}O in the Universe. The reasons supporting this assertion are the following.

    - An analysis of the surface abundances of very metal-poor halo stars indicates a high oxygen to iron ratio. According to chemical evolution

models (see Chapter 4), this reflects the fact that these stars are formed from material which has been enriched by oxygen-rich ejecta from massive stars.

- Observations of the surface abundances of naked He-burning stellar cores, namely WC and WO stars, confirm that nuclear burning reactions produce large amounts of oxygen.

- Since He-burning also occurs in low and intermediate mass stars, why do these types of stars hardly contribute to ^{16}O synthesis? The reason is that in these stars most, if not all, of the material processed by He burning will remain locked in the remnant (a white dwarf), and thus will not be ejected into the interstellar medium at the end of the star lifetime. For massive stars, the CO-core masses are sufficiently large for a significant fraction to be ejected by the stellar winds (in the case of the WC-WO stars) or at the time of the supernova explosion.

2. In order to constrain the predictions of galaxy chemical evolution models, which aim at reproducing observed abundance patterns in the Universe (see Chapter 4), the abundances observed *at the surface* of stars are sometimes used. This is of course legitimate provided the surface abundances reflect those of the ISM at the birth of the star, *i.e.* if the surface abundances have not changed during the stellar lifetime. The causes for changing the surface abundances can be mass loss, mass accretion from a close companion and internal mixing processes induced by, for instance, rotation or convection. The most interesting targets for constraining the chemical evolution models are single, low-mass main-sequence stars (which are slow rotators). Even in that case, various diffusion processes may change the surface abundances, but the situation is much more reliable than looking at the surface abundances of more evolved stars. At least, any other choice must be carefully considered and critically discussed with respect to any process which may have changed the surface abundances. This is the case, for example, when using planetary nebulae as oxygen abundance indicators in galaxies, as discussed in Chapter 2.

Chapter 4

THE EVOLUTION OF OXYGEN IN GALAXIES

4.1 Preliminaries

This chapter deals with the overall buildup of oxygen in galaxies over the ages, which is a specific aspect of a more general topic: the chemical evolution of galaxies.

Chemical evolution is the study of the transformation of gas into stars and of the resulting evolution of the chemical composition of a galaxy. It has not yet the status of a full astrophysical theory, *e.g.* the theories of stellar evolution or of hierarchical structure formation in the Universe. The reason is our poor understanding of the driver of galactic chemical evolution, namely large-scale star formation. In contrast, the drivers of stellar evolution (energy producing nuclear reactions in plasmas heated by gravity) and of hierarchical structure formation (cold dark matter assembled by gravity in an expanding universe) are fairly well understood. For that reason, those theories can make relatively robust predictions concerning, for instance, various evolutionary timescales. This is not the case with galactic chemical evolution.

Nonetheless, galactic chemical evolution provides a useful framework in which one may interpret the large (and ever expanding) body of observational data concerning elemental and isotopic abundances in stars of various ages, in the interstellar medium (ISM) and even the intergalactic medium. In particular, galactic chemical evolution allows one to:

- *Check/constrain our understanding of stellar nucleosynthesis* (expressed through the predicted yields of stars of various masses and metallicities) in a *statistical way*, *i.e.* by comparing galactic chemical evolution results to the mean trends and dispersion of abundances and abundance ratios.

- *Establish a chronology of events* in a given system, by finding when the metallicity reached a certain value, or when some stellar source (SNIa, AGBs etc.) became an important contributor to the abundance of a given nuclide.

- *Infer how a system was formed*, by constraining the history of the star formation rate (SFR) or of various gas movements, *e.g.* infall for the local disk or outflow for the Galactic halo.

Different kinds of progressively more sophisticated models of galactic chemical evolution can be developed. In the *simple homogeneous model* ejecta of dying stars are instantaneously mixed in the ISM, which thus acquires a unique chemical composition at any time. Models of *inhomogeneous galactic chemical evolution* relax this "instantaneous mixing approximation" in a semi-analytical manner, and can account for dispersion of chemical abundances in stars and the ISM. Finally *chemo-dynamical models* also treat the dynamics of a galaxy's gas, stars and dark matter (either in a static or in a cosmological environment) providing a self-consistent framework for galactic chemical evolution (see *e.g.* Gibson *et al.* 2003 for a review). One should keep in mind, however, that (i) both the number of free parameters and the number of potentially constraining observables increase with the degree of sophistication of the model, and (ii) all models whatever their level of sophistication, suffer equally from our poor understanding of star formation (and stellar feedback in the case of chemo-dynamical models).

In Section 4.2 we develop the formalism of the galactic chemical evolution model and we present the required ingredients: stellar properties and yields, stellar initial mass function, star formation rate and gaseous flows. We also provide some useful analytical solutions of the system of galactic chemical evolution equations obtained under the so-called "instantaneous recycling approximation".

Subsequent sections describe our understanding of the chemical evolution of various galaxian subsystems, mostly in the framework of the simple, homogeneous model. In Section 4.3.1 we study the evolution of the solar vicinity, which is the best studied system (for obvious reasons). In Sections 4.3.2 and 4.3.3 we consider – rather briefly – the salient features of the evolution of two major subsystems of our Galaxy, namely the halo and the bulge. Section 4.3.4 describes our current understanding of the Milky Way (MW) disk, discussing at some length the complex ingredients (star formation, infall, radial inflows, stellar migration, etc.) that may affect its evolution. Section 4.4 deals with the evolution of other resolved spirals, Section 4.5 with the evolution of the Magellanic Clouds and Section 4.6 discusses the galaxian mass-metallicity relation. In all those cases we present the general context and focus on oxygen and the information that its study may provide for a given system. However, it will soon become clear to the reader that understanding the chemical evolution of oxygen requires considering other elements as well (*e.g.* iron), and demands many observational constraints in addition to abundances. We also point out that the oxygen abundance constraints used in the works mentioned in this chapter are not necessarily in agreement with the latest data and recommendations summarised in Chapter 2.

4.2   Chemical evolution modelling

In models of galactic chemical evolution, a galaxy consists initially of gas of primordial composition, namely with mass fractions of $X_H \sim 0.75$ for H and $X_{He} \sim 0.25$ for ^{4}He, as well as trace amounts of D, ^{3}He and ^{7}Li (abundances are given as *mass fractions X_i* for element or isotope i, with $\Sigma_i X_i = 1$). The gas is progressively converted into stars with a *star formation rate (SFR)* $\Psi(t)$, the star masses M

having a distribution $\Phi(M)$, called the *initial mass function (IMF)*[1]. Depending on its lifetime τ_M, the star of mass M created at time t dies at time $t + \tau_M$ and returns a part of its mass to the interstellar medium, either through stellar winds (in the case of low-mass and intermediate-mass stars) or through supernova explosions (in the case of massive stars[2]). The ejected material is enriched in elements synthesised by nuclear reactions in the stellar interiors, while some fragile isotopes (like D) have been destroyed. Thus, the ISM is progressively enriched in elements heavier than H, while its D content is reduced. New stellar generations are formed from this ISM, their composition being progressively more enriched in heavy elements, *i.e.* with an ever increasing *metallicity Z* (where $Z = \Sigma X_i$ for all elements i heavier than He).

In the framework of the simple model of galactic chemical evolution it is assumed that the *stellar ejecta* are immediately and efficiently mixed in the ISM[3]. As a result, the ISM is characterised at each time t by a unique chemical composition $X_i(t)$, which is also the composition of the stars formed at this time. Since the surface composition of stars on the main sequence is not affected, in general, by nuclear reactions[4], observations of stellar abundances reveal, in principle, the composition of the gas of the system at the time when those stars were formed. One may thus recover the chemical history of the system and confront observations to models of galactic chemical evolution.

4.2.1 Formalism

The galactic chemical evolution scenario sketched in the previous paragraphs can be quantitatively described by a set of integro-differential equations (Tinsley 1980).

The *evolution of the total mass of the system m(t)* is given by

$$\frac{\mathrm{d}m}{\mathrm{d}t} \;=\; [\, f \;-\; o \,]. \tag{4.1}$$

The righ hand terms are optional and describe infall of extragalactic material at a rate $f(t)$ or outflow of mass from the system at a rate $o(t)$; both terms will be discussed in Section 4.2.5. If the system evolves without any input or loss of mass,

---

[1]In principle, the IMF may depend on time, either explicitly or implicitly (*i.e.* through a dependence on metallicity, which increases with time); in that case one should adopt a star creation function $C(t, M)$ (making the solution of the galactic chemical evolution equations more difficult). In practice, however, observations indicate that the IMF does not vary with the environment, allowing the separation of the variables t and M and adopt $C(t, M) = \Psi(t)\Phi(M)$.

[2]Massive stars also eject part of their mass through a wind, either in the red giant stage (a rather negligible fraction) or in the Wolf-Rayet stage (an important fraction of their mass, in the case of the most massive stars).

[3]This is the so-called *instantaneous mixing approximation*, not to be confused with the *instantaneous recycling approximation*, to be discussed in Section 4.2.6.

[4]An exception to that rule is the fragile D, already burned in the pre-main sequence all over the star's mass; Li isotopes are also destroyed, and survive only in the thin convective envelopes of the hottest stars.

the right hand member of Equation (4.1) is equal to zero; this is the so-called *closed box model*, the simplest model of galactic chemical evolution.

The *evolution of the mass of the gas* $m_G(t)$ of the system is given by

$$\frac{\mathrm{d}m_G}{\mathrm{d}t} \;=\; -\Psi \;+\; E \;+\; [\,f \;-\; o\,] \tag{4.2}$$

where $\Psi(t)$ is the star formation rate (SFR) and $E(t)$ is the *rate of mass ejection by dying stars*

$$E(t) \;=\; \int_{M_t}^{M_U} (M - C_M)\,\Psi(t - \tau_M)\,\Phi(M)\;\mathrm{d}M \tag{4.3}$$

where the star of mass M created at the time $t - \tau_M$ dies at time t (if $\tau_M < t$) and leaves a compact object (white dwarf, neutron star, black hole) of mass C_M, *i.e.* it ejects a mass $M - C_M$ in the ISM. The integral in Equation (4.3) is weighted by the initial mass function of the stars $\Phi(M)$ and runs over all stars massive enough to have already died at time t. The least massive of them has a mass M_t and a lifetime $\tau_M \le t$. The upper mass limit of the integral M_U is the upper mass limit of the IMF and is discussed in Section 4.2.3.

Obviously, the *mass of stars* $m_S(t)$ of the system (alive + dead) can be derived through

$$m \;=\; m_S \;+\; m_G. \tag{4.4}$$

The evolution of the chemical composition of the system is described by equations similar to Equations (4.2) and (4.3). The *mass of element/isotope* i in the gas is $m_i = m_G X_i$ and its evolution is given by

$$\frac{\mathrm{d}(m_G\,X_i)}{\mathrm{d}t} \;=\; -\Psi X_i \;+\; E_i \;+\; [\,f X_{i,f} \;-\; o X_{i,o}\,] \tag{4.5}$$

i.e. star formation at a rate Ψ removes element i from the ISM at a rate ΨX_i, while at the same time stars re-inject in the ISM that element at a rate $E_i(t)$. If infall is assumed, the same element i is added to the system at a rate $f X_{i,f}$, where $X_{i,f}$ is the abundance of nuclide i in the infalling gas (usually, but not necessarily, assumed to be primordial). If outflow takes place, element i is removed from the system at a rate $o X_{i,o}$ where $X_{i,o}$ is the abundance in the outflowing gas; usually, $X_{i,o} = X_i$, *i.e.* the outflowing gas has the composition of the average ISM, but in some cases it may be assumed that the hot supernova ejecta (rich in metals) leave preferentially the system, in which case $X_{i,o} > X_i$ for metals.

The *rate of ejection of element* i *by stars* is given by

$$E_i(t) \;=\; \int_{M_t}^{M_U} Y_i(M)\,\Psi(t - \tau_M)\,\Phi(M)\;\mathrm{d}M \tag{4.6}$$

where $Y_i(M)$ is the *stellar yield of element/isotope* i, *i.e.* the mass ejected in the form of that element by the star of mass M. Note that $Y_i(M)$ may depend *implicitly* on time t, if it is metallicity dependent (see Sect. 4.2.2).

The masses involved in the system of Equations (4.1) to (4.6) may be either *physical* masses, *i.e.* m, m_G, m_S, etc. are expressed in $M_\odot$ and $\Psi(t)$, $E(t)$, etc. in $M_\odot\ \mathrm{Gyr}^{-1}$, or *reduced* masses (*mass per unit final mass of the system*), in which case m, m_G, m_S, etc. have no dimensions and $\Psi(t)$, $E(t)$, etc. are in Gyr^{-1}. The latter possibility allows one to perform calculations for a system of arbitrary mass and normalise the results to the known/assumed present-day mass of that system; note that instead of mass, one may use volume or surface mass densities.

The system of integro-differential Equations (4.1) to (4.6) can only be solved numerically unless some specific assumptions are made, in particular the instantaneous recycling approximation (to be discussed in Sect. 4.2.6). Its solution requires three types of ingredients.

- *Stellar properties*: stellar lifetimes τ_M, masses of stellar residues C_M and stellar yields $Y_i(M)$; all those quantities can be derived from the theory of stellar evolution and nucleosynthesis and depend (to various degrees) on the initial stellar metallicity Z.

- *Collective stellar properties*: the initial mass function $\Phi(M)$ and the star formation rate Ψ; none of them can be reliably derived from first principles at present, and one has to rely on empirical prescriptions.

- *Gas flows* into and out of the system (infall, inflow, outflow, wind): in simple galactic chemical evolution models these factors are optional, *i.e.* their introduction depends on the nature of the considered galactic system (*e.g.* infall for the solar neighbourhood or winds for small galaxies). In more physical (*e.g.* hydrodynamical) models in a cosmological framework, they should stem naturally from the physics of the system.

We discuss these ingredients in the following sections.

4.2.2   Stellar properties: lifetimes, residues and yields

Stellar lifetime is a strongly decreasing function of stellar mass (see Fig. 4.1). Its value depends on various factors (*e.g.* mixing, mass loss, etc.) and, most importantly, on stellar metallicity. Indeed, low metallicity stars have lower opacities and are more compact and hot than their high metallicity counterparts; as a result, their lifetimes are shorter (see Fig. 4.1 right). However, in stars with $M > 2\ M_\odot$, where H burns through the CNO cycles, this is compensated to some degree by the fact that the H-burning rate (proportional to the CNO content) is smaller, making the corresponding lifetime longer; thus, for $M > 10\ M_\odot$, low metallicity stars live slightly longer than solar metallicity stars. Of course, these results depend strongly on other ingredients, *e.g.* rotation (see Chapter 3). In principle, such variations in τ_M should be taken into account in galactic chemical evolution models; in practice, however, the errors introduced by ignoring them are smaller
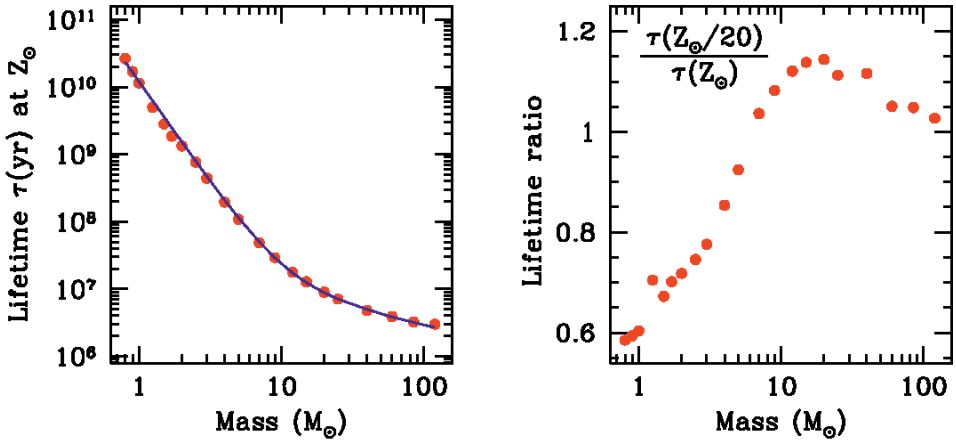
Fig. 4.1. *Left*: lifetimes of stars of solar metallicity $Z_\odot$; *points* are from Geneva stellar models (Schaller *et al.* 1992) and the *curve* is a fit to those points (see Eq. (2.7)). *Right*: ratio of stellar lifetimes at $Z_\odot/20$ and $Z_\odot$ for the same models.

than the other uncertainties of the problem, *e.g.* related to stellar yields or to the IMF[5].

The lifetime of a star of mass M (in $M_\odot$) and metallicity $Z_\odot$ can be approximated by

$$\tau(M) = 1.13 \; 10^{10} M^{-3} + 0.6 \; 10^8 M^{-0.75} + 1.2 \; 10^6 \text{ yr}. \qquad (4.7)$$

This fitting formula is displayed as a solid curve in Figure 4.1 (left). A $Z_\odot$ star of 1 $M_\odot$, like the Sun, is bound to live for 11.4 Gyr, while a 0.8 $M_\odot$ star for $\sim$23 Gyr; the latter, however, if born with a metallicity Z $\leq$ 0.05 $Z_\odot$, will live for "only" 13.8 Gyr, *i.e.* its lifetime is comparable to the age of the Universe. Stars of mass 0.8 $M_\odot$ are thus the lowest mass stars that have ever died since the dawn of time (and the heaviest stars surviving in the oldest globular clusters).

The masses of stellar residues are derived from stellar evolution calculations and confronted to observational constraints. In the regime of low- and intermediate-mass stars (LIMS[6]), *i.e.* for $M \leq 8-9$ $M_\odot$, the evolutionary outcome is a white dwarf (WD), the mass of which (in $M_\odot$) is given by Weidemann (2000):

$$C_M(WD) = 0.08 \; M + 0.47 \qquad\qquad (M < 8-9). \qquad (4.8)$$

---

[5]Metallicity dependent lifetimes *have to be taken into account* in models of the spectro-photometric evolution of galaxies, where they have a bigger impact.

[6]LIMS are defined as those stars evolving to white dwarfs. However, there is no universal definition for the mass limits characterising low- and intermediate-mass stars. The upper limit is usually taken around 8–9 $M_\odot$, although values as low as 6 $M_\odot$ have been suggested (in models with very large convective cores). The limit between low and intermediate masses is the one separating stars powered on the main sequence by the p-p chains from those powered by the CNO cycle, and is $\sim$1.2–1.7 $M_\odot$ depending on metallicity.
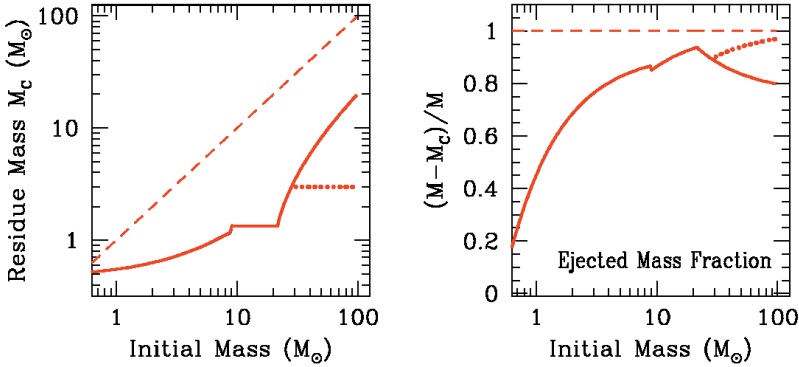
Fig. 4.2. *Left:* masses of stellar residues as a function of initial stellar mass, for stars of metallicity $Z_\odot$; for massive stars (M > 30 $M_\odot$) the two curves correspond to different assumptions about mass loss, adopted in Limongi & Chieffi (2008)(*solid curve*) and Woosley & Heger (2007) (*dotted curve*), respectively. *Right:* mass fraction of the ejecta as a function of initial stellar mass; the two curves for M > 30 $M_\odot$ result from the references in the left figure.

Stars more massive than 8–9 $M_\odot$ explode as supernovae (SN), either after electron captures in their O-Ne-Mg core (M $\leq$ 11 $M_\odot$) or after Fe core collapse (M $\geq$ 11 $M_\odot$). The nature and mass of the residue depends on the initial mass of the star and on the mass remaining before the explosion. It is often claimed that solar metallicity stars of M $\leq$ 25 $M_\odot$ leave behind a neutron star (NS), while heavier stars leave a black hole (BH). Neutron star masses are well constrained by the observed masses of pulsars in binary systems: $M_{NS} = 1.35 \pm 0.04$ $M_\odot$ (Thorsett & Chakrabarty 1999), which is adopted here

$$C_M(NS) = 1.35 \qquad\qquad (8 - 9 < M < 25) \qquad (4.9)$$

i.e. C_M is independent of the initial mass M in that case. However, black-hole masses are not known observationally as a function of the progenitor mass, and theoretical models are also quite uncertain in that respect. Thus, for solar metallicity stars with mass loss, the Frascati models (Limongi & Chieffi 2008) produce black-hole masses proportional to the initial mass, which can be approximated (in $M_\odot$) by

$$C_M(BH) = 0.24 M - 4 \qquad\qquad (M > 25) \qquad (4.10)$$

while Woosley & Heger (2007) find that, as a result of high mass losses for $M \geq$ 25 $M_\odot$, the average black-hole mass (in $M_\odot$) is

$$C_M(BH) = 3 \qquad\qquad (M > 25) \qquad (4.11)$$

(see Fig. 4.2). It is commonly accepted that black-hole masses are much larger at low metallicities, where the effects of mass loss are negligible. Note, however, that

the magnitude of the effect could be moderated in models with rotational mixing, which induces mass loss even at very low metallicities (see Chapter 3).

The quantities required in Equation (4.6) are the *stellar yields* $Y_i(M)$, representing the mass ejected in the form of element i by a star of mass M. Those quantities are obviously positive ($Y_i = 0$ in the case of an isotope totally destroyed in stellar interiors, *e.g.* deuterium). However, knowing their value is of little help in judging whether star M is an important producer of isotope i (*e.g.* by knowing that a 20 $M_\odot$ star produces 10^{-3} $M_\odot$ of Mg or 1 $M_\odot$ of O, one cannot judge whether such a star contributes significantly – if at all – to the galactic enrichment in those elements).

More insight in that respect is obtained through the *net yields* $y_i(M)$, which represent the *newly created mass of nuclide i* from a star, *i.e.*

$$y_i(M) = Y_i(M) - M_{0,i}(M) \tag{4.12}$$

where $M_{0,i}(M)$ is the mass of nuclide i originally present in the part of the star that is finally ejected:

$$M_{0,i}(M) = X_{0,i}(M - C_M) \tag{4.13}$$

and $X_{0,i}$ is the mass fraction of nuclide i in the gas from which the star is formed. Obviously, $y_i(M)$ may be positive, zero or negative, depending on whether star M creates, simply re-ejects or destroys nuclide i. Net yields *are not mandatory* in numerical models of galactic chemical evolution, but *they are used* in analytical models adopting the instantaneous recycling approximation (see Sect. 4.6).

Finally, the *production factors* (or *overproduction factors*) $f_i(M)$ are defined as

$$f_i(M) = \frac{Y_i(M)}{M_{0,i}(M)}. \tag{4.14}$$

They are useful in the sense that they immediately indicate whether star M is an important producer of nuclide i. For instance, massive stars are the exclusive producers of oxygen, for which $f \sim 10$ on average (see Fig. 4.3). If such stars produce another nuclide L with, say, $f \sim 3$ only, they are certainly important contributors, but they cannot account for the solar L/O ratio; another source is then required for nuclide L. [7]

Note that the use of production factors as defined in Equation (4.14) and described in the previous paragraph is interesting only when a comparison is made for a star of a given initial metallicity. The properties of the various quantities defined in this section are summarised in Table 4.1. An application of the definitions is given in Figure 4.3.

Regarding the nucleosynthesis products as a function of stellar mass, it is well established now that massive stars produce the quasi-totality of nuclides between carbon and the iron peak, as well as most of the trans-iron nuclei: the light s- (up

---

[7]The example is taken from the case of iron, for which another source is required beyond massive stars; that source is SNIa (see below).

Table 4.1. Yield definitions.

Nuclide i	Yields $Y_i(M)$	Net yields $y_i(M)$	Production factors $f_i(M)$
Created	$> M_{0,i}$	> 0	> 1
Re-ejected	$= M_{0,i}$	$= 0$	$= 1$
Destroyed	$< M_{0,i}$	< 0	< 1

$M_{0,i}$ is defined in Equation (4.13).
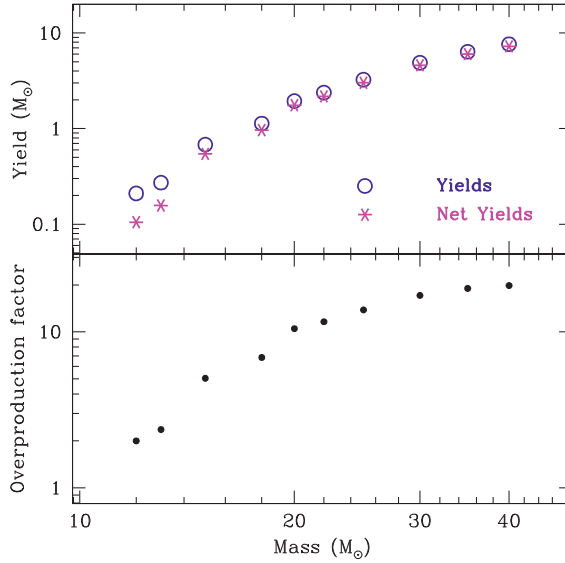
Fig. 4.3. *Top*: yields (circles) and net yields (asterisks) of oxygen as a function of stellar mass, for stellar models with no mass loss or rotation (from WW95). *Bottom*: corresponding overproduction factors. Note that, because of the form of the stellar IMF, average yields (or overproduction factors) correspond to a star of $\sim 25\ M_\odot$.

to Y), the r- (neutron-rich) and p-nuclides (neutron-poor, w.r.t. the nuclear stability valley). Oxygen is almost exclusively produced in massive stars, although its absolute yields are still subject to several uncertainties, as discussed in Chapter 3.

Intermediate mass stars synthesise substantial amounts of several nuclides, mainly in the asymptotic giant branch (AGB) phase, when H and He burn intermittently in two shells surrounding the inert CO core (see Chap. 3). Nucleosynthesis occurs in those shells, as well as in the bottom of the convective AGB envelope, if it penetrates in regions of high enough temperature (*hot bottom burning*). Such stars are the main producers of heavy s-nuclei at a galactic level and they synthesise large amounts of ^{4}He, ^{14}N, ^{13}C, ^{17}O, ^{19}F, etc. However, they are not net producers of oxygen (except at very low metallicity), while in some cases, they may even destroy part of their initial O content through hot bottom burning.

A study of the combined evolution of CNO elements (*e.g.* of N/O *vs.* O/H) should certainly take into account the role of such stars. To a first approximation, the oxygen yields of those stars can be neglected, but not their H and He ejecta that contribute to the returned mass in Equation (4.3).

Iron plays a major role in studies of galactic chemical evolution, because of its high abundance and strong spectral lines. It is produced in massive-star explosions (with fairly uncertain yields, usually taken to be 0.07 $M_\odot$, after the case of SN1987A) but also in thermonuclear supernovae (SNIa), where it is produced as radioactive ^{56}Ni. Observations of the peak luminosity of SNIa (powered by the decay of ^{56}Ni) suggest that they produce on average 0.7 $M_\odot$ of ^{56}Fe, the stable product of ^{56}Ni decay; thus, SNIa are major producers of Fe (and Fe-peak nuclides in general). In the case of the Milky Way, this can be seen as follows. The observed frequency of SNIa in external galaxies of the same morphological type (*i.e.* Sbc/d) is about 5 times smaller than the corresponding frequency of core-collapse SN (SNII+SNIb,c), see *e.g.* Mannucci *et al.* (2005). But core-collapse SN produce on average $\sim$0.1 $M_\odot$ of ^{56}Ni, that is 7 times less than SNIa. Thus, SNIa contribute at least as much as massive stars to the production of Fe and Fe-peak nuclides in the Milky Way. In the case of the solar neighbourhood, this is corroborated by another observational argument, namely the evolution of the O/Fe ratio which will be presented in Section 4.3.1.

SNIa may have long-lived progenitors, with lifetimes of up to several Gyr; this introduces a substantial delay in their rate of element ejection in the ISM. The evolution of the SNIa rate depends on the characteristics of the progenitor system, and obviously, it cannot be simply proportional to the SFR. One of the simplest parameterisations consists in assuming that the SNIa rate is the sum of two components, one proportional to the SFR and the other to the cumulative mass of the stellar population (Scannapieco & Bildsten 2005):

$$R_{SNIa}(t) \;=\; \alpha \Psi(t) \;+\beta\; m_S(t), \tag{4.15}$$

where $\Psi(t)$ and $m_S(t)$ are defined in Equations (4.2) and (4.4), respectively. The values of α and β are adjusted so as to account for the observations of SN rates in external galaxies of different morphological types. It should be noted, however, that other formulations provide an equally satisfactory fit to the data. This is the case of the widely used parameterisation of Greggio & Renzini (1983) that takes into account the time delay introduced by the evolution of the secondary star and the mass distribution of the two components of the binary system. Despite their uncertainties, due to our poor understanding of the progenitor systems of SNIa, such formulations offer more physical insight into the problem.

4.2.3   Initial Mass Function

The IMF cannot be unambiguously calculated at present from first principles (despite a large body of theoretical work, see *e.g.* Bonnell *et al.* 2006 and references therein) and it has to be derived from observations. However, this derivation is not
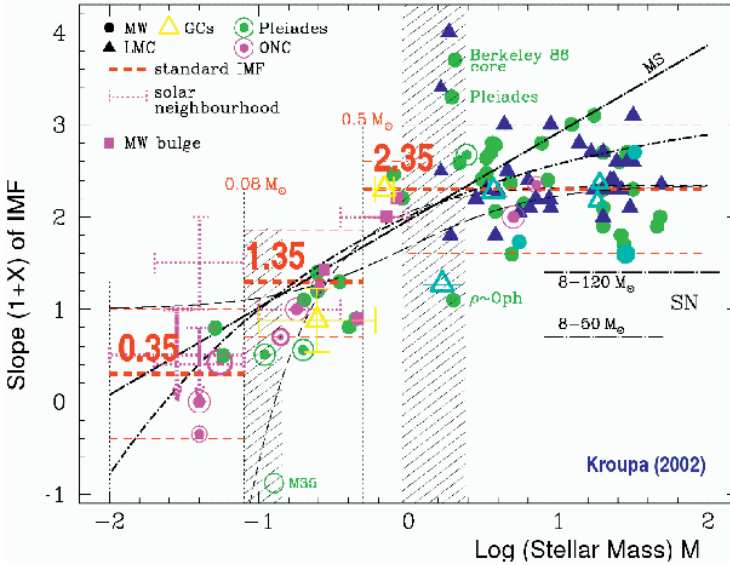
Fig. 4.4. Slope $1 + X$ of the IMF (assumed to be described by a multi-power-law form), according to observations in various astrophysical environments; the dashed horizontal lines indicate average values in three selected mass ranges, with $1 + X = 2.35$ being the classical Salpeter value (from Kroupa 2002).

straightforward and important uncertainties remain, especially concerning massive stars.

Based on observations of stars in the solar neighbourhood and accounting for various biases (but not for stellar multiplicity), Salpeter (1955) found that the local IMF in the mass range 0.3–10 $M_\odot$ is well described by a power law:

$$\Phi(M) = \frac{dN}{dM} = A\, M^{-(1+X)} \tag{4.16}$$

with slope $X = 1.35$. That slope is indeed found in a large variety of conditions, and the Salpeter IMF is often used in the whole stellar mass range, from 0.1 to 100 $M_\odot$, especially in studies of the photometric evolution of galaxies. However, it is clear now that there are less stars in the low-mass range (below 0.5 $M_\odot$) than predicted by the Salpeter slope of $X = 1.35$. For instance, Kroupa (2002) adopts a multi-slope, power-law IMF with $X = 0.35$ in the range 0.08 to 0.5 $M_\odot$ (Fig. 4.4), whereas Chabrier (2003) prefers a log-normal IMF below 1 $M_\odot$.

For galactic chemical evolution purposes, low-mass stars are "eternal" and just block matter from recycling in the ISM. More important, in that respect, is the shape of the IMF above 1 $M_\odot$. Unfortunately, the situation is not clear yet. Observations of the IMF in various environments, and in particular in young clusters (where dynamical effects are negligible), suggest that a Salpeter slope $X = 1.35$ describes the data well (see also Fig. 4.4). However, determination of

the IMF in young clusters suffers from considerable biases introduced by stellar multiplicity and pre-main sequence evolution. Moreover, in the case of the field star IMF in the solar neighbourhood, Scalo (1986) finds $X = 1.7$, *i.e.* a much steeper IMF than Salpeter.

According to Weidner & Kroupa (2006), the slope of the *stellar* IMF is indeed the one observed in clusters, but galactic chemical evolution studies involve the *galaxian IMF*, *i.e.* the sum of all cluster IMFs, which is steeper than the stellar IMF. The reason is that, although every single cluster has the same stellar IMF ($X = 1.35$), the maximum stellar mass $M_{MAX,C}$ in a cluster probably increases with the total mass of that cluster; indeed, observations reveal that small clusters may have $M_{MAX,C}$ as low as a few $M_\odot$, whereas large clusters have $M_{MAX,C}$ up to 150 $M_\odot$. If this property is general, then the resulting *galaxian* IMF is necessarily steeper. In that way, one may conciliate the results of Scalo (1986, a study still unique in its kind) with observations of cluster IMFs, which favour the Salpeter value. For Galactic chemical evolution studies, the Scalo value of $X = 1.7$ appears more appropriate, and it is indeed used in most detailed models of the local Galactic chemical evolution.

The IMF is normalised to

$$\Phi(M) = \int_{M_L}^{M_U} \Phi(M) \ M \ \mathrm{d}M = 1 \qquad (4.17)$$

where M_U and M_L are the adopted upper and lower mass limits, respectively. Typical values are $M_U \sim 100 \ M_\odot$ and $M_L \sim 0.1 \ M_\odot$, and the results depend little on the exact choice (if it is not too far from the typical values). A comparison between three normalised IMFs, namely the "reference" one (Salpeter), that proposed by Kroupa (with the Scalo slope at high masses) and that by Chabrier (with the Salpeter slope at high masses) is made in Figure 4.5.

A useful quantity is the *return mass fraction R*

$$R \ = \ \int_{M_T}^{M_U} (M - C_M) \ \Phi(M) \ \mathrm{d}M, \qquad (4.18)$$

i.e. the fraction of the mass of a stellar generation that returns to the ISM. For the three IMFs displayed in Figure 4.5, $R = 0.28$ (Salpeter), 0.30 (Kroupa+Scalo) and 0.34 (Chabrier+Salpeter), respectively; *i.e.* about 30% of the mass passing through the stellar stage returns to the ISM.

4.2.4 Star Formation Rate

Star formation is the main driver of galactic evolution and the most uncertain parameter in galactic chemical evolution studies. Despite decades of intense observational and theoretical investigation (see *e.g.* Elmegreen 2002 and references therein) our understanding of the subject remains frustratingly poor. Observations of various SFR tracers in galaxies provide only relative values, under the assumption that the IMF is the same everywhere (*e.g.* Kennicutt 1998). Moreover, those tracers reveal that star formation occurs in different ways depending
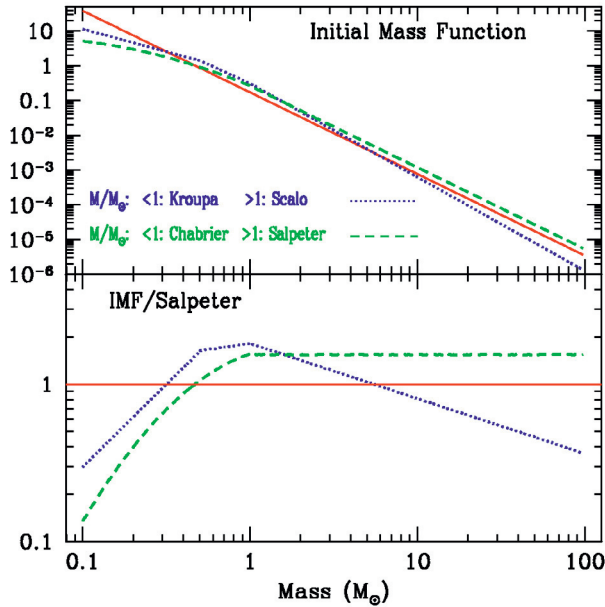
Fig. 4.5. *Top:* three initial mass functions. *Solid curve*: Salpeter (power law in the whole mass range), *dotted curve*: Kroupa (multi-slope power law for M < 1 $M_\odot$) + Scalo ($X = 1.7$ for M > 1 $M_\odot$), *dashed curve*: Chabrier (log-normal for M < 1 $M_\odot$) + Salpeter ($X = 1.35$ for M > 1 $M_\odot$). *Bottom:* ratio of the three IMFs to the one of Salpeter.

on galaxy type. In spiral disks, star formation takes place mostly inside spiral arms, in a sporadic way. In dwarf, gas-rich galaxies, it occurs in a small number of bursts, separated by long intervals of inactivity. Luminous infrared galaxies (LIRG) and starburst galaxies (as well as, most probably, ellipticals in their youth) are characterised by an intense burst of star formation, induced by the interaction (or merging) with another galaxy. Note that most star formation tracers concern stars more massive than ∼2 $M_\odot$; very little information exists for the SFR of low-mass stars, even in the Milky Way.

Today there is no universally accepted theory to predict large-scale star formation in a galaxy, given the various physical ingredients that may affect the SFR (*e.g.* density and mass of gas and stars, temperature and composition of gas, magnetic fields and frequency of collisions between giant molecular clouds, galactic rotation, etc.). Only in the case of spirals can predictions be made based on various instability criteria (*e.g.* Elmegreen 2002 for a review). In the case of other galaxies, a parameterised formulation of the SFR is adopted. Schmidt (1959) suggested that the density of the SFR Ψ is proportional to some power N of the density of gas mass m_G:

$$\Psi \ = \ \nu \, m_G^N \tag{4.19}$$

a formulation which has the merit of reminding us that stars are formed from gas after all. However, it is not clear whether *volume density ρ* or *surface density Σ* should be used in Equation (4.19). When comparing data with galactic chemical evolution models for the solar neighbourhood, Schmidt (1959) uses surface densities (Σ in $M_\odot/\text{pc}^2$). But, when finding "direct evidence for the value of N" in his paper[8] he uses volume densities (ρ in $M_\odot/\text{pc}^3$) and finds $N = 2$. Obviously, since $\Sigma = \int_z \rho(z) dz$, then $\Sigma^N \neq \int_z \rho(z)^N dz$.

It is not clear then which density should be used in the Schmidt SFR law: volume density is more "physical" (denser regions collapse more easily) but surface density is more easily measured in galaxies. Furthermore, at first sight, it seems that the density of molecular gas should be used (since stars are formed from molecular gas) and not the total gas density.

Surprisingly enough, Kennicutt (1998) finds that, in normal spirals, the surface density of SFR correlates with atomic rather than molecular gas; this conclusion is based on *average surface densities*, *i.e.* the total SFR and gas amounts of a galaxy are divided by the corresponding surface area of the disk. In fact, Kennicutt (1998) finds that a fairly good correlation exists between SFR and *total (i.e. atomic + molecular) gas*. This correlations extends over four orders of magnitude in average gas surface density ρ_S and over six orders of magnitude in average SFR surface density Ψ, from normal spirals to active galactic nuclei and starburst galaxies (see Fig. 4.6, left) and can be described as

$$\Psi \;\propto\; \Sigma^{1.4}, \tag{4.20}$$

i.e. $N = 1.4$. However, Kennicutt (1998) notes that the same data can be fitted equally well by a different N value, this time involving the *dynamical timescale* $\tau_{dyn} = R/V(R)$, where $V(R)$ is the orbital velocity of the galaxy at the optical radius R

$$\Psi \;\propto\; \frac{\Sigma}{\tau_{dyn}}. \tag{4.21}$$

More recent observations confirm Kennicutt's results, but are also compatible with other SFR laws suggested in the literature (see *e.g.* Boissier *et al.* 2003). Note that, for a given data set, the determination of coefficient ν in Equation (4.19) depends on the exponent N, and *vice versa*.

In some cases, it is useful to consider the *efficiency of star formation ε*, *i.e.* the SFR per unit mass of gas. In the case of a Schmidt law with $N = 1$, $\varepsilon = \nu = const.$, whereas in the case of $N = 2$, $\varepsilon = \nu m_G$.

Finally, one may ask whether the SFR law in Figure 4.6 extends down to lower surface densities or whether there is a star formation *threshold* in galactic disks. The data of Kennicutt (1998) and Figure 4.6 apparently suggest a lower threshold

---

[8]Schmidt (1959) describes the distributions of gas and young stars perpendicularly to the galactic plane (z direction) in terms of *volume densities $\rho_{Gas} \propto \exp(-z/h_{Gas})$* and *$\rho_{Stars} \propto \exp(-z/h_{Stars})$* with corresponding scale heights (observationally derived) $h_{Gas} = 78$ pc and $h_{Stars} = 144$ pc $\sim 2\, h_{Gas}$; from that, Schmidt deduces that $\rho_{Stars} \propto \rho_{Gas}^2$, that is $N = 2$.
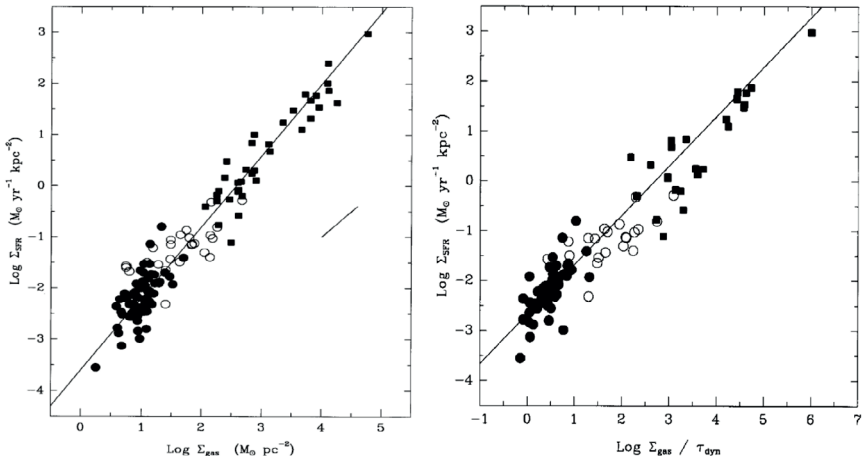
Fig. 4.6. *Left:* average surface density of star formation rate Ψ (in $M_\odot$ yr^{-1} pc^{-2}) as a function of average gas (HI+H$_2$) surface density Σ_G (in $M_\odot$ pc^{-2}) in spirals (circles) and starbursts (squares); the solid line corresponds to $\Psi \propto \Sigma^{1.4}$. *Right:* average surface density of star formation rate Ψ (in M$_\odot$ yr^{-1} pc^{-2}) as a function of Σ_G/τ_{dyn}, where the dynamical timescale τ_{dyn} is equal to R/V (for rotational velocity V at radius R); the solid line corresponds to $\Psi \propto \Sigma_G/\tau_{dyn}$. Figure taken from Kennicutt (1998).

of a few $M_\odot/$pc^2. However, more recent data, obtained with the GALEX UV satellite, reveal star formation activity even in regions of gas density as low as 0.1 $M_\odot/$pc^2 (Boissier *et al.* 2007). Those recent data imply that the threshold of star formation is much lower than thought before (and, for most practical purposes, non-existent).

4.2.5   Gaseous flows and stellar feedback

A galaxy is clearly not an isolated system, and it is expected to exchange matter (and energy) with its environment. This is true even for galaxies that are found away from galaxy groups. First of all, most of the baryonic matter in the Universe today (and in past epochs) is in the form of gas residing in the intergalactic medium, and part of it is slowly accreted by galaxies. Also, small galaxies are often found in the tidal field of larger ones, and their tidal debris (gas and/or stars) may be captured by the latter. In both cases, gaseous matter is accreted by galaxies, and in the framework of the simple galactic chemical evolution model this is generically called *infall*[9].

On the other hand, gas may leave the galaxy if it gets sufficient (i) kinetic energy or (ii) thermal energy and (iii) if its velocity becomes larger than the

---

[9]Gaseous flows in the plane of a galactic disk, due *e.g.* to viscosity, are called *inflows*; for simple galactic chemical evolution models they also constitute a form of infall.

escape velocity. Condition (i) may be met in the case of tidal stripping of gas in the field of a neighbour galaxy or in the case of ram pressure from the intergalactic medium. Condition (ii) is provided by the heating of the interstellar gas due to supernova explosions, especially if collective effects (*i.e.* a large number of SN in a small volume, leading to a super-bubble) become important. Finally, condition (iii) is more easily met in the case of small galaxies with shallow potential wells. Note that, since galaxies (*i.e.* baryons) are embedded in extended dark matter (non-baryonic) haloes, a distinction should be made between gas leaving the galaxy but still remaining trapped in the dark halo and gas leaving even the dark halo. In the former case, gas may return back to the galaxy after "floating" for some time in the dark halo and suffering sufficient cooling. In the framework of the simple galactic chemical evolution model, all those cases are described generically as *outflows*.

The rate of infall or outflow is difficult to calculate from first principles. In the case of infall, this is possible, in principle, for a hydrodynamical model evolving in an appropriate cosmological framework. In the case of outflows, the interaction between stars (SN) and the ISM, known as *feedback*, also requires detailed hydrodynamical modelling. No satisfactory models exist up to now for such complex processes. Incidentally, the treatment of feedback also affects the SFR of the system (by making gas unavailable for star formation, either by heating it or by pushing it out of the system altogether).

In simple galactic chemical evolution models, infall and outflow are treated as free parameters, adjusted so as to reproduce observed features of the galaxian systems under study. Such features are the metallicity distributions of long-lived stars or the mass-metallicity relationship of external galaxies. The former is nicely illustrated in the cases of the metallicity distribution in the local disk (Sect. 4.3.1.2), which provides strong constraints on the history of the system.

4.2.6   Analytical solutions: the instantaneous recycling approximation

The system of galactic chemical evolution Equations (4.1) to (4.6) can be solved analytically if one adopts the instantaneous recycling approximation, introduced by Schmidt (1963). Stars are divided into "eternal" stars (low-mass stars, with lifetimes far exceeding the age of the system) and "dead at birth" stars (massive stars, with lifetimes far shorter than the age of the system) for which it is assumed that $\tau_M = 0$. The dividing line between the two classes depends on the system age, and for most practical purposes it is put at 1 $M_\odot$, corresponding to an age $T \sim 12$ Gyr.

Assuming the instantaneous recycling approximation allows one to replace $\Psi(t - \tau_M)$ in the equations of galactic chemical evolution by $\Psi(t)$ and thus to take out the SFR $\Psi(t)$ from the mass integrals. The equations can then be solved analytically (see *e.g.* Tinsley 1980). Solutions involve the *return fraction R* defined

in Equation (4.18) and the yield p_i of a given nuclide, defined as

$$p_i = \frac{1}{1-R} \int_{M_T}^{M_U} y_i(M) \; \Phi(M) \; \mathrm{d}M. \qquad (4.22)$$

The yield p_i is *the newly created amount of nuclide i by a stellar generation, per unit mass of stars blocked in "eternal" objects*: indeed, $y_i(M)$ are the *net yields* of nuclide i (see Sect. 4.2.2) and $1-R$ is the mass blocked in low-mass stars and compact objects (for the normalised IMF of Eq. (4.17)). Obviously, the *stellar yields $Y_i(M)$* and *net yields $y_i(M)$* are properties of individual stars, while the *yield p_i* is an integrated property of the IMF as is the return fraction R.

With those definitions, the gas mass fraction X_i of nuclide i in the case of the closed box model is

$$X_i - X_{i,0} = p_i \ln\left(\frac{m}{m_G}\right) = p_i \ln\left(\frac{1}{\sigma}\right) \qquad (4.23)$$

where $\sigma = m_G/m$ is the *gas fraction* and $X_{i,0}$ the initial abundance ($X_{i,0} = 0$ for metals). This is the main result of the instantaneous recycling approximation, relating the chemical enrichment of the gas to the amount of gas left. It is independent of time or of the form of the SFR, and for those reasons it is a powerful tool for studying gas flows in the system. It can also be used to derive the metallicity distribution of stars and, consequently, the past history of the system (see Sect. 4.3.1).

If a simple Schmidt law of the form $\Psi = \nu m_G$ is adopted for the SFR (Eq. (4.19)) one can obtain the following solutions for the evolution of gas

$$m_G = m \; e^{-\nu(1-R)t} \qquad (4.24)$$

and for the abundances

$$X_i - X_{i,0} = p_i \; \nu \; (1-R) \; t \qquad (4.25)$$

which also satisfy the more general solution of Equation (4.23). Thus, metallicity is roughly proportional to time, a result which is approximately valid even when the instantaneous recycling approximation is relaxed. This property allows one to use the stellar "metallicity" (especially the abundance of iron, which has many strong and easily identifiable spectral lines) as a proxy for time, since stellar ages are notoriously difficult to evaluate.

The instantaneous recycling approximation turns out to be a surprisingly good approximation for nuclides produced in massive stars, *e.g.* oxygen, provided gas fractions stay above $\sim 10\%$; this is illustrated in Figure 4.7 for the case of a closed box model, with analytical solutions given by Equations (4.24) and (4.25). Analytical solutions assuming the instantaneous recycling approximation can also be obtained in the cases of gaseous flows into or out of the system. However, some specific assumptions have to be made about the form of those flows, and this limits
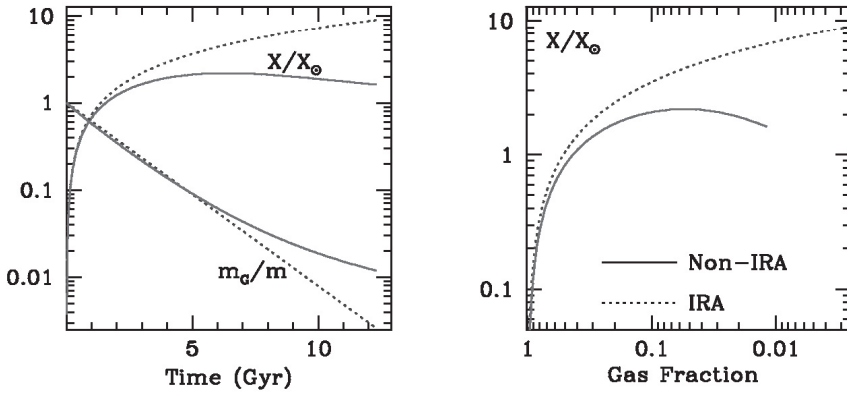
Fig. 4.7. Results of calculations for a closed box model with instantaneous recycling approximation (IRA, *dotted curves*) vs. Non-IRA (*solid curves*). *Left:* metallicity (upper curves) and gas fraction (lower curves) as a function of time. *Right:* metallicity as a function of gas fraction. It is assumed that $\Psi = 1.2 \ m_G \ \text{Gyr}^{-1}$.

their interest. For instance, in the case of outflow at a rate proportional to the SFR, $o = k\Psi$, metallicity evolves as

$$X_i - X_{i,0} = \frac{p_i}{1+k} \ln\left(\frac{1}{\sigma}\right) \tag{4.26}$$

i.e. at the same gas fraction metallicity is smaller than in the closed box or, equivalently, a larger fraction of the system has to turn into stars in order to reach the same metallicity. Equation (4.26) is formally the same as Equation (4.23), with an *effective yield*

$$p_{i,eff} = \frac{p_i}{1+k} \tag{4.27}$$

in place of the true yield p_i, and $p_{i,eff} < p_i$. It is shown (Edmunds 1990) that gas flows always produce *reduced effective yields*, *i.e.* that metallicity increases most efficiently in the closed box model. Other analytical solutions can be obtained in models with specific forms of infall, see *e.g.* Pagel (1997) or Matteucci (2001). For instance, in the case of a model with constant SFR and gas mass, driven by an infall of rate $f = \Psi(1-R)$ and zero metallicity, the resulting solution is

$$X_i - X_{i,0} = p_i \left[1 - \exp\left(1 - \frac{1}{\sigma}\right)\right]. \tag{4.28}$$

Equation (4.28) gives similar results to Equation (4.23) for gas fractions higher than ~ 0.5; for lower σ values Equation (4.28) "saturates" (*i.e.* $X_i \longrightarrow p_i$), while Equation (4.23) produces values $X_i > p_i$.

Analytical solutions obtained in the framework of the instantaneous recycling approximation can provide important constraints to various quantities of interest in galactic chemical evolution studies. For instance, it is currently admitted that
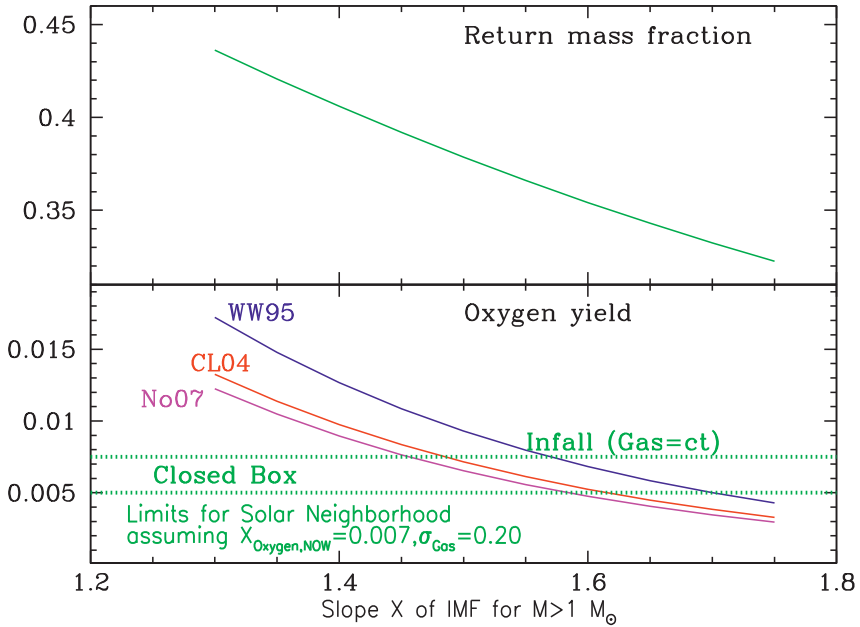
Fig. 4.8. *Top*: return mass fraction for an IMF given by Kroupa *et al.* (1993) for stars below 1 $M_\odot$ and by a power-law IMF with a slope X given in the horizontal axis. *Bottom:* oxygen yields calculated by several groups (Chieffi & Limongi 2004; Nomoto *et al.* 2006; Woosley & Weaver 1995) and integrated over the IMF, as a function of the slope X of the massive star part of the IMF. The two horizontal dotted lines correspond to empirically determined yields for a closed box model (lower) and evolution at constant gas mass (upper), adapted to match the constraints of the solar neighbourhood (*i.e.* gas fraction ∼0.20 and present-day oxygen mass fraction in the gas of $X_O \sim 7 \times 10^{-3}$). These two lines constrain the value of the oxygen yield.

the solar neighbourhood did not evolve as a closed box, but with a smoothly declining (or roughly constant) SFR, driven by continuous gas infall (see Sect. 4.3.1); in other terms, its evolution should be intermediate between the two extreme cases described by the closed box model and constant gas mass model (but not constant gas fraction!). Assuming that the present-day gas fraction is $\sigma_G \sim 0.24$ (see Sect. 4.3.1.1) and the oxygen mass fraction is $X_{O,\odot} \sim 7 \times 10^{-3}$, one can solve Equations (4.23) and (4.28) to obtain the corresponding "observationally derived" yields, which constrain the oxygen yield in the solar vicinity (see Fig. 4.8).

4.3 Chemical evolution of the Milky Way

4.3.1 The solar vicinity

Obviously, the larger the number of observables, the more useful the galactic chemical evolution framework in constraining the history of a system. The Milky
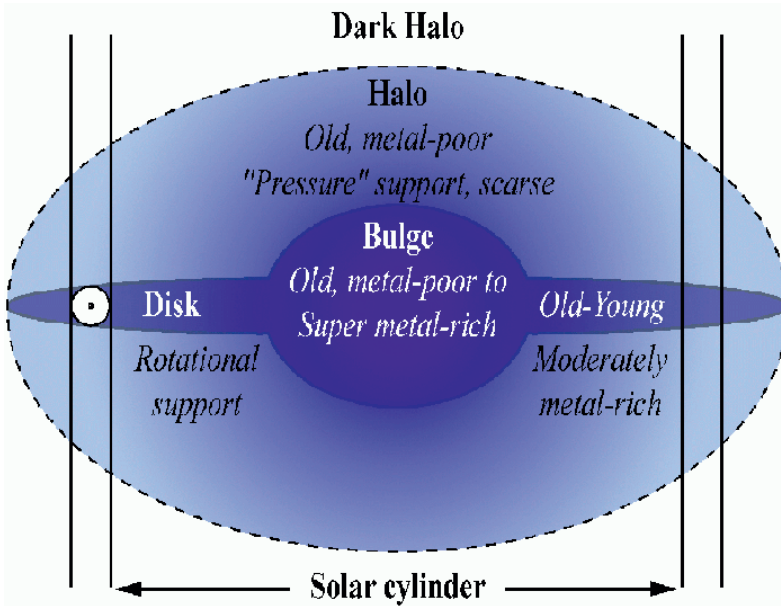
Fig. 4.9. The various components of the Milky Way (bulge, halo, disk) and their main features; a distinction should be made between the thin and the thick disks (not appearing in the figure). The solar cylinder is at 8 kpc from the centre (adapted from Pagel 1997).

Way and, in particular, the *solar cylinder* are the best observed systems today (for obvious reasons).

The solar cylinder may be defined as a cylindrical region of radius 0.5 kpc, perpendicular to the Galactic plane and centred at the position of the Sun (8 kpc from the Galactic centre, see Fig. 4.9). The interstellar gas is located near the plane and it is usually assumed to be chemically homogeneous. On the other hand, three stellar populations coexist, to various extents, in that region; they are distinguished by their kinematic and chemical properties (see Chapter 2):

- The *thin disk*: young (age $\sim$5 Gyr on average), rotationally supported, rather metal rich ([Fe/H] ~ -0.1 on average), with small vertical velocity dispersion ($\sigma_W < 25$ km s^{-1}) and scale height ($h \sim 300$ pc on average, but only $h \sim 100$ pc for the young stars, *i.e.* comparable to the scale height of the gaseous layer), dominating the total mass (75–80%).

- The *thick disk*: older than the thin disk ($\sim$10 Gyr), with greater σ_W (>35 km s^{-1}) and more extended (scale height $h \sim 1$ kpc), rotating, moderately metal poor ([Fe/H] ~ -0.7) and contributing $<20\%$ to the total surface density.

- The *Galactic halo*: old (age $\sim$12–13 Gyr), "pressure" supported, metal poor ([Fe/H] < -1) with little or no rotation, large velocity dispersion

perpendicularly to the disk and small contribution ($<5\%$) to the overall surface density.

It is tempting to assume, in the framework of the old, *monolithic collapse* scenario for the Milky Way's evolution (Eggen *et al.* 1962), a temporal continuity in the formation of those three components, *i.e.* halo $\longrightarrow$ thick disk $\longrightarrow$ thin disk[10]. Such a continuity is more difficult to establish in the modern framework of hierarchical galaxy formation: the three components may be totally uncorrelated, *e.g.* the thick disk may have been formed from tidal debris of satellite galaxies, while the thin disk probaby did so from slow accretion processes[11].

In the following we study the case of the local thin disk. In fact, if thick disk stars were mostly accreted from merging/disrupted satellites, that population cannot be considered as belonging to the early phase of the local disk. Also, in view of the large scale height of the thick disk (>1000 pc) and of the elliptical orbits of its stars (*vs.* circular orbits for those of the thin disk), one may wonder how large the local "chemical box" could be to still be considered as a single system with well-defined evolution.

4.3.1.1   Observables

In the case of the solar neighbourhood, the number of available observational data is larger than for any other Galactic system, allowing one to strongly constrain (albeit not in a unique way) the history of the system. Those data are as follows (see *e.g.* Boissier & Prantzos 1999):

- The current surface densities of gas ($\Sigma_G \sim 12\ M_\odot\ \mathrm{pc}^{-2}$), live stars ($\Sigma_* \sim 30\ M_\odot\ \mathrm{pc}^{-2}$), stellar residues ($\Sigma_C \sim 5\ M_\odot\ \mathrm{pc}^{-2}$) and total amount of baryonic matter ($\Sigma_T \sim 47\ M_\odot\ \mathrm{pc}^{-2}$), as well as the current star formation rate ($\Psi_0 = 2-5\ M_\odot\ \mathrm{pc}^{-2}\ \mathrm{Gyr}^{-1}$); the corresponding gas fraction is $\sigma \sim 0.22$.

- The elemental and isotopic abundances at solar birth ($X_{i,\odot}$, *i.e.* it is assumed that the Sun's composition is typical of the ISM 4.5 Gyr ago) and today ($X_{i,Now}$). Those two compositions are quite similar as seen in Chapter 2, suggesting little chemical evolution in the past 4.5 Gyr. Of particular importance in that respect is the abundance of deuterium, a fragile primordial isotope destroyed 100% in stellar ejecta, but continuously reintroduced in the system in the case of primordial gas infall. The evolution of the D abundance is a tracer of the amount of astration plus infall of the system and will be studied in more detail in Section 4.3.1.5.

- The stellar age-metallicity relation, traced by the Fe abundance of long-lived stars, [Fe/H]=$f(t)$ or $\log(Z) = f(t)$, Section 4.3.1.3.

---

[10]In fact, it is difficult to account for the chemical and kinematical properties of all three Galactic components in the monolithic collapse scenario.

[11]The monolithic collapse scenario may describe better the properties of the inner halo and of the bulge.

- The metallicity distribution of long-lived G-type stars $\frac{dn}{d[Fe/H]}$ or $\frac{dn}{d(logZ)}$, showing that few of them were formed at [Fe/H] < -0.7. In view of its importance, the metallicity distribution is discussed in more detail in Section 4.3.1.2.

- The oxygen $vs.$ iron relationship, interpreted in terms of a delayed (after $\sim$1 Gyr) enrichment of the ISM with products of SNIa. Since the Fe/O ratio at low metallicities (where Fe and O are produced only by massive stars) is roughly half of the solar value, and since massive stars are the unique source of oxygen, this implies that the complementary source of Fe, SNIa, contribute more than half of the solar Fe.

Among those constraints, the age-metallicity relationship and the G-dwarf metallicity distribution are the most important. In principle, by combining them, one may straightforwardly derive the SFR history (dn/dt) of the solar neighbourhood through

$$\frac{\mathrm{d}n}{\mathrm{d}t} = \frac{\mathrm{d}n}{\mathrm{d}(\log Z)} \frac{\mathrm{d}(\log Z)}{\mathrm{d}t}. \tag{4.29}$$

In practice, however, this is impossible because of the sensitivity of the result to the slope of the adopted age-metallicity relation: a small variation in the form of the age-metallicity relation produces a dramatic effect on the resulting SFR history. For that reason, the local SFR history is reconstructed only indirectly: models of the Galactic chemical evolution of the solar neighbourhood are developed, which must satisfy all the aforementioned observational constraints. Before presenting such models, we discuss in more detail two of the key observables, namely the age-metallicity relation and the metallicity distribution.

4.3.1.2   The local metallicity distribution of long-lived stars

In the framework of the closed box model of Galactic chemical evolution with the instantaneous recycling approximation, the metallicity distribution of long-lived stars can be derived as follows. In order to reach a given metallicity Z, a certain amount of stars have to be created given by Equation (4.4): $m_S = m - m_G$, or (by normalising to the total mass m):

$$n = 1 - \sigma \tag{4.30}$$

where $\sigma = m_G/m$ is the gas fraction and $n = m_S/m$ the star fraction. For a system with a final metallicity Z_1 and star fraction $n_1 = 1 - \sigma_1$, the *cumulative metallicity distribution*, *i.e.* the number of stars with metallicity lower than Z as a function of Z is given by

$$\frac{n(< Z)}{n_1} = \frac{1 - \sigma}{1 - \sigma_1}. \tag{4.31}$$

By using the fundamental result of the instantaneous recycling approximation in the case of the closed box, namely $\sigma = \exp(-Z/p)$ as resulting from Equation (4.23)
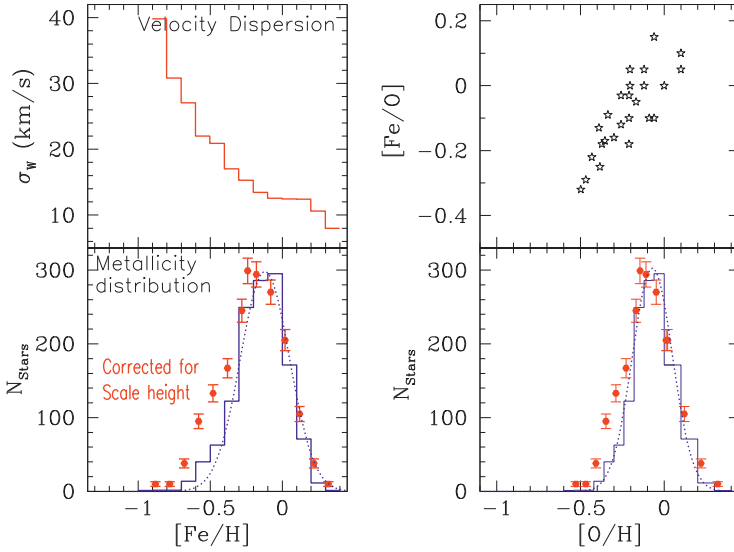
Fig. 4.10. Observations in the solar neighbourhood, as a function of [Fe/H] (*left*) and [O/H] (*right*). *Top left:* vertical velocity dispersion σ_W; *Bottom left:* metallicity distribution from Nordström *et al.* (2004) (*histogram*), fitted by a Gaussian of width $\sigma([\text{Fe/H}]) = 0.19$ dex (*dotted curve*) and corrected for velocity dispersion (*points*, from Holmberg *et al.* 2007). *Top right:* [Fe/O] *vs.* [O/H] from Edvardsson *et al.* (1993). *Bottom right:* as in bottom left, but as a function of [O/H]; note the narrower distribution (fitted with a Gaussian of width $\sigma([\text{O/H}])=0.13$ dex). Model results for the solar cylinder should be compared to the scale height corrected metallicity distribution.

and taking the derivatives of Equation (4.31), one obtains the *differential metallicity distribution*

$$\frac{\text{d}(n/n_1)}{\text{d}(\log Z)} = \frac{\ln(10)}{1 - \exp(-Z_1/p)} \ \frac{Z}{p} \ \exp(-Z/p), \qquad (4.32)$$

i.e. the number of stars per logarithmic metallicity interval as a function of metallicity Z. This relation has a maximum for $Z = p$, *i.e.* when the metallicity is equal to the yield (both metallicity and yield can be expressed in units of the solar abundance of the corresponding element). It is important to note that *the metallicity distribution is independent of the SFR* (at least in the framework of the instantaneous recycling approximation), and for that reason it provides a very powerful constrain on models of Galactic chemical evolution.

The local metallicity distribution obtained from the largest survey yet of the solar neighbourhood (the Geneva-Copenhagen survey, Nordström *et al.* 2004) appears in Figure 4.10 (histogram in bottom left panel). It peaks at [Fe/H] = −0.1, suggesting an effective yield of $p_{Fe} \sim 0.8 \, Z_\odot$. However, persisting uncertainties in metallicity calibrations may shift that peak to slightly higher values around solar. The metallicity distribution of the Geneva-Copenhagen survey can be fitted

relatively well by a Gaussian of width $\sigma[\text{Fe/H}] = 0.19$ dex (dotted curve in Fig. 4.10 bottom left). Before interpreting it in the framework of some model, corrections must be applied to account for the different scale heights of the involved stellar populations, which are attributed to the dynamical heating of the stellar disk. These scale heights are reflected in the larger velocity dispersion σ_W (vertically to the disk) with decreasing metallicity (top left panel of Fig. 4.10): the older (and more metal-poor) stars, being scattered for a longer time, obtain higher velocities and are found, on average, at larger distances from the plane. This implies that a volume limited local sample proportionally misses more of those low metallicity and old stars; therefore, appropriate corrections should be made before comparing with models. The corresponding corrected metallicity distribution (as modelled by Holmberg *et al.* 2007) appears as data points in the lower left panel of Figure 4.10. Models of the solar neighbourhood are usually made for the solar cylinder (*i.e.* all quantities are expressed per unit surface density) and their results should be compared to the *corrected metallicity distribution*. One may also use the observed iron *vs.* oxygen relationship (appearing in the top right panel of Fig. 4.10) to convert the metallicity distribution as a function of [O/H] (bottom right panel in Fig. 4.10): it is even narrower than as a function of [Fe/H], with a width of $\sigma([\text{O/H}]) = 0.12$ dex.

Equation (4.32) for the closed box model with initial metallicity $Z_0 = 0$ is depicted in Figure 4.11 (solid curve), where it is compared to data for the local disk (corrected for scale height). It predicts many more stars at low metallicities than observed, a problem known as the "G-dwarf problem"[12].

Two of the main solutions proposed for the G-dwarf problem appear also in Figure 4.11. According to the first, the disk started with an initial metallicity $Z_0 \sim 0.1\ Z_\odot(pre\text{-}enrichment)$. In that case, all metallicities in Equation (4.32) are replaced by $Z - Z_0$ and the resulting curve fits the data relatively well. The main drawback of that hypothesis is that it is hard to justify the origin of such a large pre-enrichment. It is true that the Galactic halo, which preceded disk formation, reached a maximum metallicity of $\sim 0.1\ Z_\odot$ (for Fe); but its average (stellar) metallicity is $\sim 0.03\ Z_\odot$ (for Fe), and its total mass ($\sim 4 \times 10^8\ M_\odot$, Bell *et al.* 2008) is almost 100 times smaller than that of the disk ($\sim 3.5 \times 10^{10}\ M_\odot$). There is simply not enough mass and metals produced in the halo to justify pre-enrichment of the disk to such a high level. Moreover, the halo has a low specific angular momentum (contrary to the disk), and material escaping from it should be accreted by the bulge rather than the disk.

The second hypothesis is that the disk did not evolve as a closed box, but was gradually built from *infall* of metal-free (or metal-poor) material. In the closed box, all the gas of the system is available from the very beginning; a large stellar activity is then required to enrich all that gas to, say, $0.1\ Z_\odot$, and correspondingly many long-lived stars are formed at low Z. In the case of infall, only a small

---

[12]G-type stars are bright enough for a reasonably complete sample to be constructed and long-lived enough to survive since the earliest days of the disk; the same problem is encountered if F- or K- type stars are used.
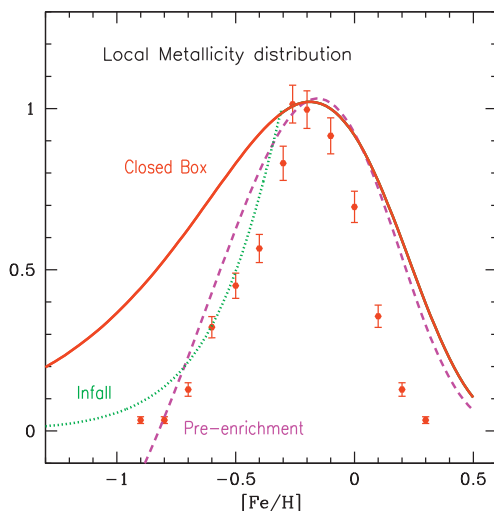
Fig. 4.11. Metallicity distribution of long-lived stars for three models: closed box, exponentially decreasing infall (with a timescale of 7 Gyr) and pre-enrichment (with $X_0 = 0.08 X_\odot$ for Fe). They are compared to the data of the Geneva-Copenhagen survey for the solar neighbourhood (corrected for scale height as in Holmberg *et al.* 2007).

amount of gas exists early on; it then takes a small number of SN to enrich it to $0.1\ Z_\odot$, and correspondingly few low-mass stars are formed at low Z.

Infall appears then as an elegant solution to the local G-dwarf problem, especially in view of the fact that gas accretion to galaxies is expected to be a common phenomenon in the Universe. The infall rate $f(t)$ must obviously be normalised

$$\int_0^T f(t)\, \mathrm{d}t = \Sigma_T \tag{4.33}$$

where Σ_T is the total surface density in the solar neighbourhood and T is the age of the Galactic disk. The infall rate is not accurately determined by the data of the local disk. An exponentially decreasing infall rate $f(t) = A \exp(-t/\tau)$ with a long characteristic timescale of $\tau \sim 7-10$ Gyr provides a reasonably good fit to the data and, in view of its simplicity, is often used in models of the solar neighbourhood (see next section). But other forms may do as well and even better; this is the case, for instance, of a Gaussian (as a function of time) infall rate, with a maximum prior to solar system formation (see *e.g.* Prantzos & Silk 1998). However, the recent update of the Geneva-Copenhagen survey (Casagrande *et al.* 2011) suggests a much more complex picture, going beyond simple ideas about infall: at every metallicity, populations of widely different ages are found in the solar neighbourhood, thus invalidating the use of simple Galactic chemical evolution models. These findings point instead towards radial migration of stars as a key phenomenon in the evolution of the Galactic disk.

4.3.1.3 The local age-metallicity relationship

Stellar ages are much harder to evaluate than stellar metallicities, and the form of the local age-metallicity relation has varied considerably over the years. The seminal work of Edvardsson *et al.* (1993) on 189 F-dwarfs established a clear trend of decreasing metallicity with age, albeit with substantial scatter (Fig. 4.11). Such a trend is compatible with (and predicted by) all simple models of local Galactic chemical evolution, either closed or open (*i.e.* with infall) models. It should be noted, however, that the adopted selection criteria in the paper of Edvardsson *et al.* (1993) introduced a bias against old metal-rich and young metal-poor stars. Also, considerable systematic errors affect estimates based on different age indicators.

The large Geneva-Copenhagen survey of Nordström *et al.* (2004), concerning ∼14 000 F and G stars with 3D kinematic information (but less accurate spectroscopy than the Edvardsson *et al.* study), provides a radically different picture: the volume-limited subsample of 462 stars with "well-defined" ages within 40 pc display a flat age-metallicity relation (an average metallicity of [Fe/H] ∼ −0.2 at all ages) with a very large scatter. The result is confirmed in the recent re-analysis of the data of the Geneva-Copenhagen survey by Casagrande *et al.* (2011). Accounting for the fact that the oldest stars have the largest age uncertainties does not modify the flatness of the age-metallicity relation. Such a trend is also obtained in Soubiran *et al.* (2008), with spectroscopic metallicities of a large sample of red giant stars. The various recent studies are in reasonable agreement for ages <8 Gyr, and start diverging at larger ages.

Evolution at quasi-constant gas surface density would lead to a flat age-metallicity relation, albeit not in the earliest times. On the other hand, the question of the intrinsic dispersion of the local age-metallicity relation is also of utmost importance. The Geneva-Copenhagen survey data suggest considerable dispersion of stellar Fe/H at all ages. Since the local ISM and nearby young stars appear to have quite a uniform composition (see Chapter 2) dispersion cannot be attributed to inhomogeneous evolution of the local disk. Radial migration of stars from regions of different metallicities (mostly the inner disk) to the solar neighbourhood appears the most probable solution (Sellwood & Binney 2002). Simple Galactic chemical evolution models provide a unique age-metallicity relation (assumed to represent an average trend), and cannot account for abundance dispersion.

4.3.1.4 A brief history of the solar neighbourhood

The observed properties of the local disk "dictate" the parameters of simple Galactic chemical evolution models that may be built for that system. The results of such a model are displayed in Figure 4.12, as a function of time (left panels) and of metallicity [Fe/H] (right panels). The various parameters of the model are adjusted as follows.

- The total amount of infalling matter is normalised to the local surface density.
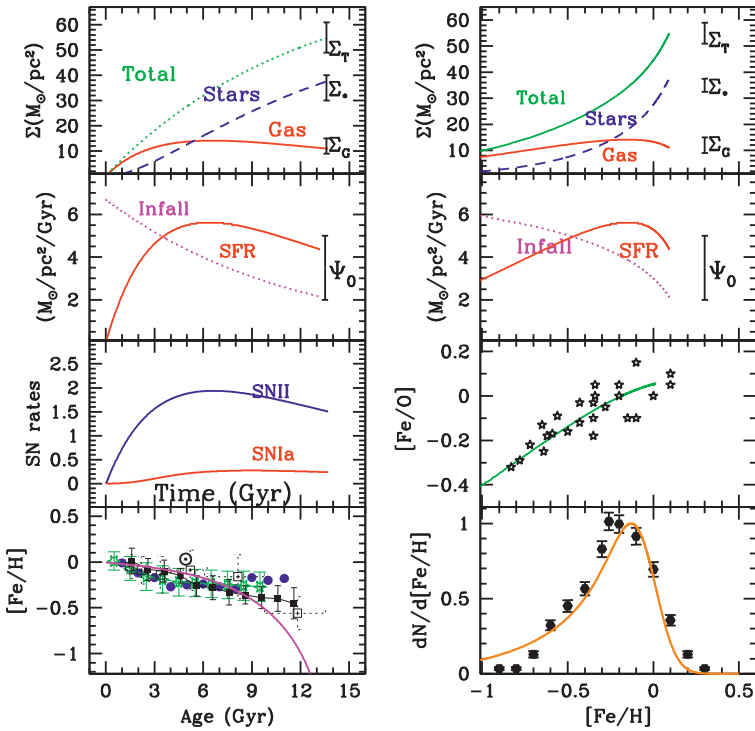
Fig. 4.12. History of the solar neighbourhood, according to a Galactic chemical evolution model with infall, constrained by various observables (updated from Boissier & Prantzos (1999). *Left:* results are plotted as a function of time (or age, for the bottom panel). Data for the present-day local disk are displayed with vertical bars. Data for the age-metallicity relation are from various sources. *Right:* results are plotted as a function of metallicity [Fe/H]. See text for comments on the various curves.

- The timescale of the adopted exponentially decreasing infall rate is sufficiently long ($\tau = 7-8$ Gyr) to reproduce the (scale height-corrected) metallicity distribution.

- The coefficient $\nu = 0.3$ Gyr^{-1} of the SFR $\Psi = \nu\, m_G$ (Eq. (2.26)) is adjusted to leave the system at 12 Gyr with a gas fraction $\sigma \sim 0.2$, as observed.

With those parameter adjustments, it remains to be seen whether the other observables of the system are reproduced. In Figure 4.12 it is seen that the current model SFR is well within observational uncertainties. Note that the derived SFR is rather flat, around an average value of $\sim 3.8\ M_\odot$/yr (alternatively, it could be fitted with a broad Gaussian).

The resulting age-metallicity relationship (left bottom panel in Fig. 4.12) fits the data approximately, but it should be stressed that uncertainties in stellar ages

are fairly large, particularly at large ages; also, dispersion in the age-metallicity relation appears to be quite large (see previous section). Thus, this observable may be of little use as a constraint for the local Galactic chemical evolution.

The rise of Fe/O (right panel of Fig. 4.12) is due to the delayed contribution of SNIa to the total amount of Fe. The adopted SNIa rate is from Greggio & Renzini (1983), and it is assumed that 0.04 of the binaries produce SNIa; the resulting SNIa rate as a function of time appears in the left panel.

Finally, the local Galactic chemical evolution model, combined with the adopted stellar yields, should also reproduce the pre-solar composition, well established from meteoritic and photospheric measurements (*e.g.* Lodders 2003). The results of such a comparison (Goswami & Prantzos 2000) show that all elements and almost all isotopes are nicely reproduced (within a factor of 2 from their pre-solar values), with key elements such as O and Fe being very well reproduced. Taking into account the huge abundance difference between O and Sc (a factor of 10^6), this agreement should be considered as a phenomenal success for stellar nucleosynthesis models. Note that this result is quite encouraging, since it shows that the adopted IMF, SFR and stellar yields reproduce the solar system composition under the assumption that it *is typical of the local ISM 4.5 Gyr ago*. If the Sun is an outlier (either because it was formed in a higher than average metallicity local cloud, or because it was born in the inner Galactic regions and radially migrated outwards), simple Galactic chemical evolution models cannot be used to explain simultaneously local and solar data. This is particularly true for the case of deuterium.

4.3.1.5   The local evolution of D/O

Modelling the Galactic chemical evolution of deuterium is a very straightforward enterprise, since this fragile isotope is 100% destroyed in stars of all masses (already on the pre-main sequence), and has no known source of substantial production other than Big Bang nucleosynthesis. In the framework of the simple closed box model with instantaneous recycling, the abundance of deuterium is given by

$$D \;=\; D_P \; \sigma^{\frac{R}{1-R}} \tag{4.34}$$

where D_P is the primordial abundance, σ the gas fraction and R the return fraction. If the boundary conditions of its evolution (namely the primordial abundance D_P and the present-day value) were accurately known, the degree of *astration*, *i.e.* the degree of processing of Galactic gas inside stars, which depends on the adopted IMF and SFR, would be severely constrained. This, in turn, would be another strong constraint for models of local Galactic chemical evolution. For typical values of $\sigma \sim 0.25$ and $R \sim 0.3$ one obtains: $D/D_P \sim 0.55$ in the closed box model, *i.e.* depletion by a factor of ~ 2. However, the true depletion factor should be smaller, because infall (of presumably primordial composition) is required for the Galactic chemical evolution of the local disk, as argued in the previous section.

The primordial abundance of D is now well determined, since observations of D in high redshift gas clouds agree with abundances derived from observations

of the cosmic microwave background combined with calculations of standard Big Bang nucleosynthesis (see *e.g.* Prantzos 2007 and reference therein). However, the present-day abundance of D in the local ISM is under debate. Indeed, UV measurements of the FUSE satellite along various lines of sight suggest substantial differences (a factor of 2 to 3) in D abundance between the Local Bubble and beyond it. Until the origin of that discrepancy is found (Hébrard 2010; Linsky 2010), the local Galactic chemical evolution of D in the past few Gyr will remain poorly understood. Naively, one may expect that a high value would imply strong late infall of primordial composition, while a low value would imply strong late astration.

A stronger indicator of the overall astration of the ISM is the D/O evolution, since D abundances decreases and O abundance increases with time (Prantzos 1996). Combining Equations (4.23) and (4.34) gives

$$\frac{D}{Z} = \frac{D_P}{p}\ \frac{\sigma^{\frac{R}{1-R}}}{\ln(1/\sigma)} \tag{4.35}$$

in the framework of the closed box model. If D_P, R and σ are known, then the current D/Z ratio can be used to test whether the system evolved as a closed box or with infall (a smaller D/Z value is obviously expected in the latter case). However, the instantaneous recycling approximation is not a good approximation for D (because it is astrated mostly by long-lived stars) and Equation (4.35) is of little help: a full non-instantaneous recycling approximation model must be used, the results of which appear in Figure 4.13 as a function of time. Comparing a closed box to an infall model (with the latter satisfying the G-dwarf Z-distribution while the former does not), it is found that the evolution of D and O in the past few Gyr can be better understood with an infall model *if the high value is adopted for local D/H* (see also Prodanović *et al.* 2010, albeit with instantaneous recycling approximation adopted).

4.3.2   The Galactic halo

The Galactic halo has a much smaller mass than any other component of the Milky Way, $\sim 4 \times 10^8\ M_\odot$ (Bell *et al.* 2008), and its rotational velocity lags behind that of the Milky Way disk by ~ 220 km s^{-1}. Therefore, it is unlikely that it had a dominant contribution to Galactic disk metal enrichment, since the amount of any ejected metal would have been insufficient; moreover, because of angular momentum conservation, it would have anyway ended up in the bulge rather than in the disk.

The available data for the chemical evolution of the halo is more scarce than for the local thin disk. Halo stars are ~ 12 Gyr old (as inferred from globular cluster isochrones and U-Th dating of some of stars), albeit with substantial error bars. In particular, the halo formation timescale is rather loosely estimated at 1–2 Gyr (from the observed dispersion in globular cluster ages). During that period, both O and Fe were produced by massive stars at similar rates, and the Fe/O ratio remained roughly constant ([Fe/O]~ -0.5 or one third solar). SNIa
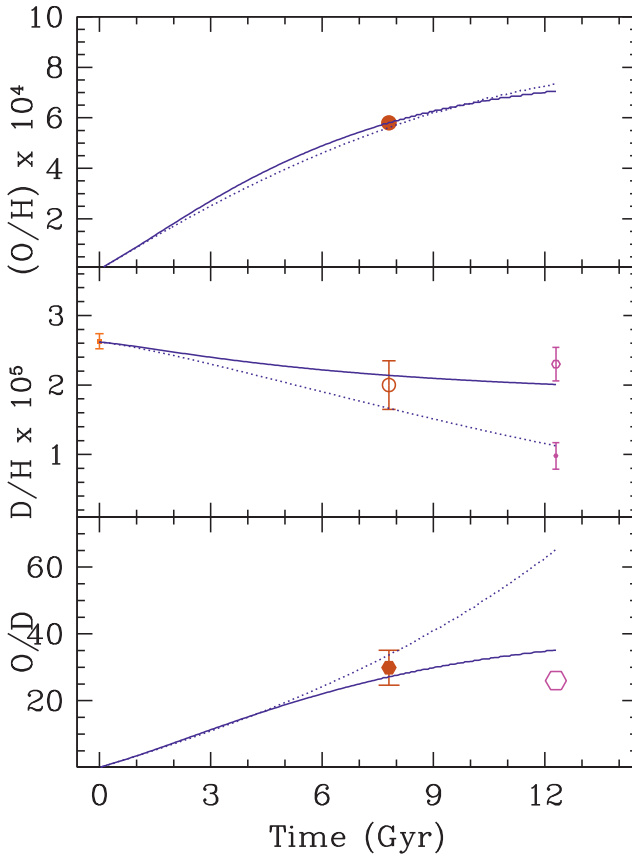
Fig. 4.13. Evolution of oxygen (mass fraction), deuterium (D/H) and the O/D ratio (by number) in the solar neighbourhood, as a function of time. The adopted model (*solid curves* in all panels) satisfies all major local observational constraints (see Fig. 4.12). Data in the *middle panel* correspond to: primordial D (resulting from standard Big Bang nucleosynthesis + baryonic density inferred from analysis of the cosmic microwave background), observations of high redshift gas clouds (DLAs), pre-solar (inferred from observations of stellar wind composition) and in the local ISM (through different interpretations of UV data from the FUSE satellite). *Dashed curves* in all panels correspond to a closed box, depleting D substantially.

became important Fe producers later, during the disk evolution (at least for local stars) thus providing ∼2/3 of the solar iron. The coincidence between those two timescales, namely for halo formation and for major SNIa activity in the solar neighbourhood, *a priori* unrelated, is not yet understood. Note that in other subsystems in the Milky Way with short formation timescales (bulge or thick disk) the Fe/O ratio does vary with metallicity (or time), showing that SNIa had time to enrich the ISM within short timescales.
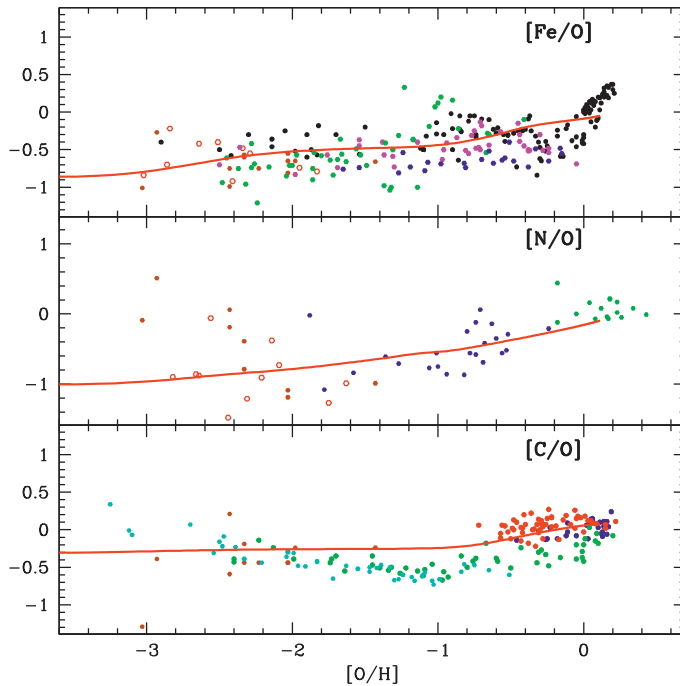
Fig. 4.14. Evolution of Fe, N and C *vs.* O/H in the Galactic halo. Data taken from various sources. The late rise of Fe/O is attributed to the action of SNIa, while those of C/O and N/O are ascribed to enhanced C and N production (not necessarily secondary) by winds from rotating massive stars.

Observations reveal constant abundance ratios of oxygen to other α elements in halo stars. Oxygen is a product of He burning in massive stars (see Chapter 3) and it is produced within a large fraction of the He core; heavier α elements (*e.g.* Si or Ca) are produced at later stages of nuclear burning, much deeper inside the star. The constancy of the O/α abundance ratios implies then that the stellar IMF did not vary substantially during halo evolution.

There is no age-metallicity relation for the halo (but note that this relation is poorly defined and of little help in the case of the local disk). Perhaps more importantly, there is no hint as to the final gas fraction of the halo (*i.e.* at the end of its evolution), which represents the main quantity for the evaluation of the degree of chemical processing (and astration) of a Galactic system.

The halo metallicity distribution provides important information on its evolution. It peaks at a low metallicity of $[Fe/H] = -1.6$ (about 30 times less than solar), and it suggests that halo evolution was dominated by an important gaseous outflow.

Observations of other elemental ratios *e.g.* N/O or C/O (see Fig. 4.14) offer some hints about the production sites and yields of those elements as a function of

metallicity rather than about the dynamics (timescales or gaseous flows) of halo formation. In particular, the evolution of N/O and C/O as a function of O/H strongly suggests that the winds of massive stars have played an important role in the enrichment of the ISM in N and C throughout the evolution of the Milky Way (see *e.g.* Chiappini *et al.* 2006 and Chapter 3).

4.3.3   The Galactic bulge

The mass of the bulge lies in the range 1–2×10^{10} $M_\odot$ (Dwek *et al.* 1995; Robin *et al.* 2003). The metallicities of stars in the bulge span a large range, from 1/10 solar to about 3 times solar. Their mean metallicity is slightly higher than solar, [Fe/H] ~ 0.15, as obtained from both photometric and spectroscopic determinations. By comparing colour-magnitude diagrams of stars in the bulge and in metal-rich globular clusters, it has been found that the populations of the two systems are coeval, with an age of $\sim$10 Gyr. Such a large age is confirmed by deep colour-magnitude diagrams of the bulge (Minniti & Zoccali 2008 and references therein).

Traces of younger populations, such as OH/IR stars, bright AGB variables, etc., appear to be confined to the Galactic plane, but the bulk of the bulge is certainly old. Such an old age is supported by the observed behaviour of the [O/Fe] ratio as a function of [Fe/H] (Fig. 4.15, top) which requires a rapid *and early* evolution of the system. On the other hand, the metallicity distribution of the bulge (Fig. 4.15, bottom) is well described by a closed box with a Fe yield slightly higher than in the solar neighbourhood. This implies that gaseous flows (infall or outflow) probably played a negligible role in the bulge evolution.

Based on those considerations, a fairly simple, one-zone model is presented for bulge evolution in Figure 4.15. It includes a rapid infall (on a timescale of 1 Gyr) and a high star formation efficiency, leading to an average age of the stellar population of $\sim$9 Gyr, in agreement with observations. Such a model reproduces well the main observational features of the bulge, as itemised below.

- The late (in terms of [Fe/H]) decline of O/Fe is the result of the high star formation efficiency, which produces an early and rapid Fe and O enrichment of the bulge. Thus Fe from SNIa arrives when the bulge is already substantially Fe enriched. Note that the opposite effect is observed in dwarf spheroidal galaxies of the Local Group.

- The age-metallicity relation, as obtained by Bensby *et al.* (2010), is also well reproduced. In the first two Gyr of its life, the bulge has already acquired a metallicity of [Fe/H] $\sim$ solar, slowly increasing to higher values (Fig. 4.15, *middle*).

- Finally, a rapid formation timescale ($\sim$1 Gyr) is required in order to reproduce the observed metallicity distribution (Fig. 4.15, *bottom*).

Note, however, that the adopted SNIa rate plays a crucial role in shaping all the above features: the success of the model depends on the prescription of the SNIa
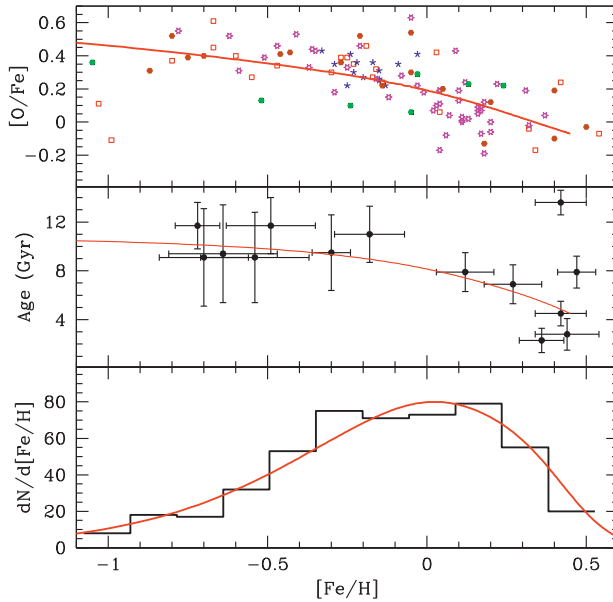
Fig. 4.15. Evolution of O/Fe (*top*), age (*middle*) and metallicity distribution (*bottom*) for stars of the Galactic bulge. Solid curve: the model. Data for O/Fe are from Chapter 2, for stellar ages from Bensby *et al.* (2010) and for the metallicity distribution from Minniti & Zoccali (2008). Because of rapid chemical evolution, the Fe contribution from SNIa appears rather late (at [Fe/H] ~ -0.3). The metallicity distribution corresponds to a closed box with $\sim$ solar Fe yield (*dotted curve in bottom panel*). The model shown here (*solid curves* in all panels) is based on a rapid, exponentially decaying infall rate on a timescale of 1 Gyr.

rate. Thus, oxygen observations alone tell us little about the bulge evolution, as is also the case for other galaxian subsystems studied in this book.

It is worth mentioning that such simple Galactic chemical evolution models provide little insight – if any at all – on the formation of the Galactic bulge. Indeed, at present there are two basic scenarios: early mergers (with galaxies already containing stars or with gas clouds leading to induced star formation during the merging event) and secular evolution where the bulge mostly formed from the inner disk (see discussion in Rahimi *et al.* 2010). In such conditions, it can only be hoped – but certainly not proved – that the simple model described above captures the essentials of bulge evolution.

4.3.4 The Galactic disk

The variation in the radial properties of the Galactic disk as well as of the disks of other spiral galaxies (see next sections) is an evidence that galactic disks did not form uniformly. Indeed, one of the main properties of disk galaxies is the

existence of abundance gradients (see Sects. 2.2.2 and 2.3.2), where the metallicity (*i.e.* O/H, Z, and several other chemical elements) decreases outwardly.

We start this section by describing how to explain the present oxygen abundance profiles along the Galactic thin disk. We illustrate how the abundance profiles can be useful to constrain the star formation histories at the different Galactocentric distances as well as the IMF. In the last part we discuss the time evolution of the oxygen gradients.

4.3.4.1   Radial profiles as witnesses of the disk formation history

Star formation history is linked to gas availability (see Sect. 4.2.4), and hence it is strongly dependent on the accretion/outflow rates of gas onto/from the disk. The accretion and outflow rates are difficult to obtain from first principles (they depend on many complex processes such as feedback). However they can be constrained by using chemical evolution models if high quality data on stellar abundances, age and kinematics along the disk are available. The same is true for the IMF and its putative time variation. These uncertain ingredients of chemical evolution models (gas flows and IMF) can be adjusted to reproduce the observed radial profiles of gas surface density as well as the chemical composition traced by stellar populations of different ages. The star formation history can then be estimated[13] once good agreement is reached between model predictions and observables, both in the solar vicinity (*e.g.* G-dwarf metallicity distribution) and in the whole disk.

There are still many open questions regarding the Milky Way and other galaxy disks. Does disk star formation drive gas out in the so-called galactic fountains? If so, will this gas return to the disk? Is this a mechanism to mix the gas from the different zones of the disk? Do we see infall? Which is the present infall rate and how does it depend on the Galactocentric distance? How did it evolve along the Milky Way history? Which was the dominant matter accretion process on the disk: gas or stellar mergers? Was it different for the thick and thin disks? What was the importance of internal processes (*e.g.* star radial migration in the disk) in shaping the abundance gradients? In particular, stellar migration drivers in disk galaxies are not yet well understood, ranging from the bar, satellite accretion, short-lived spiral arms or the combination of all of these.

We address here some of these questions, focusing on chemical evolution models and, in particular, on the role played by oxygen as a tracer of the star formation history along the galactic disk (for the solar vicinity, see Sect. 4.3.1.4).

Different mechanisms may be at work to establish the radial metallicity gradients (see Matteucci 2001, Section 6.8.1) in the gas and stars along disk galaxies. Basically, what seems to be needed is a variation of the star formation rate along the disk. Among the alternatives, the so-called *biased infall* or *inside-out formation* is the most popular. In this scenario, the Galactic disk formed by gas infall occurring at a faster rate in the innermost regions than in the outer parts. The

---

[13]Note that in systems where the star formation history can be obtained from colour-magnitude diagrams, such as dwarf galaxies, the star formation history is then an input of the models.

physical reason for a *biased infall* can be found in the fact that the gas tends to collapse faster in the centre of the spheroid such that a gradient in the gas density, being lower in the outer parts, is established. In this situation the gas continues to fall onto the disk more efficiently towards the centre than outwardly due to the stronger tidal force acting at the centre (Larson 1976; Pagel 1997). Other ways to create abundance gradients is *via* a strong metallicity dependency of the stellar yield of a certain element or of the IMF, a variation of the timescale of star formation (which is also coupled with the radial variation of the infall timescale) or a variation of the star formation efficiency.

Once gradients are established, they can be amplified or washed out by radial mixing of gas and/or stars. In any case an initial gradient needs to be present as radial flows alone cannot create one (Goetz & Koeppen 1992). The comparison between the abundance gradients traced by different stellar populations can give us hints on the importance of the mixing of gas and stars at different Galactocentric distances. As shown in the classical paper of Edmunds & Greenhow (1995), in the absence of gas flows or infall, the gas abundance gradient is steeper than the stellar one. In systems with radial flows, gradients can be either steepened or flattened depending on the flow properties (Spitoni & Matteucci 2011). Hence, systems with radial flows can make the stellar gradient equal to or steeper than the gas gradient, whereas strong infall could cause the opposite effect, a shallower stellar gradient than the gaseous one.

A further reason for the stellar abundance radial profile to be different from the gaseous one is stellar migration (Roškar *et al.* 2008). In fact, star radial migration (Sellwood & Binney 2002) could bring to the solar neighbourhood stars that were born elsewhere, although details of such mechanisms are still not very well understood. Stellar migration can affect some of the most important constraints to the chemical evolution of the Galaxy, especially those dealing with stars of a broad age range such as the G-dwarf metallicity distribution, the age-metallicity relation and the temporal evolution of the stellar abundance gradients along the disk. Clearly, the impact of radial migration depends on the initial abundance gradient and on the scatter in the ISM. These two important observational constraints are currently hotly debated in the literature (see discussion in Chapter 2). Schoenrich & Binney (2009) explored the consequences of mass exchanges between annuli by taking into account the effect of the resonant scattering of stars described in Sellwood & Binney (2002). These authors show how the radial migration could affect the abundance gradients. However, the strong mixing driven by bar resonances was not taken into account, casting thus doubts on some of the conclusions in the papers quoted above (see Brunetti *et al.* 2011, for a recent discussion on this topic).

4.3.4.2   The thin disk abundance gradient: Interpretation with purely chemical evolution models

For the thin disk in the solar vicinity a large number of observations are available, allowing one to convincingly reconstruct its formation history (Sect. 4.3.1). A consensus now exists that the thin disk in the solar vicinity must have assembled

on a relatively long timescale compared to the formation timescales of the bulge, halo or thick disk (mostly composed of old stars), through the slow accretion of metal-poor infalling gas.

In contrast, much less information is available once we step out of the solar vicinity. In this case we must rely on four basic constraints, namely the exponential stellar profile, the gaseous profile, the star formation rate profile and the abundance profiles of different chemical elements. Current abundance data are sparse for stars outside the solar neighbourhood (Sect. 2.2.2). Moreover, when abundances among relatively distant stars are known, their interpretation is difficult due to important uncertainties in extinction and distances. Despite these problems, several authors showed almost two decades ago that the *biased infall* and/or a SFR proportional to a power $k > 1$ of the gas density (see Sect. 4.2.4) can reproduce well the abundance gradients along the disk (Matteucci & Francois 1989; Tosi 1988). In the late 1980s, the value of the oxygen gradient at the present time was believed to amount to $dlog(O/H)/dR = -0.07$ dex kpc^{-1}. As shown by the critical analysis of the data carried out in Chapter 2 (see Fig. 2.21 therein) the present recommended value seems to lie between -0.03 and -0.04 dex kpc^{-1}.

Apart from the lack of an undisputed description of the *present* abundance distribution in the thin disk (not only the magnitude of the gradient is debated, but also its form – see below and Chapter 2) another important question remains. As pointed out in many papers (Chiappini *et al.* 1997, 2001; Hou *et al.* 2000; Tosi 2000) different models that are able to reproduce the solar vicinity constraints as well as the *present-day* abundance gradients predict a different *evolution* for those gradients: in some models the gradients steepen with time (Chiappini *et al.* 1997; Samland *et al.* 1997; Tosi 1988) while in others they flatten (Alibes *et al.* 2001; Hou *et al.* 2000; Portinari & Chiosi 2000)[14]. In what follows we describe the main results obtained by different groups, with the goal of understanding the key parameters governing theoretical predictions for the form and evolution of the abundance gradients in the Milky Way.

The oxygen gradient at the present time
Is the present-day oxygen gradient constant across the disk? From the observational point of view there is still no clear answer (see Chapter 2, Sect. 2.2.2). For the moment, the only safe conclusion seems to be that the oxygen abundance gradient flattens towards the inner disk (see Sect. 2.2.2.6). However, it is not clear if there is a departure from a linear gradient in the outer disk of our Galaxy, although such a flattening seems to occur in other galaxies (see discussion of the observed gradients in other nearby spiral galaxies in Chapter 2, Sect. 2.3.2).

From the theoretical point of view, in the inner disk the gradients can change due to two outstanding effects: (i) dilution by the mass return from old stars (*e.g.* Chiappini *et al.* 1997) and (ii) radial flows, which can steepen or flatten the gradient depending on flow properties such as velocity and Galactocentric distance

---

[14]Note that in none of these models, the radial migration of stars was taken into account. This would also change the expected time evolution of the abundance gradients.

where they are active (Portinari & Chiosi 2000; Edmunds & Greenhow 1995). The magnitude of the dilution due to old stellar generations depends on the adopted stellar lifetimes, IMF and star formation history.

In the outer regions the departure from a linear gradient can arise again from radial flows (Portinari & Chiosi 2000). However, in this case two other mechanisms could also be at work: (i) pre-enrichment of the outer regions by another fast evolving Galactic component such as the thick disk, halo (Chiappini *et al.* 2001) or bulge[15] (Samland *et al.* 1997) and (ii) a less efficient SFR in the outer parts due, for instance, to a gas threshold below which no stars can form (Chiappini *et al.* 2001). In addition, stellar migration can also modify a gradient traced by old stellar populations (*e.g.* Schoenrich & Binney 2009). This mechanism has been invoked to explain the observed stellar disk light profile cutoffs in many spirals (Roškar *et al.* 2008).

Chemical evolution models with independent evolving rings

In the past few years a great deal of theoretical work has appeared concerning the detailed (*i.e.* without using the instantaneous recycling approximation) chemical evolution of the Milky Way and its abundance gradients (see Matteucci 2001, 2008, for a review).

Most of these models neither consider the effects of radial flows along the disk, which are believed to be small (see discussion below), nor the effect of Galactic fountains (but see Spitoni & Matteucci 2011; Spitoni *et al.* 2008), and hence the disk is modelled by individual rings which evolve independently of each other. Also, these models do not consider the effects of star radial diffusion in the disk due to the lack of detailed information on the processes driving stellar migration. Finally, most of the models discussed in the literature consider the evolution of the Galactic thin disk as a completely separate entity (e.g. Alibes *et al.* 2001; Boissier & Prantzos 1999; Hou *et al.* 2000), *i.e.* without considering the interplay with other galactic components (*e.g.* the thick disk).

A different approach was taken by Chiappini *et al.* (1997). These authors suggested a scenario where the Galaxy formed as a result of two main infall episodes: the first built up the halo/thick disk components, and the second, the thin disk. In such a framework the thin disk was not formed from halo gas, but mainly via the slow accretion of extragalactic gas. The gas lost by the halo rapidly (in less than 1 Gyr) accumulated in the centre with the subsequent formation of the bulge. During the second episode, a much slower infall of primordial gas gave rise to the thin disk with gas accumulating faster in the inner than in the outer regions.

Turbulent, rotating, thick $(1-1.5$ kpc$)$ and clumpy star-forming disks in addition to central bulges were discovered in UV/optically selected star-forming galaxies around redshift $z = 2$ Genzel *et al.* (2008). In addition, Elmegreen & Elmegreen

---

[15]According to the model of Samland *et al.* (1997) the feedback from supernovae drives a wind of metal-rich gas from the bulge, responsible for the pre-enrichment of the thin disk. See also Samland & Gerhard (2003).

(2006) discovered the so-called *chain galaxies* in the Hubble Ultra Deep Field, where these objects show giant star-forming clumps closely centred in the mid-plane. It is tempting to consider them as the progenitors of present thick disks. Indeed, these data sets suggest thick-disk formation during a highly turbulent phase before the accreted material cools down to form a thin disk, in line with the idea of the two-infall model of Chiappini *et al.* (1997), which was based only on the study of the abundance ratios in the Milky Way (see Sect. 4.3.1 and Chiappini 2009). Note that these high redshift data (and some of the chemical properties of our own thick disk) favour smooth gas accretion rather than satellite debris accretion in the formation of the thick disk (Bournaud *et al.* 2009).

The consequences of the above scenario for the formation and evolution of abundance gradients was discussed in a subsequent work by Chiappini *et al.* (2001). They emphasise the radial abundance gradients along the thin disk and the interesting effects that can occur in the outer parts of galaxy disks. It is suggested that the mechanism for the formation of the halo/thick disk leaves detectable imprints on the chemical properties of the outer regions of the thin disk, whereas almost no imprint is expected in the inner parts. In this scenario the formation of the halo/thick-disk and that of thin disk are almost completely disentangled, although some halo/thick-disk gas falls into the thin disk providing early pre-enrichment of the gas. This pre-enrichment is almost completely erased in the inner thin disk as a result of the strong infall of primordial gas leading to further star formation and efficient chemical enrichment. However, in the outer regions, with a longer infall timescale, the effect of earlier pre-enrichment could be significant.

The impact of the earlier pre-enrichment of the thin disk gas has been studied by taking into account variations in the halo density distribution which was previously assumed constant. The possibility of different star formation thresholds in the halo and the disk components was also considered. The main conclusion was that although the halo/thick-disk evolution is unimportant for the inner thin disk region, it could have a large influence on the outer regions. As it is clearly seen in Figure 4.16, the different models predict very different radial abundance gradients in the outer regions, due to the role played by the various effects described above. It was shown for the first time that the formation of abundance gradients (and their temporal evolution) is strongly dependent on the initial conditions of thin-disk formation. Previous chemical evolution models that considered the thin disk as an independent component could not anticipate such effects.

In Cescutti *et al.* (2007), abundance gradients were computed for a large number of chemical elements, and compared with observations up to 22 kpc from the Galactic Centre. The models were first compared with a homogenous sample of Cepheids for which good distance estimates were possible between 2 and 15 kpc (Andrievsky *et al.* 2004, and references therein) (see Fig. 4.17, upper panel). The predicted gradients were then compared with other data sets including the outer parts of the disk. The gradients indicated by Cepheids and other objects in the outer parts of the disk show quite a flat behaviour which could be suggestive of a pre-enrichment of the thin disk gas in the earliest epochs of the formation of this
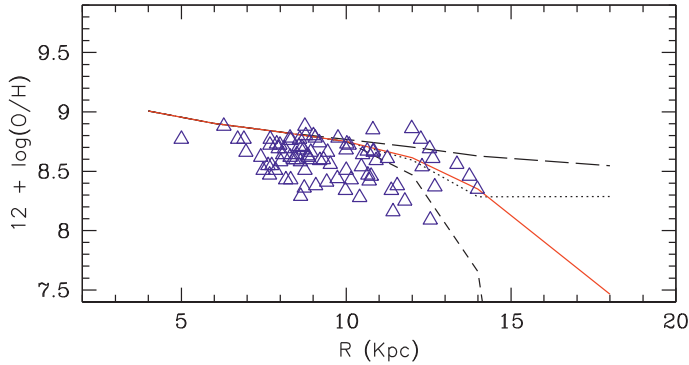
Fig. 4.16. Oxygen gradient predictions at the present time for the different cases studied in Chiappini *et al.* (2001), compared with the observed gradient traced by Cepheids (triangles) for which the Galactocentric distance was computed using the K band apparent luminosities (see Fig. 2.20; for a summary of all the different tracers of the oxygen gradient in the MW, see Sect. 2.2.2.6). The different curves correspond to the following cases: in Models A (solid line), B (long-dashed line) and C (dotted line) the thin disk has been pre-enriched by an older galactic component (halo/thick-disk). The differences are due to different assumptions on the mass profile and on the star formation threshold in the halo/thick-disk component (case C: no threshold during the halo/thick-disk phase; case B: as A but with a more extended mass density profile). Model D (short-dashed line) shows instead a case where the contribution of the halo/thick-disk phase is minimal.

component. On the other hand, as discussed in Chapter 2, for the Milky Way it is still not clear whether the oxygen gradient really flattens at large radii.

It is interesting to notice that the inside-out formation of the Galactic disk does not necessarily imply a monotonic age variation with distance from the Galactic centre as shown by Chiappini *et al.* (2001). The latter authors find that in the inner disk (4–10 kpc), the stellar ages are roughly constant (or slightly decreasing) with increasing radius, but beyond this radius, the stellar ages increase with radius because the thick disk and halo become more and more important with respect to the thin disc, also contributing to its pre-enrichment. This affects the radial variation of the mean $[\alpha/\text{Fe}]$ ratios of the stars at a given Galactocentric distance (see Fig. 4.18). Interestingly, the predictions made in 2001 happen to be in broad agreement with data in old open clusters in the outer disk (Yong *et al.* 2006), which show an enhanced $[\alpha/\text{Fe}]$. However, the interpretation of such a trend is still controversial. There are at least two alternative interpretations: (i) these old objects are just fossil records of recent accretion episodes in the outer disc, and hence are not directly linked to the disk evolution; or (ii) the stars in the outer parts of the disk came from the inner regions (including the bulge) due to stellar migration. All these different mechanisms could produce an outward increase in the $[\alpha/\text{Fe}]$ ratios. What is evident is that the outer disks contain precious information on galaxy formation.
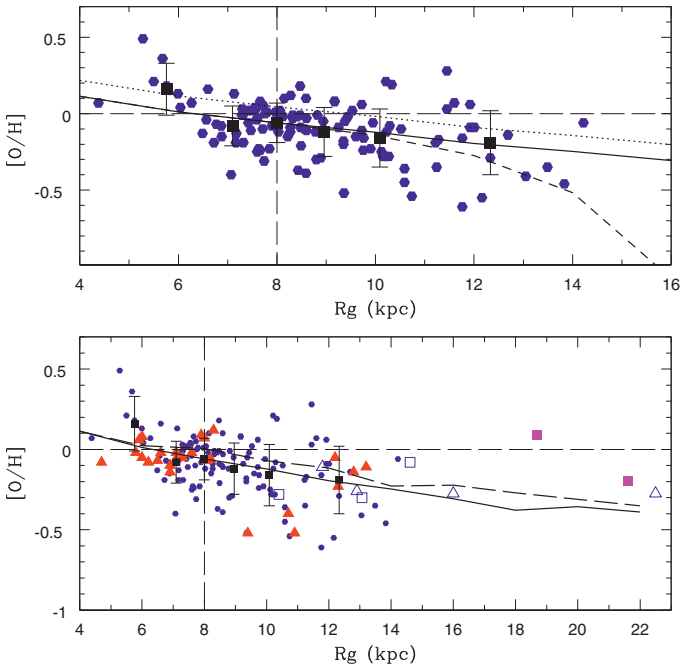
Fig. 4.17. Upper panel: oxygen gradient predicted by Cescutti *et al.* (2007) compared with a homogeneous sample of Cepheids in the 4–15 galactocentric distance range. Blue points show the data of Andrievsky *et al.* (2004), squares depict the mean values for different bins of galactocentric distance and the error bars represent the standard deviation of the mean. The solid line shows the model prediction at present time normalised to the mean value of the Cepheids around 8 kpc, whereas the dotted line shows the same model normalised to the observed solar abundances of Asplund (2005). These models are similar to Model B of Chiappini *et al.* (2001) previously discussed. The dashed line shows the predictions of Model A of Chiappini *et al.* (2001). Lower panel: the same models are now compared to other sets of data spanning larger galactocentric distances (see text for details). Solid line (same as upper panel). Long dashed: the same model but at the time of the Sun formation and normalised to Asplund (2005). Figure adapted from Cescutti *et al.* (2007).

Chemical evolution models considering radial flows and Galactic fountains

As explained before, none of the above models considered the effects of radial gas flows nor of Galactic fountains. In what follows we briefly illustrate some attempts to take these processes into account in chemical evolution models. Note, however, that this increases the number of free parameters with respect to the models discussed above.
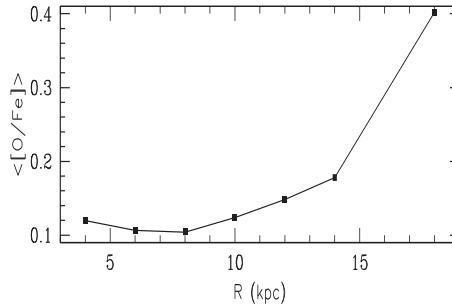
Fig. 4.18. Predicted mean [O/Fe] ratios for stars at a given Galactocentric distance, averaged by mass by Chiappini *et al.* (2001).

Radial flows towards the inner disk can be induced by different causes (see Matteucci 2001, and references therein): different angular momentum of the in-falling gas with respect to the gas in the disk, angular momentum transfer due to gas viscosity (even in the absence of infall) or shocks generated by the spiral arms (Schoenrich & Binney 2009). Current theoretical estimates for radial flows produced by the above mechanisms are in the range of 0.5–5 $\text{km}\,\text{s}^{-1}$. Stronger gas flows can occur in the inner regions due to the existence of a Galactic bar. This would explain the molecular ring of gas observed around 4 kpc from the Galactic centre.

Quantitative estimates of the effects of radial flows on the abundance gradients were presented by Portinari & Chiosi (2000). These authors have shown that the gas distribution, including the molecular ring, can be successfully reproduced by models taking into account the Galactic bar. On the other hand, their results also suggest that the Galactic bar has little effect in modifying the present oxygen abundance gradients (models with/without the bar differ by less than 0.2 dex at R = 2–3 kpc). When considering other forms of radial flows acting in the whole disk, a larger impact is found (see Fig. 4.19). More detailed models taking into account the role of the Galactic bar require N-body simulations coupled with chemical evolution models.

Finally another process to be considered is the impact of Galactic fountains, *i.e.* gas flows from the disk produced by multiple supernova explosions, on the abundance gradients. Spitoni *et al.* (2008) studied the expansion law and chemical enrichment of a supershell powered by the energetic feedback of a typical Galactic OB association at various Galactocentric radii. Sequential supernova explosions create supershells which can break out a stratified medium, producing bipolar outflows. The gas of the supershells can fragment into clouds which eventually fall toward the disk producing the so-called Galactic fountains. The authors studied the orbits of the fragments created when the supershell breaks out, and compared their kinetic and chemical properties with the available observations of high – and intermediate – velocity clouds. They found that the clouds are always formed at
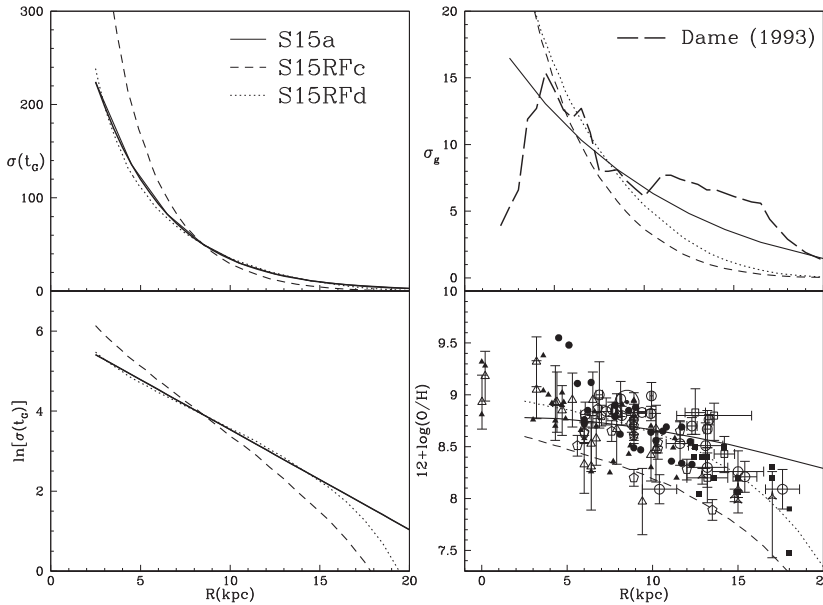
Fig. 4.19. The effect of radial flows on the radial properties of the Galactic disk. *Left panel*: total surface density σ. *Right panel*: radial gas density profile (upper) and oxygen gradient (bottom). The solid line represents a fiducial model computed without radial flows, assuming a Schmidt star formation law with $k = 1.5$. The dashed line represents the same model upon the inclusion of radial flows (assumed to happen within the star-forming disk, without inflow from the external gaseous gas, as expected if radial flows are driven by the spiral arms). In this case the overall metallicity is decreased with respect to the fiducial model. The dotted curve shows the latter model with a different IMF normalisation so that a higher fraction of stars contribute to the chemical enrichment, which would probably affect other observational constraints (see Portinari & Chiosi 2000, for details).

about 450 pc above the plane (see Fig. 4.20). If the initial metallicity is solar, the pollution from the dying stars of the OB association has a negligible effect on the chemical composition of the clouds. The maximum height reached by the clouds above the plane seldom exceeds $\sim$2 kpc, and when averaging over different throwing angles, the landing coordinate differs from the throwing coordinate by $\sim$1 kpc at most. The authors then concluded that it is unlikely that Galactic fountains can affect abundance gradients at large scales. Similar results were found by hydrodynamical simulations (Melioli et al. 2009).

4.3.4.3   Is the IMF variable? Clues from the oxygen abundance gradient

The study of the radial profiles of gas, stars and oxygen abundance along the Galactic disk can also be used to detect a possible variation of the IMF with
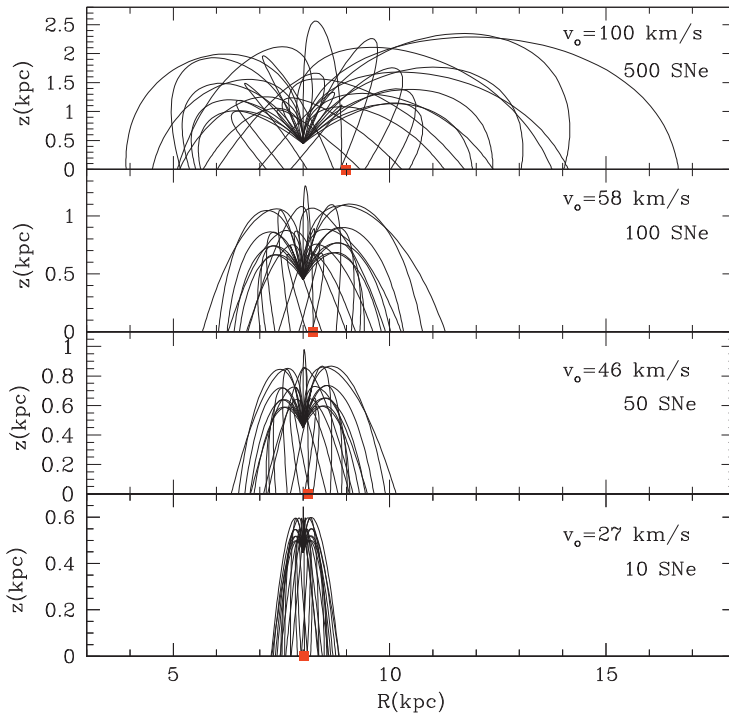
Fig. 4.20. Galactic fountains in a purely ballistic model with initial conditions: (R, z) = (8 kpc, 448 pc). Squares on the R axis are the average falling radial coordinates, and show that the clouds land at most 1 kpc away from where they were produced. As a result, the impact of Galactic fountains on the abundance gradients is found to be negligible. Figure taken from Spitoni *et al.* (2008).

metallicity. Chiappini *et al.* (2000) explored the effects of adopting time-dependent IMFs. Different cases were tested in the two-infall framework (Chiappini *et al.* 1997) with the main assumption that massive stars are preferentially formed in low metallicity regions as suggested by the simulations of Padoan *et al.* (1997). Such IMF dependency on metallicity implies that massive stars are formed preferentially at early times and at large Galactocentric distances (*i.e.* when the metallicity is low).

Results of these experiments are shown in Figure 4.21: the variable IMFs strongly dependent on metallicity were unable to reproduce all the relevant observational constraints in the Galaxy. The main reason is that the tested IMFs combined with the inside-out picture for the thin disk formation predict a flat gradient (Model B in Fig. 4.21) not in agreement with observations, and much flatter than the one predicted by a model which adopts a constant IMF (Model A). This situation cannot be reversed by increasing the star formation efficiency because in this case, although the abundance gradient is recovered, the gas density profile
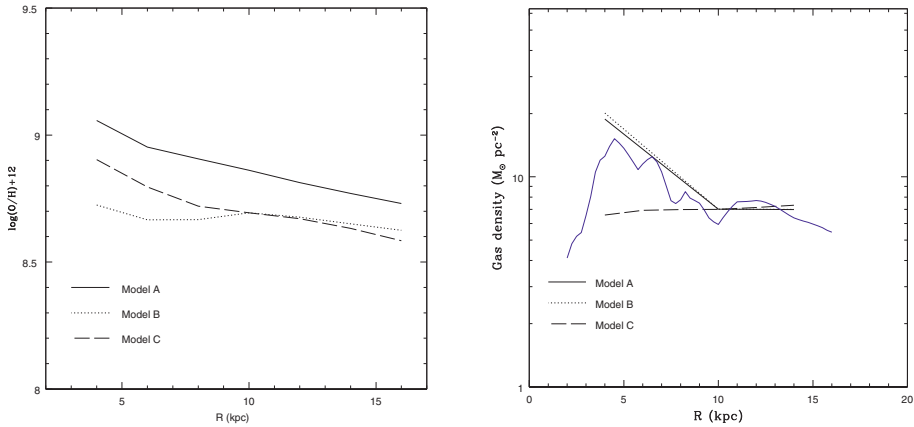
Fig. 4.21. *Left panel*: oxygen gradient – Model A: constant IMF (Scalo); Model B: variable IMF; Model C: variable IMF, intense star formation to recover oxygen gradient. *Right panel*: gas density distributions for the same models shown in the left panel. The observed gas profile is represented by the thick (blue) line. Figure updated from Chiappini *et al.* (2000).

is destroyed (Model C). The conclusion of this study is that a constant IMF, in the framework of continuous infall onto the Galactic disk, is still the best way to explain the observational constraints in the Milky Way.

4.3.4.4   The evolution of the oxygen gradient

As mentioned in the beginning of this section, chemical evolution models of the thin disk which are in good agreement with the solar vicinity constraints and with the present observed radial abundance gradients, differ on their predictions for the time evolution of gradients. Thin disk models (where this component is treated as an independent entity) usually predict the abundance gradients to flatten with the evolution of the disc. The initial gradients are very steep since in the inner parts strong star formation quickly enriches the gas, whereas in the outer parts essentially no chemical enrichment takes place. Later on, with the saturation of the chemical enrichment in the inner parts (for example, due to the restitution of low metallicity matter from the old metal-poor, low-mass stars that start dying in the inner parts), and the progressive chemical enrichment in the outer parts, the gradient gets flatter.

In contrast, models in which a pre-enrichment of the thin disk is considered, together with a threshold in the star formation rate, can predict a different gradient time evolution. This was the case of the models of Chiappini *et al.* (2001), where initially the gradients are flat due to the metallicity floor produced by the pre-enrichment from the older Galactic component. Gradients then build up with

time to the values observed at present. This buildup mostly occurs during the earliest phases of disk formation, when the star formation rate is at its maximum (during the first Gyrs of the thin-disk formation). Later on, weaker star formation leads to a slow evolution of the abundance gradient. Indeed, in models where a gas threshold for the formation of stars is assumed, a less effective evolution of the metals content in the outer parts of the galaxies takes place, such that the metallicity in the outer regions stays almost constant during galaxy evolution, leading to a mild evolution of the abundance gradients.

Gradients were also obtained in the framework of more detailed chemodynamical models (*e.g.* Samland *et al.* 1997). In this case, the models predict gradients that steepen with time. According to the latter authors, during the collapse phase, the oxygen abundance increases more rapidly in the outer regions, where the inter cloud medium (ICM) densities and low temperatures lead to effective condensation and mixing in the ISM. With time the enrichment moves inward.

The point to take from the examples above is that the temporal evolution of abundance gradients can depend on the details of the Galaxy formation process (initial conditions and radial star formation histories). Interestingly, most of the models predict a modest variation for the oxygen gradient in the last $4-5$ Gyr. Most of the evolution seems to take place in the very beginning of the history of the Galactic disk. This is compatible with the star formation history of the thin disk[16]. This means that to unveil the time evolution of the abundance gradients in the disk it will be necessary to probe abundance tracers sampling a large age baseline.

There is hope that the different scenarios for disk formation previously discussed would be validated or discarded once the temporal evolution of the abundance gradients has been recovered from observational data. Unfortunately, the answer to the question whether abundance gradients get steeper or flatter with time faces important difficulties from the observational point of view. First of all, one of the most difficult tasks in astrophysics is to assign a correct age to the different tracers, especially for objects older than $\sim$4–5 Gyr (Pont & Eyer 2004). A second known difficulty is to assign correct distances to the different objects. A third is to account for the effects of stellar migration. Gaia will contribute tremendously to improve the situation regarding the first two, and detailed dynamical models will be necessary to estimate the effects of the third point. For now, our understanding of the abundance gradient evolution in the disk remains elusive.

4.3.5   *The special case of globular clusters: direct pollution*

Section 2.2.4.3 presented the anomalies in oxygen and other chemical elements observed in Galactic globular clusters. These chemical patterns are easily understood

---

[16]For instance, in the solar vicinity, we expect a low level of star formation rate in the last 4–5 Gyrs and thus a negligible oxygen enrichment since the Sun formation. This is how the similarity of the oxygen abundance in the Sun and in the local ISM can be understood.

as the result of proton-capture nucleosynthesis in the CNO cycle and the NeNa and MgAl chains of hydrogen burning (Denissenkov & Denissenkova 1990; Langer *et al.* 1993; Prantzos *et al.* 2007). However although the CNO cycle is activated for temperatures of the order of 20×10^6 K, the NeNa and MgAl chains require temperatures around 35×10^6 K and 50×10^6 K respectively. Destruction of ^{24}Mg by proton-capture needs still higher temperatures, around 70×10^6 K (*e.g.* Arnould *et al.* 1999). Prantzos *et al.* (2007) actually showed that the observed patterns of all elements and isotopes in a typical globular cluster like NGC 6752 (see Fig. 2.30) require hydrogen burning in a temperature range around 75×10^6 K. This is much higher than the internal temperature of the low-mass stars in which we are currently observing the abundance anomalies. As a consequence, these stars must have inherited the anomalies at birth; *i.e.* the observed abundances reflect the initial composition of the protostars. It is thus clear now that a large fraction of globular cluster low-mass stars were formed from material processed through hydrogen burning at high temperature by more massive and faster evolving first generation polluter stars, and then lost and partially mixed with some original gas.

All these observations have seriously challenged the classic paradigm describing globular clusters as fairly simple aggregates of coeval stars born out of homogeneous chemical material. In other words, compelling evidence leads us to believe that at least two generations of stars succeeded in all Galactic globular clusters during their infancy. The first corresponds to the "bulk" of normal stars born with the pristine composition of the proto-cluster gas; these objects are those with the highest O and Mg and the lowest Na and Al abundances also found in their field contemporaries. The second generation consists of stars born out of material polluted to various degrees by the ejecta of more massive and short-living stars, which present lower O and Mg and higher Na and Al abundances than their first generation counterparts. Presently there are two potential polluters: massive AGB stars (Ventura *et al.* 2001) and massive stars (with initial mass higher than $\sim 20 \ M_\odot$ Decressin *et al.* 2007a,b; Prantzos & Charbonnel 2006). Both options have pros and cons, and at the present time we cannot discard any of them.

Various aspects of this "self-enrichment scenario" have been developed, *e.g.* Prantzos & Charbonnel (2006), Decressin *et al.* (2010), and Schaerer & Charbonnel (2011). The parameter space is quite large and involves (at least) the IMF (mass limit and shape) of the polluter stars, the amount and composition of their ejecta, as well as the amount of pristine gas that is mixed with these ejecta to form the observed contaminated low-mass stars. However, it is commonly accepted that, in order to reproduce the observed behaviour of oxygen and other elements, the initial stellar mass of globular clusters must have been considerably larger than their present-day value (D'Ercole *et al.* 2008; Decressin *et al.* 2010, 2007a; Prantzos & Charbonnel 2006). This reinforces the idea that these objects could have contributed significantly to reionise the intergalactic medium at high redshift (Schaerer & Charbonnel 2011). Last but not least, based on the O-Na anticorrelation, Schaerer & Charbonnel (2011) show that present-day Galactic globular

clusters must have contributed to approximately 5–20% of the low-mass stars in the Galactic halo.

4.4   The other spiral galaxies

In recent years, observations of other spiral galaxies have increased considerably. However, what we know about other spirals is not as detailed as in the case of the Milky Way, but for some of the nearer systems the situation is rapidly improving. New data are now available for the radial distributions of atomic and molecular gas, stellar light and colours, current star formation rate and chemical abundances, especially oxygen (see Chapter 2).

Most of the abundance work on external nearby spirals come from H ɪɪ regions. Abundance gradients have been measured in spirals as far as the Virgo cluster (*e.g.* for NGC 4254 by Henry, Pagel, & Chincarini 1994). However, in most cases the oxygen abundance has been obtained from the strong line method thus being uncertain (see discussions in Chapters 1 and 2). In some cases it was possible to measure the [O ɪɪɪ] λ4363 line needed to estimate the temperature, thus leading to less uncertain abundances (*e.g.* for M 101 and M 33).

More recently, it has become possible to estimate the oxygen abundance gradients from the observation of young hot stars (supergiants) in the nearest spirals, namely M 31, M 33 and NGC 300. These are very helpful to calibrate the abundances coming from the strong line method in H ɪɪ regions in the same galaxies (see a discussion in Chapter 2). However, we should keep in mind the caveats discussed in Chapters 1 and 2 (abundance uncertainties and low statistics) and that new data will surely bring some surprises in the near future.

In what follows we discuss some of the galaxies for which more data have become available and that have thus been analysed in some detail. This includes M 31, M 33, M 101 and NGC 300, all galaxies for which an extensive discussion of the available oxygen abundances was presented in Chapter 2. However, before discussing each particular galaxy, we recall here some important results concerning the relation between abundances and the more general physical properties of galaxies (see Sect. 2.3.2 for more details), as they are crucial in the theoretical interpretation of the oxygen results in each system.

Over a decade ago several authors were already suggesting that the slope and shape of the abundance profile correlated with certain global disk properties such as the presence/absence of bars (being flatter in galaxies with bars), the central metallicity (which in turn correlates with the galaxy mass) (*e.g.* Vila-Costas & Edmunds 1992; Zaritsky *et al.* 1994), or the galaxy mass or luminosity (*e.g.* Garnett *et al.* 1997 – see Sect. 2.3.2). In particular, Zaritsky *et al.* (1994) suggested that the steeper abundance gradients are observed in late-type spirals. However, Vila-Costas & Edmunds (1992) made the point that an appropriate scale length must be chosen to compare gradients in different galaxies. Garnett *et al.* (1997) showed that this trend disappears when the gradients are normalised to their disk scale length (see Matteucci 2001; Pagel 1997). In addition most of the oxygen gradients measured in external spirals seem to stay linear even at large distances

from the galactic centre (*e.g.*, van Zee *et al.* 1998), but more data are necessary to confirm this point, especially data allowing temperature-based abundance determinations (see Chapter 1).

We now discuss, for each galaxy, how the available data, and in particular the oxygen gradient, have been useful to constrain chemical evolution models (Sects. 4.4.1 to 4.4.3). Finally we discuss the lessons we can extract from these particular cases in order to gain a more global view of the main players in the formation of disk galaxies, such as the Milky Way (Sect. 4.4.4).

4.4.1   M 31: a Milky Way twin?

Among the other three disk galaxies in the Local Group, Andromeda (M 31 or NGC 224) the nearest spiral galaxy, provides a wealth of available data (on gaseous, stellar and abundance profiles) and thus a unique opportunity for testing theories of galaxy formation and evolution (*e.g.* Klypin *et al.* 2002 and references therein).

The disk of M 31 is about 2.4 times larger and 2 times more massive than the Milky Way disk, while its gas fraction is approximately half of the Galactic value. All other things being equal, this implies a higher *average* star formation efficiency for M 31. The mean disk age of Andromeda is around 6–8 Gyr and its mean metallicity is [Fe/H] ~ -0.2, albeit with substantial spread in both cases, while its total mean star formation rate is about 1 $M_\odot \, \mathrm{yr}^{-1}$ (see Yin *et al.* 2009, and references therein).

Compared with the Milky Way, M 31 appears to have been more active in the past, although its current star formation rate is smaller than that of our Galaxy. Based on a survey of spiral properties, Hammer *et al.* (2007) suggested that the Milky Way is a rather quiescent galaxy, untypical of its class, while M 31 may be closer to a typical spiral. The two ring-like structures observed in M 31 (Block *et al.* 2006) are interpreted as the result of a recent (<200 Myr ago) collision with a companion galaxy giving evidence to recent merging activity.

It has been common practice for studying the chemical evolution of the disk of M 31 to start from models already applied to the study of the Milky Way (*e.g.* Renda *et al.* 2005; Yin *et al.* 2009). Using detailed two-components (disk + halo) chemical evolution models, based on similar ideas of the two-infall model, (Chiappini *et al.* 1997), Renda *et al.* (2005) compared several radial properties (gas surface density, star formation rate and abundance gradients) in M 31 and the Milky Way. Figure 4.22 shows their results. Starting with a model computed with the same parameters as for the Milky Way (except for the scale length, which in the case of M 31 is larger) the authors find that this model overproduces the inner gas content of M 31 (upper panel, right). In order to explain the lower gas abundance in the inner regions of M 31 the authors had to invoke shorter infall timescales for the disk of this galaxy. Models computed with shorter timescales are shown by the dotted and dashed lines (right panels). In this case a better agreement is obtained. Note that the latter models produce flatter gradients as in this case there is a weaker radial dependence of the infall timescales or, in other words, the *inside-out* effect is less important than in the model represented by
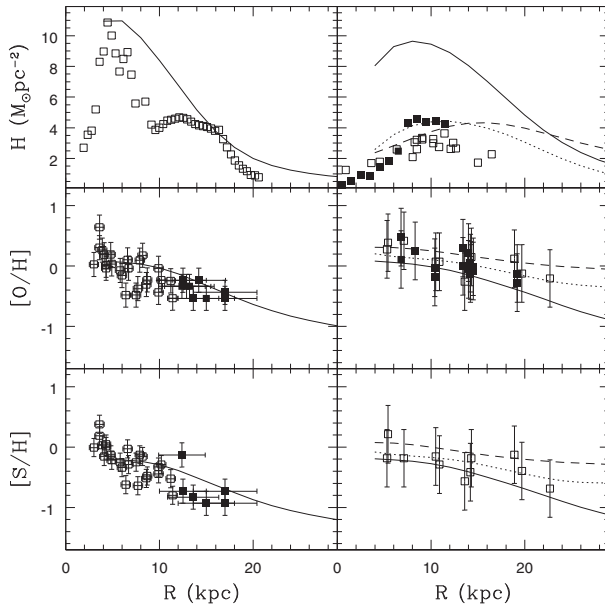
Fig. 4.22. Radial distributions of the hydrogen surface density (upper) and of the oxygen (middle) and sulphur (bottom) abundances at the present-day for the Milky Way model (left) and the M 31 models (right) compared to model predictions for the two galaxies (taken from Renda *et al.* 2005).

the solid curve. The authors concluded that M 31 must have had a higher star formation efficiency and/or shorter infall time scale than the Milky Way.

Yin *et al.* (2009) studied the chemical evolution of the disk of M 31, again using as a starting point the model of the Milky Way developed by Boissier & Prantzos (1999). These authors used an extensive data set of M 31 properties including radial profiles of gas surface density, gas fraction, star formation rate and oxygen abundances as before, but also the metallicity distribution functions at different regions of the disk (see Fig. 4.23). They found that the star formation radial profile of the Milky Way is well described by "standard" star formation laws, but not the one of M 31; they attributed the latter to a recent major perturbation of M 31 by a nearby galaxy, in line with the findings of Block *et al.* (2006).

The above detailed calculations show that all the main properties of the Milky Way disk and most of those of M 31 can be fairly well described by a unified model, provided its star formation efficiency is adjusted to be twice as large in the M 31 case (as anticipated from the lower gas fraction of that galaxy). The radial profiles of both Milky Way and M 31 are well described, albeit less successfully in the case of M 31. In particular, the model fails to match the present SFR in M 31, producing too large values in the outer disk and globally. Yin *et al.* (2009) attribute this failure to the fact that M 31 has been perturbed recently by a major
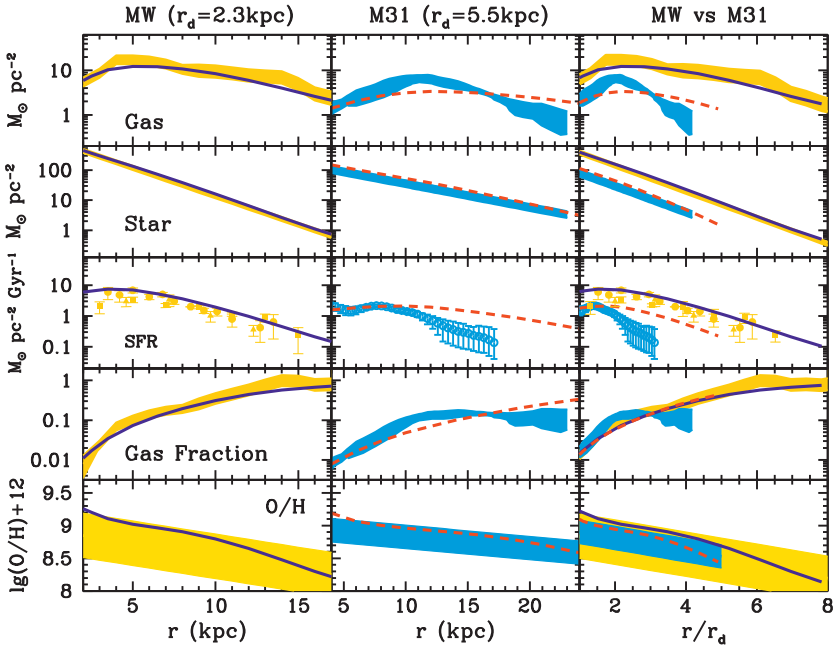
Fig. 4.23. Current profiles of gas, stars, SFR, gas fraction and oxygen abundance (from top to bottom) for the Milky Way and M 31. In the *left* and *middle* panels, profiles for the Milky Way and M 31, respectively, are expressed in terms of physical radius r (in kpc); in the *right* panels, profiles for both disks are expressed in terms of normalised radius r/r_d, where r_d is the scale-length. Observations are presented in shaded (yellow or blue) areas and model results by solid (for the Milky Way) and dashed (for M 31) curves, respectively. Figure taken from Yin *et al.* (2009).

encounter, as already anticipated by the fact that the observed SFR profile of M 31 does not seem to follow any form of the Kennicutt-Schmidt star formation law.

Interestingly, Yin *et al.* (2009) found that, when radii are expressed in terms of the corresponding scale lengths – a concern already expressed by Vila-Costas & Edmunds (1992) – the two disks display very interesting similarities in their radial profiles (Sect. 2.3). This refers, in particular, to the gas fraction, the profile of which is quasi-identical inside the innermost two scale lengths. Also, the scaled abundance gradients of the two disks are quite similar *if* one adopts for the Milky Way the lower range of reported values (see Chapter 2) and *if* one takes at face value the gradient reported for M 31 which, as shown in Chapter 2, is very uncertain. Such a similarity was found in a sample of external spirals and successfully described by the models of Boissier & Prantzos (2000), which cover a much larger range of galaxian properties than the two disks studied here (to be discussed in Sect. 4.4.4).

4.4.2   M 33 and M 101: two very different spirals with very different gradients

After Andromeda and the Milky Way, M 33 is the next large spiral galaxy in the Local Group. M 33 is a low luminosity late type galaxy (Sc) which does not show signs of recent mergers and has neither a bulge nor a bar. This galaxy is thus suited for a study with simple chemical evolution models which consider neither mergers nor gas radial flows (although radial flows induced by its spiral arms cannot be discarded).

M 33 also poses some problems to the hierarchical formation history of the Universe according to which it is very difficult to form bulgeless galaxies. In Robert Kennicutt's words, when summarising the 2007 Vatican conference on disk galaxies: *The presence of a prominent central bulge, tidal streamers, and an extended possibly disrupted outer disk in M 31 appears to be consistent with the expectations of a hierarchical formation history, but the absence (or near-absence) of a bulge, halo, or stellar streams in M 33 continues to challenge modellers.*

M 101, on the contrary, is a large galaxy with about twice the diameter of the Milky Way, and has a prominent central bulge. M 101 is not part of our Local Group but is part of another group of galaxies that has adopted its name, the M 101 Group. This galaxy has well designed spiral arms, and it is one of the galaxies for which recent studies have indicated the existence of younger stellar populations in the outer parts.

In summary, these are two spiral galaxies with very different properties. As expected, these galaxies show different oxygen gradients. While for M 33 the best observations indicate an abundance gradient between -0.045 to -0.06 dex kpc^{-1}, for M 101 a much flatter gradient is observed (around -0.027 dex kpc^{-1} – see Chapter 2). Note, however, that when expressed in terms of scale length (see Fig. 2.35), the gradient of M 101 turns out to be steeper than that of M 33.

As in the case of the Milky Way and M 31 discussed in the previous section, M 33 and M 101 were also the subject of chemical evolution studies. M 33 has been modelled by Magrini *et al.* (2007). These authors suggest that a model in which the galactic disk formed by slow accretion of extragalactic gas (their *accretion model*) is in better agreement with observations than a fast *collapse model*, where the disk is completely formed by halo gas. Their *accretion model* assumes an almost constant infall rate. As it is usually the case in pure thin-disk models (without star formation thresholds), the radial abundance gradients tend to flatten with time (but see below).

The effect of the variable star formation efficiency on the gaseous and stellar radial profiles, as well as on the oxygen gradient was investigated by Marcon-Uchida *et al.* (2010). In this paper the authors compare M 33 to M 31 and the Milky Way by means of pure thin-disk models. The role of a threshold in the star formation rate is also discussed. When comparing models with the same threshold prescriptions, the authors find that models where the star formation efficiency is a function of the galactocentric distance do predict steeper gradients than models where this parameter is assumed to be constant. From the comparison of the Milky Way, M 31 and M 33, the authors conclude that the star formation efficiency
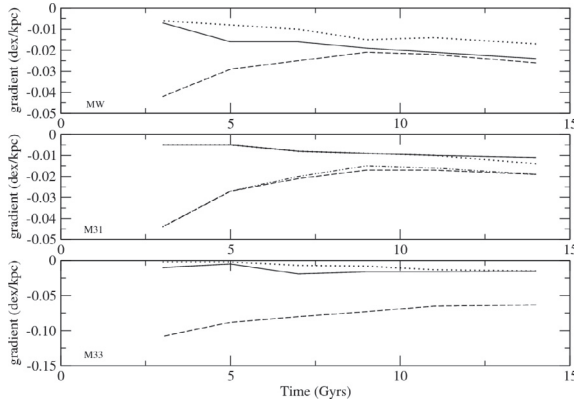
Fig. 4.24. The predicted evolution of the abundance gradients in M 33 compared to that of the Milky Way and M 31 according to the models of Marcon-Uchida *et al.* (2010) (see text for the meaning of the different curves).

increases with disk mass, again suggesting a downsizing in the star formation of spiral galaxies.

Furthermore, the authors point out that different assumptions in both the star formation efficiency and threshold gas density do play an important role in shaping not only the oxygen gradients at present time, but also their evolution. This is shown in Figure 4.24 where it can be seen that models where the star formation efficiency decreases with galactocentric distances (dashed lines in each panel) tend to predict gradients which flatten with time, whereas pure disk models where this parameter is kept constant (solid and dotted lines in each panel) predict gradients which slightly steepen with time[17]. In the top panel, the solid and dotted lines show the same models for the Milky Way but with different values for the gas threshold density, whereas in the two other panels the dotted and solid lines show models which differ in the adopted value for the star formation efficiency only.

M 101 has been modelled by Chiappini *et al.* (2003), with the specific aim of studying the carbon, nitrogen and oxygen evolution in galaxies in general. Chiappini *et al.* (2003) built a chemical evolution model suited to follow the evolutionary history of a spiral galaxy more massive than the Milky Way and took M 101 as a template. M 101 is assumed to form out of two main infall episodes, similarly to what happens for the Milky Way. The first infall episode forms the bulge, inner halo and thick disk substructures on a very short timescale. During the second infall episode the thin disk is formed, mainly through accretion of external matter of primordial chemical composition. The disk forms in an "inside-out" way, as in the case of the Milky Way. As previously discussed for M 31, the

---

[17]Note that in all the cases studied by these authors, a threshold in the star formation rate is assumed.

gas distribution and the abundance gradients are reproduced with systematically smaller timescales for the disk formation relative to the Milky Way (M 101 formed faster), and the difference between the timescales of formation of the internal and external regions is smaller than that estimated for the Milky Way. This would explain the flatter oxygen gradient of M 101 compared not only to the Milky Way but also to M 33.

The authors conclude that the fact that more luminous spirals (such as M 101) tend to have shallower abundance gradients than less luminous ones (such as M 33) can be interpreted as due to a faster formation (downsizing) of large spirals. This finding is in line with the abundance data in other spiral galaxies showing that more massive galaxies present flatter gradients (Zaritsky *et al.* 1994) and have higher average interstellar abundances (Garnett *et al.* 1997), thus suggesting that the more massive the galaxy the faster the collapse of the gas forming the disk. An interpretation is that the variation of the gas accretion timescale onto the disk should also be a function of the galaxy mass, in the sense that the more massive galaxies formed in the shorter timescale.

However, as mentioned before, if one considers the gradients in units of scale length the situation changes. In the particular case of M 101, the gradient turns out to be even steeper than in M 33 and NGC 300. This point will be further discussed in Section 4.4.4. Another caveat to the above conclusions (which are based essentially on the radial profiles of gas, current star formation and present abundance gradients) is the discovery: (i) of young stars in the outer region of M 33, suggesting recent star formation in the outskirts of this galaxy; and (ii) that the scale lengths of stellar populations in M 33 increase with age (Barker *et al.* 2007), which could be in tension with the idea of the inside-out formation of disk galaxies. However, these observations could also be an effect of stellar radial migration. Chemodynamical models are needed to address this important point.

4.4.3 NGC 300: an almost bulge-less spiral galaxy

Finally we discuss NGC 300, a member of the Sculptor group of galaxies. This galaxy is sometimes referred as the twin of M 33: both galaxies lack a bulge, have disks of similar optical size and have predominantly old and metal-poor populations when compared with the Milky Way, M 31 or M 101. However there are also fundamental differences between NGC 300 and M 33: NGC 300 does not show a disk break in its exponential profile and is much more isolated than M 33 (see Gogarten *et al.* 2010, and references therein). Hence NGC 300 offers a simple laboratory to apply isolated pure disk galaxy models (with neither bar nor bulge).

The chemical evolution of NGC 300 was studied by Molla *et al.* (1997) in comparison with other spiral galaxies for which enough data were available at the time. These authors used the gas (atomic and molecular individually) and the observed oxygen gradient in order to recover the star formation histories of the different galaxies. A radius equivalent to the one of the solar vicinity for the Milky Way was defined for each of the studied galaxies as: $R_{eq} = R_{eff}/R_{eff,MW} \times R_{\odot}$,
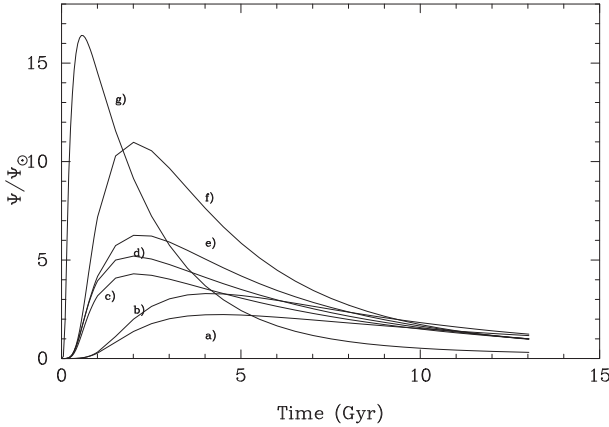
Fig. 4.25. The star formation histories of several spiral galaxies normalised to the present SFR in the solar vicinity, at a fixed galactocentric distance representing the solar vicinity in each galaxy (see text) for the following galaxies: a) NGC 300, b) M 33 (or NGC 598), c) NGC 6946, d) NGC 3198, e) NGC 628 (M74), f) the Milky Way, and g) NGC 224 (M 31). Figure taken from Molla *et al.* (1997).

where R_{eff} is the effective radius. In this way all the galaxies were put on a same scale and could be properly compared.

Figure 4.25 shows the results obtained from this kind of analysis. For our purpose here we now focus on their prediction for NGC 300 (model a) compared to that of M 33 (model b) and that of the Milky Way (model f). Here again, the same ideas discussed in the previous sections seem to be valid, namely an early-type galaxy reaches a high star formation rate at early times (*e.g.* NGC 224) while later types present delayed and less intense main star formation episodes. Among the galaxies studied here, NGC 300 is an extreme case regarding low star formation rates. The inferred star formation rate of NGC 300, at a position that would correspond to the solar vicinity in the case of the MW, is low and has been almost constant during the whole evolution of this galaxy. However, the fact that NGC 300 has a steep abundance gradient[18], steeper than the one in the MW (see Table 2.15), suggests that star formation peaked closer to the inner regions. More recently, Gogarten *et al.* (2010) determined the star formation history of NGC 300 in six radial bins via colour-magnitude diagrams obtained with the Hubble Space Telescope, finding evidence for inside-out growth of the stellar disk. Moreover, they find that the metallicity has increased with time in all radial bins, which they interpret as a lack of infall of unenriched gas. This interpretation is in broad agreement with their finding that the majority of stars in NGC 300 are older than 6 Gyr.

---

[18]When expressed in terms of scale length, the gradient of NGC 300 (traced by young objects such as H II regions and BA supergiants) turns out to be similar to the one in M 33 (see Fig. 2.35).

Note that the observations discussed above and in Chapter 2 for NGC 300 are confined to $R/R_{25} < 1.0$. Deep photometry, exploring the outer disk of NGC 300, indicates that the outer parts of this galaxy are dominated by a population older than ~ 1 Gyr (Vlajic *et al.* 2009). In addition, the inferred metallicity (although very uncertain) suggests a break in the gradient at ~ 10 kpc (*i.e.* ~ 2 R_{25}). The two possible scenarios for the break, proposed by the authors, are: (i) radial mixing of stars in the disk, bringing old stars from the inner regions to the galaxy outskirts, or (ii) a star formation that has slowly progressed outwards during the evolution of NGC 300, resulting in a moderate metallicity gradient in the inner disk, but an almost flat metallicity gradient in the outer disk (similar to what is found in chemical evolution models taking into account a threshold gas density for the star formation). However, N-body simulations for NGC 300 have shown the effects due to radial migration to be minor, compared to what is expected in the MW (see Gogarten *et al.* 2010). In any case, more data sampling the outer disk of NGC 300 are needed to better constrain its formation history.

4.4.4   A general picture for the formation of disk galaxies

From the discussion of the models for the Milky Way and other nearby galaxies it seems that galactic disks in general require slow accretion of metal-poor/primordial gas. Infall of gas is seen in the Milky Way (Sembach *et al.* 2004), in M 31 and in M 33 (Westmeier *et al.* 2005). Assuming that the Milky Way is a typical spiral galaxy and that disks in general formed by slow metal-poor gas accretion, Prantzos & Boissier (2000) made an attempt to model spirals in general. The authors extended their Milky Way chemical evolution models to other spirals by adopting scaling laws suggested in the framework of the Cold Dark Matter scenario, but assuming that all disks start forming their stars at the same time at different rates. Disk galaxies were scaled with respect to the Milky Way by means of two parameters: V_C, the maximum circular velocity and λ, the spin parameter which measures the specific angular momentum of the halo of non-baryonic matter inside of which baryonic matter condenses to form the disk. Essentially, larger values of V_C correspond to more massive disks while larger values of λ correspond to more extended disks. The authors then assume that the infall timescale is a function of the mass of the galaxy such that massive disks form faster than low-mass ones. In this way the authors are able to match, by construction, the observations discussed above, where smaller disks exhibit steeper gradients. This assumption together with the inside-out formation of galactic disks (as it seems to be the case for the Milky Way) ensures a good agreement with many of the observed properties of disk galaxies, not only chemical, but also photometric.

Their predictions for the oxygen abundance gradients in spirals of different masses and sizes are shown in Figure 4.26. As shown in that work, when expressed in dex kpc^{-1}, abundance gradients display a good correlation with disk scale lengths, better than with disk luminosity. Disks with small scale-lengths have large abundance gradients, independent of their mass. On the other hand, when expressed in dex/scale-length, observed abundance gradients show no dependence
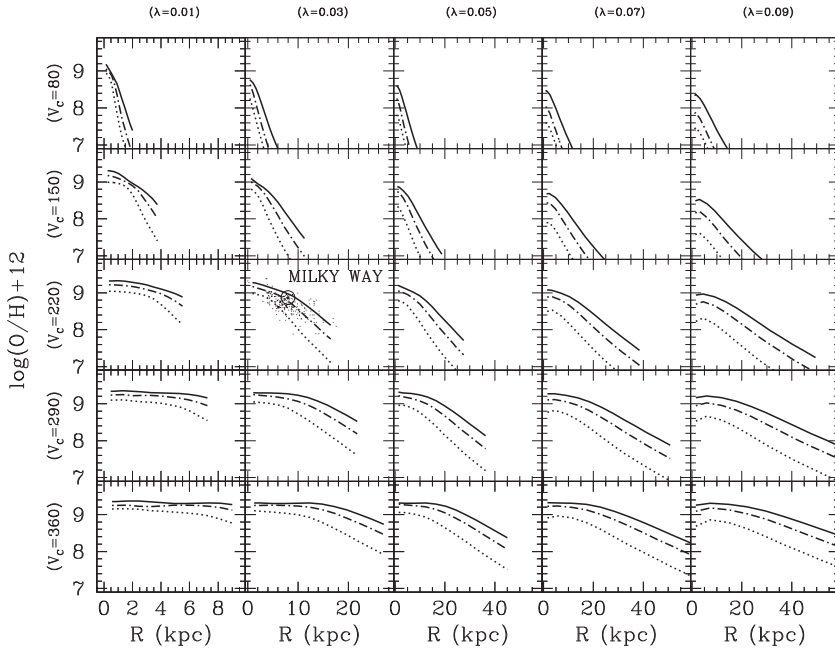
Fig. 4.26. Predictions for the oxygen gradients in spiral galaxies of different masses (V_c) and sizes (λ) at different times: 3 Gyr (dotted), 7.5 Gyr (dash-dotted) and 13.5 Gyr (solid) curves. The case with $V_c = 220$ km s^{-1} and $\lambda = 0.03$ corresponds to the Milky Way (the points in this panel show a compilation of observations of the radial oxygen gradients in the Galaxy). Figure taken from Prantzos & Boissier (2000).

on galaxy luminosity. Those properties, reproduced well by the aforementioned models, point out to a "homologous" evolution of galactic disks, as suggested already in Garnett *et al.* (1997).

In summary, from the available studies of spirals in the Local Group the idea emerges that the disk of spirals have all formed inside-out, and that the more massive disks have formed faster than the less massive ones. This can be interpreted as due to faster gas accretion rates and, consequently, more intense star formation rates in more massive galaxies.

4.5   Oxygen in the largest MW satellites: the Magellanic Clouds

The Magellanic Clouds offer the opportunity to obtain detailed chemical and dynamical information of the two nearest large galaxies to the Milky Way. The interaction of the Magellanic Clouds with our Galaxy has left traces both in the chemistry and kinematics of their stars. The motions of the stars in the Magellanic Clouds probe the Milky Way gravitational potential, and constrain cosmological simulations of the Local Group (Peebles 2010). Furthermore, the Magellanic
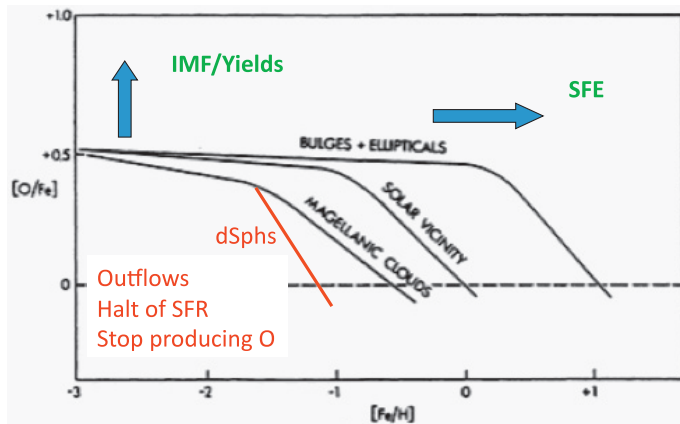
Fig. 4.27. The effect of different star formation histories in the [O/Fe] *vs.* [Fe/H] plot. The horizontal arrow indicates that a large star formation efficiency moves the *knee* of the [O/Fe] relations towards larger metallicities, whereas the *plateau* is essentially determined by the adopted IMF and stellar yields (figure adapted from Matteucci & Brocato 1990). Also indicated is a curve showing a steeper drop in the [O/Fe] ratio due to galactic outflows: the outflows deprive the galaxy of its gas, thus stopping the star formation and consequently the production of oxygen. This explains the abrupt decline in [O/Fe] in the case of outflows.

Clouds offer the opportunity to study systems with different star formation histories than that of our own Galaxy (see Fig. 4.27), and to test stellar evolution models at lower metallicities than what is possible in the solar vicinity (see discussion in Sect. 3.2.2.2).

Currently classified as an irregular galaxy, the LMC has a prominent disk and central bar (van der Marel & Cioni 2001). Does this mean that in the past the LMC was a barred spiral galaxy? The SMC, instead, resembles more a true irregular galaxy, as in this case a disk is not seen. But, how much of what we observe in these galaxies is the result of their internal evolution, and how much the result of their interaction with the Milky Way and with each other? For instance strong variations of metallicity at a fixed distance from the centre could be indicative of strong radial migration of stars in the LMC due to perturbations from the SMC and the Milky Way.

Recent spectroscopic surveys aim at obtaining detailed kinematic and chemical measurements for the different stellar populations in these galaxies to determine how much their internal evolution has been affected by the Milky Way. Indeed, oxygen abundance measurements in these neighbouring galaxies have the potential of giving insights into the above questions by revealing abundance gradients, scatter among stars of the same age and metallicity distributions of stars of all ages. More recently, it has been shown (from the comparison of colour-magnitude diagrams obtained at different positions in LMC with isochrones) that the age

of the youngest populations in LMC increases with increasing distance from the centre (Carrera *et al.* 2011).

As summarised in Chapter 2 (see Fig. 2.31), the Magellanic Clouds are less chemically enriched than the Milky Way interstellar medium in the solar vicinity. Indeed, the different oxygen tracers discussed in Chapter 2 (H II regions, B-type stars, planetary nebulae, FGK supergiants and Cepheids) give a consistent picture despite the large internal scatter within a given family of objects, namely the mean oxygen abundances of the LMC and SMC are roughly $1/2.5^{\text{th}}$ and $1/5^{\text{th}}$ of that of the Sun, respectively.

Is this because these galaxies experienced less stellar generations to enrich their interstellar medium up to the present (slower star formation history)? Or are the lower metallicities due to the fact that the smaller a galaxy, the more effective the galactic winds able to expel part of the metals? Questions like this have to be answered with the help of a chemical evolution *clock*, such as the ratio between oxygen (produced essentially in Type II supernovae) and an element produced on longer timescales, *e.g.* iron (mostly produced by Type Ia binary systems – see Chapters 3 and 4).

Previous studies have confirmed that the [O/Fe] *vs.* [Fe/H] pattern traced by LMC stars lies always below that traced by solar vicinity stars for a given metallicity, suggesting a less efficient star formation rate than in the solar vicinity (provided the IMFs are the same – see Pompéia *et al.* 2008 and references therein). Unless selective winds able to preferentially liberate oxygen are invoked, it is not possible to explain the above results by assuming that the Milky Way and the Magellanic Clouds had the same star formation history.

Pagel & Tautvaisiene (1998) investigated how well the chemical evolution of the Magellanic Clouds can be modelled with yields and time delays equal to those applying to the solar neighbourhood, but with inflow and a homogeneous wind. Their models predict current ratios of Type Ia supernova to core-collapse supernova rates enhanced by 50 and 25 per cent respectively relative to the solar neighbourhood, although these results are sensitive to detailed assumptions on the star formation history. The authors conclude that the relatively high ratio of SNIa to core-collapse supernovae observed in the LMC is most probably related to its less efficient star formation rate rather than a different IMF as suggested by other authors (see Pagel & Tautvaisiene 1998, and references therein).

For the LMC this is now confirmed from observations. Recently, Harris & Zaritsky (2009) obtained the first ever global, spatially resolved reconstruction of the star formation history of the LMC, based on the multi-band photometry of 20 million of its stars from the Magellanic Clouds Photometric Survey. The star formation history obtained by the authors is shown in Figure 4.28. Their results indicate that, following an initial burst of star formation, there was a quiescent epoch from approximately 12 to 5 Gyr ago. Star formation then resumed and has proceeded until the current time at an average rate of roughly 0.2 $M_\odot$ yr^{-1}. The authors suggest that the re-ignition of star formation about 5 Gyr ago, in both the LMC and SMC, is suggestive of a dramatic event at that time in the Magellanic system. The expected chemical enrichment from such a bursty and
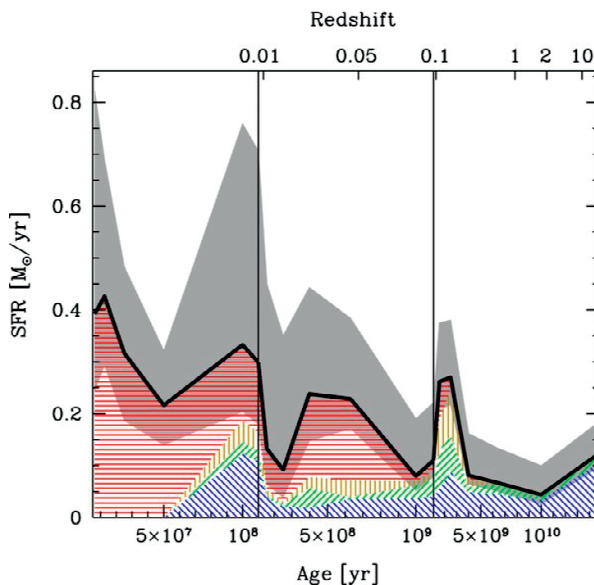
Fig. 4.28. The star formation history of the LMC inferred directly from observations. The time axis is shown with a linear scale that is broken into three segments: the left panel covers around 100 Myr, the middle panel covers around 1 Gyr, and the right panel covers around 14 Gyr. The best-fit SFR as a function of age is shown with a thick black line; the uncertainty in the fit (including covariance between age bins) is shown as a grey shaded envelope. The distribution of metallicity at each age is shown by the mix of colours below the SFR line ($Z = 0.001$ in blue and downward sloping; $Z = 0.0025$ in green and upward sloping; $Z = 0.004$ in orange and vertical; $Z = 0.008$ in red and horizontal. Figure taken from Harris & Zaritsky (2009).

weak star formation is compatible with the mean oxygen abundances discussed in Chapter 2.

4.6 The mass-metallicity relation of galaxies

The mass-metallicity[19] relation and its evolution with redshift represents one of the major constraints to the theory of galaxy formation and evolution. In simple words, the mass-metallicity relation (hereinafter $M - Z$ relation) shows that the interstellar medium of more massive galaxies is more metal rich. Even if the real form of the mass-metallicity relation seems to depend on how the metallicity is measured (see Sect. 2.3.4 for a detailed discussion on the still open issues related to the determination of the mass-metallicity relation from the observational point

---

[19]As in Section 2.4, we will use the word "metallicity" when referring to oxygen as is common practice in this field.

of view), its existence is now a well-established observational fact. The $M - Z$ relation illustrates the importance of oxygen as a tracer of the chemical enrichment of the Universe as whole, as this is the element that is taken as metallicity proxy in this kind of studies.

The $M - Z$ relation is not only a property of galaxies in the local Universe, but is also observed at different redshifts (*i.e.* in distant, and hence old galaxies) probing different epochs of galaxy evolution (see Sect. 2.4). However, at high redshifts it becomes increasingly difficult to determine the $M - Z$ relation down to the lowest masses. Recently, however, it has been realised that low-mass galaxies at redshifts as large as 5 can be revealed by Gamma-Ray bursts, thus allowing one to extend the observed $M - Z$ relation to lower-mass galaxies (Sect. 2.4.3, Laskar *et al.* 2011).

The observed $M - Z$ relation gets steeper at higher redshifts (see Fig. 2.46), suggesting that massive galaxies are enriched faster than lower-mass galaxies (a property that has been called *downsizing*). For the former a clear evolution of the $M - Z$ relation with redshift can be seen. A further thing to be noted is that many star-forming galaxies have already reached almost solar metallicities at redshifts as high as 2 (see Sect. 2.4.2).

Before discussing the several interpretations of the main driver(s) of the $M - Z$ relation at different redshifts, it is important to stress that the variation of the $M - Z$ relation with redshift cannot be interpreted as a process where the galaxies in the high redshift curves are expected to evolve into the ones in the low redshift curves (see Fig. 2.46 in Chapter 2 for the $M - Z$ relation at different redshifts). The reason for this is that the oxygen abundance (metallicity) is measured only in star-forming galaxies (via emission lines, as extensively discussed in Chapter 2), and galaxies forming stars at redshift 3 are most probably not forming stars anymore at redshift zero. However, it is worth noting that, using the fossil record of stellar populations in *local* galaxies, Vale Asari *et al.* (2009) found a similar *stellar* mass-metallicity evolution, this time the metallicity referring to a combination of abundances of different metals (iron, magnesium, among other elements).

How can the $M - Z$ relation of galaxies be explained? Are the models proposed to explain the $M - Z$ relation in the local Universe also able to reproduce the $M - Z$ relation at different redshifts? Does the $M - Z$ relation at high redshifts extend continuously to the low-mass galaxies as in the local Universe, or are there discontinuities? Is the $M - Z$ relation and its evolution well described by a single parameter or is it the result of the combination of different drivers at different redshifts? These questions have kept astronomers in this field very busy.

Let us now briefly describe the current status. The $M - Z$ relation can in principle be affected by one of the following parameters: (i) the IMF, (ii) the star formation rate, (iii) outflows (feedback) and (iv) inflows (see Spitoni *et al.* 2010, and references therein). As discussed in Section 4.2.6, the so-called instantaneous recycling approximation allows one to solve the chemical evolution equations analytically. This approximation is well suited for oxygen as this element is produced by massive stars with short lifetimes. This led several authors to consider simple chemical evolution models, with different assumptions for the

above main parameters, as tools to unravel the main driver of the $M - Z$ relation (*e.g.* Dalcanton 2007; Edmunds 2005; Garnett 2002).

Spitoni *et al.* (2010) computed the expected oxygen abundance for galaxies of a given total baryonic mass, for different assumptions on the variation of gas flows rates (both outflow and infall) and IMF with galaxy mass. It was found that both a galactic wind rate increasing with decreasing galactic mass and a flatter IMF (hence more dominated by massive stars, see also Koeppen *et al.* 2007) in more massive galaxies are equivalent solutions to explain the present $M - Z$ relation. On the other hand, a variable infall rate alone cannot reproduce the observations even at redshift zero. Note that these conclusions agree with the fact that in the local Universe low-mass galaxies do present strong outflows (*e.g.* Tremonti *et al.* 2004). Another way to reproduce the mass-metallicity relation is to assume that the efficiency of the star formation increases with galactic mass (Calura *et al.* 2009, and references therein). This assumption has the advantage to be able to explain the so-called *downsizing* observed in galaxies (*e.g.* Vale Asari *et al.* 2009). A caveat here is that, as shown by Garnett (2002), the same models should also reproduce the gas density in the studied galaxies. However, the gas densities estimates in high redshift galaxies are still very uncertain.

To break the degeneracy among the different possible solutions, the variation of the $M - Z$ relation with redshift has to be considered. Calura *et al.* (2009) investigated the evolution of the $M - Z$ relation in galaxies of different morphological types. The authors used detailed[20] chemical evolution models for elliptical, spiral and irregular galaxies. The adopted models for the different morphological types of galaxies were shown to reproduce several properties of each of these types of galaxies in the ocal Universe (*i.e.* at redshift zero), as well as other more general observational constraints such as the gas-to-light ratios and the supernova rates as a function of morphological types. The main assumption of this work was that the galaxy morphologies do not change with cosmic time.

Calura *et al.* (2009) could reproduce the $M - Z$ relation mainly by means of an increasing efficiency of star formation with mass in galaxies within all morphological types, without any need to invoke galactic outflows favouring the loss of metals in the less massive galaxies. The authors show that, by considering the $M - Z$ relation, the O/H *vs.* star formation rate (SFR), and the SFR *vs.* galactic mass diagrams at various redshifts (see Fig. 4.29), it is possible to constrain the morphology of the galaxies producing these relations. This exercise suggests that galaxies observed at $z = 3.5$ should be mainly proto-ellipticals, whereas at $z = 2.2$ the observed galaxies consist of a morphological mix of proto-spirals and proto-ellipticals. At lower redshifts, the observed $M - Z$ relation is reproduced by considering both spirals and irregulars. Galaxies with different star formation histories may overlap in the $M - Z$ diagram, but measures of abundance ratios such as [O/Fe] can help to break this degeneracy. Again, to better constrain this

---

[20]These models do not assume the instantaneous recycling approximation, and hence can fully explore the effect of different star formation histories.
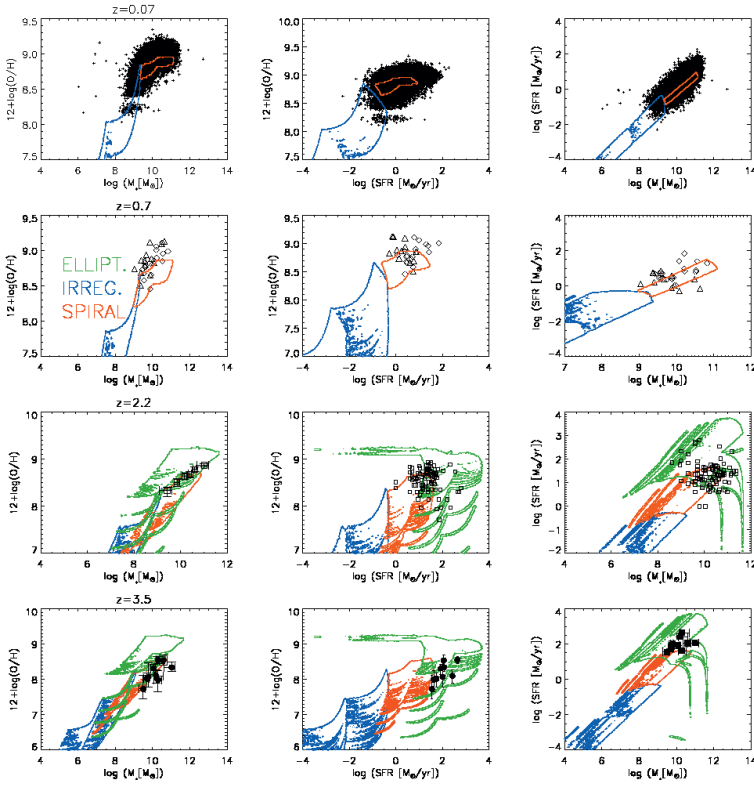
Fig. 4.29. The redshift evolution of M *vs.* Z, (O/H) *vs.* SFR, and SFR *vs.* mass for ellipticals (green contours), spirals (red contours), and irregulars (blue contours) as predicted and as observed by various authors (points) at redshifts $z = 0.07, z = 0.7, z = 2.2, z = 3.5$ (see Calura *et al.* 2009, and references therein). These particular models assume a redshift of formation $z_{\rm f} = 3$ and an age dispersion of $\Delta_{\rm t} = 3$ Gyr for ellipticals, $\Delta_{\rm t} = 5$ Gyr for spirals, and $\Delta_{\rm t} = 10$ Gyr for irregulars.

kind of models, a direct estimate of the gas density in the different galaxies would be needed (Garnett 2002).

Finally, as mentioned above Vale Asari *et al.* (2009) used the fossil record of local galaxies and found evidence of steepening of the $M - Z$ relation with time. From their analysis of galaxy stellar features, they were also able to derive the star formation histories of local galaxies. This allowed them to model the time evolution of stellar metallicity in these galaxies with a closed-box chemical evolution model, for galaxies of different types and masses, using the star formation history derived from the observations. They concluded that the $M - Z$ relation for galaxies with present-day stellar masses down to 10^{10} $M_\odot$ is mainly driven by the star formation history and not by inflows or outflows.

4.7　The global oxygen budget in the Universe

Since oxygen is produced by massive stars, and since from deep galaxy surveys or from the fossil record of local galaxies we have an idea of the history of star formation back to high redshifts (Madau *et al.* 1996; Panter *et al.* 2003), we may ask several questions regarding the total metal budget.

Have we identified correctly and at each redshift all the loci in the Universe where oxygen is found? In the local Universe, estimates give that 10% of all the metals produced by supernovae are locked in stars and 80% in stellar remnants such as white dwarfs, neutron stars and black holes (Fukugita & Peebles 2004). At higher redshifts, the first studies identified a serious "dark metal" (Pagel 2002) or "missing metals" problem (Pettini 2004). At $z \sim 2.5$, 90% of the expected metals were reported to be missing. More recent studies, however, have found that, combining the metals in galaxies and in the intergalactic medium, over 65% of the metals can be accounted for at $z \sim 2.5$, and the missing metal problem is substantially alleviated (Bouché *et al.* 2007).

Another way to look at the metal budget is to consider galaxy clusters, which evolve as closed boxes: metals lost from galaxies are captured in the hot intra-cluster medium. By analysing a dozen clusters of galaxies, Bregman *et al.* (2010) found that most of the heavy elements in the Universe were actually *not formed in galaxies* but outside galaxies by an *early* population of SNe. This study uses iron as a measurement of metallicity. A previous study at $z \sim 3$ by Sommer-Larsen & Fynbo (2008) found that only $20 - 25\%$ of the oxygen is associated with galaxies, which is consistent with the idea that most of the metals are produced outside galaxies.

Obviously, our knowledge of the global metal/oxygen budget in the Universe is still very patchy. Its improvement will require a conjunction of efforts in almost all the domains of astronomy treated in this book.

Appendix A

THE ATOMIC PHYSICS OF OXYGEN

A.1   Introduction

In this Appendix, we review the status of the atomic data sets required for handling oxygen plasma diagnostics and abundance determinations. These have been calculated and measured for several decades by a group of experienced and dedicated scientists who are determined to attain the data integrity and accuracy indispensable for astrophysical applications. In a long and arduous process, periodic revisions have certainly resulted in significant improvements but also in a few unhappy surprises.

As scientific research rapidly becomes very data intensive, atomic and molecular data activities in the field of laboratory astrophysics are reaching unprecedented levels and beginning to secure more adequate funding. We would just like to mention two recent initiatives: (i) the Virtual Atomic and Molecular Data Center (VAMDC[21] – Dubernet *et al.*, 2010; Rixon *et al.*, 2011), a large multinational consortium aimed at integrating, normalising and modernising at least 20 atomic and molecular databases into a distributed virtual warehouse; and (ii) AstroAtom[22], a blog which, by means of Web 2.0 tools, attempts to consolidate the atomic data user–producer community in astrophysics by promoting scientific exchange before formal publication.

In this report we concentrate on collisionally excited lines (Sect. A.2), but also discuss recent advances in the study of optical recombination lines (Sect. A.3), charge transfer (Sect. A.4), K-shell photoabsorption (Sect. A.5) and opacities (Sect. A.6). Whenever possible, the assessed and recommended data are organised in spreadsheets (labelled `Ion.datatype` where `Ion` is the file name and `datatype` the corresponding tab name) which are publicly available online as supplementary data from Google Docs[23]. This handy atomic database will be updated regularly and managed through subsequent releases, the initial version being referred to as V1. Statistical data-set comparisons are mainly carried out in order to give general

---

[21]http://www.vamdc.eu/
[22]https://astroatom.wordpress.com/
[23]http://bit.ly/pUwMEf

accuracy ratings, but more specific estimates may be obtained for desired items by looking through these comparisons in the spreadsheets.

A.2   Collisionally excited lines

The radiative and collisional rates considered in this review and required in the interpretation of collisionally excited lines have been computed with a suite of state-of-the-art atomic physics codes that address two important issues: configuration interaction and relativistic effects. Radiative rates (A-values) are mainly obtained with multi-configuration atomic structure codes that include the relativistic corrections with a Breit–Pauli Hamiltonian, namely SUPERSTRUCTURE (Eissner *et al.* 1974), CIV3 (Hibbert 1975), HFR (Cowan 1981), MCHF (Froese Fischer *et al.* 1997, 2007) and AUTOSTRUCTURE (Badnell 2011), and with the GRASP general purpose Dirac–Fock atomic structure package (Grant *et al.* 1980).

Electron collision rates for transitions between two atomic levels, i and j ($j > i$), can be expressed in $cm^3\,s^{-1}$ as

$$q(j, i; T) = \frac{8.631 \times 10^{-6}\Upsilon(j, i; T)}{\omega(j)T^{1/2}} \tag{A.1}$$

and

$$q(i, j) = \frac{\omega(j)}{\omega(i)} \exp\left[-\frac{\Delta E(i, j)}{\kappa T}\right] q(j, i) \tag{A.2}$$

where $\omega(j)$ and $\omega(i)$ are the statistical weights of the upper and lower levels, respectively, $\Delta E(i, j)$ is the level energy separation, T is the electron temperature in K and κ is the Boltzmann constant. The dimensionless effective collision strength $\Upsilon(j, i; T)$ is obtained by integrating the collision strength $\Omega(i, j; E)$ over a Maxwellian distribution

$$\Upsilon(j, i; T) = \int_0^\infty \Omega(i, j; E) \exp(-E_j/\kappa T)\mathrm{d}(E_j/\kappa T) \ . \tag{A.3}$$

We consider here collision strengths and, hence, effective collision strengths that are mainly calculated with the BPRM close-coupling (multichannel) Breit–Pauli R-matrix package (Berrington *et al.* 1978; Scott & Burke 1980; Scott & Taylor 1982), the intermediate-coupling frame transformation (ICFT) R-matrix method (Griffin *et al.* 1998) and the DARC Dirac Atomic R-matrix Code of P.H. Norrington and I.P. Grant (private communication).

We now proceed to evaluate for each O ion the atomic models that have been proposed and the data sets that are currently available. It will be seen that considerable efforts have been made to implement multi-level models and wide temperature ranges in order to cater for most astronomical plasma conditions.

A.2.1   O I

We consider for O I the 23-level fine-structure model (`O1.ElevIC`) computed by Tachiev & Froese Fischer (2002) with MCHF including extensive configuration

Table A.1. A-value ratios for forbidden lines in the ground configuration of O ions.

Ion	Parameter	TFF	GMZ	SZ	Z
O I	$A(^1D_2 - {}^3P_2)$	6.503E−3	6.535E−3	6.446E−3	
	$A(^1D_2 - {}^3P_1)$	2.101E−3	2.111E−3	2.151E−3	
	Ratio	3.10	3.10	3.00	
	$A(^1S - {}^1D)$	1.260E+0	1.124E+0		
	$A(^1S - {}^3P)$	7.877E−2	7.940E−2		
	Ratio	16.0	14.2		
O II	$A(^2D_{5/2} - {}^4S^o_{3/2})$	4.123E−5			3.588E−5
	$A(^2D_{3/2} - {}^4S^o_{3/2})$	1.635E−4			1.810E−4
	Ratio	0.252			0.198
O III	$A(^1D_2 - {}^3P_2)$	2.028E−2	2.041E−2	2.046E−2	
	$A(^1D_2 - {}^3P_1)$	6.951E−3	6.995E−3	6.791E−3	
	Ratio	2.92	2.92	3.01	

TFF: Tachiev & Froese Fischer (2001, 2002). GMZ: Galavís *et al.* (1997). SZ: Storey & Zeippen (2000). Z: Zeippen (1987).

interaction and relativistic Breit–Pauli corrections, which yields theoretical level energies within 1% of the spectroscopic values. Regarding the A-values for the important forbidden transitions within the ground $2s^2 2p^4$ configuration, a comparison (`O1.Aval2p4`) of the values obtained in this model with those computed by Galavís *et al.* (1997) with SUPERSTRUCTURE using a similar approximation results in good agreement: better than 10% for the magnetic dipole (M1) and 15% for the electric quadrupole (E2) transitions. It is worth mentioning that both A-value data sets are computed with the experimental level energy separations $\Delta E(i,j)$.

Storey & Zeippen (2000) have shown that the astrophysically important $A(^1D_2 - {}^3P_2)/A(^1D_2 - {}^3P_1)$ branching ratio is sensitive to the Breit–Pauli corrections to the M1 operator which have been neglected by both Tachiev & Froese Fischer (2002) and Galavís *et al.* (1997). Although the differences are small (see Table A.1), they are nevertheless relevant in plasma diagnostics and instrument calibrations; for instance, Sharpee & Slanger (2006) have estimated this ratio for O I at 2.997(16) from observations in the terrestrial nightglow which, as shown in Table A.1, is in excellent agreement with the value of 3.00 determined by Storey & Zeippen (2000).

A less satisfactory situation arises in a comparison of the theoretical $A(^1S - {}^1D)/A(^1S - {}^3P)$ ratio with those measured in the laboratory and observed in the terrestrial nightglow (Slanger *et al.* 2006). As seen in Table A.1, there is a 13% difference between the theoretical ratios which can be attributed to configuration interaction and ion model sensitivity in E2 transitions, but the atmospheric observations result in a consistent value of 9.8(10) while all laboratory measurements are above 18.6. The observed value has been recently confirmed in the auroral spectrum at 9.3(5) by Gattinger *et al.* (2009). It is difficult to agree with the assertion by Slanger *et al.* (2006) that the theoretical $A(^1S - {}^3P)$ is underestimated since the accord in Table A.1 for this transition is within 1%. Therefore, these

discrepancies between theory, laboratory and observations have not as yet been resolved and have consequences for auroral and dayglow processes.

Tachiev & Froese Fischer (2002) also provide A- and f-values for allowed transitions that are listed in `O1.AvalIC`, their f-values being within 10% of those computed by Hibbert *et al.* (1991) including configuration interaction and small energy corrections to the diagonal matrix elements, and by Tayal (2009) using a Breit–Pauli B-spline box-based R-matrix method.

Fine-structure effective collision strengths for electron impact have been computed by Bell *et al.* (1998) for transitions within the $2s^2 2p^4\ ^3P$ ground term of O I (see `O1.EColStIC`). The R-matrix method is used with a close-coupling expansion that includes pseudo-states to account for the dipole polarisability of the ^3P term, and term-energy corrections are introduced in the inner-region Hamiltonian before diagonalisation to match the spectroscopic splittings. Due to a careful study of the near-threshold behaviour of the cross section, significant differences (factors of 2 to 4) have been found with respect to previous estimates thus complying with ionospheric requirements.

Effective collision strengths have also been computed in LS coupling by Zatsarinny & Tayal (2003) with the B-spline R-matrix method for transitions involving terms of the ground and excited configurations which are listed in `O1.EColStLS`. In order to ensure proper convergence of the close-coupling expansion, a large target has been used with 26 terms comprising both bound and autoionising states represented by non-orthogonal orbitals that leads to a significant reduction of undesirable pseudo-resonances.

A more recent 38-state R-matrix calculation has been performed by Barklem (2007) to obtain excitation rates for NLTE modelling of oxygen in late-type stellar atmospheres. It excludes autoionising states and polarised pseudo-states in the close-coupling expansion, and the excitation cross sections are found to be plagued by pseudo-resonances that are somehow smoothed out, finding reasonable agreement (within a factor of 3) with Zatsarinny & Tayal (2003). In the light of these comparisons, we would rate the effective collision strengths listed by the latter as better than a factor of 2.

A.2.2   O II

For the O II atomic representation, we recommend the 62-level fine-structure model of Tachiev & Froese Fischer (2002) computed with MCHF including a Breit–Pauli Hamiltonian and extensive configuration interaction (see `O2.Elev`). The agreement of the theoretical level energies with spectroscopic measurements is better than 1%. We also consider the smaller 47-level target representations adopted in the electron impact excitation calculation of Tayal (2007), where level energies and f-values are computed with MCHF using non-orthogonal (Target A) and orthogonal (Target B) orbitals. As described by Tayal (2007), Target A is in better accord (within 2%) with the spectroscopic level energies than Target B (5%).

As shown in `O2.Aval2p3`, the A-values listed by Tachiev & Froese Fischer (2002) for the forbidden transitions within the $2s^2 2p^3$ ground configuration are

in good agreement (5%) with the earlier work by Zeippen (1987) except for the topical $^2D^o_J - ^4S^o_{3/2}$ doublet that is used in density diagnostics. It is well known that the M1 A-values for the half-filled configuration are particularly sensitive to the Breit–Pauli corrections to the transition operator, which have been neglected by Tachiev & Froese Fischer (2002) and thus lead to a 30% discrepant branching ratio (see Table A.1). We therefore recommend the A-values by Zeippen (1987).

Tachiev & Froese Fischer (2002) also list A- and f-values for allowed lines (see O2.AvalE1E2) which can be compared with the data sets by Bell *et al.* (1994) computed with the CIV3 code and by Tayal (2007). A-values in Bell *et al.* (1994) for transitions with $\log A \geq 7$ agree to within 25%, which may be considered satisfactory, while discrepancies as large as a factor of 2 are found in Tayal (2007).

The computational estimates of the effective collision strengths for transitions within the ground configuration of O II have seen interesting developments since the 5-state (LS) close-coupling calculation of Pradhan (1976). Twenty years later, McLaughlin & Bell (1998) computed new data in an 11-level (fine structure) Breit–Pauli R-matrix approximation, finding large differences that were attributed to their extended close-coupling expansion and increased resolution of the resonance structure. Moreover, the new results questioned the validity of the low-density scaling of the $^2D^o_J - ^4S^o_{3/2}$ doublet intensity ratio, assumed to be equal to the ratio of the statistical weights of the upper levels (Seaton & Osterbrock 1957), and were eventually shown to be inconsistent with observations in planetary nebulae (Copetti & Writzl 2002; Wang *et al.* 2004). Subsequent close-coupling calculations (Kisielius *et al.* 2009; Montenegro *et al.* 2006; Pradhan *et al.* 2006; Tayal 2006a, 2007) have confirmed the inaccuracies of McLaughlin & Bell (1998).

In our opinion, Kisielius *et al.* (2009) have carried out a conclusive analysis of this problem by performing a Breit–Pauli R-matrix calculation with various wave-function expansions and target orbitals, and using both *ab initio* and experimental target-level energy separations and very fine energy meshes (O2.EColSt2p3). They have found reasonable agreement (a few percent) with the results by Montenegro *et al.* (2006) and Tayal (2007), but for some transitions, *e.g.* the $^2D^o_{3/2} - ^2D^o_{5/2}$ (see Fig. A.1), noticeable discrepancies are encountered at low temperatures (36% and 25%, respectively). These are believed to be due to variations of the resonance pattern located just above the transition threshold which is sensitive to the positions of the target-level energies in the calculation, *i.e.* whether theoretical or experimental values are chosen.

Effective collision strengths for transitions to excited configurations are given in Tayal (2007) (see O2.EColSt). As pointed out by Kisielius *et al.* (2009) and confirmed by S.S. Tayal (private communications), levels 4 and 5 in Table 3 of Tayal (2007) should be interchanged in order to retrieve the correct data.

A.2.3   O III

The situation of the atomic parameters for O III is on firmer ground than that for O I although it shows some of the problems that have been previously discussed.
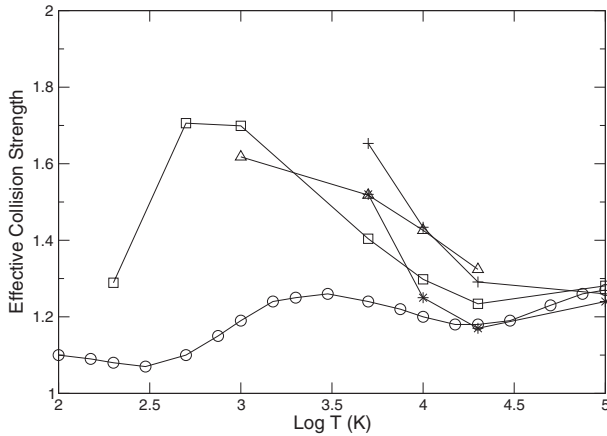
Fig. A.1. Effective collision strength for the $^2\mathrm{D}^\mathrm{o}_{3/2} - {}^2\mathrm{D}^\mathrm{o}_{5/2}$ transition in O II showing low-temperature sensitivity to the resonance structure. Circles: Kisielius *et al.* (2009) using experimental target-level energy separations. Squares: Kisielius *et al.* (2009) with theoretical target-level energy separations. Triangles: Montenegro *et al.* (2006). Crosses: Tayal (2007). Stars: McLaughlin & Bell (1998).

We consider the 46-level atomic models computed by Tachiev & Froese Fischer (2001) with the Breit–Pauli configuration-interaction MCHF code, which reproduces the measured level energies to within 1%, and by Aggarwal & Keenan (1999) with CIV3. The latter model is mainly tailored for the collisional calculation and does not include relativistic effects (see O3.Elev).

The radiative data for O III have been extensively analysed by Froese Fischer *et al.* (2009). As shown in O3.Aval2p2, *A*-values computed by Tachiev & Froese Fischer (2001) for the forbidden transitions within the $2\mathrm{s}^2 2\mathrm{p}^2$ ground configuration agree fairly well with those by Galavís *et al.* (1997), the largest discrepancy being around 25% for an E2 transition with a small ($\sim 10^{-6}$ s^{-1}) *A*-value. Their estimated lifetimes for the ^{1}S level, 523 ms and 559 ms respectively, are in very good agreement with two measurements: 530(25) ms (Träbert *et al.* 2000) and 540(27) ms (Smith *et al.* 2004). The corrections to the M1 transitions pointed out by Storey & Zeippen (2000) must be nevertheless taken into account as they have a noticeable impact on the astrophysically important $A(^1\mathrm{D}_2 - {}^3\mathrm{P}_2)/A(^1\mathrm{D}_2 - {}^3\mathrm{P}_1)$ branching ratio (see Table A.1).

A-values listed by Tachiev & Froese Fischer (2001) for E1 transitions (O3.AvalE1) can be compared with those computed by Aggarwal *et al.* (1997) who took into account extensive configuration interaction and relativistic effects with the code CIV3. For transitions with $\log A \geq 7$, the agreement is found to be better than 30% if the 11 discrepant transitions listed in Table A.2 are excluded. This rating is corroborated in a comparison of the theoretical lifetimes for the $2\mathrm{s}2\mathrm{p}^3$ $^5\mathrm{S}^\mathrm{o}_2$ level, 1.24 ms and 1.72 ms respectively, with the measurement of 1.250(13) ms by Träbert *et al.* (2000) in a heavy-ion storage ring.

Table A.2. Discrepant A-values for E1 transitions in O III.

Upper level	Lower level	AHK	TFF
$2s^2 2p3p\ ^1P_1$	$2s^2 2p3s\ ^1P_1^o$	9.27E+6	3.09E+7
$2s^2 2p3p\ ^3P_0$	$2s2p^3\ ^3P_1^o$	2.94E+7	1.30E+7
$2s^2 2p3d\ ^3F_2^o$	$2s^2 2p3p\ ^1P_1$	3.31E+7	6.06E+7
$2s^2 2p3d\ ^3F_3^o$	$2s^2 2p^2\ ^3P_2$	1.71E+7	4.08E+7
$2s^2 2p3d\ ^1D_2^o$	$2s^2 2p^2\ ^3P_1$	1.40E+7	3.45E+7
$2s^2 2p3d\ ^1D_2^o$	$2s^2 2p3p\ ^3D_1$	2.80E+7	5.54E+7
$2s^2 2p3d\ ^3P_2^o$	$2s^2 2p^2\ ^1D_2$	6.36E+6	1.02E+7
$2s^2 2p3d\ ^3P_1^o$	$2s^2 2p3p\ ^3P_1$	1.31E+7	2.19E+7
$2s^2 2p3d\ ^1P_1^o$	$2s^2 2p^2\ ^3P_0$	3.99E+6	1.57E+7
$2s^2 2p3d\ ^1P_1^o$	$2s^2 2p^2\ ^1D_2$	7.75E+8	2.86E+8
$2s^2 2p3d\ ^1P_1^o$	$2s^2 2p3p\ ^1S_0$	1.92E+7	3.45E+7

AHK: Aggarwal *et al.* (1997). TFF: Tachiev & Froese Fischer (2001).

Electron impact excitation rates for carbon-like ions, including O III, has been previously assessed by Monsignori Fossi & Landini (1994). More recently, effective collision strengths have been computed for O III with the R-matrix method by Aggarwal & Keenan (1999) for the 46-level atomic model selected above using a 26-term LS target. As specified by Aggarwal & Keenan (1999), data for the missing transitions in their original Tables 4A–B, which are reproduced in `O3.EColSt`, can be directly determined from statistical weight ratios.

Aggarwal & Keenan (1999) have compared their data set with previous computations (Aggarwal 1983, 1985, 1993; Aggarwal & Hibbert 1991) finding large discrepancies (up to a factor of 3) for some transitions at both low and high energies, which are attributed to pseudo-resonances, non-converged partial wave expansions, inadequate energy ranges and, in some cases, to unexplained reasons. However, for transitions within the ground configuration, there is good agreement with the R-matrix calculation by Lennon & Burke (1994) (well within 10%) and, for the specific $^3P - ^1D$ transition, with the absolute experimental cross section by Niimura *et al.* (2002).

A.2.4 O IV

We favour the 75-level atomic model computed by Aggarwal & Keenan (2008a) with the GRASP multi-configuration Dirac–Fock package (see `O4.Elev`). Two approximations are considered: with (AK08b) and without (AK08a) the Breit and quantum electrodynamic (QED) corrections. Energies computed for 23 levels by Tachiev & Froese Fischer (2000), for 20 levels by Corrégé & Hibbert (2004) and for 54 levels by Tayal (2006b) with different Breit–Pauli configuration-interaction methods are also tabulated. The comparison for 68 spectroscopic levels is in general very good, AK08b being on average in better accord (3%) than AK08a (5%) while values by Tachiev & Froese Fischer (2000), Corrégé & Hibbert (2004) and

Table A.3. *A*-values for forbidden and intercombination transitions in O IV.

Upper level	Lower level	GMZ	TFF	CH	AK
$2s^2 2p\ ^2P^o_{3/2}$	$2s^2 2p\ ^2P^o_{1/2}$	5.17E−4	5.22E−4		4.61E−4
$2s2p^2\ ^4P_{1/2}$	$2s^2 2p\ ^2P^o_{1/2}$	1.72E+3	1.49E+3	1.47E+3	9.42E+2
$2s2p^2\ ^4P_{1/2}$	$2s^2 2p\ ^2P^o_{3/2}$	1.76E+3	1.47E+3	1.45E+3	1.01E+3
$2s2p^2\ ^4P_{3/2}$	$2s^2 2p\ ^2P^o_{1/2}$	4.84E+1	3.91E+1	3.75E+1	2.31E+1
$2s2p^2\ ^4P_{3/2}$	$2s^2 2p\ ^2P^o_{3/2}$	3.15E+2	2.94E+2	2.90E+2	1.44E+2
$2s2p^2\ ^4P_{5/2}$	$2s^2 2p\ ^2P^o_{3/2}$	1.33E+3	1.19E+3	1.16E+3	6.54E+2

GMZ: Galavís *et al.* (1998). TFF: Tachiev & Froese Fischer (2000). CH: Corrégé & Hibbert (2004). AK: Aggarwal & Keenan (2008a).

Tayal (2006b) are well within 1%. In some of the theoretical data sets, inverted fine-structure splittings are found for some of the terms (mainly those with $L = 2$).

All these calculations list *A*-values which enable a detailed comparison (see `O4.Aval`). In Table A.3, we tabulate *A*-values for the astrophysically relevant forbidden and intercombination transitions within the $n = 2$ complex. The agreement between Tachiev & Froese Fischer (2000) and Corrégé & Hibbert (2004) is outstanding (5%) while larger differences are encountered in the data by Galavís *et al.* (1998) (20%) and Aggarwal & Keenan (2008a) (a factor of 2).

Regarding the allowed transitions within $n = 2$, it may be seen in Figure A.2 that, with respect to the *A*-values listed by Tachiev & Froese Fischer (2000), the agreement with Corrégé & Hibbert (2004) is excellent (well within 5%) while, on average, the other data sets are somewhat higher: average ratios with Galavís *et al.* (1998), Tayal (2006b) and Aggarwal & Keenan (2008a) are 1.06(4), 1.05(6) and 1.17(5), respectively. In this comparison we have corrected the *A*-value by Tayal (2006b) for the $2p^3\ ^2D^o_{3/2} - 2s2p^2\ ^2P_{1/2}$ transition which we believe was misprinted.

For allowed transitions with $\log A \geq 6$ involving excited configurations, the agreement between the data sets by Tachiev & Froese Fischer (2000), Corrégé & Hibbert (2004), Tayal (2006b) and Aggarwal & Keenan (2008a) is within a few percent except for decay transitions from the $2s^2 3p\ ^2P^o_J$ levels where very large discrepancies are encountered in Tayal (2006b) and Aggarwal & Keenan (2008a) which are difficult to explain (see Table A.4). Moreover, we are of the opinion that the differences in the radiative data computed by Aggarwal & Keenan (2008a) for both allowed and forbidden transitions within the $n = 2$ complex are not the result of the more formal treatment of the relativistic problem in the GRASP code, but perhaps due to limited configuration interaction.

Effective collision strengths for O IV have been computed with the *R*-matrix method by Blum & Pradhan (1992) and Zhang *et al.* (1994) for transitions within $n = 2$ and by Tayal (2006b) for 54 levels. On the other hand, Aggarwal & Keenan (2008a) used the Dirac *R*-matrix DARC code to obtain rates for transitions among 75 levels. Both Tayal (2006b) and Aggarwal & Keenan (2008a) have indicated
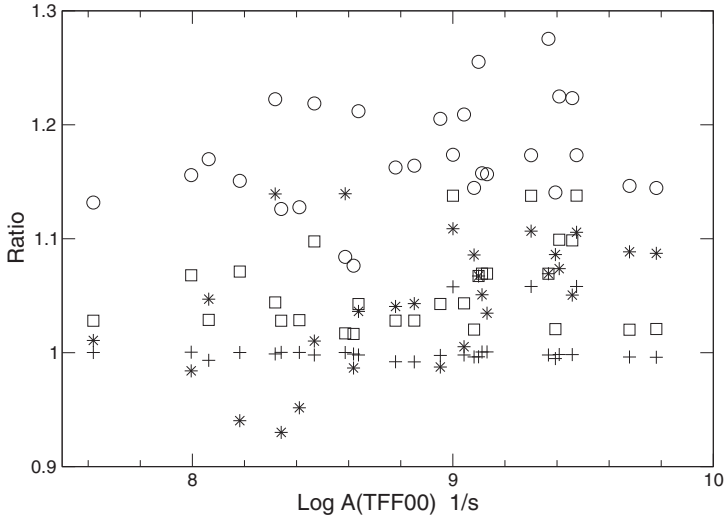
Fig. A.2. Ratios of A-values computed by Tachiev & Froese Fischer (2000) for allowed transitions within the $n = 2$ complex of O IV, A(TFF00), relative to: Galavís *et al.* (1998) (squares); Corrégé & Hibbert (2004) (crosses); Tayal (2006b) (stars); and Aggarwal & Keenan (2008a) (circles).

Table A.4. Discrepant A-values for E1 transitions in O IV.

Upper level	Lower level	TFF	CH	T	AK
$2s^2 3p\ ^2P^o_{1/2}$	$2s2p^2\ ^2D_{3/2}$	4.93E+8	4.87E+8	5.09E+8	8.20E+8
$2s^2 3p\ ^2P^o_{1/2}$	$2s2p^2\ ^2S_{1/2}$	9.31E+7	1.03E+8	5.33E+5	1.48E+8
$2s^2 3p\ ^2P^o_{1/2}$	$2s2p^2\ ^2P_{1/2}$	2.92E+6	2.96E+6	5.33E+5	3.69E+6
$2s^2 3p\ ^2P^o_{1/2}$	$2s2p^2\ ^2P_{3/2}$	1.14E+6	1.14E+6	4.17E+5	1.47E+6
$2s^2 3p\ ^2P^o_{3/2}$	$2s2p^2\ ^2D_{5/2}$	4.43E+8	4.38E+8	4.59E+8	7.37E+8
$2s^2 3p\ ^2P^o_{3/2}$	$2s2p^2\ ^2D_{3/2}$	4.92E+7	4.86E+7	5.15E+7	8.18E+7
$2s^2 3p\ ^2P^o_{3/2}$	$2s2p^2\ ^2S_{1/2}$	9.38E+7	1.03E+8	1.35E+8	1.49E+8
$2s^2 3p\ ^2P^o_{3/2}$	$2s2p^2\ ^2P_{3/2}$	3.21E+6	3.21E+6	9.67E+5	4.08E+6

TFF: Tachiev & Froese Fischer (2000). CH: Corrégé & Hibbert (2004). T: Tayal (2006b). AK: Aggarwal & Keenan (2008a).

that some of the effective collision strengths by Blum & Pradhan (1992) display anomalous increases with temperature which will not be discussed here as this calculation was corrected and superseded by Zhang *et al.* (1994). Aggarwal & Keenan (2008a) mention that the main differences with the data by Zhang *et al.* (1994) are at the lower temperatures, and that they are due to an overestimate of their top-up procedure. We do not agree with this conclusion because a comparison of the two data sets at the high-temperature end, namely $\log T = 5.7$ K, where

convergence of the partial wave expansion is more conspicuous, results in satis-factory agreement (within 10–15%). Discrepancies at the lower temperature end are mostly caused, as discussed previously, by the treatment of the resonance structure, energy meshes and target-level energy separations.

Aggarwal & Keenan (2008a) find general overall accord with Tayal (2006b), the differences being mainly at low temperatures, but warn of extensive printing errors in his tables. In conclusion, we would recommend the effective collision strengths by Zhang *et al.* (1994) and Aggarwal & Keenan (2008a) which are listed in O4.EColSt, particularly the latter due to the large number of transitions con-sidered, and suggest that the data by Tayal (2006b) should be used with caution. The overall accuracy of these collisional data sets is estimated at ∼20%.

A.2.5   O V

The 20-level atomic model we have selected for O V has been computed with the MCHF code (Froese Fischer & Tachiev 2004; Tachiev & Froese Fischer 1999) includ-ing Breit–Pauli relativistic corrections and configuration interaction (see O5.Elev), which yields level energies that on average agree with experiment to around 0.1%. We also tabulate level energies by Hibbert (1980) calculated with CIV3 in a similar approximation that are within 1%.

Tachiev & Froese Fischer (1999) tabulate A-values for both allowed (E1) and forbidden transitions (E2, M1, M2) which are compared in O5.Aval with data sets by Hibbert (1980) and Kingston & Hibbert (2000, 2001). For E1 transitions within the $n = 2$ complex, Hibbert (1980) and Kingston & Hibbert (2001) agree with Tachiev & Froese Fischer (1999) to better than 15% and 10%, respectively, while for transitions to levels in the $2s^23l$ ($l \leq 2$) configurations, Hibbert (1980) agrees to around 12%. In this comparison some of the A-values by Hibbert (1980) have been corrected for misprints. For forbidden transitions among levels of the $1s^22s^2$ and $1s^22s2p$ configurations, A-values by Kingston & Hibbert (2000) agree with those by Tachiev & Froese Fischer (1999) to better than 5%. A measurement of the radiative lifetime of the $2s2p$ $^3P_1^o$ level in a heavy-ion storage ring by Träbert *et al.* (2005) at 0.432(9) ms compares well with the theoretical values: 0.461 ms (Hibbert 1980); 0.437 ms (Tachiev & Froese Fischer 1999) and 0.481 ms (Kingston & Hibbert 2000).

Effective collision strengths for transitions among the 20 levels of the proposed atomic model have been computed by K.A. Berrington and A.E. Kingston but were never published although they have been parameterised by Kato, Lang, & Berrington (1990). For these two reasons, we have chosen not to list them in the corresponding O5 spreadsheet. On the other hand, Smith *et al.* (2005) have measured absolute effective collision strengths for the $2s^2$ $^1S - 2s2p$ $^1P^o$ transition finding good agreement (better than 25%) with theory thus providing a useful benchmark.

A.2.6   O VI

For Li-like O VI we adopt the 24-level atomic model ($1s^2nl$ for $n \leq 5$) computed by Tayal (2003), Aggarwal & Keenan (2004) and, more recently, by Liang & Badnell (2011) with the CIV3, GRASP and AUTOSTRUCTURE atomic structure codes, respectively, where the theoretical energies agree with measurements to better than 1% (see `O6.Elev`). Tayal (2003) and Aggarwal & Keenan (2004) only list A-values for allowed lines while Liang & Badnell (2011) include the forbidden transitions as well (`O6.Aval`). We also compare with the A-values for allowed lines computed by Nahar (2002) with the Breit–Pauli R-matrix method. In general, A-values for allowed lines compare very well (within a few per cent) except for the 5p–3s transition where the A-value by Tayal (2003), 3.08×10^9 s^{-1}, is notably larger than those by Nahar (2002), 1.81×10^9 s^{-1}, Aggarwal & Keenan (2004), 1.79×10^9 s^{-1}, and Liang & Badnell (2011), 1.75×10^9 s^{-1}.

Effective collision strengths have been computed with the R-matrix method including pseudo-states (Tayal 2003), the DARC code (Aggarwal & Keenan 2004) and, more recently, with the intermediate-coupling frame transformation (ICFT) R-matrix approach (Liang & Badnell 2011). All these data sets are available from `O6.EColSt`. Liang & Badnell (2011) include a target with both valence-shell ($1s^2nl$, $n \leq 5$) and inner-shell ($1s2lnl'$, $n \leq 4$) levels, and take into account radiative and Auger damping. We find very good general agreement between Tayal (2003), Aggarwal & Keenan (2004) and Liang & Badnell (2011) (around 10%), except for some transitions in Tayal (2003) with small effective collision strengths at low temperatures ($\log T < 4.5$ K) which are dominated by resonances, and for some allowed transitions for $\log T > 6$ K which are affected by partial wave convergence. This comparison also appears to indicate that, at least for valence–valence collisional transitions in O VI, damping effects on the resonance structures are still small. We confirm the reliability of these three collisional data sets.

A.2.7   O VII

Energy levels for He-like O VII have been computed by Delahaye & Pradhan (2002) for 31 levels ($n \leq 4$) with SUPERSTRUCTURE in a Breit–Pauli configuration-interaction method, and by Aggarwal & Keenan (2008b) for 49 levels ($n \leq 5$) with GRASP in a multi-configuration Dirac–Fock approach, the overall agreement with the spectroscopic measurements being better than 1%. We adopt the atomic model by Aggarwal & Keenan (2008b) in `O7.Elev`.

Aggarwal & Keenan (2008b) list A-values for both allowed and forbidden transitions with $n \leq 5$ while Delahaye & Pradhan (2002) only do so for allowed transitions with $n \leq 3$ (see `O7.Aval`). For transitions with $\log A \geq 7$, a comparison of these two data sets results in an agreement within 10%. Furthermore, Crespo López-Urrutia *et al.* (1998) report a measured lifetime for the 1s2s ^{3}S$_1$ level of 0.956(5) ms obtained with an electron beam ion trap (EBIT), which is in the same level of agreement with the theoretical estimate of 1.06 ms (Aggarwal & Keenan 2008b).

Effective collision strengths have been computed by Delahaye & Pradhan (2002) in a Breit–Pauli R-matrix method taking into account radiative damping, and by Aggarwal & Keenan (2008b) using the Dirac R-matrix DARC code. The latter have performed a detailed comparison of the two sets of rates which results in differences greater than 20% for most of the transitions listed by Delahaye & Pradhan (2002). At the lower temperatures, where the effective collision strengths are sensitive to the resonance structures, discrepancies up to a factor of 2 are found but decrease significantly with temperature; furthermore, for levels $i \geq 23$ they can be as large as an order of magnitude. Since Delahaye & Pradhan (2002) found the effects of radiative damping small in this system, such large differences are not readily explainable. As a result, we would recommend the data set by Aggarwal & Keenan (2008b) which have been rated at better than 20% for most transitions and is available in O7.EColSt.

A.2.8   O VIII

Aggarwal *et al.* (2010) have recently computed radiative and collisional rates for H-like O VIII with a 25-level ($n \leq 5$) atomic model. Level energies have been determined with the GRASP multi-configuration Dirac–Fock code with and without QED effects. C. Mendoza, A. Chechelev, P. Palmeri, P. Quinet, N.R. Badnell & T.R. Kallman (private communication) have also used this code to generate level energies (including QED effects) and A-values for this system which are used here for comparison purposes. As shown in O8.Elev, theoretical energies agree with the spectroscopic values to 3–4 parts in 10^5 if QED corrections are taking into account.

Transition probabilities for both allowed and forbidden transitions are listed in O8.Aval, the main difference between the data sets by Aggarwal *et al.* (2010) and Mendoza et al. is that the latter include the electric (E3) and magnetic (M3) octupole channels which for some transitions, *e.g.* $nd_{5/2}-n'p_{1/2}$ and $nf_{5/2}-n's_{1/2}$, are the dominant decay routes.

The effective collision strengths by Aggarwal *et al.* (2010) have been computed with the Dirac R-matrix code (DARC). Since there is no previous work to compare with, the relativistic, multi-configuration, distorted-wave Flexible Atomic Code (FAC) by Gu (2003) has been used by Aggarwal *et al.* (2010) to determine the accuracy level, finding significant resonance enhancements at the lower temperatures to arrive at an accuracy rating of better than 20%.

A.3   Optical recombination lines

In low density plasmas, metal abundances can also be estimated from the analysis of optical recombination lines. This method, compared to the most common one based on collisionally excited lines, has the advantage that the line intensity ratios relative to hydrogen depend weakly on electron temperature while collisionally excited lines display emissivities that vary exponentially with temperature.

The resulting abundances, however, have been found to be systematically larger: typically by a factor of 2 in H II regions and higher in most planetary nebulae (a factor of 70 has been reported, see Liu *et al.*, 2006; Fang *et al.*, 2011 and Chapter 2). In order to explain this dilemma, some authors, *e.g.* Liu *et al.* (2000), have proposed the existence of metal-rich, cold plasma inclusions in the diffuse gas. Others, namely Nahar *et al.* (2010), have suggested that dominant near-threshold resonance structures, such as those found in the photoionisation cross section of O II, could indeed increase the dielectronic recombination rates at very low temperatures so as to sort out the abundance anomaly.

Therefore, in this context it is important to rely outright on very well-resolved photoionisation cross sections and accurate effective recombination coefficients. In the unified method originally proposed by Storey (1994) for O II, the latter are determined directly from the photoionisation cross section of each state thus taking into account both radiative and dielectronic processes; in the case of O ions, extensive calculations have been performed in this approach by Nahar (1999, 2004).

Most of the work on the optical recombination lines have been carried out in the *LS* coupling scheme, except perhaps for the intermediate-coupling treatment of O III recombination by Kisielius & Storey (1999). As a consequence, a new set of very detailed calculations of effective recombination coefficients are currently being performed for N II (Fang *et al.* 2011) and O II (in progress) taking into account relativistic effects at very low temperatures ($\sim$100 K). It is found that the sensitivity of the individual spectral term components to temperature and density can lead to new plasma diagnostics. In the expectation of this new work, we neither include recommended photoionisation cross sections nor recombination rates for O ions in our supplementary online material.

A.4   Charge transfer

In many astrophysical plasmas containing oxygen species (*e.g.* comets, planetary atmospheres and the heliosphere), charge transfer reactions can compete with radiative and dielectronic recombination in determining ionisation fractions (Chutjian 2004; Greenwood *et al.* 2004; Koutroumpa *et al.* 2007; Stancil 2001). They essentially involve inelastic collisions between heavy particles, namely atoms, molecules and ions, whereby m electrons bound to a neutral target (X) are transferred to the incoming O-ion projectile

$$O^{q+} + X \rightarrow O^{(q-m)+} + X^{m+}. \tag{A.4}$$
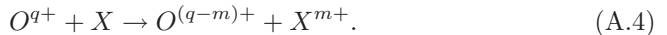
X is usually a hydrogen or helium atom (Stancil *et al.* 1999; Wu *et al.* 2009; Zhao *et al.* 2005), but H_2, H_2O, CO, CO_2 or CH_4 molecular targets may also be involved (Djurić *et al.* 2008; Greenwood *et al.* 2004; Hasan *et al.* 2001; Mawhorter *et al.* 2007). Moreover, although the reactants are usually in their ground states, the exchanged electron can recombine into an excited nl state of $O^{(q-1)+}$ which then radiates (Dalgarno & Sternberg 1982), and the inverse reactions where a neutral

O target reacts with an ionic projectile such as He$^+$ can also take place (Zhao
et al. 2004).

A keynote contribution in this field has been the comprehensive table of ana-
lytic fits to charge transfer rates for reactions between H and ions with $q = 1-4$ and
$Z \leq 30$ released by Kingdon & Ferland (1996), where quantal rates were in many
cases complemented with data computed with the Landau–Zener approximation
of the earlier days of Butler *et al.* (1979).

As described by Wang *et al.* (2002), a variety of theoretical methods are cur-
rently used to compute total and state-selective charge exchange rates accord-
ing to the nature of the projectile–target system and energy range of interest.
Good agreement with measurements is often found (see, for instance, Wu *et al.*,
2009), and online databases (*e.g.* the ORNL/UGA Charge Transfer Database for
Astrophysics[24]) are being developed.

A.5   K-shell photoabsorption

The diagnostic potential of oxygen K-shell photoabsorption is currently being ex-
ploited in the high-resolution X-ray spectra obtained with the *Chandra* and *XMM-
Newton* satellite-borne observatories. We are here concerned with inner-shell tran-
sitions in oxygen ions that give rise to spectral features such as Kα and Kβ lines
and K edges that are observed in a variety of exotic astronomical entities: Seyfert
galaxies, AGN dusty warm absorbers, black-hole candidates, black-hole binaries,
bursting neutron stars and the warm-hot intergalactic medium, to mention a few
(see García *et al.* 2005 and references therein).

Inner-shell absorption features in the X-ray spectrum of galactic sources are
being employed to determine the oxygen abundances and ionisation fractions in the
interstellar medium and to discern the phase of the absorbers, *i.e.* whether atomic
or molecular, gas or solid (Juett *et al.* 2004). It is argued that the oscillatory
modulations near the K edge due to the presence of solid particles (grains) can be
detected (Lee *et al.* 2009), but in the case of the Sco X-1 low-mass X-ray binary,
extensive spectral modelling by García *et al.* (2011) only found evidence of atomic
oxygen.

In any case, the spectral modelling of oxygen K-shell photoabsorption requires
accurate atomic data such as K-vacancy level energies, wavelengths, f-values, ra-
diative and Auger widths and high-energy photoabsorption cross sections (see the
OK spreadsheet). Although most of them are obtained through calculation, using
atomic physics codes such as those mentioned in Section A.2, laboratory wave-
lengths for oxygen K lines have been measured by Schmidt *et al.* (2004) and Gu
et al. (2005) in the high-resolution spectra of electron beam ion traps (EBIT). As
shown in Table A.5, it is evident that the theoretical efforts will never match spec-
troscopic accuracy, but on the other hand, measurements may exhibit notorious
misidentifications such as those by Gu *et al.* (2005) for O VI and O III.

---

[24]http://www-cfadc.phy.ornl.gov/astro/ps/data/

Table A.5. Comparison of EBIT and theoretical wavelengths (Å) for O K lines.

Ion	Lower level (J)	Upper level (J')	EBIT	Theory
O VI	$1s^2 2s(1/2)$	$1s2s2p(1/2, 3/2)$	$22.0194(16)^a$	22.00^c
			$22.374(8)^b$	22.05^d
				22.03^e
O V	$1s^2 2s^2(0)$	$1s2s^2 2p(1)$	$22.374(3)^a$	22.33^c
			$22.370(10)^b$	22.35^d
				22.37^e
O IV	$1s^2 2s^2 2p(1/2, 3/2)$	$1s2s^2 2p^2(1/2, 3/2)$	$22.741(5)^b$	22.78^c
				22.73^d
				22.75^e
O III	$1s^2 2s^2 2p^2(1, 2)$	$1s2s^2 2p^3(1)$	$22.071(6)^b$	23.08^c
				23.05^d
				23.07^e

^{a}EBIT measurement (Schmidt *et al.* 2004). ^{b}EBIT measurement (Gu *et al.* 2005). ^{c}HULLAC calculation (Behar & Kahn 2002). ^{d}R-matrix calculation (Pradhan *et al.* 2003). ^{e}HFR calculation (García *et al.* 2005).

The most interesting effect in K-shell photoabsorption is by far the smearing of the K-edge resonance structure by both radiative and Auger damping. When a photon promotes a K-shell electron to an excited Rydberg state

$$h\nu + 1s^2 2s^\lambda 2p^\mu \longrightarrow 1s2s^\lambda 2p^\mu n\mathrm{p} \; , \tag{A.5}$$

it decays *via* the radiative and Auger manifold

$$1s2s^\lambda 2p^\mu n\mathrm{p} \quad \xrightarrow{\mathrm{K}n} \quad 1s^2 2s^\lambda 2p^\mu + h\nu_n \tag{A.6}$$

$$\xrightarrow{\mathrm{K}\alpha} \quad 1s^2 2s^\lambda 2p^{\mu-1} n\mathrm{p} + h\nu_\alpha \tag{A.7}$$

$$\xrightarrow{\mathrm{KL}n} \begin{cases} 1s^2 2s^\lambda 2p^{\mu-1} + e^- \\ 1s^2 2s^{\lambda-1} 2p^\mu + e^- \end{cases} \tag{A.8}$$

$$\xrightarrow{\mathrm{KLL}} \begin{cases} 1s^2 2s^\lambda 2p^{\mu-2} n\mathrm{p} + e^- \\ 1s^2 2s^{\lambda-1} 2p^{\mu-1} n\mathrm{p} + e^- \\ 1s^2 2p^\mu n\mathrm{p} + e^- \; . \end{cases} \tag{A.9}$$

The radiative branches are controlled, as indicated in Equations (A.6)–(A.7), by the Kα (2p $\rightarrow$ 1s) and Kβ (K3, 3p $\rightarrow$ 1s) lines. Reaction (A.8) contains the participator Auger (KLn) channels, where the np outer electron is directly involved in the decay, while in the KLL channels (Eq. A.9) the np Rydberg electron remains a spectator. For O^{q+} ions with $0 \le q \le 5$, Auger decay dominates, and for $q \le 4$, it is almost completely through the KLL channels causing the total widths of K-vacancy resonances within each species to be approximately constant as $n \to \infty$,
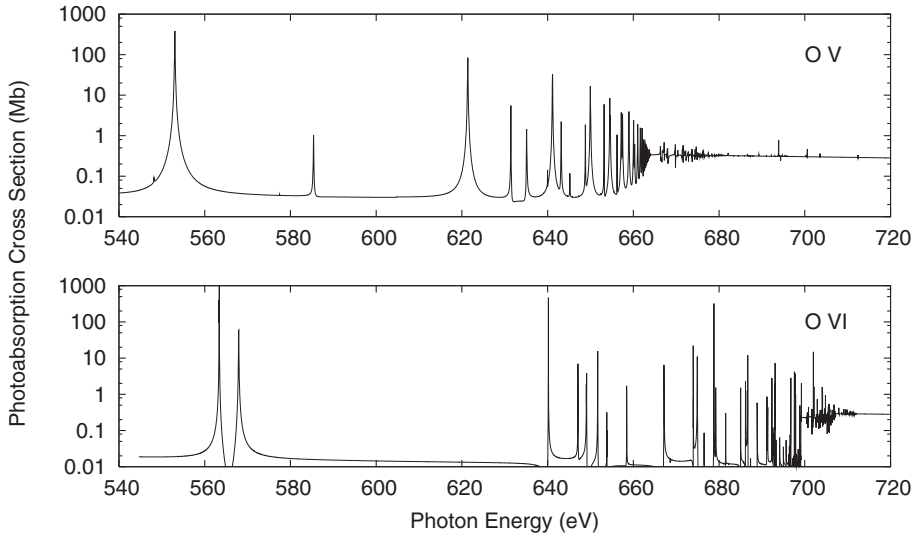
Fig. A.3. High-energy photoionisation cross section of O v (upper panel) showing the smearing of the K edge due to Auger damping. In O vi (lower panel), Auger damping does not occur thus exhibiting a sharp K edge. These cross sections are from the work by García *et al.* (2005).

thus imprinting distinctive signatures (Lorentzian profiles) on the threshold structures of the photoabsorption cross section (see Fig. A.3). This peculiar damping behaviour leads to the smearing of the K edge that has been corroborated in the laboratory (Gorczyca & McLaughlin 2000), and its theoretical treatment requires the introduction of an optical potential in the *R*-matrix formalism (Gorczyca & Robicheaux 1999).

A.6 Opacities

Rosseland mean opacities and radiative accelerations for oxygen computed by the Opacity Project can be currently retrieved online from the OPserver[25] (Mendoza *et al.* 2007). They were last revised by Seaton & Badnell (2004) and Badnell *et al.* (2005) particularly for inner-shell processes and by introducing an improved frequency mesh.

Since the OPAL Project (Rogers & Iglesias 1992) did not make mean opacities for a pure oxygen mixture directly available, and due to the downward revision of the solar oxygen abundance (Asplund *et al.* 2004) and the important contribution of this element to the Rosseland mean at the base of the solar convection zone, Badnell *et al.* (2005) have explored several possibilities that could actually lead to

[25]http://opacities.osc.edu/

enhancements of its opacity. However, contrary to the required increases of the Rosseland mean in the temperature region $2 \times 10^6 \lesssim T \lesssim 5 \times 10^6$ K (Bahcall *et al.* 2005), they did not prove to be plausible.

New light-element opacities are currently being computed (J. Colgan, private communication) with the Los Alamos ATOMIC code (Magee *et al.* 2004), and members of the Opacity Project are also expected to revise and extend their data sets in the near future, particularly by introducing improved atomic models in intermediate coupling and accurate photoionisation cross sections for neutral and near-neutral species, and by considering in detail the iron-group elements.

References

Abadi, M.G., Navarro, J.F., Steinmetz, M., & Eke, V.R., 2003, ApJ, 597, 21

Abia, C., Rebolo, R., 1989, ApJ, 347, 186

Adelberger, K.L., Steidel, C.C., Shapley, A.E., *et al.*, 2004, ApJ, 607, 226

Afflerbach, A., Churchwell, E., Acord, J.M., *et al.*, 1996, ApJS, 106, 423

Afflerbach, A., Churchwell,, E., & Werner, M.W., 1997, ApJ, 478, 190

Aggarwal, K.M., 1983, ApJS, 52, 387

Aggarwal, K.M., 1985, A&A, 146, 149

Aggarwal, K.M., 1993, ApJS, 85, 197

Aggarwal, K.M., & Hibbert, A., 1991, JPhB, 24, 3445

Aggarwal, K.M., & Keenan, F.P., 1999, ApJS, 123, 311

Aggarwal, K.M., & Keenan, F.P., 2004, PhyS, 70, 222

Aggarwal, K.M., & Keenan, F.P., 2008a, A&A, 486, 1053

Aggarwal, K.M., & Keenan, F.P., 2008b, A&A, 489, 1377

Aggarwal, K.M., Hibbert, A., & Keenan, F.P., 1997, ApJS, 108, 393

Aggarwal, K.M., Keenan, F.P., & Heeter, R.F., 2010, PhyS, 82, 015006

Aléon, J., Robert, F., Duprat, J., & Derenne, S., 2005, Nature, 437, 385

Alecian, G., & Stift, M.J., 2007, A&A, 475, 659

Alibes, A., Labay, J., & Canal, R., 2001, A&A 370, 1103

Allen, C.W., 1973, asqu.book

Allen, M.G., Groves, B.A., Dopita, M.A., Sutherland, R.S., & Kewley, L.J., 2008, ApJS, 178, 20

Allende Prieto, C., 2008, ASPC, 384, 39

Allende Prieto, C., Asplund, M., & Fabiani Bendicho, P., 2004, A&A, 423, 1109

Allende Prieto, C., Lambert, D.L., & Asplund, M., 2001, ApJ, 556, L63

Aller, L.H., 1942, ApJ, 95, 52

Aller, L.H., 1954, ApJ, 120, 401

Aller, L.H., & Czyzak, S.J., 1983, ApJS, 51, 211

Aller, L.H., Keyes, C.D., Maran, S.P., *et al.*, 1987, ApJ, 320, 159

Alloin, D., Collin-Souffrin, S., Joly M., & Vigroux, L., 1979, A&A, 78, 200

Alves-Brito, A., Meléndez, J., Asplund, M., Ramírez, I., & Yong, D., 2010, A&A, 513, A35

Amnuel, P.R., 1993, MNRAS, 261, 263

Anders, E., & Grevesse, N., 1989, GeCoA, 53, 197

Anderson, C.D., 1932, Science, 76, 238

Anderson, L.S., 1985, ApJ, 298, 848

Anderson, L.S., 1989, ApJ, 339, 558

André, M.K., *et al.*, 2003, ApJ, 591, 1000

Andrievsky, S.M., Bersier, D., Kovtyukh, V.V., *et al.*, 2002, A&A, 384, 140

Andrievsky, S.M., Kovtyukh, V.V., Korotin, S.A., Spite, M., & Spite, F., 2001, A&A, 367, 605

Andrievsky, S.M., Kovtyukh, V.V., Luck, R.E., *et al.*, 2002, A&A, 392, 491

Andrievsky, S.M., Luck, R.E., Martin, P., & Lépine, J.R.D., 2004, A&A, 413, 159

Andrievsky, S.M., Luck, R.E., & Kovtyukh, V.V., 2005, AJ, 130, 1880

Andrievsky, S.M., *et al.* 2002, A&A, 381, 32

Angulo, C., Arnould, M., Rayet, M., *et al.*, 1999, Nucl. Phys. A, 656, 3

Angulo, C., *et al.*, 1999, NuPhA, 656, 3

Antia, H.M., & Basu, S., 2011, JPhCS, 271, 012034

Arnaud M., Rothenflug R., Boulade O., Vigroux L., & Vangioni-Flam E., 1992, A&A, 254, 49

Arnould, M., Goriely, S., & Jorissen, A. 1999, A&A, 347, 572

Arnould, M., Siess, L., & Goriely, S., 2003, ASPC, 304, 284

Asari, N.V., Cid Fernandes, R., Stasinska, G., *et al.*, 2007, MNRAS, 381, 263

Asensio Ramos, A., Trujillo Bueno, J., Carlsson, M., & Cernicharo, J., 2003, ApJ, 588, L61

Asplund M., 2005, ARA&A, 43, 481

Asplund, M., & García Pérez, A.E., 2001, A&A, 372, 601

Asplund, M, Grevesse, N., & Sauval, A.J. 2005, in Cosmic Abundances as Records of Stellar Evolution and Nucleosynthesis, ed. T.G. Barnes & F.N. Bash, ASP Conf. Series, vol. 336, 25

Asplund M., Grevesse N., & Sauval A.J., 2005a, ASPC, 336, 25

Asplund, M., Grevesse, N., Sauval, A.J., & Scott, P., 2009, ARA&A, 47, 481

Asplund, M., Grevesse, N., Sauval, A.J., Allende Prieto, C., & Kiselman D., 2004, A&A, 417, 751

Asplund, M., Gustafsson, B., Kiselman, D., & Eriksson, K., 1997, A&A, 318, 521

Asplund, M., Nordlund Å., Trampedach R., & Stein R.F., 2000, A&A, 359, 743

Asplund, M., Pereira, T.,Grevesse, N., *et al.*, 2012, A&A, submitted

Assunção M., *et al.*, 2006, PhRvC, 73, 055801

Auer, L.H., & Mihalas, D., 1972, ApJS, 24, 193

Avanzini, M.B., 2011, PrPNP, 66, 412

Ayres, T.R., 2002, ApJ, 575, 1104

Ayres, T.R., 2008, ApJ, 686, 731

Ayres, T.R., Plymate, C., & Keller, C.U., 2006, ApJS, 165, 618

Badnell, N.R., 2011, CoPhC, 182, 1528

Badnell, N.R., Bautista, M.A., Butler, K., *et al.*, 2005, MNRAS, 360, 458

Böhm-Vitense, E., 1958, Z. Astrophys. 46, 108

Bahcall, J.N., & Soneira R.M., 1980, ApJS, 44, 73

Bahcall, J.N., Basu, S., Pinsonneault, M., & Serenelli, A.M., 2005, ApJ, 618, 1049

Balachandran, S.C., & Carney, B.W., 1996, AJ, 111, 946

Balachandran, S.C., Carr, J.S., & Carney, B.W., 2001, NewAR, 45, 529

Balachandran, S.C., Carr, J.S., & Carney, B.W., 2002, HiA, 12, 420

Baldwin, J.A., Ferland, G.J., Martin, P.G., *et al.*, 1991, ApJ, 374, 580

Baldwin, J.A., Phillips, M.M., & Terlevich, R., 1981, PASP, 93, 5

Ballero S.K., Matteucci, F., Origlia, L., & Rich, R.M., 2007, A&A, 467, 123

Balona, L.A., 1984, MNRAS, 211, 973

Bao, Z.Y., Beer, H., Käppeler, F., *et al.*, 2000, ADNDT, 76, 70

Baraffe, I., Chabrier, G., Allard, F., & Hauschildt, P.H. 2002, A&A, 382, 563

Barbuy, B., 1988, A&A, 191, 121

Barbuy, B., de Freitas Pacheco, J.A., & Castro, S., 1994, A&A, 283, 32

Barkat, Z., Rakavy, G., & Sack, N., 1967, Phys. Rev. Lett., 18, 379

Barker, T., 1978, ApJ, 220, 193

Barker, M.K., Sarajedini, A., Geisler, D., Harding, P., & Schommer, R., 2007, RMxAC, 29, 156

Barklem, P.S., 2007, A&A, 462, 781

Basu, S., & Antia, H.M., 1997, MNRAS, 287, 189

Basu, S., & Antia, H.M., 2004, ApJ, 606, L85

Basu, S., & Antia, H.M., 2008, PhR, 457, 217

Basu, S., Pinsonneault, M.H., & Bahcall, J.N., 2000, ApJ, 529, 1084

Battaglia, G., *et al.*, 2005, MNRAS, 364, 433

Beaulieu, J.-P., Buchler, J.R., Marquette, J.-B., Hartman, J.D., & Schwarzenberg-Czerny, A., 2006, ApJ, 653, L101

Becker, S.R., & Butler, K., 1988, A&A, 201, 232

Behar, E., & Kahn, S.M., 2002, in NASA Laboratory Astrophysics Workshop, ed. F. Salama, NASA/CP-2002-21186, GPO, Washington, DC, 23

Bekki, K., Campbell, S.W., Lattanzio, J.C., & Norris, J.E., 2007, MNRAS, 377, 335

Bell, E.F., *et al.*, 2008, ApJ, 680, 295

Bell, K.L., Berrington, K.A., & Thomas, M.R.J., 1998, MNRAS, 293, L83

Bell, K.L., Hibbert, A., Stafford, R.P., & McLaughlin, B.M., 1994, PhyS, 50, 343

Bell, R.A., Eriksson, K., Gustafsson, B., & Nordlund, Å., 1976, A&AS, 23, 37

Bensby, T., & Lundström, I., 2001, A&A, 374, 599

Bensby, T., Feltzing, S., & Lundström, I., 2004a, A&A, 415,155

Bensby, T., Feltzing, S., & Lundström, I., 2004b, A&A, 421, 969

Bensby, T., Feltzing, S., Lundström, I., & Ilyin, I., 2005, A&A, 433, 185

Bensby, T., Zenn, A.R., Oey, M.S. & Feltzing, S., 2007, ApJ 663, L13

Bensby, T., *et al.*, 2010, A&A, 512, A41

Bensby, T., *et al.*, 2010, A&A, 521, L57

Benvenuto, O.G., & De Vito, M.A., 2004, MNRAS, 352, 249

Berezinsky V., Bulanov, S., Dogiel, V., *et al.*, 1990, Astrophysics of cosmicrays, ed. V.L. Ginzburg (North-Holland)

Bergeron, J., & Herbert-Fort, S., 2005, pgqa.conf, 265

Bergeron, J., Aracil, B., Petitjean, P., & Pichon, C., 2002, A&A, 396, L11

Bernard Salas, J., Pottasch, S.R., Beintema, D.A., & Wesselius, P.R., 2001, A&A, 367, 949

Berrington, K.A., Burke, P.G., Le Dourneuf, M., *et al.*, 1978, CoPhC, 14, 367

Biermann, L., 1932, ZA, 5, 117

Binns, W.R., Wiedenbeck, M.E., Arnould, M., *et al.*, 2005, ApJ, 634, 351

Blagrave, K.P.M., Martin, P.G., & Baldwin, J.A., 2006, ApJ, 644, 1006

Blair, W.P., & Kirshner, R.P., 1985, ApJ, 289, 582

Blair, W.P., Kirshner, R.P., & Chevalier, R.A., 1982, ApJ, 254, 50

Blair, W.P., *et al.*, 2000, ApJ, 537, 667

Block, D.L., *et al.*, 2006, Nature, 443, 832

Blocker, T., 1995, A&A, 297, 727

Blum, R.D., & Pradhan, A.K., 1992, ApJS, 80, 425

Bochsler, P., 2007a, A&ARv, 14, 1

Bochsler, P., 2007b, A&A, 471, 315

Boesgaard, A.M., King, J.R., Deliyannis, C.P., & Vogt, S.S., 1999, AJ, 117, 492

Boissier, S., & Prantzos, N., 1999, MNRAS, 307, 857

Boissier, S., & Prantzos, N., 2000, MNRAS, 312, 398

Boissier, S., Prantzos, N., Boselli, A., & Gavazzi G., 2003, MNRAS, 346, 1215

Boissier, S., *et al.*, 2007, ApJS, 173, 524

Boldt, E., McDonald, F.B., Riegler, G., & Serlemitsos, P., 1966, Phys. Rev. Lett., 17, 447

Bond, J.R., Arnett, W.D., & Carr, B.J., 1984, ApJ 280, 825

Bonifacio, P., *et al.*, 2007, A&A, 462, 851

Bonnell, I.A., Clarke, C.J., & Bate, M.R., 2006, MNRAS, 368, 1296

Boothroyd, A.I., & Sackmann, I.J., 1999, ApJ, 510, 232

Boothroyd, A.I., & Sackmann, I.-J., 2003, ApJ, 583, 1004

Boothroyd, A.I., Sackmann, I.J., & Ahern, S.C., 1993, ApJ, 416, 762

Boothroyd, A.I., Sackmann, I.J., & Wasserburg, G.J., 1995, ApJ, 442, L21

Borkowski, K.J., Hendrick, S.P., & Reynolds, S.P., 2007, ApJ, 671, L45

Bouché, N., Lehnert, M.D., Aguirre, A., Péroux, C., & Bergeron, J., 2007, MNRAS, 378, 525

Bournaud, F., Elmegreen, B.G., & Martig, M., 2009, ApJ, 707, L1

Bouffard, M., Engelmann, J.J., Koch, L., *et al.*, 1982, Astrophys. Space Sci., 84, 3

Bradt, H.L., & Peters, B., 1948, Phys. Rev., 74, 1828

Bregman, J.N., Anderson , M.E., & Dai, X., 2010, ApJ, 716, L63

Bresolin, F., 2007, ApJ, 656, 186

Bresolin, F., 2011, ApJ, 730, 129

Bresolin, F., Garnett, D.R., & Kennicutt, R.C., Jr., 2004, ApJ, 615, 228

Bresolin, F., Gieren, W., Kudritzki, R.-P., Pietrzyński, G., & Przybilla, N., 2002, ApJ, 567, 277

Bresolin, F., Gieren, W., Kudritzki, R.-P., *et al.*, 2009, ApJ, 700, 309

Bresolin, F., Kudritzki, R.-P., Mendez, R.H., & Przybilla N., 2001, ApJ, 548, L159

Bresolin, F., Pietrzyński, G., Urbaneja, M.A., *et al.*, 2006, ApJ, 648, 1007

Bresolin, F., Schaerer, D., González Delgado, R.M., & Stasińska, G., 2005, A&A, 441, 981

Bresolin, F., Stasińska, G., Vílchez, J.M., Simon, J.D., & Rosolowsky, E., 2010, MNRAS, 404, 1679

Bresolin, F., Urbaneja, M.A., Gieren, W., Pietrzyński, G., & Kudritzki, R.-P., 2007, ApJ, 671, 2028

Brewer, J.P., Richer, H.B., & Crabtree, D.R., 1995, AJ, 109, 2480

Brinchmann, J., Charlot, S., White S.D.M., *et al.*, 2004, MNRAS, 351, 1151

Brook, C., Richard, S., Kawata, D., Martel, H., & Gibson, B.K., 2007, ApJ, 658, 60

Brown, P.J.F., Dufton, P.L., Lennon, D.J., & Keenan, F.P., 1986, MNRAS, 220, 1003

Brown, P.J.F., Dufton, P.L., Lennon, D.J., Keenan, F.P., & Kilkenny, D., 1986, A&A, 155, 113

Brunetti, M., Chiappini, C., & Pfenniger, D., 2011, A&A, in press

Buchmann, L., 1996, ApJ, 468, L127

Buchmann, L., & Barnes, C.A., 2006, Nucl. Phys. A, 777, 254

Buote, D.A., 2000, ApJ, 532, L113

Burgers, W., 1969, JCrGr, 5, 226

Burstein, D., Faber, S.M., Gaskell, C.M., & Krumm, N., 1984, ApJ, 287, 586

Butler, K., & Giddings, J.R, 1985, Newsl. Anal. Astron. Spectra, No. 9

Butler, S.E., Bender, C.F., & Dalgarno, A., 1979, ApJ, 230, L59

Buzzoni, A., 2002, AJ, 123, 1188

Caffau, E., Ludwig, H-G., & Steffen, M., *et al.*, 2008, A&A, 488, 1031

Cahn, J.H., Kaler, J.B., & Stanghellini, L., 1992, A&AS, 94, 399

Caldwell, J.A.R., & Ostriker, J.P., 1981, ApJ, 251, 61

Calura, F., Pipino, A., Chiappini, C., *et al.*, 2009, A&A, 504, 373

Canizares, C.R., Clark, G.W., Markert, T.H., *et al.*, 1979, ApJ, 234, L33

Carciofi, A.C., Domiciano de Souza, A., Magalhães, A.M., Bjorkman, J.E., & Vakili, F., 2008, ApJ, 676, L41

Carlsson, M., 2009, MmSAI, 80, 606

Carlsson, M., & Stein, R.F., 2002, ApJ, 572, 626

Carollo, D., *et al.*, 2007, Nature, 450, 1020

Carraro, G., Geisler, D., Villanova, S., Frinchaboy, P.M., & Majewski, S.R., 2007, A&A, 476, 217

Carrera, R., Gallart, C., Aparicio, A., & Hardy, E., 2011, ApJ, 142, 61

Carretta, E., Bragaglia, A., Gratton, R.G., D'Orazi, V., & Lucatello, S., 2009a, A&A, 508, 695

Carretta, E., Bragaglia, A., Gratton, R.G., *et al.*, 2009b, A&A, 505, 117

Carretta, E., Bragaglia, A., Gratton, R.G., & Lucatello, S., 2009c, A&A, 505, 139

Carretta, E., Bragaglia, A., Gratton, R.G., *et al.*, 2010, A&A, 516, A55

Carretta, E., Gratton, R.G., Bragaglia, A., Bonifacio, P., & Pasquini L., 2004, A&A, 416, 925

Carretta, E., Gratton, R., Cohen, J.G., Beers, T.C., & Christlieb, N., 2002, AJ, 124, 481

Carretta, E., Gratton, R.G., Lucatello, S., Bragaglia, A., & Bonifacio, P., 2005b, A&A, 441, 131

Carretta, E., Gratton, R.G., Lucatello, S., Bragaglia, A., & Bonifacio, P., 2005a, A&A, 433, 597

Carswell, B., Schaye, J., & Kim, T.-S., 2002, ApJ, 578, 43

Cartledge, S.I.B., Lauroesch, J.T., Meyer, D.M., & Sofia, U.J., 2004, ApJ, 613, 1037

Cartledge, S.I.B., Meyer, D.M., Lauroesch, J.T., & Sofia, U.J., 2001, ApJ, 562, 394

Casagrande, L., Schönrich, R., Asplund, M., *et al.*, 2011, A&A, 530, A138

Castelli, F., & Kurucz, R.L., 2003, in: IAU Symposium, Vol. 210, Modelling of Stellar Atmospheres, ed. N., Piskunov, W.W., Weiss, D.F., Gray, p. 20

Castro, M., Vauclair, S., & Richard, O., 2007, A&A, 463, 755

Caughlan, G.R., & Fowler, W.A., 1988, At. Data Nucl. Data Tables, 40, 283

Cayrel, R., Depagne, E., Spite, M., *et al.*, 2004, A&A, 416, 1117

Cedrés, B., Urbaneja, M.A., & Cepa, J., 2004, A&A, 422, 511

Centeno, R., & Socas-Navarro, H., 2008, ApJ, 682, L61

Cerviño, M., & Luridiana, V., 2004, A&A, 413, 145

Cescutti, G., Matteucci, F., Francois, P., & Chiappini, C., 2007, A&A, 462, 943

Chabrier, G., 2003, PASP, 115, 763

Chabrier, G., Baraffe, I., Allard, F., & Hauschildt, P., 2000, ApJ, 542, 464

Chafa, A., *et al.*, 2005, PhRvL, 95, 031101

Chafa, A., *et al.*, 2006, PhRvL, 96, 019902

Chafa, A., *et al.*, 2007, PhRvC, 75, 035810

Charbonnel, C., 1994, A&A, 282, 811

Charbonnel, C., 2005, IAU Symp.228 on "From lithium to uranium: Element tracers of early cosmic evolution", ed. V., Hill, P., François, F., Primas (Cambridge Univ. Press), 337

Charbonnel, C., & Lagarde, N., 2010, A&A, 422, A10

Charbonnel, C., & Zahn, J.-P., 2007, A&A, 467, L15

Charlot, S., & Longhetti, M., 2001, MNRAS, 323, 887

Charlton, J.C., Mellon, R.R., Rigby, J.R., & Churchill, C.W., 2000, ApJ, 545, 635

Chaussidon, M., 2007, leas.book, 45

Chaussidon, M., Robert, F., & McKeegan, K.D., 2006, GeCoA, 70, 5433

Chen, H.-W., Kennicutt, R.C., & Rauch, M., 2005, ApJ, 620, 703

Chiappini, C., 2009, IAU Symp., 254, 191

Chiappini, C., Górny, S.K., Stasińska, G., & Barbuy, B., 2009, A&A, 494, 591

Chiappini, C., Hirschi, R., Meynet, G., *et al.*, 2006, A&A, 449, L27

Chiappini, C., Matteucci, F., & Gratton, R., 1997, ApJ, 477, 765

Chiappini, C., Matteucci, F., & Padoan, P., 2000, ApJ, 528, 711

Chiappini, C., Matteucci, F., & Romano, D., 2001, ApJ, 554, 1044

Chiappini, C., Romano, D., & Matteucci, F., 2003, MNRAS, 339, 63

Chiba, M., & Beers, T.C., 2000, AJ, 119, 2843

Chieffi, A., & Limongi, M., 2004, ApJ, 608, 405

Christensen-Dalsgaard, J., 1982, MNRAS, 199, 735

Christensen-Dalsgaard, J., 2002, RvMP, 74, 1073

Christensen-Dalsgaard, J., di Mauro, M.P., Houdek, G., & Pijpers, F., 2009, A&A, 494, 205

Christensen-Dalsgaard, J., Proffitt, C.R., & Thompson, M.J., 1993, ApJ, 403, L75

Churchwell, E., & Walmsley, C.M., 1975, A&A, 38, 451

Chutjian, A., 2004, PhST, 110, 203

Cid Fernandes, R., Mateus, A., Sodré, L., Stasińska, G., & Gomes, J.M., 2005, MNRAS, 358, 363

Clayton, D.D., & Nittler, L.R., 2004, ARA&A, 42, 39

Clayton, R.N., 1993, AREPS, 21, 115

Clayton, R.N., Grossman, L., & Mayeda, T.K., 1973, Science, 182, 485

Clegg, R.E.S., Tomkin, J., & Lambert, D.L., 1981, ApJ, 250, 262

Cohen, J.G., 1978, ApJ, 223, 487

Collet, R., Asplund, M., & Thévenin, F., 2005, A&A, 442, 643

Conti, P.S., Greenstein, J.L., Spinrad, H., Wallerstein, G., Vardya, M.S., 1967, ApJ, 148, 105

Copetti, M.V.F., Writzl, B.C., 2002, A&A, 382, 282

Corrégé, G., Hibbert, A., 2004, ADNDT, 86, 19

Costa, R.D.D., Uchida, M.M.M., & Maciel, W.J., 2004, A&A, 423, 199

Cowan, R.D., 1981, The Theory of Atomic Structure and Spectra (Univ. of California Press, Berkeley, CA)

Cox, D.P., & Smith, B.W., 1976, ApJ, 203, 361

Crespo López-Urrutia, J.R., Beiersdorfer, P., Savin, D.W., & Widmann, K., 1998, PhRvA, 58, 238

Crockett, N.R., Garnett, D.R., Massey, P., & Jacoby, G., 2006, ApJ, 637, 741

Crowther, P.A., 2007, ARA&A, 45, 177

Crowther, P.A., Dessart, L., Hillier, D.J., Abbott, J.B., & Fullerton, A.W., 2002, A&A, 392, 653

Crowther, P.A., Morris, P.W., & Smith, J.D., 2006, ApJ, 636, 1033

Cuisinier, F., Maciel, W.J., Köppen, J., Acker, A., & Stenholm, B., 2000, A&A, 353, 543

Cummings, A.C., & Stone, E.C., 2007, Space Sci. Rev., 130, 389

Cunha, K., & Lambert, D.L., 1992, ApJ, 399, 586

Cunha, K., & Lambert, D.L., 1994, ApJ, 426, 170

Cunha, K., & Smith, V.V., 2006, ApJ, 651, 491

D'Ercole, A., Vesperini, E., D'Antona, F., McMillan, S.L.W., & recchi, S., 2008, MNRAS, 407, 854

Dababneh, S., Heil, M., Käppeler, F., *et al.*, 2003, PhRvC, 68, 025801

Daflon, S., & Cunha, K., 2004, ApJ, 617, 1115

Daflon, S., Cunha, K., & Becker, S.R., 1999, ApJ, 522, 950

Daflon, S., Cunha, K., Becker, S.R., & Smith V.V., 2001, ApJ, 552, 309

Dalcanton, J.J., 2007, ApJ, 658, 941

Dalgarno, A., & Sternberg, A., 1982, MNRAS, 200, 77P

Davidson, K., & Kinman, T.D., 1982, PASP, 94, 634

de Boer, K.S., 1981, ApJ, 244, 848

de Freitas Pacheco, J.A., Maciel, W.J., & Costa, R.D.D., 1992, A&A, 261, 579

de Mello, D.F., Daddi, E., Renzini, A., *et al.*, 2004, ApJ, 608, L29

de Séréville, N., *et al.*, 2005, Nucl. Phys., A758, 745

De, S., Baron, E., & Hauschildt, P.H., 2010, MNRAS, 401, 2081

Decin, L., Vandenbussche, B., Waelkens, C., *et al.*, 2003, A&A, 400, 679

Decourchelle, A., *et al.*, 2001, A&A, 365, L218

Decressin, T., 2007, Ph.D. Thesis (Geneva University)

Decressin, T., Baumgardt, H., Charbonnel, C., & Kroupa, P., 2010, A&A, 516, A73

Decressin, T., Charbonnel, C., & Meynet, G., 2007a, A&A, 475, 859

Decressin, T., Charbonnel, C., Siess, L., *et al.*, 2009, A&A, 505, 727

Decressin, T., Meynet, G., Charbonnel, C., Prantzos, N., & Ekström, S., 2007b, A&A, 464, 1029

Denissenkov, P.A., & Denissenkova, S.N., 1990, SvA Lett., 16, 275

Delahaye, F., & Pinsonneault, M.H., 2006, ApJ, 649, 529

Delahaye, F., & Pradhan, A.K., 2002, JPhB, 35, 3377

Deharveng, L., Caplan, J., Lequeux, J., *et al.*, 1988, A&AS, 73, 407

Deharveng, L., Peña, M., Caplan, J., & Costero, R., 2000, MNRAS, 311, 329

Dennefeld, M., & Kunth, D., 1981, AJ, 86, 989

Descouvemont, P., 1987, PhRvC, 36, 2206

Dessart, L., Crowther, P.A., Hillier, D.J., *et al.*, 2000, MNRAS, 315, 407

Dessauges-Zavadsky, M., Calura, F., Prochaska, J.X., D'Odorico, S., & Matteucci, F., 2004, A&A, 416, 79

Dessauges-Zavadsky M., Prochaska J.X., D'Odorico, S., Calura, F., & Matteucci, F., 2006, A&A, 445, 93

Dickens, R.J., Croke, B.F.W., Cannon, R.D., & Bell, R.A., 1991, Nature, 351, 212

Djurić, N., Smith, S.J., Simcic, J., & Chutjian, A., 2008, ApJ, 679, 1661

Dodorico, S., & Dopita, M., 1983, IAUS, 101, 517

Domiciano de Souza, A., Kervella, P., Jankov, S., *et al.*, 2003, A&A, 407, L47

Dopita, M.A., & Evans, I.N., 1986, ApJ, 307, 431

Dopita, M.A., & Sutherland, R.S., 1995, ApJ, 455, 468

Dopita, M.A., & Sutherland, R.S., 1996, ApJS, 102, 161

Dopita, M.A., Binette, L., Dodorico, S., & Benvenuti, P., 1984, ApJ, 276, 653

Dopita, M.A., Dodorico, S., & Benvenuti, P., 1980, ApJ, 236, 628

Dopita, M.A., Ford, H.C., & Webster, B.L., 1985, ApJ, 297, 593

Dopita, M.A., Kewley, L.J., Heisler, C.A., & Sutherland, R.S., 2000, ApJ, 542, 224

Dopita, M.A., *et al.*, 2006, ApJ, 647, 244

Drake, J.J., Smith, V.V., & Suntzeff, N.B., 1992, ApJ 395, L95

Drotleff, H.W., *et al.*, 1993, ApJ, 414, 735

Dubernet, M.L., *et al.*, 2010, JQSRT, 111, 2151

Dufour, R.J., 1984, IAUS, 108, 353

Dufour, M., & Descouvemont, P., 2001, NuPhA, 694, 221

Dufton, P.L., Fitzsimmons, A., & Howarth, I.D., 1990, ApJ, 362, L59

Dufton, P.L., McErlean, N.D., Lennon, D.J., & Ryans, R.S.I., 2000, A&A, 353, 311

Dufton, P.L., Ryans, R.S.I., Trundle, C., *et al.*, 2005, A&A, 434, 1125

Dufton, P.L., *et al.*, 2006, A&A, 457, 265

Durret, F., Lima Neto, G.B., & Forman, W., 2005, A&A, 432, 809

Dwek, E., *et al.*, 1995, ApJ, 445, 716

Ecuvillon, A., Israelian, G., Santos, N.C., *et al.*, 2006, A&A, 445, 633

Eddington, A.S., 1926, The Internal Constitution of the Stars (Cambridge: Cambridge University Press)

Edmunds, M.G., 1990, MNRAS, 246, 678

Edmunds, M.G., 2005, Astron. Geophys., 46, 4.12

Edmunds, M.G., & Greenhow, R.M., 1995, MNRAS, 272, 241

Edmunds, M.G., & Pagel, B.E.J., 1984, MNRAS, 211, 507

Edvardsson, B., Andersen, J., Gustafsson, B., *et al.*, 1993, A&A, 275, 101

Eggen, O.J., Lynden-Bell, D., & Sandage, A.R., 1962, ApJ, 136, 748

Eissner, W., Jones, M., & Nussbaumer, H., 1974, CoPhC, 8, 270

Ekström, S., Meynet, G., & Maeder, A., 2008, IAU Symp. 250, p. 209

Ekström S., *et al.*, 2011, arXiv [`arXiv:1110.5049`]

El Eid, M., 1994, A&A, 285, 915

Ellison, D.C., Drury, L.O'C., & Meyer, J.P., 1997, ApJ, 487, 197

Ellison, S.L., Kewley, L.J., & Mallen-Ornelas, G., 2005, MNRAS, 357, 354

Elmegreen, B.G., 2002, ApJ, 577, 206

Elmegreen, D.M., & Elmegreen, B.G., 2006, ApJ, 650, 644

Engelmann, J.J., Ferrando, P., Soutoul, A., *et al.*, 1990, A&A, 233, 96

Epstein, R.I., 1980, MNRAS, 193, 723

Erb, D.K., Shapley, A.E., Pettini M., *et al.*, 2006a, ApJ, 644, 813

Erb, D.K., Steidel, C.C., Shapley, A.E., *et al.*, 2006b, ApJ, 646, 107

Ercolano, B., Bastian, N., & Stasińska, G., 2007, MNRAS, 379, 945

Escudero, A.V., & Costa, R.D.D., 2001, A&A, 380, 300

Escudero, A.V., Costa, R.D.D., & Maciel, W.J., 2004, A&A, 414, 211

Esteban, C., & Peimbert, M., 1995, RMxAC, 3, 133

Esteban C., Bresolin F., Peimbert M., García-Rojas J., Peimbert A., Mesa-Delgado A., 2009, ApJ, 700, 654

Esteban C., Peimbert M., García-Rojas J., *et al.*, 2004, MNRAS, 355, 229

Esteban, C., Peimbert, M., Torres-Peimbert, S., & Escalante, V., 1998, MNRAS, 295, 401

Esteban, C., Peimbert, M., Torres-Peimbert, S., & Rodríguez, M., 2002, ApJ, 581, 241

Evans, J.W., & Michard, R., 1962, ApJ, 136, 493

Evans, C.J., Bresolin, F., Urbaneja, M.A., *et al.*, 2007, ApJ, 659, 1198

Evans, C., *et al.*, 2008, Msngr, 131, 25

Exter, K.M., Barlow, M.J., & Walton, N.A., 2004, MNRAS, 349, 1291

Fabian, A.C., & Nulsen, P.E.J., 1977, MNRAS, 180, 479

Fang, X., Storey, P.J., & Liu, X.-W., 2011, A&A, 530, A18

Farmer, C.B., & Norton, R.H., 1992, P&SS, 40, 570

Faundez-Abans, M., & Maciel, W.J., 1986, A&A, 158, 228

Feast, M.W., 1961, MNRAS, 122, 1

Feast, M.W., Abedigamba, O.P., & Whitelock, P.A., 2010, MNRAS, 408, L76

Feldman, U., & Laming, J.M., 2000, PhyS, 61, 222

Feldman, U., & Widing, K.G., 2003, SSRv, 107, 665

Feldman, U., & Widing, K.G., 2007, SSRv, 130, 115

Felten, J.E., Gould, R.J., Stein, W.A., & Woolf, N.J., 1966, ApJ, 146, 955

Ferguson, J.W., Alexander, D.R., & Allard, F., *et al.*, 2005, ApJ, 623, 585

Ferland, G.J., 2001, PASP, 113, 41

Ferrando, P., Engelmann, J.J., Goret, P., *et al.*, 1988, A&A, 193, 69

Fesen, R.A., *et al.*, 2006, ApJ, 636, 859

Fich, M., & Silkey, M., 1991, ApJ, 366, 107

Field, G.B., & Steigman, G., 1971, ApJ, 166, 59

Firnstein, M., 2011, Ph.D. Thesis (Univ. Erlangen-Nuremberg)

Fisk, L.A., Kozlovsky, B., & Ramaty, R., 1974, ApJ, 190, L35

Fitzpatrick, E.L., 1999, PASP, 111, 63

Fitzpatrick, E.L., 2004, ASPC, 309, 33

Fitzsimmons, A., Brown, P.J.F., Dufton, P.L., & Lennon, D.J., 1990, A&A, 232, 437

Flanagan, K.A., Canizares, C.R., Dewey, D., *et al.*, 2004, ApJ, 605, 230

Fludra, A., & Schmelz, J.T., 1995, ApJ, 447, 935

Fox, A.J., Petitjean, P., Ledoux, C., & Srianand, R., 2007, A&A, 465, 171

Fox, A.J., Savage, B.D., & Wakker, B.P., 2006, ApJS, 165, 229

Fox, C., Iliadis, C., Champagne, A.E., *et al.*, 2005, PhRvC, 71, 055801

Fox, C., *et al.*, 2004, PhRvL, 93, 081102

Freytag, B., Steffen M., & Dorch, B., 2002, AN, 323, 213

Friedman, S.D., Hébrard, G., Tripp, T.M., Chayer, P., & Sembach, K.R., 2006, ApJ, 638, 847

Friel, E.D., 2006, cams.book, 3

Friel, E.D., Janes, K.A., Tavarez, M., *et al.*, 2002, AJ, 124, 2693

Froese, Fischer, C., & Tachiev, G., 2004, ADNDT, 87, 1

Froese, Fischer, C., Brage, T., & Jönsson, P., 1997, Computational Atomic Structure: An MCHF Approach (Institute of Physics Publishing, Bristol, UK)

Froese, Fischer, C., Tachiev, G., Gaigalas, G., & Godefroid, M.R., 2007, CoPhC, 176, 559

Froese, Fischer, C., Tachiev, G., Rubin, R.H., & Rodríguez, M., 2009, ApJ, 703, 500

Fruchter A.S., *et al.*, 2006, Nature, 441, 463

Fuhrmann, K., 1998, A&A, 338, 161

Fukazawa, Y., Ohashi, T., Fabian, A.C., *et al.*, 1994, PASJ, 46, L55

Fukugita, M., & Peebles, P.J.E., 2004, ApJ, 616, 643

Fulbright, J.P., McWilliam, A., & Rich R.M., 2006, ApJ, 636, 821

Fulbright, J.P., McWilliam, A., & Rich, R.M., 2007, ApJ, 661, 1152

Górny, S.K., Stasińska, G., Escudero, A.V., & Costa, R.D.D., 2004, A&A, 427, 231

Görres, J., Arlandini, C., Giesen, U., *et al.*, 2000, PhRvC, 62, 055801

Güdel, M., 2004, A&ARv, 12, 71

Galarza, V.C., Walterbos, R.A.M., & Braun, R., 1999, AJ, 118, 2775

Galavís, M.E., Mendoza, C., & Zeippen, C.J., 1997, A&AS, 123, 159

Galavís, M.E., Mendoza, C., & Zeippen, C.J., 1998, A&AS, 131, 499

García-Rojas, J., & Esteban, C., 2007, ApJ, 670, 457

García Pérez, A.E., Asplund, M., Primas, F., Nissen, P.E., & Gustafsson, B., 2006, A&A, 451, 621

García, J., Mendoza, C., Bautista, M.A., *et al.*, 2005, ApJS, 158, 68

García, J., Ramírez, J.M., Kallman, T.R., *et al.*, 2011, ApJ, 731, L15

Garnett, D.R., 1992, AJ, 103, 1330

Garnett, D.R., 1999, IAUS, 190, 266

Garnett, D.R. 2002, ApJ, 581, 1019

Garnett, D.R., & Kennicutt, R.C., Jr., 1994, ApJ, 426, 123

Garnett, D.R., & Shields, G.A., 1987, ApJ, 317, 82

Garnett, D.R., Shields, G.A., Skillman, E.D., Sagan, S.P., & Dufour, R.J., 1997, ApJ, 489, 63

Gattinger, R.L., Lloyd, N.D., Bourassa, A.E., *et al.*, 2009, CaJPh, 87, 1133

Gehren, T., Kudritzki, R.P., Butler, K., & Nissen, P.E., 1985, ESOC, 21, 171

Genzel, R., Burkert, A., Bouché, N., *et al.*, 2008, ApJ, 687, 59

Ghavamian, P., Laming, J.M., & Rakowski, C.E., 2007, ApJ, 654, L69

Gibson, B.K., Kawata, D., Brook, C.B., & Connors, T.W., 2003, IAUJD, 15

Giddings, J.R., 1981, Ph.D. Thesis (University of London)

Gies, D.R., & Lambert, D.L., 1992, ApJ, 387, 673

Gilmore, G., & Reid, N., 1983, MNRAS, 202, 1025

Gnat, O., & Sternberg, A., 2007, ApJS, 168, 213

Goetz, M., & Koeppen, J., 1992, A&A, 262, 455

Gogarten, S.M., Dalcanton, J.J., Williams, B.F., *et al.*, 2010, ApJ, 712, 858

González Hernández, J.I., Rebolo, R., & Israelian, G., 2009, A&A, 499, 891

González Hernández, J.I., *et al.*, 2008, A&A, 480, 233

Gorczyca, T.W., & McLaughlin, B.M., 2000, JPhB, 33, L859

Gorczyca, T.W., & Robicheaux, F., 1999, PhRvA, 60, 1216

Goswami, A., & Prantzos, N., 2000, A&A, 359, 191

Gräfener, G., Koesterke, L., & Hamann, W.-R., 2002, A&A, 387, 244

Grant, I.P., McKenzie, B.J., Norrington, P.H., Mayers, D.F., & Pyper, N.C., 1980, CoPhC, 21, 207

Gratton, R., Bonifacio, P., Bragaglia, A., Carretta, E., *et al.*, 2001, A&A, 369, 87

Gratton, R.G., Carretta, E., Matteucci, F., & Sneden, C., 2000, A&A, 358, 671

Gratton, R., Sneden, C., & Carretta, E., 2004, ARRA, 42, 385

Gratton, R., Sneden, C., Carretta, E., & Bragaglia, A., 2000, A&A, 354, 169

Gray, D.F., 2005, The Observation and Analysis of Stellar Photospheres (Cambridge University Press, 2005)

Green, D.A., 2006, "A Catalogue of Galactic Supernova Remnants (2006 April version)", http://www.mrao.cam.ac.uk/surveys/snrs

Greenwood, J.B., Mawhorter, R.J., Cadez, I., *et al.*, 2004, PhST, 110, 358

Greggio, L., & Renzini, A., 1983, A&A, 118, 217

Grevesse, N., & Noels, A., 1993, oee..conf, 15

Grevesse, N., & Sauval, A.J., 1991, STIN, 94, 13502

Grevesse, N., & Sauval, A.J., 1998, SSRv, 85, 161

Grevesse, N., Asplund, M., & Sauval, A.J., 2007, SSRv, 130, 105

Grevesse, N., Noels, A., & Sauval, A.J., 1995, ASPC, 81, 74

Griffin, D.C., Badnell, N.R., & Pindzola, M.S., 1998, JPhB, 31, 3713

Grupp, F., Kurucz, R.L., & Tan, K., 2009, A&A, 503, 177

Gu, M.F., 2003, ApJ, 582, 1241

Gu, M.F., Schmidt, M., Beiersdorfer, P., *et al.*, 2005, ApJ, 627, 1066

Gummersbach, C.A., Kaufer, A., Schaefer, D.R., Szeifert, T., & Wolf B., 1998, A&A, 338, 881

Gursky, H., Kellogg, E., Murray, S., *et al.*, 1971, ApJ, 167, L81

Gustafsson, B., Bell, R.A., Eriksson, K., & Nordlund, Å., 1975, A&A, 42, 407

Gustafsson, B., Edvardsson, B., Eriksson, K., *et al.*, 2008, A&A, 486, 951

Gutierrez-Moreno, A., & Moreno, H., 1988, PASP, 100, 1497

Guzik, J.A., & Mussack, K., 2010, ApJ, 713, 1108

Guzik, J.A., Watson, L.S., & Cox, A.N., 2005, ApJ, 627, 1049

Haberl, F., Geppert, U., Aschenbach, B., & Hasinger, G., 2006, A&A, 460, 811

Haberreiter, M., Schmutz, W., & Hubeny, I., 2008, A&A, 492, 833

Habing, H.J., 1988, A&A, 200, 40

Haehnelt, M.G., Steinmetz, M., & Rauch, M., 1998a, ApJ, 495, 647

Haehnelt, M.G., Natarajan, P., & Rees, M.J., 1998b, MNRAS, 300, 817

Haehnelt, M.G., Steinmetz, M., & Rauch, M., 2000, ApJ, 534, 594

Hamann, W.-R., Gräfener, G., & Liermann, A., 2006, A&A, 457, 1015

Hammer, F., Puech, M., Chemin, L., Flores, H., & Lehnert, M.D., 2007, ApJ, 662, 322

Hammer, J.W., *et al.*, 2005, NuPhA, 758, 363

Han, S.R., Hyung, S., Park, H.-S., & Lee, W.-B., 2001, JKAS, 34, 67

Harissopulos, S., Becker, H.W., Hammer, J.W., *et al.*, 2005, PhRvC, 72, 062801

Harris, M.J., & Lambert, D.L., 1984a, ApJ, 281, 739

Harris, M.J., & Lambert, D.L., 1984b, ApJ, 285, 674

Harris, M.J., & Lambert, D.L., & Smith, V.V., 1985, ApJ, 299, 375

Harris, M.J., & Lambert, D.L., Hinkle, K.H., Gustafsson, B., & Eriksson, K., 1987, ApJ, 316, 294

Harris, M.J., Lambert, D.L., & Smith, V.V., 1985, ApJ, 299, 375

Harris, M.J., Lambert, D.L., & Smith V.V., 1985, ApJ, 292, 620

Harris, M.J., Lambert, D.L., & Smith, V.V., 1988, ApJ, 325, 768

Harris, J., & Zaritsky, D., 2009, Astron. J, 138, 1243

Hasan, A.A., Eissa, F., Ali, R., Schultz, D.R., & Stancil, P.C., 2001, ApJ, 560, L201

Hashizume, K., Chaussidon, M., Marty, B., & Robert, F., 2000, Science, 290, 1142

Hauck, B., Maeder, A., & Meynet, G., 1986 (Geneva University) nces.book

Hauschildt, P.H., 1992, JQSRT, 47, 433

Hauschildt, P.H., & Baron, E., 1999, JCoAM, 109, 41

Hebbard, D., 1960, Nucl. Phys., 15, 289

Hébrard, G., 2010, IAUS, 268, 59

Hébrard, G., & Moos, H.W., 2003, ApJ, 599, 297

Hébrard, G., Tripp, T.M., Chayer, P., *et al.*, 2005, ApJ, 635, 1136

Heger, A., Fryer, C.L., Woosley, S.E., Langer, N., & Hartmann, D.H., 2003, ApJ, 591, 288

Heger, A., Woosley, S., 2005, IAU Symp., 228, 297

Helmi A., 2008, A&ARv, 3

Hendrick, S.P., Reynolds, S.P., & Borkowski, K.J., 2005, ApJ, 622, L117

Henney, W.J., 2007, dmsf.book, 103

Henney, W.J., & Stasińska, G., 2010, ApJ, 711, 881

Henry, R.B.C., Kwitter, K.B., & Bates, J.A., 2000, ApJ, 531, 928

Henry, R.B.C., Kwitter, K.B., & Balick, B., 2004, AJ, 127, 2284

Henry, R.B.C., Kwitter, K.B., Jaskot, A.E., *et al.*, 2010, ApJ, 724, 748

Henry R.B.C., Pagel B.E.J., Chincarini G.L., 1994, MNRAS, 266, 421

Hernandez-Martinez, L., Peña, M., Carigi, L., & Garcia-Rojas, J., 2009, [arXiv:0906.4402]

Herrero, A., & Lennon, D.J., 2004, IAUS, 215, 209

Hess, V., 1948, Phys. Zeit., 13, 1084

Hibbert, A., 1975, CoPhC, 9, 141

Hibbert, A., 1980, JPhB, 13, 1721

Hibbert, A., Biemont, E., Godefroid, M., & Vaeck, N., 1991, JPhB, 24, 3943

Higdon, J.C., & Lingenfelter, R.E., 2005, ApJ 628, 738

Hill, V., 1996, ASPC, 99, 211

Hill, V., 1997, A&A, 324, 435

Hill, V., 1999, A&A, 345, 430

Hill, V., Andrievsky, S., & Spite, M., 1995, A&A, 293, 347

Hill, V., Barbuy, B., & Spite, M., 1997, A&A, 323, 461

Hill, V., Lecureur, A., Gómez, A., *et al.*, 2010, A&A, submitted

Hillier, D.J., & Miller, D.L., 1998, ApJ, 496, 407

Hinkle, K.H., & Lambert, D.L., 1975, MNRAS, 170, 447

Hinkle, K., Wallace, L., & Livingston, W., 1995, PASP, 107, 1042

Hirschi, R., 2007, A&A, 461, 571

Hirschi, R., Meynet, G., & Maeder, A., 2004, A&A, 425, 649

Hirschi, R., Meynet, G., & Maeder, A., 2005, A&A, 433, 1013

Holweger, H., 2001, in AIP Conf. Proc. 598, Joint SOHO/ACE Workshop: Solar and Galactic Composition, ed. R.F. Wimmer-Schweingruber (New York: AIP), 23

Holweger, H., & Müller, E.A., 1974, SoPh, 39, 19

Holmberg, J., Nordström, B., & Andersen, J., 2007, A&A, 475, 519

Hong, Y., & Fegley, B., Jr., 1998, M&PS, 33, 1101

Hopkins, A.M., 2007, ASPC, 380, 423

Hou, J.L., Prantzos N., & Boissier, S., 2000, A&A, 362, 921

Howard, J.W., Henry, R.B.C., & McCartney, S., 1997, MNRAS, 284, 465

Huang, W., & Gies, D.R., 2006, ApJ, 648, 580

Huang, W., & Gies, D.R., 2006, ApJ, 648, 591

Hubeny, I., 1998, ASPC, 138, 139

Hughes, J.P., Rakowski, C.E., Burrows, D.N., & Slane, P.O., 2000, ApJ, 528, L109

Hughes, J.P., *et al.*, 1995, ApJ, 444, L81

Hui, A.K., Armstrong, B.H., & Wray, A.A., 1978, J. Quant. Spectrosc. Radiat. Transfer, 19, 509

Hunter, I., *et al.*, 2007, A&A, 466, 277

Huss, G.R., Fahey, A.J., Gallino, R., & Wasserburg, G.J., 1994, ApJ, 430, L81

Hyung, S., Aller, L.H., & Feibelman, W.A., 1994, PASP, 106, 745

Iglesias, C.A., & Rogers, F.J., 1996, ApJ, 464, 943

Ignace, R., Cassinelli, J.P., Tracy, G., Churchwell, E., & Lamers H.J.G.L.M., 2007, ApJ, 669, 600

Israelian, G., García López, R.J., & Rebolo, R., 1998, ApJ, 507, 805

Israelian, G., Rebolo, R., García López, R.J., *et al.*, 2001, ApJ, 551, 833

Ivans, I.I., Sneden, C., Kraft, R.P., *et al.*, 1999, AJ, 118, 1273

Izotov, Y.I., Thuan, T.X., & Lipovetsky, V.A., 1994, ApJ, 435, 647

Izotov, Y.I., Stasińska, G., Meynet, G., Guseva, N.G., & Thuan, T.X., 2006, A&A, 448, 955

Jacobson, H.R., Friel, E.D., & Pilachowski, C.A., 2007, AJ, 134, 1216

Jacoby, G.H., & Ciardullo, R., 1999, ApJ, 515, 169

Jacoby, G.H., & Ford, H.C., 1986, ApJ, 304, 490

Jamet, L., Pérez, E., Cerviño, M., Stasińska, G., *et al.*, 2004, A&A, 426, 399

Jansen, R.A., Fabricant, D., Franx, M., & Caldwell, N., 2000, ApJS, 126, 331

Jaschek, C., & Jaschek, M., 1995, Science, 270, 1236

Johansson, S., Litzén, U., Lundberg, H., & Zhang, Z., 2003, ApJ, 584, L107

Johnson, E.D., *et al.*, 2006, PhRvL, 97, 192701

Jokipii, J.R., & Kota J., 2000, Astrophys. Space Science, 274, 77

José, J., & Hernanz, M., 1998, Nuclear Physics A, 621, 491

Juett, A.M., Schulz, N.S., & Chakrabarty, D., 2004, ApJ, 612, 308

Kaastra, J.S., Paerels, F.B.S., Durret, F., *et al.*, 2008, 801 [arXiv:0801.1011]

Kalirai, J.S., Bergeron, P., Hansen, B.M.S., *et al.*, 2007, ApJ, 671, 748

Kalirai, J.S., Hansen, B.M.S., Kelson D.D., *et al.*, 2008, ApJ, 676, 594

Kane, L., McKeith, C.D., & Dufton, P.L., 1980, A&A, 84, 115

Karakas, A., 2010, MNRAS, 403, 1413

Karakas, A.I., & Lugaro, M., 2010, PASA, 27, 227

Karlsson, T., Johnson, J.L., & Bromm, V., 2008, ApJ, 679, 6

Kato, T., Lang, J., & Berrington, K.A., 1990, ADNDT, 44, 133

Katsuma, M., 2008, PhRvC, 78, 034606

Kaufer, A., Szeifert, T., Krenzin, R., Baschek B., & Wolf B., 1994, A&A, 289, 740

Kaufer, A., Venn, K.A., Tolstoy, E., Pinte, C., & Kudritzki, R.-P., 2004, AJ, 127, 2723

Kauffmann, G., *et al.*, 2003, MNRAS, 346, 1055

Keeley, N., Kemper, K.W., & Khoa, D.T., 2003, NuPhA, 726, 159

Keenan, F.P., Brown, P.J.F., Dufton, P.L., & Lennon, D.J., 1984, ApJ, 279, L11

Keenan, F.P., Hibbert, A., & Dufton, P.L., 1985, A&A, 147, 89

Keller, S.C., 2004, PASA, 21, 310

Kennicutt, R.C., Jr., 1998, ARA&A, 36, 189

Kennicutt, R.C., 2008, in Formation and Evolution of Galaxy Disks, ASP Conference Series, Vol. 396, ed. J.G., Funes, S.J., & E.M. Corsini

Kennicutt, R.C., Jr., & Garnett, D.R., 1996, ApJ, 456, 504

Kennicutt, R.C., Bresolin, F., & Garnett, D.R., 2003, ApJ, 591, 801

Kewley, L.J., & Dopita, M.A., 2002, ApJS, 142, 35

Kewley, L.J., & Ellison, S.L., 2008, ApJ, 681, 1183

Kewley, L.J., & Kobulnicky, H.A., 2005, in Starbursts: From 30 Doradus to LymanBreak Galaxies, ed. R., de Grijs, R.M., González Delgado, ASSL Vol. 329 (Dordrecht: Springer), 307

Kewley, L.J., Dopita, M.A., Sutherland, R.S., Heisler, C.A., & Trevena, J., 2001, ApJ, 556, 121

Keyes, C.D., Aller, L.H., & Feibelman, W.A., 1990, PASP, 102, 59

Kilian-Montenbruck, J., Gehren, T., & Nissen, P.E., 1994, A&A, 291, 757

Kilian, J., 1992, A&A, 262, 171

Kilian, J., Montenbruck, O., & Nissen, P.E., 1994, A&A, 284, 437

Kingdon, J.B., & Ferland, G.J., 1996, ApJS, 106, 205

Kingsburgh, R.L., & Barlow, M.J., 1994, MNRAS, 271, 257

Kingsburgh, R.L., & Barlow, M.J., 1995, A&A, 295, 171

Kingston, A.E., & Hibbert, A., 2000, JPhB, 33, 693

Kingston, A.E., & Hibbert, A., 2001, JPhB, 34, 81

Kinkel, U., & Rosa M.R., 1994, A&A, 282, L37

Kiselman, D., 2001, NewAR, 45, 559

Kiselman, D., & Nordlund, A., 1995, A&A, 302, 578

Kisielius, R., & Storey, P.J., 1999, A&AS, 137, 157

Kisielius, R., Storey, P.J., Ferland, G.J., & Keenan, F.P., 2009, MNRAS, 397, 903

Klecker, B., 1995, Space Sci. Rev., 72, 419

Klypin, A., Zhao, H., & Somerville, R.S., 2002, ApJ, 573, 597

Kniazev, A.Y., Grebel, E.K., Pustilnik, S.A., Pramskij, A.G., & Zucker, D.B., 2005, AJ, 130, 1558

Kobulnicky, H.A., & Kewley, L.J., 2004, ApJ, 617, 240

Kobulnicky, H.A., & Phillips, A.C., 2003, ApJ, 599, 1031

Kobulnicky, H.A., Kennicutt, R.C., Jr., & Pizagno, J.L., 1999, ApJ, 514, 544

Kobulnicky, H.A., Willmer, C.N.A., Phillips, A.C, *et al.*, 2003, ApJ, 599, 1006

Köppen, J., Acker, A., & Stenholm, B., 1991, A&A, 248, 197

Köppen, J., Weidner, C., & Kroupa, P., 2007, MNRAS, 375, 673

Koesterke, L., Allende Prieto, C., & Lambert, D.L., 2008, ApJ, 680, 764

Korn, A.J., Keller, S.C., Kaufer A., *et al.*, 2002, A&A, 385, 143

Koutroumpa, D., Acero, F., Lallement, R., Ballet, J., & Kharchenko, V., 2007, A&A, 475, 901

Kovtyukh, V.V., Andrievsky, S.M., Belik, S.I., & Luck, R.E., 2005, AJ, 129, 433

Kovtyukh, V.V., Wallerstein, G., & Andrievsky, S.M., 2005, PASP, 117, 1173

Kroupa, P., 2002, Science, 295, 82

Kroupa, P., Tout, C.A., & Gilmore, G., 1993, MNRAS, 262, 545

Kubono, S., *et al.*, 2003, PhRvL, 90, 062501

Kudritzki, R.P., 1979, LIACo, 22, 295

Kudritzki, R.P., Pauldrach, A., & Puls, J., 1987, A&A, 173, 293

Kudritzki, R.-P., Urbaneja, M.A., Bresolin, F., *et al.*, 2008, ApJ, 681, 269

Kulkarni V.P., Fall, S.M., Lauroesch, J.T., *et al.*, 2005, ApJ, 618, 68

Kurt, C.M., & Dufour, R.J., 1998, RMxAC, 7, 202

Kunz, R., Fey, M., Jaeger, M., *et al.*, 2002, ApJ, 567, 643

Kunz, R., Jaeger, M., Mayer, A., *et al.*, 2001, PhRvL, 86, 3244

Kurucz, R.L., 1979, ApJS, 40, 1

Kurucz, R.L., 2005a, MSAIS, 8, 14

Kurucz, R.L., 2005b, MSAIS, 8, 86

Kurucz, R.L., 2005c, MSAIS, 8, 189

Kurucz, R.L., 2005d, MSAIS, 8, 73

Kurucz, R.L., 2005e, MSAIS, 8, 76

Kwitter, K.B., & Aller, L.H., 1981, MNRAS, 195, 939

Kwitter, K.B., & Henry, R.B.C., 1996, ApJ, 473, 304

Kwitter, K.B., Henry, R.B.C., & Milingo, J.B., 2003, PASP, 115, 80

La Cognata, M., *et al.*, 2008 [`nucl-ex:0806.1274v3`]

Labs, D., 1951, ZA, 29, 199

Lagarde, N., Decressin, T., & Charbonnel, C., 2012, in preparation

Lai, D.K., Bolte, M., Johnson, J.A., *et al.*, 2008, ApJ, 681, 1524

Lamb, D.Q., & Reichart, D.E., 2000, ApJ, 536, 1

Lamers, H.J.G.L.M., & Cassinelli J.P., 1999, isw.book

Landi, E., Feldman, U., & Doschek, G.A., 2007, ApJ, 659, 743

Langer, N., 2003, in "CNO in the Universe", ASP Conf. Ser., 304, ed. C., Charbonnel, D., Schaerer, & G., Meynet, 330

Langer, G.E., Hoffman, R., & Sneden, C., 1993, PASP, 105, 301

Larson, R.B., 1975, MNRAS, 173, 671

Larson, R.B., 1976, MNRAS, 176, 31

Laskar, T., Berger, E., Chary, R., AAS Meeting 218, Bull. Amer. Astronom. Soc., 43, 2011

Lazendic, J.S., Dewey, D., Schulz, N.S., & Canizares, C.R., 2006, ApJ, 651, 250

Leblanc, F., Monin, D., Hui-Bon-Hoa, A., & Hauschildt, P.H., 2009, A&A, 495, 937

Lebreton, Y., Montalbán, J., Christensen-Dalsgaard, J., Roxburgh, I.W., & Weiss, A., 2008, Ap&SS, 316, 187

Lecureur, A., 2007, Ph.D. Thesis

Lecureur, A., Hill, V., Zoccali, M., *et al.*, 2007, A&A, 465, 799

Ledoux, C., Petitjean, P., & Srianand, R., 2003, MNRAS, 346, 209

Ledoux, C., Petitjean, P., Bergeron, J., Wampler, E.J., & Srianand, R., 1998, A&A, 337, 51

Ledoux, C., Petitjean, P., Fynbo, J.P.U., Møller, P., & Srianand, R., 2006, A&A, 457, 71

Lee, T., 1978, ApJ, 224, 217

Lee, H., Grebel, E.K., & Hodge, P.W., 2003, A&A, 401, 141

Lee, H., Skillman, E.D., Cannon, J.M., *et al.*, 2006, ApJ, 647, 970

Lee, H., Zucker, D.B., & Grebel, E.K., 2007, MNRAS, 376, 820

Lee, J.-K., Rolleston, W.R.J., Dufton, P.L., & Ryans, R.S.I., 2005, A&A, 429, 1025

Lee, J.C., Xiang, J., Ravel, B., Kortright, J., & Flanagan, K., 2009, ApJ, 702, 970

Leenaarts, J., & Wedemeyer-Böhm, S., 2005, A&A, 431, 687

Leenaarts, J., & Wedemeyer-Böhm, S., 2006, A&A, 460, 301

Lehnert, M.D., & Heckman, T.M., 1994, ApJ, 426, L27

Leighton, R.B., Noyes, R.W., & Simon, G.W., 1962, ApJ, 135, 474

Leising, M., & Diehl, R., 2009 [`arXiv:0903.0772`]

Leisy, P., & Dennefeld, M., 2006, A&A, 456, 451

Leitherer, C., Robert, C., & Drissen, L., 1992, ApJ, 401, 596

Leitherer, C., *et al.*, 1999, ApJS, 123, 3

Lemasle, B., François, P., Bono, G., *et al.*, 2007, A&A, 467, 283

Lennon, D.J., & Burke, V.M., 1994, A&AS, 103, 273

Lennon, D.J., & Dufton, P.L., 1983, MNRAS, 203, 443

Lennon, D.J., Becker, S.T., Butler, K., *et al.*, 1991, A&A, 252, 498

Lennon, D.J., Dufton, P.L., Mazzali, P.A., Pasian, F., & Marconi, G., 1996, A&A, 314, 243

Lennon, D.J., Dufton, P.L., & Crowley, C., 2003, A&A, 398, 455

Lennon, D.J., Kudritzki, R.-P., Becker, S.R., Eber, F., & Butler, K., 1990, ASPC, 7, 315

Lequeux, J., Peimbert, M., Rayo, J.F., Serrano, A., & Torres-Peimbert, S., 1979, A&A, 80, 155

Leske, R.A., 2000, in AIP Conf. Proc., 516: 26[th]Int. Cosmic Ray Conf., 516, 274

Levshakov, S.A., Agafonova, I.I., Reimers, D., & Baade, R., 2003, A&A, 404, 449

Liang, G.Y., & Badnell, N.R., 2011, A&A, 528, A69

Liang, Y.C., Hammer, F., Flores, H., *et al.*, 2004, A&A, 423, 867

Lide, D.R., 1994, chcp.book

Lilly, S.J., Carollo, C.M., & Stockt, on A.N., 2003, ApJ, 597, 730

Limongi, M., & Chieffi, A., 2008, EAS Publ. Ser., 32, 233

Lind K., Charbonnel C., Decressin T., Primas F., Grundahl F., Asplund M., 2011, A&A, 527, A148

Lind, K., Primas, F., Charbonnel, C., Grundahl, F., & Asplund, M., 2009, A&A, 503, L545

Lingenfelter, R.E., & & Higdon, J.C., 2007, ApJ, 660, 330

Linsky, J.L., 2010, IAUS, 268, 53

Linsky, J.L., *et al.*, 2006, ApJ, 647, 1106

Liu, X.-W., 2002, RMxAC, 12, 70

Liu, X.-W., 2006, IAUS, 234, 219

Liu, X.-W., Barlow, M.J., Zhang, Y., Bastin, R.J., & Storey, P.J., 2006, MNRAS, 368, 1959

Liu, X.-W., Storey, P.J., Barlow, M.J., *et al.*, 2000, MNRAS, 312, 585

Livingston W., Wallace L., 1991, An Atlas of the Solar Spectrum in the infrared from 1850 to 9000 cm^{-1} (1.1 tp 5.4 μm) (NSO Technical Report, Tucson)

Lodders, K., 2003, ApJ, 591, 1220

Long, K.S., Reynolds, S.P., Raymond, J.C., *et al.*, 2003, ApJ, 586, 1162

Lopez, S., Ellison, S., D'Odorico, S., & Kim, T.-S., 2007, A&A, 469, 61

Lu, L., Sargent, W.L.W., Barlow, T.A., Churchill, C.W., & Vogt, S.S., 1996, ApJS, 107, 475

Lubowich, D.A., Pasachoff, J.M., Balonek, T.J., Millar, T.J., *et al.*, 2000, Nature, 405, 1025

Luck, R.E., & Andrievsky, S.M., 2004, AJ, 128, 343

Luck, R.E., & Heiter, U., 2006, AJ, 131, 3069

Luck, R.E., & Lambert, D.L., 1992, ApJS, 79, 303

Luck, R.E., Gieren, W.P., Andrievsky, S.M., *et al.*, 2003, A&A, 401, 939

Luck, R.E., Kovtyukh, V.V., & Andrievsky, S.M., 2006, AJ, 132, 902

Luck, R.E., Moffett, T.J., Barnes, T.G., III, & Gieren, W.P., 1998, AJ, 115, 605

Ludwig, H.-G., Caffau, E., Steffen, M., Freytag, B., Bonifacio, P., & Kučinskas, A., 2009a, MmSAI, 80, 711

Ludwig, H.-G., Behara, N.T., Steffen, M., & Bonifacio, P., 2009b, A&A, 502, L1

Ludwig H.-G., Caffau E., Steffen M., Bonifacio P., Freytag B., Cayrel R., 2010, IAUS, 265, 201

Lukasiak, A., Ferrando, P., McDonald, F.B., & Webber, R.W., 1994, ApJ, 426, 366

Lyubimkov, L.S., Rostopchin, S.I., & Lambert, D.L., 2004, MNRAS, 351, 745

Méndez, R.H., Thomas, D., Saglia, R.P., Maraston, C., Kudritzki, R.P., & Bender R., 2005, ApJ, 627, 767

Maciel, W.J., 1984, A&AS, 55, 253

Maciel, W.J., & Costa, R.D.D., 2009a, IAUS, 254, 38P

Maciel, W.J., & Koeppen, J., 1994, A&A, 282, 436

Maciel, W.J., & Quireza, C., 1999, A&A, 345, 629

Maciel W.J., Costa R.D.D., Idiart T.E.P., 2009b, RMxAA, 45, 127

Maciel, W.J., Lago, L.G., & Costa, R.D.D., 2005, A&A, 433, 127

Maciel, W.J., Lago, L.G., & Costa, R.D.D., 2006, A&A, 453, 587

Madau, P., Ferguson, H.C., Dickinson, M.E., *et al.*, 1996, MNRAS, 283, 1388

Maeder, A., 1992, A&A, 264, 105

Maeder, A., 2009, Physics, Formation and Evolution of Rotating Stars, A&A (Library, Springer)

Maeder A., & Meynet G., 1989, A&A, 210, 155

Maeder, A., & Meynet, G., 1987, A&A, 182, 243

Maeder, A., & Zahn, J.P., 1998, A&A 334, 1000

Magee, N.H., *et al.*, 2004, AIPC, 730, 168

Magrini, L., Corbelli, E., & Galli, D., 2007, A&A 470, 843

Magrini, L., Leisy, P., Corradi, R.L.M., *et al.*, 2005, A&A, 443, 115

Magrini, L., Perinotto, M., Corradi, R.L.M., & Mampaso, A., 2003, A&A, 400, 511

Magrini, L., Perinotto, M., Mampaso, A., & Corradi, R.L.M., 2004, A&A, 426, 779

Magrini, L., Stanghellini, L., & Villaver, E., 2009, ApJ, 696, 729

Magrini, L., Stanghellini, L., Corbelli, E., Galli, D., & Villaver, E., 2010, A&A, 512, A63

Magrini, L., Vílchez, J.M., Mampas, o A., Corradi, R.L.M., & Leisy P., 2007, A&A, 470, 865

Magrini, L., Vílchez, J.M., Mampaso, A., Corradi, R.L.M., & Leisy, P., 2007, A&A, 470, 865

Maiolino, R., Nagao, T., & Grazian, A., *et al.*, 2008, A&A, 488, 463

Maller, A.H., Prochaska, J.X., Somerville, R.S., & Primack, J.R., 2001, MNRAS, 326, 1475

Mannucci F., Cresci G., Maiolino R., Marconi A., & Gnerucci A., 2010, MNRAS, 408, 2115

Mannucci, F., Cresci, G., Maiolino, R., *et al.*, 2009, MNRAS, 398, 1915

Mannucci, F., Della Valle, M., Panagia, N., *et al.*, 2005, A&A, 433, 807

Marcon-Uchida, M.M., Matteucci, F., & Costa, R.D.D., 2010, A&A, 520, id.A35

Marigo, P., 2001, A&A, 370, 194

Martins, L.P., & Viegas, S.M.M., 2000, A&A, 361, 1121

Matei, C., *et al.*, 2006, PhRvL, 97, 242503

Matsushita, K., Böhringer, H., Takahashi, I., & Ikebe, Y., 2007a, A&A, 462, 953

Matsushita, K., Fukazawa, Y., Hughes, J.P. *et al.*, 2007b, PASJ 59, S327

Matteucci, F., 2001, ASSL, 253

Matteucci, F., 2008, 804 [arXiv:0804.1492]

Matteucci, F., & Broccato, 1990

Matteucci, F., & Francois, P., 1989, MNRAS, 239, 885

Mawhorter, R.J., *et al.*, 2007, PhRvA, 75, 032704

McCall, M.L., Rybski, P.M., & Shields, G.A., 1985, ApJS, 57, 1

McCarthy, J.K., Lennon, D.J., Venn, K.A., *et al.*, 1995, ApJ, 455, L135

McConnachie, A.W., & Irwin, M.J., 2006, MNRAS, 365, 902

McErlean, N.D., Lennon, D.J., & Dufton, P.L., 1999, A&A, 349, 553

McGaugh, S.S., 1991, ApJ, 380, 140

McGaugh, S.S., 1994, ApJ, 426, 135

McKeegan, K.D., & Leshin, L.A. 2001, Rev. Mineral. Geochem., 43, 279

McLaughlin, B.M., & Bell K.L., 1998, JPhB, 31, 4317

McWilliam, A., & Williams, R.E., 1991, IAUS, 148, 391

Mehlert, D., Noll S., Appenzeller, I., *et al.*, 2002, A&A, 393, 809

Meléndez, J., 2004, ApJ, 615, 1042

Meléndez, J., & Asplund, M., 2008, A&A, 490, 817

Meléndez, J., & Barbuy, B., 2002, ApJ, 575, 474

Meléndez, J., Asplund, M., Gustafsson, B., & Yong, D., 2009, ApJ, 704, L66

Meléndez, J., Barbuy, B., Bica, E., *et al.*, 2003, A&A, 411, 417

Meléndez, J., Barbuy, B., & Spite, F., 2001, ApJ, 556, 858

Meléndez, J., Shchukina, N.G., Vasiljeva, I.E., & Ramírez, I., 2006, ApJ, 642, 1082

Meléndez, J., *et al.*, 2008, A&A, 484, L21

Mendoza, C., *et al.*, 2007, MNRAS, 378, 1031

Merrill, S.P.W., 1952, ApJ, 116, 21

Mesa-Delgado, A., Esteban, C., García-Rojas, J., *et al.*, 2009, MNRAS, 395, 855

Metzger, M.R., Djorgovski, S.G., Kulkarni, S.R., *et al.*, 1997, Nature, 387, 878

Mewaldt, R.A., Cohen, C.M., Mason, G.M., *et al.*, 2007, SSRv, 130, 207

Meyer, D.M., 2001, XVIIth IAP Colloquium, Paris, ed. R., Ferlet, *et al.*, 135

Meyer, D.M., Jura, M., & Cardelli, J.A., 1998, ApJ, 493, 222

Meyer, J.P., 1985, ApJS 57, 173

Meyer, J.P., Drury, L.O'C., & Ellison, D.C., 1997, ApJ 487, 182

Meyer, B.S., & Zinner, E.K., 2006, in Meteorites and the Early Solar System II, ed. D.S., Lauretta, & H.Y., McSween, Jr. (Tucson: U. of Arizona Press), 69

Meynet, G., 1990, Ph.D. Dissertation (Geneva University)

Meynet, G., & Maeder A., 2002, A&A, 390, 561

Meynet, G., & Maeder, A., 2003, A&A, 404, 975

Meynet, G., & Maeder, A., 2005, A&A, 429, 581

Meynet, G., Ekström, S., & Maeder, A., 2006, A&A, 447, 623

Michaud, G., Proffitt, C.R., 1993, ASPC, 40, 246

Middlemass, D., 1990, MNRAS, 244, 294

Mihalas, D., 1978, Stellar Atmospheres San Francisco (W.H. Freeman and Co.)

Mihara, K., & Takahara F., 1994, PASJ, 46, 447

Milanova, Y.V., & Kholtygin, A.F., 2009, AstL, 35, 518

Miller, A.A., Smith, N., Li, W., *et al.*, 2010, AJ, 139, 2218

Minniti, D., & Zoccali, M., 2008, IAUS, 245, 323

Mishenina1, T.V., Soubiran, C., Kovtyukh, V.V., & Korotin, K., 2004, A&A, 418, 551

Mitchell, R.J., Culhane, J.L., Davison, P.J.N., & Ives, J.C., 1976, MNRAS, 176, 29P

Molaro, P., Bonifacio, P., Centurión, M., *et al.*, 2000, ApJ, 541, 54

Molla, M., Ferrini, F., & Diaz, A.I., 1997, ApJ, 475, 519

Monk, D.J., Barlow, M.J., & Clegg, R.E.S., 1988, MNRAS, 234, 583

Monsignori Fossi, B.C., & Landini, M., 1994, ADNDT, 57, 125

Montalbán, J., Miglio, A., Noels, A., Grevesse, N., & di Mauro, M.P., 2004, ESASP, 559, 574

Montenegro, M., Eissner, W., Nahar, S.N., & Pradhan, A.K., 2006, JPhB, 39, 1863

Monteverde, M.I., 1998, ASPC, 131, 188

Monteverde, M.I., & Herrero, A., 1998, Ap&SS, 263, 171

Monteverde, M.I., Herrero, A., & Lennon, D.J., 2000, ApJ, 545, 813

Monteverde, M.I., Herrero, A., Lennon, D.J., & Kudritzki, R.-P., 1997, ApJ, 474, L107

Morel, T., 2009, CoAst, 158, 122

Morel, P., & Lebreton, Y., 2008, Ap&SS, 316, 61

Morisset, C., & Georgiev, L., 2009, A&A, 507, 1517

Morisset, C., Schaerer, D., Bouret, J.-C., & Martins, F., 2004, A&A, 415, 577

Morton, D.C., 1991, ApJS, 77, 119

Morton, D.C., 2003, ApJS, 149, 205

Mottini, M., 2006, Ph.D. Thesis

Moustakas, J., & Kennicutt, R.C., Jr., 2006, ApJ, 651, 155

Moustakas, J., Kennicutt, R.C., Jr., Tremonti, C.A., *et al.*, 2010, ApJS, 190, 233

Mucciarelli, A., *et al.*, 2011, MNRAS, 65

Mukhamedzanov, A.M., *et al.*, 2008, Phys. Rev. C, 78, 015804

Mushotzky, R., Loewenstein, M., Arnaud, K.A., *et al.*, 1996, ApJ, 466, 686

Nagao, T., Maiolino, R., & Marconi, A., 2006, A&A, 459, 85

Nahar, S.N., 1999, ApJS, 120, 131

Nahar, S.N., 2002, A&A, 389, 716

Nahar, S.N., 2004, PhRvA, 69, 042714

Nahar, S.N., Montenegro, M., Eissner, W., & Pradhan, A.K., 2010, PhRvA, 82, 065401

Navarro, J.F., Frenk, C.S., & White, S.D.M., 1996, ApJ, 462, 563

Newton, J.R., Iliadis, C., Champagne, A.E., Longland, R., & Ugalde, C., 2007, PhRvC, 75, 055808

Newton, J.R., *et al.*, 2007, Phys. Rev. C 75, 055808

Nieva, M.F., & Przybilla, N., 2010, ASPC, 425, 146

Nieva M.-F., Simón-Díaz S., 2011, A&A, 532, A2

Niimura, M., Smith, S.J., & Chutjian, A., 2002, ApJ, 565, 645

Nissen, P.E., Primas, F., Asplund, M., & Lambert, D.L., 2002, A&A, 390, 235

Nittler, L.R., Alexander, C.M., Gao, X., Walker, R.M., & Zinner, E.K., 1994, Nature, 370, 443

Nittler, L.R., Alexander, C.M.O., Gao, X., Walker, R.M., & Zinner E., 1997, ApJ, 483, 475

Nittler, L.R., Alexander, C.M.O., Gallino, R., *et al.*, 2008, ApJ, 682, 1450

Nomoto, K., Tominaga, N., Umeda, H., Kobayashi, C., & Maeda, K., 2006, NuPhA, 777, 424

Nordlund, A., 1982, A&A, 107, 1

Nordlund A., & Dravins, D., 1990, A&A, 228, 155

Nordlund, A., Stein, R.F., & Asplund, A., 2009, LRSP, 6, 2

Nordström, B., *et al.*, 2004, A&A, 418, 989

Norris, J.E., Cottrell, P.L., Freeman, K.C., & Da Costa, G.S., 1981, ApJ, 244, 205

Nulsen, P.E.J., Barcons, X., & Fabian, A.C., 1998, MNRAS, 301, 168

O'Connell, R.W., 1999, ARA&A, 37, 603

O'Dell, C.R., 2001, PASP, 113, 29

Ojha, D.K., 2001, MNRAS, 322, 426

Oliveira, C.M., & Hébrard, G., 2006, ApJ, 653, 345

Oliveira, C.M., Dupuis, J., Chayer, P., & Moos, H.W., 2005, ApJ, 625, 232

Oliveira, C.M., Moos, H.W., Chayer, P., & Kruk, J.W., 2006, ApJ, 642, 283

Ortolani, S., Renzini, A., Gilmozzi, R., *et al.*, 1995, Nature, 377, 701

Osborn, W., 1971, Observatory, 91, 223

Osterbrock, D.E., & Ferland, G.J., 2006, Astrophysics of gaseous nebulae and active galactic nuclei (University Science Books)

Osterbrock, D.E., Tran, H.D., & Veilleux S., 1992, ApJ, 389, 305

Péquignot D., 2008, A&A, 478, 371

Péquignot, D., *et al.*, 2001, ASPC, 247, 533

Pérez-Montero, E., & Díaz, A.I., 2005, MNRAS, 361, 1063

Padoan, P., Nordlund, A., & Jones, B.J.T., 1997, MNRAS, 288, 145

Pagel, B.E.J., 1997, Nucleosynthesis and Chemical Evolution of Galaxies

Pagel, B.E.J., 2002, IAUS, 187, 209

Pagel, B.E.J., & Tautvaisiene, G., 1995, MNRAS, 276, 505

Pagel, B.E.J., & Tautvaisiene, G., 1998, MNRAS, 299, 535

Pagel, B.E.J., Edmunds, M.G., Fosbury, R.A.E., & Webster, B.L., 1978, MNRAS, 184, 569

Pagel, B.E.J., Edmunds, M.G., Blackwell, D.E., Chun, M.S., & Smith, G., 1979, MNRAS, 189, 95

Panter, B., Heavens, A.F., & Jimenez, R., 2003, MNRAS, 343, 1145

Paquette, C., Pelletier, C., Fontaine, G., & Michaud, G., 1986, ApJS, 61, 177

Park, S., Hughes, J.P., Burrows, D.N., *et al.*, 2003, ApJ, 598, L95

Park, S., Hughes, J.P., Slane, P.O., *et al.*, 2007, ApJ, 670, L121

Pasquali, A., & Perinotto, M., 1993, A&A, 280, 581

Pasquini, L., Bonifacio, P., Molaro, P., *et al.*, 2005, A&A, 441, 549

Patnaude, D.J., & Fesen, R.A., 2003, ApJ, 587, 221

Patriarchi, P., Morbidelli, L., & Perinotto, M., 2003, A&A, 410, 905

Pauldrach, A.W.A., Hoffmann, T.L., & Lennon, M., 2001, A&A, 375, 161

Peña, M., 2010, IAUS, 265, 155

Peebles P.J.E., 2010 [`arXiv:1009.0496`]

Peimbert, M., 1967, ApJ, 150, 825

Peimbert, M., 1978, IAUS, 76, 215

Peimbert, M., & Costero, R., 1969, BOTT, 5, 3

Peimbert, M., & Peimbert, A., 2006, IAUS, 234, 227

Peimbert, M., Bohigas, J., & Torres-Peimbert, S., 1988, RMxAA,16, 45

Peimbert, M., Peimbert, A., & Ruiz, M.T., 2000, ApJ, 541, 688

Peimbert, M., Rayo, J.F., & Torres-Peimbert, S., 1978, ApJ, 220, 516

Pellegriti, M.G., *et al.*, 2008, PhRvC, 77, 042801

Penny, L.R., Sprague, A.J., Seago, G., & Gies, D.R., 2004, ApJ, 617, 1316

Péquignot, D., Stasińska, G., & Aldrovandi, S.M.V., 1978, A&A, 63, 313

Pereira, T., Asplund, M., & Kiselman, D., 2009, A&A, 508, 1403

Perinotto, M., & Morbidelli, L., 2006, MNRAS, 372, 45

Perinotto, M., Morbidelli, L., & Scatarzi, A., 2004, MNRAS, 349, 793

Perinotto, M., Panagia, N., & Benvenuti, P., 1980, A&A, 85, 332

Peterson, R.C., 1980, ApJ, 237, L87

Peterson, J.R., Kahn, S.M., Paerels, F.B.S., *et al.*, 2003, ApJ, 590, 207

Peterson, J.R., Paerels, F.B.S., Kaastra, J.S., *et al.*, 2001, A&A, 365, L104

Petitjean, P., Ledoux, C., & Srianand, R., 2008, A&A, 480, 349

Petitjean, P., Srianand, R., & Ledoux, C., 2000, A&A, 364, L26

Pettini, M., 2004, cmpe.conf, 257

Pettini, M., & Pagel, B.E.J., 2004, MNRAS, 348, L59

Pettini, M., Ellison, S.L., Bergeron, J., & Petitjean P., 2002, A&A, 391, 21

Pettini, M., Shapley, A.E., Steidel, C.C., *et al.*, 2001, ApJ, 554, 981

Peytremann, E., 1974, A&A, 33, 203

Phillips, J.P., 2002, ApJS, 139, 199

Picaud, S., & Robin, A.C., 2004, A&A, 428, 891

Pietrzyński, G., Gieren, W., Soszyński, I., *et al.*, 2006, ApJ, 642, 216

Pilachowski, C.A., 1989, in "The abundance spread within globular clusters", ed. G., Cayrel de Strobel, M., Spite, T.L., Evans, 1

Pilyugin, L.S., & Thuan, T.X., 2005, ApJ, 631, 231

Pilyugin, L.S., Thuan, T.X., & Vílchez, J.M., 2007, MNRAS, 376, 353

Pilyugin, L.S., Vílchez, J.M., & Contini, T., 2004, A&A, 425, 849

Pilyugin, L.S., 2000, A&A, 362, 325

Pilyugin, L.S., 2001, A&A, 369, 594

Pilyugin, L.S., 2003, A&A, 399, 1003

Plez, B., 2008, PhST, 133, 014003

Pompéia, L., *et al.*, 2008, A&A, 480, 379

Pont, F., & Eyer, L., 2004, MNRAS, 351, 487

Portinari, L., & Chiosi, C., 1999, A&A, 350, 827

Portinari, L., & Chiosi, C., 2000, A&A, 355, 929

Potgieter, M.S., 2008, Adv. Space Res., 41, 245

Pottasch, S.R., Bernard-Salas, J., 2006, A&A, 457, 189

Pottasch, S.R., Bernard-Salas, J., Beintema, D.A., & Feibelman, W.A., 2004, A&A, 423, 593

Pradhan, A.K., 1976, MNRAS, 177, 31

Pradhan, A.K., Chen, G.X., Delahaye, F., Nahar, S.N., & Oelgoetz, J., 2003, MNRAS, 341, 1268

Pradhan, A.K., Montenegro, M., Nahar, S.N., & Eissner, W., 2006, MNRAS, 366, L6

Prandtl, L., 1926, in: Proc. 2nd Intern. Congr. for Applied Mechanics (Zürich 1926), 62

Prantzos, N., 1996, A&A, 310, 106

Prantzos, N., 2007, SSRv, 130, 27

Prantzos, N., 2008, EAS, 32, 311

Prantzos, N., & Boissier, S., 2000, MNRAS, 313, 338

Prantzos, N., & Charbonnel, C., 2006, A&A, 458, 135

Prantzos, N., & Silk, J., 1998, ApJ, 507, 229

Prantzos, N., Charbonnel, C., & Iliadis, C., 2007, A&A, 470, 179

Prochaska, J.X., 2006, ApJ, 650, 272

Prochaska, J.X., & Wolfe, A.M., 1997, ApJ, 487, 73

Prochaska, J.X., & Wolfe, A.M., 2002, ApJ, 566, 68

Prochaska, J.X., Chen, H.-W., Dessauges-Zavadsky, M., & Bloom, J.S., 2007, ApJ, 666, 267

Prochaska, J.X., Gawiser, E., Wolfe, A.M., Castro, S., & Djorgovski, S.G., 2003, ApJ, 595, L9

Prochaska, J.X., Howk, J.C., & Wolfe, A.M., 2003, Nature, 423, 57

Prodanović, T., Steigman, G., & Fields, B.D., 2010, MNRAS, 406, 1108

Przybilla, N., 2008, RvMA, 20, 323

Przybilla, N., Butler, K., & Kudritzki, R.-P., 2006 [arXiv:astro-ph/0611044]

Przybilla, N., Nieva, M.-F., Butler, K., 2008 [arXiv:0809.2403]

Ptuskin, V.S., & Soutoul, A., 1998, A&A, 337, 859

Puls, J., 2009, CoAst, 158, 113

Puls, J., Urbaneja, M.A., Venero, R., *et al.*, 2005, A&A, 435, 669

Quinn, P.J., Hernquist, L., & Fullagar, D.P., 1993, ApJ, 403, 74

Rahimi, A., Kawata, D., Brook, C.B., & Gibson, B.K., 2010, MNRAS, 401, 1826

Ramirez, S.V., & Cohen, J.G., 2002, AJ, 123, 3277

Ramírez, S.V., & Cohen, J.G., 2003, AJ, 125, 224

Ramírez, I., Allende Prieto, C., & Lambert, D.L., 2007, A&A, 465, 271

Ramírez, I., Asplund, M., Baumann, P., Meléndez, J., & Bensby, T., 2010, A&A, 521, A33

Ramírez, I., Meléndez, J., & Asplund, M., 2009, A&A, 508, L17

Randich, S., Primas, F., Pasquini, L., Sestito, P., & Pallavicini, R., 2007, A&A, 469, 163

Randich, S., Sestito, P., Primas, F., Pallavicini, R., & Pasquini, L., 2006, A&A, 450, 557

Rasmussen, A.P., Behar, E., Kahn, S.M., den Herder, J.W., & van der Heyden, K., 2001, A&A, 365, L231

Rauch, T., & Deetjen, J.L., 2003, ASPC, 288, 103

Rayet, M., & Hashimoto, M.-A., 2000, A&A, 354, 740

Raymond, J.C., 2004, ASSL, 317, 353

Rayo, J.F., Peimbert, M., & Torres-Peimbert, S., 1982, ApJ, 255, 1

Reames, D.V., 1999, SSRv, 90, 413

Reddy, B.E., Tomkin, J., Lambert, D.L., & Allende Prieto, C., 2003, MNRAS, 340, 304

Reddy, B.E., Lambert, D.L., & Allende Prieto, C., 2006, MNRAS, 367, 1329

Reddy, N.A., Erb, D.K., Pettini, M., Steidel, C.C., & Shapley, A.E., 2010, ApJ, 712, 1070

Reimers D., 1975, in Problems in Stellar Atmospheres and Envelopes, 229

Renda, A., Kawata, D., Fenner, Y., & Gibson, B.K., 2005, MNRAS, 356, 1071

Rich, R.M., & Origlia, L., 2005, ApJ, 634, 1293

Richer, M.G., & McCall, M.L., 2008, ApJ, 684, 1190

Richter, P., Paerels, F.B.S., & Kaastra, J.S., 2008, 801 [`arXiv:0801.0975`]

Rixon, G., *et al.*, 2011, AIPC, 1344, 107

Roškar, R., Debattista, V.P., Stinson, G.S., *et al.*, 2008, ApJ, 675, L65

Robin, A.C., Reylé, C., Derrière, S., & Picaud, S., 2003, A&A, 409, 523

Rodríguez, M., 1999, A&A, 351, 1075

Rodríguez, M., & Delgado-Inglada, G., 2011, ApJ, 733, L50

Rogers, F.J., & Iglesias, C.A., 1992, ApJS, 79, 507

Rogers, F.J., & Nayfonov, A., 2002, ApJ, 576, 1064

Rogers, A.E.E., Dudevoir, K.A., Carter, J.C., *et al.*, 2005, ApJ, 630, L41

Rolfs, C., & Rodney, W.S., 1974, NuPhA, 235, 450

Rolfs, C., & Rodney, W.S., 1988, Cauldrons in the Cosmos (The university of Chicago Press)

Rolleston, W.R.J., Brown, P.J.F., Dufton, P.L., & Howarth, I.D., 1996, A&A, 315, 95

Rolleston, W.R.J., Dufton, P.L., Fitzsimmons, A., Howarth, I.D., & Irwin, M.J., 1993, A&A, 277, 10

Rolleston, W.R.J., Dufton, P.L., & Fitzsimmons, A., 1994, A&A, 284, 72

Rolleston, W.R.J., Dufton, P.L., McErlean, N.D., & Venn, K.A., 1999, A&A, 348, 728

Rolleston, W.R.J., Smartt, S.J., Dufton, P.L., & Ryans R.S.I., 2000, A&A, 363, 537

Rolleston, W.R.J., Trundle, C., & Dufton, P.L., 2002, A&A, 396, 53

Rolleston, W.R.J., Venn, K., Tolstoy, E., & Dufton, P.L., 2003, A&A, 400, 21

Rosolowsky, E., & Simon, J.D., 2008, ApJ, 675, 1213

Ross, J.E., & Aller, L.H., 1976, Science, 191, 1223

Roters, G., Rolfs, C., Strieder, F., & Trautvetter, H.P., 1999, EpJ A, 6, 451

Rubin, R.H., Dufour, R.J., & Walter, D.K., 1993, ApJ, 413, 242

Rubin, R.H., Simpson, J.P., Haas, M.R., & Erickson, E.F., 1991, ApJ, 374, 564

Rudolph, A.L., Fich, M., Bell, G.R., *et al.*, 2006, ApJS, 162, 346

Russell, S.C., & Dopita, M.A., 1990, ApJS, 74, 93

Salaris, M., Weiss, A., & Percival, S.M., 2004, A&A, 414, 163

Salpeter, E.E., 1955, ApJ, 121, 161

Samland, M., & Gerhard, O.E., 2003, A&A, 399, 961

Samland, M., Hensler, G., & Theis, C., 1997, ApJ, 476, 544

Samland, M., Koeppen, J., Acker, A., & Stenholm, B., 1992, A&A, 264, 184

Santolaya-Rey, A.E., Puls, J., & Herrero, A., 1997, A&A, 323, 488

Sargent, W.L.W., & Searle, L., 1970, ApJ, 162, L155

Sasaki, M., Gaetz, T.J., Blair, W.P., *et al.*, 2006, ApJ, 642, 260

Saumon D., Hubbard, W.B., Burrows, A., *et al.*, 1996, ApJ, 460, 993

Savage, B.D., & Sembach, K.R., 1991, ApJ, 379, 245

Savage, B.D., & Sembach, K.R., 1996, ARA&A, 34, 279

Savage, B.D., *et al.*, 2003, ApJS, 146, 125

Savaglio, S., Glazebrook, K., Abraham, R.G., *et al.*, 2004, ApJ, 602, 51

Savaglio, S., Glazebrook, K., Le Borgne, D., *et al.*, 2005, ApJ, 635, 260

Savaglio, S., Glazebrook, K., & Le Borgne, D., 2009, ApJ, 691, 182

Sbordone, L., Bonifacio, P., Castelli, F., & Kurucz, R.L., 2004, MSAIS, 5, 93

Scalo, J.M., 1986, FCPh, 11, 1

Scannapieco E., Bildsten L., 2005, ApJ, 629, L85

Schödel, R., *et al.*, 2002, Nature, 419, 694

Schönrich, R., & Binney, J., 2009a, MNRAS, 396, 203

Schönrich, R., & Binney, J., 2009b, MNRAS, 399, 1145

Schaerer, D., & Charbonnel, C., 2011, MNRAS, 413, 2297

Schaffenberger, W., Wedemeyer-Böhm, S., Steiner, O., & Freytag, B., 2005, ESASP, 596,

Schaller, G., Schaerer, D., Meynet, G., & Maeder, A., 1992, A&AS, 96, 269

Schmelz, J.T., Nasraoui, K., Roames, J.K., Lippner, L.A., & Garst, J.W., 2005, ApJ, 634, L197

Schmidt, M., 1959, ApJ, 129, 243

Schmidt, M., 1963, ApJ, 137, 758

Schmidt, M., Beiersdorfer, P., Chen, H., *et al.*, 2004, ApJ, 604, 562

Schulte-Ladbeck, R.E., König, B., Miller, C.J., *et al.*, 2005, ApJ, 625, L79

Scott, N.S., & Burke, P.G., 1980, JPhB, 13, 4299

Scott, N.S., & Taylor, K.T., 1982, CoPhC, 25, 347

Scott, P.C., Asplund, M., Grevesse, N., & Sauval, A.J., 2006, A&A, 456, 675

Scott, P.C., Asplund, M., Grevesse, N., & Sauval, A.J., 2009, ApJ, 691, L119

Scuflaire, R., Théado, S., Montalbán, J., *et al.*, 2008, Ap&SS, 316, 83

Searle, L., 1971, ApJ, 168, 327

Searle, L., & Sargent, W.L.W., 1972, ApJ, 173, 25

Seaton, M.J., & Badnell, N.R., 2004, MNRAS, 354, 457

Seaton, M.J., & Osterbrock, D.E., 1957, ApJ, 125, 66

Sedlmayr, E., 1974, A&A, 31, 23

Sellwood, J.A., & Binney, J.J., 2002, MNRAS, 336, 785

Sembach, K.R., *et al.*, 2003, ApJS, 146, 165

de Séréville, N., *et al.*, 2005, Nucl. Phys. A 758, 745

Sfeir, D.M., Lallement, R., Crifo, F., & Welsh, B.Y., 1999, A&A, 346, 785

Shapiro, S.L., & Teukolsky, S.A., 1983 (Wiley-Interscience)

Shapley, A.E., Erb, D.K., Pettini, M., Steidel, C.C., & Adelberger, K.L., 2004, ApJ, 612, 108

Shapley, A.E., Steidel, C.C., Erb, D.K., *et al.*, 2005, ApJ, 626, 698

Sharpee, B.D., & Slanger, T.G., 2006, JPhChA, 110, 6707

Sharpee, B., Baldwin, J.A., & Williams, R., 2004, ApJ, 615, 323

Shaver, P.A., McGee, R.X., Newton, L.M., Danks, A.C., & Pottasch, S.R., 1983, MN-RAS, 204, 53

Shchukina, N.G., TrujilloBueno, J., & Asplund, M., 2005, ApJ, 618, 939

Shetrone, M.D., 1996a, AJ, 112, 2639

Shetrone, M.D., 1996b, PhDT

Shetrone, M.D., 1996c, AJ, 112, 1517

Shields, G.A., 1973, BAAS, 5, 449

Shields, G.A., 1974, ApJ, 193, 335

Shields, G.A., 1978, ApJ, 219, 565

Shields, G.A., & Searle, L., 1978, ApJ, 222, 821

Siess, L., 2007, A&A, 476, 893

Simón-Díaz, S., 2010, A&A, 510, A22

Simón-Díaz, S., & Stasińska, G., 2008, MNRAS, 389, 1009

Simón-Díaz, S., & Stasińska, G., 2011, A&A, 526, A48

Simón-Díaz, S., Herrero, A., Esteban, C., & Najarro, F., 2006, A&A, 448, 351

Simón-Díaz, S., Castro, N., Garcia, M., Herrero, A., & Markova, N., 2011, BSRSL, 80, 514

Simpson, J.A., & Connell, J.J., 2001, Space Sci. Rev., 97, 337

Slanger, T.G., Cosby, P.C., Sharpee, B.D., Minschwaner, K.R., & Siskind, D.E., 2006, JGRA, 111, 12318

Smartt, S.J., & Rolleston, W.R.J., 1997, ApJ, 481, L47

Smartt, S.J., Crowther, P.A., Dufton, P.L., *et al.*, 2001, MNRAS, 325, 257

Smartt, S.J., Venn, K.A., Dufton, P.L., *et al.*, 2001, A&A, 367, 86

Smiljanic, R., Barbuy, B., de Medeiros, J.R., & Maeder, A., 2006, A&A, 449, 655

Smiljanic, R., Gauderon, R., North, P., *et al.*, 2009, A&A, 502, 267

Smith, H.E., 1975, ApJ, 199, 591

Smith, S.J., Djurić, N., Lozano, J.A., Berrington, K.A., & Chutjian, A., 2005, ApJ, 630, 1213

Smith, L.J., Norris, R.P.F., & Crowther, P.A., 2002, MNRAS, 337, 1309

Smith, G.H., Shetrone, M.D., Bell, R.A., Churchill, C.W., & Briley, M.M., 1996, AJ, 112, 1511

Smith, S.J., Čadež, I., Chutjian, A., & Niimura, M., 2004, ApJ, 602, 1075

Smith, V.V., Cunha, K., Ivans, I.I., *et al.*, 2005, ApJ, 633, 392

Smith, V.V., Suntzeff, N.B., Cunha, K., *et al.*, 2000, AJ, 119, 1239

Smith, V.V., *et al.*, 2002, AJ, 124, 3241

Sneden, C., 2005, IAU Symp. 228 on "From lithium to uranium: Element tracers of early cosmic evolution", edited by V., Hill, P., François, & F., Primas (Cambridge Univ.Press), 337

Sneden, C., Gratton, R.G., & Crocker, D.A., 1991, A&A 246, 354

Sneden, C., Johnson, H.R., & Krupp, B.M., 1976, ApJ, 204, 281

Sneden, C., Lambert, D.L., & Whitaker, R.W., 1979, ApJ, 234, 964

Socas-Navarro, H., & Norton, A.A., 2007, ApJ, 660, L153

Sommer-Larsen, J., & Fynbo, J.P.U., 2008, MNRAS, 385, 3

Songaila, A., 2001, ApJ, 561, L153

Soubiran, C., Bienaymé, O., Mishenina, T.V., & Kovtyukh, V.V., 2008, A&A, 480, 91

Spite, M., & Spite, F., 1991, A&A, 252, 689

Spite, M., Cayrel, R., & Plez, B., 2005, A&A, 430, 655

Spite, M., Spite, F., & Barbuy, B., 1989, A&A, 222, 35

Spite, F., Spite, M., & Francois, P., 1989, A&A, 210, 25

Spitoni, E., & Matteucci, F., 2010, A&A, 514, id.A73

Spitoni, E., & Matteucci, F., 2011, A&A, in press

Spitoni, E., Recchi, S., & Matteucci, F., 2008, A&A, 484, 743

Srianand, R., Petitjean, P., Ledoux, C., Ferland, G., & Shaw, G., 2005, MNRAS, 362, 549

Stancil, P.C., 2001, ASPC, 247, 3

Stancil, P.C., Schultz, D.R., Kimura, M., *et al.*, 1999, A&AS, 140, 225

Stanghellini, L., & Haywood, M., 2010, ApJ, 714, 1096

Stanghellini, L., Guerrero, M.A., Cunha, K., Manchado, A., & Villaver, E., 2006, ApJ, 651, 898

Stanghellini, L., Shaw, R.A., & Villaver, E., 2008, ApJ, 689, 194

Starrfield, S., Iliadis, C., Hix, W.R., *et al.*, 2009, ApJ, 692, 1532

Starrfield S., Sparks, W.M., & Truran, J.W., 1974, ApJ, 192, 647

Stasińska, G., 2004, cmpe.conf, 115

Stasińska, G., 2005, A&A, 434, 507

Stasińska, G., 2006, A&A, 454, L127

Stasińska, G., 2009, elu..book, 1

Stasińska, G., 2010, IAUS, 262, 93

Stasińska, G., & Izotov, Y., 2001, A&A, 378, 817

Stasińska, G., & Izotov, Y., 2003, A&A, 397, 71

Stasińska, G., & Leitherer, C., 1996, ApJS, 107, 661

Stasińska, G., & Schaerer, D., 1999, A&A, 351, 72

Stasińska, G., & Szczerba, R., 2001, A&A, 379, 1024

Stasińska, G., Cid Fernandes, R., Mateus, A., Sodré, L., & Asari, N.V., 2006, MNRAS, 371, 972

Stasińska, G., Richer, M.G., & McCall, M.L., 1998, A&A, 336, 667

Stasińska, G., Tenorio-Tagle, G., Rodríguez, M., & Henney, W.J., 2007, A&A, 471, 193

Stasińska, G., *et al.*, 2010, A&A, 511, A44

Steffen M., Caffau E., & Ludwig H.-G., 2006, private communication

Steffen, M., Ludwig, H.-G., & Caffau, E., 2009, MmSAI, 80, 731

Steffen, M., Ludwig, H.-G., & Freytag, B., 1995, A&A, 300, 473

Steidel, C.C., Pettini, M., & Hamilton, D., 1995, AJ, 110, 2519

Steidel, C.C., Shapley, A.E., Pettini, M., *et al.*, 2004, ApJ, 604, 534

Stein, R.F., & Nordlund, A., 1998, ApJ, 499, 914

Steiner, O., & Gautschy, A., 1998, cmaf.conf

Stephenson, F.R., & Green, D.A., 2005, JHA, 36, 217

Sterling, N.C., Dinerstein, H.L., & Kallman, T.R., 2007, ApJS, 169, 37

Stix, M., 2004, suin.book

Stoesz, J.A., & Herwig, F., 2003, MNRAS, 340, 763

Stone, E.C., Cohen, C.M., & Cook, W.R., *et al.*, 1998, Space Sci. Rev., 86, 285

Storchi-Bergmann, T., Calzetti, D., & Kinney, A.L., 1994, ApJ, 429, 572

Storey, P.J., 1994, A&A, 282, 999

Storey, P.J., & Zeippen, C.J., 2000, MNRAS, 312, 813

Strom, S.E., & Kurucz, R., 1966, AJ, 71, 181

Sutherland, R.S., & Dopita, M.A., 1993, ApJS, 88, 253

Swinbank, A.M., Smail, I., Chapman, S.C., *et al.*, 2004, ApJ, 617, 64

Tachiev, G., & Froese Fischer, C., 1999, JPhB, 32, 5805

Tachiev, G., & Froese Fischer, C., 2000, JPhB, 33, 2419

Tachiev, G., & Froese Fischer, C., 2001, CaJPh, 79, 955

Tachiev, G.I., & Froese Fischer, C., 2002, A&A, 385, 716

Takahashi, I., Kawaharada, M., Makishima, K., *et al.*, 2009, ApJ, 701, 377

Talent, D.L., 1980, Ph.D. Thesis

Tamura, T., Kaastra, J.S., den Herder, J.W.A., Bleeker, J.A.M., & Peterson, J.R., 2004, A&A, 420, 135

Tanvir, N.R., *et al.*, 2009 [`arXiv:0906.1577`]

Tautvaišienė, G., Edvardsson, B., Puzeras, E., Barisevičius, G., & Ilyin, I., 2010, MNRAS, 409, 1213

Tautvaišiene, G., Edvardsson, B., Tuominen, I., & Ilyin, I., 2000, A&A, 360, 499

Tautvaišienė, G., Geisler, D., Wallerstein G., *et al.*, 2007, AJ, 134, 2318

Tayal, S.S., 2003, ApJ, 582, 550

Tayal, S.S., 2006a, JPhB, 39, 4393

Tayal, S.S., 2006b, ApJS, 166, 634

Tayal, S.S., 2007, ApJS, 171, 331

Tayal, S.S., 2009, PhyS, 79, 015303

Taylor, G.I., 1915, Trans. Royal Soc., 215, 1

Tenorio-Tagle, G., 1979, A&A, 71, 59

Tenorio-Tagle, G., 1996, AJ, 111, 1641

Thévenin, F., & Idiart, T.P., 1999, ApJ, 521, 753

Thilker, D.A., Braun, R., Walterbos, R.A.M., *et al.*, 2004, ApJ, 601, L39

Thomas, D., Johansson, J., & Maraston, C., 2011, MNRAS, 412, 2199

Thorsett, S.E., & Chakrabarty, D., 1999, ApJ, 512, 28

Tinsley, B.M., 1980, FCPh, 5, 287

Tischhauser, P., *et al.*, 2002, PhRvL, 88, 072501

Torres-Peimbert, S., & Peimbert, M., 1977, RMxAA, 2, 181

Torres-Peimbert, S., Peimbert, M., & Fierro, J., 1989, ApJ, 345, 186

Tosi, M., 1988, A&A, 197, 33

Tosi, M., 2000, emw.conf, 505

Träbert, E., Calamai, A.G., Gillaspy, J.D., *et al.*, 2000, PhRvA, 62, 022507

Träbert, E., Knystautas, E.J., Saathoff, G., & Wolf, A., 2005, JPhB, 38, 2395

Tremonti, C.A., Heckman, T.M., Kauffmann, G., *et al.*, 2004, ApJ, 613, 898

Trimble, V., 1975, RvMP, 47, 877

Trundle, C., & Lennon, D.J., 2005, A&A, 434, 677

Trundle, C., Dufton, P.L., Lennon, D.J., Smartt, S.J., & Urbaneja, M.A., 2002, A&A, 395, 519

Trundle, C., Dufton, P.L., Hunter, I., *et al.*, 2007, A&A, 471, 625

Trundle, C., Lennon, D.J., Puls, J., & Dufton, P.L., 2004, A&A, 417, 217

Tsamis, Y.G., & Péquignot, D., 2005, MNRAS, 364, 687

Tsamis, Y.G., Barlow, M.J., Liu, X.-W., Danziger, I.J., & Storey, P.J., 2003, MNRAS, 338, 687

Tur, C., Heger, A., & Austin, S.M., 2007, ApJ, 671, 821

Turck-Chièze, S., Piau, L., & Couvidat, S., 2011, ApJ, 731, L29

Turck-Chièze, S., *et al.*, 2011, JPhCS, 271, 012035

Turcotte, S., Richer, J., Michaud, G., Iglesias, C.A., & Rogers, F.J., 1998, ApJ, 504, 539

Udry, S., & Santos, N.C., 2007, ARA&A, 45, 397

Urbaneja, M.A., Herrero, A., Bresolin, F., *et al.*, 2005, ApJ, 622, 862

Urbaneja, M.A., Herrero, A., Kudritzki, R.-P., *et al.*, 2005, ApJ, 635, 311

Vale Asari, N., Stasinska, G., Cid Fernandes, R., *et al.*, 2009, MNRAS, 396, L71

van de Steene, G.C., & Zijlstra, A.A., 1994, A&AS, 108, 485

van der Hucht, K.A., 2001, NewAR, 45, 135

van der Hucht, K.A., 2006, A&A, 458, 453

van der Marel, R.P., & Cioni, M.-R.L., 2001, AJ, 122, 1807

van Zee, L., Salzer, J.J., Haynes, M.P., O'Donoghue, A.A., & Balonek, T.J., 1998, AJ, 116, 2805

Veilleux, S., Cecil, G., & Bland-Hawthorn, J., 2005, ARA&A, 43, 769

Veltz, L., *et al.*, 2008, A&A, 480, 753

Venn, K.A., McCarthy, J.K., Lennon, D.J., & Kudritzki, R.P., 1998, ASPC, 147, 54

Venn, K.A., McCarthy, J.K., Lennon, D.J., *et al.*, 2000, ApJ, 541, 610

Venn, K.A., Irwin, M., Shetrone M.D., *et al.*, 2004, AJ, 128, 1177

Venn, K.A., 1999, ApJ, 518, 405

Venn, K.A., *et al.*, 2001, ApJ, 547, 765

Ventura, P., D'Antona, F., Mazzitelli, I., & Gratton, R., 2001, ApJ, 550, L65

Vila-Costas, M.B., & Edmunds, M.G., 1992, MNRAS, 259, 121

Vilchez, J.M., & Esteban, C., 1996, MNRAS, 280, 720

Vilchez, J.M., Pagel, B.E.J., Diaz, A.I., Terlevich, E., & Edmunds, M.G., 1988, MNRAS, 235, 633

Villante, F.L., 2010, ApJ, 724, 98

Vink, J., Laming, J.M., Gu, M.F., Rasmussen, A., & Kaastra, J.S., 2003, ApJ, 587, L31

Vink, J.S., de Koter, A., & Lamers, H.J.G.L.M., 2001, A&A, 369, 574

Vitense, E., 1953, Z. Astrophys., 32, 135

Vlajic, M., Bland-Hawthorn, J.B., & Freeman, K.C., 2009, ApJ, 697, 361

von Neumann, J., Richtmyer, R.D, 1950, J. Appl. Phys., 21, 232

von Zeipel, H., 1924, MNRAS, 84, 665

Vrancken, M., Lennon, D.J., Dufton, P.L., & Lambert, D.L., 2000, A&A, 358, 639

Wagoner, R., 1967, ApJS, 18, 247

Wagoner, R.V., 1969, ApJS, 18, 247

Wakker, B.P., York, D.G., Wilhelm, R., *et al.*, 2008, ApJ, 672, 298

Walsh, J.R., Walton, N.A., Jacoby, G.H., & Peletier, R.F., 1999, A&A, 346, 753

Walter, D.K., Dufour, R.J., & Hester, J.J., 1992, ApJ, 397, 196

Wang, W., & Liu, X.-W., 2007, MNRAS, 381, 669

Wang, W., & Liu, X.-W., 2008, MNRAS, 389, L33

Wang, W., Liu, X.-W., Zhang, Y., & Barlow, M.J., 2004, A&A, 427, 873

Wang, J.G., Stancil, P.C., Raković, M.J., Schultz, D.R., & Zygelman, B., 2002, in NASA Laboratory Astrophysics Workshop, ed. F., Salama, NASA/CP-2002-21186, GPO (Washington, DC), 101

Webster, B.L., 1988, MNRAS, 230, 377

Wedemeyer, S., Freytag, B., Steffen, M., Ludwig, H.-G., & Holweger, H., 2004, A&A, 414, 1121

Wedemeyer-Böhm, S., & Rouppe van der Voort, L., 2009, A&A, 503, 225

Wedemeyer-Böhm, S., Kamp, I., Bruls, J., & Freytag, B., 2005, A&A, 438, 1043

Weidemann, V., 2000, A&A, 363, 647

Weidner, C., & Kroupa, P., 2006, MNRAS, 365, 1333

Weisberg, M.K., McCoy, T.J., & Krot, A.N., 2006, mess.book, 19

Welty, D.E., Hobbs, L.M., Lauroesch, J.T., *et al.*, 1999, ApJS, 124, 465

Werner, K., Deetjen, J.L., Dreizler, S., *et al.*, 2003, ASPC, 288, 31

Werner, N., Durret, F., Ohashi, T., Schindler, S., & Wiersma, R.P.C., 2008, in "Clusters of galaxies: beyond the thermal view", ed. J., Kaastra (Springer), previously published in Space Science Reviews, Vol. 134, issues 1-4

Westmeier, T., Braun, R., & Thilker, D., 2005, A&A, 436, 101

White III, R.E., 1991, ApJ, 367, 69

Wiedenbeck, M.E., Binns, W.R., Cummings, A.C., *et al.*, 2007, Space Sci. Rev., 130, 415

Willson, R.C., Hudson, H.S., Frohlich, C., & Brusa, R.W., 1986, Science, 234, 1114

Wise, J.H., & Abel, T., 2008, ApJ, 684, 1

Wolfe, A.M., & Prochaska, J.X., 1998, ApJ, 494, L15

Wolfe, A.M., & Prochaska, J.X., 2000, ApJ, 545, 603

Wolfe, A.M., Gawiser, E., & Prochaska, J.X., 2005, ARA&A, 43, 861

Woosley, S.E., & Bloom, J.S., 2006, ARA&A, 44, 507

Woosley, S.E., & Heger, A., 2007, PhR, 442, 269

Woosley, S.E., & Weaver, T.A., 1995, ApJS, 101, 181

Wu, Y., Qi, Y.Y., Zou, S.Y., *et al.*, 2009, PhRvA, 79, 062711

Yin, S.Y., Liang, Y.C., Hammer F., *et al.*, 2007, A&A, 462, 535

Yin, J., Hou, J.L., Prantzos, N., *et al.*, 2009, A&A, 505, 497

Yong, D., Aoki, W., & Lambert, D.L., 2006, ApJ, 638, 1018

Yong, D., Carney, B.W., & Teixera de Almeida, M.L., 2005, AJ, 130, 597

Yong, D., Carney, B.W., Teixera de Almeida, M.L., & Pohl, B.L., 2006, AJ, 131, 2256

Yong, D., Grundahl, F., Nissen, P.E., Jensen, H.R., & Lambert, D.L., 2005, A&A, 438, 875

Yong, D., Grundahl, F., Lambert, D.L., *et al.*, 2003, A&A, 402, 984

Yong, D., Grundahl, F., D'Antona, F., *et al.*, 2009, ApJ, 695, L62

Yong, D., Melendez, J., Cunha, K., *et al.*, 2008, ApJ, 689, 1020

York, D.G., Spitzer, L., Jenkins, E.B., *et al.*, 1983, ApJ, 266, L55

York D.G., *et al.*, 2000, AJ, 120, 1579

Young, P.R., 2005, A&A, 444, L45

Yuan, H.-B., Liu, X.-W., Péquignot, D., *et al.*, 2011, MNRAS, 411, 1035

Yurimoto, H., & Kuramoto, K., 2004, Science, 305, 1763

Yurimoto, H., *et al.*, 2007, in Protostars and Planets V, ed. B., Reipurth, D., Jewitt & K., Keil (Tucson: Univ. of Arizona Press), 849

Zahn, J.P., 1992, A&A, 265, 115

Zaritsky, D., Kennicutt, R.C., Jr., & Huchra, J.P., 1994, ApJ, 420, 87

Zatsarinny, O., & Tayal, S.S., 2003, ApJS, 148, 575

Zeippen, C.J., 1987, A&A, 173, 410

Zhang, Y., Liu, X.-W., Luo, S.-G., Péquignot, D., & Barlow, M.J., 2005, A&A, 442, 249

Zhang, H.L., Graziani, M., & Pradhan, A.K., 1994, A&A, 283, 319

Zhang, C.Y., 1995, ApJS, 98, 659

Zhao, L.B., Stancil, P.C., Liebermann, H.P., Funke, P., & Buenker, R.J., 2005, PhRvA, 71, 060701

Zhao, L.B., *et al.*, 2004, ApJ, 615, 1063

Zhao, M., *et al.*, 2009 [`arXiv:0906.2241`]

Zinnecker, H., 2008, in "Multiple Stars Across the H-R Diagram", ESO Astrophysics Symposia, Volume, ISBN 978-3-540-74744-4 (Springer-Verlag Berlin Heidelberg), 265

Zoccali, M., *et al.*, 2003, A&A, 399, 931

Zoccali, M., *et al.*, 2006, A&A, 457, L1

Zoccali, M., Hill, V., Lecureur, A., *et al.*, 2008, A&A, 486, 177

Zuckerman, B., 1973, ApJ, 183, 863

Index

EAS Publications Series